Hydrodynamique en rotation et instabilité dynamique du pelage des adhésifs

Pierre-Philippe Cortet

Mémoire présenté pour l'obtention du
diplôme d'Habilitation à Diriger des Recherches
de l'Université Paris-Sud par

Pierre-Philippe Cortet

Chargé de Recherche au CNRS
au Laboratoire Fluides, Automatique et Systèmes Thermiques
(UMR 7608, CNRS, Université Paris-Sud)

Hydrodynamique en rotation et Instabilité dynamique du pelage des adhésifs

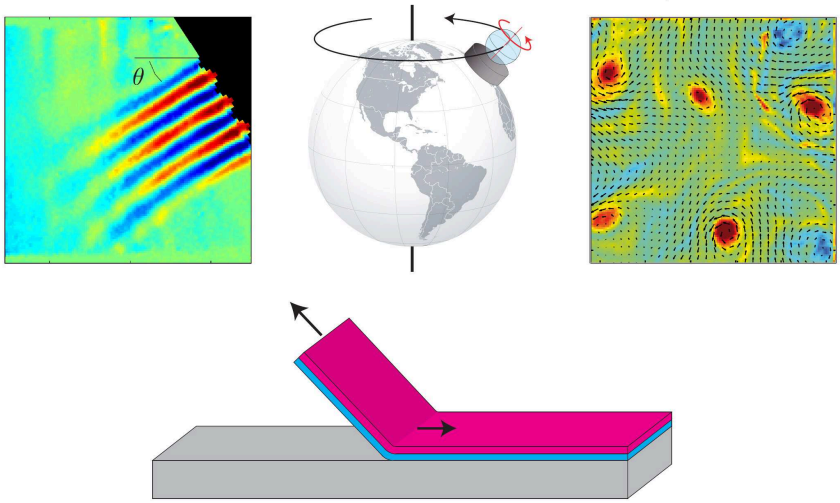

Soutenue le 4 février 2015, devant le jury composé de

Rapporteurs	Jean-Christophe Géminard	DR CNRS, École Normale Supérieure de Lyon
	Fabien Godeferd	DR CNRS, École Centrale de Lyon
	Patrice Le Gal	DR CNRS, Université d'Aix-Marseille
Examinateurs	Sergio Ciliberto	DR CNRS, École Normale Supérieure de Lyon
	Luminita Danaila	Professeur, Université de Rouen
	Élie Raphaël	DR CNRS, ESPCI de la ville de Paris
	Emmanuel Trizac	Professeur, Université Paris-Sud

Table des matières

Curriculum vitae

NOTICE INDIVIDUELLE

Naissance :	Le 27/09/1980 à Bourg-en-Bresse, France
Fonction :	Chargé de Recherche au CNRS depuis le 01/10/2009 1ère classe depuis le 01/10/2013
Laboratoire d'accueil :	Laboratoire FAST (Fluides, Automatique et Systèmes Thermiques) UMR 7608, CNRS, Université Paris-Sud
Adresse : *Téléphone* :	Laboratoire FAST, Bât. 502, Campus universitaire, 91405 Orsay Cedex 01 69 15 37 39
Email : *Page web* :	ppcortet@fast.u-psud.fr http://www.fast.u-psud.fr/~ppcortet

RÉSUMÉ DES FAITS MARQUANTS DEPUIS LE 1er OCTOBRE 2009

- **18 publications dans des revues internationales (30 depuis 2005)**
- **22 présentations orales lors de conférences (ou séminaires) dont 10 internationales (36 depuis 2005)**
- **4 contrats de financement (346 k€ dont 2 ANR)**
- **2 co-directions de thèse (2012-présent et 2009-2012), Dérogation à l'HDR obtenue en juillet 2012**
- **Responsable de 5 post-doctorats**
- **Enseignements à l'ENSTA (75 h/an depuis 2012, 60 h/an de 2010 à 2012, 15 h en 2009-2010)**

CURSUS UNIVERSITAIRE ET DIPLÔMES

2004 - 2007	Doctorat de physique de l'ENS de Lyon (mention "très honorable")
2003 - 2004	DEA Physique Statistique et Phénomènes Non-Linéaires, ENS Lyon (mention TB, rang 2)
Juillet 2003	Agrégation de Sciences Physiques (option physique) (20ème place)
2000 - 2002	Licence (mention bien) et Maîtrise (mention très bien) de physique, ENS Lyon. Second semestre de maîtrise et stage de recherche à l'Université d'Uppsala en Suède
Juillet 2000	Admission à l'École Normale Supérieure de Lyon (38ème place)
1998 - 2000	Classes préparatoires aux grandes écoles (PCSI/PC*), Lycée du Parc, Lyon

ACTIVITÉS DE RECHERCHE

Oct. 2009 - présent
Publications [1] à [18]

Chargé de Recherche au CNRS au laboratoire FAST de l'Université Paris-Sud

Activités en cours :

- *Excitation et propagation d'ondes d'inertie linéaires (avec F. Moisy, collaboration avec L. Maas, D. Cébron)*
- *Transferts d'énergie en hydrodynamique/turbulence en rotation (avec F. Moisy, collaboration avec T. Dauxois)*
- *Instabilité dynamique du pelage des adhésifs (collaboration avec M. Ciccotti, C. Creton, S. Santucci, L. Vanel)*

Activité terminée :

- *Bifurcations turbulentes de l'écoulement de von Kármán (avec A. Chiffaudel, F. Daviaud, B. Dubrulle)*

Sept. 2007 - Sept. 2009
Publications [19] à [23]

Post-Doctorat au Service de Physique de l'État Condensé du CEA Saclay

- *Multistabilité et brisure spontanée de symétrie de l'écoulement turbulent de von Kármán (avec A. Chiffaudel, F. Daviaud, B. Dubrulle)*
- *Rhéologie et statistique d'un écoulement granulaire en tambour tournant (avec D. Bonamy, O. Dauchot, F. Daviaud, B. Dubrulle)*

Sept. 2004 - Août 2007
Publications [24] à [30]

Doctorat au Laboratoire de Physique de l'ENS de Lyon
Directeurs : L. Vanel et S. Ciliberto

- *Dynamique et empreinte de fissures dans des matériaux fragiles ou visco-plastiques*

Avril-Juillet 2004

Stage de recherche de DEA au laboratoire de physique de l'ENS de Lyon sous la direction de L. Vanel et S. Ciliberto :

- *Croissance lente d'une fissure dans le polycarbonate*

Avril-Juillet 2002

Stage de recherche de maîtrise au laboratoire Ångström de l'Université d'Uppsala (Suède) sous la direction de M. Akyuz et V. Cooray :

- *Propagation of positive streamer discharges along liquid dielectric surfaces*

Juin-Juillet 2001

Stage de recherche de licence au laboratoire de physique de l'ENS de Lyon sous la direction de L. Vanel et S. Ciliberto :

- *Croissance lente d'une fissure dans le papier*

ACTIVITÉS D'ENSEIGNEMENT

2009 - présent	TD et modules expérimentaux de 2ème année et TP de 1ère année de turbulence et d'hydrodynamique à l'ENSTA (75 h/an depuis 2012, 60 h/an de 2010 à 2012, 15 h en 2009-2010)
2006 et 2007	Examinateur des TPs de physique au concours commun d'entrée aux ENS (filière PC)
2004 - 2007	Enseignement en classe de préparation à l'Agrégation de Sciences Physiques de l'ENS de Lyon en tant que moniteur (64 h/an)

2004 - 2006	Présentation d'expériences de physique auprès de classes de lycéens dans le cadre du projet pédagogique des thésards du Laboratoire de Physique de l'ENS de Lyon
2003 - 2005	Interrogations en classe préparatoire aux grandes écoles PSI* au Lycée La Martinière Monplaisir de Lyon

ENCADREMENT D'ÉTUDIANTS ET DE POST-DOCTORANTS

Sept. 2014 - Présent	Responsable du post-doctorat de Nathanaël Machicoane (50%, avec F. Moisy)
Oct. 2012 - présent	Co-directeur de la thèse de doctorat d'Antoine Campagne (50%, co-directeur F. Moisy), Dérogation à l'HDR obtenue en juillet 2012
Fév. 2014 - présent	Responsable du post-doctorat de Richard Villey (50%, avec M. Ciccotti)
Sept. 2011 - Nov. 2014	Participation à l'encadrement de la thèse de Marie-Julie Dalbe (ENS Lyon et Université Lyon 1)
Fév. 2013 - Déc. 2013	Responsable du post-doctorat de Baudouin Saintyves (50%, avec M. Ciccotti)
Déc. 2012 - Nov. 2013	Responsable du post-doctorat de Basile Gallet (50%, avec F. Moisy) qui a été recruté en tant que chercheur au CEA Saclay en décembre 2013
Juin 2011 - Juin 2012	Responsable du post-doctorat de Jean Boisson (70%, avec F. Moisy) qui a été recruté en tant qu'enseignant-chercheur à l'ENSTA en juillet 2012
Avril - Sept. 2010	Co-encadrement du post-doctorat de Claudia Guerra (LPMCN, Université Lyon 1)
Sept. 2009 - Août 2012	Co-directeur de la thèse de Cyril Lamriben (50%, directeur F. Moisy) qui a été recruté comme PRAG à l'Université Paris 10 en septembre 2012
2006 - présent	Encadrement de 5 stages de Master – 2012, Antoine Campagne, Master 2 DFE, Université Paris-Sud, – 2009, Lise Divaret, 2ème année ENSTA, – 2009, Séverine Atis, Master 2 CFP, ENS, – 2007, Caroline Cohen, Master 1 Sciences de la matière, ENS Lyon, – 2007, Guillaume Huillard, Master 1 Sciences de la matière, ENS Lyon.

FINANCEMENTS

Sept. 2012 - Août 2015	Responsable au FAST (140 k€) du financement ANR "StickSlip" (programme blanc 2012)
Oct. 2011 - Sept. 2015	Co-responsable avec F. Moisy pour le FAST (130 k€) du financement ANR "ONLITUR" (programme blanc 2011)
Juin 2011 - Juin 2012	Porteur d'un projet "RTRA-Triangle de la Physique" (56 k€) pour le financement d'une année de post-doctorat
Juin 2010	Porteur d'un projet "Attractivité 2010" de l'Université Paris Sud (20 k€)

IMPLICATION DANS LA VIE DE MON UNITÉ

2010 - présent	Responsable des séminaires communs FAST-LIMSI pour le laboratoire FAST (Co-responsable avec Georg Dietze depuis juin 2013)
2012 - présent	Correspondant communication avec le CNRS et l'Univ. Paris-Sud pour le laboratoire FAST

CURRICULUM VITAE

2013 - présent	Membre du comité de mise en place de l'Institut Pascal (IPa) de la future Université Paris-Saclay
2015 - présent	Membre du conseil de laboratoire

AUTRES ACTIVITÉS

2008 - présent	Rapporteur pour Physics of Fluids, Physical Review Letters et Physical Review E

PUBLICATIONS DANS DES REVUES À COMITÉ DE LECTURE

30 publications dans des revues internationales

Articles téléchargeables depuis l'url : http://www.fast.u-psud.fr/~ppcortet/publications

[1] A. Campagne, B. Gallet, F. Moisy, P.-P. Cortet,
Direct and inverse energy cascades in a forced rotating turbulence experiment
Physics of Fluids, **26** 125112 (2014)

[2] M.-J. Dalbe, S. Santucci, L. Vanel, P.-P. Cortet,
Peeling-angle dependence of the stick-slip instability during adhesive tape peeling
Soft Matter, **10** 9637 (2014), Sélectionné dans la collection "2014 Soft Matter Hot Papers"

[3] D. Faranda, F.M.E. Pons, B. Dubrulle, F. Daviaud, B. Saint-Michel, E. Herbert, P.-P. Cortet,
Modelling and analysis of turbulent datasets using Auto Regressive Moving Average processes
Physics of Fluids, **26** 105101 (2014)

[4] B. Gallet, A. Campagne, P.-P. Cortet, F. Moisy,
Scale-dependent cyclone-anticyclone asymmetry in a forced rotating turbulence experiment
Physics of Fluids, **26** 035108 (2014)

[5] E. Herbert, P.-P. Cortet, F. Daviaud, B. Dubrulle,
Eckhaus-like instability of large scale coherent structures in a fully turbulent von Kármán flow
Physics of Fluids, **26** 015103 (2014)

[6] M.-J. Dalbe, S. Santucci, P.-P. Cortet, L. Vanel,
Strong dynamical effects during stick-slip adhesive peeling
Soft Matter, **10** 132 (2014)

[7] O. Ramos, P.-P. Cortet, S. Ciliberto, L. Vanel,
Experimental study of the effect of disorder on subcritical crack growth dynamics
Physical Review Letters, **110** 165506 (2013)

[8] P.-P. Cortet, M.-J. Dalbe, C. Guerra, C. Cohen, M. Ciccotti, S. Santucci, L. Vanel,
Intermittent stick-slip dynamics during the peeling of an adhesive tape from a roller
Physical Review E, **87** 022601 (2013)

[9] J. Boisson, C. Lamriben, L.R.M. Maas, P.-P. Cortet, F. Moisy,
Inertial waves and modes excited by the libration of a rotating cube
Physics of Fluids, **24** 076602 (2012)

[10] J. Boisson, D. Cébron, F. Moisy, P.-P. Cortet,
Earth rotation prevents exact solid body rotation of fluids in the laboratory
EPL, **98** 59002 (2012), Sélectionné dans "EPL Highlights 2012"

[11] G. Bordes, F. Moisy, T. Dauxois, P.-P. Cortet,
Experimental evidence of a triadic resonance of plane inertial waves in a rotating fluid
Physics of Fluids, **24** 014105 (2012)

[12] P.-P. Cortet, E. Herbert, A. Chiffaudel, F. Daviaud, B. Dubrulle, V. Padilla,
Susceptibility divergence, phase transition and flow multistability of a highly turbulent closed flow
Journal of Statistical Mechanics, **P07012** (2011)

[13] C. Lamriben, P.-P. Cortet, F. Moisy,
Direct measurements of anisotropic energy transfers in a rotating turbulence experiment
Physical Review Letters, **107** 024503 (2011)

[14] C. Lamriben, P.-P. Cortet, F. Moisy, L.R.M. Maas,
Excitation of inertial modes in a closed grid turbulence experiment under rotation
Physics of Fluids, **23** 015102 (2011)

[15] P.-P. Cortet, A. Chiffaudel, F. Daviaud, B. Dubrulle,
Experimental evidence of a phase transition in a closed turbulent flow
Physical Review Letters, **105** 214501 (2010), En couverture du numéro

[16] P.-P. Cortet, C. Lamriben, F. Moisy,
Viscous spreading of an inertial wave beam in a rotating fluid
Physics of Fluids, **22** 086603 (2010)

[17] L. Vanel, S. Ciliberto, P.-P. Cortet, S. Santucci,
Time-dependent rupture and slow crack growth : Elastic and viscoplastic dynamics
Journal of Physics D : Applied Physics, **42** 214007 (2009)

[18] P.-P. Cortet, D. Bonamy, F. Daviaud, O. Dauchot, B. Dubrulle, M. Renouf,
Relevance of visco-plastic theory in a multi-directional inhomogeneous granular flow
EPL, **88** 14001 (2009)

[19] D. Bonamy, P.-H. Chavanis, P.-P. Cortet, F. Daviaud, B. Dubrulle, M. Renouf,
Euler-like modelling of dense granular flows : application to a rotating drum
European Physical Journal B, **68** 619 (2009)

[20] P.-P. Cortet, P. Diribarne, R. Monchaux, A. Chiffaudel, F. Daviaud, B. Dubrulle,
Normalized kinetic energy as a hydrodynamical global quantity for inhomogeneous anisotropic turbulence
Physics of Fluids, **21** 025104 (2009)

[21] P.-P. Cortet, G. Huillard, L. Vanel, S. Ciliberto,
Attractive and repulsive cracks in a heterogeneous material
Journal of Statistical Mechanics, **P10022** (2008)

[22] R. Monchaux, P.-P. Cortet, P.-H. Chavanis, A. Chiffaudel, F. Daviaud, P. Diribarne, B. Dubrulle,
Fluctuation-Dissipation Relations and statistical temperatures in a turbulent von Kármán flow
Physical Review Letters, **101** 174502 (2008)

[23] P.-P. Cortet, L. Vanel, S. Ciliberto,
Surface oscillations and slow crack growth controlled by creep dynamics of necking instability in a glassy film
European Physical Journal E, **27** 185 (2008)

[24] P.-P. Cortet, L. Vanel, S. Ciliberto,
Dynamical law for slow crack growth in polycarbonate films
Physical Review Letters, **99** 205502 (2007)

[25] N. Mallick, P.-P. Cortet, S. Santucci, S. G. Roux, L. Vanel,
Discrepancy between Subcritical and Fast Rupture Roughness : A Cumulant Analysis
Physical Review Letters, **98** 255502 (2007)

[26] P.-P. Cortet, M. Ciccotti, L. Vanel,
Imaging the stick-slip peeling of an adhesive tape under a constant load
Journal of Statistical Mechanics, **P03005** (2007)

[27] S. Santucci, P.-P. Cortet, S. Deschanel, L. Vanel, S. Ciliberto,
Subcritical crack growth in fibrous materials
Europhysics Letters, **74** 595 (2006)

[28] P.-P. Cortet, L. Vanel, S. Ciliberto,
Super-Arrhenius dynamics for sub-critical crack growth in two-dimensional disordered brittle media
Europhysics Letters, **74** 602 (2006)

[29] P.-P. Cortet, S. Santucci, L. Vanel, S. Ciliberto,
Slow crack growth in polycarbonate films
Europhysics Letters, **71** 242 (2005)

[30] M. Akyuz, P.-P. Cortet, V. Cooray,
Positive streamer discharges along liquid dielectric surfaces : effect of dielectric constant and surface properties
IEEE Transactions on Dielectrics and Electrical Insulation, **12** 579 (2005)

ACTES DE COLLOQUES À COMITÉ DE LECTURE

1. M.-J. Dalbe, S. Santucci, P.-P. Cortet, C. Guerra, L. Vanel,
   Stick-slip peeling of a roller adhesive tape at a constant velocity
   Comptes-rendus du 21$^{\text{ème}}$ Congrès Français de Mécanique (2013)
2. P.-P. Cortet, G. Bordes, F. Moisy, T. Dauxois,
   Instabilité d'une onde plane d'inertie par résonance triadique
   Comptes-rendus de la 16$^{\text{ème}}$ rencontre du non-linéaire, p. 13 (2013)
3. E. Herbert, S. Atis, A. Chiffaudel, P.-P. Cortet, F. Daviaud, L. Divaret, B. Dubrulle,
   A phase transition in a closed turbulent flow
   Journal of Physics : Conference Series, **318** 032003 (2011)
4. C. Lamriben, P.-P. Cortet, F. Moisy,
   Anisotropic energy transfers in rotating turbulence
   Journal of Physics : Conference Series, **318** 042005 (2011)
5. P.-P. Cortet, C. Lamriben, F. Moisy, L.R.M. Maas,
   Damping inertial modes excitation in a closed grid turbulence experiment under rotation
   Journal of Physics : Conference Series, **318** 082019 (2011)
6. L. Vanel, P.-P. Cortet, S. Ciliberto,
   Slow crack growth and creep dynamics in polycarbonate films
   Proceedings of the 14$^{\text{th}}$ International Conference on Deformation, Yield and Fracture of Polymers, p. 365 (2009)
7. P.-P. Cortet, S. Atis, A. Chiffaudel, F. Daviaud, B. Dubrulle, F. Ravelet,
   Experimental study of the von Kármán flow from $\mathrm{Re} = 10^2$ *to* 10^6
   Advances in Turbulence XII, **132** 59 (2009)

8. O. Ramos, P.-P. Cortet, G. Huillard, L. Vanel, S. Ciliberto,
   Probing the effect of disorder and interactions on crack growth dynamics
   Proceedings of the 12th International Conference on Fracture, Ottawa, Canada, vol. 5, p. 3899 (2009)
9. N. Mallick, P.-P. Cortet, S. Santucci, L. Vanel, S. G. Roux,
   Influence de la dynamique de la rupture sur l'exposant de rugosité dans les fractures 1D
   Comptes-rendus du 21ème colloque GRETSI, p. 1081 (2007)
10. P.-P. Cortet, L. Vanel, S. Ciliberto,
    Slow crack growth in polycarbonate films
    Proceedings of the 13th International Conference on Deformation, Yield and Fracture of Polymers, Kerkrade, Pays-Bas (2006)
11. S. Santucci, P.-P. Cortet, L. Vanel, S. Ciliberto,
    Physics of sub-critical crack growth in a fibrous material : Experiments and model
    Proceedings of the 11th International Conference on Fracture, Turin, Italie, vol. 7, p. 5432 (2005)

PUBLICATIONS DANS DES REVUES SANS COMITÉ (VULGARISATION)

1. J. Boisson, D. Cébron, F. Moisy, P.-P. Cortet, *Un pendule de Foucault fluide*,
   Reflets de la Physique, **31** p. 22 (2012)
2. F. Moisy, C. Lamriben, P.-P. Cortet, M. Rabaud, *Et pourtant, elle tourne...*,
   Plein Sud Spécial recherche, p. 28 (2011)

PUBLICATIONS DE JOURNALISTE SUR MON TRAVAIL (VULGARISATION)

1. Denis Delbecq, *Un pendule de Foucault version liquide*, **CNRS le journal**, **268** p. 8 (2012)
2. Denis Delbecq, *A liquid Foucault Pendulum*, **CNRS International Magazine**, **27** p. 14 (2012)

COMMUNICATIONS À DES CONFÉRENCES

1. Cours invité, "New Challenges in Turbulence Research III", 16 au 21 Mars 2014, à l'École de Physique des Houches
2. Workshop "Non-linear Hydrodynamic Waves : Wave interactions and Wave turbulence", 19 au 20 septembre 2013, à l'Université Paris Diderot, Paris
3. European Turbulence Conference 14, 1er au 4 septembre 2013, Lyon
4. Exposé long à la 16ème rencontre du non-linéaire, 25 au 27 mars 2013, à l'Université Paris Diderot, Paris
5. Journée Dynamique des Fluides du Plateau, 29 novembre 2012, Orsay
6. 65th Annual Meeting of the APS Division of Fluid Dynamics, 18 au 20 novembre 2012, San Diego, CA
7. Workshop "Rotational fluid dynamics for planetary and stellar applications", 30 et 31 mai 2012 à l'IRPHE, Marseille
8. SIG 35 Workshop on fundamental aspects of turbulence, 3 et 4 mai 2012, IHP, Paris
9. Atelier "Critères de rupture : quand et dans quelle direction ?" du GDR Mephy, 14 novembre 2011, Paris
10. Journée Dynamique des Fluides du Plateau, 9 novembre 2011, Orsay
11. 13th European Turbulence Conference, 12 au 15 septembre 2011, Varsovie, Pologne
12. Euromech Colloquium 525, "Instabilities and transition in three-dimensional flows with rotation", 21 au 23 juin 2011, Ecully, France

13. SIG 35 Workshop on statistical mechanics, fractals, instabilities and turbulence, in fluids and superfluids, 13 et 14 avril 2011, IHP, Paris
14. 63rd Annual Meeting of the APS Division of Fluid Dynamics, 21 au 23 novembre 2010, Long Beach, CA
15. Journée Dynamique des Fluides du Plateau, 15 novembre 2010, Orsay
16. Colloque Alain Bouyssy, 18 et 19 février 2010, Université Paris-Sud
17. Réunion du GDR Turbulence, 7 au 11 décembre 2009, Aussois
18. Journée Dynamique des Fluides du Plateau, 6 novembre 2009, Orsay
19. 12th European Turbulence Conference, 7 au 10 septembre 2009, Marburg, Allemagne
20. Congrès général de la SFP, 6 au 10 juillet 2009, École Polytechnique
21. Réunion du GDR MéPhy, “fracture et bandes de cisaillement”, 30 et 31 octobre 2008, ESPCI
22. Réunion du GDR Phenix, “Milieux Granulaires : Statique, Dynamique et Statistique”, 13 et 14 octobre 2008, ENS Lyon
23. Journées de Physique Statistique, 24 janvier 2008, ESPCI, Paris
24. Atelier MACODEV (cluster MAtériaux et COnception pour un DEVeloppement durable), le 3 octobre 2006, au CECAM, à Lyon
25. Workshop on “Statistical Physics in Mechanics" du 11 au 23 juin 2006 à Grasse
26. “Physics of Fracture and Friction” du 27 janvier au 6 février 2005 à Cuernavaca, Mexique

SÉMINAIRES DE LABORATOIRE

1. Laboratoire de Physique de la Matière Condensée, École Polytechnique, 15 mai 2014
2. Unité de Mécanique de l’ENSTA, Palaiseau, 9 mai 2012
3. Laboratoire de Physique de l’École Normale Supérieure de Lyon, 10 octobre 2011
4. Laboratoire FAST (Fluides, Automatique et Systèmes Thermiques), Université Paris-Sud, 20 mai 2010
5. Laboratoire FAST (Fluides, Automatique et Systèmes Thermiques), Université Paris-Sud, 9 octobre 2008
6. Laboratoire de Physique et Mécanique des Milieux Hétérogènes, ESPCI, 15 novembre 2007
7. Manufacture Française des Pneumatiques MICHELIN, Clermont-Ferrand, 13 juin 2007
8. Max Planck Institute for Dynamics and Self-Organization (Goettingen, Allemagne), 6 décembre 2006
9. Service de Physique de l’État Condensé, CEA Saclay, 18 octobre 2006
10. Group for Research and Applications in Statistical Physics, Université de Liège, 13 octobre 2006

Introduction

Depuis octobre 2009, je suis chargé de recherche au laboratoire FAST (Université Paris-Sud, CNRS), après avoir réalisé une thèse de doctorat à l'ENS de Lyon (2004-2007) ainsi que deux ans de post-doctorat au CEA Saclay (2007-2009). Au cours de ces années, j'ai mis à profit ma formation en physique statistique et non-linéaire pour me pencher sur des problèmes variés de mécanique hors-équilibre tels que la croissance de fissures, les écoulements granulaires et les écoulements turbulents et/ou en rotation. Mes travaux de recherche ont conduit à la publication de 30 articles dans des revues scientifiques internationales depuis 2005 (liste détaillée à la page viii).

Depuis mon recrutement par le CNRS, mon activité de recherche, principalement expérimentale, s'est déclinée autour de deux thématiques dominantes : la turbulence et les ondes d'inertie dans les fluides en rotation (environ 2/3 de mon temps) et l'instabilité dynamique de "stick-slip" du pelage des adhésifs ($\sim$1/3). J'ai par ailleurs consacré une plus faible partie de mon activité à prolonger une étude des bifurcations turbulentes de l'écoulement de von Kármán que j'avais entamée pendant mon post-doctorat. De manière générale, l'approche choisie dans ces recherches est de mettre en place des expériences modèles permettant d'isoler des processus physiques fondamentaux habituellement à l'œuvre au sein de systèmes plus complexes. Les applications des problématiques considérées vont de la dynamique des écoulements naturels en géo et astrophysique pour ce qui est de la mécanique des fluides, à des enjeux industriels pour ce qui est du pelage des adhésifs.

Dans ce mémoire, je présente en trois chapitres une synthèse de mes travaux de recherche des cinq dernières années, en me restreignant aux thématiques que j'ai développées à partir de mon arrivée au FAST. Je ne décris ainsi pas les travaux qui prolongent mes activités de thèse ou de post-doctorat qui ont cependant conduit à un certain nombre de publications ces dernières années ([3, 5, 7, 12, 15, 17, 18] dans la liste de la page viii). Dans chacun des chapitres de ce mémoire j'essaie d'introduire de manière pédagogique le contexte et les enjeux spécifiques aux travaux de recherche qui vont être décrits. La présentation de ces travaux consiste ensuite en un résumé qui synthétise les résultats marquants de chaque étude. Le lecteur pourra trouver plus de détails sur les études menées dans des publications qui sont annexées en fin de chapitre. Finalement, chacun des chapitres se clôt sur une série de pistes de recherche qu'il semble intéressant de développer.

Le chapitre 1 est consacré à la description de plusieurs études expérimentales des mécanismes linéaires d'excitation ou de propagation d'ondes d'inertie ou de modes résonants de ces ondes

dans des fluides en rotation. Dans des géométries expérimentales modèles, on s'intéresse en particulier à caractériser la sélection des structures spatiales des ondes par la viscosité et les conditions aux limites.

Le chapitre 2 décrit principalement mes activités sur la turbulence soumise à une rotation d'ensemble. De manière plus précise, je présente trois travaux expérimentaux où l'on caractérise quantitativement les transferts d'énergie entre échelles dans des écoulements en rotation. Le cœur de ce chapitre, qui concerne cette fois-ci les processus non-linéaires dans les fluides en rotation, repose sur deux études expérimentales de l'influence d'une rotation d'ensemble sur la cascade d'énergie entre échelles caractéristique de la turbulence.

Je présente finalement dans le chapitre 3 une activité de recherche développée en parallèle de mes travaux relevant de l'hydrodynamique. L'objet de cette étude est de progresser dans la caractérisation expérimentale et la modélisation de l'instabilité dynamique, dite de "stick-slip", intervenant lors du pelage des films adhésifs, en particulier lorsque celle-ci se développe à des vitesses de pelage élevées.

Outre le soutien des organismes de tutelle du laboratoire FAST (CNRS et Université Paris-Sud), les activités de recherche décrites dans ce manuscrit ont reçu l'appui financier de l'Agence Nationale de la Recherche (2 contrats), de l'Université Paris-Sud (1 contrat) et du "RTRA - Triangle de la Physique" (1 contrat).

Collaborations

Je profite finalement de cette introduction pour mettre en avant les personnes avec qui j'ai eu le plaisir de mener mes activités de recherche depuis le début de ma thèse, et en particulier celles qui ont contribué aux travaux présentés dans ce mémoire.

De 2004 à 2007, j'ai eu la chance de réaliser ma thèse de doctorat au Laboratoire de Physique de l'ENS de Lyon sous la direction de Loïc Vanel et de Sergio Ciliberto. Sans eux deux, je ne serai très probablement jamais devenu chercheur. Cette thèse est principalement centrée sur l'étude expérimentale de la croissance de fissures dans des matériaux fragiles ou viscoplastiques sous faible contrainte.

De 2007 à 2009, j'ai ensuite effectué un post-doctorat au CEA Saclay pendant lequel j'ai principalement travaillé avec Arnaud Chiffaudel, François Daviaud et Bérengère Dubrulle dans le cadre d'une étude expérimentale de la multistabilité et des brisures spontanées de symétrie de l'écoulement turbulent de von Kármán. Pendant ces deux années, j'ai aussi travaillé à l'analyse de données de simulations numériques d'un écoulement granulaire en tambour tournant avec Daniel Bonamy, Olivier Dauchot, François Daviaud et Bérengère Dubrulle. Ce post-doctorat a été l'occasion de découvrir deux thématiques de recherche alors nouvelles pour moi : la turbulence hydrodynamique et les écoulements granulaires. Il m'a avant tout permis de continuer à apprendre mon métier de chercheur au contact d'une assemblée de personnalités fortes et singulières.

J'ai été recruté en tant que Chargé de Recherche par le CNRS en 2009 et j'ai alors entamé, au sein du laboratoire FAST, une collaboration fructueuse avec Frédéric Moisy, à travers diverses

études expérimentales relevant de la mécanique des fluides en rotation. Je suis en pratique venu renforcer cette activité de recherche qui existait au sein du FAST depuis déjà quelques années, portée principalement par Frédéric mais aussi par Marc Rabaud. Je les remercie de m'avoir accueilli et laissé prendre une place importante dans l'équipe "Mécanique des fluides en rotation" du FAST.

Ce thème de recherche qui a depuis constitué mon activité principale m'a donné la chance d'être le co-directeur de la thèse de Cyril Lamriben (2009-2012) puis le directeur de celle d'Antoine Campagne (2012-2015), deux positions qui ont évidemment constitué une première pour moi. Dans ce même cadre, j'ai eu le plaisir d'être le responsable des post-doctorats de Jean Boisson (2011-2012) et de Basile Gallet (2012-2013) ainsi que celui débutant de Nathanaël Machicoane (2014-présent). J'ai aussi eu la joie de voir les deux premiers interrompre leur post-doctorat parce qu'ils avaient décroché un poste permanent de chercheur ou d'enseignant-chercheur. Il est finalement important pour moi de souligner le plaisir que j'ai eu à collaborer lors de diverses études expérimentales des ondes d'inertie avec David Cébron (alors en post-doctorat à l'ETH Zürich), Guilhem Bordes et Thierry Dauxois (tous deux à l'ENS Lyon, le premier réalisant sa thèse sous la direction du second) et Leo Mass (NIOZ, Pays-Bas).

À partir de 2010 et en collaboration avec Loïc Vanel (Univ. Lyon 1) et Stéphane Santucci (ENS Lyon), j'ai développé une activité de recherche nouvelle au FAST au sujet de la dynamique instable du pelage des adhésifs. J'ai dans ce contexte eu la chance de collaborer avec Marie-Julie Dalbe dans le cadre de sa thèse de doctorat à Lyon (2011-2014, Univ. Lyon 1 et ENS Lyon). Cette collaboration sur l'étude de la dynamique de pelage des adhésifs s'est rapidement étendue à l'ESPCI à travers des projets développés en commun avec Matteo Ciccotti et Costantino Creton. Cette activité de recherche a aussi été pour moi l'heureuse occasion d'encadrer les post-doctorats de Baudouin Saintyves (2013) puis de Richard Villey (2014-présent).

Chapitre 1

Ondes d'inertie linéaires

Les fluides soumis à une rotation d'ensemble sont le support d'une classe d'ondes, à la fois transverses, anisotropes et dispersives, appelées ondes d'inertie [1, 2], dont la physique repose sur l'action de rappel exercée par la force de Coriolis. Ces ondes possèdent des propriétés remarquables telles qu'une vitesse de groupe perpendiculaire à leur vitesse de phase et une direction de propagation sélectionnée par le rapport entre la fréquence de l'onde et la fréquence de rotation globale du fluide. Une autre propriété singulière est que leur longueur d'onde n'est pas liée à leur fréquence mais sélectionnée par les effets visqueux et la géométrie des conditions aux limites. Ces caractéristiques atypiques font de ces ondes un sujet d'exploration à la fois fondamental et passionnant pour le physicien. Cependant, l'intérêt de mieux les comprendre réside en premier lieu dans le rôle important qu'elles jouent dans la dynamique des écoulements géophysiques et astrophysiques [1, 3]. Les processus non-linéaires qui sont associés aux ondes d'inertie constituent notamment un ingrédient essentiel dans la construction de la bidimensionnalité des écoulements turbulents en rotation [4–6], question qui sera abordée en détail dans le chapitre 2 et qui est en réalité l'origine de l'intérêt porté aux ondes d'inertie par notre équipe.

Il est important de noter aussi que les ondes d'inertie sont cousines des ondes internes de gravité se propageant dans les fluides stratifiés et qui trouvent leur origine dans l'action de la force de flottabilité. Ces ondes partagent avec les ondes d'inertie les trois propriétés singulières mentionnées plus haut [2, 7]. Dans le contexte géo et astrophysique, les ondes internes (de gravité et/ou d'inertie) peuvent être excitées par de nombreux mécanismes et à des échelles variées. On peut mentionner l'excitation de modes résonants d'ondes d'inertie dans le cœur fluide des planètes par les forces de marée [8, 9] ou par les mouvements harmoniques perturbant la rotation de l'astre, tels la précession [10] et la libration [11]. De tels modes d'inertie peuvent aussi trouver leur origine dans des forçages locaux comme les tremblements de Terre [12, 13]. On peut souligner par ailleurs le rôle de l'interaction des mouvements de marée avec la topographie du fond des océans ou celui des ondes induites par le vent à la surface des océans dans la génération d'ondes propagatives [14]. Les ondes internes ainsi excitées à l'échelle planétaire ou à plus petite échelle sont l'objet d'instabilités lorsque les non-linéarités croissent. On peut ainsi évoquer la génération de courants moyens, tels que les vents zonaux dans l'atmosphère ou à la

surface de planètes gazeuses [9, 15, 16], ou le rôle fondamental du mélange turbulent induit par le déferlement d'ondes internes [17] dans les circulations océaniques à grandes échelles [14].

Dans ce chapitre, je décris trois expériences que j'ai menées au FAST depuis octobre 2009 dont l'objectif a été de répondre à des questions simples mais cependant fondamentales au sujet de la propagation et de l'excitation d'ondes ou de modes d'inertie dans un régime purement linéaire et visqueux. La fréquence d'une onde ne déterminant pas sa longueur d'onde, l'enjeu principal de ces études est de mieux comprendre le rôle de la viscosité dans la sélection des structures spatiales de l'onde ainsi que dans les mécanismes de son excitation. Plus précisément nous avons étudié comment la viscosité du fluide contrôle les échelles caractéristiques dans un paquet d'ondes propagatif [article Cortet *et al.* Physics of Fluids 2010 à la page 24] ainsi que les mécanismes de forçage de modes résonants dans des cavités en rotation soumises à une perturbation harmonique globale [articles Boisson *et al.* Physics of Fluids, 2012 à la page 35 et Boisson *et al.* EPL, 2012 à la page 53]. Les systèmes étudiés s'appuient toujours sur des géométries modèles avec à l'esprit l'objectif de comprendre en détail les mécanismes élémentaires en jeu.

Publications associées à ce chapitre (en annexe lorsque le chiffre est encadré)

1. P.-P. Cortet, C. Lamriben, F. Moisy,
   Viscous spreading of an inertial wave beam in a rotating fluid
   Physics of Fluids, **22** 086603 (2010)

2. J. Boisson, D. Cébron, F. Moisy, P.-P. Cortet,
   Earth rotation prevents exact solid body rotation of fluids in the laboratory
   EPL, **98** 59002 (2012), Sélectionné dans "EPL Highlights 2012"

3. J. Boisson, C. Lamriben, L.R.M. Maas, P.-P. Cortet, F. Moisy,
   Inertial waves and modes excited by the libration of a rotating cube
   Physics of Fluids, **24** 076602 (2012)

1.1 Les ondes d'inertie inviscides et linéaires

L'équation de Navier-Stokes décrivant la dynamique d'un champ de vitesse Eulérien $\mathbf{u}(\mathbf{x}, t)$ dans un référentiel tournant avec un vecteur taux rotation constant $\mathbf{\Omega} = \Omega\,\mathbf{e_z}$ s'écrit

$$\partial_t \mathbf{u} + (\mathbf{u}\cdot\nabla)\mathbf{u} = -\frac{1}{\rho}\nabla p - 2\mathbf{\Omega}\times\mathbf{u} + \nu\nabla^2\mathbf{u}, \tag{1.1}$$

où ρ est la masse volumique et ν la viscosité cinématique du fluide considéré. Dans cette équation, la rotation globale agit sur le champ de vitesse à travers la densité massique de la force de Coriolis $-2\mathbf{\Omega}\times\mathbf{u}$. Il est à noter que la densité massique de la force centrifuge a de son côté été absorbée dans le terme de gradient de pression à travers une redéfinition de la pression selon $p = p_0 - \frac{1}{2}\rho\,(\mathbf{\Omega}\times\mathbf{x})^2$ où $\mathbf{x}$ est le vecteur position depuis une origine sur l'axe de rotation. Cette absorption traduit en pratique la neutralité de la force centrifuge sur la dynamique des fluides en rotation à taux constant.

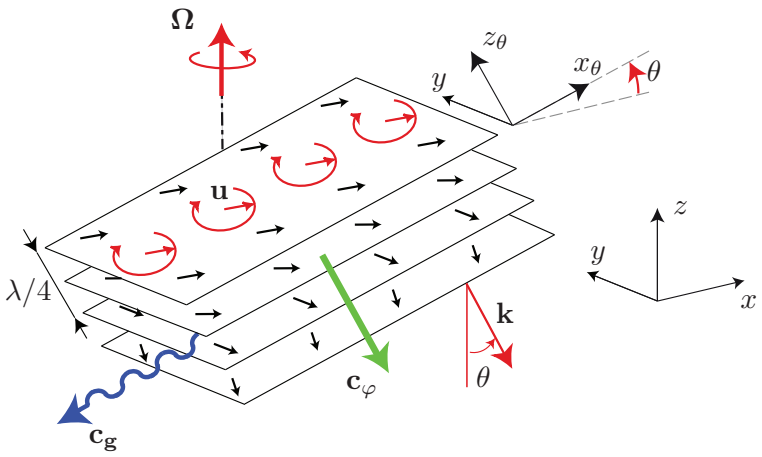

FIGURE 1.1 – Vue schématique de la géométrie d'une onde plane d'inertie d'hélicité négative $s = -1$ et définition des systèmes de coordonnées cartésiennes.

L'équation (1.1) autorise la propagation d'une classe d'ondes spécifique, les ondes d'inertie. Pour comprendre qualitativement la physique de ces ondes, on va dans un premier temps s'intéresser à la limite linéaire et inviscide de l'équation (1.1), i.e.

$$\partial_t \mathbf{u} = -\frac{1}{\rho}\nabla p - 2\mathbf{\Omega} \times \mathbf{u}. \tag{1.2}$$

Nous allons chercher des solutions particulières à cette équation en se restreignant à une structure spécifique : nous nous intéressons ainsi à déterminer sous quelles conditions un champ de vitesse à la fois contenu et uniforme dans un plan incliné d'un angle θ avec l'horizontale (l'axe de rotation est vertical par convention) peut être solution de l'équation (1.2). Nous verrons que ces deux conditions conduisent naturellement à sélectionner un champ de vitesse ondulatoire de fréquence déterminée par θ qui est en fait une onde plane d'inertie. Un tel champ de vitesse peut s'écrire $\mathbf{u}(\mathbf{x}, t) = u_{x_\theta}(z_\theta, t)\mathbf{e}_{\mathbf{x}_\theta} + u_y(z_\theta, t)\mathbf{e}_\mathbf{y}$, où $(\mathbf{e}_{\mathbf{x}_\theta}, \mathbf{e}_\mathbf{y}, \mathbf{e}_{\mathbf{z}_\theta})$ est un système de coordonnées cartésiennes attaché au plan incliné d'un angle θ comme défini à la Figure 1.1. L'idée de ce calcul, qui ne prétend à aucun caractère démonstratif, est d'appréhender qualitativement la mécanique interne d'une onde d'inertie. Le lecteur trouvera une démonstration exacte de la structure d'une onde plane dans l'article [Bordes *et al.* Physics of Fluids, 2012] à la page 88.

L'équation (1.2) devient alors

$$\partial_t u_{x_\theta} = 2\Omega\, u_y \cos\theta, \tag{1.3}$$

$$\partial_t u_y = -2\Omega\, u_{x_\theta} \cos\theta, \tag{1.4}$$

$$\frac{1}{\rho}\partial_{z_\theta} p = -2\Omega\, u_y \sin\theta. \tag{1.5}$$

La solution générale de ce système d'équations est une onde de la forme

$$u_{x_\theta}(\mathbf{x},t) = u_0\,\cos(\sigma t+\varphi(\mathbf{x})), \tag{1.6}$$
$$u_y(\mathbf{x},t) = -s\,u_0\,\sin(\sigma t+\varphi(\mathbf{x})), \tag{1.7}$$
$$p(\mathbf{x},t) = p_0\,\cos(\sigma t+\varphi(\mathbf{x})), \tag{1.8}$$

où la pulsation vérifie $\sigma = s\,2\Omega\cos\theta$ (avec $s=\pm1$) et la phase $\partial_{z_\theta}\varphi = -s\,\rho 2\Omega\sin\theta\,u_0/p_0$ et $\partial_{x_\theta}\varphi = \partial_y\varphi = 0$. Cette solution particulière de l'équation de Navier-Stokes en référentiel tournant est une onde plane d'inertie (oscillation temporelle sinusoïdale et gradient de phase uniforme) dont la relation $\sigma/2\Omega = s\,\cos\theta$ est la relation de dispersion. On voit que cette dernière relation n'autorise les ondes d'inertie à se propager que pour des fréquences inférieures à la fréquence de Coriolis 2Ω. La forme obtenue du champ de vitesse $\mathbf{u}(\mathbf{x},t)$ correspond à un mouvement de translation circulaire à la pulsation $|\sigma| = 2\Omega\cos\theta$ de l'ensemble du plan incliné d'un angle θ et toujours dans le sens anticyclonique (i.e. opposé à la rotation globale, cf. Figure 1.1). La phase évoluant linéairement avec la coordonnée z_θ normale au plan dans lequel a lieu le mouvement, les plans parallèles inclinés de θ sont en fait animés du même mouvement de translation circulaire mais avec un déphasage proportionnel à leur distance. Ce déphasage construit un cisaillement qui a pour conséquence un champ de vorticité $\boldsymbol{\omega}$ parallèle en chaque point au vecteur vitesse $\mathbf{u}$ (Figure 1.1). C'est de cet alignement entre vorticité et vitesse que vient un autre nom parfois utilisé pour désigner les ondes d'inertie, les "ondes hélicoïdales". Le signe de s détermine celui de l'hélicité de l'onde $\boldsymbol{\omega}\cdot\mathbf{u}$.

On note par ailleurs que le vecteur d'onde

$$\mathbf{k} = \nabla\varphi = -s\,\rho\,2\Omega\sin\theta\,u_0/p_0\,\mathbf{e_{z_\theta}}, \tag{1.9}$$

est normal au plan dans lequel le mouvement a lieu, ce qui fait des ondes d'inertie des ondes transverses. Sa norme et donc la longueur d'onde n'est pas déterminée par la valeur de la pulsation σ grâce au degré de liberté que constitue dans (1.9) la présence du rapport u_0/p_0 entre l'amplitude des oscillations de vitesse et de pression. Si on exprime le vecteur d'onde $\mathbf{k} = (k_x\mathbf{e_x}, 0, k_z\mathbf{e_z})$ dans le système de coordonnées cartésiennes $(\mathbf{e_x},\mathbf{e_y},\mathbf{e_z})$ attaché au vecteur taux de rotation $\boldsymbol{\Omega} = \Omega\,\mathbf{e_z}$ (Figure 1.1), la relation de dispersion des ondes d'inertie peut se réécrire sous la forme

$$\frac{\sigma}{2\Omega} = s\,\frac{k_z}{|\mathbf{k}|}, \tag{1.10}$$

dont on déduit les expressions de la vitesse de phase $\mathbf{c}_\varphi = s\,\sigma\mathbf{k}/|\mathbf{k}|^2$ et de la vitesse de groupe $\mathbf{c_g} = \nabla_{\mathbf{k}}\sigma$ qui se révèlent perpendiculaires l'une à l'autre. Comme déjà évoqué, la phase de l'onde se propage ainsi dans la direction perpendiculaire au plan dans lequel a lieu le mouvement alors que la propagation de l'énergie, selon $\mathbf{c_g}$, se fait dans le plan dans lequel a lieu le mouvement (selon son intersection avec le plan contenant $\boldsymbol{\Omega}$ et $\mathbf{k}$, i.e. selon $\mathbf{e_{x_\theta}}$ dans la Figure 1.1).

1.2 La plateforme tournante “Gyroflow”

Les études expérimentales présentées dans ce chapitre et le chapitre suivant ont pour outil principal une plateforme tournante, baptisée “Gyroflow”, qui a été livrée au FAST à l'été 2009 par un bureau d'étude l'ayant conçue et réalisée. Mon arrivée au sein du FAST en octobre 2009 a ainsi coïncidé avec la mise en route des toutes premières expériences sur cette plateforme.

Cette plateforme mécanique de précision, de 2 m de diamètre, peut embarquer jusqu'à une tonne de matériel en rotation, comprenant en particulier les cuves où les écoulements sont générés. Cette plateforme présente des fluctuations relatives de la vitesse de rotation inférieures à 5×10^{-4} pour des fréquences de rotation allant jusqu'à 30 tours/min. Au-delà de ses qualités mécaniques, son atout majeur est de permettre d'embarquer dans le référentiel tournant et de piloter à distance via un collecteur tournant un système de vélocimétrie par images de particules (PIV) et les dispositifs expérimentaux permettant de générer les écoulements. Les dimensions de cette plateforme nous ont ainsi autorisé à réaliser des mesures de champs de vitesse dans des plans quelconques du référentiel tournant et plus récemment de mettre en place un système de PIV stéréoscopique donnant accès aux trois composantes du champ de vitesse dans un plan.

À titre illustratif, le lecteur pourra cliquer sur les liens suivants pour visionner deux films illustrant les expériences de turbulence en rotation réalisées sur la plateforme “Gyroflow” et décrites dans le chapitre 2 de ce manuscrit :
- Turbulence de grille en rotation et en déclin, http://youtu.be/G0WFWlPuaQQ,
- Turbulence en rotation forcée par des générateurs de tourbillons, http://youtu.be/xzvZGKPPnBQ.

1.3 Étalement visqueux d'un paquet d'ondes localisé

Comme nous venons de le voir, la relation de dispersion des ondes d'inertie relie la direction de propagation de l'onde au rapport entre la fréquence de l'onde et la fréquence dite de Coriolis 2Ω mais laisse libre la longueur d'onde. Cette propriété a par exemple pour conséquence des lois de réflexion anormales, l'inclinaison de l'onde par rapport à l'axe de rotation étant conservée mais pas la longueur d'onde [2, 18]. De manière générale, cette propriété de liberté de la longueur d'onde est la source de questions relatives à la structure spatiale que prendra une onde excitée à une certaine fréquence. En considérant toujours la limite linéaire de l'équation du mouvement, la forme du champs de phase $\varphi(\mathbf{x})$ d'une onde d'inertie oscillant à la pulsation $|\sigma| = 2\Omega \cos\theta$ sera déterminée de manière subtile par la combinaison des effets visqueux et des conditions aux limites.

J'ai abordé l'étude de ce type de problèmes par une question d'apparence très simple : quelle est la structure spatiale du faisceau d'ondes issu d'une source ponctuelle ? Cette question avait en pratique déjà reçue une réponse aussi bien d'un point de vue expérimental [19–21] que théorique [19, 22, 23] dans le cas des ondes internes de gravité mais restait encore ouverte dans le cas des fluides en rotation. On note cependant l'étude précoce de Görtler [24] qui a visualisé en 1957 les faisceaux coniques d'ondes d'inertie produits par un disque horizontal oscillant verticalement (Figure 1.2). Expérimentalement, une explication à ce retard tient sûrement à la difficulté de

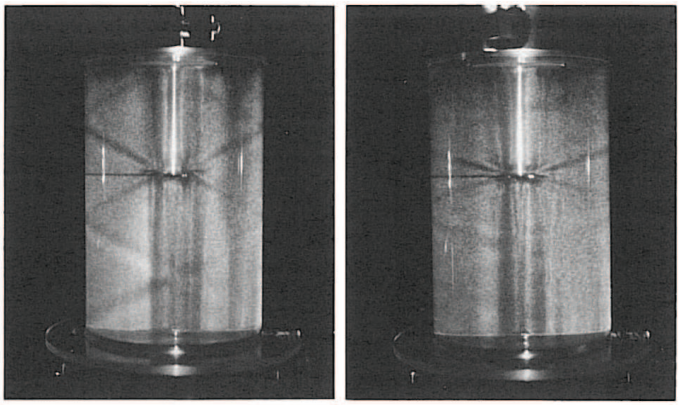

FIGURE 1.2 – Faisceaux d'ondes d'inertie produits par l'oscillation verticale (à la pulsation σ) d'un disque horizontal dans un cylindre en rotation (au taux Ω) pour $\sigma/2\Omega = 0.87 \simeq \cos(30^o)$ à gauche et $\sigma/2\Omega = 0.95 \simeq \cos(18^o)$ à droite (Extrait de Görtler 1957 [24]). La visualisation est réalisée au moyen d'un liquide de type Kalliroscope© soulignant les plans de cisaillement produits par le faisceau d'ondes conique.

réaliser des mesures quantitatives des champs de vitesse dans le référentiel en rotation avant l'avènement de systèmes "légers" de vélocimétrie par image de particules (PIV), la contrainte étant de pouvoir embarquer l'ensemble du système. En comparaison, l'ombroscopie et plus récemment la strioscopie synthétique ont permis des mesures plus précoces des ondes internes de gravité. D'un point de vue plus fondamental, l'influence plus faible de la rotation par rapport à la stratification dans de nombreuses applications océanographiques explique sûrement le moindre intérêt porté aux ondes d'inertie dans ce type de configurations propagatives [3]. Il faut cependant souligner la reproduction de l'expérience de Görtler réalisée au FAST avant mon arrivée en 2009 par Messio *et al.* [25]. Dans cette étude, les mesures de champs de vitesse par PIV réalisées dans un plan horizontal seulement n'ont toutefois pas permis d'étudier quantitativement l'évolution visqueuse du paquet d'ondes.

J'ai mis en place une expérience dans laquelle un fin cylindre horizontal est oscillé verticalement dans un aquarium rempli d'eau, l'ensemble étant entraîné en rotation sur la plateforme "Gyroflow" du FAST (Figure 1.3). L'écoulement excité dessine alors quatre paquets d'ondes, invariants dans la direction horizontale parallèle au cylindre, formant une croix connue sous le nom de "croix de Saint-André" dans le contexte des ondes internes de gravité. La configuration bidimensionnelle que nous avons choisie présente l'avantage que l'évolution de l'onde avec la distance à la source est pleinement contrôlée par les effets visqueux alors que dans le cas d'une source quasi-ponctuelle, comme dans les expériences de Görtler [24] et Messio *et al.* [25], le déclin de l'onde ajoute les effets d'étalement géométrique aux effets visqueux conduisant à une décroissance rapide de l'onde plus difficile à caractériser quantitativement. Nous avons ainsi étudié l'étalement visqueux des paquets d'ondes émis en fonction de la distance à la source (Figure 1.3) grâce à des mesures du champs de vitesse dans un plan vertical obtenues par vélocimétrie par image de particules (PIV) dans le référentiel tournant. Nous avons montré que cet étalement

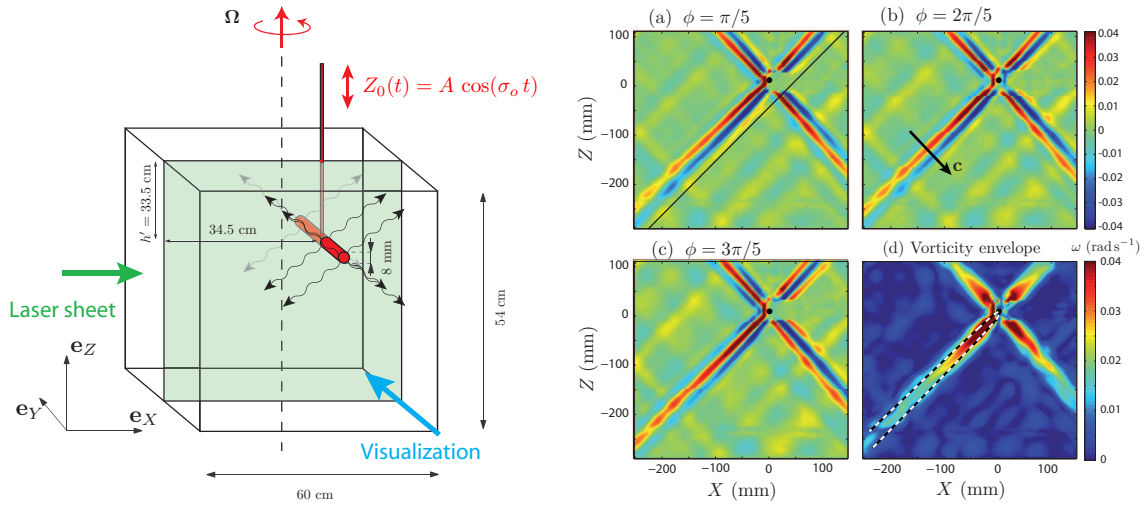

FIGURE 1.3 – **Gauche** : Vue schématique de l'expérience. Un cylindre de 8 mm de diamètre est oscillé verticalement selon $Z_0(t) = A\cos(\sigma_0 t)$ avec $A = 2$ mm et $\sigma_0/2\pi = 0.2$ Hz. Des mesures de PIV sont réalisées dans le plan vertical (X, Z) dans le référentiel tournant. **Droite** : Champ de vorticité ω_Y pour $\sigma_0/2\Omega = 0.67$ à différentes phases (a) $\phi = \pi/5$, (b) $\phi = 2\pi/5$ et (c) $\phi = 3\pi/5$. La ligne noire dans la figure (a) indique la direction de propagation prédite par la relation de dispersion. (d) montre l'enveloppe des oscillations de vorticité. La ligne pointillée noire et blanche reporte la prédiction de l'épaisseur du faisceau selon la théorie de similitude.

était en accord quantitatif avec des prédictions théoriques que nous avons obtenues en nous inspirant des solutions autosimilaires de Thomas et Stevenson (1972) pour les ondes internes de gravité [22].

On donne dans la suite quelques éléments permettant de comprendre les lois d'échelles proposées. Cependant, pour connaître le détail de l'approche théorique et des travaux expérimentaux, le lecteur pourra se reporter à l'article [Cortet *et al.* Physics of Fluids, 2010] qui vient compléter cette section à la page 24. Dans un fluide visqueux, l'énergie d'une onde plane d'inertie est dissipée par le mouvement de cisaillement entre les plans oscillants inclinés la composant (Figure 1.1). Cette atténuation visqueuse conduit à un déclin exponentiel de l'amplitude de l'onde le long de sa direction de propagation (selon $\mathbf{c_g}$). À partir de l'équation de Navier-Stokes en référentiel tournant (1.1), on prédit que le facteur d'atténuation sur une distance x_θ est

$$\epsilon_{|\mathbf{k}|} = \exp(-\ell^2 |\mathbf{k}|^3 x_\theta),$$

pour un vecteur d'onde $\mathbf{k}$, où on a introduit une longueur visqueuse

$$\ell = \left(\frac{\nu}{\sqrt{(2\Omega)^2 - \sigma^2}} \right)^{1/2}. \tag{1.11}$$

En faisant l'hypothèse que le cylindre excite un large spectre de nombres d'ondes, la loi de déclin précédente prédit que les grands nombres d'onde vont être préférentiellement atténués. À

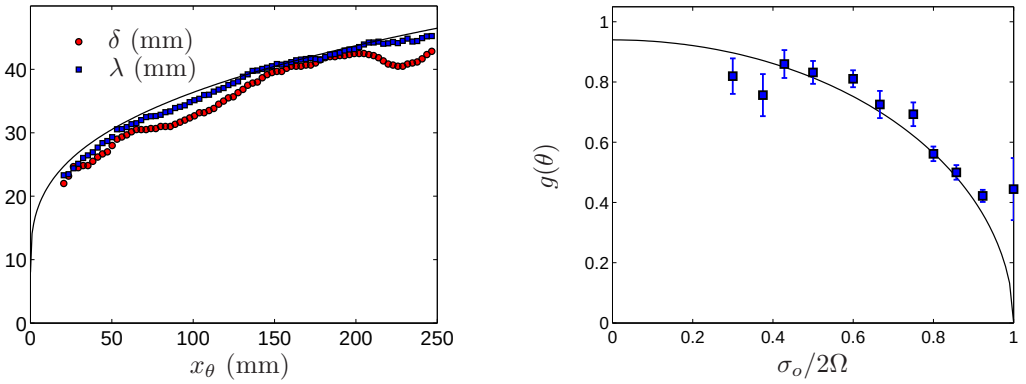

FIGURE 1.4 – **Gauche** : Largeur à mi-hauteur δ de l'enveloppe en vorticité du faisceau d'ondes et longueur d'onde apparente λ en fonction de la distance x_θ au générateur pour $\sigma_0/2\Omega = 0.67$. Prédiction théorique en trait continu. **Droite** : Facteur d'efficacité du générateur, i.e. rapport de la vitesse imposée par le générateur au préfacteur en vitesse du déclin visqueux. L'efficacité est déterminée par la projection du mouvement vertical du générateur sur le plan dans lequel les mouvements des ondes se développent, i.e. $g = \sqrt{1-(\sigma_0/2\Omega)^2}$ (courbe noire).

la distance r de la source, le plus grand nombre d'onde pour lequel l'énergie aura diminuée d'un certain facteur ϵ^*, est $k_{\max} = (\ell^2 x_\theta)^{-1/3} \ln \epsilon^*$. Le paquet d'ondes résulte alors de l'interférence entre les ondes ayant survécues, de nombres d'onde compris entre 0 et $k_{\max}$. La largeur de celui-ci peut ainsi être estimée comme $\delta(x_\theta) \sim k_{\max}^{-1} \sim \ell^{2/3} x_\theta^{1/3}$.

Nous avons en fait dérivé ce résultat de manière analytique en s'inspirant des solutions auto-similaires des équations du mouvement proposées par Thomas et Stevenson [22] dans le cas d'un paquet d'ondes de gravité. Le point de départ consiste à introduire une coordonnée transverse réduite $\eta = z_\theta / x_\theta^{1/3} \ell^{2/3}$ et d'y ajouter une hypothèse d'écoulement quasi-parallèle. On peut alors montrer qu'une solution autosimilaire existe qui s'est révélée en accord quantitatif avec nos mesures comme l'illustre la Figure 1.4 (Gauche). Finalement, nous avons pu montrer expérimentalement que le préfacteur de l'amplitude de l'onde dans les lois de déclins visqueux pouvait s'interpréter directement comme la projection de la vitesse imposée par le générateur sur le plan dans lequel les ondes d'inertie oscillent (Figure 1.4 Droite) illustrant la grande efficacité du générateur.

Cette caractérisation quantitative de la croix de Saint-André dans le cas des ondes d'inertie a été rendue possible par la grande stabilité mécanique de notre plateforme tournante capable d'embarquer un système de PIV. Cette première étude réalisée en 2009 sur la plateforme "Gyroflow" du FAST a ainsi aussi eu pour rôle d'appréhender les capacités exceptionnelles de ce dispositif expérimental alors nouveau.

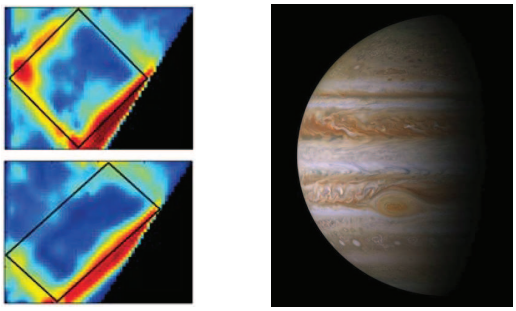

FIGURE 1.5 – **Gauche** : Deux exemples d'attracteurs d'ondes excités par la libration longitudinale d'un canal possédant une face inclinée (extrait de Manders et Mass [27]). Enveloppe des oscillations de vitesse dans le plan vertical pour deux fréquences de libration ($\sigma/2\Omega \simeq 0.71$ et 0.74, mesure par PIV). **Droite** : Vue de Jupiter et de ces vents zonaux en surface prise par la sonde spatiale Cassini (NASA/JPL/Space Science Institute).

1.4 Excitation de modes d'inertie dans des cavités en rotation perturbées par un mouvement harmonique

Comme nous l'avons évoqué en préambule de ce chapitre, dans un volume clos, une assemblée d'ondes d'inertie peut être sujette à une résonance liée aux réflexions multiples sur les parois de la cavité. Lorsque celles-ci sont uniquement perpendiculaires et parallèles à l'axe de rotation, une telle résonance conduit à ce qu'on appelle un mode d'inertie, i.e. un mode propre inviscide de la géométrie considérée [1, 26], pour lequel l'ensemble du fluide est entraîné dans un mouvement oscillant. Lorsque la cavité contient une paroi inclinée, le mécanisme de focalisation-défocalisation [18] induit par les lois de réflexion anormales des ondes d'inertie peut au contraire conduire à une concentration de l'énergie selon un faisceau localisé et fermé appelé attracteur d'ondes [27] (Figure 1.5 Gauche). Certaines géométries spécifiques, telles que les sphéroïdes [28], autorisent cependant aussi l'existence de modes résonants d'inertie, qui peuvent ainsi se développer dans le cœur et les calottes fluides des planètes. De tels modes d'inertie ont par exemple été mis en évidence dans le noyau externe de la Terre par des mesures de gravimétrie [12, 13].

Dans le contexte géo et astrophysique, de nombreux mouvements harmoniques peuvent être à l'origine de l'excitation d'ondes d'inertie dans l'atmosphère, les océans et le noyau liquide des planètes. Il a été démontré en particulier [11, 29–32] que des modes d'inertie peuvent être excités dans une cavité sphérique par une libration longitudinale, qui consiste en une oscillation du taux de rotation planétaire autour de sa moyenne, ainsi que par la précession des planètes [10, 33, 34] et les forces de marées [8, 9]. Les modes ainsi excités pourraient contribuer, à travers leur auto-interaction non-linéaire à la génération de vents zonaux, comme ceux visibles à la surface des planètes gazeuses telles que Jupiter (Figure 1.5 Droite) [9, 16, 35]. La description de ces modes et de leurs non-linéarités apparaît donc comme un enjeu important dans la compréhension des écoulements à l'échelle planétaire. Il est cependant nécessaire de remarquer que les perturbations harmoniques à la rotation des planètes sont aussi à l'origine d'autres processus non-linéaires conduisant par exemple, dans les systèmes en forte libration, aux rouleaux de Taylor-Görtler près

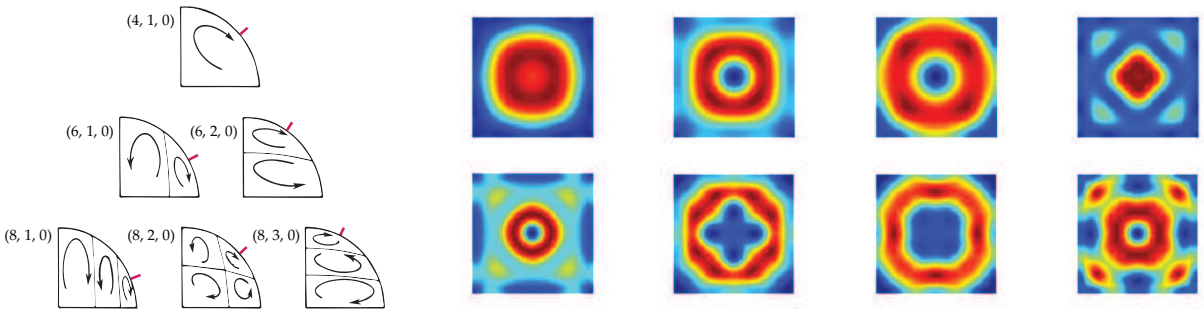

FIGURE 1.6 – **Gauche** : Structure spatiale dans le plan méridien des modes d'inertie de bas ordre dans une sphère (de haut en bas et de gauche à droite, fréquences $\sigma/2\Omega \simeq 0.65, 0.47, 0.83, 0.36, 0.68$ et 0.90, adapté de Greenspan [1]). Le trait rose indique la latitude critique correspondant à chaque mode. **Droite** : Structure spatiale (énergie cinétique) dans le plan équatorial de quelques modes d'inertie inviscides de bas ordre dans un cube (de haut en bas et de gauche à droite, fréquences $\sigma/2\Omega \simeq 0.42, 0.36, 0.28, 0.25, 0.23, 0.23, 0.21$ et 0.19, communication privée de Leo Maas).

de l'équateur [11, 36] ou à l'apparition de vents zonaux sous la forme d'écoulements redressés dans les couches limites d'Ekman [37, 38]. Finalement, les déplacements de masse fluide induits par les perturbations harmoniques à la rotation des planètes peuvent aussi être à l'origine de couples gravitationnels qui rétroagissent sur le mouvement de la planète rendant ces problèmes très complexes. Nous nous restreindront ici à l'étude des seuls effets directs des perturbations harmoniques à la rotation de la cavité sur les mouvements du fluide.

Les fréquences de résonance des modes d'inertie inviscides ont été calculées de manière analytique dans quelques géométries comme pour les modes de Kelvin dans un cylindre [39] ou les modes de cavités sphériques et sphéroïdes (Figure 1.6 Gauche) [1, 28]. Dans le dernier cas, une correction visqueuse à la fréquence de résonance ainsi que le taux de dissipation visqueux de chaque mode ont pu être calculés. Dans le cas d'une cavité parallélépipédique, les fréquences et les structures spatiales des modes inviscides ont été prédites numériquement (Figure 1.6 Droite) par Leo Maas [40] du Royal Netherlands Institute for Sea Research avec qui nous avons collaboré sur cette thématique de recherche.

Ainsi, si la zoologie des modes d'inertie est bien établie pour les géométries les plus usuelles, l'efficacité des mécanismes visqueux d'injection d'énergie dans ces modes par un mouvement harmonique des parois de la cavité est quant à elle beaucoup moins bien connue. Depuis mon arrivée au laboratoire FAST en 2009, nous avons mené deux études expérimentales qui ont consisté à caractériser cette efficacité dans deux cas particuliers, le cube en libration et la sphère en précession, en se concentrant sur le régime purement linéaire dans un premier temps. Je résume dans les deux sous-sections qui suivent les résultats obtenus lors ces travaux qui sont présentés en détail dans les articles (Boisson *et al.* Physics of Fluids, 2012) à la page 35 et (Boisson *et al.* EPL, 2012) à la page 53 en annexe à ce chapitre.

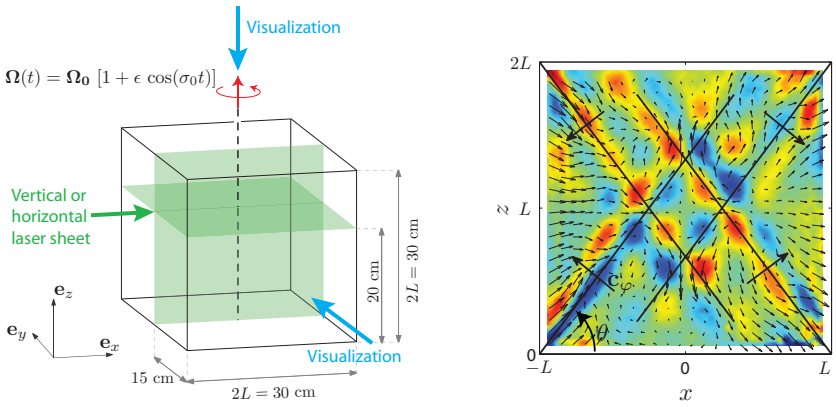

FIGURE 1.7 – **Gauche** : Vue schématique de l'aquarium cubique en libration autour de son axe central. Des mesures par PIV sont réalisées dans le référentiel en libration à la fois dans une section horizontale et verticale. $\Omega_0 = 0.419$ rad s^{-1} (4 rpm) et $\epsilon = 2\%$ à 16%. **Droite** : Structure spatiale dans le plan vertical méridien $y = 0$ de l'écoulement oscillant pour $\epsilon = 2\%$ et $\sigma_0/2\Omega_0 = 0.60$ en l'absence de mode d'inertie. En trait gras, on a souligné la direction de propagation des ondes d'inertie prévue par la relation de dispersion $\cos\theta = \sigma_0/2\Omega_0$.

1.4.1 Excitation de modes d'inertie dans un cube en libration

- Collaboration avec L. Maas (NIOZ, Pays-Bas)
- Post-doctorat de J. Boisson (juin 2011 - juin 2012, co-responsable avec F. Moisy)
- Thèse de C. Lamriben (Sept. 2009 - Août 2012, co-directeur avec F. Moisy)

Nous avons étudié le mécanisme d'excitation de modes d'inertie dans un cube en libration longitudinale (Figure 1.7), i.e. soumis à un taux de rotation oscillant selon

$$\Omega(t) = \Omega_0\ [1 + \epsilon\ \cos(\sigma_0 t)]\,. \tag{1.12}$$

Cette géometrie peut sembler singulière dans le contexte astrophysique mais possède cependant la propriété remarquable que les latitudes critiques de la cavité sont toujours confondues avec les arêtes du cube. En ces latitudes, des faisceaux d'ondes propagatifs sont usuellement excités en direction du cœur de l'écoulement par un mouvement harmonique de la cavité : c'est le phénomène d'éruption de la couche limite d'Ekman [33, 41]. Pour une fréquence σ_0 donnée, ces latitudes critiques se situent de manière générale là où la direction du mouvement d'une onde d'inertie est tangent à la surface de la cavité, i.e. en $\theta = \cos^{-1}(\sigma_0/2\Omega_0)$. Pour une cavité dont les parois sont uniquement perpendiculaires et parallèles à l'axe de rotation, les latitudes critiques sont ainsi naturellement confondues avec les arêtes horizontales, indépendamment de la fréquence $\sigma_0/2\Omega_0 < 1$ en jeu. Cette propriété confère à la géométrie cubique un caractère atypique, mais d'un certain point de vue modèle, par rapport aux cas sphérique et ellipsoïdal. Elle permet par ailleurs à travers la brisure de la symétrie par rotation autour de l'axe du cube de tester le rôle des symétries du forçage sur la sélectivité des mécanismes visqueux d'excitation des

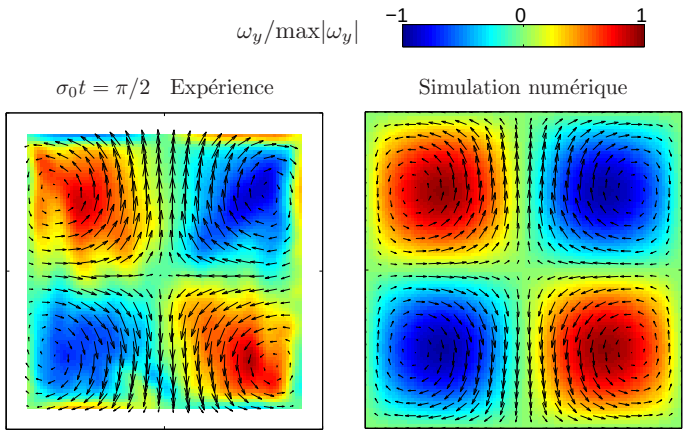

FIGURE 1.8 – Champs de vitesse (dans le plan) et de vorticité (hors plan, codé en couleur) dans le plan vertical méridien $y = 0$. **Gauche** : Mesures expérimentales pour $\epsilon = 0.04$ et $\sigma_0/2\Omega_0 = 0.674$ correspondant à la résonance du mode d'inertie [2,1,+] (nomenclature définie dans Boisson *et al.* Physics of Fluids, 2012, page 35). **Droite** : Structure du mode inviscide [2,1,+] prédit numériquement à la fréquence correspondante.

modes résonants. Finalement, elle permet de tester l'écart, lié aux effets visqueux, aux prédictions numériques des modes inviscides proposées par Leo Mass.

L'écoulement excité a été étudié par des mesures de PIV dans le référentiel en libration successivement dans un plan vertical puis horizontal (Figure 1.7). Nous avons montré que les mouvements de base consistent en un écoulement 2D lié à la conservation inviscide de la vorticité absolue dans le référentiel du laboratoire, i.e. $\boldsymbol{\omega}(t) + 2\boldsymbol{\Omega}(t) = 2\boldsymbol{\Omega}_0$ où $\boldsymbol{\omega}$ est la vorticité dans le référentiel en libration. À celui-ci s'ajoute, lorsque $\sigma_0 < 2\Omega_0$, des faisceaux d'ondes d'inertie trouvant leur source aux arêtes horizontales du cube et se propageant vers le cœur de l'écoulement selon les directions $\theta = \pm\cos(\sigma_0/2\Omega_0)$ imposées par la relation de dispersion. Ces faisceaux d'onde, similaires aux éruptions mentionnées plus tôt, sont le fruit de l'oscillation des couches limites d'Ekman sur les parois horizontales du cube. Celles-ci résultent de l'équilibre [1], quantifié par le nombre d'Ekman $E = \nu/2\Omega_0 L^2$, entre les forces visqueuses et de Coriolis induites par le mouvement oscillant des parois horizontales dans le référentiel tournant au taux moyen Ω_0. Même si le rapport d'aspect de notre cavité est ici de 1, la longueur L utilisée dans la définition de E s'attache de manière générale à quantifier le confinement vertical du système. Cet équilibre s'effectue sur une couche limite d'épaisseur typique $\delta = L\sqrt{E}$ dans laquelle se développe un écoulement alternativement centrifuge et centripète d'amplitude $\epsilon\,\Omega_0\cos(\sigma_0\,t)\,r$ où r est la distance à l'axe de rotation. Dans la limite des oscillations rapides qui est la nôtre, i.e. $\sigma_0 \gg \sqrt{E}\,\Omega_0 \sim 10^{-2}\,\Omega_0$, ce mouvement oscillant, lorsqu'il atteint les arêtes du cube, joue le rôle de source des faisceaux d'ondes d'inertie. La conséquence importante de ce mécanisme est que la viscosité est bien un ingrédient clé dans l'excitation des ondes d'inertie mais que celles-ci sont cependant nourries en vitesse selon une loi inertielle ne faisant pas intervenir la viscosité [33].

Pour certaines fréquences spécifiques de libration, nous avons réussi à exciter, en plus de cet écoulement primaire, un écoulement dont les caractéristiques correspondaient au mode inviscide

obtenu numériquement (Figure 1.8). Le résultat principal de notre étude est que, cependant, seul un sous-ensemble des modes d'inertie prédits, ceux respectant strictement les symétries du forçage, est effectivement excité. En effet, aucun des modes inviscides brisant une de ces symétries (invariance par rotation de $\pi/2$ et π autour de l'axe de rotation, symétrie miroir par rapport à l'équateur) n'a ainsi pu être observé, illustrant la grande sélectivité de l'excitation des modes visqueux. Notre interprétation de cette sélectivité repose sur le fait que ce sont les faisceaux d'ondes issus des arêtes qui réalisent le transfert d'énergie entre les mouvements oscillants des parois de la cavité et le mode d'inertie. Ces faisceaux respectant naturellement les symétries du forçage, ils ne peuvent exciter efficacement que les modes respectant aussi ces symétries. Un indice fort dans ce sens est qu'aux fréquences de résonance des modes effectivement excités, le motif dessiné par les faisceaux d'ondes issus des arêtes a la particularité de devenir quasi-périodique tout en respectant les nombres d'onde du mode.

1.4.2 Étude du mode de "tilt-over" dans une sphère en précession

- Collaboration avec D. Cébron (ETH Zürich, puis ISTerre, CNRS et Univ. Grenoble 1)
- Post-doctorat de J. Boisson (juin 2011 - juin 2012, co-responsable avec F. Moisy)

Lors de l'analyse des expériences de cube en libration décrites dans la partie précédente, nous avons notamment calculé la densité spectrale de puissance associée aux séries temporelles des champs de vitesse (cf. Figure 3 dans [Boisson *et al.* Physics of Fluids, 2012] à la page 35). La conclusion de ces données était que la quasi-totalité de l'énergie était contenue dans une fine bande de fréquences autour de la fréquence de libration traduisant la réponse linéaire de l'écoulement au forçage. Nous avons cependant remarqué la présence d'un pic secondaire de faible amplitude à la fréquence moyenne de rotation de la plateforme. Après avoir dans un premier temps pensé que ce pic d'amplitude indépendante de l'intensité de la libration était lié à un défaut mécanique dans la rotation de la plateforme, nous avons découvert une structure et une dynamique singulière de l'écoulement associé (extrait par filtrage de Fourier temporel) suggérant une physique beaucoup plus intéressante.

Nous avons alors réalisé que cet écoulement synchronisé avec la rotation de la plateforme correspondait à un mode d'inertie connu en géométrie sphérique sous le nom de mode de "tilt-over". Celui-ci consiste dans le référentiel non-tournant (du laboratoire pour nous) en une rotation solide autour d'un axe équatorial fixe [1] qui vient s'ajouter à la rotation globale au taux Ω_0 autour de l'axe vertical. Dans notre expérience, cet écoulement est excité par la rotation de la Terre qui entraîne la rotation de notre plateforme dans un lent mouvement de précession (Figure 1.9). Nous nous sommes alors attachés à vérifier expérimentalement cette hypothèse en mettant une sphère remplie d'eau en simple rotation solide. Le choix de revenir à une géométrie sphérique a été fait pour se placer dans le cadre naturel des travaux théoriques concernant l'écoulement dans le cœur des planètes en précession [10, 42–44]. Les écoulements induits par la précession de cavité sphérique ou sphéroïde ont en effet reçu une attention considérable depuis les travaux pionniers de Poincaré [45] de par l'importance astrophysique de ce problème [10, 35]. Dans le

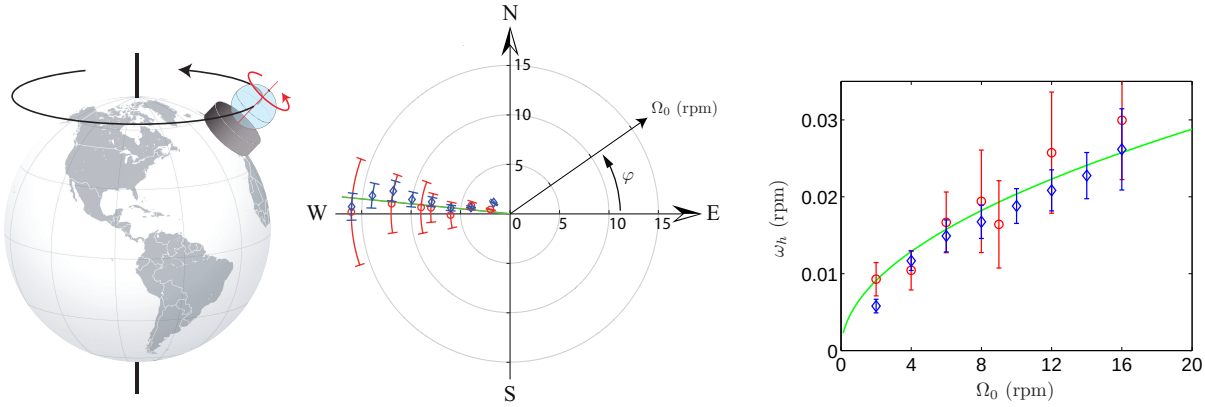

FIGURE 1.9 – **Gauche** : La rotation de la Terre induit un mouvement de précession sur la sphère en rotation. **Centre** : Angle φ entre la projection horizontale de l'axe de rotation de l'écoulement de tilt-over et l'Est en fonction du taux de rotation Ω_0 de la sphère. La ligne continue verte montre la prédiction théorique $\varphi = 174.35°$. Les données indiquées avec un $\circ$ sont extraites des champs de PIV dans le plan horizontal et celles avec un $\diamond$ dans le plan vertical. **Droite** : Taux de rotation horizontal ω_h de l'écoulement de tilt-over en fonction du taux de rotation Ω_0 de la sphère. La ligne continue représente la prédiction théorique.

cas de la Terre par exemple, la précession qui se fait sur une période très longue de 26 000 ans induit de larges excursions de l'axe de rotation du noyau liquide [46]. Il a par ailleurs été proposé que les écoulements dus à la précession aient une contribution significative dans la génération des champs magnétiques planétaires [35, 47, 48].

Je donne dans la suite de cette section quelques éléments d'ordre de grandeur pour comprendre la physique de base de cet écoulement de tilt-over induit par précession mais le lecteur pourra se reporter à une lecture de l'article (Boisson *et al.* EPL, 2012) à la page 53 pour une description plus précise de nos mesures et du modèle permettant de les interpréter.

Dans la limite linéaire, lorsque l'on soumet une sphère en rotation à une précession définie par le vecteur $\mathbf{\Omega}_p$, le fluide dans le cœur de la sphère conserve un mouvement de rotation solide de vecteur $\boldsymbol{\omega}$ (fixe dans le référentiel de précession) mais dont l'amplitude et l'orientation s'écarte de la rotation $\mathbf{\Omega_0}$ de la sphère. L'amplitude de cet écart est déterminée de manière non-triviale par la valeur du nombre de Poincaré Ω_p/Ω_0 et du nombre d'Ekman $E = \nu/(2\Omega_0 R^2)$ où R est le rayon de la sphère. Dans la limite de forte rotation et de faible précession, plus précisément lorsque $\Omega_p/\Omega_0 \ll \sqrt{E} \ll 1$, la perturbation du vecteur rotation du cœur fluide $\boldsymbol{\omega}$ est faible et la correction $\boldsymbol{\omega}' = \boldsymbol{\omega} - \mathbf{\Omega_0}$ devient perpendiculaire à $\mathbf{\Omega}_0$. L'écoulement de tilt-over peut alors être décrit comme un des modes résonants d'inertie des cavités sphériques, excité dans ce cas par la précession (Figure 1.5 et [1]) : c'est le mode de fréquence propre Ω_0 et de nombre d'onde azimutal $m = 1$. Le cœur fluide ne tournant pas à la même vitesse que les parois de la sphère, des couches visqueuses vont venir adapter la différence de vitesse sur l'épaisseur typique des couches d'Ekman $\delta = R\sqrt{E}$. Dans cette limite, l'amplitude ω' de l'écoulement de tilt-over peut se déterminer simplement dans le référentiel tournant à $\mathbf{\Omega}_0$ en écrivant l'équilibre entre le couple exercé par la force de Coriolis due à la précession agissant sur le cœur de l'écoulement et le

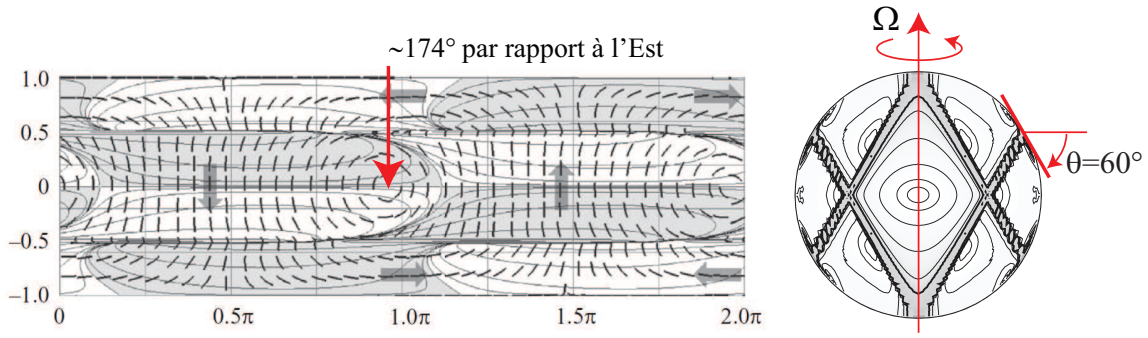

FIGURE 1.10 – Écoulement prévu théoriquement par Kida dans une sphère en très faible précession au nombre d'Ekman $E = 10^{-12}$. Figures adaptées de [44]. C'est l'écart à la rotation imposée qui est représenté. **Gauche** : Projection de Mercator du champs de vitesse sur une calotte sphérique de rayon $R - 4\delta$ où δ est l'épaisseur de la couche d'Ekman. L'orientation de la vorticité horizontale dans le cœur de l'écoulement fait un angle d'environ 174° avec l'Est (en utilisant la convention de notre expérience). **Droite** : Courbes de niveau de la norme du champ de vitesse dans un plan méridien illustrant les faisceaux d'ondes excités aux latitudes critiques $\theta = \arccos(0.5) = 60°$.

couple visqueux exercé par les couches limites en surface qui prédit finalement $\omega' \sim E^{-1/2}\,\Omega_p$. Ainsi, bien que la rotation de la Terre ($\Omega_p \simeq 6.9\,10^{-4}$ rpm) soit très lente devant la rotation de notre sphère ($\Omega_0 \in [2; 16]$ rpm), la correction introduite à la rotation du fluide est observable, comme amplifiée par le faible nombre d'Ekman (typiquement $E \sim 10^{-4}$ dans notre expérience). L'énergie qui vient alimenter l'écoulement de tilt-over est en fait prélevée dans le mouvement de rotation et la précession n'intervient que comme catalyseur pour convertir une partie de l'énergie de la rotation en mouvement fluide oscillant dans le référentiel tournant.

Les premiers indices expérimentaux d'un écoulement de tilt-over excité par la rotation de la Terre dans une expérience de laboratoire ont été rapportés par Vanyo et Dunn [49] en 2000 grâce à une visualisation par colorant. Simultanément à notre étude de ce problème, l'équipe de Daniel Lathrop [50] à l'Université du Maryland, a elle aussi mis en évidence cet écoulement de tilt-over grâce à des mesures de sonde Doppler ultrasonores le long d'un axe vertical dans une coquille de 3 m de diamètre en rotation. Cependant, aucun de ces deux travaux n'a permis une comparaison quantitative avec la théorie de l'écoulement de "tilt-over" dans une sphère en précession [10].

Nous avons ainsi réalisé des mesures de PIV successivement dans une coupe horizontale et verticale d'une sphère remplie d'eau en rotation sur la plateforme "Gyroflow" (Figure 1.9). Ces mesures constituent en pratique la première étude expérimentale directe des champs de vitesse de l'écoulement de tilt-over excité par précession. De manière plus anecdotique, cette expérience permettant de détecter quantitativement la rotation de la Terre peut être qualifiée d'analogue fluide au célèbre pendule de Foucault. Notre article décrivant ces résultats a ainsi été sélectionné dans "EPL Highlights 2012" et a fait l'objet d'adaptation sous la forme de plusieurs articles de vulgarisation.

Les mesures réalisées ont constitué un vrai défi expérimental de par la faiblesse de l'écou-

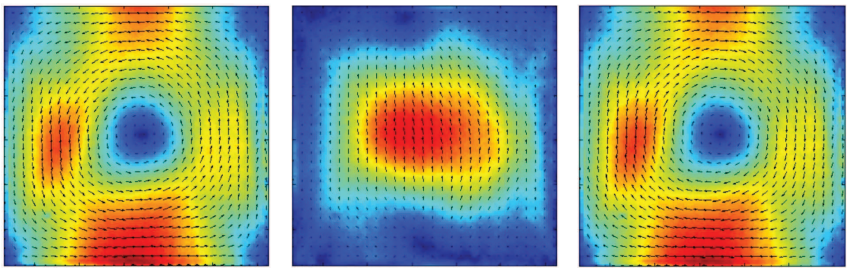

FIGURE 1.11 – Expérience de cube en rotation constante. Visualisation de l'écoulement induit par la rotation de la Terre. Champs de vitesse mesurés dans le référentiel en rotation dans un plan vertical excentré, avec un déphasage de $\pi/2$ entre chaque image. Les couleurs représentent la norme de la vitesse. On retrouve la structure d'écoulement de rotation solide d'axe horizontal fixe dans le référentiel du laboratoire autour duquel nous sommes en train de tourner. Échelle de vitesse de 0 à 50 μm s^{-1}. **Gauche** : rotation anti-horaire. **Centre** : écoulement montant. **Droite** : rotation horaire.

lement qui consiste en son cœur et dans le référentiel du laboratoire en une rotation solide légèrement inclinée de 0.1 à 0.2° par rapport à la rotation imposée par la sphère. En pratique, nous avons été capables de détecter ce très faible écart à la rotation verticale grâce à la sensibilité de notre système de PIV dans le référentiel tournant (jusqu'à 10 μm s^{-1}). Nos mesures ont finalement montré un accord quantitatif avec la théorie de Busse [10] pour le cœur de l'écoulement de tilt-over aussi bien pour son amplitude que pour son orientation (Figure 1.9). Nous avons aussi mis en évidence que les mouvements du fluide s'éloignaient d'une rotation solide le long des parois de la sphère, sur une épaisseur d'environ $0.3\,R$ beaucoup plus grande que celle prévue pour les couches d'Ekman $\sqrt{E}\,R \simeq 0.01R$. Cet écart est en fait lié à l'excitation de faisceaux d'ondes d'inertie aux latitudes critiques que nous avons réussi à mettre en évidence en soustrayant la rotation solide de tilt-over à l'écoulement total. Nos observations sont compatibles avec les prédictions théoriques récentes de Kida [44] (Figure 1.10) pour l'épaisseur typique des faisceaux émis $2R\,E^{1/5} \simeq 0.3\,R$.

L'atout de cette expérience où la précession est imposée par la rotation de la Terre est que nous avons été capable d'embarquer un système de PIV dans le deuxième référentiel tournant ce qui paraît extrêmement ardu dans une "vraie" expérience de précession [42, 51, 52] où deux rotations non-coaxiales sont imposées en série par l'expérimentateur. L'inconvénient et non des moindres est que l'on ne peut évidemment pas jouer sur les paramètres de la précession et que l'on est en conséquence confiné dans une gamme restreinte de régimes de l'écoulement.

Il est finalement intéressant de rappeler que nous avons observé un écoulement analogue, excité lui aussi par la rotation de la Terre, dans nos expériences de cube en rotation ou en libration (Figure 1.11). Cet écoulement consiste lui aussi dans son cœur en une rotation solide d'axe légèrement penché par rapport à la rotation du cube. Il est cependant remarquable que dans un cube une telle structure spatiale ne correspond en aucun cas à celle d'un mode d'inertie dont la fréquence de résonance serait proche de Ω_0. Ce résultat souligne que l'écoulement de tilt-over est robuste et définit une sorte d'écoulement irréductible lors d'une expérience de fluide en rotation au laboratoire (sauf à aligner l'axe de rotation de l'expérience avec celui de la Terre). Bien que

faible, la présence de cet écoulement lors d'études en laboratoire peut cependant perturber la détection d'écoulements secondaires liés notamment aux non-linéarités.

1.5 Perspectives

Les trois études expérimentales qui ont été présentées dans ce chapitre pourraient faire l'objet de prolongement dans mes activités de recherche à venir. J'évoque dans cette partie quelques pistes de recherche qui nous paraissent intéressantes dans ce cadre.

1.5.1 Étude du déclin visqueux d'un paquet d'ondes propagatif

Le premier projet mené sur la plateforme tournante "Gyroflow" en 2009 et décrit dans la partie 1.3 de ce chapitre a consisté en une étude de l'étalement visqueux du paquet d'ondes émis par une source ponctuelle bidimensionnelle. Cette étude a permis de valider l'adaptation aux ondes d'inertie de l'approche théorique auto-similaire de Thomas et Stevenson [22] à travers une vérification de la loi de puissance décrivant l'épaississement du faisceau. La validation expérimentale de cette prédiction a cependant laissé en suspens la question subtile de la loi d'échelle régissant le déclin visqueux de l'amplitude de l'onde. Bruno Voisin (LEGI, CNRS et Université de Grenoble), qui travaille à la modélisation des ondes internes et avec qui nous collaborerons sur ce projet, prédit en effet que les coefficients des équations différentielles régissant la forme du paquet d'ondes en champ lointain sont dépendants de l'ordre de la polarité de la source ponctuelle (monopolaire, dipolaire ...). Une conséquence directe est alors une dépendance de l'exposant de déclin de l'onde avec l'ordre de la polarité de la source.

Le projet que nous proposons ici consiste à explorer expérimentalement la décroissance visqueuse des faisceaux d'ondes d'inertie issus de sources ponctuelles monopolaire et dipolaire (dans une géométrie 2D) avec pour objectif de mettre en évidence une différence entre les deux exposants de déclin.

1.5.2 Propagation d'ondes d'inertie dans un fluide en rotation inhomogène

Une autre perspective de travail que j'envisage au sujet des faisceaux d'ondes propagatifs consiste dans le développement d'expériences de propagation d'ondes d'inertie dans des fluides en rotation (légèrement) inhomogène, un domaine d'étude presque vierge. On pense en particulier à générer une ou plusieurs "interfaces" entre des zones de taux de rotation légèrement différents. L'idée est ici de sonder si de telles inhomogénéités de l'"indice du milieu", c'est-à-dire de la fréquence de Coriolis 2Ω, conduisent à des effets de réflexion-réfraction, à de l'effet tunnel... Le défi expérimental consiste ici à produire une interface entre deux zones dont les taux de rotation sont suffisamment différents pour observer des effets sur une onde traversant celle-ci. Dans le même temps, le contraste de rotation devra être maintenu suffisamment faible pour éviter les instabilités de l'interface ou la création de recirculations trop importantes liées à des phénomènes de pompage d'Ekman. Bien entendu, ce projet impliquera aussi des développements théoriques

pour modéliser les phénomènes observés en prolongeant par exemple les travaux de Phillips [18] sur la réflexion des ondes internes.

1.5.3 Écoulements excités dans des cavités en rotation perturbées par un mouvement harmonique intense

Un autre prolongement des études décrites dans ce chapitre (à la partie 1.4 cette fois-ci) pourrait se concrétiser sous la forme d'expériences de libration ou de précession de cavités dans lesquelles le forçage serait plus intense que dans les expériences déjà réalisées, permettant d'atteindre des régimes non-linéaires. L'objectif est ici d'étudier certaines instabilités que peuvent subir les écoulements excités (sans se restreindre aux modes d'inertie comme écoulement de base) et la transition vers des régimes turbulents qui peut s'en suivre. La motivation de ce type d'études est d'apporter des repères pour comprendre les origines de la turbulence dans le cœur fluide des planètes, tout en gardant à l'esprit que la dynamique de ces écoulements astrophysiques relève de l'interaction d'un nombre important de processus, bien au-delà de ceux liés aux seuls effets de la rotation.

Un premier projet part du constat que, en conséquence de l'interaction gravitationnelle avec des astres compagnons, la forme usuelle de la frontière entre le cœur liquide des planètes et leur manteau solide diffère souvent de manière significative d'une sphère [53] ou même d'une forme axisymétrique, i.e. sphéroïde. De cette constatation naît l'intérêt d'étudier des cavités non-axisymétriques qui donnent naissance à des instabilités spécifiques lorsque que la déformation équatoriale de la cavité présente un mouvement relatif par rapport à la rotation globale du fluide. L'exemple le plus célèbre est l'instabilité elliptique [54] qui se développe dans les cavités dont l'équateur est déformé par des forces de marée [55–58]. Il a récemment été montré que ce type d'instabilités pouvaient aussi se développer dans les cavités ellipsoïdales en libration [59] ou en précession [60]. Dans ce contexte, nous pourrions nous intéresser à une instabilité analogue prédite théoriquement et numériquement par David Cébron (ISTerre, CNRS et Univ. Grenoble 1) dans un cube en libration (d'amplitude plus importante que celle que nous avons étudiée jusqu'à présent). Ce travail permettrait de tester expérimentalement dans le cas quadrupolaire les prédictions de travaux numériques et théoriques dans les cavités multipolaires en libration [61]. L'instabilité en question est le fruit d'une déstabilisation tridimensionnelle de l'écoulement de base 2D. Elle conduit à l'excitation de deux modes d'inertie à travers une résonance triadique avec l'écoulement oscillant de base. Il est prévu numériquement que cette instabilité conduise finalement à une dynamique cyclique de l'écoulement alternant entre des phases laminaires et turbulentes. Ce projet pourrait idéalement se faire en collaboration avec David Cébron avec qui nous avons déjà travaillé sur l'étude de l'écoulement de faible précession en régime linéaire décrit à la partie 1.4.2.

Le principe expérimental consistera à mettre en place sur la plateforme tournante un moteur puissant permettant d'imposer un mouvement d'oscillation intense à une cavité remplie d'eau dans le référentiel tournant de la plateforme. De grandes amplitudes de libration pourront ainsi être atteintes, à la différence des expériences présentées en section 1.4.1 : l'inertie de plateforme

tournante ne sera en effet plus à entraîner dans un mouvement de libration mais seulement celle de la cavité.

Ce même moteur embarqué dans le référentiel tournant de la plateforme pourra de manière opportune servir aussi à la mise en précession d'une cavité remplie de fluide en introduisant une inclinaison entre l'axe du moteur embarqué et celui de rotation de la plateforme. Le projet expérimental auquel nous songeons ici a pour but d'explorer les régimes de l'écoulement excité dans une sphère en précession plus largement que dans les expériences décrites dans la section 1.4.2 où la précession était imposée par la rotation de la Terre. Nous envisageons plus précisément de sonder les domaines de stabilité (en fonction du nombre d'Ekman et du taux de précession, i.e. le nombre de Poincaré) des régimes laminaires et turbulents dans les sphères et les sphéroïdes en précession. Ce sujet de recherche complexe de l'instabilité des écoulements de précession reste assez vierge vis-à-vis de la caractérisation des régimes turbulents, hormis les travaux expérimentaux de Goto *et al.* [62, 63] et sera donc exploratoire dans une large mesure. Les mécanismes d'instabilité de l'écoulement de précession en géométrie sphérique et sphéroïde sont en effet encore matière à débat avec la proposition de mécanismes inertiels (par résonance paramétrique de l'écoulement de base avec des modes d'inertie [64, 65]) et de mécanismes visqueux (par instabilité des faisceaux d'ondes émis aux latitudes critiques). Comme dans le cas de l'instabilité elliptique, des dynamiques cycliques de l'écoulement, alternant entre des phases laminaires et turbulentes, ont été observées dans des simulations numériques directes [66]. Les études théoriques de Kida [67] ont plus récemment proposé que la limite de stabilité de l'écoulement soit franchie lorsque le taux de précession $\Gamma = \Omega_p/\Omega_0$ devient plus grand que E^α avec différents exposants α selon que l'instabilité dominante soit inertielle ou visqueuse. L'objectif expérimental que nous envisageons dans un tel projet est d'explorer ce type de limite de stabilité et d'essayer de participer à la cartographie des régimes de l'écoulement dans l'espace (Γ, E).

Viscous spreading of an inertial wave beam in a rotating fluid

Pierre-Philippe Cortet,[a] Cyril Lamriben, and Frédéric Moisy
Laboratoire FAST, CNRS UMR 7608, Université Paris-Sud, Université Pierre-et-Marie-Curie, Bât. 502, Campus Universitaire, 91405 Orsay, France

(Received 23 March 2010; accepted 3 August 2010; published online 30 August 2010)

We report experimental measurements of inertial waves generated by an oscillating cylinder in a rotating fluid. The two-dimensional wave takes place in a stationary cross-shaped wavepacket. Velocity and vorticity fields in a vertical plane normal to the wavemaker are measured by a corotating particle image velocimetry system. The viscous spreading of the wave beam and the associated decay of the velocity and vorticity envelopes are characterized. They are found in good agreement with the similarity solution of a linear viscous theory, derived under a quasiparallel assumption similar to the classical analysis of Thomas and Stevenson ["A similarity solution for viscous internal waves," J. Fluid Mech. **54**, 495 (1972)] for internal waves. © *2010 American Institute of Physics*. [doi:10.1063/1.3483468]

I. INTRODUCTION

Rotating and stratified fluids both support the propagation of waves, referred to as inertial and internal waves, respectively, which share numbers of similar properties.[1,2] These waves are of first importance in the dynamics of the ocean and the atmosphere,[3] and play a key role in the anisotropic energy transfers and in the resulting quasi-two-dimensional nature of turbulence under strong rotation and/or stratification.[4]

More specifically, rotation and stratification both lead to an anisotropic dispersion relation in the form $\sigma=f(k_z/|\mathbf{k}|)$, where σ is the pulsation, $\mathbf{k}$ is the wave vector, and the z axis is defined either by the rotation axis or the gravity.[2] This particular form implies that a given excitation frequency σ selects a single direction of propagation, whereas the range of excited wavelengths is set by boundary conditions or viscous effects. A number of well-known properties follow from this dispersion relation, such as perpendicular phase velocity and group velocity, and anomalous reflection on solid boundaries.[2,5]

Most of the laboratory experiments on internal waves in stratified fluids have focused on the properties of localized wave beams, of characteristic thickness and wavelength which are much smaller than the size of the container, excited either from local[6–10] or extended[11] sources. On the other hand, most of the experiments in rotating fluids have focused on the inertial modes or wave attractors in closed containers,[12–16] whereas less attention has been paid to localized inertial wave beams in effectively unbounded systems. Inertial modes and attractors are generated either from a disturbance of significant size compared to the container,[12] or more classically from global forcing (precession or modulated angular velocity).[13–16] Localized inertial waves generated by a small disturbance were visualized from numerical simulations by Godeferd and Lollini,[17] and were recently investigated using particle image velocimetry (PIV) by Messio *et al.*[18] In this latter experiment, the geometrical properties of the conical wavepacket emitted from a small oscillating disk was characterized, by means of velocity measurements restricted to a horizontal plane normal to the rotation axis, intersecting the wavepacket along an annulus.

The weaker influence of rotation compared to stratification in most geophysical applications probably explains the limited number of references on inertial waves compared to the abundant literature on internal waves (see Ref. 19 and references therein). Another reason might be that quantitative laboratory experiments on rotating fluids are more delicate to perform than for stratified fluids: Mounting the measurement devices, such as cameras and light sources for PIV, on the rotating frame implies technical issues (connection wiring and mechanical vibrations). Moreover, only PIV is available for quantitative investigation of the wave structure for inertial waves, whereas other optical methods, such as shadowgraphy, or more recently synthetic Schlieren,[8] are also possible for internal waves.

The purpose of this paper is to extend the results of Messio *et al.*,[18] using a newly designed rotating turntable, in which the velocity field can be measured over a large vertical field of view using a corotating PIV system. In the present experiment, the inertial wave is generated by a thin cylindrical wavemaker, producing a two-dimensional cross-shaped wave beam, and special attention is paid to the viscous spreading of the wave beam. The beam thickness and the vorticity decay are found to compare well with a similarity solution, analogous to the one derived by Thomas and Stevenson[7] for internal waves.

II. THEORETICAL BACKGROUND

A. Geometry of the wave pattern

A detailed description of the structure of a plane monochromatic inertial wave in an inviscid fluid can be found in Ref. 18 and only the main properties are recalled here. We consider a fluid rotating at constant angular velocity $\mathbf{\Omega}=\Omega\mathbf{e}_Z$, where the direction $\mathbf{e}_Z$ of the reference frame

[a]Electronic mail: ppcortet@fast.u-psud.fr.

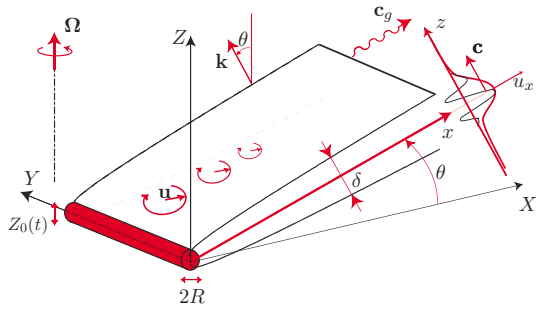

FIG. 1. (Color online) Geometry of an inertial wave beam emitted in an infinite medium from a localized oscillating cylindrical wavemaker invariant in the Y-direction.

$(\mathbf{e}_X, \mathbf{e}_Y, \mathbf{e}_Z)$ is vertical (see Fig. 1). Fluid particles forced to oscillate with a pulsation $\sigma < 2\Omega$ describe anticyclonic circular trajectories in tilted planes. A propagating wave defined by a wavevector $\mathbf{k}$ normal to these oscillating planes is a solution of the linearized inviscid equations, satisfying the following dispersion relation:

$$\sigma = 2\mathbf{\Omega} \cdot \mathbf{k}/k = 2\Omega \cos\,\theta. \tag{1}$$

In this relation, only the angle of $\mathbf{k}$ with respect to the rotation axis is prescribed, whereas its magnitude is set by the boundary conditions. For such anisotropic dispersion relation, the phase velocity, $\mathbf{c} = \sigma\mathbf{k}/k^2$, is normal to the group velocity,[2] $\mathbf{c}_g = \nabla_{\mathbf{k}}\sigma$ (see Fig. 1).

If one now considers a wave forced by a thin horizontal velocity disturbance invariant in the Y direction, although the velocity field still has three components, the wave pattern is two-dimensional, varying only in the (X,Z) vertical plane. The wave pattern consists in four plane beams making angle $\pm\theta$ with respect to the horizontal, drawing the famous *St. Andrew's cross* familiar in the context of internal waves.[6] In the following, we consider only one of those four beams, with $X > 0$ and $Z > 0$, and we define in Fig. 1 the associated local system of coordinates $(\mathbf{e}_x, \mathbf{e}_y, \mathbf{e}_z)$: The axis $\mathbf{e}_x$ is in the direction of the group velocity, $\mathbf{e}_z$ is directed along the wavevector $\mathbf{k}$, and $\mathbf{e}_y = \mathbf{e}_Y$ is along the wavemaker.

Considering the idealized case of an infinitely thin cylinder oscillating with an infinitely small amplitude (a Dirac disturbance), a white spectrum of wavevectors is excited, all aligned with $\mathbf{e}_z$. In an inviscid fluid, the interference of this infinite set of plane waves will cancel out everywhere except in the $z=0$ plane, where all the wave phases coincide, resulting in a single, infinitely thin oscillating sheet of fluid describing circular trajectory normal to $\mathbf{e}_z$. Of course, for a disturbance of finite size, finite amplitude, and in a viscous fluid, the constructive interferences will spread over a layer of finite thickness around the $z=0$ plane, as discussed in the following section.

B. Viscous spreading

In a viscous fluid, the energy of the wave beam is dissipated because of the shearing motion between oscillating planes. As the energy propagates away from the source, the larger wavenumbers will be damped first so that the spectrum of the wave beam gradually concentrates toward lower wavenumbers, resulting in a spreading of the wave beam away from the source.

Although the viscous attenuation of a single Fourier component yields a purely exponential decay, the attenuation of a localized wave follows a power law with the distance from the source, which originates from the combined exponential attenuation of its Fourier components. A similarity solution for the viscous spreading of a wave beam was derived by Thomas and Stevenson[7] in the case of internal waves, and was extended to the case of coupled internal-inertial waves by Peat.[20] The derivation in the case of a pure inertial wave is detailed in the Appendix, and we provide here only a qualitative argument for the broadening of the wave beam.

During a time t, the amplitude of a planar monochromatic wave of wavevector $\mathbf{k}$ is damped by a factor $\epsilon_k = \exp(-\nu k^2 t)$ as it travels a distance $x = c_g t$ along the beam, where c_g is the group velocity. Using $c_g = (2\Omega/k)\sin\,\theta = (\sigma/k)\tan\,\theta$, the attenuation factor writes

$$\epsilon_k = \exp(-\ell^2 k^3 x),$$

where we introduce the viscous lengthscale,

$$\ell = \left(\frac{\nu}{\sigma \tan\,\theta}\right)^{1/2}. \tag{2}$$

For a wave beam emitted from a thin linear source at $x=0$, an infinite set of plane waves is generated, and the energy of the largest wavenumbers will be preferentially attenuated as the wave propagates in the x direction. At a distance x from the source, the largest wavenumber, for which the energy has decayed by less than a given factor ϵ^*, is $k_{\max} = (\ell^2 x)^{-1/3} \ln \epsilon^*$. At distance x, the wave beam thus results from the interference of the remaining plane waves of wavenumbers ranging from 0 to $k_{\max}$. Its thickness can be approximated by $\delta(x) \sim k_{\max}^{-1}$, yielding $\delta(x)/\ell \sim (x/\ell)^{1/3}$. Mass conservation across a surface normal to the group velocity implies that the velocity amplitude of the wave must decrease as $x^{-1/3}$.

More specifically, introducing the reduced transverse coordinate $\eta = z/x^{1/3}\ell^{2/3}$, a similarity solution exists for the velocity envelope,

$$u_0(x) = U_0^* \frac{E_0(\eta)}{E_0(0)} \left(\frac{\ell}{x}\right)^{1/3}, \tag{3}$$

where U_0^* is the velocity scale of the wave and the analytical expression of the nondimensional envelope $E_0(\eta)$ is given in the Appendix. Similarly, the vorticity envelope can be written as

$$\omega_0(x) = W_0^* \frac{E_1(\eta)}{E_1(0)} \left(\frac{\ell}{x}\right)^{2/3}, \tag{4}$$

with W_0^* as the vorticity scale. Although the normalized velocity envelope $E_0(\eta)/E_0(0)$ has larger tails than the vorticity one $E_1(\eta)/E_1(0)$, they turn out to be almost equal for $\eta < 4$.

The width at midheight, defined such that $E_m(\eta_{1/2}/2) = E_m(0)/2$, with $m=0,1$, is $\eta_{1/2} \simeq 6.84$ for both envelopes so that the width of the beam in dimensional units is

$$\delta(x) \simeq 6.84\ell\left(\frac{x}{\ell}\right)^{1/3}. \quad (5)$$

C. Finite size effect of the source

The similarity solution described here applies only in the case of a source of size much smaller than the viscous scale ℓ. In the case of internal waves, Hurley and Keady[21] (see also Ref. 9) showed that for a source of large extent, vertically vibrated with a small amplitude, the wave could be approximately described as originating from two virtual sources, respectively, located at the top and bottom of the disturbance. Following qualitatively this approach in the case of inertial waves forced by a horizontal cylinder of radius R, the boundaries of the upper wave are given by $z_{\text{up}}^{\pm} = R \pm \delta(x)/2$, and those of the lower wave are given by $z_{\text{down}}^{\pm} = -R \pm \delta(x)/2$. The lower boundary of the upper source intersects the upper boundary of the lower source at a distance x_i, such that $z_{\text{up}}^{-}(x_i) = z_{\text{down}}^{+}(x_i)$, yielding $\delta(x_i) = 2R$. Using the numerical factor given in Eq. (5), the distance x_i writes

$$\frac{x_i}{R} \simeq 0.025\left(\frac{R}{\ell}\right)^2. \quad (6)$$

For large wavemakers ($R/\ell \gg 0.025^{-1/2} \simeq 6.3$), one has two distinct wave beams for $x \ll x_i$, and one single merged beam for $x \gg x_i$. On the other hand, for smaller wavemakers, the merging of the two wave beams occurs virtually inside the source, which can be effectively considered as a point source. In this case, the effective beam width far from the source may be simply written as

$$\delta_{\text{eff}}(x) \simeq 2R + \delta(x). \quad (7)$$

III. THE EXPERIMENT

A. Experimental setup

The experimental setup consists in a cubic glass tank, of 60 cm sides and filled with 54 cm of water (see Fig. 2), mounted on the new precision rotating turntable "Gyroflow," with 2 m diameter. The angular velocity Ω of the turntable is set in the range of 0.63–2.09 rad s^{-1}, with relative fluctuations $\Delta\Omega/\Omega$ less than 5×10^{-4}. A cover is placed at the free surface, preventing from disturbances due to residual surface waves. The rotation of the fluid is set long before each experiment (at least 1 h) in order to avoid transient spin-up recirculation flows and to achieve a clean solid body rotation.

The wavemaker is a horizontal cylinder of radius $R=4$ mm and length $L=50$ cm, hung at 33.5 cm below the cover by a thin vertical stem with 3 mm diameter. It is off-centered in order to increase the size of the investigated wave beam in the quadrant $X<0$ and $Z<0$. The vertical oscillation $Z_0(t) = A\cos(\sigma_o t)$, with $A=2$ mm, is achieved by a step-motor, coupled to a circular camshaft which converts the rotation into a sinusoidal vertical oscillation. In the present experiments, the wavemaker frequency is kept constant, equal to $\sigma_o = 1.26$ rad s^{-1}, and the angular velocity of the turntable is used as the control parameter. This allows the velocity disturbance $\sigma_o A = 2.5$ mm s^{-1} to be fixed, whereas the angle of the inertial wave beam with respect to the horizontal, $\theta = \cos^{-1}(\sigma_o/2\Omega)$, is varied between 0° and 72°. The velocity and vorticity profiles are examined at distances x between 30 and 300 mm from the wavemaker. The three-dimensional effects originating from the finite length L of the cylinder can be safely neglected since $x < 0.6L$. The Reynolds number based on the wavemaker velocity is $\text{Re} = \sigma_o A(2R)/\nu \simeq 20$ so that the flow in the vicinity of the wavemaker is essentially laminar. Except in Sec. IV B, where the transient regime is described, measurements start after several wavemaker periods in order to achieve a steady state.

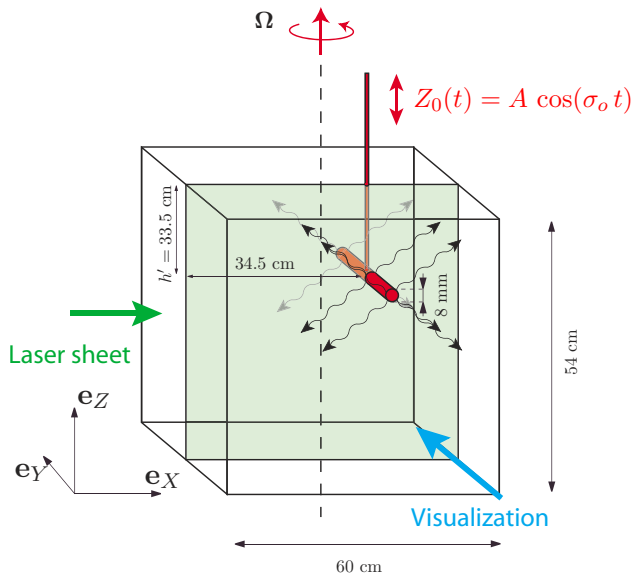

FIG. 2. (Color online) Schematic view of the experimental setup. The horizontal 8 mm diameter cylinder is oscillating vertically according to $Z_0(t) = A\cos(\sigma_o t)$, with $A=2$ mm and $\sigma_o = 0.2$ Hz. PIV measurements in a vertical plane (X,Z) in the rotating frame are achieved by a vertical laser sheet and a camera at 90°.

For the forcing frequency σ_o considered here, the characteristic boundary layer thickness is $\delta_S = (\nu/\sigma_o)^{1/2} \simeq 0.9$ mm. This thickness also gives the order of magnitude of the viscous length $\ell = \delta_S/\sqrt{\tan\theta}$ [see Eq. (2)], for angles not too close to 0 and $\pi/2$. The wavemaker radius being chosen such that $R/\ell \simeq 4$, the small source approximation is satisfied according to the criterion discussed in Sec. II C.

B. PIV measurements

Velocity fields in a vertical plane (X,Z) are measured using a 2D particle image velocimetry system. The flow is seeded by 10 μm tracer particles, and illuminated by a vertical laser sheet, generated by a 140 mJ Nd:YAG (yttrium aluminum garnet) pulsed laser. A vertical 43×43 cm^2 field of view is acquired by a 2048×2048 pixel camera synchronized with the laser pulses. The field of view is set on the

lower left wave beam. For each rotation rate, a set of 2000 images is recorded, at a frequency of 2 Hz, representing ten images per wavemaker oscillation period.

PIV computations are performed over successive images, on 32×32 pixel interrogation windows with 50% overlap, leading to a spatial resolution of 3.4 mm.[22] In the following, the two quantities of interest are the velocity component u_x, obtained from the measured components u_X and u_Z projected along the direction of the wave beam, and the vorticity component ω_y normal to the measurement plane.

The velocity along the wave beam typically decreases from 1 to 0.1 mm s^{-1}, and is measured with a resolution of 0.02 mm s^{-1}. Two sources of velocity noise are present, both of the order of 0.2 mm s^{-1}, originating from residual modulations of the angular velocity of the turntable, and from thermal convection effects due to a slight difference between the water and the room temperature. The residual velocity modulations, of the order of $L_0\Delta\Omega/2$ (where L_0 is the tank size and $\Delta\Omega\simeq5\times10^{-4}$ Ω), are readily removed by computing the phase-averaged velocity fields $\mathbf{u}(x,z,\phi)$ from the instantaneous velocity $\mathbf{u}_{\text{inst}}(x,z,t)$. Here the phase-averaged field at a given phase $\phi\in[0,2\pi]$ is defined as

$$\mathbf{u}(x,z,\phi)=\frac{1}{N}\sum_{n=1}^{N}\mathbf{u}_{\text{inst}}\left[x,z,\left(\frac{\phi}{2\pi}+n\right)T\right], \tag{8}$$

where $T=2\pi/\sigma_o$ is the oscillation period and $N=200$ is the number of recorded periods. Thermal convective motions, in the form of slowly drifting ascending and descending columns, could be reduced but not completely suppressed by this phase-averaging, and represent the main source of uncertainty in these experiments. However, the vorticity level associated to those convective motions appears to be negligible compared to the typical vorticity of the inertial wave. Therefore, the vorticity profiles of the wave could be safely computed from the phase-averaged velocity fields.

IV. GENERAL PROPERTIES OF THE WAVE PATTERN

A. Visualization of the wave beams

Figure 3 is a close-up view of the velocity and vorticity fields at $\sigma_o/2\Omega=0.67$, showing velocity vectors almost parallel to the beam direction $\mathbf{e}_x$ and vorticity layers of alternating sign. The angle of the beam with respect to the horizontal (see the black line) accurately follows the prediction of the dispersion relation (1), as shown in Fig. 4. In Figs. 5(a)–5(c), phase-averaged horizontal vorticity fields ω_y are shown for three equally spaced values of the phase. One can clearly see the location of the inertial wave inside a wavepacket that draws the classical four-ray St. Andrew's cross. The evolution of the vorticity field from Fig. 5(a) to Fig. 5(c) illustrates the propagation of the phase, in directions normal to the beams and toward the rotation axis. Some reflected wave beams of much smaller amplitude may also be distinguished on the background.

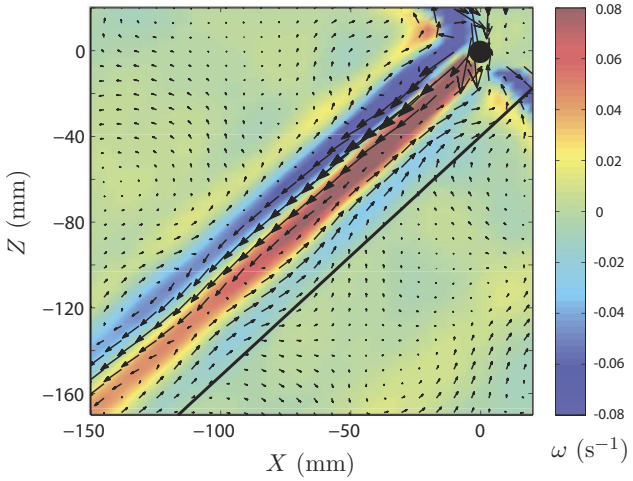

FIG. 3. (Color) Close-up view of the phase-averaged velocity (arrows) and vorticity ω_y (shade/color mapped) for an experiment performed at $\sigma_o/2\Omega=0.67$. The black line shows the direction predicted by the dispersion relation $\cos\theta=\sigma_o/2\Omega$. The filled black circle represents the oscillating cylinder. The velocity field on the right of the cylinder is not resolved because the particles are not illuminated by the laser sheet originating from the left.

B. Transient experiments

In order to characterize the formation of the inertial wave pattern as the oscillation is started, a series of transient experiments have been performed. In the case of a pure monochromatic plane wave, the front velocity of the wavepacket would be simply given by the group velocity. However, in the case of a localized wave beam, since each Fourier component k travels with its own group velocity $c_g=(\sigma/k)\tan\theta$, the shape of the wavepacket gradually evolves as the wave propagates. A rough estimate for the front velocity can be readily obtained from $V_f\simeq\sigma(\lambda/2\pi)\tan\theta$, where λ is the apparent wavelength of the wave, simply estimated as twice the distance between the locations of two successive vorticity extrema.

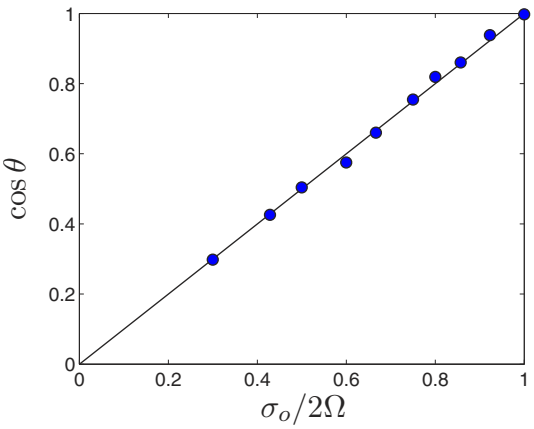

FIG. 4. (Color online) Cosine of the measured average beam angle, $\cos\theta$, as a function of the frequency ratio $\sigma_o/2\Omega$. The angle is determined from the location of the maximum of the vorticity envelope. The line shows the dispersion relation (1). Experimental uncertainties are of the order of the marker size.

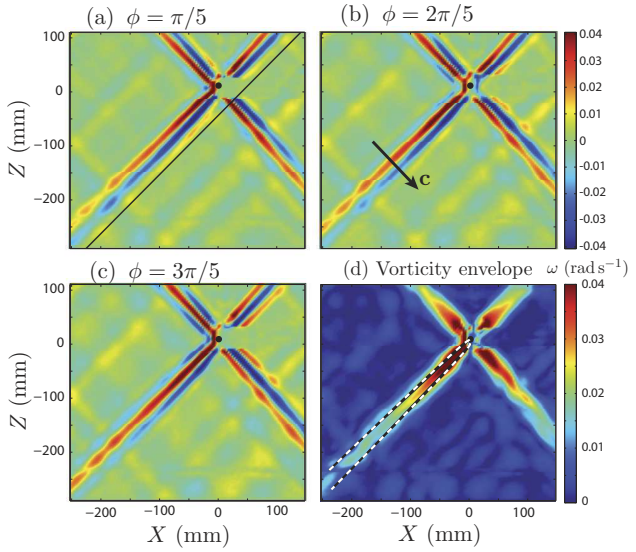

FIG. 5. (Color) Phase-averaged horizontal vorticity field ω_y for $\sigma_o/2\Omega=0.67$ at different phases: (a) $\phi=\pi/5$, (b) $\phi=2\pi/5$, and (c) $\phi=3\pi/5$. The black line in (a) draws the direction predicted by the dispersion relation. (d) Vorticity envelope field ω_0 (see Sec. V). The dashed black and white lines show the wave beam thickness predicted by the similarity solution [see Eq. (7)].

Figure 6 shows spatiotemporal diagrams of the vorticity $\omega_y(x,z=0,t)$ at the center of the beam as a function of the distance x from the wavemaker, for $\sigma_o/2\Omega$ between 0.85 and 0.50. Superimposed to these spatiotemporal images, we show the front velocity $V_f \simeq \sigma(\lambda/2\pi)\tan\theta$, starting from $x=0$ at $t=0$. Qualitative agreement with the spatiotemporal

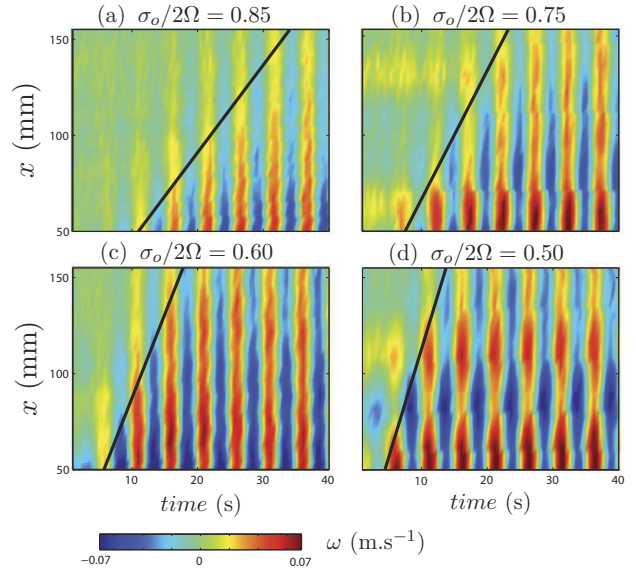

FIG. 6. (Color) Spatiotemporal representation of the vorticity ω_y along the wave beam, where space is the distance x to the oscillating cylinder, for experiments performed at $\sigma_o/2\Omega=0.85,0.75,0.60,0.50$. Black lines originating at $(x=0,t=0)$ trace the front velocity $V_f=\sigma(\lambda/2\pi)\tan\theta$ estimated from the apparent wavelength (see Sec. V A). $t=0$ corresponds to the start of the oscillation.

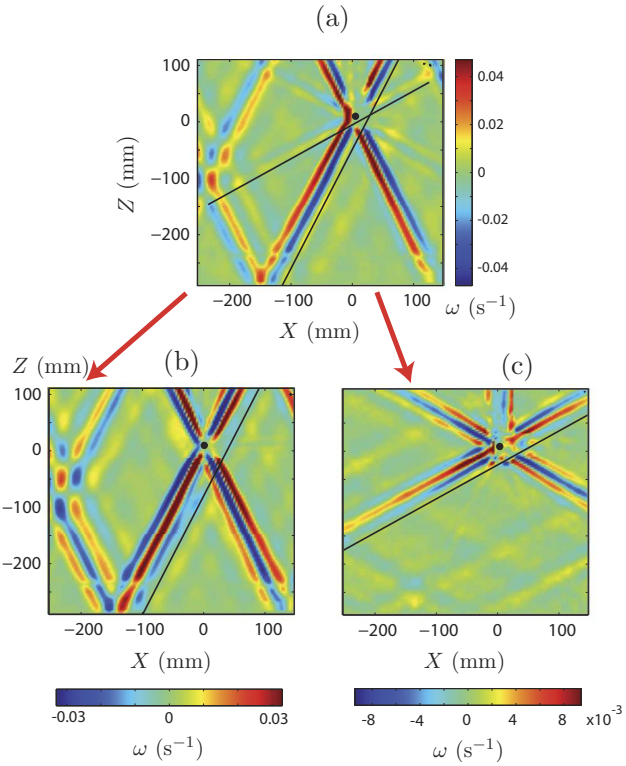

FIG. 7. (Color) (a) Phase-averaged vorticity field ω_y for an experiment performed at $\sigma_o/2\Omega=0.43$, showing both the fundamental $(n=1)$ and the second harmonic $(n=2)$ wave beams. The corresponding frequency-filtered vorticity fields are extracted in (b) and (c).

diagrams is obtained, indicating that the propagation of the wave envelope is indeed compatible with this simple estimate of the front velocity.

Further quantitative estimate of the front velocity would require us to extract the instantaneous wave envelope from those spatiotemporal diagrams, which is difficult because the front velocity and the phase velocity are of the same order. This property actually prevents a safe extraction of a longitudinal wavepacket envelope using standard temporal averaging over small time windows.

C. Generation of harmonics

Returning to steady waves, we now characterize the generation of higher order wave beams that take place at low forcing frequency. According to the dispersion relation, an harmonic wave of order $n \geq 2$ is allowed to develop whenever $n\sigma_o/2\Omega < 1$. Such harmonic waves of order $n \geq 2$ may originate either from a residual nonharmonic component of the wavemaker oscillation profile $Z_0(t)$, or from inertial nonlinear effects in the flow in the vicinity of the wavemaker, which may exist at the Reynolds number $\mathrm{Re} \simeq 20$ considered here.

In Fig. 5, for $\sigma_o/2\Omega=0.67$, only the fundamental wave $(n=1)$ can be seen. On the other hand, in Fig. 7(a), for $\sigma_o/2\Omega=0.43$, a second harmonic wave beam is clearly present, propagating at an angle closer to the horizontal, as expected from the dispersion relation. This is confirmed by Figs. 7(b) and 7(c), showing the corresponding frequency-

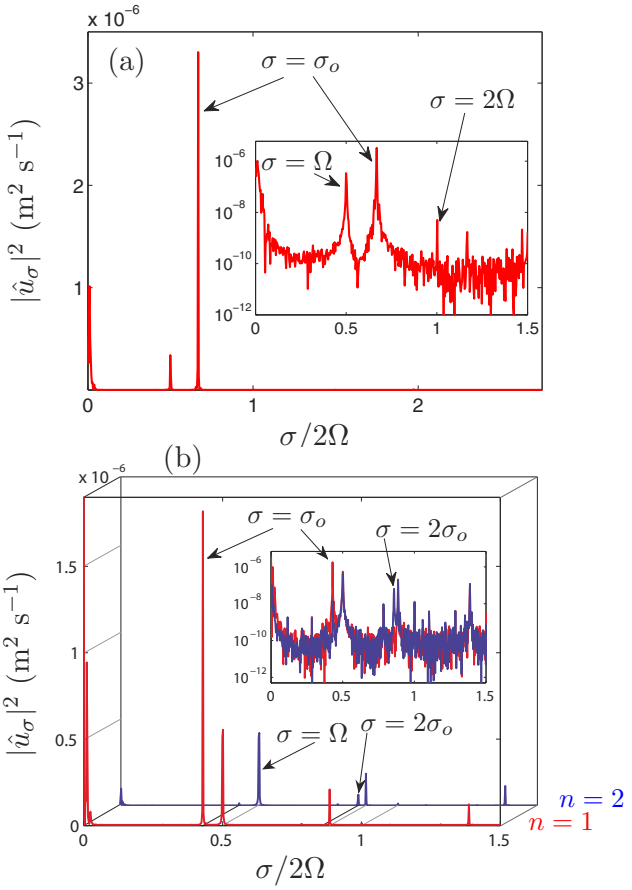

FIG. 8. (Color online) Energy spectrum of the velocity time series measured at the center of the wave beam of interest, at a fixed distance $x_0=100$ mm from the wavemaker. (a) $\sigma_o/2\Omega=0.67$, showing a single peak at the forcing frequency. (b) $\sigma_o/2\Omega=0.43$, showing measurements performed in the fundamental beam $n=1$ (light gray in print, red online) and in the second harmonic beam $n=2$ (dark gray in print, blue online). In (a) and (b), the inset shows the same spectrum in semilogarithmic coordinates. Additional peaks are present at $\sigma/2\Omega=0.5$ and 1, originating from mechanical noise of the rotating platform.

filtered phase-averaged vorticity fields, in (b) for the fundamental $n=1$ and in (c) for the second harmonics $n=2$.

In order to further characterize this generation of harmonics, we have performed a spectral analysis of the time series of the longitudinal velocity $u_x(t)$, measured at a given distance $x_0=100$ mm from the source, at the center of each wave beam. The energy spectrum $|\hat{u}_\sigma|^2$, where $\hat{u}_\sigma$ is the temporal Fourier transform of $u_x(t)$, is shown in Fig. 8 for the two cases $\sigma_o/2\Omega=0.67$ and 0.43. In both cases, the spectra are clearly dominated by the fundamental forcing frequency σ_o. Two other peaks are also found, at $\sigma=\Omega$ and $\sigma=2\Omega$, originating from the residual modulation of the angular velocity of the platform, as discussed in Sec. III B (the energy of those peaks is typically three to ten times smaller than the fundamental one). It has been checked that these two peaks are also present when the cylinder is not oscillating, confirming that they are not linked to the inertial wave beam. Computing the velocity field bandpass filtered at $\sigma=\Omega$ actually shows that the mechanical noise at Ω excites a high order spatial structure characteristic of a resonating inertial mode of the container.[23] This is not the case for the peak at $\sigma=2\Omega$, which theoretically cannot be associated to an inertial mode. One can also see a peak at $\sigma\simeq 0$, probably originating from the slowly drifting thermal convection columns discussed in Sec. III B, which are of significant amplitude compared to the inertial waves.

As expected, no harmonic frequency $n\sigma_o$ $(n\geq 2)$ is found in the spectrum for $\sigma_o/2\Omega=0.67$ [see Fig. 8(a)], but a second harmonic $n=2$ is indeed present for $\sigma_o/2\Omega=0.43$ [see Fig. 8(b)]. In this case, the energy ratio of the first to the second harmonics, each of them being measured at a distance $x_0=100$ mm from the source on the corresponding beam, is $|\hat{u}_{2\sigma}|^2/|\hat{u}_\sigma|^2\simeq 0.036$. (Note that the additional peak at $\sigma/2\Omega=0.89$, immediately to the right of the second harmonic peak at $2\sigma_o/2\Omega=0.86$, originates from a residual vibration of the camera with respect to the water tank at this particular angular velocity Ω). As $\sigma_o/2\Omega$ is further decreased, the ratio $|\hat{u}_{2\sigma}|^2/|\hat{u}_\sigma|^2$ increases, reaching 0.05 for $\sigma_o/2\Omega=0.30$, and even higher order harmonics emerge, although with very weak amplitude.

V. TEST OF THE SIMILARITY SOLUTION

A. Velocity and vorticity envelopes

We now focus on the dependence of the wavepacket shape and the viscous spreading of the wave beam with the distance x from the source. Figures 9(a) and 9(b) illustrate the shape of the phase-averaged velocity and vorticity profiles, respectively, for two values of the phase ϕ_0 and $\phi_0+2\pi/5$. The wavepacket envelopes are defined as

$$u_0(x,z)=\sqrt{2\langle u_x(x,z,\phi)^2\rangle_\phi}$$

(and similarly for ω_0), where $\langle\cdot\rangle_\phi$ is the average over all phases ϕ. Although the measured normalized envelopes compare well with the normalized envelopes predicted from the similarity solutions $[E_m(\eta)/E_m(0)$, with $m=0$ for the velocity and $m=1$ for the vorticity], the agreement is actually better for the vorticity. This is probably due to the velocity contamination originating from the residual angular velocity modulation of the platform and the slight thermal convection effects discussed in Sec. III B. The better defined vorticity envelopes actually confirm that those velocity contaminations have a negligible vorticity contribution. For this reason, we will concentrate only on the vorticity field in the following.

It is worth to examine here the singular situation $\sigma_o/2\Omega=1$, in which the similarity solution is no longer valid. In this situation, the phase velocity is strictly vertical and the group velocity vanishes. The upward and downward beams are expected to superimpose and generate a stationary wave pattern in the horizontal plane $Z=z=0$. Figure 10 shows the velocity envelope $u_0(x_0,z)$ and three phase-averaged profiles as a function of the transverse coordinate z. The observed wave is actually stationary at the center of the wavepacket (see the velocity node and vorticity maximum for $z=0$), and shows outward propagation on each side of the wavepacket.

Returning to the standard situation $\sigma_o/2\Omega<1$, the vorticity amplitude at a given location x is defined as the maximum of the vorticity envelope at the center of the beam,

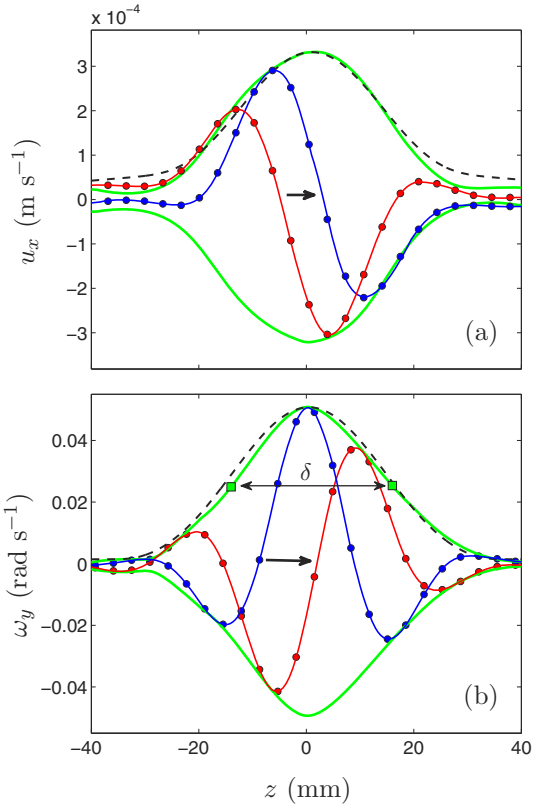

FIG. 9. (Color online) (a) Velocity envelope $u_0(x_0,z)$ and two velocity profiles $u_x(x_o,z,\phi)$ for two values of the phase ϕ, as a function of the transverse coordinate z at a fixed distance x_o=100 mm from the wavemaker for $\sigma_o/2\Omega$=0.67. (b) Corresponding vorticity envelope $\omega_0(x_0,z)$ and vorticity profiles $\omega_y(x_0,z,\phi)$. (●) Data points with spline interpolations of the profiles in continuous lines. Light gray (green online) continuous lines: Envelopes computed from the interpolated profiles. Dashed curves: similarity solution normalized by the measured maximum. Both profiles are averaged over a distance range $90<x<110$ mm from the wavemaker. δ is the envelope thickness at midheight.

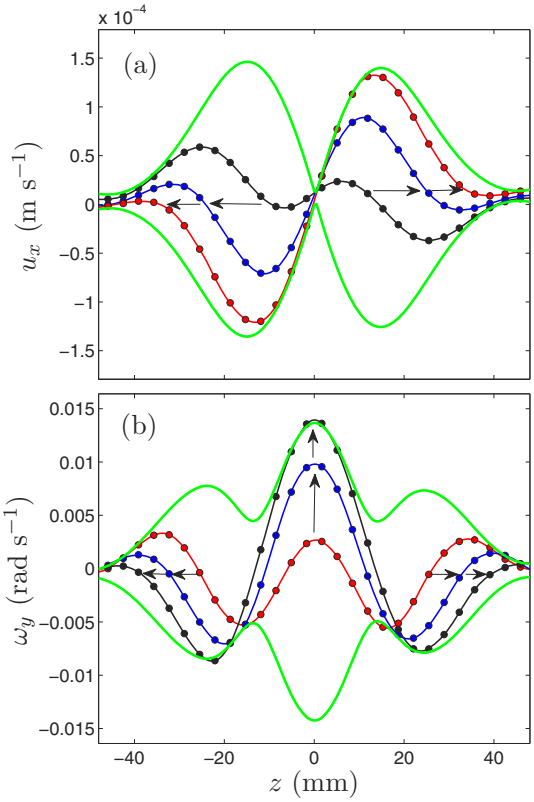

FIG. 10. (Color online) (a) Velocity envelope $u_0(x_0,z)$ and three velocity profiles $u_x(x_0,z,\phi)$ as a function of the transverse coordinate z at a fixed distance x_o=70 mm (average over $50<x<90$ mm) from the wavemaker for $\sigma_o/2\Omega$=1. (b) Corresponding vorticity envelope and vorticity profiles. The arrows indicate the time evolution of the profiles. The interference of the upward and downward wave beams produces a stationary wave pattern at z=0 with a velocity node and a vorticity maximum. Same data representations as in Fig. 9.

$\omega_{\max}(x)=\omega_0(x,z=0)$. The thickness of the wavepacket $\delta(x)$ is defined from the width at midheight of the envelope, such that

$$\omega_0[x,\delta(x)/2]=\omega_{\max}(x)/2.$$

This beam thickness δ depends both on the distance x from the source and on the viscous length ℓ [see Eqs. (5) and (7)]. In order to check those two dependencies, δ is plotted in Fig. 11(a) as a function of x at fixed $\sigma_o/2\Omega$, and in Fig. 11(b) as a function of $\sigma_o/2\Omega$ at fixed x_0. The agreement with the effective wave beam thickness $\delta_{\text{eff}}=2R+6.84\ell(x/\ell)^{1/3}$ is correct, to within 10%, which justifies the simple analysis of merged beams originating from the two virtual sources located at the top and bottom of the wavemaker. The oscillations of δ probably originate from the interaction of the principal wave beam with reflected ones. Figure 11(a) also shows the apparent wavelength $\lambda(x)$ of the wave, simply defined as twice the distance between a maximum and a minimum of the phase-averaged vorticity profiles. This apparent wavelength turns out to be even closer to the expected lengthscale δ_{eff} of Eq. (7), to within 4%, suggesting that λ is less affected by the background noise than the beam thickness. A good agreement between both δ and λ and prediction (7) is also obtained as $\sigma_o/2\Omega$ (and hence ℓ) is varied at fixed x_0, as shown in Fig. 11(b). Here again, the interaction with reflected wave beams is probably responsible for the significant scatter in this figure.

B. Decay of the vorticity envelope

The decay of the vorticity amplitude $\omega_{\max}(x)$ as a function of the distance x from the source is shown in Fig. 12. Taking the similarity solution (4) at the center of the wave beam z=0 yields

$$\omega_{\max}(x)=W_0^*\left(\frac{\ell}{x}\right)^{2/3}. \tag{9}$$

Letting the vorticity scale W_0^* as a free parameter, a power law $x^{-2/3}$ is found to provide a good fit for the overall decay of $\omega_{\max}(x)$. Some marked oscillations are however clearly visible, e.g., at x between 220 and 320 mm for $\sigma_o/2\Omega$ =0.85. Those oscillations appear at locations where reflected wave beams interact with the principal one, inducing modulations of the wave amplitude. This interpretation is confirmed by the fact that (i) the observed modulation has a wavelength of 45 mm, which corresponds to the apparent wavelength of the wave, and that (ii) in Fig. 5, corresponding

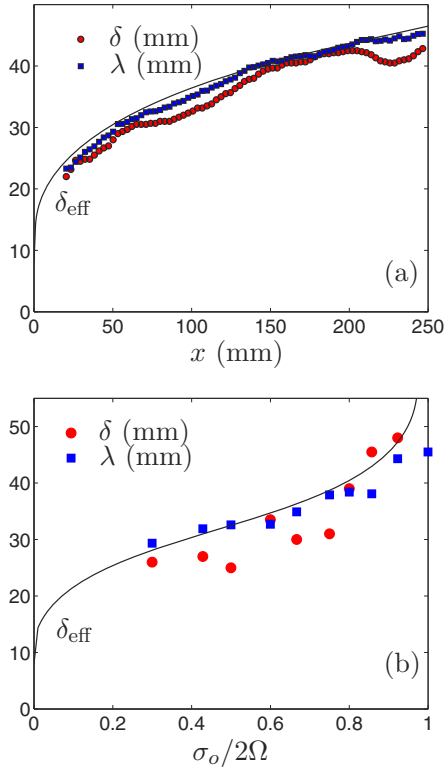

FIG. 11. (Color online) (●) Wave beam thickness δ and (■) apparent wavelength λ; (a) as a function of the distance x from the wavemaker for $\sigma_o/2\Omega=0.67$; (b) as a function of $\sigma_o/2\Omega$ at a distance $x_o=100$ mm from the wavemaker. In both plots, the line shows the predicted effective wave beam thickness δ_{eff} (7).

to $\sigma_o/2\Omega=0.67$, a modulation of the principal wave beam by a reflected one can be clearly seen at a distance of about 250 mm from the source.

The vorticity scale W_0^* is theoretically related to the velocity scale U_0^* through the relation $W_0^*=[E_1(0)/E_0(0)]U_0^*/\ell \simeq 0.506U_0^*/\ell$ (see the Appendix). Since the wavemaker velocity is $\sigma_o A$, the velocity scale U_0^* is expected to write in the form $\sigma_o A g(\theta)$, where the unknown function $g(\theta)$ describes the forcing efficiency of the wavemaker. Accordingly, the forcing efficiency can be deduced from the vorticity data, by computing

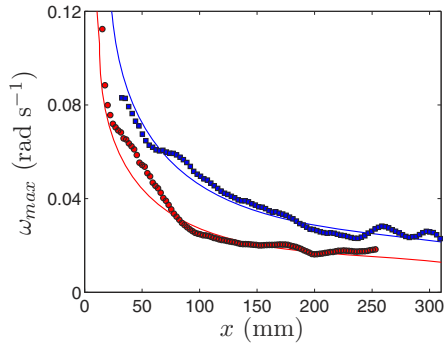

FIG. 12. (Color online) Vorticity amplitude $\omega_{\max}(x)$ as a function of the distance x from the wavemaker, and best fit with the law $W_0^*(x/\ell)^{-2/3}$. (■) $\sigma_o/2\Omega=0.67$. (●) $\sigma_o/2\Omega=0.85$.

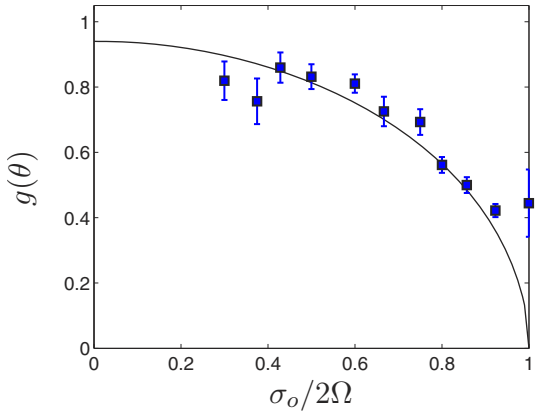

FIG. 13. (Color online) Forcing efficiency $g(\theta)$ defined from Eq. (10) as a function of $\sigma_o/2\Omega$. Squares and errorbars represent the mean and the standard deviation for each $\sigma_o/2\Omega$, respectively, reflecting the variability of $\omega_{\max}$ along x. The line shows the best fit according to Eq. (11), with $g_0=0.94\pm0.10$.

$$g(\theta)=\frac{W_0^*}{0.506\sigma_o A/\ell}=\frac{\omega_{\max}(x/\ell)^{2/3}}{0.506\sigma_o A/\ell} \tag{10}$$

for each value of $\sigma_o/2\Omega$. Measurements of $g(\theta)$ are plotted as a function of $\sigma_o/2\Omega$ in Fig. 13. As expected, this forcing efficiency decreases as $\sigma_o/2\Omega$ is increased, i.e., as the wave beam becomes closer to the horizontal. In the limit $\sigma_o/2\Omega\to1$, the vertically oscillating wavemaker becomes indeed very inefficient to force the quasihorizontal velocities of the wave.

An analytical expression for the function $g(\theta)$ would require us to solve exactly the velocity field in the vicinity of the wavemaker and, in particular, the coupling between the oscillating boundary layer and the wave far from the source, which is beyond the scope of this paper. In the case of a cylinder, a naive estimate of $g(\theta)$ could however be obtained, assuming that the effective velocity forcing is simply given by the projection of the wavemaker velocity along the wave beam direction, yielding

$$g(\theta)=g_0\sin\theta=g_0\sqrt{1-\left(\frac{\sigma_o}{2\Omega}\right)^2}, \tag{11}$$

with g_0 a constant to be determined. A best fit of the experimental values of $g(\theta)$ with this law leads to $g_0 \simeq 0.94\pm0.10$ (see Fig. 13), and reproduces well the decrease of $g(\theta)$ as $\sigma_o/2\Omega$ is increased. The fact that g_0 is found close to 1 indicates that the inertial wave beam is essentially fed by the oscillating velocity field in the close vicinity of the wavemaker. The discrepancy at large forcing frequency may be due to the breakdown of the similarity solution as the angle θ approaches 0.

VI. STOKES DRIFT

We finally consider the possibility of Stokes drifts which may take place in a localized inertial wave beam. Two drift mechanisms may be expected in this geometry: a first one in the vertical plane (x,z) and a second one along the invariant direction y. The first drift mechanism is similar to the one

discussed by Kistovich and Chashechkin[24] in the case of a two-dimensional internal wave beam, leading to a mass transport of different signs on each side of the wave beam. The second drift mechanism is specific to the inertial wave and originates from the circular motion in the (x,y) plane of the wave.

The physical mechanism for this second drift is as follows. A fluid particle in the inertial wave approximately describes a circular orbit. During this orbit, the particle experiences a larger velocity along y when it is closer than when it is further from the wavemaker (see Fig. 1), resulting in a net mass transport along y. This is similar to the classical Stokes drift for surface waves, which is horizontal because of the decay of the velocity magnitude with depth.[25] Here the drift is due to the viscous decay of the wave which takes place along the direction of propagation and is expected, in general, in the direction given by $\mathbf{\Omega}\times\mathbf{c}_g$.

Attempts to detect this effect have been carried out from PIV measurements in vertical planes (Y,Z). Because of the weakness of the considered drift, the measurements have been performed very close to the wavemaker, for X between 5 and 30 mm, where a stronger effect is expected. However, those attempts were not successful, probably because the drift, if present, is hidden by the stronger fluid motions induced by the residual thermal convection columns, as discussed in Sec. III B.

The magnitude of the expected Stokes drift cannot be easily inferred from the complex motion of the fluid particles close to the wavemaker. An estimate could however be obtained in the far field, from the similarity solution of the wave beam. We consider, for simplicity, a particle lying at the center of the wave beam $(z=0)$, at a mean distance x_0 from the source, describing approximate circles of gyration radius $a\simeq|\mathbf{u}(x_0)|/\sigma$ in the tilted plan (x,y). The expected drift velocity $\bar{\mathbf{v}}_S$ can be approximated by computing the velocity difference between the two extreme points x_0-a and x_0+a of the orbit, yielding, to first order in a/x_0, to[26]

$$\bar{v}_{Sy}(x_0)\simeq\frac{2}{3}\frac{U_0^{*2}\ell^{2/3}}{\sigma x_0^{5/3}}. \tag{12}$$

The steep decrease as $x_0^{-5/3}$ confirms that the drift should be essentially present close to the wavemaker. Although this formula is expected to apply only in the far-field wave (typically for $x_0>40\ell$, see the Appendix), its extrapolation close to the wavemaker, for $x_0\simeq 10\ell\simeq 2R$, gives $\bar{v}_{Sy}\simeq 0.1$ mm s^{-1}. This expected drift velocity is about 10% of the wave velocity at the same location, but it turns out to remain smaller than the velocity contamination due to the thermal convection columns. Although the phase-averaging proved to be efficient to extract the inertial wave field from the measured velocity field because of a sufficient frequency separation between convection effects and the inertial wave, it fails here to extract the much weaker velocity signal expected from this drift since it is of zero frequency and hence mixed with the very low frequency of those convective motions.

VII. CONCLUSION

In this paper, particle image velocimetry measurements have been used to provide quantitative insight into the structure of the inertial wave emitted by a vertically oscillating horizontal cylinder in a rotating fluid. Large vertical fields of view could be achieved, thanks to a new rotating platform, allowing for direct visualization of the cross-shaped St. Andrew's wave pattern.

It must be noted that performing accurate PIV measurements of the very weak signal of an inertial wave is a challenging task. In spite of the high stability of the angular velocity of the platform $(\Delta\Omega/\Omega<5\times10^{-4})$, the velocity signal-to-noise ratio remains moderate here. Additionally, slowly drifting vertical columns are present because of residual thermal convection effects, and are found to account for most of velocity noise in these experiments. Those thermal convection effects are very difficult to avoid in large containers, even in an approximately thermalized room. However, this noise can be significantly reduced by a phase-averaging over a large number of oscillation periods. This concern is not present for internal waves in stratified fluids because residual thermal motions are inhibited by the stable stratification. This emphasizes the intrinsic difficulty of experimental investigation of inertial waves, in contrast to internal waves which have been the subject of a number of studies (although it must be noted that achieving a strictly linear stratification through the whole fluid volume, and hence a strictly homogeneous Brunt–Väsäilä frequency, is also a delicate issue).

In this article, emphasis has been given on the spreading of the inertial wave beam induced by viscous dissipation. The attenuation of a two-dimensional wave beam emitted from a linear source is purely viscous, whereas it combines viscous and geometrical effects in the case of a conical wave emitted from a point source. The linear theory presented in this paper is derived under the classical boundary layer assumption first introduced by Thomas and Stevenson[7] for two-dimensional internal waves in stratified fluids. The measured thickening of the wave beam and the decay of the vorticity envelope are quantitatively fitted by the scaling laws of the similarity solutions of this linear theory, $\delta(x)\sim x^{1/3}$ and $\omega_{\max}(x)\sim x^{-2/3}$, where x is the distance from the source. More precisely, we have shown that the amplitude of the vorticity envelope could be correctly predicted from the velocity disturbance induced by the wavemaker, by introducing a simple forcing efficiency function $g(\theta)$, where θ is the angle of the wave beam.

Finally, it is shown that an attenuated inertial wave beam should, in principle, generate a Stokes drift along the wavemaker, in the direction given by $\mathbf{\Omega}\times\mathbf{c}_g$, where $\mathbf{c}_g$ is the group velocity. However, in spite of the high precision of the rotating platform and the PIV measurements, attempts to detect this drift were not successful in the present configuration. Velocity fluctuations induced by thermal convection effects probably hide this slight mean drift velocity, suggesting that an improved experiment with a very carefully controlled temperature stability would be necessary to detect this very weak effect.

ACKNOWLEDGMENTS

We acknowledge A. Aubertin, L. Auffray, C. Borget, G.-J. Michon, and R. Pidoux for experimental help, and T. Dauxois, L. Gostiaux, M. Mercier, C. Morize, M. Rabaud, and B. Voisin for fruitful discussions. The new rotating platform Gyroflow was funded by the ANR (Grant No. 06-BLAN-0363-01 "HiSpeedPIV") and the "Triangle de la Physique."

APPENDIX: SIMILARITY SOLUTION FOR A VISCOUS PLANAR INERTIAL WAVE

In this appendix, we derive the similarity solution for a viscous planar inertial wave, following the procedure first described by Thomas and Stevenson[7] for internal waves.

We consider the inertial wave emitted from a thin linear disturbance invariant along the Y axis and oscillating along Z with a pulsation σ in a viscous fluid rotating at angular velocity $\mathbf{\Omega}=\Omega\mathbf{e}_Z$. Since the linear source is invariant along Y, so will the wave beams, and the energy propagates in the (X,Z) plan. In the following, we consider only the wave beam propagating along $X>0$ and $Z>0$.

The linearized vorticity equation is

$$\partial_t\boldsymbol{\omega}=(2\mathbf{\Omega}\cdot\nabla)\mathbf{u}+\nu\nabla^2\boldsymbol{\omega}.$$

Recasting the problem in the tilted frame of the wave, $(\mathbf{e}_x,\mathbf{e}_y,\mathbf{e}_z)$, with $\mathbf{e}_y=\mathbf{e}_Y$ and $\mathbf{e}_x$ tilted of an angle $\theta=\cos^{-1}(\sigma/2\Omega)$ with the horizontal, one has $\mathbf{\Omega}=\Omega(\sin\theta\mathbf{e}_x+\cos\theta\mathbf{e}_z)$ so that $(2\mathbf{\Omega}\cdot\nabla)=2\Omega(\sin\theta\partial_x+\cos\theta\partial_z)=\sigma(\tan\theta\partial_x+\partial_z)$. Assuming that the flow inside the wave beam is quasiparallel (boundary layer approximation), i.e., such that $|u_x|,|u_y|\gg|u_z|$, $|\omega_x|,|\omega_y|\gg|\omega_z|$, and $\nabla^2\simeq\partial_z^2$, the linearized vorticity equation reduces to

$$\partial_t\omega_x=\sigma(\tan\theta\partial_x+\partial_z)u_x+\nu\partial_z^2\omega_x, \tag{A1}$$

$$\partial_t\omega_y=\sigma(\tan\theta\partial_x+\partial_z)u_y+\nu\partial_z^2\omega_y. \tag{A2}$$

We introduce the complex velocity and vorticity fields in the (x,y) plan as

$$U=u_x+iu_y,\quad W=\omega_x+i\omega_y.$$

Since, within the quasiparallel approximation, one has $W=i\partial_zU$, the combination (A1)+i(A2) yields

$$i\partial_t\partial_zU=\sigma(\tan\theta\partial_x+\partial_z)U+i\nu\partial_z^3U. \tag{A3}$$

Searching solutions in the form $U=U_0e^{-i\sigma t}$, Eq. (A3) becomes

$$\partial_xU_0+i\ell^2\partial_z^3U_0=0, \tag{A4}$$

where we have introduced the viscous scale ℓ (2). Equation (A4) admits similarity solutions as a function of the variable

$$\eta=\frac{z}{x^{1/3}\ell^{2/3}}, \tag{A5}$$

which are of the form

$$U_0(x,z)=\tilde{U}_0\left(\frac{\ell}{x}\right)^{1/3}f(\eta), \tag{A6}$$

where $\tilde{U}_0$ is a velocity scale and $f(\eta)$ is a nondimensional complex function of the reduced transverse coordinate η. Plugging such similarity solution (A6) into Eq. (A4) shows that $f(\eta)$ is a solution of the ordinary differential equation

$$3f'''+i(f+\eta f')=0, \tag{A7}$$

which is identical to Eq. (16) derived by Thomas and Stevenson[7] for the pressure field of internal waves. Following their development, we introduce the family of functions f_m defined through

$$f_m(\eta)=c_m+is_m=\int_0^\infty K^me^{-K^3}e^{iK\eta}dK, \tag{A8}$$

where c_m and s_m are real, and such that $f_0(\eta)$ is a solution of Eq. (A7).

The velocity in the plan of the wave beam is therefore given by $u_x=\Re\{U\}$ and $u_y=\Im\{U\}$, leading to

$$u_x=\frac{U_0^*}{E_0(0)}\left(\frac{\ell}{x}\right)^{1/3}[c_0(\eta)\cos(\sigma t)+s_0(\eta)\sin(\sigma t)],$$

$$u_y=\frac{U_0^*}{E_0(0)}\left(\frac{\ell}{x}\right)^{1/3}[s_0(\eta)\cos(\sigma t)-c_0(\eta)\sin(\sigma t)],$$

with $U_0^*=E_0(0)\tilde{U}_0\simeq0.893\tilde{U}_0$, where we introduce the family of envelopes $E_m(\eta)=|f_m(\eta)|=(c_m^2+s_m^2)^{1/2}$ for $m=0,1$.

Similarly, the vorticities in the plan of the wave beam are $\omega_x=\Re\{W\}$ and $\omega_y=\Im\{W\}$ so that

$$\omega_x=\frac{W_0^*}{E_1(0)}\left(\frac{\ell}{x}\right)^{2/3}[-c_1(\eta)\cos(\sigma t)-s_1(\eta)\sin(\sigma t)],$$

$$\omega_y=\frac{W_0^*}{E_1(0)}\left(\frac{\ell}{x}\right)^{2/3}[-s_1(\eta)\cos(\sigma t)+c_1(\eta)\sin(\sigma t)],$$

with $W_0^*=[E_1(0)/E_0(0)]U_0^*/\ell\simeq0.506U_0^*/\ell$.

The velocity and vorticity envelopes, defined as $u_0=(\langle u_x^2\rangle+\langle u_y^2\rangle)^{1/2}$ and $\omega_0=(\langle\omega_x^2\rangle+\langle\omega_y^2\rangle)^{1/2}$, where $\langle\cdot\rangle$ is the time-average over one wave period, are given by

$$u_0=U_0^*\left(\frac{\ell}{x}\right)^{1/3}\frac{E_0(\eta)}{E_0(0)},$$

$$\omega_0=W_0^*\left(\frac{\ell}{x}\right)^{2/3}\frac{E_1(\eta)}{E_1(0)}.$$

The two normalized envelopes $E_m(\eta)/E_m(0)$ are compared in Fig. 14. Interestingly, they closely coincide up to $\eta\simeq4$, but the vorticity envelope decreases much more rapidly than the velocity envelope as $\eta\to\infty$ (one has $E_m\propto1/\eta^{m+1}$ for $\eta\gg1$). The thickness $\eta_{1/2}$ of the two envelopes, defined such that

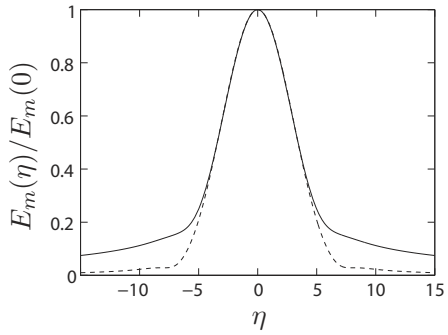

FIG. 14. Normalized velocity [(—) $m=0$] and vorticity [(- -) $m=1$] envelopes of the similarity solutions.

$E_m(\eta_{1/2}/2)=E_m(0)/2$, turns out to be almost equal: $\eta_{1/2}\simeq 6.841$ for $m=0$ and $\eta_{1/2}\simeq 6.834$ for $m=1$. In dimensional units, the wave thickness is thus given by Eq. (5).

It is interesting to note that velocity and vorticity in the present analysis are analogous to the pressure and velocity in the analysis of Thomas and Stevenson.[7] One consequence is that the lateral decay of the velocity envelope is sharper for an internal wave (as $1/\eta^2$) than for an inertial wave (as $1/\eta$).

Finally, the z component of the velocity is obtained using incompressibility $(\partial_x u_x+\partial_z u_z=0)$,

$$u_z=\frac{1}{3}\frac{U_0^*}{E_0(0)}\left(\frac{\ell}{x}\right)\eta[c_0(\eta)\cos(\sigma t)+s_0(\eta)\sin(\sigma t)], \tag{A9}$$

which is zero in the center of the wave beam $(\eta=0)$. Interestingly, the envelope of u_z is given by $\eta E_0(\eta)$, which tends toward 1 as $\eta\to\infty$ so that no thickness could be defined for u_z.

The streamlines projected in the vertical plane (x,z) can be deduced from the ratio of the velocity components,

$$\frac{u_z}{u_x}=\frac{1}{3}\frac{z}{x}, \tag{A10}$$

which integrates to $x=cz^{1/3}$. This result shows that the streamlines lie in surfaces of constant η, invariant along y. As a consequence, a particle trajectory is an approximate circle wrapped on a curved surface, such that $z=\eta^*\ell^{2/3}x^{1/3}$, with η^* given by the initial location of the particle.

Finally, we note that the quasiparallel approximation used in the present analysis is satisfied for $|u_z|/|u_x|\ll 1$. Using $|u_z|/|u_x|=\eta^{1/3}(\ell/x)^{1/3}/3$, and evaluating the envelope ratio at the boundary of the wave, i.e., for $\eta=\eta_{1/2}/2\simeq 3.42$, this criterion is satisfied within 10% for $x>38\ell$.

[1] H. Greenspan, *The Theory of Rotating Fluids* (Cambridge University Press, London, 1968).
[2] J. Lighthill, *Waves in Fluids* (Cambridge University Press, London, 1978).
[3] J. Pedlosky, *Geophysical Fluid Dynamics* (Springer-Verlag, Heidelberg, 1987).
[4] C. Cambon, "Turbulence and vortex structures in rotating and stratified flows," Eur. J. Mech. B/Fluids **20**, 489 (2001).
[5] O. M. Phillips, "Energy transfer in rotating fluids by reflection of inertial waves," Phys. Fluids **6**, 513 (1963).
[6] D. E. Mowbray and B. S. H. Rarity, "A theoretical and experimental investigation of the phase configuration of internal waves of small amplitude in a density stratified liquid," J. Fluid Mech. **28**, 1 (1967).
[7] N. H. Thomas and T. N. Stevenson, "A similarity solution for viscous internal waves," J. Fluid Mech. **54**, 495 (1972).
[8] B. R. Sutherland, S. B. Dalziel, G. O. Hughes, and P. F. Linden, "Visualization and measurement of internal waves by 'synthetic Schlieren.' Part 1. Vertically oscillating cylinder," J. Fluid Mech. **390**, 93 (1999).
[9] M. R. Flynn, K. Onu, and B. R. Sutherland, "Internal wave excitation by a vertically oscillating sphere," J. Fluid Mech. **494**, 65 (2003).
[10] L. Gostiaux, T. Dauxois, H. Didelle, J. Sommeria, and S. Viboud, "Quantitative laboratory observations of internal wave reflection on ascending slopes," Phys. Fluids **18**, 056602 (2006).
[11] L. Gostiaux, H. Didelle, S. Mercier, and T. Dauxois, "A novel internal waves generator," Exp. Fluids **42**, 123 (2007).
[12] D. Fultz, "A note on overstability and the elastoid-inertia oscillations of Kelvin, Soldberg, and Bjerknes," J. Meteorol. **16**, 199 (1959).
[13] A. D. McEwan, "Inertial oscillations in a rotating fluid cylinder," J. Fluid Mech. **40**, 603 (1970).
[14] R. Manasseh, "Distortions of inertia waves in a rotating fluid cylinder forced near its fundamental mode resonance," J. Fluid Mech. **265**, 345 (1994).
[15] L. R. M. Maas, "Wave focusing and ensuing mean flow due to symmetry breaking in rotating fluids," J. Fluid Mech. **437**, 13 (2001).
[16] P. Meunier, C. Eloy, R. Lagrange, and F. Nadal, "A rotating fluid cylinder subject to weak precession," J. Fluid Mech. **599**, 405 (2008).
[17] F. S. Godeferd and L. Lollini, "Direct numerical simulations of turbulence with confinement and rotation," J. Fluid Mech. **393**, 257 (1999).
[18] L. Messio, C. Morize, M. Rabaud, and F. Moisy, "Experimental observation using particle image velocimetry of inertial waves in a rotating fluid," Exp. Fluids **44**, 519 (2008).
[19] B. Voisin, "Limit states of internal wave beams," J. Fluid Mech. **496**, 243 (2003).
[20] K. S. Peat, "Internal and inertial waves in a viscous rotating stratified fluid," Appl. Sci. Res. **33**, 481 (1978).
[21] D. G. Hurley and G. Keady, "The generation of internal waves by vibrating elliptic cylinders. Part 2. Approximate viscous solution," J. Fluid Mech. **351**, 119 (1997).
[22] DAVIS, LaVision GmbH, Anna-Vandenhoeck-Ring 19, 37081 Goettingen, Germany, complemented with the PIVMat toolbox for MATLAB, http://www.fast.u-psud.fr/pivmat.
[23] L. R. M. Maas, "On the amphidromic structure of inertial waves in a rectangular parallelepiped," Fluid Dyn. Res. **33**, 373 (2003).
[24] Y. V. Kistovich and Y. D. Chashechkin, "Mass transport and the force of a beam of two-dimensional periodic internal waves," J. Appl. Math. Mech. **65**, 237 (2001).
[25] M. S. Longuet-Higgins, "Mass transport in water waves," Philos. Trans. R. Soc. London, Ser. A **245**, 535 (1953).
[26] A numerical integration of the particle trajectory in the center of the beam $(z=0)$ actually shows that the numerical prefactor in Eq. (12) is 1.047 instead of 2/3.

Inertial waves and modes excited by the libration of a rotating cube

Jean Boisson,[1,a)] Cyril Lamriben,[1,b)] Leo R. M. Maas,[2,c)]
Pierre-Philippe Cortet,[1,d)] and Frédéric Moisy[1,e)]
[1]*Laboratoire FAST, CNRS, Université Paris-Sud, UPMC, France*
[2]*NIOZ Royal Netherlands Institute for Sea Research, Texel, The Netherlands*

(Received 8 March 2012; accepted 9 June 2012; published online 9 July 2012)

We report experimental measurements of the flow in a cubic container submitted to a longitudinal libration, i.e., a rotation modulated in time. Velocity fields in a vertical and a horizontal plane are measured in the librating frame using a corotating particle image velocimetry system. When the libration frequency σ_0 is smaller than twice the mean rotation rate, Ω_0, inertial waves can propagate in the interior of the fluid. At arbitrary excitation frequencies $\sigma_0 < 2\Omega_0$, the oscillating flow shows two contributions: (i) a basic flow induced by the libration motion, and (ii) inertial wave beams propagating obliquely upward and downward from the horizontal edges of the cube. In addition to these two contributions, inertial modes may also be excited at some specific resonant frequencies. We characterize in particular the resonance of the mode of lowest order compatible with the symmetries of the forcing, noted [2,1,+]. By comparing the measured flow fields to the expected inviscid inertial modes computed numerically [L. R. M. Maas, "On the amphidromic structure of inertial waves in rectangular parallelepiped," Fluid Dyn. Res. **33**, 373 (2003)], we show that only a subset of inertial modes, matching the symmetries of the forcing, can be excited by the libration. © *2012 American Institute of Physics*. [http://dx.doi.org/10.1063/1.4731802]

I. INTRODUCTION

Rotating fluids support the existence of a singular class of waves called inertial waves,[1–3] which are anisotropic and propagate because of the restoring nature of the Coriolis force. These waves exist only for excitation frequencies σ_0 lower than twice the rotation rate Ω_0. In a confined volume of fluid, inertial waves may become phase-coherent and experience a resonance due to multiple reflections over the container walls, leading to the so-called inertial modes. These inertial modes are relevant to geophysical and astrophysical flows (in liquid cores of planets and stars), but also to mechanical engineering flows (e.g., in liquid-filled projectiles).

Inviscid inertial modes are the eigenmodes of a given container geometry, and can be found in general when the walls are either normal, or parallel to the rotation axis,[1,4] but also in some specific cases such as spheres, spheroids[5] and, to some extent, in spherical shells (namely for so-called R-modes that lack radial displacement). However, in general, when sloping walls are present, the wave focusing and defocusing induced by the peculiar reflection law of inertial waves[6] precludes the existence of inviscid eigenmodes, and the concentration of energy along particular beams leads to wave attractors.[7] The resonance frequencies of inviscid inertial modes can be derived analytically only in some specific geometries, such as cylinders, spheres, and spheroids.[1,5,8] In the case of a

[a)]Electronic mail: boisson@fast.u-psud.fr.
[b)]Electronic mail: lamriben@fast.u-psud.fr.
[c)]Electronic mail: Leo.Maas@nioz.nl.
[d)]Electronic mail: ppcortet@fast.u-psud.fr.
[e)]Electronic mail: moisy@fast.u-psud.fr.

parallelepipedic container, such as used in the experiments presented here, the frequencies and the spatial structure of the inviscid inertial modes have been determined numerically.[9]

In geophysical and astrophysical flows, several types of forcing may be at the origin of the excitation of inertial modes. Inertial modes have been excited experimentally in a spherical cavity by a longitudinal libration[10]—i.e., a time modulation of the rotation rate—and have recently been described in numerical simulations in spheres and spherical shells.[11–14] Precession[15–17] and periodic deformation of the walls modeling gravitational tides[18,19] are other examples of forcing, providing an efficient generation of inertial modes. These inertial modes have been proposed to contribute, through nonlinear self-interaction, to the generation of steady zonal flows, which are visible for instance in the atmosphere of gaseous planets like Jupiter.[19–21]

Although axisymmetric geometries have been primarily considered to observe and characterize inertial modes, non-axisymmetric geometries such as parallelepipeds[9] are also of fundamental interest. In particular, the symmetries of the container, the symmetries of the forcing, and the role of viscosity, are critical parameters in determining which inertial modes can be excited.

Inertial modes may be present in any laboratory experiment performed in a rotating container. They have been for instance detected in ensemble averages of turbulence generated by the translation of a grid in a rotating container.[22–24] When present, these modes may couple to the turbulence, and have a profound influence on its statistical properties. In particular, turbulence in the presence of inertial modes, which are non homogeneous by nature, cannot be considered as freely decaying, raising the issue of the relevance of the homogeneous framework to describe rotating turbulence in laboratory experiments.

In this paper, we investigate the spatial structure of the oscillating flow generated by the longitudinal libration of a cube, and we characterize the efficiency of this configuration to excite inertial modes. Measurements are performed both in a vertical and in a horizontal plane (the rotation axis is vertical) using a co-rotating two-dimensional particle image velocimetry (PIV) system. For libration frequencies lower than twice the rotation rate $\sigma_0 < 2\Omega_0$, we observe, in addition to the basic oscillating flow induced by the libration, the propagation of oblique inertial wave beams emitted from the horizontal edges of the cube. These wave beams, similar to the ones observed in cylindrical geometry,[4,25] originate from the convergence of Ekman fluxes near the edges of the container. In addition, for a specific libration frequency in the explored range $\sigma_0/2\Omega_0 \in [0.60; 0.73]$, libration also excites an inertial mode, of spatial structure in close agreement with the inviscid computation of Ref. 9. Our results suggest that, among all the eigen modes predicted numerically, only a small subset of low order modes matching exactly the symmetries of the cube libration can be actually excited.

II. EXPERIMENTAL SETUP

A. Flow geometry and rotating platform

The experimental setup, sketched in Fig. 1, consists in a closed cubic glass tank, of inner size $2L = 30$ cm, filled with water and mounted on a precision rotating turntable of 2 m in diameter. We use a coordinate system centered on the horizontal square, $-L \le x, y \le L$, with the horizontal walls at $z = 0$ and $z = 2L$, perpendicular to the rotation vector $\mathbf{\Omega} = \Omega(t)\mathbf{e}_z$. The mean angular velocity of the rotating platform is set to $\Omega_0 = 0.419$ rad s^{-1} (4 rpm). The Ekman number of the system, which compares the viscous to the Coriolis force, is $E = \nu/(2\Omega_0 L^2) = 5.3 \times 10^{-5}$. The rotation of the fluid is set long before the start of the libration, at least 1 h, in order for transient spin-up recirculations to be damped. Once the solid-body rotation is reached, the turntable is submitted to a longitudinal libration, which consists in a modulation of the angular velocity $\Omega(t)$ around Ω_0 at a frequency σ_0 with a peak-to-peak amplitude $2\epsilon\,\Omega_0$,

$$\Omega(t) = \Omega_0\,[1 + \epsilon\,\cos(\sigma_0 t)]\,. \tag{1}$$

In the frame rotating at constant velocity Ω_0, the libration of the cube is described by the angle

$$\varphi(t) = \epsilon\frac{\Omega_0}{\sigma_0}\sin(\sigma_0 t). \tag{2}$$

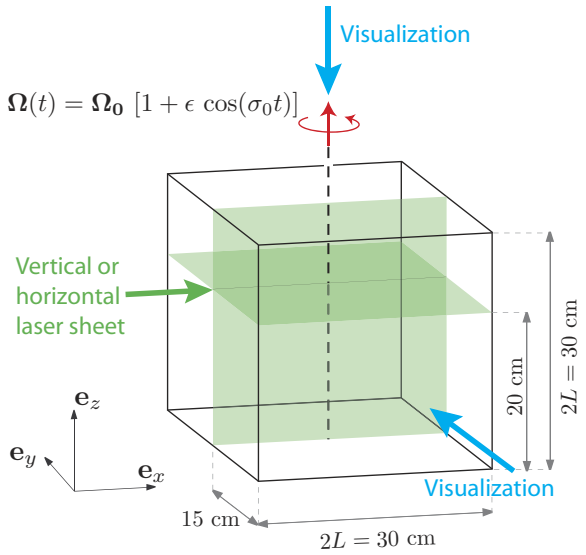

FIG. 1. Schematic view of the $(30\ \text{cm})^3$ water tank mounted on the rotating platform. The bottom and top walls are located at $z = 0$ and $z = 2L$, and the origin of the coordinates (x, y) is taken at the center of the square cross section. Two-dimensional PIV measurements are achieved in the vertical plane $y = 0$ and in the horizontal plane $z = 4L/3$ in the librated frame using a corotating laser sheet and a camera aiming normally at it.

The normalized libration amplitude ϵ, which is the Rossby number of the problem, is varied between 2% and 16%. In order to excite inertial waves, the libration frequency σ_0 can take in principle any value in the range $[0, 2\Omega_0]$. In this paper, we focus on the restricted range $\sigma_0/2\Omega_0 \in [0.60; 0.73]$. For these frequencies, the peak-to-peak libration angle $\Delta\varphi = 2\epsilon\Omega_0/\sigma_0$ lies in the range from 1° to 13° for $\epsilon = 2\%$ to 16%. The relative precision in the control of the instantaneous rotation rate is better than 10^{-3}. After the start of the libration, we wait at least half an hour before the data acquisition (which represents $8\tau_E$, where $\tau_E = L(\nu\Omega_0)^{-1/2}$ is the Ekman time scale) in order to reach a stationary regime.

B. Particle image velocimetry (PIV) measurements

Velocity fields are measured in the librated reference frame using a two-dimensional PIV system mounted on the rotating platform (Fig. 1).[26,27] Measurements are performed either in the vertical plane $y = 0$ or in the horizontal plane $z = 4L/3 = 20$ cm. This last particular choice is motivated by the fact that $z = 4L/3$ does not correspond to a node for the inertial modes considered in this paper (the centered horizontal plane $z = L$ is a node for the inertial modes of even vertical wavenumber n). The flow is seeded with 10 μm tracer particles, and illuminated by a corotating laser sheet generated by a 140 mJ Nd:YAG pulsed laser. For both horizontal and vertical measurements, the entire $30 \times 30\ \text{cm}^2$ flow sections are imaged through the transparent sides of the tank with a high resolution 2048×2048 pixels camera aiming normally at the laser sheet.

Each acquisition consists in at least 1000, and up to 3000, images taken at a sampling rate between $12\sigma_0$ and $36\sigma_0$, which correspond to at least 80 libration periods. The sampling rate is chosen according to the libration amplitude in order to keep a typical particle displacement of the order of 5 pixels between two successive images. PIV fields are computed over successive images using 32×32 pixels interrogation windows with 50% overlap, leading to a spatial resolution of 3.5 mm. This resolution is not enough to resolve the thickness of the Ekman boundary layers, $\delta_E = LE^{1/2} \simeq 1$ mm, but is appropriate for the flow structures associated to inertial waves and modes in the bulk of the fluid.

III. BASIC LIBRATION FLOW

A. Inviscid solution

We first characterize the basic flow response to the libration forcing. Since in the present experiments the modulation period $2\pi/\sigma_0 \simeq [20; 25]$ s is much shorter than the Ekman time $\tau_E \simeq 230$ s (which is the time scale required for the angular velocity of the fluid to match that of the boundaries), the core of the flow can be considered as essentially inertial, and rotating at the constant rotation rate Ω_0. In the frame rotating at Ω_0, the flow is therefore approximately at rest, and surrounded by oscillating recirculations induced by the periodic motion of the walls.

The inviscid response to the libration of an arbitrary container, whose walls are either parallel, or normal to the rotation axis, can be derived by assuming that the flow is strictly two-dimensional. In the absence of viscosity, the *absolute vorticity* of the fluid in the frame of the laboratory,

$$\boldsymbol{\omega}_a = \boldsymbol{\omega} + 2\Omega(t)\mathbf{e}_z,$$

must be conserved, and hence given by the mean vorticity $2\Omega_0\mathbf{e}_z$. Here, $\boldsymbol{\omega}$ is the *relative vorticity*, as measured in the libration frame. If viscosity is present, this result remains approximately valid far from the boundaries, with the additional assumption that $\sigma_0/\Omega_0 \gg E^{1/2}$ (i.e., for a rapid libration compared to the Ekman time scale). With the total angular velocity of the libration given by Eq. (1), the relative vorticity $\boldsymbol{\omega}$ is therefore vertical, homogeneous, and given by

$$\omega_z(t) = \frac{\partial u_y}{\partial x} - \frac{\partial u_x}{\partial y} = -2\epsilon\Omega_0 \cos(\sigma_0 t). \tag{3}$$

In an axisymmetric container, the resulting flow is an oscillating solid body rotation of angular velocity $-\epsilon\Omega_0\cos(\sigma_0 t)$: this simply describes a fluid at rest in the frame rotating at constant rate Ω_0. The case of a non-axisymmetric container is more complex, and can be solved in terms of a streamfunction $\psi(x, y, t) = \Psi(x, y)\cos(\sigma_0 t)$, such that $(u_x, u_y) = (-\partial_y\psi, \partial_x\psi)$. Equation (3) therefore takes the form of a Poisson equation for the spatial part of the streamfunction,

$$\Delta\Psi = -2\epsilon\Omega_0.$$

The solution of this equation for a square domain, subject to the condition that the streamfunction vanishes at the boundary, is given in the Appendix, in Eq. (A3). The streamlines are circular near the center of the container, as in a solid-body rotation, but they become gradually more square near the boundaries (see the velocity field in Fig. 2(a)).

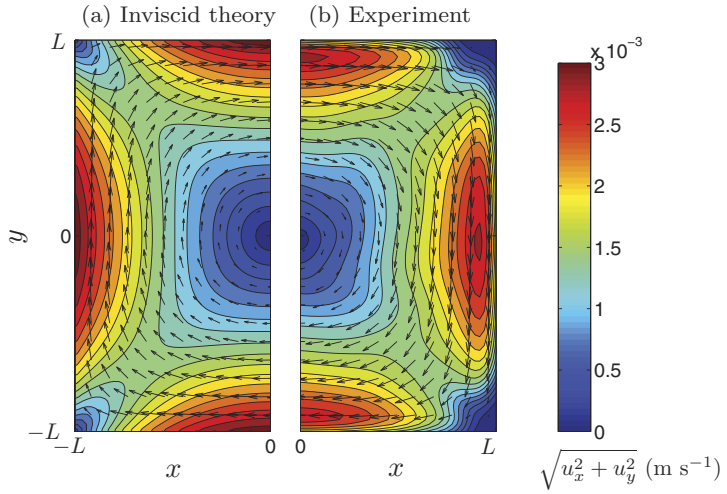

FIG. 2. Velocity fields excited by libration in a container of square cross-section. (a) Inviscid solution, computed from Eq. (A3). (b) PIV measurements at the phase $\sigma_0 t = 0$ (maximum libration velocity). The libration frequency is $\sigma_0/2\Omega_0 = 0.648$ (corresponding to the mode [2, 2, +], which is not resonant in this experiment), and its amplitude is $\epsilon = 0.04$.

B. Experimental measurements of the libration flow

Figure 2 compares the measured libration flow obtained by PIV and the inviscid solution (A3). The velocity field shown here is taken at the phase $\sigma_0 t = 0$ corresponding to the maximum amplitude of the libration, when the flow in the librated frame is anticyclonic (i.e., $\omega_z = -2\epsilon\Omega_0$). The libration frequency σ_0 is chosen here far from any resonant frequency of inertial mode. The agreement between the measured field and the inviscid solution is excellent in most of the flow section, except near the boundaries. It must be noted that the vanishing of the velocity near the boundaries may be affected by the PIV resolution (about 3 mm), which is of the same order as the expected boundary layer thickness.

An interesting feature of Fig. 2(b) is the wavy shape of the experimental iso-velocity lines: this is a first indication that, in addition to the basic libration flow, the flow also contains a wave component. This additional component is further described in Sec. V.

For all the libration amplitudes investigated here ($\epsilon = 2\%$ to 16%), the fluid response to the forcing is found to remain essentially linear. This is demonstrated in Fig. 3, where the temporal energy spectra $E(\sigma)$ are shown for different forcing amplitude ϵ. Here, the spectrum is defined as $E(\sigma) = \langle|\hat{\mathbf{u}}_\sigma|^2\rangle_{xy}$, where $\hat{\mathbf{u}}_\sigma(x, y)$ is the temporal Fourier transform computed at each location, and $\langle\rangle_{xy}$ is the spatial average over the horizontal plane. The Fourier transform is computed over at least 80 periods of libration.

All spectra show a narrow peak at the forcing frequency σ_0, well above the white noise level of the PIV measurements. We note that, since we are only interested here in forcing frequencies $\sigma_0 > \Omega_0$, higher harmonics $n\sigma_0$, if present, are beyond the upper limit $2\Omega_0$, and are therefore not governed by the dynamics of inertial waves.

We can note that, for all forcing amplitudes ϵ, the peak at σ_0 contains at least 97% of the total flow energy. The remaining energy is associated to secondary peaks at $\sigma = 0$, $\sigma = \Omega_0$, and higher harmonics ($\sigma > 2\Omega_0$). The secondary peak at $\sigma = \Omega_0$, mostly visible at low ϵ, corresponds to a residual fluid motion synchronized with the platform rotation rate. The peak at $\sigma = 0$ can be associated to the generation of a weak mean flow. This mean flow is probably a nonlinear response to the libration forcing, and is not investigated in the present paper.

In order to improve the signal-to-noise ratio, we perform, in the following, a band-pass filtering of the velocity fields at the forcing frequency σ_0. This procedure consists in filtering the Fourier transform $\hat{\mathbf{u}}_\sigma$ at all σ except in a narrow region centered on σ_0 of width $\delta\sigma/2\Omega_0 = 0.024$ (which

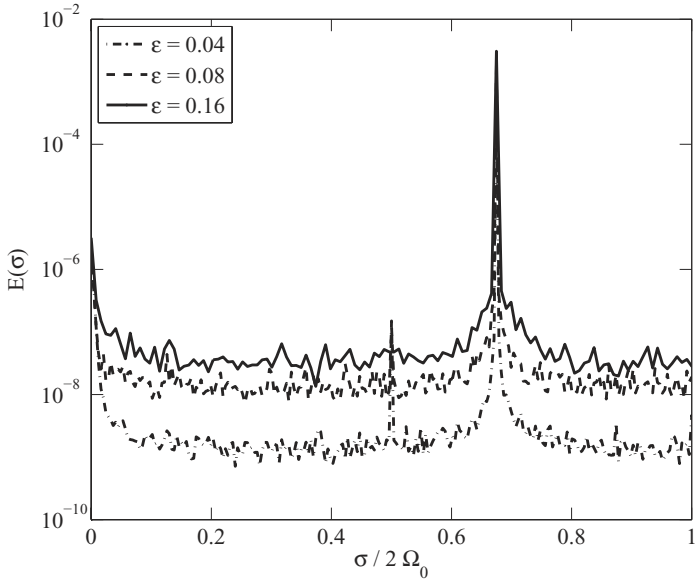

FIG. 3. Temporal energy spectra $E(\sigma)$ for a forcing frequency $\sigma_0/2\Omega_0 = 0.675$ (corresponding to the mode [2, 1, +]), for three libration amplitudes $\epsilon = 0.04$, 0.08, and 0.16.

contains the energy of the peak to within 1%), and computing the inverse Fourier transform of the resulting filtered field.

IV. INVISCID INERTIAL MODES AND SYMMETRIES OF THE LIBRATION FORCING

A. Inviscid inertial modes

The eigen frequencies and the spatial structures of the inertial modes in a parallelepiped whose sides are parallel or perpendicular to the rotation axis have been determined numerically for an inviscid fluid in Ref. 9. These predictions have been achieved from the numerical resolution of the eigenproblem defined from the inviscid linearized equations in a rotating frame. Any frequency σ_0 in the range $[0, 2\Omega_0]$ corresponds to an inertial mode. Accordingly, an infinity of inviscid modes may be excited if the system is forced at a given frequency with a finite bandwidth.

Following the notation introduced in Ref. 24, we label the inertial modes as $[n, m, s]$. The first index n is the normalized vertical wavenumber, such that the velocity field $\mathbf{u}$ shows n recirculation cells in the vertical direction. With the container walls taken at $z = 0$ and $z = H$, the velocity field has the form

$$\mathbf{u}_\perp(x, y, z, t) = \cos\left(\pi n \frac{z}{H}\right) \breve{\mathbf{u}}_\perp(x, y, t), \tag{4}$$

$$u_z(x, y, z, t) = \sin\left(\pi n \frac{z}{H}\right) \breve{u}_z(x, y, t), \tag{5}$$

with $\mathbf{u}_\perp = u_x \mathbf{e}_x + u_y \mathbf{e}_y$ (we restrict to $H = 2L$ in this paper). Inertial modes are therefore stationary in the vertical direction, but their horizontal structure $\breve{\mathbf{u}}(x, y, t)$ may be either stationary (the so-called "sloshing" modes), or propagating. The second index m enumerates the eigen frequencies of modes of sign s from the largest one ($m = 1$) down. Larger values of m essentially correspond to finer structures in the horizontal plane. Since each mode m is expressed in terms of an infinite amount of horizontal Fourier modes, the index m is not directly related to a number of nodes as for the vertical index n. Finally, the sign s refers to the invariance of the mode with respect to the rotation of angle π about the z axis. More precisely, a mode $\mathbf{u}(x, y, z, t)$ has symmetry s if

$$\begin{pmatrix} u_x \\ u_y \\ u_z \end{pmatrix} (-x, -y, z, t) = s \begin{pmatrix} -u_x \\ -u_y \\ u_z \end{pmatrix} (x, y, z, t). \tag{6}$$

The resonance frequencies of inertial modes $[n, m, s]$ are increasing functions of n and, at fixed n and s, decreasing functions of m. This behavior essentially originates from the dispersion relation for plane inertial waves,

$$\sigma = 2\Omega_0 \cos\theta, \tag{7}$$

where θ is the angle between the wavevector $\mathbf{k}$ and the rotation axis, $\cos\theta = k_z/|\mathbf{k}|$. Low frequencies σ are therefore associated to nearly horizontal $\mathbf{k}$, i.e., to small k_z and hence to small n, or/and to large $k_{x,y}$ and hence to large m.

B. Symmetry properties and boundary conditions for a viscous fluid

In the case of a viscous fluid, the no-slip boundary condition at the walls is expected to affect the spatial structure of the inertial modes. The spectrum and spatial structure of viscous inertial modes in a rotating parallelepiped have not been computed yet. It is therefore of first interest to check as to what extent the inviscid modes found numerically could be recovered in a viscous fluid at a finite Ekman number. Since viscosity damps preferentially the high order modes (i.e., the modes with large indices n and/or m), we expect the libration to force more efficiently modes of low order. This is straightforward for the vertical wavenumber n, which is naturally associated to a viscous damping proportional to νn^2. No equivalent simple law exists for the horizontal index m, but we can similarly expect that lower m, associated to larger scales in the horizontal plane, will be favored in the presence of viscosity.

TABLE I. List of all the inviscid inertial modes [n, m, s], truncated at $n \leq 4$ and $m \leq 6$, in the range of frequencies $\sigma_0/2\Omega_0 \in [0.60; 0.73]$. n is the normalized vertical wavenumber, m characterizes the horizontal structure, and $s = \pm$ refers to the symmetry or antisymmetry of the mode with respect to rotation of angle π about the rotation axis (see Ref. 9 for details). The * symbol marks the four modes having symmetries compatible with the libration forcing: even n and $s = +$.

Mode [n, m, s]	Frequency $\sigma/2\Omega_0$
[2, 1, +]*	0.6742
[2, 2, +]*	0.6484
[3, 2, −]	0.7271
[3, 3, −]	0.6857
[3, 4, −]	0.6848
[3, 3, +]	0.6485
[3, 4, +]	0.6258
[4, 5, +]*	0.6960
[4, 6, +]*	0.6945
[4, 5, −]	0.6889
[4, 6, −]	0.6643

From the symmetries of the boundary conditions, it is possible to anticipate which inertial modes are compatible with the libration forcing. In the frame rotating at constant velocity Ω_0, the angular oscillation of the top and bottom walls is described by the velocity $\mathbf{u}(x, y, z = 0) = \mathbf{u}(x, y, z = 2L) = \epsilon\Omega_0 \cos(\sigma_0 t)(-y\mathbf{e}_x + x\mathbf{e}_y)$ which, according to Eq. (6), has symmetry $s = +$. Moreover, the no-slip boundary conditions impose equal horizontal velocity at the top and bottom walls, which is satisfied only for even vertical wavenumbers n (the basic libration flow described in Sec. III is vertically invariant, and is hence associated to $n = 0$). Finally, there is the possibility that particular symmetries associated to the second index m may even further reduce the set of modes compatible with the symmetries of the libration forcing. According to these symmetry properties, the longitudinal libration is expected to excite only a subset of the modes [n, m, s] among those having even n and $s = +$.

It must be noted that those symmetry arguments state which modes are forbidden by this forcing, but they do not state which modes, among the allowed ones, are effectively excited by the libration. In other words, we would like to address the question of how the fluid motion induced by the oscillating walls, and in particular close to the edges of the cube, will be transmitted to the inertial modes, and to characterize the efficiency of this transmission.

In the following, we investigate the flow response for libration frequencies in the vicinity of two inertial modes of low order allowed by the symmetries of the forcing: [2,1,+] and [2,2,+]. More specifically, we systematically characterize the flow in the range $\sigma_0/2\Omega_0 \in [0.60; 0.73]$ surrounding these two modes. The list of all modes in this range, truncated at $n \leq 4$ and $m \leq 6$, is given in Table I. Among these modes, only the four ones [2,1,+], [2,2,+], [4,5,+], and [4,6,+] (marked by a * symbol) have the correct symmetries (even n and $s = +$) and could be observed in principle. However, we will show in the following that viscous effects and additional symmetry properties actually select only the single mode [2,1,+] in this list.

V. EDGE BEAMS AND INERTIAL MODES

A. Flow in the vertical plane: Non-resonant case

We first describe the flow in the vertical plane $y = 0$ in the absence of inertial modes. The velocity $\mathbf{u}_{x,z}$ and the vorticity $\omega_y(x, z)$ shown in Fig. 4 for $\epsilon = 0.02$ are for forcing frequencies $\sigma_0/2\Omega_0 = 0.60$ (a) and 0.73 (b), chosen far from any low order inertial mode. Fields are not displayed in lateral strips of 12 mm width along the walls due to poor quality of the data induced by light

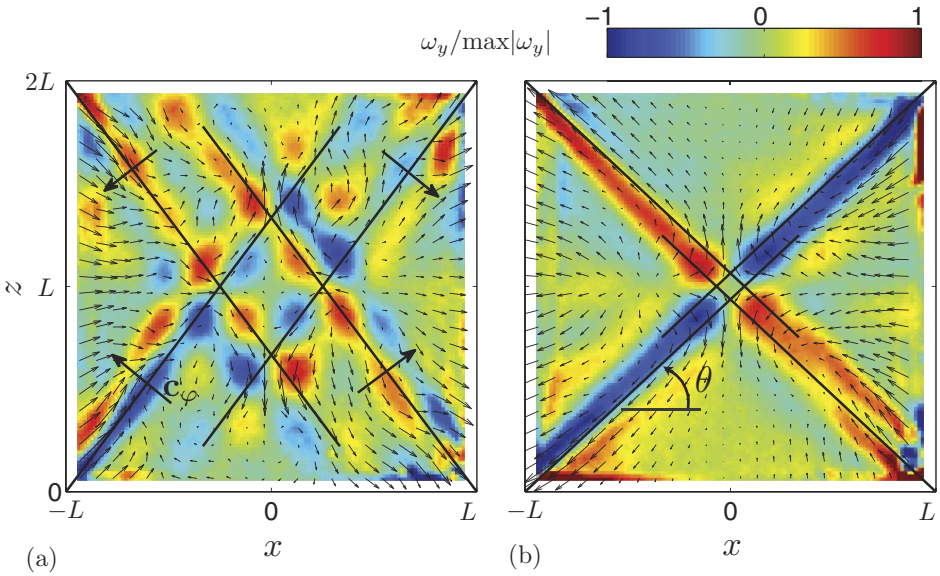

FIG. 4. Spatial structure, in the vertical plane $y = 0$, of the oscillating flow excited with $\epsilon = 0.02$ and at frequencies $\sigma_0/2\Omega_0 = 0.60$ (a) and 0.73 (b), in the absence of inertial modes. The velocity fields are extracted by temporal band-pass filtering around the excitation frequency. The arrow fields illustrate the (x, z) components of the velocity field at a given arbitrary phase of the oscillation, and the gray shade/color maps the corresponding normalized vorticity $\omega_y/\max|\omega_y|$. Resolution of the velocity fields has been reduced by a factor 5 for better visibility. In (a), bold arrows show the direction of the phase velocity $\mathbf{c}_\varphi$ for each wave beam. In (a) and (b), the solid black lines show the expected direction predicted for each wave beam from the dispersion relation, $\cos\theta = \sigma_0/2\Omega_0$.

reflections. Since the basic libration flow is normal to the plane $y = 0$, the vertical flows here show the x and z deviations from the libration flow, and contain therefore only the contributions from the wave component of the flow.

We observe that the libration excites a cross shaped pattern made of four oblique shear layers originating from the bottom and top edges of the cube. These shear layers actually correspond to propagative inertial waves in two-dimensional plane wave packets, which contain approximately one wavelength in their transverse direction. There are actually eight two-dimensional wave packets emitted from the four upper and the four lower edges of the container; only the four ones emitted from the edges defined by $x = \pm L$, $z = 0, 2L$ can be seen in the vertical cut $y = 0$. The direction of the beams is found in good agreement with the dispersion relation (7), as shown by the black lines in Fig. 4 making an angle $\theta = \cos^{-1}(\sigma_0/2\Omega_0)$ with the horizontal. In these wave beams, fluid particles describe an anticyclonic circular motion at frequency σ_0 in the planes inclined at angles $\pm\theta$ with the horizontal (the sign depends on the considered beam). The shearing motion traced by the vorticity ω_y is related to the variation of the wave phase in the direction normal to $\pm\theta$. We also observe that the phase of the wave travels normal to the beam, with a phase velocity $\mathbf{c}_\varphi$ directed towards the vertical wall from which originates the beam. In Fig. 4(a) [$\theta = \cos^{-1}(0.60) \simeq 53°$], the four wave beams show interferences at their intersections, which make the wave pattern rather complex. On the contrary, in Fig. 4(b) [$\theta = \cos^{-1}(0.73) \simeq 43°$], the opposite wave beams are almost aligned for this particular frequency. As a consequence, the wave beams show constructive interferences, leading to almost standing waves along the diagonals, but propagative outwards on their sides.

These edge beams are similar to the ones observed in cylindrical containers, e.g., in the early experiment of McEwan[4] (forced by a tilted top lid) and in the numerical simulations of Duguet *et al.*[25] (forced by an oscillating axial compression). Similar beams are also found in the recent simulations of Sauret *et al.*[28] (forced by a longitudinal libration) although in this case, the beam angle is apparently not directly related to the libration frequency, and probably results from the turbulence in the boundary layers over the sidewalls. In all these references, the container is cylindrical, resulting in conical edge beams, emitted from the two circular edges and focusing towards the rotation axis. In our non-axisymmetric geometry, since the disturbance sources are linear segments, there are eight two-dimensional edge beams emitted from the four upper and the four lower edges of the container.

These edge beams originate from the oscillating outward (resp. inward) Ekman layers on the upper and lower walls associated with the prograde (resp. retrograde) part of the libration motion. Far from the lateral walls, where the streamlines of the libration flow are approximately axisymmetric, this flow is approximately radial, of order $\epsilon\Omega_0\sqrt{x^2+y^2}$. In the classical axisymmetric spin-up problem, the horizontal flow in the unsteady (but slowly varying) Ekman layer is vertically deflected into Stewartson layers along the lateral walls.[1] However, in the rapidly oscillating situation examined here, the matching condition between the Ekman and Stewartson layers cannot be satisfied, and the flow in the Ekman layer detaches when it reaches the lateral walls, generating an oscillating shear layer in the bulk,[16] of characteristic velocity $\epsilon\Omega_0 L$. As a consequence, although the velocity scale of the edge beams is inertial, viscosity is responsible for this flow feature.

The width of these edge beams can be compared to predictions from a viscous theory. Because of viscous damping, it is known that a wave beam spreads as $\ell^{1/3}$, where ℓ is the distance from the source.[29,30] More precisely, the thickening of the full-width half maximum $\delta(\ell)$ of a self-similar plane beam emitted by a linear disturbance of small size can be computed,[31]

$$\delta(\ell) \simeq 6.84L\left(\frac{E}{\sin\theta}\right)^{1/3}\left(\frac{\ell}{L}\right)^{1/3}, \tag{8}$$

with $E = \nu/(2\Omega_0 L^2)$. According to this model, a wave beam emitted from an edge reaches the central area of the container after a distance $\ell^* = L/\sin\theta$ (for $\theta > 45^\circ$), where its width is $\delta(\ell^*) \simeq 6.84(\sin\theta)^{-2/3} L E^{1/3} \simeq 4.2-5.0$ cm for the range of angles considered here. This prediction provides correct agreement with the observations in Fig. 4, showing the beams of thickness of order of 3−4 cm near the center. Note that the case $\theta \simeq 45^\circ$is specific: the overlap of the upper and lower wave beams leads to a different scaling,[25] $\delta \simeq E^{1/4}$.

B. Flow in the vertical plane: Resonant case

We still examine here the structure of the flow in the vertical plane, but now at frequencies where inertial modes are expected. We select the two frequencies $\sigma_0/2\Omega_0 = 0.674$ and 0.648, corresponding to the inviscid predictions for the modes [2,1,+] and [2,2,+], respectively (see Table I). The velocity and vorticity fields are shown in Fig. 5, at the phases $\sigma_0 t = 0$ (a,d) and $\pi/2$ (b,e) of the libration. In the frame rotating at constant velocity Ω_0, the phase $\sigma_0 t = 0$ corresponds to $\varphi = 0$ and $\Omega(t) = \epsilon\Omega_0$ (i.e., maximum rotation rate), whereas $\sigma_0 t = \pi/2$ corresponds to φ maximum and $\Omega(t) = 0$ [see Eqs. (1)−(2)].

Looking first at the velocity fields (b) and (e), both frequencies show two oscillating cells in the vertical direction, as expected for a mode $n = 2$ (see also the movies available at Ref. 32). These oscillating cells are mainly visible at the phase $\sigma_0 t = \pi/2$, when the angle φ is maximum and the libration motion vanishes. At this phase, the velocity fields clearly satisfy the $s = +$ symmetry, with $u_x(-x, z) = -u_x(x, z)$ and $u_z(-x, z) = u_z(x, z)$. On the other hand, at the phase $\sigma_0 t = 0$ corresponding to the maximum libration velocity (a,d), the x and z components of the velocity associated to this mode $n = 2$ vanish and one recovers the propagative edge beams already evidenced in Fig. 4.

Looking now at the vorticity field reveals finer structures of the flow. At phase $\sigma_0 t = 0$ (a,d), the typical cross shaped pattern composed of four edge beams is found for both forcing frequencies. On the other hand, at phase $\pi/2$ (b,e), the shape of the vorticity field is found to depend now on the forcing frequency. Whereas it keeps approximately its cross-shape structure for $\sigma_0/2\Omega_0 = 0.648$ (e), it shows four nearly circular extrema of alternate signs for $\sigma_0/2\Omega_0 = 0.674$ (b). This indicates that, at $\sigma_0 t = \pi/2$, the four recirculation cells dominate the vorticity for $\sigma_0/2\Omega_0 = 0.674$ (b), whereas their vorticity is partially hidden by the strong edge beams for $\sigma_0/2\Omega_0 = 0.648$ (e).

In order to understand the different behaviors between the two frequencies, we compare now the experimental fields with the numerical predictions of the inviscid modes [2,1,+] and [2,2,+], shown in Figs. 5(c) and 5(f), respectively (movies of the numerical modes are also provided at Ref. 32). Note that the phase of the numerical fields is arbitrary since they are not related to any specific forcing: the numerical fields in Fig. 5 have been simply chosen here at phases which provide

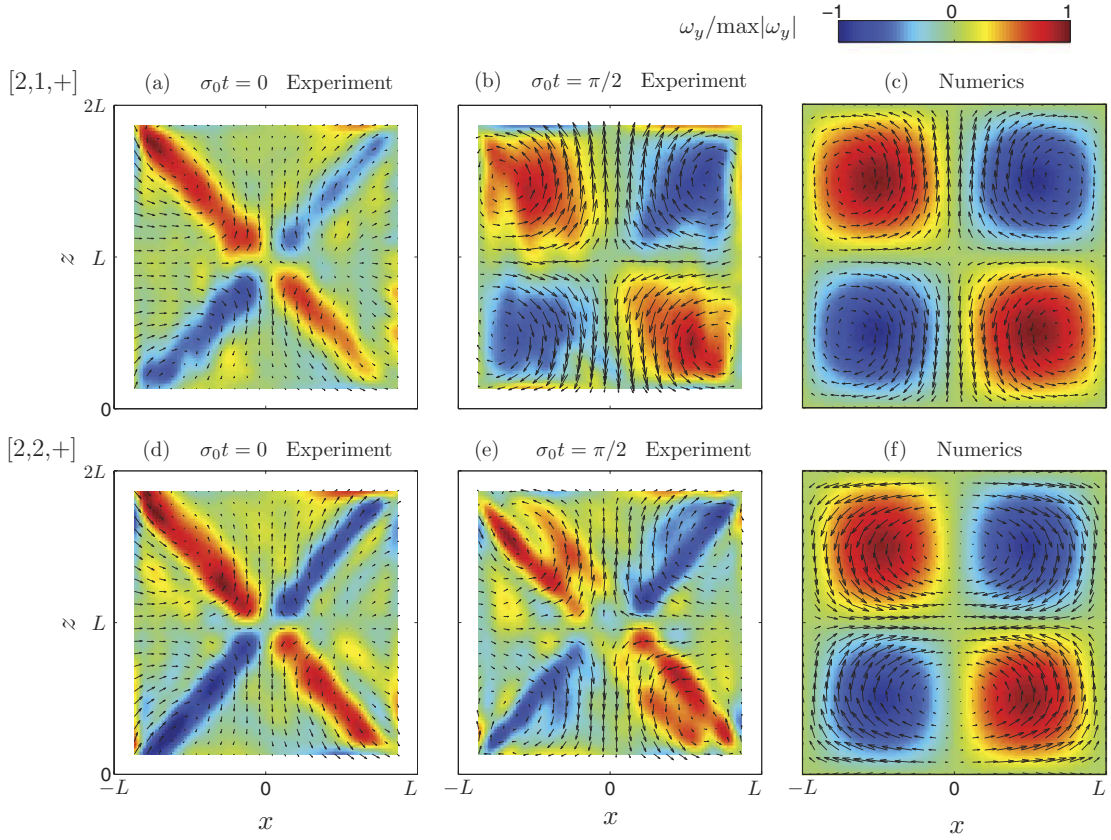

FIG. 5. Spatial structure, in the vertical plane $y = 0$, of the oscillating flow excited with $\epsilon = 0.04$ and at frequency $\sigma_0/2\Omega_0 = 0.674$ (a)−(c) and $\sigma_0/2\Omega_0 = 0.648$ (d)−(f). (a), (b), (d), and (e) correspond to the experimental fields extracted by temporal band-pass filtering around the excitation frequency. (c) and (f) show the corresponding numerical inviscid modes [2,1,+] and [2,2,+] expected at the same frequency. The libration phase is $\sigma_0 t = 0$ for (a) and (d), and $\sigma_0 t = \pi/2$ for (b) and (e). The gray shade/color maps the normalized vorticity field $\omega_y/\max|\omega_y|$. Resolution of the velocity fields has been reduced by a factor 5 for better visibility (see also Ref. 32).

a good visual correspondence with the experimental fields. Although the vorticity patterns of modes [2,1,+] and [2,2,+] look similar, with four extrema of alternate signs, their velocity fields are very different: the vertical velocity is maximum on the vertical axis for [2,1,+], but it is zero for [2,2,+]. The smooth pattern of ω_y found experimentally in Fig. 5(b) matches actually well the prediction for [2,1,+]. On the other hand, the comparison fails for Fig. 5(e), both for the velocity and vorticity fields, suggesting that the mode [2,2,+] cannot be excited by the longitudinal libration.

We can interpret these observations as follows. For $\sigma_0/2\Omega_0 = 0.674$, the flow is a superimposition of the pattern of propagative edge beams and a resonant stationary [2,1,+] mode. Whenever the libration angle is zero (i.e., at phases $\sigma_0 t = 0$ and π), the instantaneous amplitude of the [2,1,+] mode vanishes, and only the edge beams remain visible. Turning now to the case $\sigma_0/2\Omega_0 = 0.648$, the mode [2,2,+] is apparently not excited, and the edge beam pattern remains visible all the time. Interestingly, it seems that a flow reminiscent of the mode [2,1,+] is excited instead (see Fig. 5(e)), although with a weak amplitude, probably because of the closeness of the eigen frequencies (less than 4%) of the two modes. It will indeed be confirmed in Sec. VI that the resonance of the [2,1,+] mode spreads over a significant frequency range because of viscosity.

C. Flow in the horizontal plane

We finally turn to visualizations in the horizontal plane $z = 4L/3$, still for the two frequencies $\sigma_0/2\Omega_0 = 0.674$ and 0.648. In order to focus on the wave component of the flow, we remove, in the

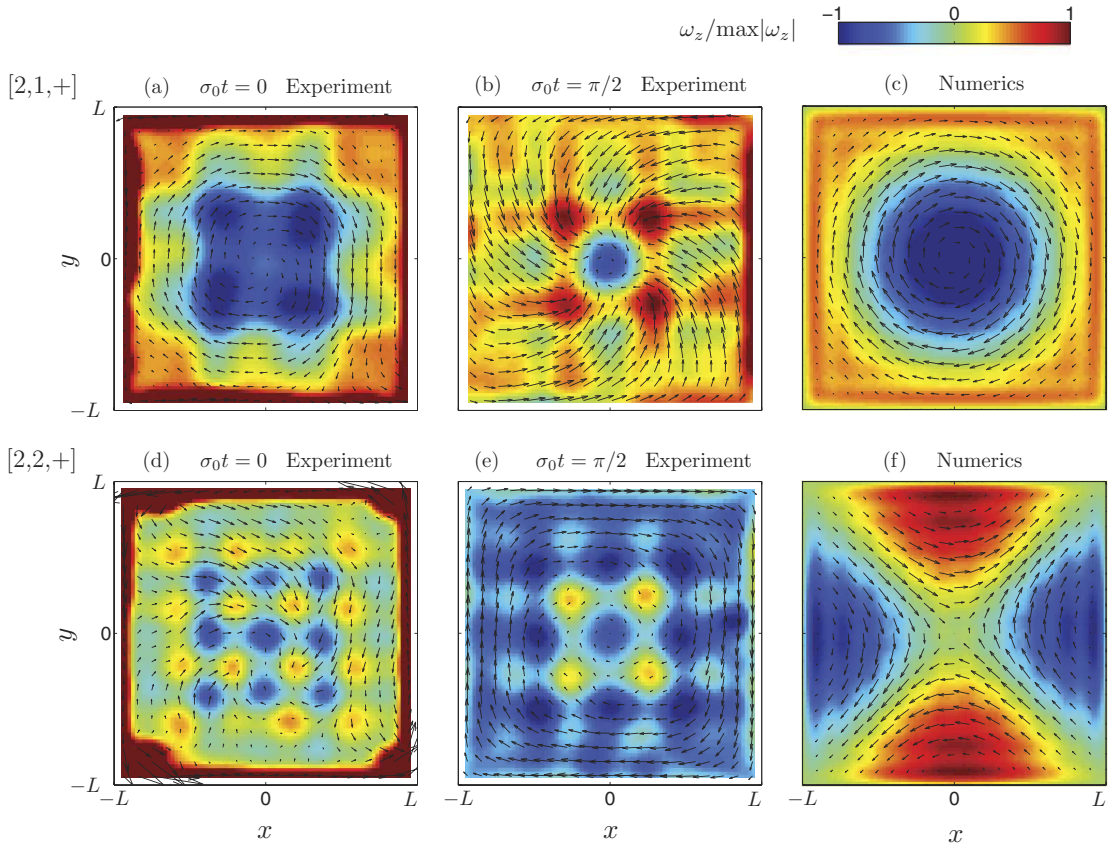

FIG. 6. Spatial structure, in the horizontal plane $z = 4L/3$, of the wave component of the flow $\mathbf{u}'$ excited with $\epsilon = 0.04$ and at frequency $\sigma_0/2\Omega_0 = 0.674$ (a)−(c) and $\sigma_0/2\Omega_0 = 0.648$ (d)−(f). Same layout as in Fig. 5.

following, the libration component,

$$\mathbf{u}'(x, y, t) = \mathbf{u}(x, y, t) - \mathbf{u}_{lib}(x, y)\cos(\sigma_0 t), \tag{9}$$

where $\mathbf{u}(x, y, t)$ is the total velocity measured by PIV, and $\mathbf{u}_{lib}(x, y) = \nabla \times (\Psi \mathbf{e}_z)$ is the inviscid libration flow computed from Eq. (A3). In Fig. 6, we show the resulting horizontal velocity $u'_{x,y}$ and the corresponding vertical vorticity $\omega'_z(x, y)$ fields for both frequencies, for the same phases $\sigma_0 t = 0$ and $\pi/2$ as previously. Here again, measurements are not displayed in lateral strips of width 6 mm along the walls because of the poor quality of the PIV data.

For both frequencies, the horizontal flow shows a complex spatial structure, which verifies the relation $u'_{x,y}(-x, -y) = -u'_{x,y}(x, y)$, confirming the $s = +$ symmetry of the flow. Both frequencies show a clear square pattern of vorticity extrema, which is the trace of the interferences between the eight propagative inertial wave beams emitted from the eight horizontal edges of the container. Note that since the libration flow has constant vorticity far from the boundaries, one has $\omega'_z = \omega_z + 2\epsilon\Omega_0 \cos(\sigma_0 t)$, so the vorticity patterns computed from the total flow and from its wave component are identical. The amplitude of the wave component in the bulk of the flow is typically a factor 10 below the libration velocity scale $\epsilon\Omega_0 L$, indicating a weak efficiency of the excitation of inertial waves by libration.

In Figs. 6(c) and 6(f), we show for comparison the numerical predictions of the inviscid modes [2,1,+] and [2,2,+] in the horizontal plane. The mode [2,1,+] (c) consists in a nearly axisymmetric flow, in which each velocity vector describes an elliptic oscillation in the anticyclonic direction. During one period of the mode, the flow goes through the following sequence: cyclonic, centrifugal, anticyclonic, centripetal (see Ref. 32). The mode [2,2,+] (f) has a very different structure: it has four vortices located along the sidewalls, with a hyperbolic point in the middle. This pattern is essentially

rotating as a whole around the rotation axis, with only weak deformations near the walls due to the non-axisymmetry of the container.

The comparison between the numerical inviscid modes and the experimental measurements is revealing. The structure of the mode [2,1,+] can be easily recognized in the experimental data, superimposed to the square pattern of the interfering edge waves. For instance, the numerical mode chosen at the phase shown in Fig. 6(c) matches well the experimental flow at the libration phase $\sigma_0 t = 0$ [Fig. 6(a)]. At this phase, the flow is normal to the plane $y = 0$, in agreement with the vanishing of the mode in the vertical plane observed at the same phase in Fig. 5(a). On the other hand, the structure of the inviscid mode [2,2,+] cannot be recognized in the experimental data at any phase,[32] confirming that this mode cannot be excited by libration. For both frequencies, the vorticity field is essentially dominated by the interfering edge waves, and is always different from the vorticity of the predicted inviscid modes [Figs. 6(c) and 6(f)].

The absence of mode [2, 2, +] in the experimental fields may be understood from symmetry arguments. In addition to the $s = +$ symmetry, which corresponds to an invariance under a rotation of π about the z axis, the [2,1,+] mode also turns out to be invariant under a rotation of $\pi/2$ about the z axis [Fig. 6(c)], which exactly matches the symmetry of the libration forcing for a cube. On the contrary, the mode [2,2,+] has only the π symmetry, and it is antisymmetric with respect to the rotation of $\pi/2$ about z. Taking into account this additional symmetry explains why only [2,1,+] is excited by the libration and not [2,2,+], even when the forcing frequency exactly matches the predicted frequency. Excitation of [2,2,+] would require two adjacent walls to move in opposition of phase, which is not possible with a rigid container.

These observations confirm that the libration forcing is able to excite only a subset of the possible inertial modes. Excitable modes [n, m, s] have even n and $s = +$, and must in addition be symmetric under the rotation of $\pi/2$ about z, which is satisfied for [2,1,+] but not for [2,2,+].

VI. RESONANCE CURVE

We finally describe the energy of the oscillating flow as the libration amplitude ϵ and the forcing frequency $\sigma_0/2\Omega_0$ are varied. First, we have varied the libration amplitude ϵ for the two frequencies $\sigma_0/2\Omega_0 = 0.648$ and 0.674 corresponding to the (excitable) mode [2,1,+] and the (non excitable) mode [2,2,+]. The energy of the wave component $\mathbf{u}'(x, y, t)$ of the flow [see Eq. (9)] is plotted in Fig. 7 as a function of ϵ for these two frequencies. This energy is computed over the horizontal components of the velocity in the horizontal plane $z = 4L/3$,

$$k_h = \overline{\langle u_x'^2 + u_y'^2 \rangle}_{x,y}, \tag{10}$$

where the overbar stands for time average.

For both frequencies, the scaling of the energy is compatible with ϵ^2, confirming that the wave component of the flow essentially responds linearly to the excitation amplitude ϵ in the range

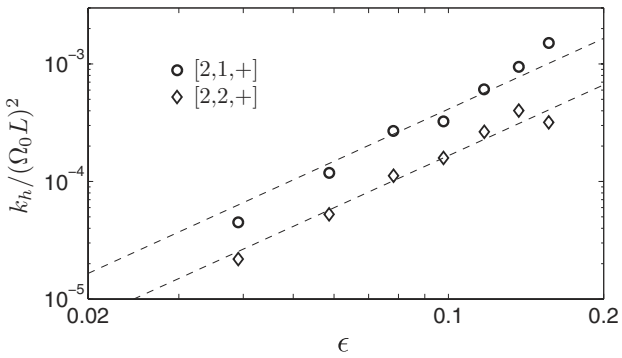

FIG. 7. Normalized kinetic energy $k_h/(\Omega_0 L)^2$ of the wave component of the flow in the horizontal plane $z = 4L/3$ as a function of the excitation amplitude ϵ, for libration frequencies corresponding to the [2,1,+] (○) and [2,2,+] (◇) modes. The dashed lines show the best fits in ϵ^2.

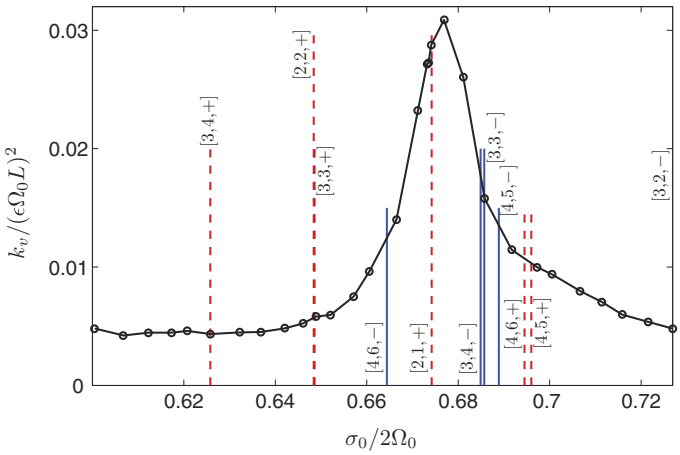

FIG. 8. Normalized kinetic energy $k_v/(\epsilon\Omega_0 L)^2$ in the vertical plane $y = 0$ as a function of the excitation frequency $\sigma_0/2\Omega_0$ for an excitation amplitude $\epsilon = 0.02$. The vertical lines indicate the eigen frequencies of the inviscid modes of low order (only modes with $n \leq 4$ and $m \leq 6$ are shown). Solid lines correspond to $s = -$ modes and dashed lines to $s = +$ modes. The size of the vertical segments is taken proportional to $1/n$.

0.02−0.16. The energy for the frequency corresponding to [2,1,+] is a factor 2.5 above that for [2,2,+]. Since we know that the mode [2,2,+] is not excited, the curve for [2,2,+] essentially corresponds to the interfering propagating edge beams. The additional amount of energy in [2,1,+] therefore corresponds to the resonant mode [2,1,+]. These curves suggest that, in the horizontal plane, the energy of the mode [2,1,+] and that of the edge waves are of the same order.

In order to characterize in more detail the resonance of the mode [2,1,+], we have also computed the energy in the vertical plane $y = 0$,

$$k_v = \overline{\langle u_x^2 + u_z^2 \rangle}_{x,z}. \tag{11}$$

The libration flow being normal to the measurement plane, it does not contribute to k_v, so this definition essentially describes the energy of the wave component of the flow. Focusing on a single value of the excitation amplitude, $\epsilon = 0.02$, we have performed a systematic scan over the excitation frequency $\sigma_0/2\Omega_0$ in the range [0.60; 0.73]. Since the energy basically scales as ϵ^2, the energy k_v in Fig. 8 is normalized now by $(\epsilon\Omega_0 L)^2$, which represents the order of magnitude of the energy of the basic libration flow.

The resonance curve shows a well-defined peak of energy $k_v \simeq 3 \times 10^{-2}\,(\epsilon\Omega_0 L)^2$, centered on $\sigma_0/2\Omega_0 = 0.676 \pm 0.003$, and of width at half maximum $\Delta\sigma/2\Omega_0 \simeq 0.02$. The peak frequency is very close to the numerical prediction for the inviscid mode [2,1,+], $\sigma_0/2\Omega_0 = 0.6742$, confirming that this mode is the only one which is significantly excited in the frequency range investigated here. We can note a slight shift of about $\sigma_0/2\Omega_0 \simeq +0.002$ between the predicted and the observed peak, which probably originates from a viscous detuning effect. Although this detuning has not been computed for the inertial modes of a parallelepiped, it is essentially similar to the one found for the inertial modes of a sphere.[1] The frequency shift for the sphere has been actually determined analytically, and is of the order of $\sigma_0/2\Omega_0 \simeq (0.02 - 0.05)\sqrt{E}$ for low order modes. This would give $\sigma_0/2\Omega_0 \simeq 0.002$−$0.004$ for $E = 5.3 \times 10^{-5}$, which is consistent with the shift observed here for the cube.

The resonance peak is surrounded by a nearly constant plateau at $k_v \simeq (5 \pm 1) \times 10^{-3}(\epsilon\Omega_0 L)^2$, which accounts for the wave beams emitted from the edges of the container. This plateau confirms that the edge beams are always present in the flow, and are hidden only at the particular frequencies at which a mode is excited. It is worth noting that the width of the resonance peak is significantly larger than the width of the peak at σ_0 in the temporal energy spectra of the flow (see Fig. 3). This suggests that the quality of the resonance of the mode [2,1,+] is not fixed by the precision of the libration forcing, but is rather governed by the viscosity. This is confirmed by the fact that the

resonance width $\Delta\sigma/2\Omega_0 \sim 0.02$ is of the order of $(\Omega_0\tau_E)^{-1} \simeq 0.01$, where $\tau_E = L/\sqrt{\nu\Omega_0}$ is the Ekman time scale.

As expected, inertial modes which do not have the symmetries of the libration forcing (e.g., [3,4,+] or [3,3,+], with odd n) are not found in the resonance curve. More interestingly, the even and symmetric (with respect to rotation of π) mode [2,2,+] is not found either, confirming that the antisymmetry (with respect to rotation of $\pi/2$) of this particular mode is not compatible with the symmetry of the libration. However, it appears that at this frequency, the system still lies in the far tail of the [2,1,+] resonance, which probably explains the residual flow structure associated to the mode [2,1,+] found in Fig. 5(e). We can conclude that, because of viscous effects and symmetry properties, the libration forcing selects only one single resonant inertial mode in the range [0.60; 0.73]. The slight asymmetry in the tails of the resonance curve might be due to the presence of the modes [4,5,+] and [4,6,+] at frequencies slightly larger than the [2,1,+] peak. It turns out that [4,5,+] has the $\pi/2$ symmetry, whereas [4,6,+] has the π symmetry only; it is therefore conceivable that a slight contribution of the mode [4,5,+] is responsible for the asymmetric shape of the resonance curve.

VII. EXCITATION OF INERTIAL MODES BY THE EDGE BEAMS

The present results raise the question of the relation between the inertial modes and the edge beams originating from the convergence of Ekman fluxes near the edges of the container. Interestingly, for forcing frequencies close to the frequency of low-order symmetric inertial modes $[n, 1, +]$ with even n, the edge beams form a periodic ray pattern in the vertical plane (x, z). This is illustrated in Figs. 9(a) and 9(c) for libration frequencies corresponding to the modes [2,1,+] and [4,1,+], showing one and two X-shaped patterns, respectively. This figure suggests that the periodicity of the rays leads to the formation of a standing wave, since energy can propagate along these rays either way. It motivates the use of a two-dimensional simplification, in which the planar wave beams emitted from the edges of the cube propagate in the vertical plane along rays, at an angle given by the dispersion relation (7). This 2D approximation does not apply near the corners, where the flow must be three-dimensional. But away from the walls, the edge beams essentially protrude in the bulk of the fluid, as if the container were infinitely long in the along-edge direction.

We consider, in the following, the 2D ray orbits in a vertical plane originating from the edges of the cube. These orbits can be characterized by integers, (i, j), denoting the number of reflections from vertical (i) and horizontal (j) boundaries. Here, we count edge reflections as reflections on *both* the vertical as well as the horizontal walls. The orbits in Figs. 9(b) and 9(d) therefore classify as (1, 1) and (2, 1) periodic orbits, respectively. The angle which the beam makes with the horizontal is $\theta_{ij} = \tan^{-1}(j/i)$, yielding a normalized frequency

$$\frac{\sigma_{ij}}{2\Omega_0} = \cos\left(\tan^{-1}\left(\frac{j}{i}\right)\right) = \frac{i}{\sqrt{i^2 + j^2}},$$

similar to the expression for the eigenfrequencies of the transverse modes of an infinite channel.[9] The frequencies σ_{ij} are dense in $[0, 2\Omega_0]$. This spectrum is degenerate: patterns (i, j) and (i', j') have the same frequency if $i'/i = j'/j$ (such degeneracy is not obvious for the inertial modes in the parallelepiped). The resulting ray pattern may be associated with a set of cells, with hyperbolic points at the intersection between rays. Restricting to ray patterns compatible with symmetries of the libration, this construction yields $2i \times 2j$ cells [see dashed lines in Figs. 9(b) and 9(d)], corresponding to an $n = 2i$ inertial mode structure. No similar connection can be made between index m and j from this simple geometrical construction, because m is not related to the number of cells in the horizontal direction.

If we compare the frequencies of the periodic patterns (i, j) and the frequencies of the inertial modes $[n, m, s]$, we obtain a reasonable agreement for $n = 2i$, $m = 1$, and $s = +$ (see Table II). The discrepancy is 4.7% for [2, 1, +], and decreases for larger n. We can also note that, for $j > 1$, it is always possible to find, among the modes having $n = 2i$ and $s = +$, a mode $m > 1$ such that $\sigma_{ij} \simeq \sigma_{nms}$ to within a few %. For instance, for $(i, j) = (1, 2)$, one has $\sigma_{12}/2\Omega_0 = 0.447$, which is close to the frequencies of modes [2, 4, +] and [2, 5, +] (0.465 and 0.434, respectively). One

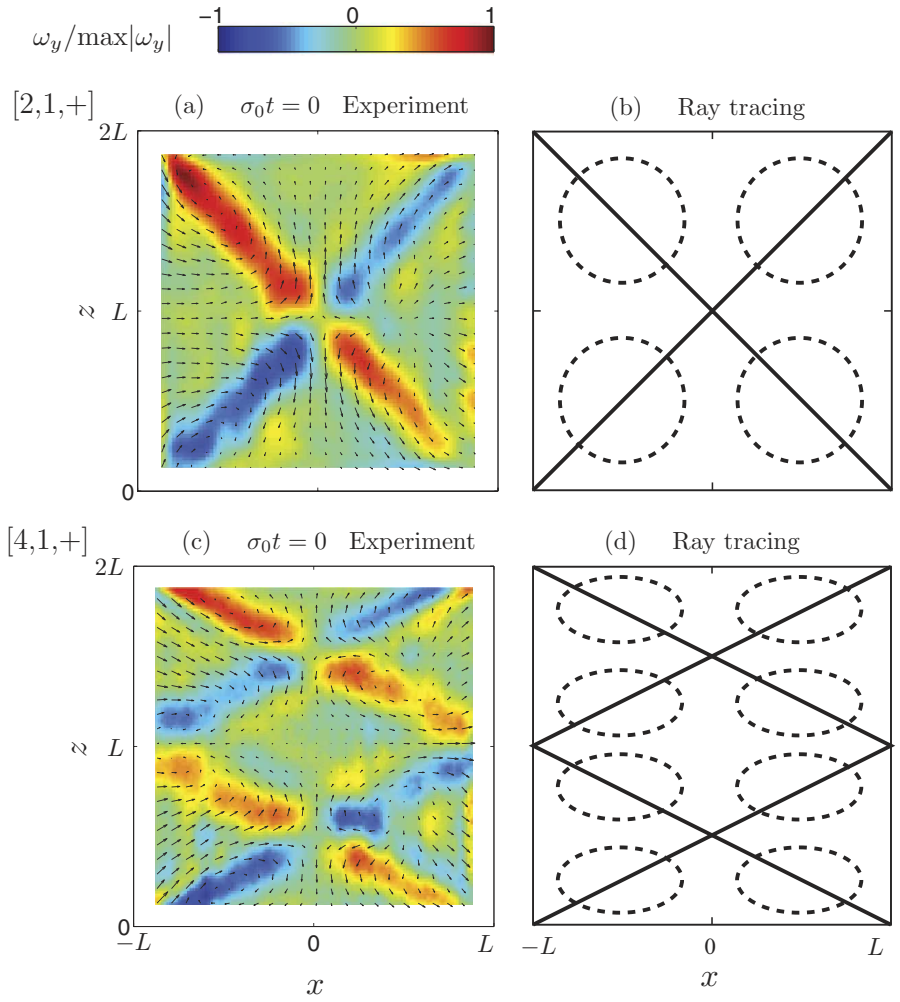

FIG. 9. (a) and (c) Flow in the vertical plane $y = 0$ corresponding to the modes [2, 1, +] and [4, 1, +]; (b) and (d) corresponding ray-tracing patterns (1,1) and (2,1). Figures are taken at the libration phase $\sigma_0 t = 0$, for which, the mode has zero amplitude, so only the wave beams are visible.

explanation for the apparent ability of strictly 2D periodic orbits to predict eigenfrequencies of the 3D problem quite accurately may lie in the fact that while the eigenspectrum is dense, there are indications that the density of states (the amount of eigenfrequencies per frequency increment) may be nonuniform. Computations in long channels[9] show that eigenfrequencies cluster preferentially around the eigenfrequencies of strictly transverse modes of an infinitely long channel, and there are indications that this also applies to the higher vertical modes (large n) in a cube.

The coincidence between the frequencies of inertial modes and periodic beam patterns of similar spatial structure suggests the following mechanism for the excitation of modes in a librated container. A given libration frequency induces a set of inertial wave beams originating from the detachment of the oscillating Ekman layers at the edges. If the libration frequency is close to an inertial mode,

TABLE II. Comparison between the frequencies of the periodic edge beam patterns (i, 1) and the frequencies of the inertial modes with $[n, 1, +] = [2i, 1, +]$.

Pattern (i, j)	θ_{ij}	$\sigma_{ij}/2\Omega_0$	Mode $[n, m, s]$	$\sigma_{nms}/2\Omega_0$	Difference (%)
(1,1)	45°	0.707	[2,1,+]	0.674	4.7
(2,1)	26.6°	0.894	[4,1,+]	0.875	2.1
(3,1)	18.4°	0.949	[6,1,+]	0.938	1.2

the resulting edge beam pattern is nearly periodic, and has the same symmetries as the mode—this is at least the case for the two modes [2,1,+] and [4,1,+] shown in Fig. 9. This suggests that the edge beams can supply energy to the modes directly in the bulk of the flow, with the correct vertical periodicity. The libration flow, being associated to $n = 0$ (vertical invariance), is unable to excite these modes other than viscously, through the edge beams, because it lacks the vertical structure of the inertial modes. This may be different in the presence of sloping boundaries, which enforce vertical motions, and may excite inertial waves inviscidly. We may conclude that inertial modes are excited with an *inertial* velocity scale $\epsilon\Omega_0 L$, but this excitation requires the presence of edge beams induced by the *viscous* oscillating Ekman layers.

VIII. CONCLUSION

In *symmetric* containers, i.e., axisymmetric containers or containers whose side walls are either parallel or perpendicular to the rotation axis, longitudinal libration produces an inviscid type of fluid response that conserves absolute vorticity. However, by friction at bottom, top, and side walls, this leads to a periodic mass flux in boundary layers adjacent to the horizontal walls. Convergence and divergence of these Ekman fluxes near the edges spawn free shear layers that are inclined with respect to the rotation axis.[16,25,33] Their angle is set by the ratio of the modulation frequency to the Coriolis frequency. Expulsion of Ekman mass fluxes takes place where the topography has the same inclination, at so-called *critical* slopes. In containers where changes in the orientation of the boundary occur suddenly (such as near the edges of the cube studied here), these critically sloping regions are "buried" in these horizontal edges. The free shear layers thus spawn from the edges, and are here termed "edge beams."

In a 2D approximation, these edge beams propagate along periodic paths. For paths that are short enough, upon a few reflections energy folds back onto itself and an inertial mode may establish itself: a vertically standing large-scale structure that may either be propagating, or standing ("sloshing") horizontally. In our experiment, symmetries, due to the way that the fluid is forced into motion by means of libration, allow the realization of only a particular subset of all possible theoretical inertial modes. Latitudinal libration (libration along an axis normal to the rotation axis) might provide a mechanism by means of which also the other, anti-symmetric modes can be excited, e.g., the mode [1,1,−], which consists in a single oscillating cell.

Previous studies in cylindrical domains suggest that the resonant forcing (and, therefore, amplification) of a vertically standing inertial mode opens the possibility of elliptic instability (vortex breakdown). This should be manifested as a sudden collapse of the inertial wave mode. This has so far not been seen in our experiments in a cube, but is not ruled out either. Another peculiarity of the theoretical inviscid wave field in the cube is the appearance of many horizontal scales of motion, even for "large-scale" modes (i.e., having low vertical wave number and high frequency).[9] These scales are required by the wave field in order to match the rotational (circular) to the geometrical (square) symmetries. A more detailed experimental observation of an inertial mode is required to investigate this property. Finally, it is of interest to examine as to what extent edge beams and inertial modes can play a role in containers whose symmetry is broken.

ACKNOWLEDGMENTS

We acknowledge A. Aubertin, L. Auffray, C. Borget, and R. Pidoux for experimental help, and Y. Duguet, W. Herreman, and M. Rabaud for fruitful discussions. J.B. is supported by the "Triangle de la Physique." This work is supported by the ANR (Grant No. ANR-2011-BS04-006-01) "ONLITUR." The rotating platform "Gyroflow" was funded by the "Triangle de la Physique."

APPENDIX: THE INVISCID BASE FLOW IN A LIBRATING CUBE

In this section, we derive the streamfunction describing the inviscid flow generated by the libration of a parallelepiped container of square cross section. The Euler equation in the librated

frame of reference writes

$$\frac{\partial \mathbf{u}}{\partial t} + (\boldsymbol{\omega} + 2\Omega) \times \mathbf{u} = -\nabla\Big(\frac{p}{\rho} + \frac{1}{2}|\Omega(t) \times \mathbf{r}|^2 + \frac{1}{2}|\mathbf{u}|^2\Big) - \frac{d\Omega}{dt} \times \mathbf{r}, \tag{A1}$$

with $\boldsymbol{\Omega}(t)$, the total angular velocity, of vertical component given by Eq. (1). This equation contains three terms related to the (modulated) background rotation: (1) the Coriolis acceleration (last term on left-hand side), (2) the centrifugal force (second term on right-hand, that can be absorbed in a reduced pressure), and (3) the Euler force (last term on right-hand side), due to the modulation of the rotation rate.[34] Here, $\boldsymbol{\omega}$ is the relative vorticity vector, $\boldsymbol{\omega} = \nabla \times \mathbf{u}$. Taking the curl of the Euler equation (A1), we obtain the vorticity equation:

$$\frac{\partial \boldsymbol{\omega}}{\partial t} + \mathbf{u} \cdot \nabla(\boldsymbol{\omega} + 2\Omega) - (\boldsymbol{\omega} + 2\Omega) \cdot \nabla \mathbf{u} = -2\frac{d\boldsymbol{\Omega}}{dt}.$$

This equation tells that relative vorticity changes due to advection of absolute vorticity,

$$\boldsymbol{\omega}_a = \boldsymbol{\omega} + 2\Omega$$

(second term on left-hand side), vortex tilting by sheared motion (third term), or by changes in the rotation rate (right-hand side).

Note that for forcing by libration, the driving term on the right of the vorticity equation is present in the vertical direction only and is independent of the vertical coordinate. Since the boundaries are not inclined relative to the rotation axis, this motivates looking for velocity fields that are z-independent as well. In fact, the vanishing of the vertical velocity at the horizontal bottom and top walls suggests looking for solutions of zero vertical velocity. The vertical component of the vorticity $\omega_a = \boldsymbol{\omega}_a \cdot \mathbf{e}_z$ (which at this point is the only nonvanishing component) thus satisfies

$$\frac{\partial \omega_a}{\partial t} = 0.$$

Since the horizontal velocity field is nondivergent ($\partial_x u_x + \partial_y u_y = 0$), we can introduce a streamfunction such that $(u_x, u_y) = (-\partial_y \psi, \partial_x \psi)$. The spatial part $\Psi(x, y)$ of streamfunction, $\psi(x, y, t) = \Psi(x, y) \cos(\sigma_0 t)$, therefore satisfies a Poisson equation,

$$\Delta \Psi = -2\epsilon \Omega_0, \tag{A2}$$

subject to the condition that in the librating frame, the solid boundary at $x = \pm L$ and $y = \pm L$ acts as a streamline. We introduce the normalized coordinates $(\tilde{x}, \tilde{y}) = (x, y)/L$. The solution of Eq. (A2) is the sum of a particular solution, Ψ_p, and a homogeneous solution, Ψ_h, such that $\Delta \Psi_h = 0$. A particular solution is

$$\Psi_p = \epsilon \Omega_0 (1 - \tilde{x}^2),$$

that matches the right hand forcing term and satisfies the boundary condition at $\tilde{x} = \pm 1$, but is *nonvanishing* at $\tilde{y} = \pm 1$. The homogeneous solution, Ψ_h, also vanishes at $\tilde{x} = \pm 1$, but annihilates $\Psi_p(\tilde{x})$ at $\tilde{y} = \pm 1$. It is given by

$$\Psi_h = -4\epsilon \Omega_0 \sum_{n=0}^{\infty} (-1)^n \frac{\cos(d_n \tilde{x}) \cosh(d_n \tilde{y})}{d_n^3 \cosh(d_n)},$$

where

$$d_n \equiv (2n + 1)\frac{\pi}{2}.$$

For convenience, we finally symmetrize the solution, by simply computing $(\Psi(\tilde{x}, \tilde{y}) + \Psi(\tilde{y}, \tilde{x}))/2$, yielding

$$\Psi = \epsilon \Omega_0 \Big(1 - \frac{1}{2}(\tilde{x}^2 + \tilde{y}^2) - 2\sum_{n=0}^{\infty} (-1)^n \frac{\cos(d_n \tilde{x}) \cosh(d_n \tilde{y}) + \cos(d_n \tilde{y}) \cosh(d_n \tilde{x})}{d_n^3 \cosh(d_n)}\Big). \tag{A3}$$

[1] H. Greenspan, *The Theory of Rotating Fluids* (Cambridge University Press, London, 1968).
[2] J. Pedlosky, *Geophysical Fluid Dynamics* (Springer-Verlag, Heidelberg, 1987).
[3] J. Lighthill, *Waves in Fluids* (Cambridge University Press, London, 1978).
[4] A. D. McEwan, "Inertial oscillations in a rotating fluid cylinder," J. Fluid Mech. **40**, 603–639 (1970).
[5] K. K. Zhang, X. H. Liao, and P. Earnshaw, "On inertial waves and oscillations in a rapidly rotating spheroid," J. Fluid Mech. **504**, 1–40 (2004).
[6] O. M. Phillips, "Energy transfer in rotating fluids by reflection of inertial waves," Phys. Fluids **6**(4), 513 (1963).
[7] A. A. M. Manders and L. R. M. Maas, "Observations of inertial waves in a rectangular basin with one sloping boundary," J. Fluid Mech. **493**, 59 (2003).
[8] G. K. Batchelor, *An Introduction to Fluid Dynamics* (Cambridge University Press, Cambridge, 1967)
[9] L. R. M. Maas, "On the amphidromic structure of inertial waves in rectangular parallelepiped," Fluid Dyn. Res. **33**, 373–401 (2003).
[10] K. D. Aldridge and A. Toomre, "Axisymmetric inertial oscillations of a fluid in a rotating spherical container," J. Fluid Mech. **37**, 307−323 (1969).
[11] M. Rieutord, "Linear theory of rotating fluids using spherical harmonics. II. Time-periodic flows," Geophys. Astrophys. Fluid Dyn. **59**, 185−208 (1991).
[12] A. Tilgner, "Driven inertial oscillations in spherical shells," Phys. Rev. E **59**, 1789−1794 (1999).
[13] J. Noir, F. Hemmerlin, J. Wicht, S. Baca, and J. Aurnou, "An experimental and numerical study of librationally driven flow in planetary cores and subsurface oceans," Phys. Earth Planet Inter. **173**, 141−152 (2009).
[14] M. A. Calkins, J. Noir, J. D. Eldredge, and J. M. Aurnou, "Axisymmetric simulations of libration-driven fluid dynamics in a spherical shell geometry," Phys. Fluids **22**, 086602 (2010).
[15] F. H. Busse, "Steady fluid flow in a precessing spheroidal shell," J. Fluid Mech. **33**(4), 739 (1968).
[16] R. R. Kerswell, "On the internal shear layers spawned by the critical regions in oscillatoray Ekman boundary layers," J. Fluid Mech. **298**, 311 (1995).
[17] J. Noir, D. Jault, and P. Cardin, "Numerical study of the motions within a slowly precessing sphere at low Ekman number," J. Fluid Mech. **437**, 283 (2001).
[18] S. T. Suess, "Viscous flow in a deformable rotating container," J. Fluid Mech. **45**, 189−201 (1971).
[19] C. Morize, M. Le Bars, P. Le Gal, and A. Tilgner, "Experimental determination of zonal winds driven by tides," Phys. Rev. Lett. **104**, 214501 (2010).
[20] W. V. R. Malkus, "Precession of earth as cause of geomagnetism," Science **160**, 259 (1968).
[21] A. Tilgner, "Zonal wind driven by inertial modes," Phys. Rev. Lett. **99**, 194501 (2007).
[22] S. B. Dalziel, "Decay of rotating turbulence: Some particle tracking experiments," Appl. Sci. Res. **49**, 217−244 (1992).
[23] G. P. Bewley, D. P. Lathrop, L. R. M. Maas, and K. R. Sreenivasan, "Inertial waves in rotating grid turbulence," Phys. Fluids **19**, 071701 (2007).
[24] C. Lamriben, P.-P. Cortet, F. Moisy, and L. R. M. Maas, "Excitation of inertial modes in a closed grid turbulence experiment under rotation," Phys. Fluids **23**, 015102 (2011).
[25] Y. Duguet, J. F. Scott, and L. Le Penven, "Oscillatory jets and instabilities in a rotating cylinder," Phys. Fluids **18**, 104104 (2006).
[26] DaVis, LaVision GmbH, Anna-Vandenhoeck-Ring 19, Goettingen, Germany.
[27] F. Moisy, PIVMat toolbox for Matlab, Laboratory FAST, University Paris-Sud, France.
[28] A. Sauret, D. Cébron, M. Le Bars, and S. Le Dizès, "Fluid flows in a librating cylinder," Phys. Fluids **24**, 026603 (2012).
[29] K. S. Peat, "Internal and inertial waves in a viscous rotating stratified fluid," Appl. Sci. Res. **33**(5–6), 481–499 (1977).
[30] A. Tilgner, "Oscillatory shear layers in source driven flows in an unbounded rotating fluid," Phys. Fluids **12**, 1101 (2000).
[31] P.-P. Cortet, C. Lamriben, and F. Moisy, "Viscous spreading of an inertial wave beam in a rotating fluid," Phys. Fluids **22**, 086603 (2010).
[32] See supplementary material at http://dx.doi.org/10.1063/1.4731802 for movies of the experimental fields compared to the numerical inviscid modes.
[33] A. Swart, L. R. M. Maas, U. Harlander, and A. Manders, "Experimental observation of strong mixing due to internal wave focusing over sloping terrain," Dyn. Atmosph. Oceans **50**, 16−34 (2010).
[34] I. Tolstoy, *Wave Propagation* (McGraw-Hill, New York, 1973).

epl A Letters Journal Exploring the Frontiers of Physics

June 2012

EPL, **98** (2012) 59002 www.epljournal.org
doi: 10.1209/0295-5075/98/59002

Earth rotation prevents exact solid-body rotation of fluids in the laboratory

J. Boisson[1(a)], D. Cébron[2(b)], F. Moisy[1(c)] and P.-P. Cortet[1(d)]

[1] *Laboratoire FAST, CNRS, Univ Paris-Sud, UPMC Univ Paris 06 - France, EU*
[2] *Institut für Geophysik, ETH Zürich - Switzerland*

received 1 April 2012; accepted in final form 18 May 2012
published online 12 June 2012

PACS 92.10.Ei – Coriolis effects
PACS 47.32.-y – Vortex dynamics; rotating fluids
PACS 92.10.hj – Internal and inertial waves

Abstract – We report direct evidence of a secondary flow excited by the Earth rotation in a water-filled spherical container spinning at constant rotation rate. This so-called *tilt-over flow* essentially consists in a rotation around an axis which is slightly tilted with respect to the rotation axis of the sphere. In the astrophysical context, it corresponds to the flow in the liquid cores of planets forced by precession of the planet rotation axis, and it has been proposed to contribute to the generation of planetary magnetic fields. We detect this weak secondary flow using a particle image velocimetry system mounted in the rotating frame. This secondary flow consists in a weak rotation, thousand times smaller than the sphere rotation, around a horizontal axis which is stationary in the laboratory frame. Its amplitude and orientation are in quantitative agreement with the theory of the tilt-over flow excited by precession. These results show that setting a fluid in a perfect solid-body rotation in a laboratory experiment is impossible —unless by tilting the rotation axis of the experiment parallel to the Earth rotation axis.

Introduction. – There are few examples of fluid mechanics experiments at the laboratory scale in which the Earth's Coriolis force has a measurable influence. Such experiments may be considered as fluid analogues to the Foucault pendulum. The most popular instance is certainly the drain of a bathtube vortex [1]. Although this is the subject of common misconception, it is actually possible to detect the influence of the Earth's rotation on the vortex, but only under extremely careful experimental conditions, far from the everyday experience [2]. Thermal convection is another example, in which a slow drift of the large-scale flow due to the Earth rotation has been detected in very controlled systems [3,4].

In this letter we describe an experiment which may be considered as the most simple fluid Foucault pendulum: it consists in a volume of water enclosed in a spherical container spinning at constant rotation rate Ω_0 (fig. 1). After a transient known as spin-up, the water is expected to rotate as a solid body at the same rate Ω_0 [5]. The timescale for this spin-up is classically given by the Ekman time $\tau_E = R\,(\nu\Omega_0)^{-1/2}$, where R is the radius of the sphere and ν the kinematic viscosity of the fluid. For a typical laboratory experiment using water, this timescale is usually of the order of a minute, so after a few tens of minutes a perfect solid-body rotation should be reached, with the fluid exactly at rest in the frame of the container. If this simple experiment is performed on Earth, it is expected that the Earth rotation could prevent from reaching this idealized solid rotation state [6,7]. A weak secondary flow, known as *tilt-over* flow [5,8,9], is induced by the precession of the rotation vector $\boldsymbol{\Omega}_0$ of the container by the Earth rotation vector $\boldsymbol{\Omega}_p$. Seen from the laboratory frame of reference, the fluid particles rotating at velocity $\mathbf{u}_0 = \boldsymbol{\Omega}_0 \times \mathbf{r}$ experience a Coriolis force per unit mass $\mathbf{f}_c = -2\boldsymbol{\Omega}_p \times \mathbf{u}_0$. This Coriolis force disturbs the fluid particles periodically at frequency Ω_0, and tends to deflect their trajectory towards the plane normal to $\boldsymbol{\Omega}_p$.

Precession driven flows in spherical or spheroidal containers and in spheroidal shells have received considerable interest since Poincaré [10], because of their importance to geophysical and astrophysical flows [8,9]. In the case of the Earth, rotating with a period $T_0 \sim 1$ day, the precession of its rotation axis, at a period $T_p \simeq$ 26000 years, could produce large excursions of the

(a) E-mail: boisson@fast.u-psud.fr
(b) E-mail: david.cebron@erdw.ethz.ch
(c) E-mail: moisy@fast.u-psud.fr
(d) E-mail: ppcortet@fast.u-psud.fr

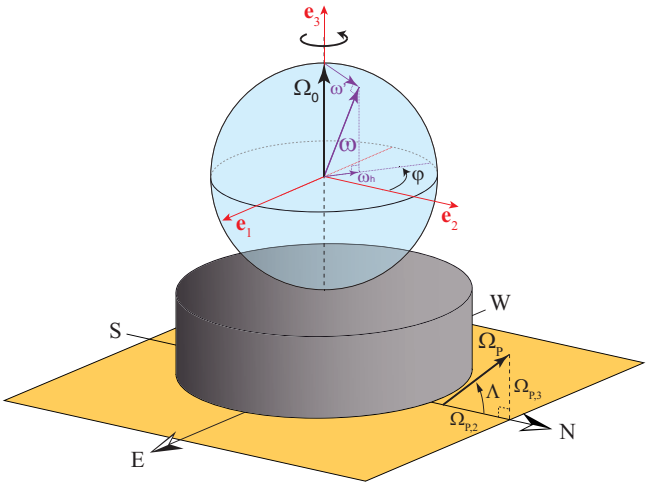

Fig. 1: (Color online) Sketch of the rotating platform and the water filled sphere. ($\mathbf{e}_1$, $\mathbf{e}_2$, $\mathbf{e}_3$) is a Cartesian coordinates system attached to the laboratory frame. The platform is rotating at $\boldsymbol{\Omega}_0 = \Omega_0\,\mathbf{e}_3$ in the laboratory. $\boldsymbol{\Omega}_p$ is the Earth rotation vector at the latitude $\Lambda = 48.70^\circ$ of the laboratory. $\boldsymbol{\omega}$ is the rotation vector of the tilt-over flow in the bulk. The rotation vectors are not to scale.

rotation axis of the liquid core [11]. Precession driven flows have also been proposed by Malkus [9] to contribute to the generation of planetary magnetic fields, which has been later confirmed by Kerswell [12] and Tilgner [13]. Kida [14] recently proposed a complete solution for the flow in a rapidly rotating sphere under weak precession, including a detailed analysis of the conical shear layers detached from the critical latitudes.

First evidence of a tilt-over flow excited by the Earth rotation in a laboratory experiment has been reported by Vanyo and Dunn [6], using visualizations by dyes and buoyant tracers, but without quantitative determination of the tilt-over flow properties. Recently, Triana *et al.* [7] obtained indirect evidence of this effect, from one-dimensional velocity profiles in a rotating water-filled spherical shell, 3 m in diameter, containing an inner co-rotating sphere. However, no quantitative agreement with the theory of Busse [8] could be obtained in their experiment.

Based on the same idea, we provide in this letter, by means of particle image velocimetry measurements (PIV), the first direct visualization of the precession flow driven by the Earth rotation in a sphere rotating in the laboratory. These measurements are a technical challenge, because of the weakness of the velocity signal of this tilt-over flow (the fluid rotation axis is tilted by less than 0.2° with respect to the sphere rotation axis). A quantitative agreement with the theory of Busse is demonstrated, both for the magnitude and the orientation of the secondary circulation.

Physical origin of the tilt-over flow. – Poincaré [10] first analyzed the precession flow in a sphere in the singular case of a perfect fluid. He showed that the inviscid solution consists in a solid-body rotation around an axis parallel to $\boldsymbol{\Omega}_p$, but of undefined amplitude. In the presence of weak viscosity, far from the boundaries, the tilt-over flow may still be described as a solid-body rotation, with a rotation vector $\boldsymbol{\omega}$ tilted with respect to $\boldsymbol{\Omega}_0$, and stationary in the *precessing frame* (the laboratory frame here). We note in the following $\boldsymbol{\omega}' = \boldsymbol{\omega} - \boldsymbol{\Omega}_0$ the rotation vector of the fluid in the bulk measured in the rotating frame.

Remarkably, the presence of viscosity, even weak, drastically changes the rotation vector of the fluid $\boldsymbol{\omega}$ compared to the inviscid solution of Poincaré. The orientation and amplitude of $\boldsymbol{\omega}$ for a viscous fluid are now nontrivial functions of the Poincaré number Ω_p/Ω_0 and of the Ekman number $E = \nu/(\Omega_0 R^2)$. In the limit $\Omega_p/\Omega_0 \ll \sqrt{E} \ll 1$, the rotation vector $\boldsymbol{\omega}$ is almost equal to $\boldsymbol{\Omega}_0$, and the small correction $\boldsymbol{\omega}'$ is almost normal to $\boldsymbol{\Omega}_0$. This tilt-over flow has been described by Busse [8] as one among a dense family of inertial modes, of eigenfrequency given by Ω_0 (see ref. [5] for a general description of inertial modes in a sphere). When forced by precession, the magnitude ω' of this tilt-over flow can be determined by a simple balance between the Coriolis torque (in the bulk) and the viscous torque (at the surface of the container). The Coriolis torque is of order $\Gamma_c \sim \rho R^4 f_c \sim \rho R^5 \Omega_p \Omega_0 \cos\Lambda$, with ρ the fluid density and $\cos\Lambda = |\boldsymbol{\Omega}_0 \times \boldsymbol{\Omega}_p|/\Omega_0\Omega_p$. The viscous stress is given by $\sigma \sim \rho\nu\Delta u/\delta$, where $\Delta u \simeq \omega' R$ is the small velocity jump between the container wall and the fluid bulk, and $\delta = (\nu/\Omega_0)^{1/2}$ is the thickness of the Ekman boundary layer. The resulting viscous torque is of order $\Gamma_\nu \sim R^3\sigma \sim \rho\nu\omega' R^4/\delta$. Balancing the two torques gives the simple relation

$$\omega' \sim E^{-1/2}\Omega_p \cos\Lambda. \qquad (1)$$

Although very weak, this tilt-over correction may be significantly larger than the Earth rotation rate in a typical laboratory experiment where $E \ll 1$.

Experimental setup. – The experimental setup, sketched in fig. 1, consists in a spherical glass tank, of inner radius $R = 115 \pm 0.25$ mm, filled with water and mounted on the center of a precision rotating turntable of 2 m in diameter. We use two Cartesian coordinate systems, both with origin at the center of the sphere: i) $(\mathbf{e}_1, \mathbf{e}_2, \mathbf{e}_3)$, attached to the laboratory reference frame (fig. 1), with $\mathbf{e}_1$ pointing to East, $\mathbf{e}_2$ pointing to North and $\mathbf{e}_3$ along the vertical; ii) $(\mathbf{e}_x, \mathbf{e}_y, \mathbf{e}_z)$, attached to the rotating platform (fig. 2), with $\mathbf{e}_z = \mathbf{e}_3$, in which the measurements are performed.

The platform is rotating in the laboratory frame with a rotation vector $\boldsymbol{\Omega}_0 = \Omega_0\,\mathbf{e}_3$. The angular velocity Ω_0 is varied between 2 and 16 rpm, with temporal fluctuations less than $\pm 5 \times 10^{-4}$. The Ekman number $E = \nu/(\Omega_0 R^2)$ varies between 3.6×10^{-4} and 4.6×10^{-5} in this range of Ω_0. In fig. 1, the rotation vector of the Earth $\boldsymbol{\Omega}_p$ is also shown, for the latitude $\Lambda = 48.70^\circ$ of our laboratory in Orsay. The relative scale of the vectors $\boldsymbol{\Omega}_0$ and $\boldsymbol{\Omega}_p$ is obviously not realistic in this figure: the Earth rotation rate is $\Omega_p \simeq 6.9 \times 10^{-4}$ rpm $\sim 2\pi/(1\text{ day})$, which yields

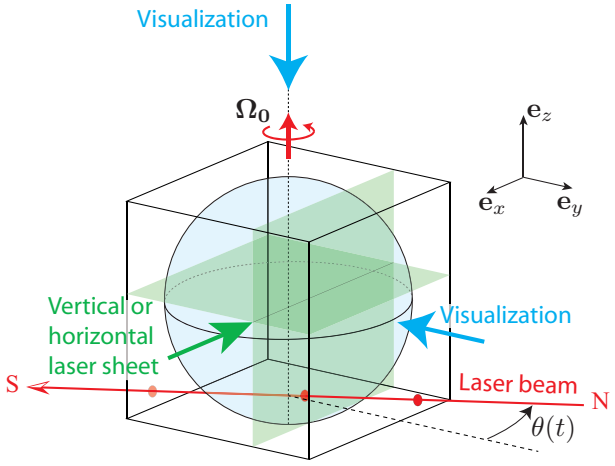

Fig. 2: (Color online) Schematic view of the cubic water tank containing the 115 mm radius glass sphere, mounted together on the rotating platform. PIV measurements are achieved in off-centered vertical and horizontal planes, located at $y_{\rm mes} = +22$ mm and $z_{\rm mes} = +22$ mm, using a corotating laser sheet and a camera aiming normally at it. The angle $\theta(t)$ between the images and the North direction is determined using a continuous laser beam aligned along the North-South orientation and crossing the rotation axis.

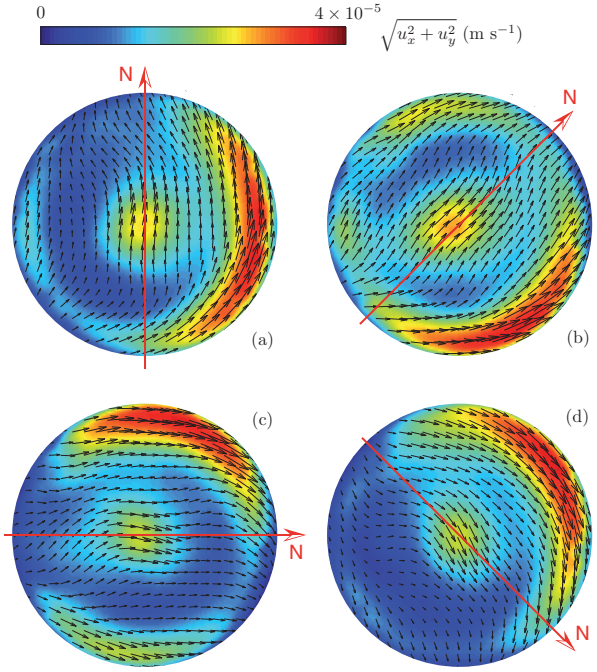

Fig. 3: (Color online) Horizontal velocity fields measured in the rotating frame, in the off-centered horizontal plane at $z_{\rm mes}/R \simeq 0.19$ for $\Omega_0 = 6$ rpm ($E = 1.2 \times 10^{-4}$), with a phase shift of $\pi/4$ between each image. The platform rotation is anticlockwise. The red arrows indicate the direction of the North at each time. Resolution of the velocity fields has been reduced by a factor 5 for better visibility.

a Poincaré number Ω_p/Ω_0 ranging from 3.5×10^{-4} to 4.3×10^{-5}.

After the start of the platform rotation, we wait at least $\tau_w = 2$ hours before data acquisition in order to reach a stationary regime. This waiting time represents at least $30\,\tau_E$, where $\tau_E = R\,(\nu\Omega_0)^{-1/2}$ is the Ekman spin-up time. This indicates that the solid-body rotation state should be reached, apart from precession effects, with a relative precision better than $\exp(-\tau_w/\tau_E) \simeq 10^{-13}$.

Velocity fields are measured in the rotating frame using a two-dimensional PIV system [15] mounted on the rotating platform, in either a vertical $(\mathbf{e}_x, \mathbf{e}_z)$- or a horizontal $(\mathbf{e}_x, \mathbf{e}_y)$-plane (fig. 2). These measurement planes are off-centered, at $y_{\rm mes}/R = z_{\rm mes}/R \simeq 0.19$ (see fig. 2), in order to get better insight in the spatial structure of the flow. Optical distortions are reduced by immersing the glass sphere in a square glass tank of 300 mm side also filled with water. The distortion is found less than 5% for $r < 0.9R$. The fluid is seeded with 10 μm tracer particles, and illuminated by a corotating laser sheet generated by a 140 mJ Nd:YAG pulsed laser. For both horizontal and vertical measurements, the sphere cross-section is imaged with a high-resolution 2048×2048 pixels camera aiming normally at the laser sheet.

For each rotation rate Ω_0, a set of 2000 images is acquired, covering at least 80 rotation periods. The sampling rate is synchronized with the platform rotation rate, with a number of images per rotation ranging from 24 (for low Ω_0) to 9 (for large Ω_0). PIV fields are computed over successive images using 32×32 pixels interrogation windows with 50% overlap, leading to a spatial resolution of about 2 mm. This resolution is not enough to resolve the thickness of the Ekman boundary layers, $\delta \simeq R\,E^{1/2} = 0.8$–$2.2$ mm, but is appropriate for the large scales of the precession flow expected in the bulk.

In view of the very low velocity expected for the precession flow, the resolution of the velocity measurement is critical in our experiment. The characteristic velocities of the flow encountered in this work ranges from 0.01 to 0.4 mm s^{-1} for Ω_0 between 2 and 16 rpm. For the sampling rates considered here, these velocities correspond to a typical frame-by-frame particle displacement of 0.16 to 2.6 pixels only. Although very weak, such displacement may actually be measured using PIV with sub-pixel interpolation of the correlation peak. For interrogation windows of size 32×32 pixels, an accuracy of 0.05 pixel can be achieved using this technique [15,16], yielding a signal-to-noise ratio ranging from 3 (low Ω_0) to 50 (large Ω_0).

The orientation of the experiment with respect to the Earth rotation axis is monitored using a continuous laser beam aligned along the North-South direction and passing through the rotation axis of the sphere (see fig. 2). The beam crosses the cubic glass tank and is therefore visible on the recorded images. The angle $\theta(t)$ between the South-North direction and the measurement fields (see fig. 2) can be determined for each image with a precision better than $\pm 0.5°$.

Structure of the tilt-over flow. – We first show in fig. 3 the flow measured in the horizontal plane in the rotating frame for a rotation rate $\Omega_0 = 6$ rpm. This flow

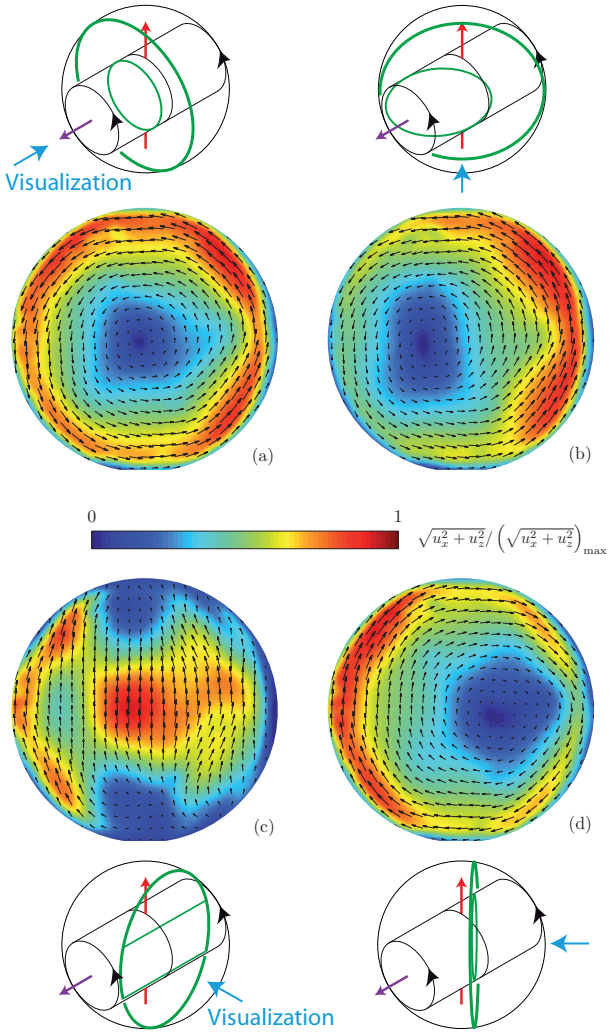

Fig. 4: (Color online) Vertical velocity fields measured in the rotating frame, in the off-centered vertical plane at $y_{\rm mes}/R \simeq 0.19$ for $\Omega_0 = 6\,$rpm ($E = 1.2\times10^{-4}$), with a phase shift of $\pi/4$ between each image. The color maps the vertical velocity norm normalized by its maximum in each field. The phase origin is not the same as in fig. 3.

represents the departure between the total flow in the laboratory frame and the solid-body rotation at Ω_0. In order to improve the quality of the velocity fields shown here, a phase average is performed over the velocity fields at the platform rotation rate Ω_0. This procedure allows to decrease the broad-band PIV measurement noise by a factor $N^{1/2}$, where N is the number of recorded rotation periods ($N \geqslant 80$). The spatial structure of the precession flow can finally be extracted with a signal-to-noise ratio of at least 30 for all rotations rates.

The four snapshots shown in fig. 3 are separated by a phase shift of $\pi/4$, with a phase origin chosen such that $\mathbf{e}_x = \mathbf{e}_1$ (*i.e.*, $\mathbf{e}_y$ pointing to the North). In spite of the very weak velocity signal (of order of $0.04\,\mathrm{mm\,s^{-1}}$, to be compared to the typical velocity of the sphere boundaries, $\Omega_0\, R \simeq 72\,\mathrm{mm\,s^{-1}}$), we clearly observe a well-defined flow pattern, which is rotating as a whole at the platform rotation rate but in the opposite direction. This weak flow is therefore stationary in the laboratory frame. Assuming that the total flow in the laboratory frame is a solid-body rotation of vector $\boldsymbol{\omega}$ slightly tilted with respect to $\boldsymbol{\Omega}_0$, the measured flow must be a solid-body rotation of rotation vector $\boldsymbol{\omega}' = \boldsymbol{\omega} - \boldsymbol{\Omega}_0$. Since the measurement plane is shifted at $z_{\rm mes}/R \simeq 0.19$, the resulting horizontal velocity field must be uniform in the bulk, given by $\boldsymbol{\omega}' \times (z_{\rm mes}\mathbf{e}_3)$, and rotating in the anticyclonic direction at frequency Ω_0, which is precisely what we observe. Snapshots at other values of Ω_0 show essentially the same flow patterns.

Measurements in the vertical plane, shown in fig. 4, confirm this flow structure. In this configuration, the camera is now rotating around the vortex of quasi-horizontal rotation vector $\boldsymbol{\omega}'$ stationary in the laboratory frame. The 4 snapshots taken over half a rotation around the vortex actually show the following sequence: (a) anticlockwise, with $\boldsymbol{\omega}'$ pointing towards the camera; (b) intermediate; (c) ascending, with $\boldsymbol{\omega}'$ pointing to the left; (d) intermediate. If the tilt-over flow were a pure solid-body rotation, the ascending flow in the snapshot (c) would be uniform, given by $\boldsymbol{\omega}' \times (y_{\rm mes}\mathbf{e}_y)$, which is approximately the case far from the boundaries. The wall region where the flow departs from a pure uniform flow has a thickness of order of $0.3\,R$, which is much larger than the expected Ekman thickness $E^{1/2}R \simeq 0.01\,R$. The tilt-over flow is therefore not exactly a pure solid-body rotation, in agreement with numerical results obtained in a spherical shell with a very small stress-free inner solid core [17]. Indeed, because of the breakdown of the Ekman layer at the so-called critical circles, a pure solid-body rotation cannot be a uniformly valid solution [14].

Viscous prediction for the tilt-over flow forced by precession. – We compute here the rotation vector $\boldsymbol{\omega}$ in the bulk of the fluid viewed from the precessing frame of reference (here the laboratory frame), following refs. [18,19]. The differential rotation between the fluid in the bulk rotating at $\boldsymbol{\omega}$ and the sphere boundary rotating at $\boldsymbol{\Omega}_0$ is matched across an Ekman boundary layer of typical thickness $RE^{1/2}$. We therefore assume $E \ll 1$, such that a separation between a bulk flow and a thin boundary layer may be assumed. In the steady state, the viscous torque $\boldsymbol{\Gamma}_\nu$ exerted by the boundary layers on the fluid in the bulk is balanced by the Coriolis torque $\boldsymbol{\Gamma}_c$ (note that the pressure torque is zero here because of spherical symmetry). This balance, projected along $\boldsymbol{\omega}$ and along two directions normal to $\boldsymbol{\omega}$, yields the following nonlinear system of equations [5,19],

$$\omega_1^2 + \omega_2^2 = \omega_3(\Omega_0 - \omega_3), \tag{2}$$

$$\frac{\Omega_p}{\sqrt{E}}\left(\omega_3\cos\Lambda - \omega_2\sin\Lambda\right) = \lambda_r\omega_1\omega_3^{1/4}\Omega_0^{3/4} + \lambda_i\omega_2\frac{\Omega_0^{5/4}}{\omega_3^{1/4}}, \tag{3}$$

$$\frac{\Omega_p}{\sqrt{E}}\omega_1\cos\Lambda = \lambda_r\Omega_0^{3/4}\omega_3^{1/4}(\Omega_0 - \omega_3), \tag{4}$$

where λ_r and λ_i are, respectively, the non-dimensional viscous damping rate and viscous correction to the eigenfrequency of the tilt-over mode. Their values have been obtained by Greenspan [5] and completed by Zhang *et al.* [20], $\lambda_r = -2.62$ and $\lambda_i = 0.258$. In presence of viscosity, the eigenfrequency Ω_0 of the inviscid tilt-over mode becomes $\Omega_0 + (\lambda_i + \mathrm{i}\lambda_r)\sqrt{E}\sqrt{\Omega_0\,\omega}$ [18,20], which means that, if the precession forcing is switched off, the tilt-over mode starts to rotate in the inertial frame at a frequency $\lambda_i\sqrt{E}\sqrt{\Omega_0\,\omega}$, while exponentially decaying at a rate $|\lambda_r|\sqrt{E}\sqrt{\Omega_0\,\omega}$.

Equation (2) reflects the fact that the work done per unit time by the viscous torque is zero, $\boldsymbol{\Gamma}_\nu \cdot \boldsymbol{\omega} = 0$, since the work done by the Coriolis force is zero by definition. This equation, which can be recast into $\boldsymbol{\omega} \cdot (\boldsymbol{\omega} - \boldsymbol{\Omega}_0) = 0$, simply expresses the so-called "no spin-up" condition, indicating that there is no differential rotation between the fluid and the sphere in the direction of the fluid rotation. This right angle between $\boldsymbol{\omega}$ and $\boldsymbol{\omega}' = \boldsymbol{\omega} - \boldsymbol{\Omega}_0$ indicates that the rotation rate $|\boldsymbol{\omega}|$ of the fluid is lower than Ω_0.

If we further assume that the Poincaré number Ω_p/Ω_0 is small compared to $E^{1/2}$, the rotation vector $\boldsymbol{\omega}$ is almost aligned with $\boldsymbol{\Omega}_0$, and the system of equations (2)–(4) can be simplified. More precisely, this regime applies for rotation rates $\Omega_0 \gg \Omega_{0,c}$, with

$$\Omega_{0,c} = \left(\frac{\Omega_p R \sin\Lambda}{\lambda_r\sqrt{\nu}}\right)^2. \tag{5}$$

This condition is comfortably satisfied in the present experiments, with $\Omega_{0,c} \simeq 5.2 \times 10^{-5}$ rpm. In this limit, the components of the tilt-over flow can be explicitly derived

$$\omega_1 \simeq \frac{\Omega_p \cos\Lambda}{\lambda_r}\left(\frac{\Omega_0 R^2}{\nu}\right)^{1/2}, \tag{6}$$

$$\omega_2 \simeq \frac{\lambda_i}{\lambda_r}\omega_1, \tag{7}$$

$$\omega_3 \simeq \Omega_0. \tag{8}$$

The horizontal projection of $\boldsymbol{\omega}$ in the laboratory frame, $\boldsymbol{\omega}_h = \omega_1\mathbf{e}_1 + \omega_2\mathbf{e}_2$, has therefore an amplitude

$$\omega_h = \frac{\Omega_p \cos\Lambda}{|\lambda_r|}\left(\frac{\Omega_0 R^2}{\nu}\right)^{1/2}\left(1 + \frac{\lambda_i^2}{\lambda_r^2}\right)^{1/2}, \tag{9}$$

which has indeed the expected form (1). Note that, in the limit considered here ($\Omega_p/\Omega_0 \ll \sqrt{E}$), the horizontal projection $\boldsymbol{\omega}_h$ measured in the experiment almost coincides with $\boldsymbol{\omega}'$.

In this limit, the angle φ between $\boldsymbol{\omega}_h$ and $\mathbf{e}_1$ (the East direction) is constant, and given by

$$\varphi = \arctan\left(\frac{\omega_2}{\omega_1}\right) = \arctan\frac{\lambda_i}{\lambda_r} = 174.35^\circ, \tag{10}$$

showing that $\boldsymbol{\omega}_h$ points almost to the West (along $-\mathbf{e}_1$), with a slight component to the North. Remarkably, this asymptotic angle obtained in the limit of large Ω_0 is almost perpendicular to the inviscid prediction of Poincaré, for which $\boldsymbol{\omega}_h$ points to the North (*i.e.*, $\varphi = 90^\circ$). This indicates that, even for very low viscosity, the boundary layers have a critical influence on the tilt-over flow, provided that $\Omega_p/\Omega_0 \ll E^{1/2}$.

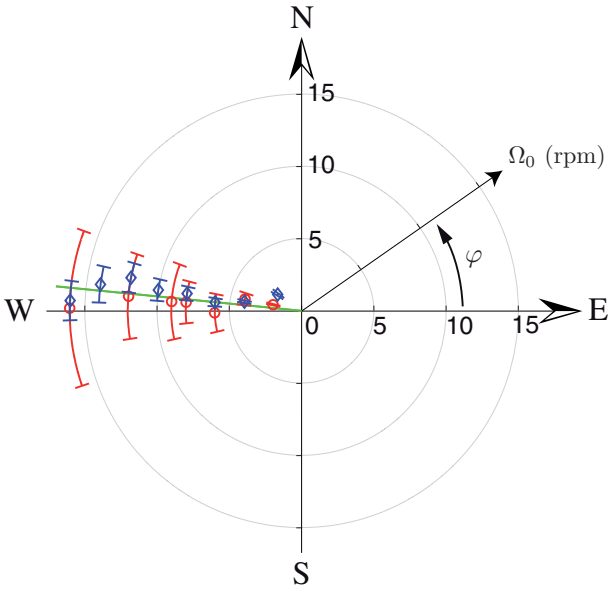

Fig. 5: (Color online) Angle φ between the rotation vector of the tilt-over flow and $\mathbf{e}_1$ (*i.e.*, East) as a function of the rotation rate Ω_0 in polar coordinates. Measurements are obtained in the horizontal (○) and the vertical (◊) plane, respectively. The continuous line shows the theoretical prediction $\varphi = 174.35^\circ$ (10).

Comparison with the experimental tilt-over flow. – The rotation rate ω_h of the tilt-over flow and its angle φ with the East have been systematically determined for Ω_0 ranging from 2 to 16 rpm. These data have been extracted independently from the raw velocity fields measured in the vertical and horizontal planes, and are compared here with the theoretical predictions (9) and (10) in figs. 5 and 6.

Measurements of the vortex angle φ from the PIV data in the vertical plane have been obtained as follows: the horizontal vorticity, spatially averaged over a central region of 50 mm radius, shows a harmonic oscillation at frequency Ω_0. At each period, the delay between the time $t_{\max}$ of maximum vorticity (when $\boldsymbol{\omega}_h$ points to the camera) and the time at which the North-South laser beam is aligned with the camera axis is computed. Knowing the instantaneous angle $\theta(t)$ between the camera incidence and the South-North direction, we can simply deduce the angle of the vortex as $\varphi = \theta(t_{\max}) + 90^\circ$. An independent estimate for φ has been determined from the data in the horizontal plane, by computing the time-averaged (and spatially averaged over the region $|\mathbf{r}| < 50$ mm) angle of the velocity with respect to the East direction $\mathbf{e}_1$.

The rotation rate ω_h of the horizontal component of the tilt-over flow has been determined from the vertical cuts

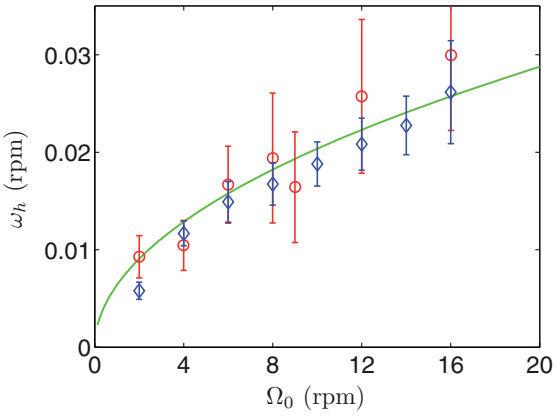

Fig. 6: (Color online) Horizontal rotation rate ω_h of the tilt-over flow as a function of the rotation rate of the platform Ω_0, measured in the horizontal ($\circ$) and vertical ($\Diamond$) planes. The continuous line shows the prediction (9).

as half the spatially averaged (over a central disk of radius 50 mm) vorticity, measured at the times $t_{\max}$ of maximum vorticity. ω_h has also been determined independently from the horizontal cuts, as $\omega_h = \langle |\mathbf{u}_h| \rangle / z_{\mathrm{mes}}$, where $\langle \cdot \rangle$ is an average over time and over the region $|\mathbf{r}| < 50$ mm, and z_{mes} is the height of the measurement plane.

For both measurements in the horizontal and vertical planes, one value of φ and ω_h is obtained at each rotation period. From this set, the average and standard deviation are computed over the 80 periods recorded for each rotation rate. In addition to the temporal fluctuations, the errorbars in figs. 5 and 6 also include the variations of φ and ω_h when varying the radius of the averaging region between 25 and 75 mm. For both quantities, the estimates determined from the two measurement planes closely agree, although data from the horizontal plane systematically show a larger scatter.

The vortex angle measured from both vertical and horizontal planes, $\varphi \simeq 173 \pm 4^\circ$ and $175 \pm 11^\circ$, respectively (fig. 5), are in good agreement with the theoretical prediction (10) (see footnote [1]). Similarly, the rotation rate ω_h measured in both planes closely follow the prediction (9) to within 20% over the range $\Omega_0 = 2$–16 rpm (fig. 6). The agreement of ω_h and φ with the theoretical predictions is remarkable in view of the very weak velocity signal, providing strong evidence that the weak secondary flow that we observe originates from the precession of the experiment by the Earth rotation. The magnitude of the secondary rotation lies in the range $(1.5\text{–}3)\times 10^{-3}\,\Omega_0$, confirming that the rotation vector $\boldsymbol{\omega}$ of the fluid is almost aligned with $\boldsymbol{\Omega}_0$, with a very weak angular departure of $\omega_h/\Omega_0 < 0.2^\circ$.

[1] A possible residual ellipticity of the sphere would lead to slightly different angles φ. Considering a prolate or an oblate spheroid, of ellipticity given by the maximum deviation of the radius of the sphere ($R = 115 \pm 0.25$ mm), yields predictions for φ between 170 and 180° for the range of Ω_0 considered here, which is compatible with the present data.

Conclusion. – Measuring the influence of the Earth rotation at the laboratory scale is a technical challenge. In the fluid analogue of the Foucault pendulum presented in this letter, the very weak precession driven flow would have been impossible to detect directly from the laboratory frame. Probing the flow in the rotating frame naturally subtracts the first-order rotation and allows us to detect this slight correction. We note that such residual tilt-over flow forced by the Earth rotation defines an irreducible background flow which should be present in every rotating fluid experiments, routinely used as models for geophysical and astrophysical flows in the laboratory.

* * *

We acknowledge D. Lathrop, C. Lamriben and M. Rabaud for fruitfull discussions, and A. Aubertin, L. Auffray, C. Borget, A. Campagne and R. Pidoux for experimental help. JB is supported by the "Triangle de la Physique". This work is supported by the ANR through grant No. ANR-2011-BS04-006-01 "ONLITUR". The rotating platform "Gyroflow" was funded by the "Triangle de la Physique".

REFERENCES

[1] Perrot M., *C. R. Acad. Sci.*, **XLIX** (1859) 637.
[2] Shapiro A. H., *Nature*, **196** (1962) 1080.
[3] Pantaloni J., Cerisier P., Bailleux R. and Gerbaud C., *J. Physique Lett.*, **42** (1981) L147.
[4] Brown E. and Ahlers G., *Phys. Fluids*, **18** (2006) 125108.
[5] Greenspan H., *The Theory of Rotating Fluids* (Cambridge University Press, London) 1968.
[6] Vanyo J. P. and Dunn J. R., *Geophys. J. Int.*, **142** (2000) 409.
[7] Triana S. A., Zimmerman D. S. and Lathrop D. P., *J. Geophys. Res.*, **117** (2012) B04103.
[8] Busse F. H., *J. Fluid Mech.*, **33** (1968) 739.
[9] Malkus W. V. R., *Science*, **160** (1968) 259.
[10] Poincaré R., *Bull. Astron.*, **27** (1910) 321.
[11] Greff-Lefftz M. and Legros H., *Science*, **286** (1999) 1707.
[12] Kerswell R. R., *J. Fluid Mech.*, **321** (1996) 335.
[13] Tilgner A., *Phys. Fluids*, **17** (2005) 034104.
[14] Kida S., *J. Fluid Mech.*, **680** (2011) 150.
[15] DaVis by LaVision GmbH complemented by the PIVMat toolbox for Matlab, `http://www.fast.u-psud.fr/pivmat`.
[16] Raffel M., Willert C., Wereley S. and Kompenhans J., *Particle Image Velocimetry* (Springer-Verlag, Berlin) 2007.
[17] Tilgner A. and Busse F. H., *J. Fluid Mech.*, **426** (2001) 387.
[18] Noir J., Cardin P., Jault D. and Masson J.-P., *Geophys. J. Int.*, **154** (2003) 407.
[19] Cébron D., Le Bars M. and Meunier P., *Phys. Fluids*, **22** (2010) 101063.
[20] Zhang K., Liao X. and Earnshaw P., *J. Fluid Mech.*, **504** (2004) 1.

Chapitre 2

Transferts d'énergie en hydrodynamique en rotation

Comme nous l'avons vu dans le premier chapitre, une rotation d'ensemble affecte fortement la dynamique des fluides en autorisant la propagation d'une classe d'ondes –les ondes d'inertie– aux propriétés singulières, dont en premier lieu l'indépendance de la longueur d'onde avec la fréquence. Jusqu'ici, on s'est intéressé à comprendre, dans plusieurs situations modèles, comment dans la limite linéaire les effets visqueux couplés aux conditions aux limites gouvernent les structures spatiales de l'écoulement. Dans ce chapitre, nous allons toujours nous intéresser aux effets d'une rotation d'ensemble mais cette fois-ci dans des régimes non-linéaires de l'équation de Navier-Stokes. Notre intérêt se tournera naturellement en direction de la turbulence dans un fluide en rotation, sujet de recherche aux motivations géophysiques et astrophysiques fortes.

À travers l'action de la force de Coriolis, la rotation modifie profondément les propriétés statistiques et géométriques de la turbulence hydrodynamique [6, 68]. Les effets qui sont aujourd'hui bien établis peuvent se résumer en trois points :

- La rotation d'ensemble induit une anisotropie de la turbulence qui la rapproche d'un état asymptotique bidimensionnel, invariant le long de l'axe de rotation [69, 70]. D'un point de vue géométrique, cette tendance se traduit par l'émergence de tourbillons persistants alignés avec la rotation [71, 72].
- Les transferts d'énergie des grandes vers les petites échelles et la dissipation qui en résulte, caractéristiques majeures de la turbulence tridimensionnelle, sont inhibés par la rotation [69, 70, 73, 74].
- La statistique des champs de vitesse brise la symétrie miroir par rapport aux plans verticaux, i.e. parallèles à l'axe de rotation. De manière plus intuitive, cela se traduit par une présence dominante de tourbillons cycloniques, i.e. tournants dans le même sens que la rotation d'ensemble, par rapport aux tourbillons anticycloniques. C'est l'asymétrie cyclone-anticyclone [71, 72, 75].

Depuis la fin des années 1970, de nombreux travaux expérimentaux, numériques et théoriques ont fournit un support solide à ces trois propriétés de la turbulence en rotation. Il serait trop

long d'en détailler l'historique ici et le lecteur est invité à se reporter aux livres de référence de Sagaut et Cambon [6] et de Davidson [68] traitant attentivement du cas de la turbulence en rotation.

Si les trois propriétés évoquées ci-dessus sont à présent bien caractérisées, les processus physiques qui leurs donnent jour ne sont en revanche toujours compris que de manière partielle. Dans ce cadre, les études expérimentales qui sont décrites dans ce chapitre concernent une question centrale relative à la turbulence en rotation et transverse aux points précédents : Comment la rotation d'ensemble affecte les transferts d'énergie entre échelles ? Cette question débouche en fait sur deux problématiques auxquelles nous nous sommes intéressé : (i) Comment l'interaction entre la rotation et les transferts d'énergie construit l'anisotropie de la turbulence ? (ii) Comment cette anisotropie peut elle-même influencer en retour les transferts d'énergie ? Nos travaux de recherche ont eu pour ambition d'apporter de nouveaux éléments pour répondre à ces questions en s'appuyant sur des systèmes expérimentaux modèles et sur les techniques modernes de vélocimétrie par images de particules. Les progrès récents dans ce type de méthodes de mesure ont en effet ouvert la voie aux analyses en échelles spatiales des statistiques anisotropes des champs de vitesse, qui restaient auparavant inaccessibles.

Dans ce chapitre, je présente les résultats de trois études expérimentales que j'ai menées au FAST depuis 2009. Leurs présentations successives constituent en pratique la trame d'une discussion abordant certaines questions clés et parfois encore ouvertes relatives à l'influence d'une rotation d'ensemble sur les transferts d'énergie entre échelles en mécanique des fluides. Dans le premier travail présenté [article Bordes *et al.* Physics of Fluids, 2012 à la page 88], on s'intéresse au mécanisme non-linéaire permettant les transferts d'énergie à l'intérieur d'une triade résonante d'ondes d'inertie. Ce processus est fondamental car il constitue la brique élémentaire de l'anisotropie des transferts d'énergie à l'origine de la bidimensionalisation de la turbulence. On présentera ensuite deux expériences où l'on génère à proprement parler une turbulence en rotation : (i) une turbulence de grille en déclin qui nous a permis d'étudier l'anisotropie des transferts d'énergie dans un plan parallèle à l'axe de rotation et (ii) une expérience de turbulence forcée qui nous a permis de mettre en évidence l'apparition d'une cascade d'énergie d'abord double puis purement inverse dans le plan normal à l'axe de rotation. Les résultats importants de ces deux études seront résumés dans ce chapitre, mais le lecteur est invité à la lecture de deux articles publiés et d'un projet d'article qui les décrivent en détail : article (Lamriben *et al.* Physical Review Letters, 2011) à la page 122, article (Cortet *et al.* en préparation pour Journal of Turbulence, 2015) à la page 126 et article (Campagne *et al.* Physics of Fluids, 2014) à la page 103.

Publications associées à ce chapitre (en annexe lorsque le chiffre est encadré)

1. C. Lamriben, P.-P. Cortet, F. Moisy, L.R.M. Maas,
   Excitation of inertial modes in a closed grid turbulence experiment under rotation
   Physics of Fluids, **23** 015102 (2011)

2. C. Lamriben, P.-P. Cortet, F. Moisy,
   Direct measurements of anisotropic energy transfers in a rotating turbulence experiment

Physical Review Letters, **107** 024503 (2011)

3. G. Bordes, F. Moisy, T. Dauxois, P.-P. Cortet,
Experimental evidence of a triadic resonance of plane inertial waves in a rotating fluid
Physics of Fluids, **24** 014105 (2012)

4. B. Gallet, A. Campagne, P.-P. Cortet, F. Moisy,
Scale-dependent cyclone-anticyclone asymmetry in a forced rotating turbulence experiment
Physics of Fluids, **26** 035108 (2014)

5. A. Campagne, B. Gallet, F. Moisy, P.-P. Cortet
Direct and inverse energy cascades in a forced rotating turbulence experiment
Physics of Fluids, **26** 125112 (2014)

6. P.-P. Cortet, F. Moisy
Scale-dependent anisotropy in decaying rotating turbulence
en préparation pour **Journal of Turbulence**

2.1 Hydrodynamique et turbulence en rotation

2.1.1 Équation du mouvement

Dans ce chapitre, nous nous plaçons à nouveau dans le cadre de l'équation de Navier-Stokes en référentiel tournant

$$\partial_t \mathbf{u} + (\mathbf{u}\cdot\nabla)\mathbf{u} = -\frac{1}{\rho}\nabla p - 2\boldsymbol{\Omega}\times\mathbf{u} + \nu\nabla^2\mathbf{u}, \tag{2.1}$$

i.e. l'équation décrivant la dynamique d'un champ de vitesse Eulérien $\mathbf{u}(\mathbf{x},t)$ dans un référentiel tournant avec un taux $\boldsymbol{\Omega} = \Omega\,\mathbf{e_z}$. L'équation (2.1) peut se réécrire sous la forme

$$Ro_t\,\partial_t \mathbf{u}^* + Ro\,(\mathbf{u}^*\cdot\nabla)\mathbf{u}^* = -\nabla p^* - 2\mathbf{e_z}\times\mathbf{u}^* + \frac{Ro}{Re}\,\nabla^2\mathbf{u}^*, \tag{2.2}$$

où l'on a adimensionné les différents termes en utilisant des échelles de vitesse U, de longueur L et de fréquence σ caractéristiques de l'écoulement. Cette équation fait apparaître trois nombres sans dimension qui, si on choisit les échelles U, L et σ de manière pertinente (ce qui n'est pas évident !), vont contrôler le régime dans lequel l'écoulement se développe :

– Le nombre de Reynolds

$$Re = \frac{UL}{\nu} \simeq \frac{|(\mathbf{u}\cdot\nabla)\mathbf{u}|}{|\nu\nabla^2\mathbf{u}|},$$

qui compare l'intensité du terme non-linéaire d'advection à celle de la diffusion visqueuse,

– Le nombre de Rossby

$$Ro = \frac{U}{2\Omega L} = \frac{1}{2\Omega\,\tau_{nl}} \simeq \frac{|(\mathbf{u}\cdot\nabla)\mathbf{u}|}{|2\boldsymbol{\Omega}\times\mathbf{u}|}, \tag{2.3}$$

qui compare l'intensité du terme non-linéaire à la force de Coriolis. $1/\tau_{nl} = U/L$ mesure

la fréquence caractéristique associée aux effets non-linéaires,

– Le nombre de Rossby temporel

$$Ro_t = \frac{\sigma}{2\Omega} \simeq \frac{|\partial_t \mathbf{u}|}{|2\mathbf{\Omega} \times \mathbf{u}|},$$

qui compare l'intensité du terme non-stationnaire à la force de Coriolis, σ étant le taux caractéristique d'évolution du champs de vitesse Eulérien.

Ce dernier nombre sans dimension s'identifiera au nombre de Rossby Ro lorsque l'écoulement devient "suffisamment" non-linéaire pour que son évolution temporelle soit dominée par les non-linéarités : dans ce cas, la fréquence σ s'identifie à $1/\tau_{nl}$ et $Ro_t \simeq Ro$. La distinction entre les deux nombres de Rossby se révèle cependant nécessaire dans la limite faiblement non-linéaire de l'équation (2.1) où $\sigma\,\tau_{nl} \gg 1$. Dans cette limite, l'écoulement est en pratique composé d'ondes d'inertie dont l'interaction non-linéaire modifie l'amplitude selon une dynamique lente devant la période des ondes. On note aussi que dans (2.2) apparaît le rapport $Ro/Re = \nu/2\Omega L^2 = E(H/L)^2$ qui, lorsque l'écoulement est confiné sur une hauteur H selon l'axe de rotation, est lié au nombre d'Ekman $E = \nu/2\Omega H^2$ introduit au chapitre précédent. On rappelle que ce nombre E contrôle la physique des couches limites visqueuses aux parois (non-parallèles à $\mathbf{\Omega}$) des écoulements en rotation.

On peut essayer de dresser une liste des différents régimes d'écoulement attendus selon la valeur de ces nombres sans dimension en se restreignant cependant aux écoulements turbulents, ou plus exactement à grand nombre de Reynolds $Re \gg 1$:

– $Ro = Ro_t \gg 1$. L'écoulement est fortement non-linéaire et la rotation négligeable. On retrouve la turbulence tridimensionnelle classique.

– $Ro \ll 1$ et $Ro_t \ll 1$. C'est au contraire la limite d'une rotation infiniment forte décrite par le théorème de Taylor-Proudman. On verra dans la partie 2.1.3 que celui-ci prévoit un écoulement bidimensionnel, invariant le long de l'axe de rotation, mais perdant par la même occasion son caractère turbulent, ou plus précisément non-linéaire.

– $Ro \ll 1$ et $Ro_t \leqslant 1$. L'écoulement est composé d'ondes d'inertie en interaction non-linéaire faible. Celles-ci échangent alors de l'énergie à travers le processus non-linéaire élémentaire appelé résonance triadique et qui sera décrit dans la partie 2.2.

– $Ro \simeq Ro_t = O(1)$ ou $\ll 1$. Les non-linéarités sont suffisamment grandes pour dominer la dynamique rapide de l'écoulement. En parallèle, le nombre de Rossby est d'ordre 1 ou éventuellement petit mais fini, de telle manière que la rotation interagit fortement avec les non-linéarités de l'équation de Navier-Stokes. Nous appellerons "turbulence en rotation" ce dernier régime de l'équation (2.1). C'est celui qui nous intéressera principalement dans ce chapitre puisqu'il correspond à la situation la plus pertinente pour décrire les écoulements naturels et qu'il contient par ailleurs la physique la plus riche. Il sera abordé dans la partie 2.3.

Il est important toutefois d'apporter un bémol à cette tentative de dresser un panorama des régimes de l'équation de Navier-Stokes en rotation (2.1). Le large spectre de fréquences

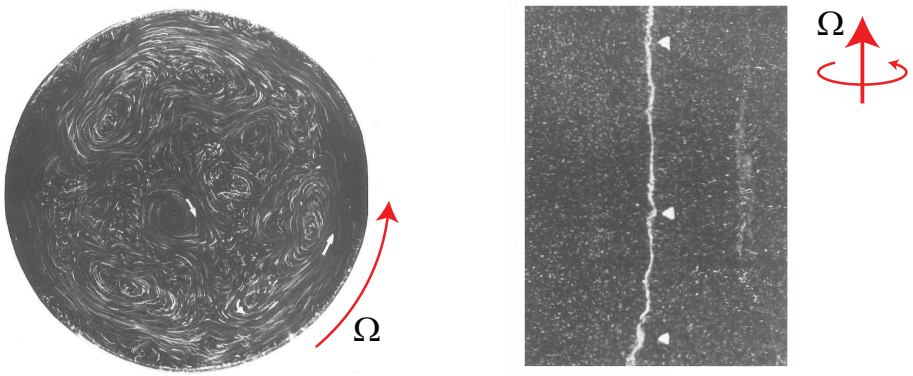

FIGURE 2.1 – Expérience de grille oscillée dans un cylindre en rotation de Hopfinger *et al.* [71]. La grille horizontale est oscillée verticalement (en bas de la cuve) et l'axe de rotation est vertical. Figures adaptées de [71]. **Gauche** : Vue de dessus dans un plan normal à l'axe de rotation. Photographie posée de trajectoires de bulles dans l'écoulement. **Droite** : Photographie de l'écoulement dans un plan parallèle à l'axe de rotation vertical. Les bulles s'agrègent dans le cœur des tourbillons.

temporelles caractéristique des écoulements turbulents, l'indépendance des échelles spatiales et temporelles dans la relation de dispersion des ondes d'inertie, les modifications possibles de l'intensité et du sens des cascades d'énergie par la rotation, l'effet singulier mais important du confinement vertical, font qu'il est en pratique souvent difficile voire impossible de choisir des échelles temporelle, spatiale et de vitesse qui permettent de caractériser de manière univoque le régime d'un écoulement turbulent en rotation. Un même écoulement, selon les échelles considérées, peut ainsi explorer simultanément plusieurs des régimes évoqués dans la liste précédente. D'une certaine manière, la suite de ce chapitre essaiera humblement d'apporter quelques éléments pour se repérer dans le vaste espace des paramètres de la mécanique des fluides en rotation.

2.1.2 Bidimensionnalisation de la turbulence par la rotation

L'effet le plus marqué que produit une rotation d'ensemble sur un écoulement turbulent est de le diriger vers un état anisotrope 2D. Cette bidimensionnalisation fait uniquement référence à une invariance de l'écoulement le long de l'axe de rotation $\mathbf{e_z}$ et en aucun cas à la disparition de la composante selon $\mathbf{e_z}$ du champs de vitesse. Cette tendance a été mise en évidence dans de nombreux travaux expérimentaux et numériques aussi bien dans l'espace physique [69, 71] que dans l'espace spectral (ou des échelles) [76–79]. Ainsi, le couplage entre la force de Coriolis et les non-linéarités construit un transfert d'énergie des modes 3D en direction des modes 2D qui se traduit dans l'espace physique par une structuration de la turbulence en colonnes parallèles à l'axe de rotation [71, 72, 80–82]. On peut s'arrêter ici plus particulièrement sur deux observations expérimentales pionnières mettant en évidence cette tendance.

Sur la Figure 2.1, on reproduit des photographies prises dans le référentiel tournant pendant une expérience de turbulence menée par Hopfinger *et al.* [71] où une grille horizontale est oscillée verticalement en bas d'un cylindre en rotation. Ces prises de vue légèrement posées montrent

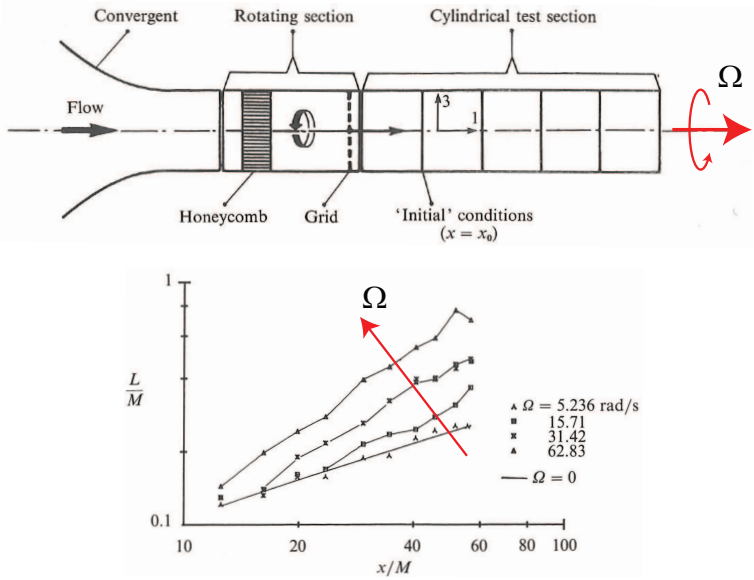

FIGURE 2.2 – Expérience de turbulence de grille en rotation de Jacquin *et al.* [69]. Figures adaptées de [69]. **Haut** : Schéma du dispositif expérimental de soufflerie avec section tournante. **Bas** : Échelle intégrale (longueur de corrélation du champ de vitesse) le long de l'axe de rotation en fonction de la distance à la grille et du taux de rotation. M est la taille des mailles de la grille.

la trajectoire de petites bulles faisant office de traceurs de l'écoulement. Celles-ci ont aussi tendance à s'agréger dans les zones de basse pression, permettant ainsi d'identifier les zones tourbillonaires. On observe ainsi sur la Figure 2.1(Droite) l'émergence de tourbillons alignés avec l'axe de rotation, illustrant la tendance de l'écoulement à l'invariance le long de l'axe de rotation.

Une autre illustration remarquable de la bidimensionnalisation de la turbulence en rotation a été obtenue par Jacquin *et al.* [69] dans une expérience de turbulence de grille en soufflerie (Figure 2.2). Dans cette expérience, l'air est entraîné en rotation par une section tournante de la soufflerie dans laquelle un nid d'abeille a été inséré avant la grille. Des mesures au fil chaud de séries temporelles de la vitesse dans l'écoulement turbulent ont alors notamment permis de mesurer la longueur de corrélation du champs de vitesse selon l'axe de rotation. Sur la Figure 2.2, on constate que cette longueur croît avec la distance à la grille (de manière usuelle), mais aussi avec le taux de rotation Ω du fluide, illustrant la croissance d'une invariance le long de l'axe rotation, sur la base de quantités statistiques cette fois-ci.

2.1.3 Le théorème de Taylor-Proudman

Un résultat souvent mentionné pour interpréter la bidimensionnalisation de la turbulence en rotation est le théorème de Taylor-Proudman [1, 83, 84]. Celui-ci consiste en la limite de l'équation de Navier-Stokes en référentiel tournant lorsque les deux nombres de Rossby, linéaire Ro_t et non-linéaire Ro, s'annulent, autrement dit lorsque la rotation est infiniment grande. Dans

cette limite, l'équation (2.1) traduit un simple équilibre, dit "géostrophique", entre le gradient de pression et la force de Coriolis

$$\frac{1}{\rho}\nabla p = -2\mathbf{\Omega} \times \mathbf{u}. \tag{2.4}$$

Cet équilibre a pour première conséquence un alignement des isobares avec le champ de vitesse. La deuxième conséquence est obtenue en prenant le rotationnel de l'équation (2.4),

$$(\mathbf{\Omega} \cdot \nabla)\mathbf{u} = 0,$$

qui prédit une invariance du champ de vitesse dans la direction de l'axe de rotation. L'écoulement ainsi obtenu est parfaitement bidimensionnel, i.e. indépendant de la coordonnée z, mais toujours avec trois composantes non-nulles du champ de vitesse. On parlera dans le suite de champ de vitesse 2D-3C.

Il est important de souligner ici que le théorème de Taylor-Proudman est un résultat purement linéaire puisque le terme d'advection de l'équation de Navier-Stokes en est absent. Dans une telle limite, l'écoulement ne peut être considéré comme turbulent puisqu'aucune non-linéarité n'est à l'œuvre alors que celles-ci constituent le moteur des transferts d'énergie entre échelles, i.e. l'essence même de la turbulence. Le théorème de Taylor-Proudman décrit ainsi un écoulement compatible avec l'état asymptotique de la turbulence en rotation lorsque le nombre de Rossby décroît vers zéro. Il n'explique cependant en rien les processus physiques, non-linéaires, qui construisent l'invariance de l'écoulement selon l'axe de rotation. La "turbulence en rotation" correspond donc à un régime de nombre de Rossby $Ro = O(1)$ ou $Ro \ll 1$, mais fini de manière à observer une interaction effective entre le terme non-linéaire de l'équation de Navier-Stokes et la force de Coriolis.

2.1.4 Les écoulements 2D en rotation

Il est instructif aussi de considérer le cas particulier d'un écoulement parfaitement 2D (mais toujours 3C) à nombre de Rossby fini, i.e. $Ro \neq 0$. Dans cette situation, le champs de vitesse horizontal peut se paramétrer grâce à une fonction de courant $\psi(\mathbf{x})$ telle que $\mathbf{u} = (\partial_y\psi, -\partial_x\psi, u_z)$. L'équation du mouvement peut alors se réécrire

$$\partial_t\mathbf{u} + (\mathbf{u} \cdot \nabla)\mathbf{u} = -\frac{1}{\rho}\nabla\tilde{p} + \nu\nabla^2\mathbf{u}, \tag{2.5}$$

où la force de Coriolis a été absorbée dans le gradient de pression selon $\tilde{p} = p + 2\rho\Omega\psi$. Cette formulation nous montre que la rotation n'a en pratique plus prise sur les écoulements 2D-3C, invariants le long de l'axe de rotation, et ce quelque soit la valeur du nombre de Rossby.

À la lumière des trois dernières sous-sections, on réalise qu'à mesure que la rotation dirige un écoulement vers l'état 2D-3C, elle perd son influence sur celui-ci. Cette constatation illustre à nouveau le fait que c'est bien le régime de nombre de Rossby fini, associé à un écoulement anisotrope mais pas encore 2D, qui constitue un réel enjeu de recherche.

Dans la suite de ce chapitre, nous allons présenter trois travaux expérimentaux que nous avons

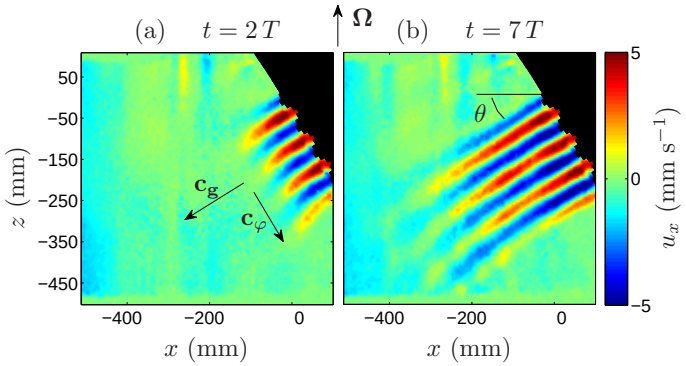

FIGURE 2.3 – Champ de vitesse horizontal respectivement 2 (a) et 7 (b) périodes d'oscillation après le démarrage du générateur pour $\sigma_0/2\Omega = \cos\theta = 0.84$. On a représenté la direction de propagation de la phase selon la vitesse de phase $\mathbf{c}_\varphi$ et celle du front de l'onde selon la vitesse de groupe $\mathbf{c_g}$.

menés au FAST depuis 2009 correspondant au régime dont on vient de dessiner les contours. Notre ambition a été d'apporter des éléments expérimentaux nouveaux à la compréhension de l'influence d'une rotation d'ensemble sur les transferts d'énergie entre échelles en turbulence. On s'intéressera dans un premier temps au régime faiblement non-linéaire à travers une expérience modèle illustrant la résonance triadique d'ondes d'inertie, mécanisme élémentaire à l'origine de l'anisotropie des flux d'énergie en turbulence en rotation. Nous décrirons ensuite deux études qui ont permis les premières caractérisations expérimentales directes des flux d'énergie entre échelles dans une turbulence en rotation.

2.2 Transferts d'énergie en régime faiblement non-linéaire

2.2.1 Instabilité d'une onde plane d'inertie par résonance triadique

- Collaboration avec G. Bordes et T. Dauxois (ENS Lyon)

Dans cette partie, je présente une étude expérimentale qui isole le processus élémentaire de résonance triadique d'ondes d'inertie, dominant les échanges d'énergie dans la limite faiblement non-linéaire de l'équation de Navier-Stokes en rotation. Dans le cadre d'une description spectrale de la turbulence en rotation, nous allons voir que la résonance triadique conduit à un transfert de l'énergie vers des vecteurs d'onde $\mathbf{k}$ de composante verticale k_z toujours plus faible, rapprochant ainsi l'écoulement de l'état asymptotique 2D associé aux vecteurs d'onde de composante $k_z = 0$.

Le premier succès de notre étude a consisté à réussir à exciter pour la première fois expérimentalement une onde plane d'inertie (Figure 2.3). Pour cela, nous avons utilisé un générateur conçu, dans l'équipe de Thierry Dauxois à l'ENS de Lyon, initialement pour étudier la physique des ondes internes dans les fluides stratifiés [85, 86]. Ce générateur, que nous avons placé dans un grand aquarium sur la plateforme tournante "Gyroflow", est constitué d'un empilement de plaques placées autour d'un arbre à cames hélicoïdal. La phase des cames est décalée d'une

plaque à l'autre de telle manière que la tranche des plaques dessine un profil sinusoïdal. Ce profil voit alors sa phase se propager le long de la surface alors que le mouvement des plaques y est perpendiculaire, reproduisant des conditions aux limites proches de celles d'une onde plane d'inertie. Grâce à des mesures de PIV dans un plan vertical du référentiel tournant, nous avons alors observé que l'onde excitée subit une instabilité qui donne naissance à deux ondes planes secondaires de fréquences plus faibles. Nous avons pu extraire les fréquences σ_i et les vecteurs d'ondes $\mathbf{k_i}$ des deux ondes secondaires et démontrer qu'elles respectent des conditions de résonance triadique temporelle $\sigma_0 + \sigma_1 + \sigma_2 = 0$ et spatiale $\mathbf{k_0} + \mathbf{k_1} + \mathbf{k_2} = 0$ avec l'onde primaire (Figure 2.4). Il est important de noter ici que ce type d'instabilité sous-harmonique d'une onde propagative avait déjà été étudié en détail dans le cas des ondes internes de gravité [87–89], mais que son observation expérimentale dans le cas des ondes d'inertie n'avait pas encore été réalisée.

Le caractère sous-harmonique des ondes issues de l'instabilité, i.e. $|\sigma_{1,2}| < |\sigma_0|$, couplé à la relation de dispersion des ondes d'inertie $|\sigma_i|/2\Omega = |k_z^i|/|\mathbf{k_i}|$, implique alors que les transferts d'énergie se font systématiquement en direction de vecteurs d'ondes plus normaux à l'axe de rotation que le vecteur initial [4] (Figure 2.4). Dans la limite faiblement non-linéaire de l'équation de Navier-Stokes, i.e. pour un fort taux de rotation ($Ro \ll 1$), la turbulence en rotation consiste en une superposition d'ondes d'inertie en interaction faible pour laquelle la résonance triadique constitue ainsi le mécanisme élémentaire de création d'anisotropie. Pour fixer les idées, dans les expériences présentées ici, le nombre de Rossby est de l'ordre de $Ro \simeq 0.05$ à 0.1 et celui de Reynolds de l'ordre de $Re \simeq 40$. On note ainsi la robustesse du processus de résonance triadique qui reste ici pertinent alors que la limite de forte rotation est en pratique encore lointaine.

Il a été proposé que cette limite faiblement non-linéaire ($Ro \ll 1$) de la turbulence en rotation puisse être décrite par les modèles dits de "turbulence d'ondes", de "turbulence faible" ou encore "Asymptotique Quasi-Normal Markovien" (AQNM) [90–93]. Ce type d'approches s'appuie, lors de la description des transferts d'énergie entre échelles spatiales, sur une séparation d'échelles temporelles entre la dynamique "ondulatoire" rapide et linéaire d'un coté et la dynamique lente et non-linéaire de l'autre. Ces modèles conduisent finalement à des prédictions sur les lois d'échelles anisotropes suivies par la densité spectrale (spatiale) d'énergie en supposant la conservation du flux d'énergie entre échelles. Ces modèles n'ont cependant pu recevoir aucun support expérimental à ce jour, notamment à cause de la difficulté pratique d'atteindre les régimes de faible nombre de Rossby et fort nombre de Reynolds et celle de réaliser des mesures sur de larges gammes d'échelles spatiales dans un contexte anisotrope.

2.2.2 Décomposition en modes hélicoïdaux et turbulence d'ondes d'inertie

Application de la décomposition en modes hélicoïdaux à la description de l'instabilité sous-harmonique

Dans la suite de cette partie, nous allons présenter succinctement le principe de la modélisation théorique de l'instabilité d'une onde d'inertie par résonance triadique. Le but sera ici notamment de discuter les limites de ce type d'approche de "turbulence d'ondes" pour la description de la turbulence en rotation faiblement et fortement non-linéaire. Le lecteur pourra se

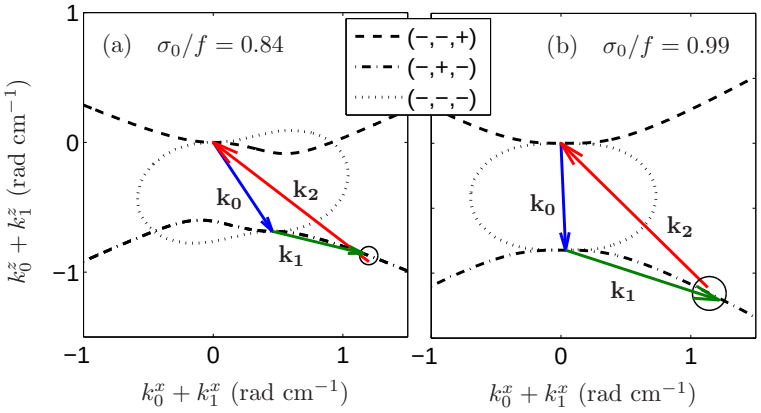

FIGURE 2.4 – Courbes de résonance théoriques pour les ondes primaires définies par (a) $[s_0 = -1, \sigma_0/2\Omega = 0.84, |\mathbf{k_0}| = 0.82$ rad cm$^{-1}]$ et (b) $[s_0 = -1, \sigma_0/2\Omega = 0.99, |\mathbf{k_0}| = 0.82$ rad cm$^{-1}]$. Ces courbes représentent l'ensemble des vecteurs $\mathbf{k}_0 + \mathbf{k}_1 = (k_0^x + k_1^x, k_0^z + k_1^z)$ satisfaisant aux conditions de résonance. Les vecteurs d'onde mesurés expérimentalement sont représentés par les flèches. Les cercles représentent la prédiction théorique du couple d'ondes secondaires maximisant le taux de croissance de l'instabilité [déterminé en utilisant comme amplitude de l'onde primaire $A_0 = 0.29 \pm 0.07$ cm s^{-1} pour (a) et $A_0 = 0.34 \pm 0.11$ cm s^{-1} pour (b)]. Le diamètre des cercles quantifie l'incertitude sur la prédiction théorique liée à la variabilité de l'amplitude A_0 de l'onde primaire dans la zone où se produit l'instabilité.

reporter à l'article (Bordes *et al.* Physics of Fluids, 2012) à la page 88 pour une description plus technique de cette étude.

Pour décrire la dynamique non-linéaire conduisant à l'instabilité présentée dans la sous-partie précédente, nous nous sommes appuyé sur la décomposition des champs de vitesse sur la base complète des modes hélicoïdaux introduite par Waleffe *et al.* [4, 94, 95] au début des années 1990

$$\mathbf{u}(\mathbf{x},t) = \sum_{\substack{\mathbf{k} \\ s_\mathbf{k}=\pm 1}} A_{s_\mathbf{k}}(\mathbf{k},t)\, \mathbf{h}_{s_\mathbf{k}}(\mathbf{k}) e^{i\mathbf{k}\cdot\mathbf{x}} \quad \text{avec} \quad \mathbf{h}_{s_\mathbf{k}}(\mathbf{k}) = \frac{\mathbf{k}}{|\mathbf{k}|} \times \frac{\mathbf{k}\times\mathbf{e_z}}{|\mathbf{k}\times\mathbf{e_z}|} + i s_\mathbf{k} \frac{\mathbf{k}\times\mathbf{e_z}}{|\mathbf{k}\times\mathbf{e_z}|}, \qquad (2.6)$$

où $s_\mathbf{k} = \pm 1$ mesure le signe de l'hélicité et $A_{s_\mathbf{k}}(\mathbf{k},t)$ l'amplitude de chaque mode. Le vecteur complexe $\mathbf{h}_{s_\mathbf{k}}(\mathbf{k})$ définit un champ de vitesse transverse au vecteur d'onde $\mathbf{k}$ et polarisé circulairement. On peux noter que cette décomposition est équivalente à celle dite de Craya-Herring [6, 76, 96, 97] qui l'a largement précédée historiquement. Elle permet une réécriture de l'équation de Navier-Stokes en une série d'équations décrivant l'évolution temporelle de l'amplitude $A_{s_\mathbf{k}}(\mathbf{k},t)$ de chaque mode en fonction de la somme des interactions non-linéaires entre les couples résonants spatialement d'autres modes, les coefficients d'interaction ayant été dérivés analytiquement.

Lorsque les équations du mouvement supportent la propagation d'une classe d'ondes (Alfvén, de gravité, d'inertie...) et dans une limite faiblement non-linéaire, on décompose alors généralement l'amplitude $A_{s_\mathbf{k}}(\mathbf{k},t)$ des modes en une oscillation sinusoïdale rapide modulée par une amplitude évoluant lentement sous l'action des non-linéarités $A_{s_\mathbf{k}}(\mathbf{k},t) = B_{s_\mathbf{k}}(\mathbf{k},t)\, e^{-i\sigma_\mathbf{k} t}$. Les

équations de la dynamique s'écrivent alors sous la forme

$$\left(\frac{\partial}{\partial t}+\nu\mathbf{k}^2\right)B_{s_\mathbf{k}}(\mathbf{k},t)=\frac{1}{2}\sum_{\mathbf{k}+\mathbf{p}+\mathbf{q}=\mathbf{0}}C^{s_\mathbf{k}s_\mathbf{p}s_\mathbf{q}}_{\mathbf{kpq}}\,B^*_{s_\mathbf{p}}B^*_{s_\mathbf{q}}\,e^{i(\sigma_\mathbf{k}+\sigma_\mathbf{p}+\sigma_\mathbf{q})t}. \tag{2.7}$$

Il est remarquable de noter que ces équations d'interaction restent inchangées par la présence d'une rotation d'ensemble. Ainsi, même si elle est applicable dans le contexte de la turbulence isotrope [94], la décomposition en modes hélicoïdaux est en réalité taillée pour la mécanique des fluides en rotation, d'autant plus qu'un mode hélicoïdal $\mathbf{h}_{s_\mathbf{k}}(\mathbf{k})e^{i(\mathbf{k}\cdot\mathbf{x}-\sigma_\mathbf{k}t)}$ s'identifie exactement à une onde plane d'inertie lorsqu'on lui associe leur relation de dispersion $\sigma_\mathbf{k}=s_\mathbf{k}\,2\Omega\,k_z/|\mathbf{k}|$. En restreignant la décomposition (2.6) à trois ondes d'inertie et en supposant leur résonance temporelle $\sigma_0+\sigma_1+\sigma_2=0$, il nous a alors été aisé de prédire une croissance exponentielle de l'amplitude des ondes secondaires aux temps courts [4] et d'en calculer le taux de croissance

$$\gamma=\sqrt{\frac{\nu^2}{4}\left({\mathbf{k_1}}^2-{\mathbf{k_2}}^2\right)^2+C_1C_2|A_0|^2}-\frac{\nu}{2}({\mathbf{k_1}}^2+{\mathbf{k_2}}^2), \tag{2.8}$$

pour une onde primaire d'amplitude A_0 et de vecteur d'onde $\mathbf{k_0}$ ($C_1=C^{s_1s_0s_2}_{\mathbf{k_1k_0k_2}}$ et $C_2=C^{s_2s_0s_1}_{\mathbf{k_2k_0k_1}}$). Nous avons alors pu déterminer parmi tous les couples d'ondes secondaires résonants avec l'onde primaire celui associé au taux de croissance maximal et ce en excellent accord avec nos résultats expérimentaux (Figure 2.4).

Il est remarquable de noter que dans cette approche théorique, la physique des ondes d'inertie n'apparaît pas explicitement dans les équations (2.7) et n'intervient qu'indirectement dans les coefficients d'interaction $C^{s_\mathbf{k}s_\mathbf{p}s_\mathbf{q}}_{\mathbf{kpq}}$ entre les modes et donc dans le taux de croissance de l'instabilité (2.8) à travers les contraintes imposées aux vecteurs d'ondes par la relation de dispersion et la résonance temporelle. Cette propriété met en valeur la subtilité de l'action de la force de Coriolis sur les transferts d'énergie entre échelles.

Décomposition en modes hélicoïdaux et turbulence en rotation

Nous allons à présent essayer de pointer du doigt les limites de l'approche théorique utilisée ici dans l'objectif de décrire la turbulence en rotation, définie par $Re\gg1$ et $Ro\ll1$ dans la limite faiblement non-linéaire ou $Ro\simeq1$ dans celle fortement non-linéaire.

On peut noter dans un premier temps que le taux de croissance γ (2.8) de l'instabilité d'une onde plane d'inertie prédit ici est fortement dépendant du nombre de Reynolds $Re_0=A_0/|\mathbf{k_0}|\nu$ associé à l'onde primaire. Dans la limite des faibles nombres de Reynolds $Re_0\ll1$, le taux de croissance maximal est atteint pour $|\mathbf{k_2}|\simeq|\mathbf{k_0}|\gg|\mathbf{k_1}|$, correspondant à un transfert d'énergie vers les grandes échelles. Dans cette limite, l'instabilité devient cependant infiniment longue à se mettre en place puisque $\max_{(\mathbf{k_1}+\mathbf{k_2}=-\mathbf{k_0})}(\gamma)\underset{Re_0\to0}{\sim}Re_0^4$. Dans un système réel à faible nombre de Reynolds $Re_0\ll1$, l'instabilité serait de toute manière interdite par la taille finie du système L, n'autorisant pas l'excitation de vecteurs d'onde plus faibles que $2\pi/L$. Au contraire dans la limite inviscide, i.e. des nombres de Reynolds infinis, le couple d'ondes secondaires le plus instable vérifie

$|\mathbf{k_1}|/|\mathbf{k_0}| \simeq |\mathbf{k_2}|/|\mathbf{k_0}| \to \infty$ suggérant un transfert d'énergie vers les échelles infiniment petites. La réalité est ici cependant plus subtile car le taux de croissance de l'instabilité est peu sélectif pour les grands nombres de Reynolds : il présente en pratique des valeurs significatives pour toutes les triades telles que $|\mathbf{k_1}| \simeq |\mathbf{k_2}| \geqslant |\mathbf{k_0}|$ prédisant qu'une large gamme de couples d'ondes résonantes va pouvoir échanger efficacement de l'énergie avec l'onde primaire. La conséquence de cette limite est qu'au sein d'une turbulence en rotation, une onde d'inertie pourra échanger de l'énergie avec un spectre d'échelles d'autant plus large que le nombre de Reynolds est grand, conduisant à une cascade purement directe [90] et non-locale d'énergie. Dans nos expériences où $Re_0 \simeq 40$, nous avons étudié un régime intermédiaire, finalement assez singulier, où la résonance triadique conduit à une instabilité sélective (cf. Figure 6 de l'article Bordes *et al.* Physics of Fluids, 2012 à la page 88) faisant émerger une triade particulière telle que $|\mathbf{k_1}| \simeq |\mathbf{k_2}| \simeq |\mathbf{k_0}|$ (Figure 2.4). La situation que nous avons observée dans notre expérience, où les effets visqueux jouent un rôle majeur dans la sélection d'une triade résonante particulière, illustre malgré tout le mécanisme à l'origine de l'anisotropie des transferts d'énergie en turbulence en rotation faiblement non-linéaire, qui lui est robuste quel que soit le nombre de Reynolds Re_0.

Pour décrire nos observations expérimentales, nous sommes partis de la réécriture -exacte- de l'équation de Navier-Stokes en terme de modes hélicoïdaux. Nous avons assimilé chaque mode à une onde d'inertie $B_{s_\mathbf{k}}(\mathbf{k},t)\,\mathbf{h}_{s_\mathbf{k}}(\mathbf{k})e^{i(\mathbf{k}\cdot\mathbf{x}-\sigma_\mathbf{k}t)}$ en faisant une hypothèse de séparation d'échelles temporelles qui revient à supposer que le taux d'évolution non-linéaire γ de l'amplitude $B_{s_\mathbf{k}}(\mathbf{k},t)$ est faible devant la fréquence d'oscillation $\sigma_\mathbf{k}$. Cette hypothèse équivaut à considérer le nombre de Rossby temporel associé aux ondes grand devant le nombre de Rossby non-linéaire, i.e.

$$\frac{\gamma}{2\Omega} = Ro \ll \underbrace{\frac{\sigma_{\mathbf{k_i}}}{2\Omega} = Ro_t}_{=O(1)} \leqslant 1.$$

On constate que nous avons fait ici une hypothèse de faible non-linéarité, qui bien que modérément vérifiée dans nos expériences où $Ro \simeq 0.1$, conduit à une prédiction quantitative des couples d'ondes secondaires observées.

La deuxième hypothèse que nous avons faite est celle de la résonance temporelle des trois ondes d'inertie, i.e. $\sigma_0+\sigma_1+\sigma_2 = 0$. Cette hypothèse simplificatrice traduit de manière intuitive le fait que, dans l'équation (2.7), seules les interactions où la phase $(\sigma_0+\sigma_1+\sigma_2)t$ évolue lentement devant les effets non-linéaires produisent un transfert efficace d'énergie, les autres étant sujettes à un effet de "brouillage de phase". En pratique, pour décrire une turbulence réelle, la prise en compte dans les transferts d'énergie de l'ensemble des triades de modes hélicoïdaux, en relaxant la condition de résonance temporelle, est nécessaire : c'est l'objet des modèles de "fermeture" de type EDQNM (Eddy Damped Quasi-Normal Markovian) [6, 76] ou des modèles de turbulence d'ondes [90, 98–100]. Ces approches prédisent de manière générale que le temps de transfert de l'énergie à travers une échelle k évolue comme $\tau_{tr}(k) \sim \tau_{nl}^2/\tau_{dec}$, où $\tau_{nl} = 1/(ku_k)$ est le temps non-linéaire et τ_{dec} le temps de décorrélation associés aux ondes à l'échelle k (u_k mesure ici la vitesse typique associée au nombre d'onde k). Dans une limite fortement non-linéaire, i.e. de rotation faible ici, la physique des ondes ne gère plus la dynamique rapide des modes hélicoïdaux

et le temps de décorrélation s'identifie au temps non-linéaire. On retrouve alors le temps de transfert de l'énergie de la turbulence isotrope $\tau_{tr} = \tau_{nl}$. En revanche, dans une turbulence en rotation plus forte ($Ro \ll 1$), le temps de décorrélation imposé par la physique des ondes d'inertie est l'inverse du taux de rotation $\tau_{dec} = 1/\Omega$, conduisant à un temps de transfert de l'énergie $\tau_{tr} \sim \tau_{nl}/Ro$ plus grand d'un facteur $1/Ro$ que dans le cas sans rotation [76, 90, 98–100]. Au passage, on peut ainsi interpréter la réduction par la rotation des transferts d'énergie des grandes vers les petites échelles, évoquée en introduction de ce chapitre. En effet, on prédit ici que le taux de transfert de l'énergie entre échelles devient $\epsilon \simeq u_k^2/\tau_{tr} \simeq Ro\,\epsilon_{3D}$, où ϵ_{3D} est le taux de transfert en turbulence isotrope. En s'appuyant sur la prédiction précédente pour le temps associé au transfert d'énergie entre échelles $\tau_{tr} \sim \tau_{nl}/Ro$, on déduit que l'ensemble des triades telles que $(\sigma_0 + \sigma_1 + \sigma_2)\tau_{tr} \ll 1$ ou encore

$$\frac{\sigma_0 + \sigma_1 + \sigma_2}{2\Omega} \ll Ro^2,$$

vont finalement être capables d'échanger efficacement de l'énergie. Cette constatation dessine la complexité de la turbulence en rotation dans un régime "fortement" non-linéaire qui ne pourra certainement plus être décrit par la superposition des processus élémentaires de résonance triadique [101].

Un dernier point remarquable de la décomposition en modes hélicoïdaux est que les coefficients d'interaction $C^{s_\mathbf{k} s_\mathbf{p} s_\mathbf{q}}_{\mathbf{kpq}}$ des équations (2.7) deviennent strictement nuls si l'une des trois ondes d'inertie considérées a la composante verticale de son vecteur d'onde nulle $k_z = 0$ [95]. Cette remarque est importante puisqu'elle traduit dans l'espace spectral le fait que le mode 2D, parfois qualifié de "mode tourbillon", ne peut pas échanger d'énergie avec les ondes 3D à travers le processus de résonance triadique [102]. Cette propriété est intrinsèquement liée à la condition que les modes hélicoïdaux respectent la relation de dispersion des ondes d'inertie et donc à la faible non-linéarité de l'écoulement. À $Ro \to 0$, le mode 2D-3C évolue donc indépendamment des ondes d'inertie. Il présente alors les caractéristiques traditionnelles de la turbulence 2D : cascade inverse de la vitesse horizontale et cascade directe de la composante verticale de la vitesse qui se comporte comme un scalaire passif advecté-diffusé [103]. Une augmentation des non-linéarités et la possibilité associée d'échanger de l'énergie à l'intérieur de triades presque mais pas exactement résonantes permet cependant des transferts d'énergie entre les modes 3D et 2D [4]. Ces transferts ont été mis en évidence dans des simulations numériques directes [4, 81, 104] qui ont notamment montré que le mode tourbillon 2D est alimenté en énergie à grande échelle à travers des triades quasi-résonantes impliquant deux ondes de faible fréquence et de petites échelles horizontales. Il est important de souligner finalement que, dans un système réel ou même dans les simulations numériques (aux conditions aux limites périodiques [4, 81]), les effets du confinement H de l'écoulement dans la direction de l'axe de rotation vont de toute manière empêcher l'existence de nombres d'onde verticaux $|k_z| < 2\pi/H$. Le confinement vertical, considéré explicitement dans certaines études théoriques de turbulence d'ondes [105], réintroduit donc finalement à travers une discrétisation de l'espace spectral un couplage entre le mode tourbillon et les ondes 3D.

2.3 Transferts d'énergie en turbulence en rotation

2.3.1 Transferts d'énergie en turbulence homogène isotrope

La cascade d'énergie des grandes vers les petites échelles, et la fameuse loi des 4/5ème de Kolmogorov qu'on lui associe, sont reconnues comme les résultats les plus robustes concernant la turbulence homogène et isotrope [6, 106]. La description théorique de cette cascade d'énergie a été développée à la fois dans l'espace spectral, à travers l'équation de Lin [6], et dans l'espace des échelles, à travers l'équation de Kármán-Howarth [106]. Bien que légèrement plus difficile d'interprétation, cette dernière est en général privilégiée par les expérimentateurs [107] : Les moments des incréments de vitesse qui interviennent dans celle-ci sont en effet raisonnablement accessibles à partir de mesures de vitesse. Au contraire, le calcul des transformées de Fourier spatiales nécessaire à l'accès aux termes de l'équation de Lin est en général périlleux, du fait des gammes d'échelles restreintes accessibles avec les techniques de vélocimétrie par imagerie. On peux noter que l'équation de Lin est en revanche le cadre naturel pour l'analyse des transferts d'énergie dans les simulations numériques qui font de manière usuelle apparaître des conditions aux limites périodiques. Cette dualité spectral-spatial [6, 108] de la description des transferts d'énergie en turbulence constitue à la fois une richesse pour l'interprétation des phénomènes mais aussi une difficulté lors de la confrontation des résultats numériques et expérimentaux.

Équation de Lin

L'équation de Lin, dans sa version anisotrope, décrit la dynamique de la densité spectrale (spatiale) de puissance des champs de vitesse que l'on appelle plus simplement "spectre d'énergie" $e(\mathbf{k}, t)$ et qui mesure la densité d'énergie associée à chaque vecteur d'onde $\mathbf{k}$ [6]. Cette équation qui suppose l'homogénéité statistique de la turbulence mais pas son isotropie s'écrit sous la forme

$$\left(\frac{\partial}{\partial t} + 2\nu\mathbf{k}^2\right) e(\mathbf{k}, t) = T^{(e)}(\mathbf{k}, t), \tag{2.9}$$

où $T^{(e)}(\mathbf{k}, t)$ mesure le flux d'énergie alimentant le vecteur d'onde $\mathbf{k}$ et $2\nu\mathbf{k}^2 e(\mathbf{k}, t)$ la dissipation d'énergie à cette échelle. Même si nous n'expliciterons pas son expression ici, le terme de flux d'énergie $T^{(e)}(\mathbf{k}, t)$ rend compte, sous la forme de corrélations triples de la transformée de Fourier du champ de vitesse, de l'interaction non-linéaire du vecteur d'onde $\mathbf{k}$ avec tous les couples de vecteurs d'ondes $(\mathbf{p}, \mathbf{q})$ avec qui il résonne spatialement [6, 76]. Ce terme de transfert est intimement lié aux interactions triadiques décrites par la décomposition de l'équation de Navier-Stokes en modes hélicoïdaux (2.7). Dans le contexte anisotrope, l'équation de Lin doit être complétée par une équation de conservation du spectre de polarisation et du spectre d'hélicité pour obtenir une description complète du problème. On peux noter aussi que les modèles EDQNM mentionnés dans la partie précédente consistent en une fermeture de l'équation (2.9), i.e. une modélisation du terme de transfert d'énergie $T^{(e)}(\mathbf{k}, t)$, en termes de corrélations doubles de la transformée de Fourier du champ de vitesse. Ces modèles sont particulièrement adaptés à la description de

la turbulence en rotation à travers la prise en compte du caractère ondulatoire et anisotrope de l'écoulement [6, 108].

Dans le cadre de l'équation (2.9), la conservation du flux d'énergie entre échelles, caractéristique de la gamme d'échelles inertielle de la turbulence homogène et isotrope à grand nombre de Reynolds, se traduit par la nullité de $T^{(e)}(k,t)$, qui nous dit que l'énergie arrivant des grandes échelles est intégralement transmise aux plus petites. C'est en réalité seulement le signe de l'intégrale cumulative $\Pi(k) = \int_0^k T^{(e)}(p,t)dp$ qui renseigne sur le sens de la cascade d'énergie, négatif pour une cascade directe des grandes vers les petites échelles et positif pour une cascade inverse. Pour une turbulence homogène, isotrope et stationnaire, cette intégrale est en effet bien négative dans la gamme inertielle, puisque $\Pi(\infty) = \int_0^\infty T^{(e)}(p,t)dp = 0$ et qu'aux grands k (aux petites échelles), où la dissipation d'énergie a lieu, $T^{(e)}(k) = 2\nu k^2 E(k) > 0$.

Équation de Kármán-Howarth

L'équation de Kármán-Howarth, qui constituera la pierre angulaire des travaux présentés dans la suite de ce chapitre, décrit la conservation dans l'espace des échelles du moment d'ordre deux, $E(\mathbf{r},t) = \langle(\delta\mathbf{u})^2\rangle$, des incréments de vitesse, définis comme la différence $\delta\mathbf{u}(\mathbf{x},\mathbf{r},t) = \mathbf{u}(\mathbf{x}+\mathbf{r},t) - \mathbf{u}(\mathbf{x},t)$ du champ de vitesse entre un point $\mathbf{x}+\mathbf{r}$ et un point $\mathbf{x}$. C'est une équation exacte, dérivée en prenant la moyenne statistique du produit de l'équation de Navier-Stokes aux points $\mathbf{x}$ et $\mathbf{x}+\mathbf{r}$ [68]. La moyenne considérée est *a priori* une moyenne d'ensemble. Celle-ci est cependant souvent remplacée par une moyenne spatiale sur $\mathbf{x}$, dans le contexte de la turbulence homogène, et/ou une moyenne temporelle lorsque la turbulence est statistiquement stationnaire. La moyenne angulaire $\mathcal{E}(r) = 1/(4\pi)\int_{\theta=0}^{\pi}\int_{\varphi=0}^{2\pi} E(\mathbf{r})\sin\theta d\theta d\varphi$ de $E(\mathbf{r},t)$ peut être interprétée comme l'énergie contenue dans les structures turbulentes d'échelles inférieures à $r = |\mathbf{r}|$ [*]. Dans le cas particulier d'une turbulence isotrope, $E(\mathbf{r}) = \mathcal{E}(|\mathbf{r}|)$ mesure donc directement l'énergie cumulée de 0 à r, dont l'équation Kármán-Howarth décrit la conservation.

L'écriture la plus générale de cette équation pour une turbulence homogène, en laissant la porte ouverte à une anisotropie, est l'équation de Kármán-Howarth-Monin (KHM) [106, 109]

$$\frac{1}{4}\partial_t E(\mathbf{r},t) = -\Pi(\mathbf{r},t) + \frac{1}{2}\nu\nabla_{\mathbf{r}}^2 E - \epsilon + \frac{1}{2}\langle\delta\mathbf{u}\cdot\delta\mathbf{f}\rangle, \tag{2.10}$$

où $-\Pi(\mathbf{r},t)$ est le terme de transfert d'énergie entre échelles spatiales, $\frac{1}{2}\nu\nabla_{\mathbf{r}}^2 E$ est un terme de diffusion visqueuse (dans l'espace des échelles), $\epsilon = \nu\langle(\partial_i u_j + \partial_j u_i)^2\rangle/2$ le taux de dissipation de l'énergie (totale) et $\frac{1}{2}\langle\delta\mathbf{u}\cdot\delta\mathbf{f}\rangle$ un terme d'injection par une force volumique $\mathbf{f}(\mathbf{x},t)$. Pour les échelles supérieures à celle du forçage L_{inj}, ce dernier terme s'identifie à la puissance P injectée par le travail de la force $\mathbf{f}$. Il est à noter que ce terme est nul dans les expériences et la majorité des écoulements naturels (sauf dans un contexte magnétohydrodynamique). Il est en pratique majoritairement introduit, dans les simulations numériques et les approches théoriques, comme un outil permettant de rendre compte d'une injection d'énergie qui respecte l'homogénéité

∗. Cette quantité contient en réalité aussi r^2-fois l'enstrophie associée aux échelles supérieures à r. Cette dernière contribution est toutefois négligeable pour les échelles grandes devant celles où la dissipation a lieu [68].

statistique. Au contraire, dans les expériences de laboratoire où la turbulence est stationnaire et le forçage assuré par le mouvement d'objets solides, l'injection d'énergie dans l'équation de KHM, considérée sur un certain volume de contrôle, est assurée par un transport d'énergie dans l'espace réel (i.e. $\mathbf{x}$) qui est intrinsèquement associé à des inhomogénéités de la statistique turbulente. Ce point est discuté en détail dans la partie V de notre article (Campagne *et al.* Physics of Fluids, 2014) à la page 103 qui explicite l'extension inhomogène de l'équation de KHM permettant de rendre compte de l'injection d'énergie. Cette remarque est finalement l'occasion de souligner qu'il est impossible de construire une expérience de turbulence statistiquement stationnaire et homogène en laboratoire. L'un ou l'autre sont possibles bien entendu mais pas les deux simultanément, dans quel cas tous les termes de (2.10) sont nuls.

Le terme de flux d'énergie,

$$\Pi(\mathbf{r},t) = \frac{1}{4}\boldsymbol{\nabla}_{\mathbf{r}} \cdot \langle (\delta\mathbf{u})^2 \delta\mathbf{u} \rangle, \tag{2.11}$$

est égal à la divergence dans l'espace des échelles d'un champs vectoriel de densité de flux d'énergie $\mathbf{F} = \langle (\delta\mathbf{u})^2 \delta\mathbf{u} \rangle$ construit à partir de moments d'ordre trois des incréments de vitesse. On note que comme pour l'équation de Lin, les transferts d'énergie sont caractérisés par des corrélations triples des vitesses.

La moyenne angulaire $\mathcal{E}(r)$ de $E(\mathbf{r})$ représentant l'énergie associée aux échelles de 0 à r, la moyenne angulaire $\mathcal{P}(r) = 1/(4\pi) \int_{\theta=0}^{\pi} \int_{\varphi=0}^{2\pi} \Pi(\mathbf{r}) \sin\theta d\theta d\varphi$ peut directement être interprétée comme le flux d'énergie des échelles plus petites que $r = |\mathbf{r}|$ vers les échelles plus grandes que r. Pour une turbulence isotrope, le signe de $\Pi(\mathbf{r}) = \mathcal{P}(|\mathbf{r}|)$ indique ainsi le sens de la cascade d'énergie, directe si $\Pi(\mathbf{r}) < 0$ et inverse si $\Pi(\mathbf{r}) > 0$.

Pour une turbulence homogène et isotrope à grand nombre de Reynolds, Kolmogorov dans ses articles de 1941 [110] a fait l'hypothèse de l'existence d'une gamme d'échelles dite inertielle, $\eta \ll r \ll L_{\text{inj}}$, pour laquelle tous les termes de (2.10) (dépendants de l'échelle r) deviennent négligeables sauf le transfert d'énergie, conduisant à la relation $\Pi(\mathbf{r}) = -\epsilon < 0$ (η est l'échelle en dessous de laquelle la diffusion visqueuse redevient importante dans (2.10), tel que $\nu\nabla^2_{\mathbf{r}} E \simeq 2\epsilon$ pour $r \ll \eta$). Cette équation, équivalente à la célèbre loi des 4/5ème de Kolmogorov $S_3(r) = \langle (\delta\mathbf{u}\cdot\mathbf{r}/r)^3 \rangle = -4/5\epsilon r$, prédit un flux d'énergie des grandes vers les petites échelles indépendant de r, et donc conservé. Elle a reçu de nombreuses confirmations expérimentales et numériques depuis ([107] et les références citées). Le même type de raisonnement a plus tard été développé pour la turbulence bidimensionnelle [111–113], où il a été proposé l'existence d'une gamme inertielle aux échelles plus grandes que l'échelle d'injection $r \gg L_{\text{inj}}$ et fait l'hypothèse que la puissance injectée P y domine largement la dissipation ϵ. On prédit cette fois-ci la relation $\Pi(\mathbf{r}) = +P > 0$, équivalente à la loi $S_3(r) = \langle (\delta\mathbf{u}\cdot\mathbf{r}/r)^3 \rangle = +3/2Pr$, révélant une cascade inverse d'énergie vers les grandes échelles mise en évidence dans de nombreuses expériences [114–116] et simulations numériques [117–119].

2.3.2 Transferts d'énergie en turbulence en rotation

En présence de rotation, il est remarquable de noter que les équations de Lin et de Kármán-Howarth-Monin restent inchangées. Cette propriété traduit le fait que la force de Coriolis n'agit que de manière indirecte sur la distribution de l'énergie à travers son influence sur les flux d'énergie, respectivement $T(\mathbf{k},t)$ ou $\Pi(\mathbf{r},t)$. Comme déjà mentionné, cette action bien qu'indirecte est cependant capable de rendre la turbulence fortement anisotrope et les interprétations des équations de Lin et de Kármán-Howarth-Monin en terme de cascade d'énergie ne conservent alors strictement leur sens que prises en moyenne angulaire $(1/(4\pi)\int_{\theta=0}^{\pi}\int_{\varphi=0}^{2\pi}\sin\theta d\theta d\varphi)$. Par exemple, le terme de flux d'énergie entre échelles $\Pi(\mathbf{r},t)$ ne peux plus être associé à la notion de flux des échelles plus grandes que $|\mathbf{r}|$ vers les échelles plus petites que $|\mathbf{r}|$, puisqu'il dépend à présent de l'orientation du vecteur séparation $\mathbf{r}$.

Malgré ce bémol, les quantités considérées dans (2.10) portent toujours des informations clés sur la construction de l'anisotropie de la turbulence par la rotation et restent donc d'un intérêt fondamental. En effet, pour une turbulence isotrope les surfaces de niveau de $E(\mathbf{r})$ sont des sphères tandis qu'elles deviennent des cylindres alignés avec l'axe de rotation pour une turbulence 2D. La compréhension des processus non-linéaires, i.e. des flux d'énergie $\Pi(\mathbf{r})$, construisant à travers l'équation de KHM l'anisotropie de $E(\mathbf{r})$ conserve ainsi une importance majeure.

2.3.3 Flux horizontaux d'énergie : expérience de turbulence forcée en rotation

- Doctorat d'A. Campagne (octobre 2012 - septembre 2015, co-directeur avec F. Moisy)
- Post-doctorat de B. Gallet (décembre 2012 - novembre 2013, co-responsable avec F. Moisy)

Comme nous l'avons vu dans la sous-partie 2.3.1, la turbulence 3D est associée à une cascade directe d'énergie des grandes vers les petites échelles et au contraire la turbulence 2D à une cascade inverse. À un nombre de Rossby fini, la tendance à la bidimensionnalisation induite par la rotation entraîne la turbulence vers un état anisotrope intermédiaire entre 3D et 2D. Il se pose alors naturellement la question de la direction des flux d'énergie dans le plan perpendiculaire à l'axe de rotation.

Cette question a été principalement abordée au moyen de simulations numériques directes de turbulence forcée [4, 102, 120–126]. Dans ces simulations où l'énergie est injectée à un taux constant à un nombre d'onde particulier k_f, l'action de la rotation se manifeste notamment à travers une croissance avec le temps du spectre d'énergie $e(k_\perp, k_\parallel)$ aux grandes échelles horizontales $(k_\perp < k_f, k_\parallel = 0)$ (Figure 2.5 Gauche), signe d'une cascade inverse dans le plan horizontal ($k_\perp$ et $k_\parallel$ sont respectivement les composantes du vecteur d'onde normale et parallèle à l'axe de rotation). L'énergie à grandes échelles ne subissant que très peu la dissipation visqueuse, ces études rapportent une croissance avec le temps de l'énergie totale. Certaines d'entre elles [102, 123–125] présentent par ailleurs une mesure directe des flux d'énergie, inverses pour $k < k_f$ et directs pour $k > k_f$, révélant la possibilité d'une double cascade alimentée à l'échelle k_f (Figure 2.5 Droite). Des indices plus ténus d'une cascade inverse ont aussi été mis en évidence dans des simulations

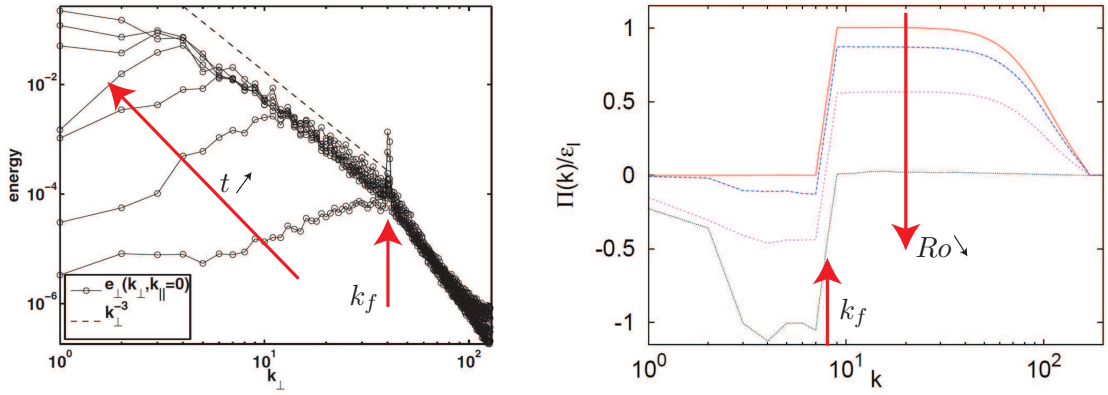

FIGURE 2.5 – **Gauche** : Évolution temporelle du spectre d'énergie $e(k_\perp, k_\parallel = 0)$ (mode 2D) dans une simulation numérique directe forcée à l'échelle k_f. Adapté de Sen *et al.* [124]. **Droite** : Moyenne angulaire du flux d'énergie entre échelles pour différentes valeurs du nombre de Rossby Ro dans une simulation numérique directe forcée à l'échelle k_f : on observe la croissance d'une cascade inverse ($k < k_f$) et la décroissance de la cascade directe ($k > k_f$) lorsque Ro décroît. Adapté de Deusebio *et al.* [126].

directes de turbulence en déclin et en rotation [127, 128]. Dans l'ensemble, ces simulations indiquent que l'apparition et le cas échéant l'amplitude d'une cascade inverse d'énergie dans une turbulence en rotation dépend fortement, évidemment du nombre de Rossby, mais aussi de la nature du forçage (2D ou 3D, 2C ou 3C, hélicitaire ou non). On souligne aussi le rôle important du confinement vertical H, le nombre de Rossby critique en dessous duquel une cascade inverse apparaît croissant rapidement lorsque $k_f\, H$ diminue [4, 121, 126].

Malgré la qualité des travaux mentionnés ci-dessus, un certain nombre de caractéristiques intrinsèques aux simulations numériques homogènes rendent utiles les études expérimentales. L'injection de l'énergie à un nombre d'onde k_f particulier semble par exemple fixer de manière artificielle l'échelle d'inversion de la cascade d'énergie entre directe et inverse. La croissance non-transitoire de l'énergie avec le temps semble aussi une conclusion problématique de ces simulations numériques, intrinsèquement liée au caractère irréaliste de la turbulence homogène forcée stationnairement en présence de cascade inverse. Dans les deux cas, ces caractéristiques disparaîtront dans un écoulement réel forcé par des parois mobiles, où l'échelle d'inversion de la cascade sera libre et la turbulence statistiquement inhomogène et stationnaire. La différence fondamentale entre les systèmes numériques et expérimentaux relève de l'injection d'énergie qui est liée, dans les simulations numériques, à une force volumique statistiquement homogène et, dans les écoulements réels, aux inhomogénéités.

Il existe cependant assez peu de caractérisations expérimentales des flux d'énergie entre échelles dans une turbulence en rotation. Celles-ci ont en pratique pris leur essort avec la démocratisation des techniques de PIV dans les années 2000. On peux citer les travaux de Baroud *et al.* en 2002 [129] en turbulence forcée (inhomogène stationnaire) et de Morize *et al.* en 2005 [75] en turbulence de grille en déclin (homogène instationnaire) qui ont permis les premières mesures des moments d'ordre trois des incréments longitudinaux de vitesse $S_3(r_\perp)$ dans un plan horizon-

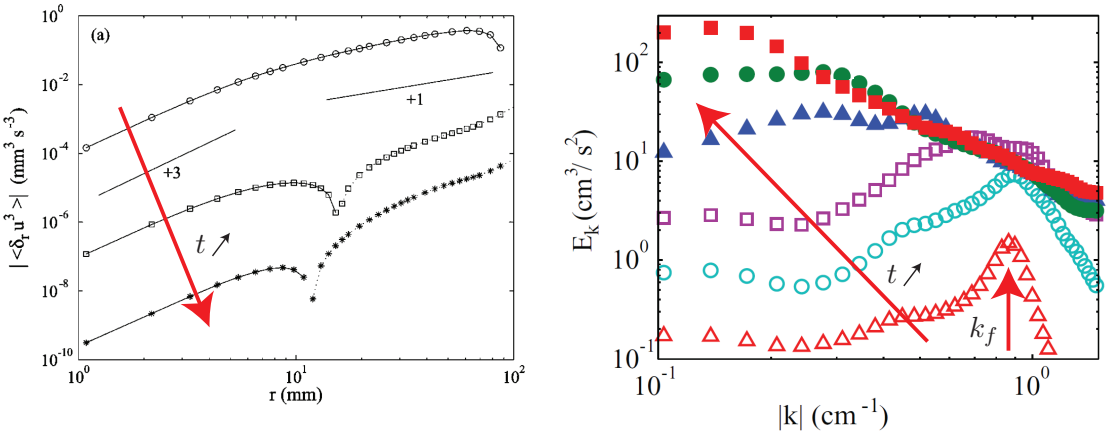

FIGURE 2.6 – **Gauche** : Évolution temporelle de la valeur absolue du moment d'ordre trois des incréments longitudinaux de vitesse $S_3(r)$ dans le plan horizontal d'une expérience de turbulence de grille en déclin et en rotation. Adapté de Morize *et al.* [75]. On observe un changement de signe de $S_3(r)$ qui se propage vers les petites échelles avec le temps. **Droite** : Évolution temporelle du spectre d'énergie du champ de vitesse horizontale dans un plan horizontal dans une expérience de turbulence forcée en rotation. Adapté de Yarom *et al.* [130]

tal du référentiel tournant. Ces travaux ont mis en évidence la possibilité d'une cascade inverse d'énergie à travers l'observation d'un changement de signe de $S_3(r_\perp)$ aux grandes échelles (Figure 2.6 Gauche). Comme nous l'avons vu en 2.3.1, on sait en effet que le signe de cette quantité est associé au sens de la cascade d'énergie dans un contexte isotrope. Dans le contexte anisotrope, aucune relation théorique ne permet cependant de reconstruire les flux d'énergie $\Pi(\mathbf{r})$ à partir de $S_3(r_\perp)$ de sorte que ces résultats ne permettent pas d'établir avec certitude la direction des transferts d'énergie. Cette même question de l'émergence d'une cascade inverse en turbulence en rotation a été abordée plus récemment par Yarom *et al.* [130] qui ont étudié l'évolution temporelle du spectre spatial de l'énergie pendant la phase transitoire d'une expérience de turbulence en rotation forcée à petite échelle. Ils ont mis en évidence une croissance avec le temps (transitoire bien sûr) de l'énergie associée aux grandes échelles horizontales qui est un signe fort de cascade inverse (Figure 2.6 Droite). La nature à la fois instationnaire et inhomogène de l'écoulement étudié laisse cependant la possibilité que l'énergie qui alimente les grandes échelles soit apportée par un transport spatial (et non seulement en échelles) et ne permet donc pas d'interpréter définitivement ces observations.

Dans notre article (Campagne *et al.* Physics of Fluids, 2014) à la page 103 nous avons tenté d'apporter de nouveaux éléments en réalisant les premières mesures directes de $\Pi(\mathbf{r})$ dans le plan horizontal d'une expérience de turbulence en rotation. Dans cette expérience (http://youtu.be/xzvZGKPPnBQ) une turbulence statistiquement stationnaire ($Re \simeq 300$, $0.07 < Ro < \infty$) est excitée par une arène de dix générateurs de dipôles de tourbillons verticaux, constitués de volets se fermant périodiquement, qui injectent des fluctuations turbulentes tridimensionnelles en direction du centre de l'expérience (Figure 2.7). Ces générateurs [131, 132] ont été développés au LadHyX à l'École

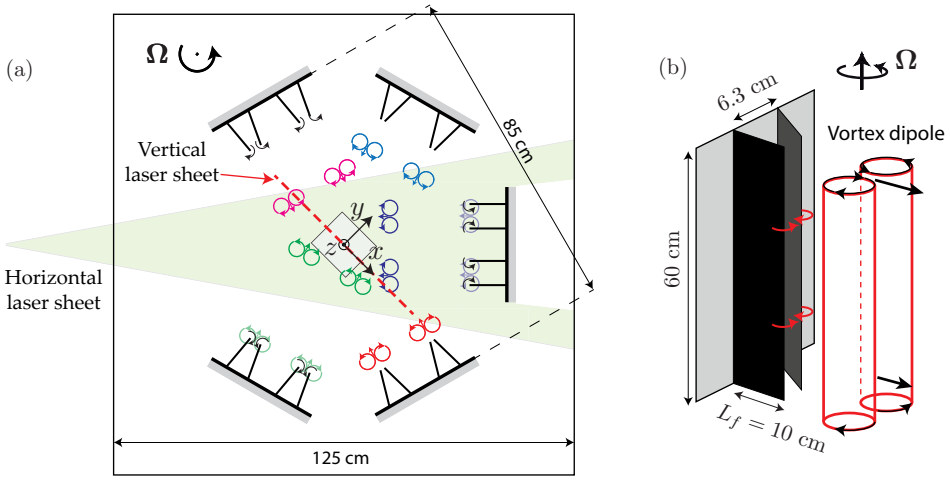

FIGURE 2.7 – (a) Schéma de l'arène de 10 générateurs de dipôles de tourbillons placée dans un aquarium parallélépipédique sur la plateforme tournante "Gyroflow". Le vecteur taux de rotation $\mathbf{\Omega}$ est vertical et le système est vu de dessus. Le rectangle au centre de l'arène indique la région horizontale où les champs de vitesse 2D-3C ont été mesurés par PIV stéréoscopique. On a représenté de manière idéalisée quelques dipôles de tourbillons avant qu'ils n'interagissent au centre de l'arène. Ceux-ci advectent de fortes fluctuations tridimensionnelles. (b) Vue en perspective d'une paire de volets constituant un générateur de dipôles de tourbillons.

Polytechnique par P. Augier, J.-M. Chomaz et P. Billant, qui nous les ont amicalement prêtés. Ce système a été placé dans un grand aquarium tournant sur la plateforme "Gyroflow". Nous avons mis en œuvre des mesures de PIV stéréoscopique permettant d'accéder aux trois composantes des champs de vitesse dans un plan (vertical ou horizontal) du référentiel tournant, ce qui constitue un enjeu important dans ce contexte anisotrope. Ce système expérimental a alors ouvert la voie à une étude détaillée des transferts d'énergie entre échelles en nous donnant accès à des statistiques importantes (10 000 champs de vitesse mesurés par vitesse de rotation) pour le calcul statistiquement exigeant des flux d'énergie.

Dans un premier temps, ces expériences ont donné lieu à une caractérisation de la dépendance en échelles de la statistique de l'asymétrie entre cyclones (tourbillons tournant dans le même sens que la rotation globale) et anticyclones induite par la rotation. Nous avons pour cela introduit des outils (corrélations triples de vitesse en deux points), nouveaux dans ce contexte, dont l'interprétation a été testée analytiquement à l'aide de distributions aléatoires de tourbillons. Ce travail a par ailleurs été l'occasion de valider un modèle phénoménologique simple décrivant les lois d'échelle suivies par la déviation standard des fluctuations de vitesse. Ces travaux ont été publiés dans "Physics of Fluids" en 2014 (B. Gallet *et al.*, Phys. Fluids **26**, 035108 (2014) [133]).

Le résultat central de ces expériences est la mesure des flux d'énergie entre échelles $\Pi(\mathbf{r})$ dans le plan horizontal. Sans rotation d'ensemble, ces flux révèlent une cascade directe de l'énergie des grandes vers les petites échelles, classique de la turbulence tridimensionnelle (Figure 2.8). Avec une rotation d'ensemble, on observe dans le plan horizontal l'émergence d'une double cascade de l'énergie horizontale (associée aux composantes horizontales du champ de vitesse).

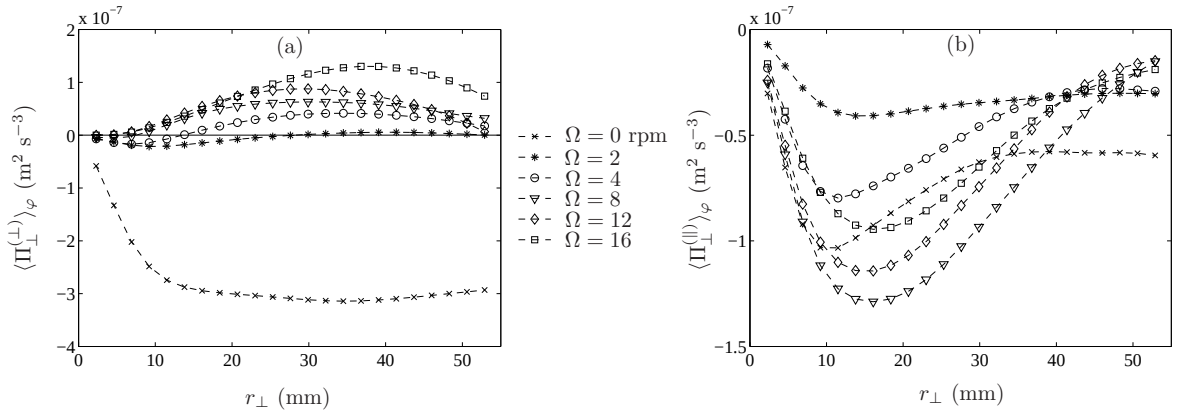

FIGURE 2.8 – Flux d'énergie $\Pi_\perp(r_\perp) = \Pi_\perp^{(\perp)}(r_\perp) + \Pi_\perp^{(\parallel)}(r_\perp)$ dans le plan horizontal en fonction de l'échelle horizontale $r_\perp$ pour différents taux de rotation. (a) Flux d'énergie horizontale $\Pi_\perp^{(\perp)}(r_\perp)$ dans le plan horizontal présentant une cascade directe à $\Omega = 0$ ($\Pi < 0$) puis une double cascade et enfin une pure cascade inverse ($\Pi > 0$) lorsque que Ω augmente. (b) Flux d'énergie verticale $\Pi_\perp^{(\parallel)}(r_\perp)$ dans le plan horizontal présentant une cascade directe pour tout Ω et tout $r_\perp$ ($\Pi < 0$).

Celle-ci est composée d'une cascade directe à petites échelles et d'une cascade inverse à grandes échelles, l'échelle d'inversion décroissant avec le taux de rotation (Figure 2.8a). Au contraire, on observe pour l'énergie associée à la composante verticale du champ de vitesse une cascade dans le plan horizontal toujours directe (Figure 2.8b). Aux échelles où l'énergie horizontale subit une cascade directe, la cascade directe de l'énergie verticale est associée à la physique de la turbulence tridimensionnelle. Au contraire, aux échelles où l'énergie horizontale subit une cascade inverse, la cascade directe de l'énergie verticale traduit une dynamique d'étirement-repliement typique d'un scalaire passif en turbulence 2D [134, 135]. Finalement, il est important de souligner que dans notre expérience forcée par le mouvement de parois solides, l'injection de l'énergie dans l'équation de KHM intervient à travers un transport spatial, des générateurs vers le centre de l'arène, intrinsèquement lié aux inhomogénéités. Nous avons réussi à mesurer ce terme d'injection d'énergie pour les expériences aux taux de rotation les plus élevés.

Notre travail expérimental apporte ici trois résultats ayant un caractère nouveau : (i) la confirmation expérimentale directe de l'émergence d'une double cascade d'énergie liée à la rotation, (ii) la décroissance de l'échelle d'inversion de la cascade avec le taux de rotation, (iii) la prise en compte de l'ensemble des termes de la version inhomogène de l'équation de KHM qui permet de révéler l'"histoire" des flux d'énergie dans l'espace des échelles. Nos résultats apparaissent comme complémentaires de ceux des simulations numériques homogènes à travers une prise en compte du caractère nécessairement inhomogène des écoulements turbulents forcés en rotation développant une cascade inverse. L'enjeu principal qui émerge de nos travaux est de mieux comprendre ce qui fixe l'échelle d'inversion de la cascade d'énergie dans le plan horizontal d'une turbulence en rotation. Dans ce cadre, il semble nécessaire pour progresser que nos résultats puissent être confrontés à des simulations numériques laissant libre l'échelle d'inversion, ainsi qu'à d'autres résultats expérimentaux.

2.3.4 Flux d'énergie dans le plan vertical : expérience de turbulence de grille en déclin et en rotation

- Collaboration avec L. Maas (NIOZ, Pays-Bas)
- Doctorat de C. Lamriben (septembre 2009 - août 2012, co-directeur avec F. Moisy)

Un autre sujet d'étude auquel nous avons consacré un temps important est la caractérisation expérimentale de l'anisotropie de la turbulence en rotation et plus précisément de sa répartition en échelles. La rotation étant absente, explicitement en tout cas, de l'équation de KHM (2.10), une question importante ici est de mieux comprendre comment l'anisotropie des flux d'énergie $\Pi(\mathbf{r},t)$ dans le plan vertical construit l'anisotropie de la distribution de l'énergie $E(\mathbf{r},t)$.

Dans ce contexte, une approche d'analyse dimensionnelle a été proposée dans les années 1990 [136–138] prédisant que l'influence de la rotation est plus prononcée aux grandes qu'aux petites échelles. Celle-ci se base sur la construction d'un nombre de Rossby $Ro_r = (\Omega\tau_r)^{-1}$ dépendant de l'échelle où τ_r est un temps caractéristique associé aux structures de taille r. L'idée est alors d'utiliser les lois bien établies de la turbulence isotrope, $\tau_r \sim \epsilon^{-1/3} r^{2/3}$, pour construire une relation

$$Ro_r = \left(\frac{r_\Omega}{r}\right)^{2/3}, \tag{2.12}$$

faisant apparaître l'échelle dite de Zeman [136–138]

$$r_\Omega = \epsilon^{1/2}\Omega^{-3/2}. \tag{2.13}$$

La décroissance (2.12) de Ro_r avec r prédit que, si une turbulence initialement isotrope est soumise à l'influence de la force de Coriolis, cette dernière n'affectera pas les échelles plus petites que l'échelle de Zeman r_Ω qui sont associées à des dynamiques rapides devant la rotation. Les échelles plus grandes que r_Ω sont au contraire lentes et donc affectées par la rotation. Pour ces dernières, les lois d'échelles utilisées pour construire le nombre de Rossby Ro_r (2.12) deviennent cependant obsolètes *a priori* et il semble difficile de discuter plus avant la dépendance en échelles de l'influence de la rotation de cette manière. La physique des ondes d'inertie ne couplant pas les échelles temporelles et spatiales, les structures plus lentes que la rotation et donc affectées par celles-ci semblent en effet possiblement pouvoir apparaître à toutes échelles, révélant la complexité de cette question de la dépendance en échelles de l'anisotropie.

Les formalismes de turbulence d'ondes d'inertie [90, 91] s'attachent justement à décrire les lois d'échelle de la distribution de l'énergie dans la limite des fortes rotations $Ro \to 0$. Ils prédisent en pratique une anisotropie croissante lorsque l'échelle considérée diminue. Galtier [139] a proposé une interprétation de ce résultat à travers une analyse dimensionnelle qui associe un temps caractéristique $\tau_r \sim r^{-1/3}$ à l'échelle r [140, 141] en prenant en compte la conservation de l'énergie et de l'hélicité par les équations inviscides du mouvement. La réalité d'une telle anisotropie plus forte aux petites échelles dans la limite $Ro \to 0$ est renforcée par son observation dans les simulations numériques de turbulence d'ondes de Bellet *et al.* [142] (modèle asymptotique quasi-normal markovien). Il est important de souligner que dans ces modèles asymptotiques, l'échelle

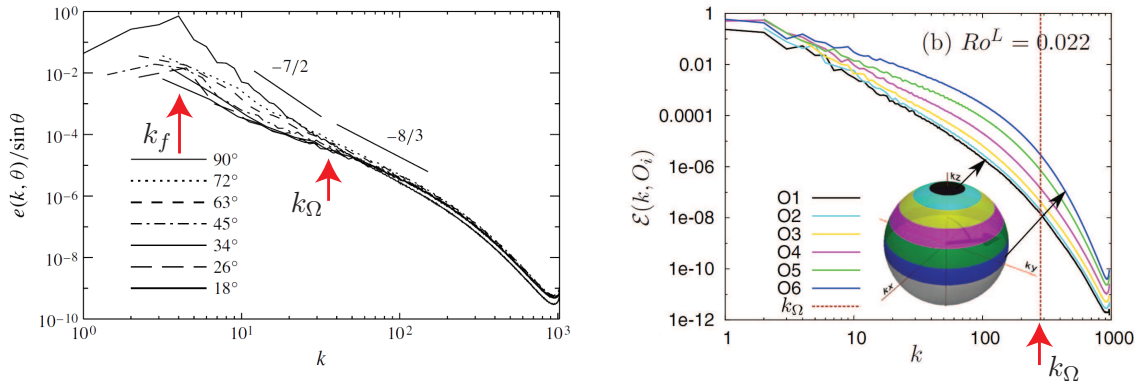

FIGURE 2.9 – Distribution angulaire de la densité spectrale d'énergie, tracée en fonction de la norme du nombre d'onde et paramétrée par la colatitude. On a reporté le nombre d'onde de Zeman $k_\Omega = 2\pi/r_\Omega$ et le cas échéant celui d'injection k_f. **Gauche** : Simulations numériques directes avec forçage hélicitaire au nombre d'onde k_f de Mininni *et al.* [78]. **Droite** : Simulations numériques directes de turbulence en rotation en déclin depuis un état initial isotrope de Delache *et al.* [79].

de Zeman r_Ω est infiniment faible. Ces approches ne sont donc pas incompatibles avec l'existence d'un retour à l'isotropie pour $r < r_\Omega$ à nombre de Rossby fini, ou, plus précisément, dans une situation où l'échelle de Zeman r_Ω appartiendrait à la gamme inertielle.

La question de la répartition en échelles de l'anisotropie de la turbulence en rotation a été assez peu abordée à travers les simulations numériques directes. On peut mentionner les simulations de turbulence en déclin et en rotation depuis un état initial isotrope (non hélicitaire) de Yoshimatsu *et al.* [143] et Delache *et al.* [79]. Ces études mettent en évidence une anisotropie de la distribution d'énergie respectivement maximum aux plus petites échelles de la turbulence dans [143] et à une échelle proche de l'échelle de Zeman dans [79] (Figure 2.9 Droite). On note que ces résultats sont tous deux compatibles avec le scénario dressé par les modèles de turbulence d'ondes d'inertie (pour $r > r_\Omega = 2\pi/k_\Omega$) si on lui associe un retour à l'isotropie pour $r < r_\Omega$. Au contraire, les simulations de turbulence stationnaire de Mininni *et al.* [78] avec un forçage hélicitaire révèlent une anisotropie de la distribution de l'énergie croissant avec l'échelle, i.e. décroissant entre le nombre d'onde associé à l'injection k_f et celui de Zeman $k_\Omega = 2\pi/r_\Omega$ (Figure 2.9 Gauche). L'anisotropie disparaît ensuite aux échelles plus petites que l'échelle de Zeman. Un retour à l'isotropie similaire a été mis en évidence dans les simulations de turbulence forcée de Naso et Godeferd [144] à travers l'étude du tenseur des gradients de vitesse en fonction d'une échelle de filtrage. Hormis un retour à l'isotropie pour les échelles r plus petites que l'échelle de Zeman r_Ω, les simulations numériques directes de turbulence en rotation semblent donc indiquer des résultats contrastés et dépendant de manière subtile des détails des simulations (turbulence forcée ou en déclin, hélicitaire ou non,...). On souligne cependant le fait que dans les simulations de turbulence en déclin depuis un état initial isotrope [79, 143] l'anisotropie observée est intégralement construite par l'action de la rotation sur les transferts d'énergie entre échelles ce qui n'est pas nécessairement le cas pour les simulations forcées.

D'un point de vue expérimental, il n'existe pas à notre connaissance, avant l'étude présentée

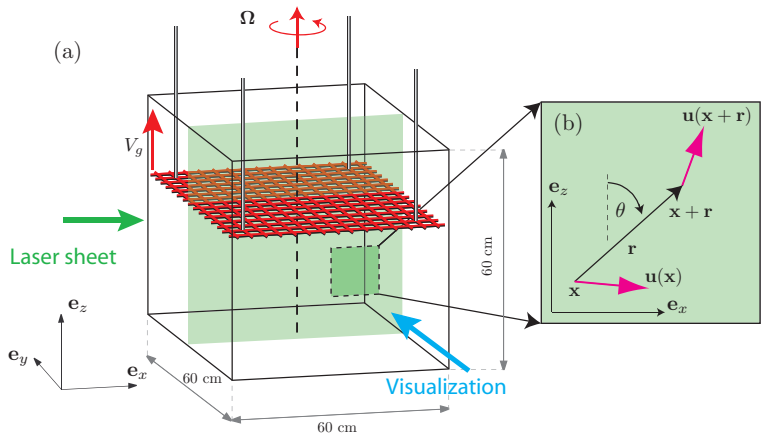

FIGURE 2.10 – (a) Schéma du dispositif expérimental de turbulence de grille. L'aquarium tourne à Ω de 0 à 16 rpm (1.68 rad s^{-1}). La grille est translatée de bas en haut à $V_g = 1$ m s^{-1} et des mesures de PIV sont réalisées dans le plan vertical (x, z) du référentiel tournant durant le déclin de la turbulence. (b) Zone de mesure et définition de l'incrément de vitesse $\delta\mathbf{u} = \mathbf{u}(\mathbf{x}+\mathbf{r}) - \mathbf{u}(\mathbf{x})$.

ici, de travaux donnant accès à la distribution de l'énergie et encore moins des transferts d'énergie dans un plan vertical de l'espace des échelles. On peut expliquer cette absence par la difficulté de réaliser des mesures de vélocimétrie dans le plan vertical d'une expérience en rotation. À la vue des résultats contrastés des travaux numériques évoqués plus tôt, il apparaît cependant souhaitable d'accéder à ce genre de données dans une situation expérimentale.

Notre équipe au FAST a ainsi tenté d'apporter des éléments expérimentaux à travers une expérience de turbulence quasi-homogène en déclin et en rotation. Ces travaux, dont nous résumons les points marquants dans la suite de cette partie, sont décrits pour partie dans l'article (Lamriben *et al.* Physical Review Letters, 2011) à la page 122 et plus en détail dans l'article (Cortet *et al.* en préparation pour Journal of Turbulence, 2015) à la page 126. Dans cette expérience (Figure 2.10), la turbulence est générée par la translation rapide d'une grille dans un aquarium cubique placé sur la plateforme "Gyroflow" (http://youtu.be/G0WFWlPuaQQ). L'intensité des fluctuations turbulentes est initialement suffisamment forte pour que l'écoulement ne soit pas sensible à la rotation ($Re \simeq 1000$, $Ro \geqslant 1$). La turbulence possède ainsi initialement des propriétés proches de l'isotropie et ce pour tous les taux de rotation Ω étudiés ($\leqslant 16$ rpm). La turbulence va ensuite décliner sous l'action de la dissipation visqueuse et l'intensité relative de la rotation globale va augmenter progressivement ($Re(t) \simeq 1000 \to 200$, $Ro(t) \simeq 1 \to 10^{-2}$). Nous avons ainsi pu étudier la construction des effets de la rotation, et notamment la croissance de l'anisotropie pendant le déclin de la turbulence (Figure 2.11).

Lors de ces expériences, nous avons dans un premier temps observé que lorsque qu'une grille "simple" est utilisée, une partie importante de l'énergie est injectée dans un écoulement reproductible. Nous avons montré que cet écoulement est composé de modes résonants d'ondes d'inertie de la cavité cubique. Un travail important a alors été consacré à caractériser ces modes dont les structures spatiales et les fréquences de résonance se sont révélées correspondre aux

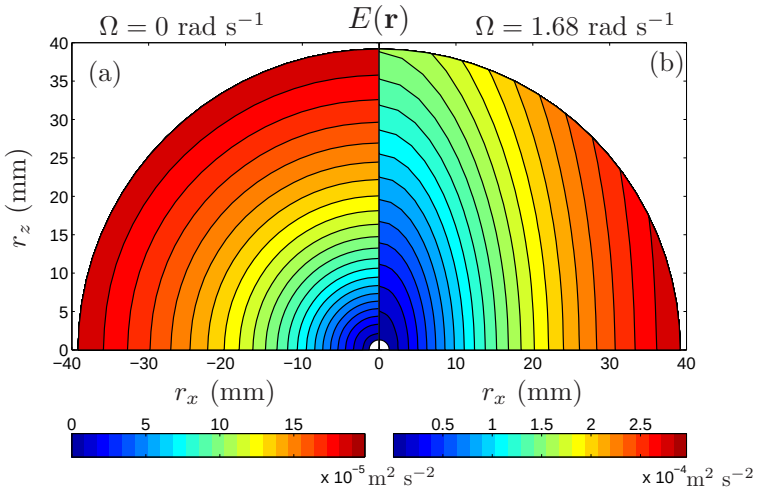

FIGURE 2.11 – Distribution d'énergie $E(\mathbf{r}, t)$ au temps $t\,V_g/M = 400$ après la translation de la grille pour (a) $\Omega = 0$ et (b) $\Omega = 1.68$ rad s^{-1} (16 rpm). $V_g = 1$ m s^{-1} est la vitesse et $M = 40$ mm la maille de la grille excitant la turbulence à $t = 0$.

prédictions numériques faites par Leo Mass (Professeur au Royal Netherlands Institute for Sea Research) (cf. section 1.4.1). Les échanges locaux d'énergie possibles entre ces modes et la partie "turbulente" de l'écoulement suggèrent qu'une telle turbulence ne peut être ni homogène ni même en déclin libre. Une tâche indispensable pour que notre étude puisse être menée dans de bonnes conditions a donc été d'inhiber l'excitation de ces modes, ce qui a été rendu possible par l'ajout de plusieurs parois verticales en amont de la grille. Ces travaux ont ainsi démontré que l'on pouvait effectivement générer une turbulence quasi-homogène, initialement isotrope, et en déclin libre dans une géométrie confinée en rotation ce qui était jusqu'alors contesté [145]. Ce travail, publié dans "Physics of Fluids" (C. Lamriben *et al.*, Phys. Fluids **23**, 015102 (2011) [146]), a été l'occasion d'amorcer notre collaboration avec Leo Mass pour lequel nous avons obtenu un mois d'un poste de professeur invité en 2012.

Pour chaque taux de rotation étudié, 600 déclins ont été déclenchés et mesurés dans un plan vertical parallèle à l'axe de rotation grâce à un système de PIV embarqué dans le référentiel tournant (Figure 2.10). À partir de cette statistique d'ensemble, limitée mais représentant un travail très important, nous avons pu accéder à des estimateurs de la distribution d'énergie $E(\mathbf{r}, t)$ et des transferts d'énergie $\Pi(\mathbf{r}, t)$ dans l'espace des échelles. Nos mesures de PIV d'alors n'étant pas encore stéréoscopiques, nous n'avons en effet eu accès qu'à des champs de vitesse 2D2C. Nos mesures de $E(\mathbf{r}, t)$ et de $\Pi(\mathbf{r}, t)$ ne constituent donc à strictement parler que des estimateurs puisque certains termes manquent. Il est cependant important de noter que l'axi-symétrie de notre turbulence permet de reconstruire à partir des mesures 2D2C la distribution exacte d'énergie $E(\mathbf{r}, t)$, ce qui n'est malheureusement pas le cas pour les transferts $\Pi(\mathbf{r}, t)$. Les conclusions présentées dans la suite sont donc exactes pour $E(\mathbf{r}, t)$ mais partiellement sujettes à caution pour les transferts d'énergie $\Pi(\mathbf{r}, t)$. On peut cependant souligner à nouveau le caractère pionnier de ces mesures expérimentales de flux d'énergie qui justifie leur intérêt malgré leur

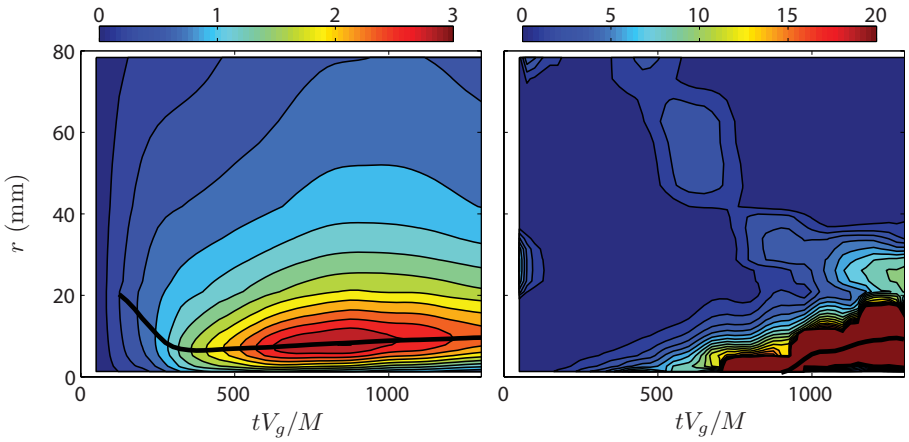

FIGURE 2.12 – Dépendance avec l'échelle r et le temps t des facteurs d'anisotropie de la distribution de l'énergie $(E(r,\theta=\pi/2,t)-E(r,\theta=0,t))/E(r,\theta=0,t)$ (**Gauche**) et des transferts d'énergie $(\Pi(r,\theta=\pi/2,t)-\Pi(r,\theta=0,t))/\Pi(r,\theta=0,t)$ (**Droite**) pour l'expérience au taux de rotation le plus grand $\Omega = 16$ rpm. (r,θ,φ) correspond aux coordonnées sphériques avec θ la colatitude, i.e. $\theta = 0$ selon l'axe de rotation et $\theta = \pi/2$ selon l'équateur.

nature incomplète.

Un premier résultat fort de ces expériences a été de révéler que l'anisotropie des transferts d'énergie $\Pi(\mathbf{r},t) = \frac{1}{4}\boldsymbol{\nabla}_\mathbf{r}\cdot\mathbf{F}$ n'est quasiment pas liée à l'émergence d'une composante non-radiale de la densité de flux d'énergie dans l'espace des échelles $\mathbf{F} = \langle(\delta\mathbf{u})^2\delta\mathbf{u}\rangle$ mais à l'apparition d'une dépendance de son amplitude avec la direction angulaire du vecteur séparation $\mathbf{r}$. Ces résultats, publiés dans l'article (Lamriben *et al.* Physical Review Letters, 2011) (à la page 122), apportent en pratique les premières mesures directes de l'influence de la force de Coriolis sur les flux d'énergie dans le plan vertical. Nos mesures ont aussi mis en évidence que l'anisotropie des flux d'énergie $\Pi(\mathbf{r},t)$ est maximale aux plus petites échelles qui, aux temps courts, se trouvent être plus petites que l'échelle de Zeman (Figure 2.12 Droite). Cette anisotropie se propage ensuite lentement vers les échelles plus grandes sur un temps caractéristique $1/\Omega$. Ces résultats restent largement inexpliqués par les travaux théoriques existants [139] et nous espérons qu'ils pourront susciter de nouveaux efforts dans ce domaine. Il semble par ailleurs intéressant que nos mesures puissent être confrontées à des résultats numériques [147] ainsi qu'à d'autres résultats expérimentaux qui s'appuieraient cette fois-ci sur des données 2D-3C donnant accès à une mesure complète des flux d'énergie.

Au contraire des flux d'énergie, l'anisotropie de la distribution d'énergie présente un maximum à une échelle intermédiaire $r_{\text{aniso}}(t)$ dont l'évolution temporelle est non-monotone (Figure 2.12 Gauche). Cette échelle décroît dans un premier temps, de manière compatible avec le déclin de l'échelle de Zeman $r_\Omega = \epsilon(t)^{1/2}\Omega^{-3/2}$, lié au déclin du taux de dissipation de l'énergie. Lorsque l'échelle de Zeman devient plus faible que la coupure visqueuse de la cascade d'énergie, nos données montrent que $r_{\text{aniso}}(t)$ croît ensuite lentement en suivant l'échelle de Kolmogorov $\eta(t) = (\nu^3/\epsilon(t))^{1/4}$. Le premier régime que nous rapportons ici avec une anisotropie de l'énergie

maximale à l'échelle de Zeman $r_{\text{aniso}}(t) \sim r_\Omega(t)$ est compatible avec les observations de Delache *et al.* [79], tandis que le deuxième régime, où l'échelle d'anisotropie maximale correspond à celle de coupure visqueuse, reproduit les résultats des simulations numériques de Yoshimatsu *et al.* [143]. On remarque l'atout lié au caractère déclinant de notre turbulence qui fournit, à travers la décroissance des nombres de Reynolds $Re(t)$ et de Rossby $Ro(t)$, une manière intéressante d'explorer dans une même expérience les deux régimes $r_\Omega \gg \eta$ (i.e. $ReRo^2 \gg 1$) et $r_\Omega \ll \eta$ (i.e. $ReRo^2 \ll 1$). On souligne aussi à nouveau le fait que, le forçage initial construisant une turbulence isotrope comme dans les simulations des références [143] et [79], cette expérience permet de s'assurer que l'anisotropie observée est pleinement liée aux effets de la rotation sur les transferts d'énergie. On peux finalement noter que nos mesures présentent en revanche un désaccord avec les résultats de Mininni *et al.* [78]. Celui-ci semble possiblement lié au caractère hélicitaire du forçage utilisé dans ces simulations qui, couplé à la rotation, pourrait imposer une anisotropie supplémentaire aux grandes échelles. Une clarification de ce désaccord semble nécessaire pour une compréhension plus profonde de la répartition en échelles de l'anisotropie de la turbulence en rotation, appelant à de nouveaux travaux expérimentaux et numériques. On souligne cependant que nos travaux confirment pour la première fois expérimentalement le scénario, proposé par la turbulence d'ondes et supporté par les simulations numériques [142], [143] et [79], selon lequel l'anisotropie de l'énergie décroît avec l'échelle pour les échelles plus grandes que celle de Zeman.

2.4 Perspectives

Les deux expériences de turbulence en rotation que nous avons développées depuis 2009 ont permis d'accéder à des résultats expérimentaux ayant un caractère novateur dans un domaine dominé par les approches numériques. Nos travaux apparaissent comme complémentaires des simulations numériques (directes ou non), en particulier grâce à un certain nombre de différences notables : injection d'énergie large bande *vs.* injection à une échelle imposée, inhomogénéité *vs.* homogénéité, analyse en échelles *vs.* analyse spectrale.

Dans cette dernière partie, nous présentons deux pistes nouvelles de recherche —une nouvelle analyse de données et une nouvelle expérience— qu'il nous parait intéressant de suivre.

2.4.1 Analyse en échelles spatiales et temporelles

Un premier projet que nous envisageons de développer dans un futur proche consiste à analyser simultanément dans l'espace des échelles spatiales et temporelles les champs de vitesse dans le plan vertical de l'expérience de turbulence forcée présentée dans la partie 2.3.3. L'idée au cœur de cette étude est d'aller à la recherche d'ondes d'inertie dans cet écoulement turbulent en rotation avec à l'esprit une possible confrontation avec les formalismes de turbulence d'ondes. Un enjeu est ici de tester la pertinence de ce type de modèles pour décrire au moins certaines échelles de cette turbulence en rotation expérimentale. Il s'agira d'abord de tester les hypothèses en jeu et en premier lieu la présence d'ondes d'inertie avant de pouvoir se confronter à certaines prédictions

théoriques. Un autre objectif de cette étude est de caractériser l'anisotropie de l'écoulement simultanément en échelles spatiales et en échelles temporelles. L'idée est ici de "décortiquer" ce qui compose l'anisotropie de la turbulence en rotation plus finement que lors de l'analyse des expériences de turbulence en déclin décrites à la section 2.3.4. On note qu'une telle analyse spatiotemporelle est impossible pour ces expériences de turbulence de grille en déclin, l'évolution temporelle de l'écoulement étant trop rapide par rapport aux échelles de temps que l'on souhaite analyser.

D'un point de vue technique, cette étude est complexe car l'analyse spectrale spatiotemporelle (i.e. par transformée de Fourier spatiotemporelle) qui est naturelle dans l'objectif de la détection d'une assemblée d'ondes semble ici compromise. Les gammes d'échelles spatiales en jeu dans l'écoulement étant aussi grandes voir plus grandes que celles accessibles par nos mesures de PIV, les transformées de Fourier spatiales (anisotropes) des champs de vitesse apparaissent ici comme un outil dangereux, fortement biaisé par le caractère non-périodique des champs de vitesse. Notre idée pour contourner ce problème est de développer une analyse mixte spectrale en temps (s'appuyant sur nos séries temporelles de 10 000 champs) et en deux points dans l'espace pour accéder à une description spatiotemporelle pertinente. On calculera en pratique la corrélation $R_\omega(\mathbf{r}) = |\langle \tilde{\mathbf{u}}(\omega, \mathbf{x}) \cdot \tilde{\mathbf{u}}^*(\omega, \mathbf{x}+\mathbf{r})\rangle_{\mathbf{x}}|$ entre les points $\mathbf{x}$ et $\mathbf{x}+\mathbf{r}$ de la transformée de Fourier temporelle $\tilde{\mathbf{u}}(\omega, \mathbf{x})$ du champ de vitesse. Les cartes de $R_\omega(\mathbf{r})$ nous permettront finalement de caractériser la distribution anisotrope de l'énergie associée à chaque pulsation ω.

2.4.2 Taux de transfert de l'énergie et rotation d'ensemble

Comme nous l'avons évoqué à plusieurs reprises dans ce chapitre, les formalismes de turbulence d'ondes prédisent que, dans la limite des fortes rotation $Ro \to 0$, le taux de transfert de l'énergie des grandes vers les petites échelles est diminué d'un facteur Ro par rapport au cas isotrope. Cette approche prédit ainsi que le taux de dissipation de l'énergie, qui s'identifie au taux de transfert de la cascade directe, suit une loi de la forme

$$\epsilon \underset{Re=\infty}{=} G(Ro)\,\frac{U^3}{L}, \tag{2.14}$$

où $G(Ro)$ serait constant pour $Ro \gg Ro_c$, conduisant au résultat de la turbulence isotrope, et au contraire proportionnel à Ro, $G(Ro) \propto Ro$, pour $Ro \ll Ro_c$, Ro_c étant un nombre de Rossby critique *a priori* d'ordre 1. Les conditions sous lesquelles une telle loi (2.14) pourrait décrire les taux de transfert (direct) et de dissipation dans une turbulence en rotation sont encore l'objet de vifs débats. Cette question a en pratique été discutée principalement à travers les implications de (2.14) sur l'exposant de la décroissance de l'énergie cinétique dans une turbulence en déclin [148, 149], certaines observations numériques ou expérimentales [74, 82, 150] soutenant et d'autres [128, 149, 151] contredisant la présence du régime où $G(Ro) \propto Ro$.

La détermination pratique de l'exposant de déclin d'une turbulence expérimentale est quelque chose de difficile, l'exposant dépendant souvent de manière non négligeable de la définition de l'origine des temps. Par ailleurs, les prédictions théoriques de cet exposant sont seulement des

conséquences indirectes de la loi (2.14) faisant appel à d'autres hypothèses. Il parait donc utile, dans l'objectif de tester les conditions de validité de l'équation (2.14), d'essayer de mesurer directement le taux ϵ de transfert, de dissipation, ou, dans une expérience forcée, d'injection de l'énergie.

Les expériences de turbulence de grille en rotation et en déclin décrites dans la partie 2.3.4 ont ainsi permis une mesure directe du taux de dissipation de l'énergie à travers son taux de déclin. Ces données révèlent une loi d'échelle identique à celle de la turbulence isotrope, avec un facteur $G(Ro)$ indépendant de Ro, et ce malgré un nombre de Rossby ultime de $Ro \simeq 10^{-2}$. On réalise que, de manière remarquable, les effets de la rotation sur l'anisotropie de la turbulence sont ici déjà forts alors que le taux global de transferts de l'énergie semble lui encore pas (ou peu) affecté par la rotation.

Pour essayer d'apporter des éléments complémentaires à cette étude expérimentale et éventuellement de mettre en évidence un régime où $G(Ro) \propto Ro$, il paraît nécessaire d'être capable d'explorer de manière versatile des gammes plus larges de nombre de Rossby. Dans cet objectif, nous projetons de développer un nouveau dispositif expérimental consistant en une hélice en rotation dans un cylindre rempli d'eau, l'ensemble étant lui même mis en rotation par notre plateforme tournante [†]. Cette nouvelle expérience a pour ambition d'aborder la question des lois d'échelles de la dissipation de l'énergie en turbulence en rotation (Eq. 2.14) d'un point de vue expérimental différent des études décrites en 2.3.3 et 2.3.4 : le taux de dissipation d'énergie sera ici mesuré à travers la puissance injectée et non via les transferts d'énergie entre échelles. L'hélice en rotation à un taux ω sera entraînée par un servo-moteur brushless de précision permettant une mesure directe de la puissance injectée à travers celle du couple $\Gamma(t)$ imposé instantanément. En comparaison des expériences de turbulence de grille, ce système aura l'avantage de permettre une exploration plus facile de larges gammes des nombres de Reynolds et de Rossby. Le moteur embarqué permettra en effet de balayer aisément au moins deux décades de fréquence de rotation ω de l'hélice. Les dimensions et la forme de l'hélice pourront aussi être modifiées facilement permettant un changement de plusieurs ordres de grandeur dans la gamme de travail pour le couple Γ : en régime turbulent sans rotation, on sait que le couple évolue selon $\Gamma \propto \rho R^4 H \omega^2$ où R et H mesurent respectivement le rayon et la hauteur de l'hélice et ρ la masse volumique du fluide.

†. L'idée de cette expérience nous a été soufflée par Stéphan Fauve il y a maintenant quelques années déjà.

Experimental evidence of a triadic resonance of plane inertial waves in a rotating fluid

Guilhem Bordes,[1,a)] Frédéric Moisy,[2,b)] Thierry Dauxois,[1,c)] and Pierre-Philippe Cortet[2,d)]
[1]*Laboratoire de Physique de l'École Normale Supérieure de Lyon, CNRS and Université de Lyon, 46 Allée d'Italie, 69007 Lyon, France*
[2]*Laboratoire FAST, CNRS, Univ Paris-Sud, UPMC Univ Paris 06, France*

(Received 12 October 2011; accepted 16 December 2011; published online 11 January 2012)

Plane inertial waves are generated using a wavemaker, made of oscillating stacked plates, in a rotating water tank. Using particle image velocimetry, we observe that, after a transient, the primary plane wave is subject to a subharmonic instability and excites two secondary plane waves. The measured frequencies and wavevectors of these secondary waves are in quantitative agreement with the predictions of the triadic resonance mechanism. The secondary wavevectors are found systematically more normal to the rotation axis than the primary wavevector: this feature illustrates the basic mechanism at the origin of the energy transfers towards slow, quasi two-dimensional, motions in rotating turbulence. © *2012 American Institute of Physics*. [doi:10.1063/1.3675627]

I. INTRODUCTION

Rotating and stratified fluids support the existence of two classes of anisotropic dispersive waves, called, respectively, inertial and internal waves, which play a major role in the dynamics of astrophysical and geophysical flows.[1–3] These waves share a number of similar properties, such as a group velocity normal to the phase velocity. Remarkably, in both cases, the frequency of the wave selects only its direction of propagation, whereas the wavelength is selected by other physical properties of the system, such as the boundary conditions or the viscosity.[2,4,5]

Most of the previous laboratory experiments on inertial waves in rotating fluids have focused on inertial modes or wave attractors in closed containers,[6–12] whereas less attention has been paid to propagative inertial wave beams. Inertial modes and attractors are generated either from a disturbance of significant size compared to the container[6] or more classically from global forcing.[7–12] Inertial modes are also detected in the ensemble average of rotating turbulence experiments in closed containers.[13,14] On the other hand, localized propagative inertial wave beams have been investigated recently in experiments using particle image velocimetry (PIV).[15,16]

A monochromatic internal or inertial wave of finite amplitude may become unstable with respect to a parametric subharmonic instability.[17–20] This instability originates from a nonlinear resonant interaction of three waves and induces an energy transfer from the primary wave towards two secondary waves of lower frequencies. This instability has received considerable interest in the case of internal gravity waves,[20] because it is believed to provide an efficient mechanism of dissipation in the oceans, by allowing a transfer of energy from the large to the small scales.[21–23]

Parametric instability is a generic mechanism expected for any forced oscillator. A pendulum forced at twice its natural frequency provides a classical illustration of this mechanism. Here, the "parameter" is the natural frequency of the pendulum, which is modulated in time through variations of the gravity or pendulum length. Weakly nonlinear theory shows that the energy of the

[a)]Electronic mail: guilhem.bordes@ens-lyon.fr.
[b)]Electronic mail: moisy@fast.u-psud.fr.
[c)]Electronic mail: thierry.dauxois@ens-lyon.fr.
[d)]Electronic mail: ppcortet@fast.u-psud.fr.

excitation, at frequency σ_0, is transferred to the pendulum at its natural frequency $\sigma_0/2$, resulting in an exponential growth of the oscillation amplitude.

In the case of inertial (resp. internal) waves, the "parameter" is now the so-called Coriolis frequency $f = 2\Omega$, with Ω the rotation rate (resp. the Brunt-Väisälä frequency N). In the presence of a primary wave of frequency σ_0, this "parameter" becomes locally modulated in time at frequency σ_0, and is hence able to excite secondary waves of lower natural frequency. However, here a continuum of frequencies can be excited, so that the frequencies σ_1 and σ_2 of the secondary waves are not necessarily half the excitation frequency, but they nevertheless have to satisfy the resonant condition $\sigma_1 + \sigma_2 = \sigma_0$. Interestingly, in the absence of dissipation, the standard pendulum-like resonance $\sigma_1 = \sigma_2 = \sigma_0/2$ is recovered both for inertial and internal waves, and the corresponding secondary waves have vanishing wavelengths.[20] Viscosity is responsible here for the lift of degeneracy, by selecting a maximum growth rate corresponding to finite wavelengths, with frequencies σ_1 and σ_2 splitted on both sides of $\sigma_0/2$.[24]

The parametric subharmonic instability has been investigated in detail for internal gravity waves.[20,24] On the other hand, this instability mechanism has received less attention in the case of pure inertial waves (i.e., in absence of stratification), probably because of the lower importance of rotation effects compared to stratification effects in most geophysical flows. It has been observed in numerical simulations of inertial modes in a periodically compressed rotating cylinder.[10,11] To our knowledge, parametric instability in the simpler geometry of plane inertial waves has not been investigated so far and is the subject of this paper. A fundamental motivation for this work is the key role played by triadic interactions of inertial waves in the problem of the generation of slow quasi-2D flows in rotating turbulence.[25–27] The parametric subharmonic instability indeed provides a simple but nontrivial mechanism for anisotropic energy transfers from modes of arbitrary wavevectors towards lower frequency modes of wavevector closer to the plane normal to the rotation axis (i.e., more "horizontal" by convention). Note that this nonlinear mechanism may however be in competition with a linear mechanism—the radiation of inertial waves along the rotation axis—which has also been shown to support the formation of vertical columnar structures.[28] The relative importance of these two mechanisms is governed by the Rossby number, defined as $Ro = (\tau_{\rm nl}\Omega)^{-1}$, with Ω^{-1} the linear timescale and $\tau_{\rm nl} = L/U$ the nonlinear timescale based on the characteristic velocity U and length scale L. In rotating turbulence with $Ro \ll 1$, the anisotropy growth should hence be dominated by the nonlinear triadic interactions, whereas for $Ro = O(1)$, both mechanisms should be at play.

In this paper, we report the first experimental observation of the destabilization of a primary plane inertial wave and the subsequent excitation of subharmonic secondary waves. To produce a plane inertial wave of sufficient spatial extent, and hence of well-defined wavevector $\mathbf{k}_0$, we have made use of a wave generator already developed for internal waves in stratified fluids.[29–31] Wave beams of tunable shape and orientation can be generated with this wavemaker. We show that, after a transient, the excited plane wave undergoes a parametric subharmonic instability. This instability leads to the excitation of two secondary plane waves, with wavevectors which are systematically more "horizontal" than the primary wavevector. We show that the predictions from the resonant triadic interaction theory for inertial waves, as described by Smith and Waleffe,[25] are in excellent agreement with our experimental results. In particular, the frequencies and wavenumbers of the secondary waves accurately match the expected theoretical values.

II. INERTIAL PLANE WAVE GENERATION

A. Structure of a plane inertial wave

We first briefly recall the main properties of inertial waves in a homogeneous fluid rotating at a constant rate Ω. In the rotating frame, the restoring nature of the Coriolis force is responsible for the propagation of the inertial waves, for frequencies $\sigma \leq f$, where $f = 2\Omega$ is the Coriolis parameter. Fluid particles excited at frequency σ describe anticyclonic circles in a plane tilted at an angle $\theta = \cos^{-1}(\sigma/f)$ with respect to the horizontal, and the phase of this circular motion propagates perpendicularly to this tilted plane.

The equations of motion for a viscous fluid in a frame rotating at a rate $\Omega = f/2$ around the axis z are

$$\partial_t \mathbf{u} + (\mathbf{u}\cdot\nabla)\mathbf{u} = -\frac{1}{\rho}\nabla p - f\mathbf{e}_z \times \mathbf{u} + \nu\nabla^2\mathbf{u}, \tag{1}$$

$$\nabla\cdot\mathbf{u} = 0, \tag{2}$$

where $\mathbf{u} = (u_x, u_y, u_z)$ is the velocity field in cartesian coordinates $\mathbf{x} = (x, y, z)$. In the following, we restrict to the case of a flow invariant along the horizontal direction y. The fluid being incompressible, the motion in the vertical plane (x, z) may be described by a streamfunction $\psi(x, z)$, such that $\mathbf{u} = (\partial_z\psi, u_y, -\partial_x\psi)$. Neglecting viscosity, the linearized equations for small velocity disturbances are

$$\partial_t\partial_z\psi = -\frac{1}{\rho}\partial_x p + fu_y, \tag{3}$$

$$\partial_t u_y = -f\partial_z\psi, \tag{4}$$

$$-\partial_t\partial_x\psi = -\frac{1}{\rho}\partial_z p. \tag{5}$$

These equations may be combined to obtain the equation of propagation for inertial waves

$$\partial_{tt}(\partial_{xx} + \partial_{zz})\psi + f^2\partial_{zz}\psi = 0. \tag{6}$$

Considering a plane wave solution of frequency σ and wavevector $\mathbf{k} = (k, 0, m)$

$$\psi(x, z, t) = \psi_0 e^{i(\mathbf{k}\cdot\mathbf{x}-\sigma t)} + \text{c.c.} \tag{7}$$

where c.c. means complex conjugate. We obtain the anisotropic dispersion relation for inertial waves

$$\sigma = sf\frac{m}{\kappa} = sf\cos\theta, \tag{8}$$

with $\kappa = (k^2 + m^2)^{1/2}$, $s = \pm 1$, and θ the angle between $\mathbf{k}$ and the rotation axis (see Fig. 1). We see from Eq. (8) that a given frequency σ lower than f selects a propagation angle $\pm\theta$, without specifying the norm of the wavevector κ. The corresponding velocity field is given by

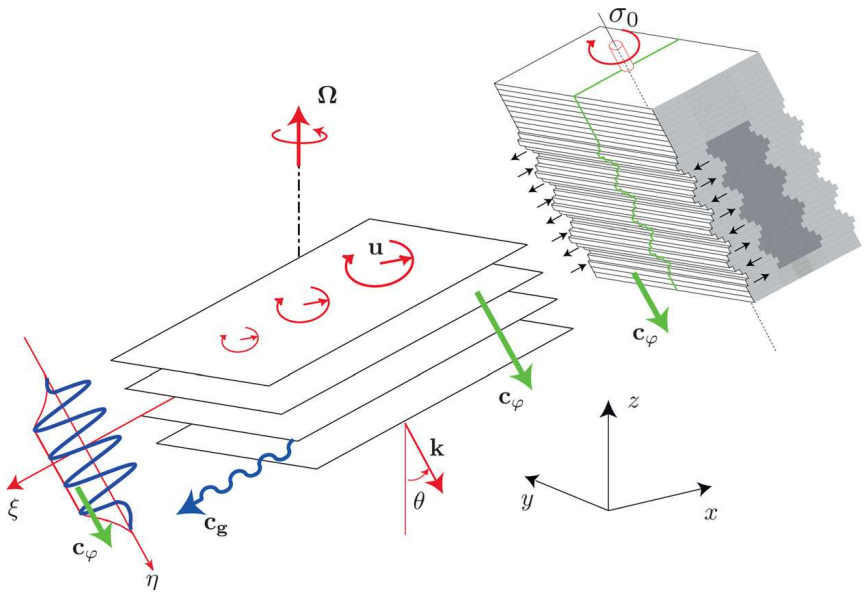

FIG. 1. (Color online) Schematic representation of the wave generator. The excited plane inertial wave has a frequency σ_0, a downward phase velocity, a negative helicity ($s_0 = -1$), and propagates at an angle $\theta = \cos^{-1}(\sigma_0/f)$, with $f = 2\Omega$ the Coriolis parameter.

$$u_x = im\psi_0 e^{i(kx+mz-\sigma t)} + \text{c.c.} \tag{9}$$

$$u_y = s\kappa\psi_0 e^{i(kx+mz-\sigma t)} + \text{c.c.} \tag{10}$$

$$u_z = -ik\psi_0 e^{i(kx+mz-\sigma t)} + \text{c.c.} \tag{11}$$

We recover here that the fluid particles describe anticyclonic circular motions in tilted planes perpendicular to $\mathbf{k}$, as sketched in Fig. 1. The wave travels with a phase velocity $\mathbf{c}_\varphi = \sigma\mathbf{k}/\kappa^2$ and a group velocity $\mathbf{c}_g = \nabla_\mathbf{k}\sigma$ normal to $\mathbf{c}_\varphi$. The vorticity $\boldsymbol{\omega} = \nabla \times \mathbf{u}$, given by

$$\boldsymbol{\omega} = -s\kappa\mathbf{u}, \tag{12}$$

is associated to the shearing motion between planes of constant phase. Because the velocity and vorticity are aligned, inertial waves are also called *helical waves*, and the sign s in Eq. (8) identifies to the sign of the wave helicity $\mathbf{u}\cdot\boldsymbol{\omega}$, with $s = +1$ for a right-handed wave and $s = -1$ for a left-handed wave. For instance, in the classical St. Andrew's wave pattern emitted from a linear source,[16] the two upper beams are right-handed and the two lower beams are left-handed, although the fluid motion is always anticyclonic.

B. Generation of a plane inertial wave

In order to generate a plane inertial wave, we have made use of a wavemaker, introduced by Gostiaux *et al.*,[29] which was originally designed to generate internal gravity waves (see Mercier *et al.*[31] for a detailed characterization of the wavemaker). This wavemaker consists in a series of oscillating stacked plates, designed to reproduce the fluid motion in the bulk of an internal gravity wave invariant along y. The use of this internal wave generator for the generation of inertial waves is motivated by the similarity of the spatial structure of the two types of waves in the vertical plane (x, z). However, the fluid motion in the internal wave is a simple oscillating translation in the direction of the group velocity, whereas fluid particles describe anticyclonic circular translation in the case of inertial waves. As a consequence, the oscillating plates of the wavemaker only force the longitudinal component of the circular motion of the inertial waves, whereas the lateral component is let to freely adjust according to the spatial structure of the wave solution.

The wavemaker is made of a series of 48 parallelepipedic plates stacked around a helical camshaft, with the appropriate shifts between successive cames in order to form a sinusoidal profile at the surface of the generator. We introduce the local coordinate system (ξ, y, η), tilted at an angle θ about y, where ξ is along the wave propagation and η is parallel to the camshaft axis (see Fig. 1). The group velocity and the phase velocity of the wave are oriented along ξ and η, respectively. As the camshaft rotates at frequency σ_0, the plates, which are constrained in the y direction, oscillate back and forth along ξ. The sign of the rotation of the helical camshaft selects the helicity of the excited wave and hence an upward or downward phase velocity. In the present experiment, the rotation of the camshaft is set to produce a downward phase velocity, resulting in a left-handed inertial wave of negative helicity $s_0 = -1$.

The cames are 14 cm wide in the y direction, and their eccentricities are chosen to produce a sinusoidal displacement profile, $\xi_0(\eta) = \xi_o \sin(\kappa_0\eta)$, of wavelength $\lambda = 2\pi/\kappa_0 = 7.6$ cm and amplitude $\xi_o = 0.5$ cm at the center of the beam. The wave beam has a width 30.5 cm with a smooth decrease to 0 at the borders and contains approximately 4 wavelengths. The generator is only forcing the ξ component of the inertial wave, and the y component is found to adjust according to the inertial wave structure after a distance of order of 2 cm.

The wavemaker is placed in a tank of 120 cm length, 80 cm width, and 70 cm depth which is filled with 58 cm of water. The tank is mounted on the precision rotating platform "Gyroflow" of 2 m in diameter. The angular velocity Ω of the platform is set in the range 1.05–3.15 rad s^{-1}, with relative fluctuations $\Delta\Omega/\Omega$ less than 10^{-3}. A cover is placed at the free surface, preventing from disturbances due to residual surface waves. The rotation of the fluid is set long before each experiment (at least 1 h) in order to avoid transient spin-up recirculations and to achieve a clean solid body rotation.

The propagation angle θ of the inertial wave is varied by changing the rotation rate of the platform, while keeping the wavemaker frequency constant, $\sigma_0 = 1.05$ rad s^{-1}. This allows to have a

fixed wave amplitude $\sigma_0 \xi_o = 0.52$ cm s^{-1} for all angles. The Coriolis parameter has been varied in the range $f = 1.004\sigma_0$ to $3\sigma_0$, corresponding to angles θ from 5° to 70°. For each value of the rotation rate, the axis of the wavemaker camshaft is tilted to the corresponding angle $\theta = \cos^{-1}(\sigma_0/f)$, in order to keep the plate oscillation aligned with the fluid motion in the excited wave. As a consequence, the efficiency of the forcing should not depend significantly on the angle θ. For each experiment, the fluid is first reset to a solid body rotation before the wavemaker is started.

C. PIV measurements

Velocity fields are measured using a 2D PIV system[32,33] mounted on the rotating platform. The flow is seeded by 10 μm tracer particles, and illuminated by a vertical laser sheet, generated by a 140 mJ Nd:YAG pulsed laser. A vertical 59 × 59 cm^2 field of view is acquired by a 14 bits 2048 × 2048 pixels camera synchronized with the laser pulses. For each rotation rate, a set of 3200 images is recorded, at a frequency of 4 Hz, representing 24 images per wavemaker period. This frame rate is set to achieve a typical particle displacement of 5–10 pixels between each frame, ensuring an optimal signal-to-noise ratio for the velocity measurement. PIV computations are performed over successive images on 32 × 32 pixels interrogation windows with 50% overlap. The spatial resolution is 4.6 mm, which represents 17 points per wavelength of the inertial wave.

Figure 2 shows typical instantaneous horizontal velocity fields after 2 and 7 periods $T = 2\pi/\sigma_0$ from the start of generator, for an experiment performed with $\sigma_0/f = 0.84$. A well defined truncated plane wave propagates downward, making an angle $\theta = \cos^{-1}(\sigma_0/f) \simeq 34^o$ to the horizontal. The front of the plane wave is propagating at a velocity 8.3 ± 0.6 mm s^{-1}, which agrees well with the expected group velocity $c_g = f \sin\theta/\kappa = 8.5$ mm s^{-1}. The phase velocity is downward, normal to the group velocity, and also agrees with the expected value $c_\varphi = \sigma_0/\kappa = 12.7$ mm s^{-1}.

Two sources of noise have been identified, which can be seen in the temporal energy spectrum of the velocity fields (Fig. 3, described in Sec. III A): an oscillatory motion at frequency $\sigma = \Omega = 0.5f$, due to a residual modulation of the rotation rate of the platform, and slowly drifting thermal convection structures at frequency $\sigma \to 0$, due to slight temperature inhomogeneities in the tank. Both effects contribute to a velocity noise of order of 0.2 mm s^{-1}, i.e., 25 times lower than the wave amplitude close to the wavemaker. This noise could be safely removed using a temporal Fourier filtering of the velocity fields at the forcing frequency σ_0. This filtering, however, fails in the particular case where $\sigma_0 = \Omega$, for which the mechanical noise of the platform cannot be filtered out of the inertial wave signal.

The wavemaker is found to successfully generate well defined plane waves for frequencies $\sigma_0 \geq 0.65f$. For lower frequency, i.e., for steeper angle of propagation [$\theta = \cos^{-1}(\sigma_0/f) > 50^o$], the wave pattern shows significant departure from the expected plane wave profile, which may be

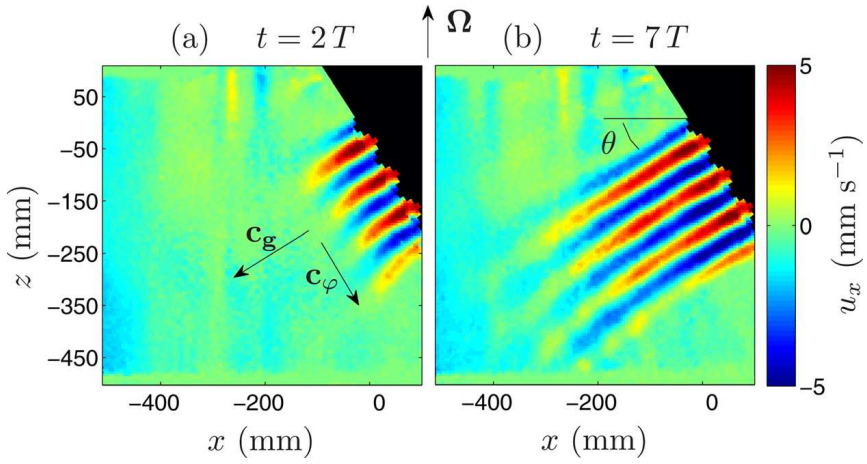

FIG. 2. (Color online) Horizontal velocity field after 2 and 7 periods from the start of the wavemaker for $\sigma_0/f = 0.84$. The wavemaker is on the top-right, forcing a wave propagating along $\mathbf{c_g}$ with a phase propagating along $\mathbf{c}_\varphi$.

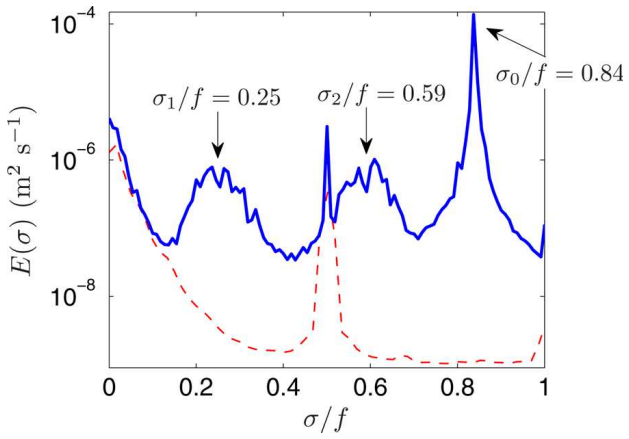

FIG. 3. (Color online) Temporal energy spectra for two experiments performed at rotation rate $\Omega = 0.63$ rad s^{-1} with (continuous line) and without (dashed line) the wavemaker operating at $\sigma_0/f = 0.84$. The spectrum with the generator working has been computed on the time interval between 24 and 116 periods after the start of the generator. The peak at $\sigma/f = 0.5$ present in the two spectra is the trace of the mechanical noise of the platform at the rotation frequency $\sigma = \Omega$, whereas the low frequencies are due to thermal convection effects (see text).

attributed to the interference of the incident wave with the reflected wave on the bottom of the tank.

III. SUBHARMONIC INSTABILITY

A. Experimental observations

After a few excitation periods, the front of the inertial wave has travelled outside the region of interest, and the inertial wave can be considered locally in a stationary regime. However, after typically 15 wavemaker periods (the exact value depends on the ratio σ_0/f), the inertial wave becomes unstable and shows slow disturbances of scale slightly smaller than the excited wavelength.

We have characterized this instability using Fourier analysis of the PIV time series. We compute, at each location (x, z) of the PIV field, the temporal Fourier transform of the two velocity components over a temporal window Δt,

$$\widehat{\mathbf{u}}_\sigma(x,z) = \frac{1}{\sqrt{2\pi}} \int_{t_0}^{t_0+\Delta t} \mathbf{u}(x,z,t) e^{i\sigma t} dt. \tag{13}$$

The temporal energy spectrum is then defined as

$$E(\sigma) = \langle |\widehat{\mathbf{u}}_\sigma|^2 \rangle_{x,z}, \tag{14}$$

where $\langle \cdot \rangle_{x,z}$ is the spatial average over the PIV field.

If we compute $E(\sigma)$ over a temporal window Δt spanning a few excitation periods, we observe, as t_0 is increased, the emergence of two broad peaks at frequencies smaller than the excitation frequency σ_0, suggesting the growth of a subharmonic instability. These two subharmonic peaks can be seen in Fig. 3, for an experiment performed at rotation rate $\Omega = 0.63$ rad s^{-1} with the wavemaker operating at $\sigma_0/f = 0.84$. Here, the temporal window Δt is chosen equal to 92 wavemaker periods, yielding a spectral resolution of $\Delta\sigma = 2\pi/\Delta t \simeq 9 \times 10^{-3} f$. The two secondary peaks are centered on $\sigma_1/f = 0.25 \pm 0.03$ and $\sigma_2/f = 0.59 \pm 0.03$, and their sum matches well with the forcing frequency $\sigma_0/f = 0.84$, as expected for a subharmonic resonance. The significant width of the secondary peaks, of order $0.07\,f$, indicates that this resonance is weakly selective. This broad-band selection will be further discussed in Sec. IV B.

The subharmonic instability of the primary wave is found for all forcing frequencies σ_0 ranging from $0.65\,f$ to f; the measured frequencies $\sigma_{1,2}$ are given in Table I. The absence of clear subharmonic instability at lower forcing frequency may be due to an intrinsic stability of the primary

TABLE I. Frequencies of the secondary waves σ_1/f and σ_2/f, determined from the peaks in the temporal energy spectra, as a function of the frequency of the primary wave σ_0/f. The uncertainty for σ_1/f and σ_2/f is ± 0.03.

σ_0/f	$(\sigma_1+\sigma_2)/f$	σ_1/f	σ_2/f
0.64	0.64	0.19	0.45
0.71	0.71	0.21	0.50
0.84	0.84	0.25	0.59
0.91	0.94	0.27	0.67
0.95	0.97	0.29	0.68
0.98	0.98	0.32	0.66
0.99	1.00	0.34	0.66

wave for $\sigma_0 < 0.65f$, or to the low quality of the plane wave at steep angles because of the interference with the reflected wave beam on the bottom of the tank.

Using temporal Hilbert filtering,[30,34] the spatial structure of the wave amplitude $\mathbf{u}_o(\mathbf{x})$ and phase $\varphi(\mathbf{x},t) = \mathbf{k}\cdot\mathbf{x} - \sigma t$ can be extracted for each secondary wave. The procedure consists in (i) computing the Fourier transform $\widehat{\mathbf{u}}_\sigma(x,z)$ of the velocity field according to Eq. (13), with a temporal window Δt of at least 42 excitation periods; (ii) band-pass filtering $\widehat{\mathbf{u}}_\sigma(x,z)$ around the frequency of interest σ_1 or σ_2 with a bandwidth of $\delta\sigma = 2.0\times 10^{-2}f$ but without including the associated negative frequency; and (iii) reconstructing the complex velocity field by computing the inverse Fourier transform (including a factor 2, which accounts for the redundant negative frequency, in order to conserve energy),

$$\mathbf{u}_H(\mathbf{x},t) = \mathbf{u}_o(\mathbf{x})e^{i\varphi(\mathbf{x},t)}. \tag{15}$$

The physical velocity field is given by $Re(\mathbf{u}_H)$. The wave amplitude $\mathbf{u}_o$ and phase field φ are finally obtained from the Hilbert-filtered field $\mathbf{u}_H$.

In Figs. 4(c) and 4(d), for the experiment at $\sigma_0/f = 0.84$, we show the maps of the phase of the secondary waves, extracted from Hilbert filtering at frequencies σ_1 and σ_2, respectively. It is worth to note, as can be verified from Fig. 3, that the corresponding typical velocity amplitude is at least ten times smaller than for the primary wave [see Fig. 4(a)]. The spatial structures of the phase of these secondary waves are not as clearly defined as for the primary wave [Fig. 4(b)]. In particular, dislocations can be distinguished in the phase field. The finite extent of the primary wave and its spatial decay due to viscous attenuation are probably responsible for this departure of the secondary waves from pure plane waves. It is also important to note that the monochromaticity of the first subharmonic wave [Fig. 4(c)] is affected by interferences with its reflection on the wavemaker which is due to the fact that this secondary wave is propagating toward the wavemaker. However, to a reasonable degree of accuracy, the two secondary waves can be considered locally as plane waves, characterized by local wavevectors $\mathbf{k}_1$ and $\mathbf{k}_2$.

B. Helical modes

The approximate plane wave structure of the two secondary waves suggests to analyze the instability in terms of a triadic resonance between the primary wave, of wavevector $\mathbf{k}_0$, and the two secondary waves, of wavevectors $\mathbf{k}_1$ and $\mathbf{k}_2$. This resonance may be conveniently analyzed in the framework of the helical decomposition, introduced by Waleffe,[35,36] which we briefly recall here.

Helical modes have been introduced as a general spectral decomposition basis, which is useful to analyze the energy transfers via triadic interactions. Although this decomposition also applies for non-rotating flows, it is particularly relevant for rotating flows, because inertial plane waves have exactly the structure of helical modes.[36] Any velocity field can actually be decomposed as a superposition of helical modes of amplitudes $A_{s_\mathbf{k}}(\mathbf{k},t)$

$$\mathbf{u}(\mathbf{x},t) = \sum_{\mathbf{k}}\sum_{s_\mathbf{k}=\pm 1} A_{s_\mathbf{k}}(\mathbf{k},t)\mathbf{h}_{s_\mathbf{k}}(\mathbf{k})e^{i(\mathbf{k}\cdot\mathbf{x}-\sigma^{\mathbf{k}}_{s_\mathbf{k}}t)}, \tag{16}$$

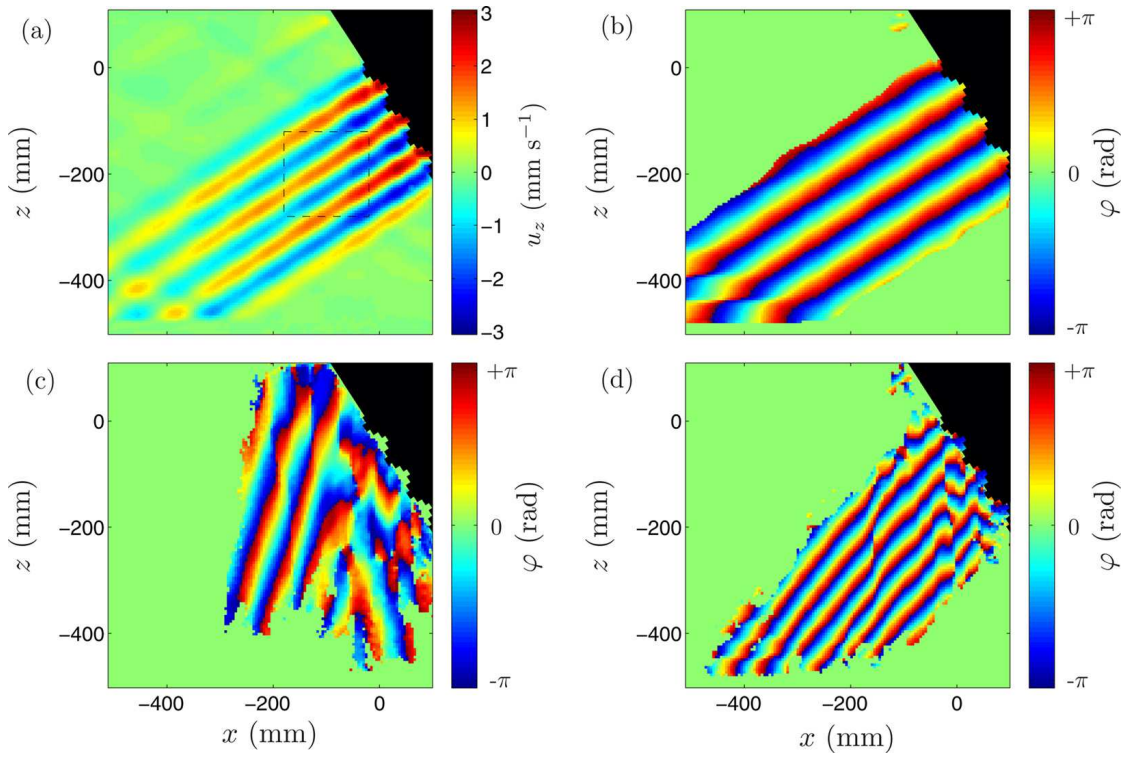

FIG. 4. (Color online) Hilbert filtered vertical velocity (a) and phase (b) of the primary wave at $\sigma_0/f = 0.84$, and phase of the Hilbert filtered first [(c), $\sigma_1/f = 0.25$] and second [(d), $\sigma_2/f = 0.59$] subharmonic waves. The phase is displayed only where the wave amplitude is larger than $1.3 \times 10^{-1}\sigma_0\xi_0$ for (b) and $7.7 \times 10^{-3}\sigma_0\xi_0$ for (c) and (d). In (a), the square in dashed lines indicates the region where the primary wave amplitude A_0 has been measured.

where $\sigma^{\mathbf{k}}_{s_\mathbf{k}}$ is the frequency associated to a plane wave of wavevector $\mathbf{k}$ and helicity sign $s_\mathbf{k}$. The helical mode $\mathbf{h}_{s_\mathbf{k}}(\mathbf{k})$ is normal to $\mathbf{k}$ (by incompressibility) and given by

$$\mathbf{h}_{s_\mathbf{k}}(\mathbf{k}) = \frac{\mathbf{k}}{|\mathbf{k}|} \times \frac{\mathbf{k} \times \mathbf{e_z}}{|\mathbf{k} \times \mathbf{e_z}|} + i s_\mathbf{k} \frac{\mathbf{k} \times \mathbf{e_z}}{|\mathbf{k} \times \mathbf{e_z}|}, \tag{17}$$

where $s_\mathbf{k} = \pm 1$ is the sign of the mode helicity.[37] Injecting the decomposition (16) into the Navier-Stokes equation (1) yields

$$\left(\frac{\partial}{\partial t} + \nu\kappa^2\right) A_\mathbf{k} = \frac{1}{2} \sum C^{s_\mathbf{k} s_\mathbf{p} s_\mathbf{q}}_{\mathbf{kpq}} A^*_\mathbf{p} A^*_\mathbf{q} e^{i(\sigma_\mathbf{k} + \sigma_\mathbf{p} + \sigma_\mathbf{q})t}, \tag{18}$$

with stars denoting complex conjugate, and $A_\mathbf{k}$, $\sigma_\mathbf{k}$ being short-hands for $A_{s_\mathbf{k}}(\mathbf{k}, t)$, $\sigma^{\mathbf{k}}_{s_\mathbf{k}}$. In Eq. (18), the sum is to be understood over all wavevectors $\mathbf{p}$ and $\mathbf{q}$ such that $\mathbf{k} + \mathbf{p} + \mathbf{q} = \mathbf{0}$ and all corresponding helicity signs $s_\mathbf{p}$ and $s_\mathbf{q}$. In the following, the equation $\mathbf{k} + \mathbf{p} + \mathbf{q} = \mathbf{0}$ will be referred to as the spatial resonance condition for a triad of helical modes. The interaction coefficient is given by

$$C^{s_\mathbf{k} s_\mathbf{p} s_\mathbf{q}}_{\mathbf{kpq}} = \frac{1}{2}\left[s_\mathbf{q}\kappa_\mathbf{q} - s_\mathbf{p}\kappa_\mathbf{p}\right]\left(\mathbf{h}^*_{s_\mathbf{p}}(\mathbf{p}) \times \mathbf{h}^*_{s_\mathbf{q}}(\mathbf{q})\right) \cdot \mathbf{h}^*_{s_\mathbf{k}}(\mathbf{k}). \tag{19}$$

C. Resonant triads

The helical mode decomposition (16) applies for any velocity field, containing an arbitrary spectrum of wavevectors. We restrict in the following the analysis to a set of three interacting inertial waves of wavevectors ($\mathbf{k}$, $\mathbf{p}$, $\mathbf{q}$). Equation (18) shows that the amplitude of the mode of wavevector $\mathbf{k}$ is related to the two other modes $\mathbf{p}$ and $\mathbf{q}$ according to

$$\left(\frac{\partial}{\partial t}+\nu\kappa^2\right)A_{\mathbf{k}}=C_{\mathbf{k}}A^*_{\mathbf{p}}A^*_{\mathbf{q}}e^{i(\sigma_{\mathbf{k}}+\sigma_{\mathbf{p}}+\sigma_{\mathbf{q}})t}, \tag{20}$$

where $C_{\mathbf{k}}$ is short-hand for $C^{s_{\mathbf{k}}s_{\mathbf{p}}s_{\mathbf{q}}}_{\mathbf{kpq}}=C^{s_{\mathbf{k}}s_{\mathbf{q}}s_{\mathbf{p}}}_{\mathbf{kqp}}$. Cyclic permutation of **k**, **p,** and **q** in Eq. (20) gives the two other relevant interaction equations between the three waves. We further restrict the analysis to plane inertial waves invariant along y (i.e., $\mathbf{k}\cdot\mathbf{e_y}=\mathbf{0}$). The three considered helical modes (17) therefore reduce to

$$\mathbf{h}_{s_{\mathbf{r}}}(\mathbf{r})=\frac{m_{\mathbf{r}}\mathbf{e_x}-k_{\mathbf{r}}\mathbf{e_z}}{\kappa_{\mathbf{r}}}-is_{\mathbf{r}}\mathbf{e_y}, \tag{21}$$

where **r** stands for **k**, **p,** or **q**. From Eq. (21), the interaction coefficients (19) can be explicitly computed

$$C_{\mathbf{k}}=\frac{i}{2\kappa_{\mathbf{k}}\kappa_{\mathbf{p}}\kappa_{\mathbf{q}}}\left[m_{\mathbf{p}}k_{\mathbf{q}}-m_{\mathbf{q}}k_{\mathbf{p}}\right]\left[\kappa^2_{\mathbf{q}}-\kappa^2_{\mathbf{p}}+s_{\mathbf{q}}s_{\mathbf{k}}\kappa_{\mathbf{q}}\kappa_{\mathbf{k}}-s_{\mathbf{p}}s_{\mathbf{k}}\kappa_{\mathbf{p}}\kappa_{\mathbf{k}}\right] \tag{22}$$

and similarly for the two cyclic permutations.

Since in Eq. (20) and in its two cyclic permutations, the $A_{\mathbf{r}}(t)$ coefficients have to be understood as complex velocity amplitudes evolving slowly compared to wave periods $2\pi/\sigma_{\mathbf{r}}$; temporal resonance is needed in addition to spatial resonance for the left-hand coefficients $A_{\mathbf{r}}$ to be nonzero. Using 0, 1, 2 for reindexing the three waves **k**, **p,** and **q**, this leads to the triadic resonance conditions

$$\mathbf{k_0}+\mathbf{k_1}+\mathbf{k_2}=\mathbf{0}, \tag{23}$$

$$\sigma_0+\sigma_1+\sigma_2=0. \tag{24}$$

We consider in the following that only the primary wave A_0, of given frequency σ_0, wavevector $\mathbf{k_0}=(k_0,m_0)$ and helicity sign s_0, is present initially in the system (i.e., $A_{1,2}(0)=0$). The two secondary waves $(s_1,\sigma_1,\mathbf{k_1})$ and $(s_2,\sigma_2,\mathbf{k_2})$ which could form a resonant triad with the primary wave may be determined using the resonance conditions (23) and (24). From the dispersion relation for inertial waves (8), the resonance conditions lead to

$$s_0\frac{m_0}{\sqrt{k_0^2+m_0^2}}+s_1\frac{m_1}{\sqrt{k_1^2+m_1^2}}-s_2\frac{m_0+m_1}{\sqrt{(k_0+k_1)^2+(m_0+m_1)^2}}=0. \tag{25}$$

For a given primary wave (s_0,k_0,m_0), the solution of this equation for each sign combination (s_0,s_1,s_2) is a curve in the (k_1,m_1) plane (see Fig. 5). Without loss of generality, once we have taken $s_0=-1$ (which corresponds to the experimental configuration), it is necessary to consider four sign combinations: $(-,-,-)$, $(-,+,-)$, $(-,-,+)$, and $(-,+,+)$. Notice that the three first combinations always admit solutions, whereas the fourth one, $(-,+,+)$, admits a solution only if $|m_0|\leq\kappa_0/2$, i.e., $\theta>60^{\circ}$. The exchange of $\mathbf{k}_1$ and $\mathbf{k}_2$ keeps the $(-,-,-)$ and $(-,+,+)$ resonances unchanged, but exchanges the $(-,-,+)$ and $(-,+,-)$ resonances. Eventually, three independent sign combinations remain: $(-,-,-)$, $(-,\mp,\pm)$, and $(-,+,+)$.

D. Experimental verification of the resonance condition

The predictions of the triadic resonance theory are compared here with the measured wavevectors of the secondary waves. Figure 5 shows the theoretical resonance curves for two forcing frequencies, $\sigma_0/f=0.84$ and 0.99. For both curves, helicity sign and wavenumber of the primary wave are chosen according to the experimental values, $s_0=-1$ and $\kappa_0=0.82$ rad cm^{-1}.

For both frequencies σ_0 considered here, only the three first sign combinations admit solutions. The $(-,-,-)$ combination gives a closed loop, whereas the two others, $(-,\mp,\pm)$, give infinite branches, tending asymptotically to constant angles. The limit of large secondary wavevectors is such that $|\sigma_1|=|\sigma_2|=|\sigma_0|/2$: when a wave $\mathbf{k}_0$ excites two waves of wavelength $\lambda\ll 2\pi/\kappa_0$, both secondary waves have frequency $\sigma_0/2$, with opposite wavevectors, leading to a stationary wave pattern. However, such large wavenumbers are prevented by viscosity, as will be shown in Sec. IV A.

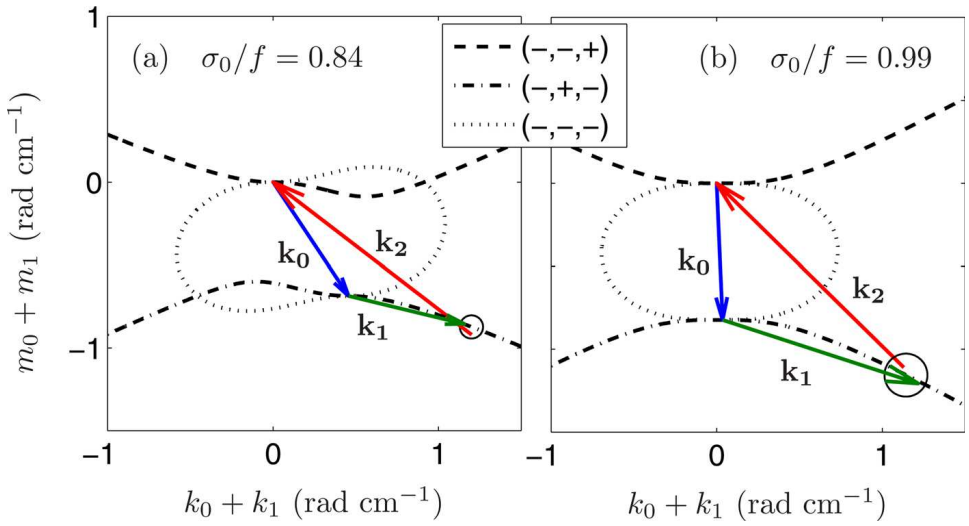

FIG. 5. (Color online) Resonance curves for the primary waves (a) $[s_0 = -1, \sigma_0 = 0.84f, \kappa_0 = 0.82$ rad cm$^{-1}]$ and (b) $[s_0 = -1, \sigma_0 = 0.99f, \kappa_0 = 0.82$ rad cm$^{-1}]$. The curves represent the location of $\mathbf{k}_0 + \mathbf{k}_1 = (k_0 + k_1, m_0 + m_1)$ satisfying Eq. (25) for the 3 possible combinations of signs. The wavevectors measured experimentally are shown using arrows. The circle is the theoretical prediction for the location of $\mathbf{k}_0 + \mathbf{k}_1$ obtained from the maximum growth rate criterion, determined using the experimental primary wave amplitude $[A_0 = 0.29 \pm 0.07$ cm s^{-1} for (a) and $A_0 = 0.34 \pm 0.11$ cm s^{-1} for (b)]. The diameter of the circle measures the uncertainty of the prediction due to the uncertainty on the wave amplitude A_0.

Figure 5 also shows the measured secondary wavevectors $\mathbf{k}_1$ and $\mathbf{k}_2$. These wavevectors are obtained from the phase fields $\varphi_{1,2}$ extracted by Hilbert filtering, using

$$\mathbf{k}_{1,2} = \nabla \varphi_{1,2}. \tag{26}$$

These measurements are then averaged over regions of about $(130\,\text{mm})^2$ where the secondary waves can be considered as reasonably spatially monochromatic. It must be noted that a same plane wave can be equivalently described by $(s, \sigma > 0, \mathbf{k})$ and $(s, -\sigma < 0, -\mathbf{k})$. Since we always consider primary waves with positive frequency $\sigma_0 > 0$, according to Eq. (24), the subharmonic frequencies $\sigma_{1,2}$ have to be taken negative. As a consequence, the Hilbert filtering should be performed for the negative peaks in the temporal Fourier transform, in order to produce phase fields with the appropriate sign. Practically, the Hilbert filtering has been performed around the positive peaks $-\sigma_{1,2}$, and the signs of the measured wavevectors have been changed accordingly.

The secondary wavevectors $\mathbf{k}_1 = (k_1, m_1)$ and $\mathbf{k}_2 = (k_2, m_2)$ measured experimentally, shown in Fig. 5, are in good agreement with the triadic condition (23), forming a triangle such that $\mathbf{k}_0 + \mathbf{k}_1 + \mathbf{k}_2 = 0$. Moreover, the apex of the triangle, at $\mathbf{k}_0 + \mathbf{k}_1$, falls onto one of the three resonant curves. The selected resonant curve corresponds to the sign combination $(-, +, -)$, in agreement with the observed experimental helicities. We actually verify that $s_1 = \sigma_1 \kappa_1 / f m_1$ is positive ($\sigma_1 < 0$ and $m_1 < 0$) and that $s_2 = \sigma_2 \kappa_2 / f m_2$ is negative ($\sigma_2 < 0$ and $m_2 > 0$), confirming the $(-, +, -)$ nature of the experimental resonance.

Interestingly, the shape of the triangle $\mathbf{k}_0 + \mathbf{k}_1 + \mathbf{k}_2 = 0$ in Fig. 5 indicates that the group velocity of the secondary wave $\mathbf{k}_1$ is oriented towards the wavemaker. Indeed, we recall that, for a given wavevector $\mathbf{k}$, the group velocity $\mathbf{c}_g$ is normal to $\mathbf{k}$, and the vertical projections of $\mathbf{c}_g$ and $\mathbf{k}$ are oriented in the same direction if $\sigma > 0$ and in opposite directions if $\sigma < 0$. Accordingly, Fig. 5 shows that $\mathbf{c}_{g0}$ and $\mathbf{c}_{g2}$ are oriented downward, pointing from the wavemaker towards the bottom of the tank, whereas $\mathbf{c}_{g1}$ is oriented upward, pointing towards the wavemaker. As a consequence, the secondary wave $\mathbf{k}_1$ is fed by the primary wave but releases its energy back to the wavemaker.

For all the primary wave angles for which the instability is observed, the secondary waves are systematically such that $|\sigma_1|$ and $|\sigma_2|$ are lower than $|\sigma_0|$. The dispersion relation hence yields secondary wavevectors $\mathbf{k}_{1,2}$ more horizontal than $\mathbf{k}_0$, as illustrated in Fig. 5. This property, which actually follows from the conservation of energy and helicity,[25] illustrates the natural tendency of rotating flows to transfer energy towards slow quasi-two-dimensional modes. If the process is repeated, as in rotating turbulence, the energy becomes eventually concentrated on nearly

horizontal wavevectors, corresponding to a quasi-2D flow, with weak dependence along the rotation axis.[26,27]

IV. SELECTION OF THE MOST UNSTABLE RESONANT TRIAD

A. Maximum growth rate criterion

In order to univocally predict the resonant secondary waves, a supplementary condition must be added to Eq. (25): we assume that the selected resonant triad is the one with the largest growth rate. Going back to the wave interaction equations (20) associated to the temporal resonance condition (24), the amplitudes of the secondary waves are governed by

$$\frac{dA_1}{dt} = C_1 A_0^* A_2^* - \nu\kappa_1^2 A_1, \tag{27}$$

$$\frac{dA_2}{dt} = C_2 A_0^* A_1^* - \nu\kappa_2^2 A_2, \tag{28}$$

with $C_{1,2}$ given by Eq. (22) taking $\mathbf{k} = \mathbf{k}_{1,2}$ (see also Appendix A in Ref. 25). Solving this system with initial conditions $A_{1,2}(0) = 0$, and assuming that A_0 remains almost constant at short time, lead to the solutions

$$A_{1,2}(t) = B_{1,2}(e^{\gamma_+ t} - e^{\gamma_- t}), \tag{29}$$

where the growth rates $\gamma_\pm$ write

$$\gamma_\pm = -\frac{\nu}{2}(\kappa_1^2 + \kappa_2^2) \pm \sqrt{\frac{\nu^2}{4}(\kappa_1^2 - \kappa_2^2)^2 + C_1 C_2 |A_0|^2}. \tag{30}$$

In the following, we consider the primary wave amplitude as real without loss of generality, so $|A_0| = A_0$.

The coefficient γ_- is always negative, so the stability of the system is governed by the sign of γ_+, which we simply note γ in the following. Interestingly, this growth rate γ depends on the amplitude A_0 of the primary wave. As a consequence, the primary wave is unstable with respect to a given set of secondary waves, selected by the resonance condition and unequivocally denoted by κ_1, only if A_0 exceeds the threshold $A_c(\kappa_1) = \nu\kappa_1\kappa_2/\sqrt{C_1 C_2}$ in which case $\gamma(\kappa_1) > 0$. In other words, for a given couple of secondary waves (denoted by κ_1) to be possibly growing, the Reynolds number based on the primary wave, $Re_0 = A_0/(\kappa_0\nu)$, must exceed a critical value $Re_c(\kappa_1) = A_c(\kappa_1)/(\kappa_0\nu)$ for the onset of the parametric instability. This critical Reynolds number is actually an increasing function of κ_1 and tends to zero as $\kappa_1 \to 0$, showing that whatever the value of Re_0, there is always a continuum of resonant triads with $Re_0 > Re_c(\kappa_1)$, i.e., with a positive growth rate. The main consequence is that, whatever the value of Re_0, the most unstable triad always has a positive (maximum) growth rate, and the parametric instability does not have any Re_0 threshold to proceed.

If viscosity can be neglected, Eq. (30) reduces to $\gamma = \sqrt{C_1 C_2} A_0$. In the limit of large secondary wavenumbers $\kappa_{1,2} \gg \kappa_0$, one has $\mathbf{k}_1 \simeq -\mathbf{k}_2$, and the growth rate γ is found to tend asymptotically toward a maximum value,[24] i.e., the selected secondary waves have frequency exactly half the forcing frequency. Taking viscosity into account reduces the growth rate of the large wavenumbers, and hence selects finite wavenumbers. Equation (30) indicates that larger wavenumbers are selected for larger primary wave amplitudes A_0 and/or lower viscosity, i.e., for larger Reynolds number Re_0.

B. Selection of the most unstable wavenumbers

In Fig. 6, the predicted growth rates γ are plotted for the three possible sign combinations, for the primary wave defined by $s_0 = -1, \sigma_0 = 0.84f$, $\kappa_0 = 0.82$ rad cm^{-1}. These growth rates have been computed using the primary wave amplitude averaged over the area where the secondary wavevectors have been measured (see the square in Fig. 4(a)), $A_0 = 0.29$ cm s^{-1}. For the 3 types of resonance, the growth rates tend to zero when $k_1 \to -k_0/2$ and $k_1 \to \infty$ (because of viscosity). If the secondary waves $\mathbf{k}_1$ and $\mathbf{k}_2$ are exchanged, which amounts to exchange the $(-,-,+)$ and

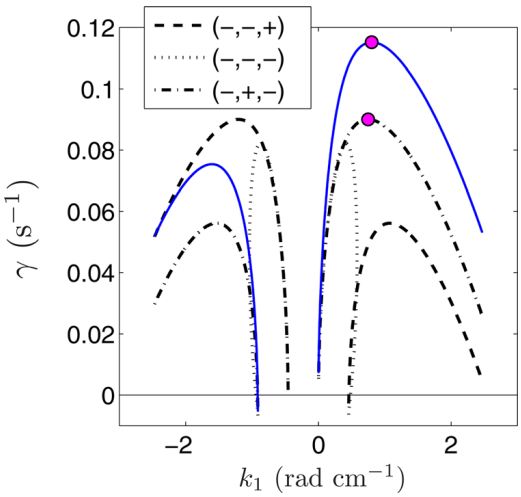

FIG. 6. (Color online) Growth rates γ as a function of k_1, computed from Eq. (30), for the three possible resonances for a primary wave ($s_0 = -1, \sigma_0 = 0.84f$, $\kappa_0 = 0.82$ rad cm^{-1}). The growth rates have been computed using the average value $A_0 = 0.29$ cm s^{-1} for the primary wave amplitude. For resonance $(-,+,-)$, an additional curve (continuous line) has been computed using a wave amplitude 25% larger.

$(-,+,-)$ resonances, the same growth rates are obtained: the curves for $(-,-,+)$ and $(-,+,-)$ are symmetrical with respect to $k_0/2$.

Interestingly, the growth rate is positive for a broad range of wavenumbers. Together with the broad subharmonic peaks observed in the temporal spectrum of Fig. 3, this confirms that the parametric resonance is weakly selective in this system. Values of k_1 corresponding to significant growth rates are of the same order of magnitude as the primary wavenumber $\kappa_0 = 0.82$ rad cm^{-1}, indicating that the viscosity has a significant effect on the selection of the excited resonant triad. For the value of σ_0/f considered in Fig. 6, the maximum growth rate is obtained for the $(-,+,-)$ resonance, for $k_1^{\max} = 0.75$ rad cm^{-1}. The corresponding predicted wavevector $\mathbf{k}_1$ is represented as a circle in the resonance curve of Fig. 5(a), and is found in excellent agreement with the experimental measurement of $\mathbf{k}_1$ (shown with an arrow).

Because of the viscous attenuation, the primary wave amplitude A_0 actually depends on the distance from the wavemaker. In the measurement area shown in Fig. 4(a), spatial variations of $\pm 25\%$ are found around the average $A_0 = 0.29$ cm s^{-1}. Since the growth rate (30) depends on A_0, this introduces an uncertainty on the predicted value of γ and consequently on the selected secondary wavenumbers. In order to appreciate the influence of the measured value of A_0 on the predicted triadic resonance, we also plot in Fig. 6 the growth rate of the selected $(-,+,-)$ resonance, but for a value of A_0 increased by an amount of 25% (continuous line), which corresponds to the wave amplitude in the close vicinity of the wavemaker. The maximum growth rate is actually found to strongly depend on A_0, with an increase of 30%, indicating that the onset of the parametric instability will take place first close to the wavemaker. This strong sensitivity would make any direct comparison with an experimental growth rate too difficult. On the other hand, the selected wavenumber $k_1^{\max}$ is quite robust, showing a slight increase of 6% only when A_0 is increased by 25%. As a consequence, the uncertainty in the measurement of A_0, which is unavoidable because of the viscous attenuation of the primary wave, does not affect significantly the prediction for the most unstable secondary wavevectors.

The size of the circles in Figs. 5(a) and 5(b) illustrates the uncertainty in the determination of the most unstable wavevectors due to the spatial variation of A_0. The relative uncertainty lies in the range 5%–15% for the range of wave frequencies considered here. In spite of this uncertainty, we can conclude that the secondary wavevectors predictions from the maximum growth rate criterion are in good agreement with the observed resonant triads.

C. Dependence of the secondary waves properties on the primary wave frequency

We finally characterize here the evolution of the secondary wave properties (frequencies and wavenumbers) as the frequency of the primary wave is changed. For a given primary wave

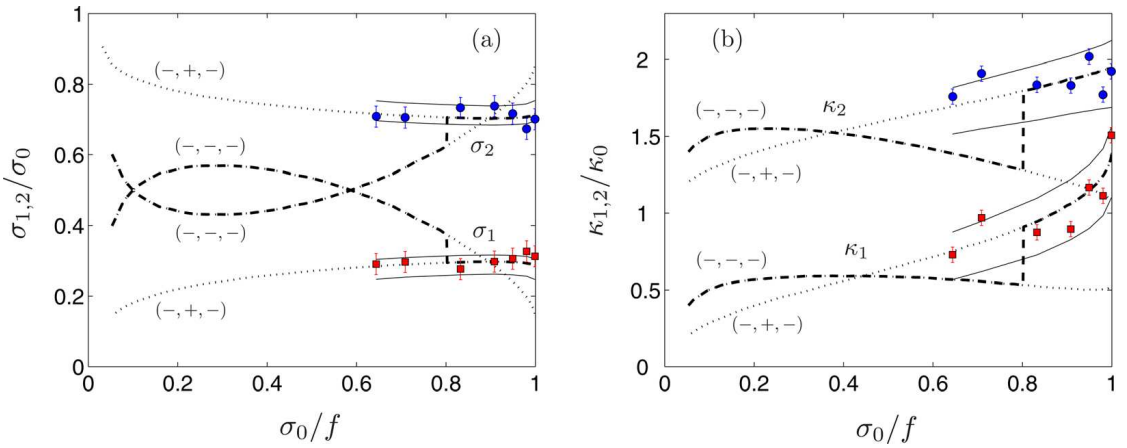

FIG. 7. (Color online) Normalized frequencies $\sigma_{1,2}/\sigma_0$ (a), and wavenumbers $\kappa_{1,2}/\kappa_0$ (b) of the secondary waves, as a function of the primary wave frequency σ_0/f. Filled circles and squares with errorbars correspond to experimental measurements. Predictions from the triadic resonance instability are represented with dashed thick lines (using absolute maximum growth rate criterion) and dotted lines (using maximum growth rate criterion for the $(-,-,-)$ and $(-,+,-)$ resonances). Predictions for the most unstable resonance are $(-,-,-)$ for $\sigma_0/f < 0.79$ and $(-,+,-)$ for $\sigma_0/f > 0.79$. These predictions have been computed with a typical amplitude $A_0 = 0.30$ cm s^{-1} for the primary wave. Continuous solid lines show the allowed range around the $(-,+,-)$ curves, determined by considering an uncertainty of $\pm 50\%$ on A_0.

amplitude A_0, the secondary frequencies $\sigma_{1,2}$ and wavenumbers $\kappa_{1,2}$ have been systematically computed according to the maximum growth rate criterion and are reported in Fig. 7 as a function of $\sigma_0/f \in [0, 1]$. The dotted lines correspond to the $(-,-,-)$ and $(-,+,-)$ resonances, whereas the dashed thick lines are computed from the absolute maximum growth rate among all the possible resonances. For $\sigma_0/f > 0.79$, the growth rate is maximum on the $(-,\pm,\mp)$ branch, whereas for $\sigma_0/f < 0.79$, it is maximum on the $(-,-,-)$ branch.

In Fig. 7, we also show the experimental measurements of $\sigma_{1,2}$ and $\kappa_{1,2}$ for the range of primary wave frequencies for which a subharmonic instability is observed, $0.65 < \sigma_0/f < 0.99$. The errorbars show the uncertainties computed from the measured frequencies and wavenumbers. The agreement with the predictions from the triadic resonance theory is excellent for the $(-,+,-)$ branch. However, it is not clear why all the measurements actually follow the $(-,+,-)$ branch, although the $(-,-,-)$ branch is expected to be more unstable for the two data points at $\sigma_0/f < 0.79$.

The limited spatial extent of the primary wave along its transverse direction (which represents 4 wavelengths only) and its amplitude decay along its propagation direction (because of viscous attenuation) may be responsible for this unexpected stability of the $(-,-,-)$ branch at low σ_0/f. Indeed, the $(-,-,-)$ branch is associated to wavelengths significantly larger than the primary wavelength, so that a large spatial region of nearly homogeneous primary wave amplitude is required to sustain such large wavelength secondary waves. On the other hand, the $(-,+,-)$ resonance generates lower wavelengths, which can more easily fit into the limited extent of the primary wave. Finite size effects may, therefore, explain both the preferred $(-,+,-)$ resonance at $\sigma_0/f < 0.79$ and the unexpected global stability of the primary wave for $\sigma_0/f < 0.65$. Confinement effects are not described by the present triadic resonance theory, which assumes plane waves of infinite spatial extent. Apart from this open issue, we can conclude that, at least for sufficiently large forcing frequency, the observed secondary frequencies and wavenumbers are in good quantitative agreement with the predictions from the triadic resonance theory.

V. DISCUSSION AND CONCLUSION

Using a wavemaker initially designed to generate beams of *internal* gravity waves in stratified fluids, we have successfully generated well-defined plane *inertial* waves in a rotating water tank. Spectral analysis, performed on particle image velocimetry measurements of this plane inertial wave, has revealed the onset of a parametric instability, leading to the emergence of two secondary subharmonic waves. The wavevectors and frequencies of the primary and secondary waves are found in good agreement with the spatial and temporal resonance conditions for a resonant

triad of inertial waves. Moreover, using the triadic resonance theory for inertial waves derived by Smith and Waleffe,[25] the growth rate of the instability has been computed, yielding predictions for the secondary wavevectors and frequencies in agreement with the measurements. At low forcing frequency, we observe a departure from these predictions which may be associated to the finite size of the primary wave. These finite size effects cannot actually be described within the triadic resonant theory, which relies on plane waves of infinite extent.

Triadic resonant instability for inertial and internal waves shares a number of common properties. In particular, equations governing the wave amplitudes equivalent to Eqs. (27) and (28) may also be derived for a triad of internal waves, but in this case, they concern the amplitude of streamfunctions and not of velocities.[24] The interaction coefficients for internal waves $\tilde{C}_r$ (with $r = 0, 1, 2$) can be readily obtained from the interaction coefficients for inertial waves C_r through a simple exchange of the vertical and horizontal components of the wavevectors, and introducing a prefactor

$$\tilde{C}_r(k,m) = \frac{\kappa_p \kappa_q}{\kappa_r} C_r(m,k). \tag{31}$$

The $\kappa_p\kappa_q/\kappa_r$ prefactor between the two types of coefficients comes from the fact the wave amplitude is directly given by the velocity $\mathbf{u}$ in the case of inertial waves, whereas it is given by the streamfunction $\tilde{\psi} \sim u/\kappa$ in the case of internal waves. The exchange of the vertical and horizontal components of the wavevectors comes from the comparison between the dispersion relations for inertial and internal waves, $\sigma/f = sm/\kappa$ and $\sigma/N = sk/\kappa$, respectively, with $f = 2\Omega$ the Coriolis parameter and N the Brunt–Väisälä frequency. The inviscid growth rate of the parametric instability $\tilde{\gamma}$ for the internal waves is actually equal to the one of inertial waves γ through

$$\tilde{\gamma} = \sqrt{\tilde{C}_1 \tilde{C}_2} \tilde{A}_0 = \sqrt{C_1 C_2} \kappa_0 \tilde{A}_0 = \gamma, \tag{32}$$

where $\tilde{A}_0$ is the primary internal wave amplitude (homogeneous to a streamfunction). Here, the inertial wave amplitude A_0 (homogeneous to a velocity) identifies with $\kappa_0 \tilde{A}_0$. This equality between inertial and internal growth rates finally shows that the predicted secondary waves should be identical for the two types of waves.

Interacting inertial waves are of primary importance for the dynamics of rotating turbulence. In the limit of low Rossby numbers $Ro = U/\Omega L$, where U and L are the characteristic velocity and length scales, rotating turbulence can be described as a superposition of weakly interacting inertial waves, whose interactions are directly governed by triadic resonances. This is precisely the framework of wave turbulence as analyzed in Refs. 38 and 39 in the context of rotating turbulence. The parametric instability between three inertial waves can be seen as an elementary process by which energy is transferred between wavevectors in rotating turbulence. This anisotropic energy transfer takes place both in scales (or wavenumbers) and directions (or angles). The *angular* energy transfer is always directed towards more horizontal wavevectors, providing a clear mechanism by which slow quasi-2D motions become excited.[25] However, the nature of energy transfers through triadic resonance in terms of *wavenumbers* (or *scales*) —i.e., whether the energy proceeds from large to small scales or inversely—is found to depend on wave amplitude and viscosity. Indeed, it can be shown theoretically, within the present triadic resonance framework, that waves of amplitude large compared to $\nu\kappa_0$ are unstable with respect to secondary waves of large wavenumbers, producing a direct energy cascade towards small scales. On the other hand, waves of amplitude much lower than $\nu\kappa_0$ are found to excite secondary waves of smaller wavenumber, hence producing an inverse energy cascade towards larger scales. The net result of this competition is delicate to decide and may contain an answer to the debated issue concerning the direction of the energy cascade in rapidly rotating turbulence.

ACKNOWLEDGMENTS

We thank M. Moulin for the technical work and improvement made on the wavemaker, and C. Borget for experimental help with the rotating platform. The collaboration between FAST

laboratory and ENS Lyon Physics laboratory is funded by the ANR Grant No. ANR-2011-BS04-006-01 "ONLITUR." The rotating platform "Gyroflow" was funded by the ANR Grant No. 06-BLAN-0363-01 "HiSpeedPIV" and by the "Triangle de la Physique." ENS Lyon's research work has been also partially supported by the ANR Grant No. ANR-08-BLAN-0113-01 "PIWO."

[1]H. Greenspan, *The Theory of Rotating Fluids* (Cambridge University Press, London, 1968).
[2]J. Lighthill, *Waves in Fluids* (Cambridge University Press, London, 1978).
[3]J. Pedlosky, *Geophysical Fluid Dynamics* (Springer-Verlag, Heidelberg, 1987).
[4]O. M. Phillips, "Energy transfer in rotating fluids by reflection of inertial waves," Phys. Fluids **6**, 513 (1963).
[5]L. Gostiaux, T. Dauxois, H. Didelle, J. Sommeria, and S. Viboud, "Quantitative laboratory observations of internal wave reflection on ascending slopes," Phys. Fluids **18**, 056602 (2006).
[6]D. Fultz, "A note on overstability and the elastoid-inertia oscillations of Kelvin, Soldberg, and Bjerknes," J. Meteorol. **16**, 199 (1959).
[7]A. D. McEwan, "Inertial oscillations in a rotating fluid cylinder," J. Fluid Mech. **40**, 603 (1970).
[8]R. Manasseh, "Distortions of inertia waves in a rotating fluid cylinder forced near its fundamental mode resonance," J. Fluid Mech. **265**, 345 (1994).
[9]L. R. M. Maas, "Wave focusing and ensuing mean flow due to symmetry breaking in rotating fluids," J. Fluid Mech. **437**, 13 (2001).
[10]Y. Duguet, J. F. Scott, and L. Le Penven, "Instability inside a rotating gas cylinder subject to axial periodic strain," Phys. Fluids **17**, 114103 (2005).
[11]Y. Duguet, J. F. Scott, and L. Le Penven, "Oscillatory jets and instabilities in a rotating cylinder," Phys. Fluids **18**, 104104 (2006).
[12]P. Meunier, C. Eloy, R. Lagrange, and F. Nadal, "A rotating fluid cylinder subject to weak precession," J. Fluid Mech. **599**, 405 (2008).
[13]G. P. Bewley, D. P. Lathrop, L. R. M. Maas, and K. R. Sreenivasan, "Inertial waves in rotating grid turbulence," Phys. Fluids **19**, 071701 (2007).
[14]C. Lamriben, P.-P. Cortet, F. Moisy, and L. R. M. Maas, "Excitation of inertial modes in a closed grid turbulence experiment under rotation," Phys. Fluids **23**, 015102 (2011).
[15]L. Messio, C. Morize, M. Rabaud, and F. Moisy, "Experimental observation using particle image velocimetry of inertial waves in a rotating fluid," Exp. Fluids **44**, 519 (2008).
[16]P.-P. Cortet, C. Lamriben, and F. Moisy, "Viscous spreading of an inertial wave beam in a rotating fluid," Phys. Fluids **22**, 086603 (2010).
[17]S. A. Thorpe, "On standing internal gravity waves of finite amplitude," J. Fluid Mech. **32**, 489 (1969).
[18]A. D. McEwan, "Degeneration of resonantly-excited standing internal gravity waves," J. Fluid Mech. **50**, 431 (1971).
[19]D. Benielli and J. Sommeria, "Excitation and breaking of internal gravity waves by parametric instability," J. Fluid Mech. **374**, 117 (1998).
[20]C. Staquet and J. Sommeria, "Internal gravity waves: From instabilities to turbulence," Annu. Rev. Fluid Mech. **34**, 559 (2002).
[21]D. J. Olbers and N. Pomphrey, "Disqualifying 2 candidates for the energy-balance of oceanic internal waves," J. Phys. Oceanogr. **11**, 1423 (1981).
[22]E. Kunze and S. G. Llewellyn Smith, "The role of small-scale topography in turbulent mixing of the global ocean," Oceanography **17**, 55 (2004).
[23]J. A. MacKinnon and K. B. Winters, "Subtropical catastrophe: Significant loss of low-mode tidal energy at 28.9°," Geophys. Res. Lett. **32**, L15605, doi:10.1029/2005GL023376 (2005).
[24]C. R. Koudella and C. Staquet, "Instability mechanisms of a two-dimensional progressive internal gravity wave," J. Fluid Mech. **548**, 165 (2006).
[25]L. M. Smith and F. Waleffe, "Transfer of energy to two-dimensional large scales in forced, rotating, three-dimensional turbulence," Phys. Fluids **11**, 1608 (1999).
[26]P. Sagaut and C. Cambon, *Homogeneous Turbulence Dynamics* (Cambridge University Press, London, 2008).
[27]C. Lamriben, P.-P. Cortet, and F. Moisy, "Direct Measurements of anisotropic energy transfers in a rotating turbulence experiment," Phys. Rev. Lett. **107**, 024503 (2011).
[28]P. J. Staplehurst, P. A. Davidson, and S. B. Dalziel, "Structure formation in homogeneous freely decaying rotating turbulence," J. Fluid Mech. **598**, 81 (2008).
[29]L. Gostiaux, H. Didelle, S. Mercier, and T. Dauxois, "A novel internal waves generator," Exp. Fluids **42**, 123 (2007).
[30]M. Mercier, N. Garnier, and T. Dauxois, "Reflection and diffraction of internal waves analyzed with the Hilbert transform," Phys. Fluids **20**, 086601 (2008).
[31]M. Mercier, D. Martinand, M. Mathur, L. Gostiaux, T. Peacock, and T. Dauxois, "New wave generation," J. Fluid Mech. **657**, 310 (2010).
[32]DaVis, LaVision GmbH, Anna-Vandenhoeck-Ring 19, 37081 Goettingen, Germany.
[33]F. Moisy, See http://www.fast.u-psud.fr/pivmat for PIVMat toolbox for MATLAB.
[34]V. Croquette and H. Williams, "Nonlinear waves of the oscillatory instability on finite convective rolls," Physica D **37**, 300 (1989).
[35]F. Waleffe, "The nature of triad interactions in homogeneous turbulence," Phys. Fluids A **4**(2), 350 (1992).
[36]F. Waleffe, "Inertial transfers in the helical decomposition," Phys. Fluids A **5**(3), 577 (1993).
[37]The definition of the helical mode used here corresponds to the one in Ref. 25. In Refs. 35 and 36, the helical mode is defined as the complex conjugate of Eq. (17), resulting in a sign change of the helicity.
[38]S. Galtier, "Weak inertial-wave turbulence theory," Phys. Rev. E **68**, 015301(R) (2003).
[39]C. Cambon, R. Rubinstein, and F. S. Godeferd, "Advances in wave turbulence: Rapidly rotating flows," New J. Phys. **6**, 73 (2004).

PHYSICS OF FLUIDS **26**, 125112 (2014)

Direct and inverse energy cascades in a forced rotating turbulence experiment

Antoine Campagne,[1] Basile Gallet,[1,2] Frédéric Moisy,[1]
and Pierre-Philippe Cortet[1]
[1]*Laboratoire FAST, CNRS, Université Paris-Sud, 91405 Orsay, France*
[2]*Laboratoire SPHYNX, Service de Physique de l'État Condensé, DSM, CEA Saclay, CNRS, 91191 Gif-sur-Yvette, France*

(Received 24 June 2014; accepted 11 December 2014; published online 31 December 2014)

We present experimental evidence for a double cascade of kinetic energy in a statistically stationary rotating turbulence experiment. Turbulence is generated by a set of vertical flaps, which continuously injects velocity fluctuations towards the center of a rotating water tank. The energy transfers are evaluated from two-point third-order three-component velocity structure functions, which we measure using stereoscopic particle image velocimetry in the rotating frame. Without global rotation, the energy is transferred from large to small scales, as in classical three-dimensional turbulence. For nonzero rotation rates, the horizontal kinetic energy presents a double cascade: a direct cascade at small horizontal scales and an inverse cascade at large horizontal scales. By contrast, the vertical kinetic energy is always transferred from large to small horizontal scales, a behavior reminiscent of the dynamics of a passive scalar in two-dimensional turbulence. At the largest rotation rate, the flow is nearly two-dimensional, and a pure inverse energy cascade is found for the horizontal energy. To describe the scale-by-scale energy budget, we consider a generalization of the Kármán-Howarth-Monin equation to inhomogeneous turbulent flows, in which the energy input is explicitly described as the advection of turbulent energy from the flaps through the surface of the control volume where the measurements are performed. [http://dx.doi.org/10.1063/1.4904957]

I. INTRODUCTION

Global rotation is a key ingredient of many geophysical and astrophysical flows. Through the action of the Coriolis force, rotating turbulence tends to approach two-dimensionality, i.e., invariance along the rotation axis (hereafter denoted as the vertical axis by convention).[1–3] Energetic 2D and 3D flow features therefore coexist in rotating turbulence, and the question of the direction of the energy cascade between spatial scales naturally arises: In 3D, energy is transferred from large to small scales[1,2,4] whereas it is transferred from small to large scales in 2D, as first proposed by Kraichnan.[5–7] In rotating turbulence, energy transfers depend on the Rossby number Ro, which compares the rotation period Ω^{-1} to the turbulent turnover time. In the limit of small Ro, the fluid motions evolving on a time scale much slower than the rotation period Ω^{-1} are 2D3C (two-dimensional, three-component), a result known as the Taylor-Proudman theorem, while the faster motions of frequency up to 2Ω are in the form of 3D inertial waves.[8] In this limit, 3D energy transfers occur through resonant and quasi-resonant triadic interactions of inertial waves,[9–13] which drive energy in a *direct* cascade, with a net transfer towards slow, small-scale, nearly 2D modes.[10,14,15] Exactly resonant triads cannot however drive energy from 3D modes to the exactly 2D mode. In the limit of vanishing Rossby number, only those exact resonances are efficient, so the 2D3C mode is autonomous:[16] It follows a purely 2D dynamics unaffected by rotation, with an inverse cascade of horizontal energy and a passive-scalar mixing of the vertical velocity.[4,7] This decoupling implies that, if energy is supplied to the 3D modes only, the 2D mode should not be excited and no inverse cascade should be observed.

In contrast with this asymptotic limit, most experiments and numerical simulations correspond to moderate Rossby numbers. They exhibit the emergence of large-scale columnar structures, which suggests a net transfer from the 3D "wave" modes to the 2D3C "vortex" mode.[17–25] For such moderate Rossby numbers, near-resonant triadic interactions, which are increasingly important as *Ro* is increased, allow for non-vanishing energy transfers between 3D and 2D modes,[10,19,20,26,27] thus providing a mechanism for the emergence of inverse energy transfers: once energy is transferred to the 2D vortex mode, local 2D interactions are expected to build an upscale energy cascade. Even for a purely 3D forcing, the vortex mode grows as a result of near-resonant triads involving one 2D mode, and two large-vertical-scale and small-horizontal-scale 3D modes:[20] this vortex mode then triggers inverse energy transfers between purely 2D modes. This intermediate Rossby number regime is of first practical interest: the Rossby number of most laboratory experiments and geophysical/astrophysical flows is indeed of the order of $10^{-1} - 10^{-2}$. In these situations, a natural question is to what extent direct and inverse cascades may coexist, and what sets their relative amplitudes as the Rossby number is varied.

Inverse energy cascade in rotating turbulence has been mostly investigated numerically, in the simplified configuration of a body force acting at an intermediate wave number k_f in a periodic box.[11,22,25,26,28–32] In this setup, the inverse cascade is manifested through a growth of the energy spectrum, and hence an inverse spectral transfer, at wave numbers $k_\perp < k_f$ (with $k_\perp$, the wave number component normal to the rotation axis). As for 2D turbulence, the kinetic energy increases during this transient regime, until energetic domain size structures are formed[33] or additional large-scale dissipation comes into play. Although much weaker, an inverse transfer of energy is also found in numerical simulations of decaying rotating turbulence.[19,34,35] Overall, these simulations indicate that, in addition to the Rossby number, the nature of the forcing, in particular, its *dimensionality* (2D vs. 3D), *componentality* (2C vs. 3C), and helicity content, plays a key role for the existence and intensity of the inverse cascade.[27,29] In addition, since shallow domains resemble 2D systems, which enhance the inverse cascade, another key parameter in this problem is the vertical confinement: the critical Rossby number under which the inverse cascade appears increases as the ratio of the box height to the forcing scale gets smaller.[11,30,31]

Although these numerical simulations have provided valuable insight about the conditions under which an inverse cascade takes place in rotating turbulence, the most common assumptions of homogeneity and narrow-band spectral forcing are of limited practical interest. More general forcing functions are considered in the simulations of Bourouiba *et al.*,[20] with energy input either in a large range of vertical scales and a single horizontal scale, or vice-versa. In most flows encountered in the laboratory and in geophysical/astrophysical contexts, energy injection in a given control volume is broadband and results from the spatial gradients of turbulent energy. As a consequence, the well-separated inverse and direct cascades obtained in numerical simulations with a separating wave number fixed at the forcing wave number k_f are not relevant to describe real flows with boundary forcing. Furthermore, flows of geophysical relevance can often be considered to be in statistically steady state. Such stationary states are easily achieved in laboratory experiments, whereas they generally correspond to prohibitively long integration times for numerical simulation. This provides another justification for considering the problem of the energy cascade directions of rotating turbulence experimentally.

We therefore built an experiment aimed at studying such stationary rotating turbulence. Designing a rotating turbulence experiment which unambiguously exhibits an inverse cascade is however difficult for several reasons. First, in a statistically steady turbulence experiment, an inverse cascade can be identified only from measurements of energy transfers, i.e., from third-order velocity correlations. These measurements require very large data sets from advanced image-based diagnostic such as stereoscopic particle image velocimetry (PIV).[36] Second, it is possible to separate the scale-by-scale energy fluxes from the spatial transport of energy only under the assumption of weak inhomogeneity of the flow, which is difficult to satisfy with boundary forced experiments.

Because of these difficulties, experimental evidence of inverse cascade in rotating turbulence is scarce. Indirect evidence was first provided by Baroud *et al.*[37] in forced turbulence and later by Morize *et al.*[38] in decaying turbulence. In both experiments, it is reflected in a change of sign of the third-order moment of the longitudinal velocity increments in the plane normal to

the rotation axis, $S_3(r_\perp) = \langle(\delta u_L)^3\rangle$ (where δu_L is the velocity increment projected along the horizontal separation $\mathbf{r}_\perp$). Simple relations between $S_3(r_\perp)$ and the energy flux exist only either in the 3D3C (three-dimensional, three-component) isotropic case or in the 2D2C (two-dimensional, two-component) isotropic case, but not in the general axisymmetric case, so the change of sign of S_3 cannot be unambiguously related to inverse energy transfers in these experiments. More recently, evidence of inverse energy transfers has been reported by Yarom *et al.*,[39] from the transient evolution of the energy spectrum in a forced rotating turbulence experiment. However, because of the unstationary and inhomogeneous nature of their experiment, it is delicate to distinguish the *scale-by-scale* energy transfers at a given spatial location from the *spatial* energy transport from the turbulence production device to the measurement area. In all these experiments, the aspect ratio is of order unity, so the 2D features of turbulence are essentially due to rotation and not confinement. The extreme case of rotating shallow water experiments is indeed known to produce a purely 2D dynamics with an inverse energy cascade even at small rotation rate (see, e.g., Afanasyev and Craig[40]). The integral scale measurements of van Bokhoven *et al.*,[41] in which both the fluid height and the rotation rate are varied, also confirm the combined roles of these two parameters in the generation of large-scale quasi-2D vortices.

In this paper, we investigate the interplay between direct and inverse energy cascades in a statistically stationary rotating turbulence experiment from direct measurements of scale-by-scale energy transfers. Turbulence is generated by a set of vertical flaps which continuously inject velocity fluctuations towards the center of a rotating water tank. The flaps are vertically invariant, but instabilities in their vicinity induce 3D turbulent fluctuations, so the forcing injects energy both in the 2D and 3D modes. We compute the energy transfers from the divergence of the two-point third-order velocity structure functions extracted from stereoscopic particle image velocimetry measurements in the rotating frame. We observe the emergence of a double cascade of energy, direct at small scales and inverse at large scales, the extension and magnitude of the inverse cascade increasing with global rotation. This overall behavior of the total kinetic energy is the superposition of different behaviors for the horizontal and vertical velocities: for rapid global rotation, the horizontal energy exhibits an inverse cascade, whereas the vertical energy follows a direct cascade. The inverse cascade of horizontal energy is found only at large scale for moderate rotation rate but gradually spreads down to the smallest scales as the rotation rate is increased. These findings are compatible with a 2D3C dynamics at large rotation rate, with the horizontal velocity following a 2D dynamics and the vertical velocity behaving as a passive scalar.

The energy transfers in homogeneous (but not necessarily isotropic) turbulence can be described in the physical space using the Kármán-Howarth-Monin (KHM) equation.[4,36,42] This approach holds for homogeneous decaying turbulence and for stationary turbulence forced by a homogeneous body force. However, it breaks down in boundary-forced experiments, in which inhomogeneities induce a transport of kinetic energy from the forcing region to the region where measurements are performed. Extended versions of the KHM equation including the effects of inhomogeneities have been proposed and proved useful to describe the energy budget in simple configurations, e.g., in wind-tunnel experiments.[43–47] Here, we make use of the inhomogeneous generalization of the KHM equation proposed by Hill.[44] The measurement of the different terms of this equation in the case of the largest rotation rate, which is closer to the asymptotic 2D3C state, allows us to clarify the effect of the inhomogeneous forcing in this experiment.

II. EXPERIMENTAL SETUP

The experimental setup is similar to the one described in Gallet *et al.*,[48] and only the features specific to the present experiments are described in detail here. The setup consists of a glass tank of 125×125 cm^2 square base and 65 cm height, filled with 50 cm of water and mounted on a precision rotating platform of 2 m diameter (see Fig. 1(a)). We have carried out experiments at five rotation rates Ω in the range from 0.21 to 1.68 rad s^{-1} (2–16 rpm), together with a reference experiment without rotation ($\Omega = 0$). The rotation rate is constant to better than 10^{-3} relative fluctuations. In the central region of the tank, we use a glass lid to avoid the paraboloidal deformation of the free surface and to allow for visualization from above. This lid is 43 cm above the bottom of the tank.

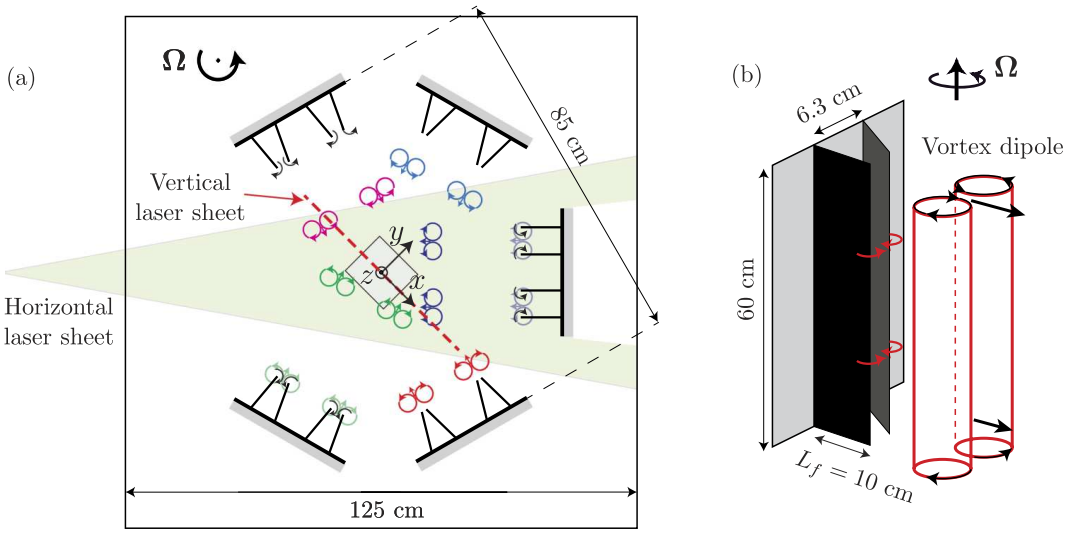

FIG. 1. (a) Schematic of the experiment: An arena of 10 pairs of vertical flaps is placed in a parallelepipedic water tank rotating at angular velocity Ω. The rotation vector **Ω** is vertical and the system is viewed from above. The rectangle at the center of the arena indicates the horizontal region where 2D-3C velocity fields are measured by stereoscopic particle image velocimetry. The drawing shows idealized vortex dipoles emitted by the generators, before they interact in the center of the arena. (b) Perspective view of a pair of flaps.

A statistically stationary turbulent flow is produced by a set of ten vortex dipole generators. They are arranged in 5 blocks of 2 generators located around a hexagonal arena of 85 ± 5 cm width, each of them being oriented towards the center of the arena (Fig. 1(a)). One side of the hexagon is left open to illuminate the center of the arena with a horizontal laser sheet. This forcing device was initially designed to generate turbulence in stratified fluids and is described in detail in Refs. 49 and 50. Each generator consists of a pair of vertical flaps, 60 cm high and $L_f = 10$ cm long, each flap rotating about one of its vertical edges (Fig. 1(b)). Thanks to DC motors and a system of gears and cams, the pairs of flaps are driven in a periodic motion of 8.5 s duration and 9° amplitude: the two flaps being initially parallel, they first rotate with an angular velocity $\omega_f = 0.092$ rad s^{-1} during 1.7 s until their tips almost touch each other. They remain motionless during 3.4 s, before reopening during 1.7 s until they reach the initial parallel configuration again. They finally remain motionless during the last 1.7 s of the cycle. The motions of the two adjacent pairs of flaps of a given block are in phase, but an arbitrary phase shift is set between the five blocks. The rotation of the platform is set long before the start of this forcing device, at least 1 h, in order for transient spin-up recirculations to be damped. Once solid-body rotation is reached, we start the generators, and a statistically stationary state is reached in the center of the tank after a few minutes.

The Reynolds number based on the flap length L_f and flap angular velocity ω_f is $Re_f = \omega_f L_f^2/\nu = 920$. The flow generated by the closing of the flaps consists of an initially vertically invariant vortex dipole (Fig. 1(a)) which quickly becomes unstable and produces small-scale 3D turbulent fluctuations. This turbulent burst self-advects towards the center of the arena because of the persistent large-scale vortex dipole component. The Rossby number based on the flap angular velocity is low, $Ro_f = \omega_f/2\Omega \in [0.03, 0.22]$ (see Table I), indicating that the flow generated by the flap motion is influenced by rotation right from the generators (except for the non-rotating experiment). Turbulence in the center of the flow can be also characterized locally by the turbulent Reynolds and Rossby numbers based on the r.m.s. velocity $u_{\rm rms}$ and the horizontal integral scale $L_\perp$ defined in Eq. (4) (see Sec. IV A): $Re = u_{\rm rms} L_\perp/\nu$ and $Ro = u_{\rm rms}/2\Omega L_\perp$ (values are given in Table I).

The three components of the velocity field $\mathbf{u}(\mathbf{x},t) = (u_x, u_y, u_z)$ are measured in a horizontal and a vertical plane in the rotating frame (Fig. 1(a)) using a stereoscopic particle image velocimetry (PIV) system.[51,52] The two regions of interest are centered with respect to the arena of generators. It is a square of about 14×14 cm^2 in a vertical plane along the diagonal of the base of the tank and a square of 12×12 cm^2 in a horizontal plane at mid-depth. The flow is seeded with 10 μm tracer particles and illuminated by a laser sheet generated by a double 140 mJ Nd:YAG pulsed

TABLE I. Flow parameters for the different rotation rates Ω: Rossby number based on the flap velocity Ro_f, rate of turbulence k/K, inhomogeneity factor γ, horizontal integral scale $L_\perp$, turbulent Reynolds number Re, and Rossby number Ro. These figures are computed from the stereoscopic PIV data in the horizontal plane (Fig. 1(a)). See text for definitions.

Ω (rpm)	0	2	4	8	12	16
Ro_f	∞	0.22	0.11	0.055	0.037	0.028
k/K	0.48	0.79	0.89	0.95	0.94	0.97
γ	0.17	0.15	0.06	0.05	0.04	0.10
$L_\perp$ (mm)	24	43	45	44	42	38
Re	140	230	350	420	400	330
Ro	∞	0.30	0.20	0.13	0.087	0.068

laser mounted on the rotating platform (Fig. 1(a)). The illuminated flow section is imaged with two double-buffer cameras aiming at the laser sheet under different incidence angles. Images are taken from above through the glass lid for the measurements in the horizontal plane and from two adjacent vertical sides of the tank for the measurements in the vertical plane.

Each acquisition consists of 3 600 quadruplets of images (one pair per camera) recorded at 0.35 Hz with a 50 ms time lag between the two images of a given pair. The 3 velocity components are computed in the two-dimensional measurement plane using stereoscopic reconstruction. The cross-correlations are based on interrogation windows of 32×32 pixels with 50% overlap. The resulting 2D3C velocity fields are sampled on a grid of 105×105 (respectively, 80×80) vectors with a spatial resolution of 1.15 mm (respectively, 1.75 mm) in the horizontal (respectively, vertical) plane.

III. LOCAL HOMOGENEITY AND AXISYMMETRY

In this experiment, kinetic energy is injected by the generators located around the region of interest, so an inward transport of energy takes place from the generators to the center of the arena. An important feature of turbulence in this configuration is the presence or not of a mean flow induced by the generators: this indicates whether the transport of energy can be mainly attributed to a reproducible flow or to turbulent fluctuations. This can be addressed by performing a Reynolds decomposition of the velocity field

$$\mathbf{u}(\mathbf{x},t) = \bar{\mathbf{u}}(\mathbf{x}) + \mathbf{u}'(\mathbf{x},t), \tag{1}$$

where $\bar{\mathbf{u}}(\mathbf{x})$ is the time-averaged velocity field and $\mathbf{u}'(\mathbf{x},t)$ its turbulent part. From this decomposition, we can compute the turbulent and total kinetic energies, $k = \langle \overline{\mathbf{u}'(\mathbf{x},t)^2} \rangle_\mathbf{x}/2$ and $K = \langle \overline{\mathbf{u}(\mathbf{x},t)^2} \rangle_\mathbf{x}/2$, respectively, where $\langle \cdot \rangle_\mathbf{x}$ is a spatial average over the horizontal region of interest. The turbulence rate k/K is about 50% in the non-rotating experiment but rapidly increases up to 97% as the rotation rate Ω is increased (see Table I) indicating that, under rotation, the turbulent structures are essentially self-advected from the generators towards the center of the arena. In the following, we therefore focus on the turbulent component $\mathbf{u}'(\mathbf{x},t)$ which dominates the flow in the rotating case.

Although turbulence is necessarily inhomogeneous in this configuration, with more energy near the generators than at the center of the flow, we may expect a reasonable local homogeneity in the measurement area because of its small size (square of about 13 cm side) compared to the distance to the generators (33 cm from the center of the arena to the tip of the flaps). Before investigating the scale-by-scale energy distribution and energy transfers from spatially averaged two-point statistics, it is therefore important to quantify the degree of homogeneity of the flow. Since most of the energy is turbulent, we can quantify the level of homogeneity by the spatial standard deviation of the turbulent kinetic energy

$$\gamma = \frac{\langle [k(\mathbf{x}) - k]^2 \rangle_\mathbf{x}^{1/2}}{k}, \tag{2}$$

with $k(\mathbf{x}) = \overline{\mathbf{u}'(\mathbf{x},t)^2}/2$ the *local* time-averaged turbulent energy (such that $k = \langle k(\mathbf{x})\rangle_{\mathbf{x}}$). This ratio is given in Table I. It is smaller than 10% for $\Omega > 4$ rpm, indicating a reasonable degree of homogeneity in the region of interest.

A last single-point quantity of interest to characterize the turbulence field in this configuration is the spatially averaged velocity correlation tensor, $\langle\overline{u_i'u_j'}\rangle_{\mathbf{x}}$ (the trace of this tensor is twice the turbulence kinetic energy). For axisymmetric turbulence with respect to z, one has $\langle\overline{u_x'^2}\rangle_{\mathbf{x}} = \langle\overline{u_y'^2}\rangle_{\mathbf{x}} \neq \langle\overline{u_z'^2}\rangle_{\mathbf{x}}$ (i.e., turbulence is isotropic in the horizontal plane), with zero non-diagonal components. For 3D isotropic turbulence, the three diagonal components are equal (i.e., $\langle\overline{u_i'u_j'}\rangle_{\mathbf{x}} = \frac{2}{3}k\,\delta_{ij}$). This tensor therefore characterizes the *componentality* of turbulence, i.e., the isotropy with respect to the velocity components. It must not be confused with the *dimensionality* of turbulence, which characterizes the dependence of the two-point velocity statistics with respect to orientation of the separation vector joining the two points (investigated in Sec. IV).

In Fig. 2, we see that turbulence is nearly axisymmetric, with $\langle\overline{u_x'^2}\rangle_{\mathbf{x}} \simeq \langle\overline{u_y'^2}\rangle_{\mathbf{x}}$ to within 3% in the rotating case and 10% in the non-rotating case, and with the three non-diagonal components less than 10% of the diagonal components. As expected, turbulence is never isotropic, even in the case $\Omega = 0$, for which $\langle\overline{u_x'^2}\rangle_{\mathbf{x}} \simeq \langle\overline{u_y'^2}\rangle_{\mathbf{x}} \simeq 2\langle\overline{u_z'^2}\rangle_{\mathbf{x}}$. This anisotropy originates from the vertically invariant forcing by the flaps, which induces significantly weaker vertical velocity fluctuations than horizontal ones. As the rotation rate Ω increases, $\langle\overline{u_z'^2}\rangle_{\mathbf{x}}$ remains roughly constant, whereas $\langle\overline{u_x'^2}\rangle_{\mathbf{x}}$ and $\langle\overline{u_y'^2}\rangle_{\mathbf{x}}$ first increase with Ω before saturating beyond 8 rpm ($Ro \simeq 0.13$). At large Ω, the vertical kinetic energy represents about 10% of the total energy.

IV. SCALE-BY-SCALE ENERGY DISTRIBUTION AND TRANSFERS

We now focus on the scale-by-scale energy distribution and energy transfers. For this we must use two-point quantities: let us consider two points A and B in the turbulent flow at positions $\mathbf{x}_A$ and $\mathbf{x}_B$. We define the mid-point position $\mathbf{X} = (\mathbf{x}_A + \mathbf{x}_B)/2$ and the separation vector $\mathbf{r} = \mathbf{x}_B - \mathbf{x}_A$. Using cylindrical coordinates, the separation $\mathbf{r}$ writes $(r_\perp,\varphi,r_\parallel)$, with $r_\perp = (r_x^2 + r_y^2)^{1/2}$ and $r_\parallel = r_z$. In homogeneous turbulence, all statistical averages are functions of the separation vector $\mathbf{r}$ only. However, inhomogeneity plays a key role in boundary forced experiments, and we thus consider the inhomogeneous framework in which ensemble averages remain functions of both $\mathbf{r}$ and $\mathbf{X}$.

The centered velocity increment for separation $\mathbf{r}$, mid-point $\mathbf{X}$, and time t is

$$\begin{aligned}\delta\mathbf{u}'(\mathbf{X},\mathbf{r},t) &= \mathbf{u}_B'(\mathbf{X},\mathbf{r},t) - \mathbf{u}_A'(\mathbf{X},\mathbf{r},t)\\ &= \mathbf{u}'(\mathbf{x}_B = \mathbf{X} + \mathbf{r}/2,t) - \mathbf{u}'(\mathbf{x}_A = \mathbf{X} - \mathbf{r}/2,t).\end{aligned}$$

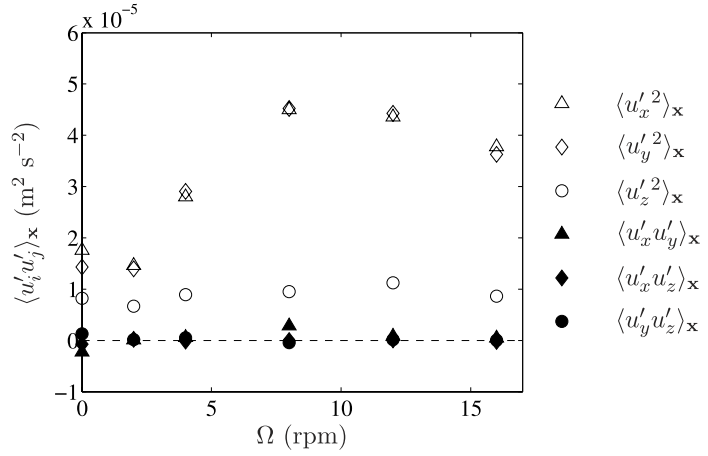

FIG. 2. Components of the velocity correlation tensor $\langle\overline{u_i'u_j'}\rangle_{\mathbf{x}}$ (with $(i, j) \in (x, y, z)$) as a function of Ω averaged over the horizontal region of interest. The non-diagonal components are nearly zero and $\langle\overline{u_x'^2}\rangle_{\mathbf{x}} \simeq \langle\overline{u_y'^2}\rangle_{\mathbf{x}}$, indicating statistically axisymmetric turbulence. Ω = 0, 2, 4, 8, 12, 16 rpm corresponds to turbulent Rossby number $Ro = \infty$, 0.30, 0.20, 0.13, 0.087, 0.068, respectively.

To perform an energy budget in this inhomogeneous context, we first need to define a control region for the mid-point $\mathbf{X}$: we consider only points A and B for which $\mathbf{X}$ lies in square S_X of side 40 mm centered in the PIV field. The relatively small size of the square allows for the separation $|\mathbf{r}|$ to be as large as 80 mm with the two points A and B still lying in the PIV field. The statistical averages are defined as an average over time and over all the positions of $\mathbf{X}$ inside S_X. In the following, the spatial average $\langle . \rangle_{\mathbf{X}}$ over $\mathbf{X} \in S_X$ will simply be denoted by $\langle . \rangle$.

Defining the statistics from centered or non-centered increments would be equivalent for homogeneous turbulence, and most of the remainder of this section can be understood in this framework. However, the use of centered increments plays a key role in Sec. V where we discuss the scale-by-scale energy budget: there is a balance at every scale $\mathbf{r}$ between viscous dissipation, nonlinear transfers between different scales (flux in $\mathbf{r}$ space), and advection of kinetic energy at scale $\mathbf{r}$ through the boundaries of the domain S_X (flux in $\mathbf{X}$ space). The latter term is the source term of the energy budget, which vanishes if turbulence is assumed to be homogeneous.

A. Energy distribution

We characterize the distribution of the turbulent energy among spatial scales by the anisotropic second-order structure function, defined as the variance of the centered velocity increments[55]

$$E(\mathbf{r}) = \langle \overline{(\delta \mathbf{u}')^2} \rangle. \tag{3}$$

The angular average of this quantity, $\mathcal{E}(r) = 1/(4\pi) \int_{\theta=0}^{\pi} \int_{\varphi=0}^{2\pi} E(r,\theta,\varphi) \sin\theta d\theta d\varphi$, where (r, θ, φ) is the usual spherical coordinate system, can be interpreted as the energy contained in eddies of size r or less, provided that r is larger than the dissipative scale.[2,53] For isotropic turbulence, $E(\mathbf{r}) = \mathcal{E}(r)$ therefore directly measures the cumulative energy from 0 to r. For anisotropic turbulence, $E(\mathbf{r})$ contains in addition key information on the anisotropic distribution of energy among eddies of characteristic horizontal and vertical scale given by $r_\perp$ and $r_\parallel$, respectively. For isotropic turbulence, the isosurfaces of $E(\mathbf{r})$ are spherical, while for axisymmetric turbulence about the vertical they are invariants with respect to rotations around the r_z axis. Two-dimensional turbulence would give exactly cylindrical iso-$E(\mathbf{r})$ (invariant by translation along r_z), which is a special case of axisymmetric turbulence.

Figure 3 shows the maps of the normalized energy distributions, $E(\mathbf{r})/E_0$, in the horizontal (r_x, r_y) and vertical (r_x, r_z) planes for $\Omega = 0$ and 16 rpm, with $E_0 = \langle \overline{\mathbf{u}_A'^2 + \mathbf{u}_B'^2} \rangle_{\mathbf{X}}$ taken at $\mathbf{r} = r_{\max}\mathbf{e}_\perp$ and $r_{\max} = 80$ mm as the maximum separation.[56] In Figs. 3(a) and 3(b), the iso-contours of $E(\mathbf{r})$ are nearly circular in the horizontal plane, both without and with rotation, indicating the good level of two-point axisymmetry of turbulence. For the largest horizontal scales considered here ($|\mathbf{r}| = 80$ mm), E/E_0 reaches 0.98 for $\Omega = 0$, indicating that nearly all the turbulent energy is contained in the range of scales of interest, whereas it reaches 0.89 only at $\Omega = 16$ rpm, indicating that structures larger than the maximum available scale still contain energy. This is a first indication of the emergence of large horizontal structures in the presence of rotation. This effect can be further quantified by the horizontal integral scale,

$$L_\perp = \int_0^{r^*} C(r_\perp) dr_\perp, \tag{4}$$

with $C(r_\perp) = 1/(2\pi) \int_0^{2\pi} C(\mathbf{r}_\perp) d\varphi$ and $C(\mathbf{r}_\perp) = 2 \langle \mathbf{u}_A' \cdot \mathbf{u}_B' \rangle_{\mathbf{X}} / E_0$ as the two-point correlation function. The conventional definition is such that $r^* = \infty$, but using here a finite truncation at r^*, chosen such that $C(r^*) = 0.25$, is necessary because $C(r_\perp)$ does not reach 0 at the maximum available scale $r_\perp = 80$ mm. Values of $L_\perp$ are given in Table I. In the absence of rotation, $L_\perp \simeq 24$ mm, which corresponds to the characteristic size of the turbulent fluctuations generated by the flaps. As Ω is increased, $L_\perp$ grows by nearly a factor of 2 compared to the non-rotating case, confirming the generation of large-scale structures.

We now turn to the energy distribution in the vertical plane (Figs. 3(c) and 3(d)). $E(\mathbf{r})$ is anisotropic both with and without rotation, with a trend towards vertical elongation of the contour lines at large scales. This anisotropy is, however, weak at $\Omega = 0$ and affects preferentially the large

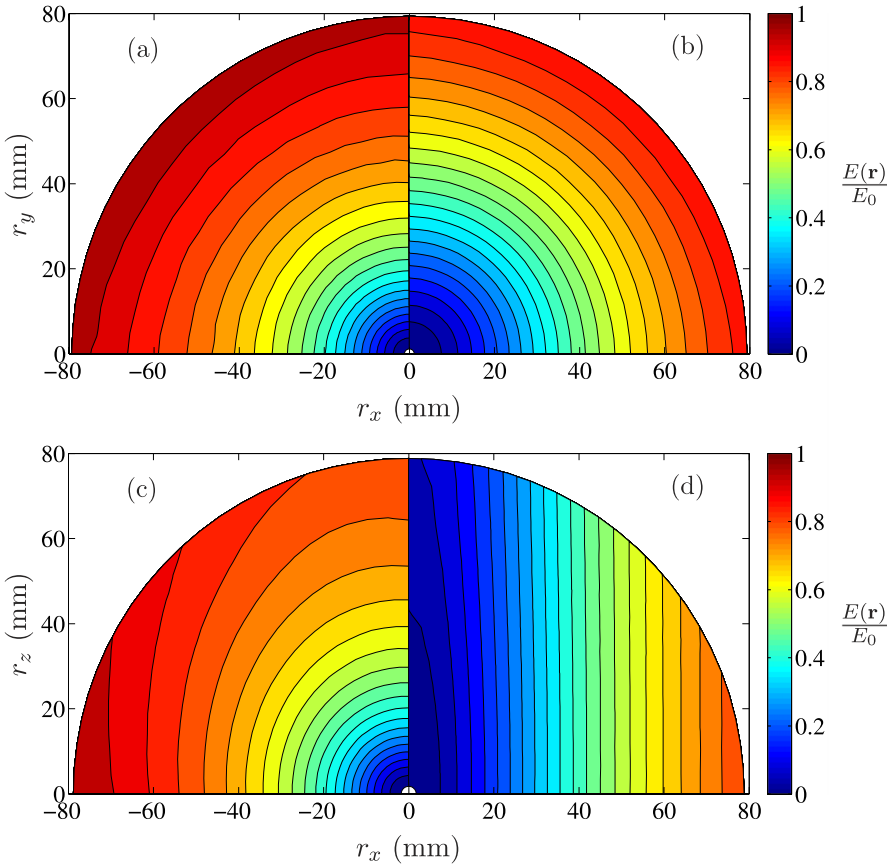

FIG. 3. Maps of the normalized energy distribution $E(\mathbf{r})/E_0$, (a) and (b) in the horizontal (r_x,r_y) plane, and (c) and (d) in the vertical (r_x,r_z) plane. (a) and (c) correspond to the experiment with $\Omega = 0$ ($Ro = \infty$), and (b) and (d) to $\Omega = 16$ rpm ($Ro = 0.068$).

scales: this is a direct consequence of the vertical invariance of the forcing device, which creates a nearly 2D flow at large scale carrying small-scale 3D fluctuations. The anisotropy is much more pronounced in the presence of rotation and persists down to the smallest scales, indicating a trend towards quasi-2D turbulence. This scale dependence of the anisotropy can be quantified by the ratio

$$A_E(r) = \frac{E_\perp(r) - E_\parallel(r)}{E_\perp(r) + E_\parallel(r)}, \tag{5}$$

with $E_\perp(r) = E(r_x = r, r_z = 0)$ and $E_\parallel(r) = E(r_x = 0, r_z = r)$. This ratio is zero for 3D isotropic turbulence and 1 for 2D turbulence. The plot of $A_E(r)$ in Fig. 4 shows a growth of anisotropy with r at all rotation rates. This growth is weak for $\Omega = 0$ (with A_E increasing from -0.01 to 0.1), indicating that the 2D nature of the forcing has a weak influence at these scales in the center of the tank. The anisotropy is much stronger when $\Omega \neq 0$: $A_E(r)$ first grows rapidly from $r = 0$ to $r \sim 10$ mm before saturating. For the largest available rotation rate, $\Omega = 16$ rpm, turbulence is nearly 2D for $r > 10$ mm, with $A_E(r) \simeq 0.85$, but remains significantly 3D at smaller scales.

B. Energy transfers

We now consider the scale-by-scale energy transfers defined from third-order moments of velocity increments. We start from the Kármán-Howarth-Monin equation for time-dependent homogeneous (but not necessarily isotropic) turbulence[4,42]

$$\frac{1}{4}\partial_t E(\mathbf{r},t) = -\Pi(\mathbf{r},t) + \frac{1}{2}\nu\nabla^2_{\mathbf{r}} E - \epsilon, \tag{6}$$

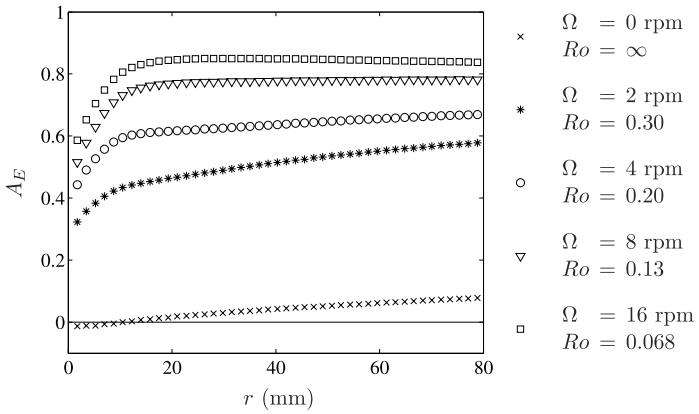

FIG. 4. Scale-dependent anisotropy factor $A_E(r)$ (Eq. (5)) of the energy distribution as a function of r for different rotation rates ($A_E = 0$ for 3D isotropic turbulence and $A_E = 1$ for 2D3C turbulence).

where $E(\mathbf{r},t) = \langle(\delta\mathbf{u}')^2\rangle_{\mathbf{X},E}$ and

$$\Pi(\mathbf{r},t) = \frac{1}{4}\boldsymbol{\nabla}_\mathbf{r}\cdot\langle(\delta\mathbf{u}')^2\delta\mathbf{u}'\rangle_{\mathbf{X},E} \tag{7}$$

is the energy transfer term in scale-space (with $\boldsymbol{\nabla}_\mathbf{r}\cdot$ the divergence with respect to the vector separation $\mathbf{r}$), and $\epsilon = \nu\langle(\partial_i u_j' + \partial_j u_i')^2\rangle_{\mathbf{X},E}/2$ the instantaneous energy dissipation rate. Here, the brackets $\langle\cdot\rangle_{\mathbf{X},E}$ represent spatial and ensemble average. Similar to the angular average $\mathcal{E}(r)$ of $E(\mathbf{r})$, which represents the cumulative energy from scale 0 to r, the angular average $\mathcal{P}(r) = (4\pi)^{-1}\int_{\theta=0}^{\pi}\int_{\varphi=0}^{2\pi}\Pi(r,\theta,\varphi)\sin\theta d\theta d\varphi$ can be interpreted as the energy flux from scales smaller than $r = |\mathbf{r}|$ towards scales larger than r. For isotropic turbulence, the sign of $\Pi(\mathbf{r}) = \mathcal{P}(r)$, therefore, gives the direction of the energy cascade, forward if $\Pi(\mathbf{r}) < 0$ and inverse if $\Pi(\mathbf{r}) > 0$. In the inhomogeneous case, additional terms corresponding to advection of energy between different regions of the turbulent flow appear in Eq. (6). In the absence of body forces, which are not relevant in our experiment, advection of energy from outside the control domain is the only source term to sustain stationary turbulence: we will come back to this point in Sec. V.

In the following, we focus on stationary turbulence, and we take $\partial_t E = 0$ in Eq. (6). The ensemble average $\langle\cdot\rangle_E$ can be therefore replaced by a temporal average, which we denote as $\bar{\cdot}$. For axisymmetric turbulence, it is convenient to decompose the flux (7) into its perpendicular (horizontal) and parallel (vertical) contributions,

$$\begin{aligned}\Pi(\mathbf{r}) &= \Pi_\perp(\mathbf{r}) + \Pi_\parallel(\mathbf{r})\\ &= \frac{1}{4}\boldsymbol{\nabla}_\perp\cdot\langle\overline{(\delta\mathbf{u}')^2\delta\mathbf{u}_\perp'}\rangle + \frac{1}{4}\nabla_\parallel\langle\overline{(\delta\mathbf{u}')^2\delta u_\parallel'}\rangle,\end{aligned} \tag{8}$$

with $\boldsymbol{\nabla}_\perp = \mathbf{e}_x\partial_{r_x} + \mathbf{e}_y\partial_{r_y}$ and $\nabla_\parallel = \partial_{r_z}$. We focus in the following on pure horizontal separations by setting $r_\parallel \equiv r_z = 0$, and we perform an azimuthal average over φ to improve the statistics. Both contributions from Eq. (8) are then functions of the horizontal separation $r_\perp$ only.

For strictly 2D turbulence, vertical invariance implies $\Pi_\parallel = 0$. The vertical flux $\Pi_\parallel$ cannot be measured here, because we cannot access the vertical derivative $\nabla_\parallel$ from measurements in the horizontal plane. In principle, one could use the data in the vertical plane, but we found significant departure from axisymmetry for third-order quantities (although second-order quantities are found nearly axisymmetric, as shown in Fig. 3(a)). This lack of axisymmetry can be circumvented by performing an azimuthal average with respect to φ, which is possible in the horizontal plane only.

For the non-rotating experiment, Fig. 5 shows that the horizontal flux $\Pi_\perp(r_\perp)$ is negative at all scales, as expected for a direct energy cascade from large to small scales, with $\Pi_\perp \to 0$ as $r_\perp \to 0$ in the viscous range. The observed 10% decrease in $|\Pi_\perp(r_\perp)|$ for $r_\perp$ beyond 15 mm might be due to the vertical invariance of the forcing device: the large scales are slightly 2D (see Fig. 4), which may enhance the inverse energy transfers and reduce the direct ones. However, as discussed in Sec. V, boundary-driven flows display some inhomogeneity at large scale, which challenges the

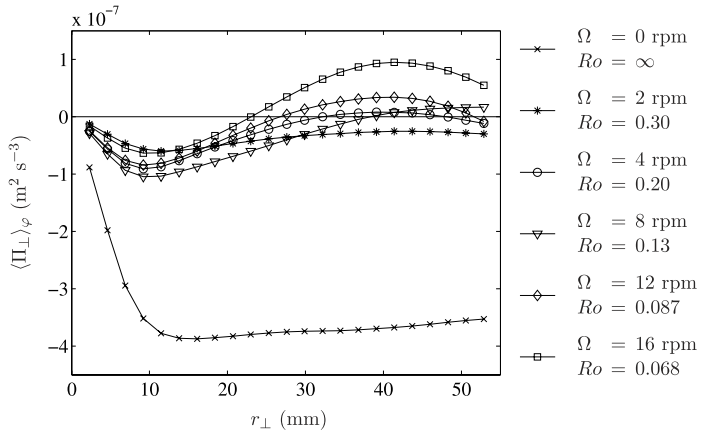

FIG. 5. Azimuthal average of the horizontal energy flux, $\langle \Pi_\perp \rangle_\varphi$, as a function of horizontal separation $r_\perp$ and for various rotation rates Ω. These data are computed from measurements in the horizontal plane. A negative value (respectively, positive) corresponds to a direct (respectively, inverse) energy transfer.

interpretation of $\Pi_\perp$ in terms of pure scale-by-scale energy transfers. Therefore, we do not elaborate more on the behavior of $\Pi_\perp$ at scales larger than $r_\perp > 40$ mm (see details in Sec. V).

For increasing rotation rates, $\Pi_\perp(r_\perp)$ strongly decreases at intermediate scales in absolute value, and eventually a change of sign is observed at large scales beyond 4 rpm ($Ro \simeq 0.2$). This indicates the onset of an inverse energy cascade, which spreads towards smaller scales as Ω increases. Remarkably, the double cascade persists even at the largest rotation rate ($\Omega = 16$ rpm, $Ro \simeq 0.068$), with the coexistence of an inverse flux ($\Pi_\perp > 0$) at large scales and a direct flux ($\Pi_\perp < 0$) at small scales. This implies that, on average, energy must be supplied at intermediate scales (of the order of 25 mm for $\Omega = 16$ rpm): we return to this point in Sec. V.

C. Horizontal transfers of horizontal and vertical energy

The energy flux $\Pi_\perp(r_\perp)$ contains both the horizontal flux of horizontal energy, $(\delta \mathbf{u}'_\perp)^2$, and the horizontal flux of vertical energy, $(\delta u'_\parallel)^2$. To get further insight into the double cascade observed in Fig. 5, we decompose $\Pi_\perp$ as follows:

$$\Pi_\perp(r_\perp) = \Pi_\perp^{(\perp)}(r_\perp) + \Pi_\perp^{(\parallel)}(r_\perp) \tag{9}$$

$$= \frac{1}{4}\boldsymbol{\nabla}_\perp \cdot \langle \overline{(\delta \mathbf{u}'_\perp)^2 \delta \mathbf{u}'_\perp} \rangle + \frac{1}{4}\boldsymbol{\nabla}_\perp \cdot \langle \overline{(\delta u'_\parallel)^2 \delta \mathbf{u}'_\perp} \rangle. \tag{10}$$

These two contributions are shown in Fig. 6. Interestingly, we observe that $\Pi_\perp^{(\parallel)}$ remains negative at all rotation rates, indicating that vertical energy is always transferred from large to small horizontal scales, whereas $\Pi_\perp^{(\perp)}$ becomes positive as the rotation rate is increased, a signature of the onset of an inverse cascade for the horizontal energy. In the non-rotating case, this negative flux $\Pi_\perp^{(\parallel)}$ is compatible with the classical direct cascade framework of 3D turbulence. By contrast, in the presence of rotation, for the scales at which the inverse cascade of $(\delta \mathbf{u}'_\perp)^2$ is observed, the direct cascade of $(\delta u'_\parallel)^2$ is reminiscent of the behavior of a passive scalar advected by a two-dimensional flow; the stretching and folding of the vertical velocity by the horizontal flow produce small scales through filamentation, inducing a direct horizontal cascade of vertical velocity.[7,42,54] We provide in Sec. V further assessment of this picture.

Figure 6 also indicates that the horizontal flux of vertical energy $\Pi_\perp^{(\parallel)}$ is a significant contribution to $\Pi_\perp$ for all rotation rates. For the low rotation rate $\Omega = 2$ rpm ($Ro = 0.3$), although a significant inverse cascade already takes place at large scale for the horizontal energy ($\Pi_\perp^{(\perp)} > 0$), it is hidden by a stronger direct cascade of vertical energy ($\Pi_\perp^{(\parallel)} < 0$). This results in an overall direct cascade of total energy ($\Pi_\perp < 0$). For larger rotation rates, the inverse cascade of horizontal energy becomes dominant, eventually leading to $\Pi_\perp^{(\perp)} > 0$ at all scales for $\Omega \geq 12$ rpm. The crossover scale

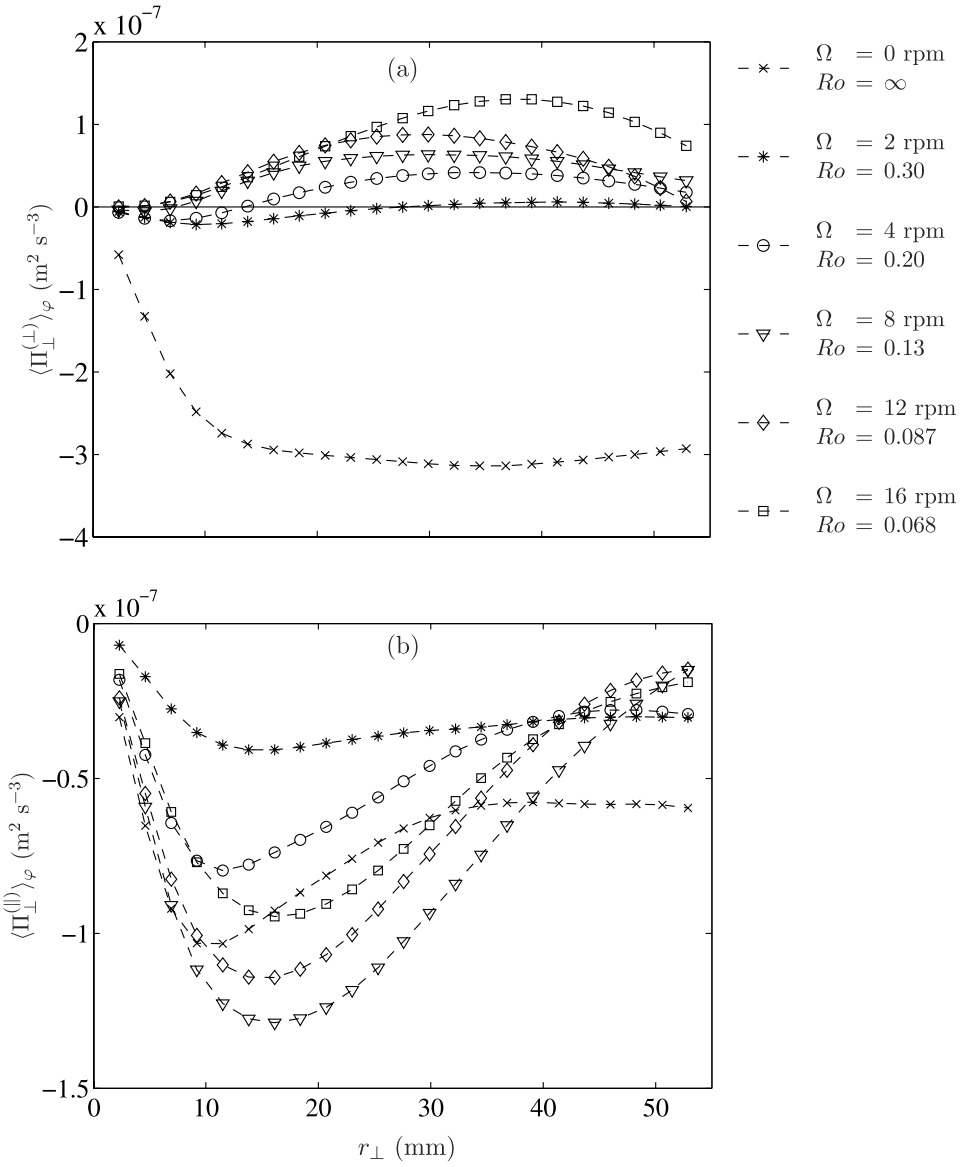

FIG. 6. Horizontal flux of (a) horizontal energy $\Pi_\perp^{(\perp)}(r_\perp)$, and (b) vertical energy, $\Pi_\perp^{(\parallel)}(r_\perp)$, at various rotation rates Ω. A negative flux corresponds to a direct energy transfer (from large to small scales) whereas a positive flux corresponds to an inverse energy transfer.

separating the direct and inverse cascades of horizontal energy rapidly decreases as Ω increases, going from ∼ 30 mm for Ω = 2 rpm to zero for Ω ≥ 12 rpm (and then $\Pi_\perp^{(\perp)} > 0$ over the whole range of scales).

V. SCALE-BY-SCALE ENERGY BUDGET

A. Inhomogeneous Kármán-Howarth-Monin equation

To provide a physical interpretation for the sign of the scale-by-scale energy flux $\Pi(\mathbf{r})$, we must describe carefully the energy input in the experiment and in particular, its scale dependence. In numerical simulations of homogeneous stationary turbulence, this source term usually originates from a random body force acting on a narrow range of scales. By contrast, here the fluid motion is driven by moving solid boundaries, so the energy injection in a given control volume away from the forcing must originate from the transport of energy through the surface delimiting the control volume. Since a non-trivial stationary state cannot be described by the homogeneous non-forced

KHM equation (6), which contains no source term, we must consider explicitly the effects of the inhomogeneities in the following.

We consider here the inhomogeneous generalization of the KHM equation proposed by Hill.[44] We briefly recall the derivation of this equation, with the addition of the Coriolis force. Let us start from the incompressible Navier-Stokes (NS) equation in the rotating frame

$$\partial_t \mathbf{u} + (\mathbf{u}\cdot\nabla)\mathbf{u} = -\boldsymbol{\nabla} p - 2\boldsymbol{\Omega}\times\mathbf{u} + \nu\boldsymbol{\nabla}^2\mathbf{u}, \tag{11}$$

with p the pressure modified by the centrifugal force and normalized by the fluid density. Taking the difference between points $\mathbf{x}_B = \mathbf{X} + \mathbf{r}/2$ and $\mathbf{x}_A = \mathbf{X} - \mathbf{r}/2$ and taking the scalar product with $\delta\mathbf{u} = \mathbf{u}_B - \mathbf{u}_A$ yield

$$\begin{aligned}\partial_t(\delta\mathbf{u})^2 + \boldsymbol{\nabla}_\mathbf{r}\cdot(\delta\mathbf{u})^2\delta\mathbf{u} =& 2\nu\boldsymbol{\nabla}_\mathbf{r}^2(\delta\mathbf{u})^2 - 4\tilde{\epsilon}\\ &+ \boldsymbol{\nabla}_\mathbf{X}\cdot\left[-(\delta\mathbf{u})^2\tilde{\mathbf{u}} - 2\delta p\delta\mathbf{u} + \frac{\nu}{2}\boldsymbol{\nabla}_\mathbf{X}\left((\delta\mathbf{u})^2 - 8\tilde{\boldsymbol{\tau}}\right)\right],\end{aligned} \tag{12}$$

with $\delta p = p_B - p_A$. Quantities with $\tilde{\cdot}$ denote the average between the two points: $\tilde{\mathbf{u}} = (\mathbf{u}_A + \mathbf{u}_B)/2$, $\tilde{p} = (p_A + p_B)/2$, and $\tilde{\epsilon} = (\epsilon_A + \epsilon_B)/2$, with $\epsilon = \frac{\nu}{2}(\partial_j u_i + \partial_i u_j)^2$ the local energy dissipation rate. The last term of the equation involves the velocity correlation tensor $\tilde{\boldsymbol{\tau}} = (\boldsymbol{\tau}_A + \boldsymbol{\tau}_B)/2$, with $\tau_{ij} = u_i u_j$. Importantly, all the terms in Eq. (12) are functions of $(\mathbf{X},\mathbf{r},t)$, and the nonlinear term splits into a scale-to-scale transfer term (divergence with respect to separation $\mathbf{r}$) and a transport term (divergence with respect to mid-point $\mathbf{X}$).

We consider both the spatial average $\langle\cdot\rangle_\mathbf{X}$ over a control volume V_X and the ensemble average $\langle\cdot\rangle_E$ of Eq. (12). Using the divergence theorem to express the inhomogeneous terms as a flux through the closed surface S_X delimiting the control volume V_X, we obtain

$$\partial_t\langle(\delta\mathbf{u})^2\rangle_{\mathbf{X},E} + \boldsymbol{\nabla}_\mathbf{r}\cdot\langle(\delta\mathbf{u})^2\delta\mathbf{u}\rangle_{\mathbf{X},E} = 2\nu\boldsymbol{\nabla}_\mathbf{r}^2\langle(\delta\mathbf{u})^2\rangle_{\mathbf{X},E} - 4\langle\tilde{\epsilon}\rangle_{\mathbf{X},E} + \Phi_{\text{inh}}(\mathbf{r}), \tag{13}$$

where the flux term writes

$$\Phi_{\text{inh}}(\mathbf{r}) = \frac{1}{V_X}\oint_{S_X}\left(-\langle(\delta\mathbf{u})^2\tilde{\mathbf{u}}\rangle_E - 2\langle\delta p\,\delta\mathbf{u}\rangle_E + \frac{\nu}{2}\boldsymbol{\nabla}_\mathbf{X}\langle(\delta\mathbf{u})^2 - 8\tilde{\boldsymbol{\tau}}\rangle_E\right)\cdot d\mathbf{S}_\mathbf{X}. \tag{14}$$

The unit vector, $d\mathbf{S}_\mathbf{X}$, is directed outward of the control volume by convention. In the scale-by-scale budget (13), the energy input (or output) at a given scale $\mathbf{r}$ is ensured by the term $\Phi_{\text{inh}}(\mathbf{r})$, which originates from the inhomogeneities in the pressure and velocity statistics. For homogeneous turbulence, one has $\langle\tilde{\epsilon}\rangle_{\mathbf{X},E} = \langle\epsilon\rangle_{\mathbf{x},E}$ and $\Phi_{\text{inh}} = 0$, so Eq. (13) becomes the usual KHM equation (6).

The flux term (14) contains three contributions:

(i) $\oint -\langle(\delta\mathbf{u})^2\tilde{\mathbf{u}}\rangle_E\cdot d\mathbf{S}_\mathbf{X}$ is the flux of cumulative energy $(\delta\mathbf{u})^2$ through the surface S_X due to advection by the velocity $\tilde{\mathbf{u}} = (\mathbf{u}_A + \mathbf{u}_B)/2$. It is positive when $\tilde{\mathbf{u}}$ is directed into the control volume. Note that this term takes a simple form in the classical configuration of a wind-tunnel: the transport velocity $\tilde{\mathbf{u}}$ is essentially replaced by the uniform mean velocity $\mathbf{U_0}$, and the energy flux per unit surface becomes $\oint -\langle(\delta\mathbf{u})^2\rangle_E\,\mathbf{U_0}\cdot d\mathbf{S}_\mathbf{X}$. The inward flux of $(\delta\mathbf{u})^2$ through the upstream face of the control volume is larger than the outward flux through the downstream face, hence a net flux of kinetic energy into the control volume, which is dissipated at the same rate by viscosity. By contrast, the time-averaged velocity is negligible in the present experiment when $\Omega > 0$, and energy input in the control volume proceeds through advection of turbulent kinetic energy by the turbulent velocity itself.

(ii) The term $\oint -2\langle\delta p\,\delta\mathbf{u}\rangle_E\cdot d\mathbf{S}_\mathbf{X}$ originates from the work of the pressure force through the boundary of the control volume. This term cannot be measured experimentally. However, under the assumption of local axisymmetry and homogeneity at small scale, this term is expected to be much smaller than the advection term for scales much smaller than the characteristic scale of inhomogeneity (see Appendix).

(iii) The diffusion term in Eq. (14) is weak because it corresponds to derivatives with respect to $\mathbf{X}$, which are negligible compared to derivatives with respect to $\mathbf{r}$ at small scales for weakly inhomogeneous turbulence (see Appendix).

We stress the fact that the present inhomogeneous KHM equation has a clear interpretation for scales smaller than the characteristic scale of inhomogeneity, for which the contribution from the pressure can be neglected. This is because the two-point velocity-pressure correlation can be written either as a divergence with respect to $\mathbf{X}$ or with respect to $\mathbf{r}$, so the interpretation of Π as the only scale-by-scale transfer term becomes questionable when the velocity-pressure correlation is significant, i.e., for large (inhomogeneous) scales. In the following, we show that interesting modifications of the energy transfers by global rotation occur in the range of scales for which the velocity-pressure correlation is indeed negligible.

B. Scale-by-scale budget for 2D3C flows

For rapid global rotation, the flow becomes weakly dependent on the vertical coordinate far from the horizontal boundaries. In the following, we assume a purely 2D3C velocity field in the bulk of the flow, and write separate equations for the evolution of the horizontal and vertical energies. In this 2D limit, the same analysis as in Sec. V A, but performed here on the horizontal components of Eq. (11) only, yields

$$\partial_t \langle (\delta \mathbf{u}_\perp)^2 \rangle_{\mathbf{X},E} + \boldsymbol{\nabla}_\mathbf{r} \cdot \langle (\delta \mathbf{u}_\perp)^2 \delta \mathbf{u}_\perp \rangle_{\mathbf{X},E} = 2\nu \boldsymbol{\nabla}_\mathbf{r}^2 \langle (\delta \mathbf{u}_\perp)^2 \rangle_{\mathbf{X},E} - 4\langle \tilde{\epsilon}_\perp^{(\perp)} \rangle_{\mathbf{X},E} + \Phi_{\mathrm{inh}}^{(\perp)}(\mathbf{r}) \tag{15}$$

with

$$\Phi_{\mathrm{inh}}^{(\perp)}(\mathbf{r}) = \frac{1}{V_X} \oint_{S_X} \left(-\langle (\delta \mathbf{u}_\perp)^2 \tilde{\mathbf{u}}_\perp \rangle_E - 2\langle \delta p \, \delta \mathbf{u}_\perp \rangle_E + \frac{\nu}{2} \boldsymbol{\nabla}_\mathbf{X} \langle (\delta \mathbf{u}_\perp)^2 - 8\tilde{\boldsymbol{\tau}}_\perp \rangle_E \right) \cdot d\mathbf{S}_\mathbf{X}, \tag{16}$$

where the subscript $\perp$ in $\delta \mathbf{u}_\perp$, $\tilde{\mathbf{u}}_\perp$, and $\tilde{\boldsymbol{\tau}}_\perp$ indicates that only the horizontal velocity components are considered, and the $\tilde{\cdot}$ indicates that the quantity is a mid-point average. This equation is an inhomogeneous version of the KHM equation for the horizontal flow only. Similarly, from the vertical component of the NS equation, one can also compute the budget for the vertical energy,

$$\partial_t \langle (\delta u_\parallel)^2 \rangle_{\mathbf{X},E} + \boldsymbol{\nabla}_\mathbf{r} \cdot \langle (\delta u_\parallel)^2 \delta \mathbf{u}_\perp \rangle_{\mathbf{X},E} = 2\nu \boldsymbol{\nabla}_\mathbf{r}^2 \langle (\delta u_\parallel)^2 \rangle_{\mathbf{X},E} - 4\langle \tilde{\epsilon}_\perp^{(\parallel)} \rangle_{\mathbf{X},E} + \Phi_{\mathrm{inh}}^{(\parallel)}(\mathbf{r}) \tag{17}$$

with

$$\Phi_{\mathrm{inh}}^{(\parallel)}(\mathbf{r}) = \frac{1}{V_X} \oint_{S_X} \left(-\langle (\delta u_\parallel)^2 \tilde{\mathbf{u}}_\perp \rangle_E + \frac{\nu}{2} \boldsymbol{\nabla}_\mathbf{X} \langle (\delta u_\parallel)^2 - 8\tilde{\tau}_\parallel \rangle_E \right) \cdot d\mathbf{S}_\mathbf{X}, \tag{18}$$

where the subscript $\parallel$ refers to the vertical component of the velocity. This equation is an inhomogeneous generalization of Yaglom's equation for a passive scalar field:[42,54] the tracer $u_\parallel$ enters and leaves the control volume through advection by the horizontal velocity $\tilde{\mathbf{u}}_\perp$. Inside the control volume, nonlinearities transfer the vertical energy between different scales $\mathbf{r}$ through stretching and folding by the horizontal field, and viscosity damps the strong gradients created by these processes. We stress the fact that Eq. (17) does not involve pressure: all the terms in this equation can be accessed through stereo-PIV measurements in a horizontal plane.

C. Experimental assessment of the horizontal and vertical kinetic energy budget

In the following, we focus on the highest rotation rate, $\Omega = 16$ rpm ($Ro = 0.068$), for which we expect the turbulent flow to reach a quasi-2D3C state, so that we can apply the $\perp$ vs. $\parallel$ decomposition of the inhomogeneous KHM equation derived above. Note that in this case, the ensemble-averaged flow is negligible (see Table I), so we simply consider $\mathbf{u} = \mathbf{u}'$.

We consider for the control domain a centered square in the square PIV field, with a maximum separation $r_\perp = 60$ mm. One can think about the corresponding control volume as a parallelepiped of arbitrary vertical length, with zero fluxes through the top and bottom boundaries. Because turbulence is stationary in the experiment, we replace the ensemble average $\langle \cdot \rangle_E$ by a temporal one, which we denote $\bar{\cdot}$.

1. Horizontal kinetic energy budget

Let us first consider the energy budget for the horizontal kinetic energy. In statistically steady state, Eq. (15) writes

$$\tilde{\epsilon}_\perp^{(\perp)} = -\Pi_\perp^{(\perp)} + D_\perp^{(\perp)} + A_\perp^{(\perp)} + W_p + NT^{(\perp)} \tag{19}$$

with

$$\epsilon_\perp^{(\perp)} = \frac{\nu}{2}\langle\overline{(\partial_\alpha u_\beta + \partial_\beta u_\alpha)^2}\rangle, \qquad D_\perp^{(\perp)} = \frac{\nu}{2}\boldsymbol{\nabla}_\perp^2\langle\overline{(\delta\mathbf{u}_\perp)^2}\rangle, \tag{20}$$

$$A_\perp^{(\perp)} = -\frac{1}{4V_X}\oint_{S_X}\overline{(\delta\mathbf{u}_\perp)^2\tilde{\mathbf{u}}_\perp}\cdot d\mathbf{S}_\mathbf{X}, \qquad W_p = -\frac{1}{2V_X}\oint_{S_X}\overline{\delta p\delta\mathbf{u}_\perp}\cdot d\mathbf{S}_X. \tag{21}$$

For sake of simplicity, $\langle\overline{\tilde{\epsilon}_\perp^{(\perp)}}\rangle$ and $\langle\overline{\epsilon_\perp^{(\perp)}}\rangle$ will be simply noted as $\tilde{\epsilon}_\perp^{(\perp)}$ and $\epsilon_\perp^{(\perp)}$ in the following.

The horizontal flux of horizontal energy $\Pi_\perp^{(\perp)}$ is defined in Eq. (9), and $\epsilon_\perp^{(\perp)}$ is the dissipation of the horizontal velocity by the horizontal shearing (with summation over $\alpha, \beta = x, y$), such that $D_\perp^{(\perp)}(r_\perp \to 0) = \epsilon_\perp^{(\perp)}$. In Eq. (19), $NT^{(\perp)}$ contains the viscous contribution from inhomogeneities, which we neglect in the following (it is at least 2 orders of magnitude smaller than the other terms), and the vertical transport, which we cannot compute from 2D3C measurements. Here, $\langle.\rangle$ still denotes the spatial average over $\mathbf{X} \in V_X$. Under the assumption of weak inhomogeneity, the velocity-pressure flux, W_p, is expected to be small compared to the transport $A_\perp^{(\perp)}$ (see Appendix), and the remaining terms in Eq. (19) can be readily computed from the 2D-3C PIV measurements.

Figure 7(a) shows the three measurable terms of the rhs of Eq. (19) together with their sum, $S^{(\perp)} = -\Pi_\perp^{(\perp)} + D_\perp^{(\perp)} + A_\perp^{(\perp)}$. These terms are averaged over the azimuthal angle φ. We observe a good agreement between $\tilde{\epsilon}_\perp^{(\perp)}$ and the sum $S^{(\perp)}$ for scales smaller than 40 mm, to within 20%. The approximation of locally homogeneous and axisymmetric turbulence, with a negligible velocity-pressure flux W_p, thus seems valid at small scales. For larger scales, we observe a significant departure between $\tilde{\epsilon}_\perp^{(\perp)}$ and $S^{(\perp)}$, up to a factor of 2 at $r_\perp \simeq 60$ mm: for such large scales, the turbulent flow cannot be considered as locally homogeneous anymore; the non-measured pressure term W_p cannot be neglected, so the interpretation of $\Pi_\perp^{(\perp)}$ as a scale-by-scale energy transfer becomes incorrect.

Focusing on scales smaller than 40 mm, the advection of horizontal kinetic energy $A_\perp^{(\perp)}$ is the only source term in the energy budget. This source term is maximum at large scales, as expected, but it remains significant over the whole range of scales, suggesting a broad-band energy injection in this system. If $E(r_\perp)$ is interpreted as a cumulative energy for eddies of horizontal scale $r_\perp$ or less, the scale-by-scale energy density has the form $dE/dr_\perp$, so the corresponding forcing density is $dA_\perp/dr_\perp$. Since we observe $A_\perp \simeq r_\perp^{1.5}$ at intermediate scales, the forcing density scales as $r_\perp^{0.5}$, and it remains significant over the range of scales considered here. This broad-band energy injection is an important feature of boundary-forced inhomogeneous turbulence and is in strong contrast with the narrow-band forcing often considered in numerical simulations of homogeneous rotating turbulence.

Although the inverse cascade is evident from this horizontal energy budget, it must be noted that its magnitude remains moderate: $\Pi_\perp^{(\perp)}$ is never the dominant contribution to the budget, even at the crossover between the viscous diffusion and the forcing. A well developed inverse cascade over a wide range of quasi-homogeneous scales at much larger Reynolds number would be characterized by $\Pi_\perp^{(\perp)} \simeq A_\perp \gg \tilde{\epsilon}_\perp^{(\perp)}$. Here, the amount of energy transferred to large scales remains at the best of the same order as the small-scale viscous dissipation $\tilde{\epsilon}_\perp^{(\perp)}$.

2. Vertical kinetic energy budget

We now consider the vertical kinetic energy budget using Eq. (17) in statistically steady state

$$\tilde{\epsilon}_\perp^{(\parallel)} = -\Pi_\perp^{(\parallel)} + D_\perp^{(\parallel)} + A_\perp^{(\parallel)} + NT^{(\parallel)}, \tag{22}$$

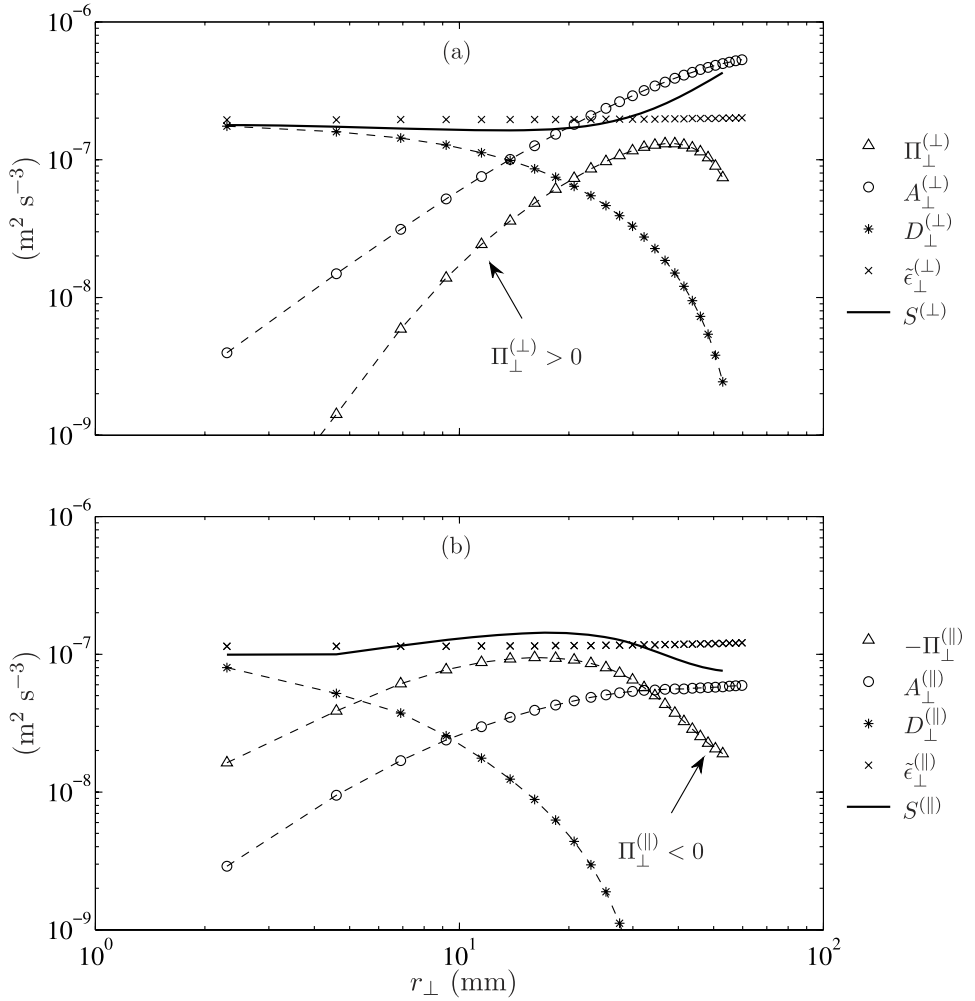

FIG. 7. Scale-by-scale energy budget in the horizontal plane, for (a) the horizontal kinetic energy $(\delta \mathbf{u}'_\perp)^2$ and (b) the vertical kinetic energy $(\delta u'_\parallel)^2$: Horizontal flux $\Pi_\perp^{(\perp)}$ (respectively, $\Pi_\perp^{(\parallel)}$), transport $A_\perp^{(\perp)}$ (respectively, $A_\perp^{(\parallel)}$), diffusion $D_\perp^{(\perp)}$ (respectively, $D_\perp^{(\parallel)}$), and dissipation rate $\tilde{\epsilon}_\perp^{(\perp)}$ (respectively, $\tilde{\epsilon}_\perp^{(\parallel)}$) of horizontal energy (respectively, vertical energy). $S^{(\perp)} = -\Pi_\perp^{(\perp)} + D_\perp^{(\perp)} + A_\perp^{(\perp)}$ and $S^{(\parallel)} = -\Pi_\perp^{(\parallel)} + D_\perp^{(\parallel)} + A_\perp^{(\parallel)}$ are the sums of the measurable right-hand side terms in the energy budgets (19) and (22), respectively. In (a), the horizontal flux of horizontal energy is inverse, from small to large scales ($\Pi_\perp^{(\perp)} > 0$), whereas in (b) the horizontal flux of vertical energy is direct, from large to small scales ($\Pi_\perp^{(\parallel)} < 0$).

where

$$\epsilon_\perp^{(\parallel)} = \nu \langle \overline{(\nabla_\perp u_\parallel)^2} \rangle, \qquad D_\perp^{(\parallel)} = \frac{\nu}{2} \boldsymbol{\nabla}_\perp^2 \langle \overline{(\delta u_\parallel)^2} \rangle, \tag{23}$$

$$A_\perp^{(\parallel)} = -\frac{1}{4V_X} \oint_{S_X} \overline{(\delta u_\parallel)^2 \tilde{\mathbf{u}}_\perp} \cdot d\mathbf{S}_\mathbf{X}. \tag{24}$$

For sake of simplicity, $\langle \overline{\tilde{\epsilon}_\perp^{(\parallel)}} \rangle$ and $\langle \overline{\epsilon_\perp^{(\parallel)}} \rangle$ will be simply noted as $\tilde{\epsilon}_\perp^{(\parallel)}$ and $\epsilon_\perp^{(\parallel)}$ in the following.

The horizontal flux of vertical energy $\Pi_\perp^{(\parallel)}$ is defined in Eq. (9) and $\epsilon_\perp^{(\parallel)}$ is the dissipation of the vertical velocity by the horizontal shearing, with $D_\perp^{(\parallel)}(r_\perp \to 0) = \epsilon_\perp^{(\parallel)}$. The viscous contribution from inhomogeneities $NT^{(\parallel)}$ is once again discarded for simplicity. A key feature of Eq. (22) is that it does not involve pressure: All the terms can therefore be readily measured from stereo-PIV measurements and the equation should be satisfied for scales at which quasi-two-dimensionality holds.

The terms of Eq. (22) are shown in Fig. 7(b), together with the sum of the right-hand side terms $S^{(\parallel)} = -\Pi_\perp^{(\parallel)} + D_\perp^{(\parallel)} + A_\perp^{(\parallel)}$. Once again, there is a good overall agreement between $\tilde{\epsilon}_\perp^{(\parallel)}$ and $S^{(\parallel)}$ for $r_\perp \leq 40$ mm, clearly indicating a direct cascade of vertical kinetic energy. The picture here is simpler than the horizontal energy budget: the vertical energy is advected into the control domain

($A_\perp^{(\|)}$), it is transferred by the nonlinearities to smaller scales ($\Pi_\perp^{(\|)}$), and it is dissipated at small scales by viscosity ($D_\perp^{(\|)}$). We can assume that the instabilities of the vortex dipoles generated near the flaps and away from the measurement domain are the source of vertical energy at large scale. Note that for very large Reynolds numbers, an inertial range of scales $r_\perp$ with constant flux of vertical energy is expected, characterized by $\Pi_\perp^{(\|)}(r_\perp) = -\epsilon_\perp^{(\|)}$. Although this is not achieved at the moderate Reynolds number of this experiment, we can, nonetheless, define a significant range of scales, centered around 10-20 mm, for which $-\Pi_\perp^{(\|)}$ is close to $\epsilon_\perp^{(\|)}$ within 20%.

3. Large-scale energy dissipation

For the largest rotation rate, the scenario of a double cascade, towards small scales for the vertical energy and towards large scales for the horizontal energy, is well established from Figs. 7(a) and 7(b), at least for scales $r_\perp \leq 40$ mm. At larger scales, the departure between $\tilde{\epsilon}_\perp^{(\perp)}$ and $S^{(\perp)}$ may originate both from a departure from two-dimensionality or from the non-measured velocity-pressure correlation. Although less pronounced, there is also a discrepancy between $\tilde{\epsilon}_\perp^{(\|)}$ and $S^{(\|)}$ at large scale, which indicates a departure from a pure 2D3C state and possibly an influence of the horizontal top and bottom boundaries.

We are therefore left with the following question: what sink of energy absorbs the inverse horizontal energy flux at large scales? A first candidate is Ekman friction on the horizontal boundaries. Assuming that the flow is 2D3C in the central region of the tank, we consider the laminar scaling for the Ekman layer thickness, $\delta_E \simeq \sqrt{\nu/\Omega}$, and we deduce a typical energy dissipation $\epsilon_\Omega = \sqrt{\nu\Omega}u_\perp^2/H$, where H is the water depth and $u_\perp$ is the characteristic horizontal velocity. For $\Omega = 16$ rpm, we obtain $\epsilon_\Omega \simeq 10^{-7}$ m^2 s^{-3}, which turns out to be of the order of the other terms of Eq. (19) (see Fig. 7). A significant fraction of the input horizontal kinetic energy could therefore be dissipated at large scale through Ekman friction. However, this order of magnitude strongly relies on the boundary layers being laminar, which seems questionable in the present experiment.

As an alternate explanation for the energy sink at large scales, we may invoke a feedback of the large-scale flow on the forcing device; the large-scale flow resulting from the inverse cascade induces large-scale pressure forces that transfer some kinetic energy back to the flaps, reducing the overall energy input in the system. In this scenario, the flaps inject energy at intermediate scales and receive energy from the large-scale flow through the work of the pressure forces. In the framework of Eq. (19), the corresponding sink of energy is taken into account by the spatial flux and pressure terms: energy at large scales is transferred outside of the control volume, towards the flaps. Unfortunately, testing this scenario would require a precise measurement of the energy input by the flaps and is beyond the scope of the present study.

VI. CONCLUSION

In this paper, we provide experimental evidence of a double energy cascade, direct at small scales and inverse at large scales, in a forced rotating turbulence experiment. Since turbulence is statistically steady, the inverse cascade does not manifest through a temporal growth of kinetic energy, but it is characterized by a change of sign of the scale-by-scale energy flux. As the rotation rate is increased, the inverse cascade becomes more pronounced and spreads down to the smallest scales. As compared to previous experimental observations of an inverse cascade in rotating turbulence,[37–39] here we provide for the first time a direct scale-by-scale measurement of the energy transfers in the horizontal plane. This allows us to distinguish between the horizontal transfers of vertical and horizontal kinetic energies. At the largest rotation rate, this double cascade of the total energy can be described as the superposition of an inverse cascade of horizontal energy and a direct cascade of vertical energy. This is consistent with the 2D3C dynamics expected in the limit of small Rossby numbers, with the vertical velocity behaving as a passive scalar transported by the horizontal flow.

Contrary to numerical simulations, in which energy is usually supplied by a homogeneous body force acting on a prescribed narrow range of wave numbers, in most experiments and in many

natural flows, energy is supplied at the boundaries. For a control domain away from those boundaries, energy is advected from the boundaries into the domain. This spatial flux of energy, which is strongly related to the inhomogeneities of the turbulent statistics, results in an effective broad-band energy injection term. In order to interpret the energy transfers in such an experiment, it is therefore necessary to separate the contributions from the spatial transport and from the scale-by-scale transfers. We have performed this analysis using the inhomogeneous generalization of the KHM equation proposed by Hill,[44] and we have measured directly the energy transport term for scales at which the velocity-pressure correlations can be neglected (quasi-homogeneous approximation). Because of this effective broad-band forcing, the inversion scale, which separates the direct and inverse cascades, is not directly prescribed by the geometry of the forcing device and decreases with the imposed rotation rate. Modelling this inversion scale as a function of the Rossby number and forcing geometry remains an open issue of first interest for flows of oceanic and atmospheric relevance, such as convectively driven rotating flows.

ACKNOWLEDGMENTS

We acknowledge P. Augier, P. Billant, and J.-M. Chomaz for kindly providing the flap apparatus; and A. Aubertin, L. Auffray, C. Borget, and R. Pidoux for their experimental help. This work is supported by the ANR Grant No. 2011-BS04-006-01 "ONLITUR". The rotating platform "Gyroflow" was funded by the "Triangle de la Physique". FM would like to thank the Institut Universitaire de France for its support.

APPENDIX: LOCALLY HOMOGENEOUS AND AXISYMMETRIC TURBULENCE

In this appendix, we show how one can neglect the velocity-pressure correlations in the inhomogeneous KHM equations (13)–(15) under the assumptions of local homogeneity and axisymmetry.

Let us first consider that the turbulence is invariant to a reflection with respect to a horizontal plane (non-helical turbulence). Let us then denote as L_{inh} the typical scale of the inhomogeneity of the turbulence statistics, and focus on small separations $r \ll L_{\mathrm{inh}}$, or equivalently $r/L_{\mathrm{inh}} = \zeta \ll 1$. We decompose the velocity and pressure fields into $\mathbf{u} = \mathbf{V} + \mathbf{v}$ and $p = P + q$, where $\mathbf{V}$ and P contain the large scales of the flow and $\mathbf{v}$ and q are the small-scale fluctuations. One can think about $\mathbf{V}$ and P as coarse-grained versions of the velocity and pressure fields on a scale that is smaller than L_{inh} but larger than the range of scales, r, of interest. Then, $\mathbf{v} = \mathbf{u} - \mathbf{V}$ and $q = p - P$ are the small-scale remainders.

Local axisymmetry and homogeneity consist in assuming that the statistics of $\mathbf{v}$ and q are axisymmetric and homogeneous for separations $r \ll L_{\mathrm{inh}}$. Let us evaluate the different terms in the integrand of (14) under this assumption.

The pressure term decomposes into

$$\langle \delta\mathbf{u}\delta p\rangle = \langle \delta\mathbf{V}\delta P\rangle + \langle \delta\mathbf{V}\delta q\rangle + \langle \delta\mathbf{v}\delta P\rangle + \langle \delta\mathbf{v}\delta q\rangle . \tag{A1}$$

Because P and $\mathbf{V}$ evolve on a spatial scale $r \ll L_{\mathrm{inh}}$,

$$\delta P \simeq \mathbf{r}\cdot\boldsymbol{\nabla} P \sim \frac{r}{L_{\mathrm{inh}}} P = \zeta P. \tag{A2}$$

Similarly, $\delta\mathbf{V} \sim \zeta\mathbf{V}$. Hence, $\langle \delta\mathbf{V}\delta P\rangle = O(\zeta^2)$, $\langle \delta\mathbf{V}\delta q\rangle = O(\zeta)$, and $\langle \delta\mathbf{v}\delta P\rangle = O(\zeta)$. We deal with the term $\langle \delta\mathbf{v}\delta q\rangle$ using the assumption of local homogeneity and axisymmetry: under a rotation of angle π around a vertical axis passing through the mid-point $\mathbf{X}$, followed by a reflection with respect to the horizontal plane containing $\mathbf{X}$, $\mathbf{v}$ becomes $\mathbf{v}'$, $\mathbf{v}'$ becomes $-\mathbf{v}$, q' becomes q, and q becomes q'. Hence, $\delta\mathbf{v}\delta q$ becomes $-\delta\mathbf{v}\delta q$, so that on statistical average this quantity vanishes: $\langle \delta\mathbf{v}\delta q\rangle = 0$. As a consequence, the velocity-pressure correlation term $(\delta\mathbf{u}\delta p)$ is of order $O(\zeta)$ in the weakly inhomogeneous limit. We therefore expect $(\delta\mathbf{u}\delta p)$ to be negligible compared to the transport term $\langle(\delta\mathbf{u})^2\tilde{\mathbf{u}}\rangle$, which is of order $O(\zeta^0)$.

The viscous term in the integrand of (14) is of order

$$\nu \frac{\langle (\delta \mathbf{u})^2 \rangle}{L_{\text{inh}}} \sim \frac{\nu}{|\tilde{\mathbf{u}}| L_{\text{inh}}} \langle (\delta \mathbf{u})^2 \tilde{\mathbf{u}} \rangle . \tag{A3}$$

It is therefore negligible compared to the advective term of the integrand, because the Reynolds number based on L_{inh} is large. Note that because $r \ll L_{\text{inh}}$, derivatives with respect to r are much larger than derivatives with respect to X. In the ensemble average of Eq. (12), the "inhomogeneous" viscous contribution can be estimated as $\nu \boldsymbol{\nabla}_{\mathbf{X}}^2 \left((\delta \mathbf{u})^2 \right) \sim \zeta^2 \nu \boldsymbol{\nabla}_{\mathbf{r}}^2 \langle (\delta \mathbf{u})^2 \rangle$, hence it is negligible compared to the "homogeneous" viscous contribution $2\nu \boldsymbol{\nabla}_{\mathbf{r}}^2 \langle (\delta \mathbf{u})^2 \rangle$. For weakly inhomogeneous turbulence, one can therefore keep the latter while neglecting the former.

To conclude, the advective term, $\left((\delta \mathbf{u})^2 \tilde{\mathbf{u}} \right)$, is the dominant term in the integrand of Eq. (14). For weakly inhomogeneous turbulence, one can therefore retain only this term of the integrand, which ensures the injection of kinetic energy into the control volume.

[1] P. Sagaut and C. Cambon, *Homogeneous Turbulence Dynamics* (Cambridge University Press, Cambridge, 2008).
[2] P. A. Davidson, *Turbulence in Rotating, Stratified and Electrically Conducting Fluids* (Cambridge University Press, Cambridge, 2013).
[3] F. S. Godeferd and F. Moisy, "Structure and dynamics of rotating turbulence: A review of recent experimental and numerical results," Appl. Mech. Rev. (2015).
[4] U. Frisch, *Turbulence - The Legacy of A. N. Kolmogorov* (Cambridge University Press, Cambridge, 1995).
[5] R. Kraichnan, "Inertial ranges in two-dimensional turbulence," Phys. Fluids **10**, 1417 (1967).
[6] E. Lindborg, "Can the atmospheric kinetic energy spectrum be explained by two-dimensional turbulence?," J. Fluid Mech. **388**, 259 (1999).
[7] P. Tabeling, "Two-dimensional turbulence: A physicist approach," Phys. Rep. **362**, 1 (2002).
[8] H. Greenspan, *The Theory of Rotating Fluids* (Cambridge University Press, 1968).
[9] C. Cambon and L. Jacquin, "Spectral approach to non-isotropic turbulence subjected to rotation," J. Fluid Mech. **202**, 295 (1989).
[10] F. Waleffe, "Inertial transfers in the helical decomposition," Phys. Fluids A **5**, 677 (1993).
[11] L. M. Smith and F. Waleffe, "Transfer of energy to two-dimensional large scales in forced, rotating three-dimensional turbulence," Phys. Fluids **11**, 1608 (1999).
[12] F. Waleffe, "The nature of triad interactions in homogeneous turbulence," Phys. Fluids A **4**, 350 (1992).
[13] G. Bordes, F. Moisy, T. Dauxois, and P.-P. Cortet, "Experimental evidence of a triadic resonance of plane inertial waves in a rotating fluid," Phys. Fluids **24**, 014105 (2012).
[14] S. Galtier, "Weak inertial-wave turbulence theory," Phys. Rev. E **68**, 015301 (2003).
[15] C. Cambon, R. Rubinstein, and F. S. Godeferd, "Advances in wave turbulence: Rapidly rotating flows," New J. Phys. **6**, 73 (2004).
[16] L. Bourouiba, "Model of a truncated fast rotating flow at infinite Reynolds number," Phys. Fluids **20**, 075112 (2008).
[17] E. J. Hopfinger, F. K. Browand, and Y. Gagne, "Turbulence and waves in a rotating tank," J. Fluid Mech. **125**, 505 (1982).
[18] P. Bartello, O. Métais, and M. Lesieur, "Coherent structures in rotating three-dimensional turbulence," J. Fluid Mech. **273**, 1 (1994).
[19] L. Bourouiba and P. Bartello, "The intermediate Rossby number range and two-dimensional three-dimensional transfers in rotating decaying homogeneous turbulence," J. Fluid Mech. **587**, 139 (2007).
[20] L. Bourouiba, D. N. Straube, and M. L. Waite, "Non-local energy transfers in rotating turbulence at intermediate Rossby number," J. Fluid Mech. **690**, 129 (2012).
[21] F. Moisy, C. Morize, M. Rabaud, and J. Sommeria, "Decay laws, anisotropy and cyclone-anticyclone asymmetry in decaying rotating turbulence," J. Fluid Mech. **666**, 5 (2011).
[22] P. D. Mininni, A. Alexakis, and A. Pouquet, "Scale interactions and scaling laws in rotating flows at moderate Rossby numbers and large Reynolds numbers," Phys. Fluids **21**, 015108 (2009).
[23] P. D. Mininni and A. Pouquet, "Rotating helical turbulence. II. Intermittency, scale invariance, and structures," Phys. Fluids **22**, 035106 (2010).
[24] A. Pouquet and P. D. Mininni, "The interplay between helicity and rotation in turbulence: Implications for scaling laws and small-scale dynamics," Philos. Trans. R. Soc., A **368**, 1635 (2010), revue sur scaling, mais sans cascade inverse.
[25] A. Pouquet, A. Sen, D. Rosenberg, P. D. Mininni, and J. Baerenzung, "Inverse cascades in turbulence and the case of rotating flows," Phys. Scr. **T155**, 014032 (2013).
[26] Q. Chen, S. Chen, G. L. Eyink, and D. D. Holm, "Resonant interactions in rotating homogeneous three-dimensional turbulence," J. Fluid Mech. **542**, 139 (2005).
[27] L. M. Smith and Y. Lee, "On near resonances and symmetry breaking in forced rotating flows at moderate Rossby number," J. Fluid Mech. **535**, 111 (2005).
[28] M. Hossain, "Reduction in the dimensionality of turbulence due to a strong rotation," Phys. Fluids **6**, 1077 (1994).
[29] A. Sen, P. D. Mininni, D. Rosenberg, and A. Pouquet, "Anisotropy and nonuniversality in scaling laws of the large-scale energy spectrum in rotating turbulence," Phys. Rev. E **86**, 036319 (2012).
[30] L. M. Smith, J. R. Chasnov, and F. Waleffe, "Crossover from two- to three-dimensional turbulence," Phys. Rev. Lett. **77**, 2467 (1996).
[31] E. Deusebio, G. Boffetta, E. Lindborg, and S. Musacchio, "Dimensional transition in rotating turbulence," Phys. Rev. E **90**, 023005 (2014).

[32] P. K. Yeung and Ye Zhou, "Numerical study of rotating turbulence with external forcing," Phys. Fluids **10**, 2895 (1998).
[33] B. Gallet and W. R. Young, "A two-dimensional vortex condensate at high Reynolds number," J. Fluid Mech. **715**, 359 (2013).
[34] M. Thiele and W.-C. Muller, "Structure and decay of rotating homogeneous turbulence," J. Fluid Mech. **637**, 425 (2009).
[35] T. Teitelbaum and P. D. Mininni, "The decay of turbulence in rotating flows," Phys. Fluids **23**, 065105 (2011).
[36] C. Lamriben, P.-P. Cortet, and F. Moisy, "Direct measurements of anisotropic energy transfers in a rotating turbulence experiment," Phys. Rev. Lett. **107**, 024503 (2011).
[37] C. N. Baroud, B. B. Plapp, Z.-S. She, and H. L. Swinney, "Anomalous self-similarity in a turbulent rapidly rotating fluid," Phys. Rev. Lett. **88**, 114501 (2002).
[38] C. Morize, F. Moisy, and M. Rabaud, "Decaying grid-generated turbulence in a rotating tank," Phys. Fluids **17**, 095105 (2005).
[39] E. Yarom, Y. Vardi, and E. Sharon, "Experimental quantification of inverse energy cascade in deep rotating turbulence," Phys. Fluids **25**, 085105 (2013).
[40] Y. D. Afanasyev and J. D. C. Craig, "Rotating shallow water turbulence: Experiments with altimetry," Phys. Fluids **25**, 106603 (2013).
[41] L. J. A. van Bokhoven, H. J. H. Clercx, G. J. F. van Heijst, and R. R. Trieling, "Experiments on rapidly rotating turbulent flows," Phys. Fluids **21**, 096601 (2009).
[42] A. S. Monin and A. M. Yaglom, *Statistical Fluid Mechanics* (MIT Press, Cambridge, 1975), Vol. 2.
[43] E. Lindborg, "Correction to the four-fifths law due to variations of the dissipation," Phys. Fluids **11**, 510 (1999).
[44] R. J. Hill, "Exact second-order structure function relationships," J. Fluid Mech. **468**, 317 (2002).
[45] R. A. Antonia and P. Burattini, "Approach to the 4/5 law in homogeneous isotropic turbulence," J. Fluid Mech. **550**, 175 (2006).
[46] L. Danaila, R. A. Antonia, and P. Burattini, "Comparison between kinetic energy and passive scalar energy transfer in locally homogeneous isotropic turbulence," Phys. D **241**, 224 (2012).
[47] L. Danaila, J. F. Krawczynski, F. Thiesset, and B. Renou, "Yaglom-like equation in axisymmetric anisotropic turbulence," Phys. D **241**, 216 (2012).
[48] B. Gallet, A. Campagne, P.-P. Cortet, and F. Moisy, "Scale-dependent cyclone-anticyclone asymmetry in a forced rotating turbulence experiment," Phys. Fluids **26**, 035108 (2014).
[49] P. Billant and J.-M. Chomaz, "Experimental evidence for a new instability of a vertical columnar vortex pair in a strongly stratified fluid," J. Fluid Mech. **418**, 167 (2000).
[50] P. Augier, P. Billant, M. E. Negretti, and J.-M. Chomaz, "Experimental study of stratified turbulence forced with columnar dipoles," Phys. Fluids. **26**, 046603 (2014).
[51] DaVis, LaVision GmbH, Anna-Vandenhoeck-Ring 19, Goettingen, Germany.
[52] F. Moisy, PIVMat toolbox for Matlab, http://www.fast.u-psud.fr/pivmat.
[53] P. A. Davidson, *Turbulence: An Introduction for Scientists and Engineers* (Oxford University Press, Oxford, 2004).
[54] A. M. Yaglom, "On the local structure of a temperature field in a turbulent flow," Dokl. Akad. Nauk SSSR **69**(6), 743 (1949).
[55] This anisotropic second order structure function (3) is directly related to the 3D turbulent energy spectrum $e(\boldsymbol{\kappa})$: $E(\mathbf{r}) = 4\left(k - \iiint e(\boldsymbol{\kappa})\mathrm{e}^{i\boldsymbol{\kappa}\cdot\mathbf{r}}d^3\boldsymbol{\kappa}\right)$, with k the turbulent kinetic energy and $\boldsymbol{\kappa}$ the wavevector.
[56] The normalization by $E_0 = \langle\overline{\mathbf{u}_A'^2 + \mathbf{u}_B'^2}\rangle_{\mathbf{X}}$ is chosen so that $E(\mathbf{r})/E_0 = 1$ when an exact decorrelation of $\mathbf{u}'_A$ and $\mathbf{u}'_B$ is observed beyond $r_\perp = r_{\max}$. Note that normalizing by $2\langle\overline{\mathbf{u}'^2}\rangle_{\mathbf{X}}$ would give very similar results, to within 3%, because of the nearly homogeneous turbulence in the region of interest.

Direct Measurements of Anisotropic Energy Transfers in a Rotating Turbulence Experiment

Cyril Lamriben, Pierre-Philippe Cortet, and Frédéric Moisy

Laboratoire FAST, CNRS, Univ Paris-Sud, UPMC Univ Paris 06, Bâtiment 502, Campus universitaire, 91405 Orsay, France

(Received 28 February 2011; published 7 July 2011)

We investigate experimentally the influence of a background rotation on the energy transfers in decaying grid turbulence. The anisotropic energy flux density $\mathbf{F}(\mathbf{r}) = \langle \delta\mathbf{u}(\delta\mathbf{u})^2 \rangle$, where $\delta\mathbf{u}$ is the vector velocity increment over separation $\mathbf{r}$, is determined for the first time by using particle image velocimetry. We show that rotation induces an anisotropy of the energy flux $\nabla \cdot \mathbf{F}$, which leads to an anisotropy growth of the energy distribution $E(\mathbf{r}) = \langle (\delta\mathbf{u})^2 \rangle$, in agreement with the von Kármán–Howarth–Monin equation. Surprisingly, our results prove that this anisotropy growth is essentially driven by a nearly radial, but orientation-dependent, energy flux density $\mathbf{F}(\mathbf{r})$.

DOI: 10.1103/PhysRevLett.107.024503 PACS numbers: 47.27.−i, 47.32.Ef

The energy cascade from large to small scales and the associated Kolmogorov 4/5th law are recognized as the most fundamental results of homogeneous and isotropic turbulence [1,2]. In the presence of a background rotation, a situation which is relevant for most geophysical and astrophysical flows, the scale-to-scale energy transfers are modified by the Coriolis force, yielding a gradual columnar structuring of turbulence along the rotation axis [3–7]. The Taylor-Proudman theorem is often invoked, however improperly, to justify the resulting quasi-2D nature of turbulence under rotation. Indeed, this theorem is a purely linear result, which applies only in the limit of a zero Rossby number (i.e., infinite rotation rate), and is therefore incompatible with turbulence; it cannot describe the anisotropic energy transfers responsible for the nontrivial organization of rotating turbulence which are a subtle nonlinear effect taking place only at a nonzero Rossby number. To date, no direct evidence for these anisotropic energy transfers towards the 2D state in the physical space has been obtained. In this Letter, we report for the first time direct measurements of the physical-space energy transfers in decaying rotating turbulence using particle image velocimetry (PIV) and provide new insight into the anisotropy growth of turbulence at a finite, and hence geophysically relevant, Rossby number.

If homogeneity (but not necessarily isotropy) holds, the energy distribution and energy flux density in the space of separations $\mathbf{r}$ are described by the fields

$$E(\mathbf{r}, t) = \langle (\delta\mathbf{u})^2 \rangle \quad \text{and} \quad \mathbf{F}(\mathbf{r}, t) = \langle \delta\mathbf{u}(\delta\mathbf{u})^2 \rangle, \qquad (1)$$

respectively, where $\mathbf{u}(\mathbf{x}, t)$ is the turbulent velocity, $\delta\mathbf{u} = \mathbf{u}(\mathbf{x} + \mathbf{r}, t) - \mathbf{u}(\mathbf{x}, t)$ is the velocity vector increment over $\mathbf{r}$ (Fig. 1), and $\langle \cdot \rangle$ denotes spatial and ensemble averages. These key quantities satisfy the von Kármán–Howarth–Monin (KHM) equation [1,8], which describes the evolution of the energy distribution in the space of separations,

$$\frac{1}{2}\frac{\partial}{\partial t} R = \frac{1}{4}\nabla \cdot \mathbf{F} + \nu \nabla^2 R, \qquad (2)$$

where $R(\mathbf{r}, t) = \langle \mathbf{u}(\mathbf{x}, t) \cdot \mathbf{u}(\mathbf{x} + \mathbf{r}, t) \rangle = \langle \mathbf{u}^2 \rangle - E(\mathbf{r}, t)/2$ is the two-point velocity correlation and ν the kinematic viscosity. Importantly, this equation is still valid for homogeneous anisotropic turbulence [9] and, in particular, for axisymmetric turbulence in a rotating frame (here axisymmetry is to be understood in the statistical sense, with respect to $\mathbf{r}$). For stationary (forced) turbulence, this equation reduces to $\nabla \cdot \mathbf{F} = -4\epsilon$ in the inertial range, where ϵ stands for the rates of injected and dissipated energy. In the isotropic case, this constant-flux relation yields a purely radial flux density $\mathbf{F}(\mathbf{r}) = -(4/3)\epsilon\mathbf{r}$, describing the usual energy cascade from large to small scales. This result is actually identical to the celebrated Kolmogorov's 4/5th law, classically expressed in terms of the 3rd-order longitudinal structure function, $\langle \delta u_L^3 \rangle = -(4/5)\epsilon r$, where $\delta u_L = \delta\mathbf{u} \cdot \mathbf{r}/r$ is the longitudinal velocity increment.

In decaying rotating homogeneous turbulence, Eq. (2) shows that, starting from an isotropic initial energy distribution $E(\mathbf{r}, 0)$, an anisotropy growth in $E(\mathbf{r}, t)$ is expected if an anisotropic energy flux $\nabla \cdot \mathbf{F}$ is induced by the Coriolis force. However, the flux density $\mathbf{F}(\mathbf{r})$ itself has never been

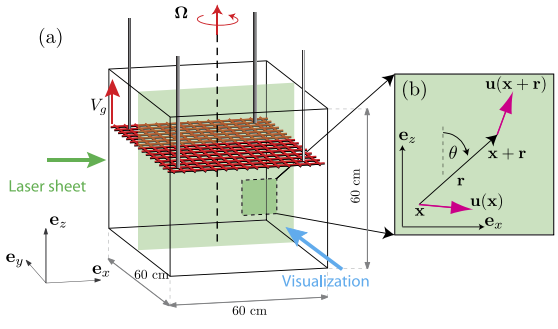

FIG. 1 (color online). (a) Experimental setup. The water-filled tank is rotating at $0 \leq \Omega \leq 1.68$ rad s^{-1}. The grid is towed from the bottom to the top, and PIV measurements are performed in the vertical plane (x, z) in the rotating frame during the turbulence decay. (b) Definition of the vector velocity increment $\delta\mathbf{u} = \mathbf{u}(\mathbf{x} + \mathbf{r}) - \mathbf{u}(\mathbf{x})$.

measured, and its precise form, which reveals the fundamental action of rotation on turbulence, is so far unknown. The only experimental attempts to characterize the energy transfers in rotating turbulence were restricted to measurements of $\langle \delta u_L^3 \rangle$ in the plane normal to the rotation axis [10,11], hence ignoring the anisotropic nature of those transfers. Recent theoretical efforts have been made to generalize the 4/5th law, assuming weak anisotropy [12] or considering the full anisotropic problem but restricted to the stationary case [9].

Experiments.—The experimental setup is similar to the one described in Ref. [13] and is briefly recalled here [Fig. 1(a)]. Turbulence is generated by towing a square grid at a velocity $V_g = 1.0\ \mathrm{m\,s^{-1}}$ from the bottom to the top of a cubic glass tank, of height 60 cm, filled with 52 cm of water. The grid consists in 8 mm thick bars with a mesh size $M = 40$ mm. The whole setup is mounted on a precision rotating turntable 2 m in diameter. Runs for three rotation rates, $\Omega = 0.42$, 0.84, and $1.68\ \mathrm{rad\,s^{-1}}$ (4, 8, and 16 rpm, respectively), as well as a reference run without rotation, have been carried out. The initial Reynolds number based on the grid mesh is $\mathrm{Re}_g = V_g M/\nu = 40\,000$, and the initial Rossby number $\mathrm{Ro}_g = V_g/2\ \Omega \mathrm{M}$ ranges from 7.4 to 30, indicating that the flow in the close wake of the grid is fully turbulent and weakly affected by rotation. During the turbulence decay, the instantaneous Rossby number $\mathrm{Ro}(t) = \langle \mathbf{u}^2 \rangle^{1/2}/2\ \Omega \mathrm{M}$ decreases with time down to 10^{-2}, spanning a range in which influence of rotation is expected. An important concern about grid turbulence experiments in a confined rotating domain is the excitation of reproducible inertial modes [14]. Here, we use the modified grid introduced in Ref. [13], which was shown to significantly reduce the generation of these modes. Consequently, turbulence can be considered here as almost freely decaying and homogeneous, a necessary condition for the validity of the KHM equation (2).

Velocity measurements are performed in the rotating frame by using a corotating PIV system. Two velocity components (u_x and u_z) are measured, in a vertical $16 \times 16\ \mathrm{cm}^2$ field of view, where z is the rotation axis. During the decay of turbulence, 60 image pairs are acquired by a double-frame 2048^2-pixel camera, at a rate of 1 pair per second. The PIV resolution 1.3 mm is sufficient to resolve the inertial range but fails to resolve the dissipative scale (the Kolmogorov scale is of the order of 0.2 mm right after the grid translation [11]).

Only surrogates of $E(\mathbf{r})$ and $\mathbf{F}(\mathbf{r})$ (1) can be computed from the measured 2D velocity fields. These surrogate quantities are defined as

$$\tilde{E}(\mathbf{r}) = \langle \delta u_x^2 + \delta u_z^2 \rangle_{x,z}, \qquad \tilde{\mathbf{F}}(\mathbf{r}) = \langle \delta \mathbf{u} (\delta u_x^2 + \delta u_z^2) \rangle_{x,z}, \quad (3)$$

where the spatial average is restricted to the measurement plane and $\mathbf{r} = r_x \mathbf{e}_x + r_z \mathbf{e}_z$. For each time after the grid translation, these quantities are computed for all separations $\mathbf{r}$ in the PIV field of view and are ensemble-averaged over 600 realizations of the turbulence decay. The fields $\tilde{E}(\mathbf{r})$ and $\tilde{\mathbf{F}}(\mathbf{r})$ are remapped on a spherical coordinate system (r, θ, ϕ), where $r = |\mathbf{r}|$ and θ is the polar angle between $\mathbf{e}_z$ and $\mathbf{r}$; the invariance with respect to the (non-measured) azimuthal angle ϕ is assumed by axisymmetry. Although relations between the surrogates (3) and the exact 3-component quantities (1) can be derived for isotropic turbulence, no general relation holds in the anisotropic case, so we do not apply any correction weight in $\tilde{E}$ and $\tilde{\mathbf{F}}$. Since only the surrogates are considered in this Letter, we simply drop the tildes $\tilde{\cdot}$ in the following.

The convergence of the statistics from experimental measurements is very delicate to achieve, in particular, for the computation of $\mathbf{F}(\mathbf{r})$, which is a 3rd-order moment of a zero-mean velocity increment. We found that, by using a set of 600 realizations of the turbulence decay, a convergence better than 5% at small scales, and of the order of 20% at scales $r \simeq M$, could be achieved for $\mathbf{F}(\mathbf{r})$. The convergence for $E(\mathbf{r})$ is better than 1% for all scales up to $r \simeq M$.

Energy distribution.—The map of energy distribution $E(\mathbf{r})$ for separations $\mathbf{r}$ in the vertical plane is plotted in Fig. 2, at a time $tV_g/M = 400$ after the grid translation. The iso-E curves are found to be nearly circular for $\Omega = 0$ [Fig. 2(a)], showing the good level of isotropy of our grid turbulence without rotation. On the other hand, they are highly anisotropic at the same time for $\Omega = 16$ rpm (corresponding to 4.3 tank rotations), with a strong depletion of $E(\mathbf{r})$ along the rotation axis z [Fig. 2(b)]. The depletion of $E(\mathbf{r})$ corresponds to an enhanced velocity correlation $R(\mathbf{r})$ along the rotation axis, reflecting the classical trend

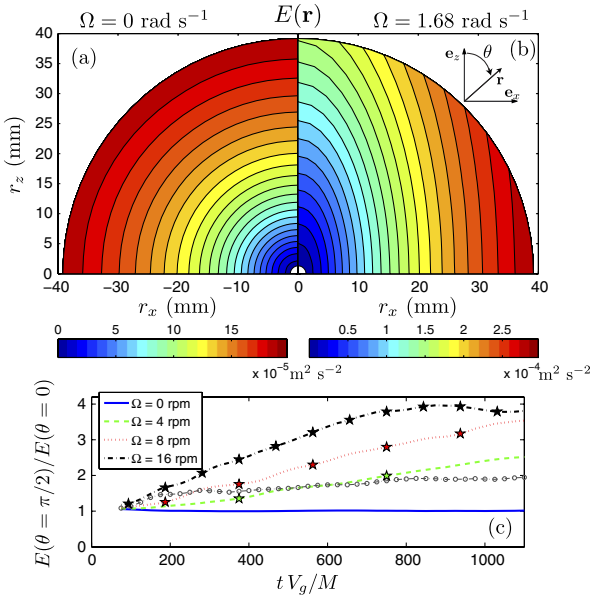

FIG. 2 (color online). Energy distribution $E(\mathbf{r})$ at time $tV_g/M = 400$ after the grid translation, for (a) $\Omega = 0$ and (b) $\Omega = 1.68\ \mathrm{rad\,s^{-1}}$ (16 rpm). (c) Horizontal-to-vertical energy ratio as a function of time at scale $r = 10$ mm for various Ω; ○, additional curve at $r = 30$ mm for $\Omega = 16$ rpm. Stars indicate integer numbers of tank rotations.

towards a 2D flow invariant along z. Importantly, an isotropic energy distribution is found in the 3 rotating cases just after the grid translation, as demonstrated in Fig. 2(c), where the time evolution of the horizontal-to-vertical energy ratio $E(\theta = 0)/E(\theta = \pi/2)$ is plotted for an inertial-range separation $r = 10$ mm. This confirms that the initial grid turbulence is isotropic even when $\Omega \neq 0$ and that the subsequent anisotropy growth is a pure effect of the background rotation. Figure 2(c) also shows that the anisotropy growth rate is essentially proportional to Ω [5,7]. Interestingly, the anisotropy is found to be more pronounced at small scales, as shown by the lower anisotropy ratio plotted for $r = 30$ mm. It is worth noting that this stronger anisotropy at small scales is in contradiction with the naive assumption that large scales, having a slower dynamics, are more affected by rotation than the faster and supposedly still 3D small scales.

Energy transfers: Isotropic case.—We now turn to the energy flux density, and we first present in Fig. 3(b) measurements of $\mathbf{F}(\mathbf{r})$ for $\Omega = 0$, at the same time $tV_g/M = 400$. This vector field is found to be remarkably radial, pointing towards the origin, giving direct evidence of the isotropic energy cascade in the physical space, from the large to the small scales, in the nonrotating case. Finer assessment of the isotropy of $\mathbf{F}$ can be achieved by introducing the following three scalar quantities: the deviation angle $\alpha(\mathbf{r})$ from the radial direction [Fig. 3(d)], the magnitude $|\mathbf{F}|$ [Fig. 3(a)], and the energy flux $\nabla \cdot \mathbf{F}$ [Fig. 3(c)].

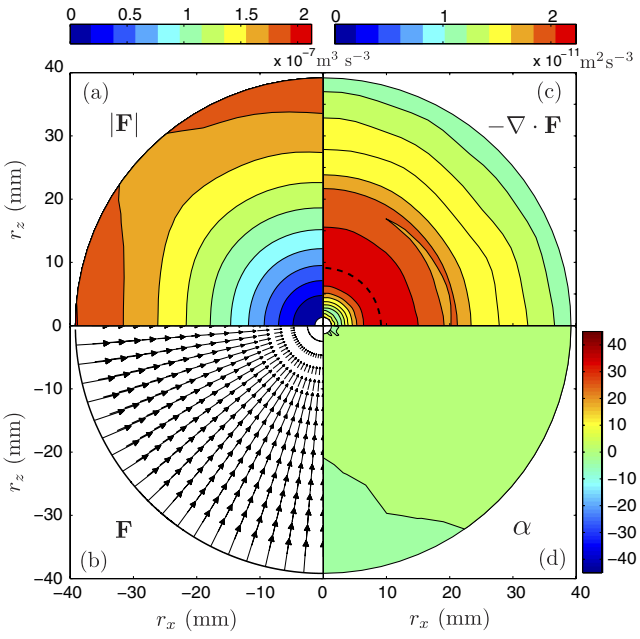

FIG. 3 (color online). Energy flux density $\mathbf{F}(\mathbf{r})$ in the nonrotating case, at time $tV_g/M = 400$ after the grid translation. (a) Flux density magnitude $|\mathbf{F}|$. (b) Raw vector field $\mathbf{F}$. (c) Energy flux $\nabla \cdot \mathbf{F}$. (d) Deviation angle $\alpha(\mathbf{r})$, defined as $\sin\alpha(\mathbf{r}) = \mathbf{e}_y \cdot (\mathbf{e}_r \times \mathbf{F})/|\mathbf{F}|$; isoangle lines are separated by 5°. The dashed line in (c) shows the "crest line," following the local maximum of $-\nabla \cdot \mathbf{F}$.

The very weak angle measured for $r \leq M$, $\alpha(\mathbf{r}) \simeq 2° \pm 2°$, confirms the almost purely radial nature of $\mathbf{F}$. The isotropy of the flux density magnitude is not as good: The iso-$|\mathbf{F}|$ are nearly circular up to $r \simeq 30$ mm but show slight departure from isotropy at larger r, suggesting that this quantity is very sensitive to a residual anisotropy of the large-scale flow. However, the iso-$\nabla \cdot \mathbf{F}$ remain remarkably circular up to $r \simeq M$, showing that the residual large-scale anisotropy has indeed a weak influence on the energy flux for $r \leq M$. The energy flux $\nabla \cdot \mathbf{F}$ shows a broad negative minimum in an annular region spanning over $r \simeq 5$–20 mm, providing an indication of the extent of the inertial range (we recall that, in the inertial range, $\nabla \cdot \mathbf{F} = -4\epsilon$), and decreases to zero at both small and large scales.

Energy transfers: Rotating case.—We consider now the energy transfers in the rotating case, shown in Fig. 4 at the same time $tV_g/M = 400$. Interestingly, the flux density $\mathbf{F}$ is found to remain nearly radial for all separations, in qualitative agreement with recent predictions [9], except at the smallest scales, for $r < 10$ mm, where a marked deflection towards the rotation axis is observed. Such a horizontally tilted $\mathbf{F}$ is indeed consistent with an asymptotic 2D flow, for which $\mathbf{F}$ must be a strictly horizontal vector and a function of the horizontal component of the separation only. This small-scale anisotropy is best appreciated from the map of the deviation angle α [Fig. 4(d)], showing a region of nonzero α at small scale only. Note that a horizontally tilted $\mathbf{F}$ exists only for intermediate angle θ since axisymmetry requires a radial $\mathbf{F}$ for $\theta = 0$ and $\pi/2$. The 2D trend is remarkably weak in terms of the orientation of $\mathbf{F}(\mathbf{r})$ in the inertial range, compared to the strong anisotropy observed for the energy distribution $E(\mathbf{r})$

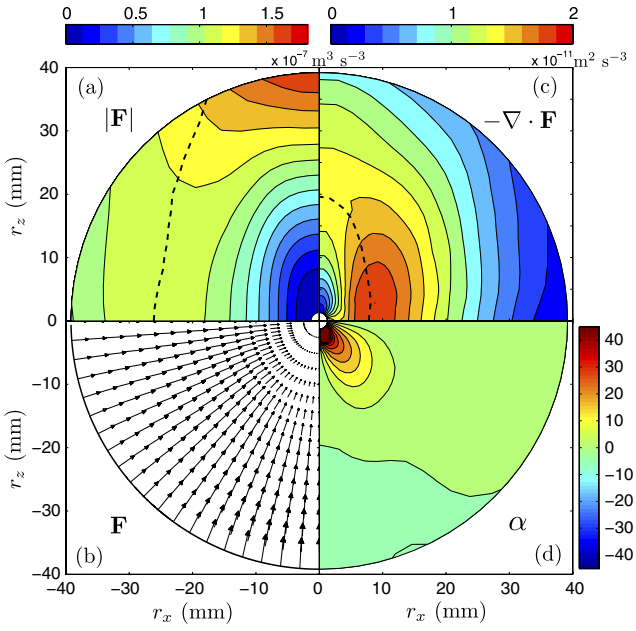

FIG. 4 (color online). Energy flux density $\mathbf{F}(\mathbf{r})$ in the rotating case ($\Omega = 16$ rpm), at time $tV_g/M = 400$ after the grid translation. The same layout as for Fig. 3 is used.

at comparable scales: α is only in the range 0–10° in the inertial range and increases up to 25° ± 5° for $r \to 0$, with no significant dependence with Ω.

If we focus on the flux density magnitude $|\mathbf{F}|$, which is essentially given by the radial component $-F_r = -\mathbf{F} \cdot \mathbf{e}_r$, a clear anisotropy is now found at all scales. This suggests that the anisotropy of the energy transfers is mostly driven by the θ dependence of F_r and not by the growth of a nonzero polar component $F_\theta = \mathbf{F} \cdot \mathbf{e}_\theta$. The maximum of $|\mathbf{F}|$ is systematically encountered near the rotation axis, at rather large scales, centered around 50–80 mm [outside the range shown in Fig. 4(a)]. The local maximum of $|\mathbf{F}|$ on the horizontal axis is encountered at smaller scales, as evidenced by the crest line in Fig. 4(a).

The flux map $\nabla \cdot \mathbf{F}$ [Fig. 4(c)] shows an overall anisotropic structure similar to that of $|\mathbf{F}|$ but essentially shifted towards smaller scales. The inertial range, where the flux $\nabla \cdot \mathbf{F}$ is negative and approximately constant, becomes vertically elongated as time proceeds. Actually, although $|\mathbf{F}|$ is maximum along the rotation axis, it is spread over a wider range of scales, leading to a weaker flux $\nabla \cdot \mathbf{F}$ along z than along x and hence a less intense vertical energy cascade. Here again, this is consistent with a 2D trend, which should yield a vanishing energy flux along the rotation axis. The horizontal-to-vertical flux ratio in Fig. 5 illustrates this vanishing vertical energy cascade as time proceeds, an effect which is clearly enhanced as the rotation rate is increased.

It must be noted that the spatial structure of the flux $\nabla \cdot \mathbf{F}$ is in good qualitative agreement with the KHM equation (2). Indeed, by neglecting the viscous term, the vertically elongated region where $\nabla \cdot \mathbf{F} < 0$ induces a stronger reduction of the velocity correlation R along x than along z, resulting in a relative growth of the vertical correlation along z and hence a vertical depletion of the energy distribution $E = 2(\langle \mathbf{u}^2 \rangle - R)$. We can conclude that the measured flux density $\mathbf{F}$ contains, through its divergence, a spatial structure consistent with the anisotropy growth of E observed in Fig. 2. Interestingly, in line with the stronger anisotropy of $E(\mathbf{r})$ found at smaller scales, the flux is also found to be more anisotropic at smaller scales. This is clearly demonstrated by the spatiotemporal diagram in Fig. 5(a), showing that the anisotropy first appears at small scales and then propagates towards larger scales as time proceeds.

Conclusion.—We report the first direct measurements of the energy flux density $\mathbf{F}$ in the physical space in a decaying rotating turbulence experiment. Although the alternative description of the energy transfers in the spectral space is more natural for theory or numerics [2–4,6], the direct use of the KHM equation (2) in the physical space, which is better suited for experiments, reveals here new and unexpected behaviors. The spatial structure of the measured energy distribution and energy flux $\nabla \cdot \mathbf{F}$ are found to be in good qualitative agreement with the KHM equation which, to our knowledge, has never been assessed experimentally. Surprisingly, the anisotropy growth of the energy distribution is primarily driven by an almost radial, but orientation-dependent, flux density $\mathbf{F}$, except at small scales where $\mathbf{F}$ shows a horizontal tilt, compatible with a trend towards a 2D state. It is also demonstrated that the anisotropy is paradoxically stronger at small scales and propagates towards larger scales as time proceeds, an unexpected result which should motivate new theoretical efforts.

We acknowledge S. Galtier, J.-P. Hulin, and M. Rabaud for fruitful discussions and Triangle de la Physique for funding of the "Gyroflow" platform.

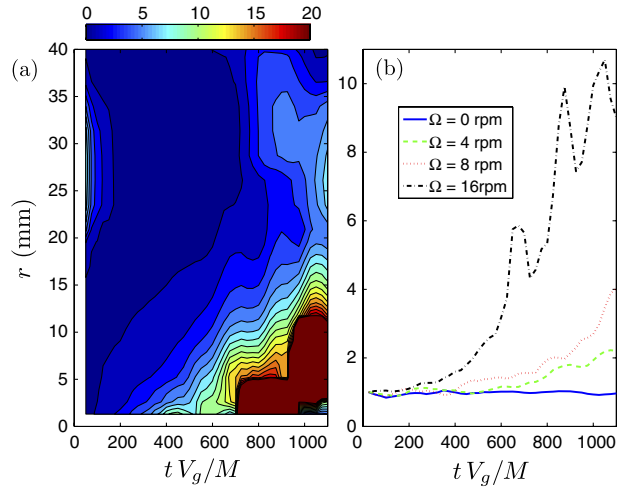

FIG. 5 (color online). (a) Spatiotemporal diagram of the horizontal-to-vertical energy flux ratio $\nabla \cdot \mathbf{F}(\theta = \pi/2)/\nabla \cdot \mathbf{F}(\theta = 0)$, showing the anisotropy growing from small to large scales. (b) Time evolution of the energy flux ratio at scale $r = 10$ mm for various Ω.

[1] U. Frisch, *Turbulence—The Legacy of A. N. Kolmogorov* (Cambridge University Press, Cambridge, England, 1995).
[2] P. Sagaut and C. Cambon, *Homogeneous Turbulence Dynamics* (Cambridge University Press, Cambridge, England, 2008).
[3] C. Cambon and L. Jacquin, J. Fluid Mech. **202**, 295 (1989).
[4] F. Waleffe, Phys. Fluids A **5**, 677 (1993).
[5] P. J. Staplehurst, P. A. Davidson, and S. B. Dalziel, J. Fluid Mech. **598**, 81 (2008).
[6] P. D. Mininni and A. Pouquet, Phys. Fluids **22**, 035106 (2010).
[7] F. Moisy *et al.*, J. Fluid Mech. **666**, 5 (2011).
[8] A. S. Monin and A. M. Yaglom, *Statistical Fluid Mechanics* (MIT, Cambridge, MA, 1975), Vol. 2.
[9] S. Galtier, Phys. Rev. E **80**, 046301 (2009).
[10] C. N. Baroud *et al.*, Phys. Rev. Lett. **88**, 114501 (2002).
[11] C. Morize, F. Moisy, and M. Rabaud, Phys. Fluids **17**, 095105 (2005).
[12] S. Chakraborty and J. K. Bhattacharjee, Phys. Rev. E **76**, 036304 (2007).
[13] C. Lamriben *et al.*, Phys. Fluids **23**, 015102 (2011).
[14] G. P. Bewley *et al.*, Phys. Fluids **19**, 071701 (2007).

Journal of Turbulence
Vol. 00, No. 00, 2014, 1–27

Scale-dependent anisotropy in decaying rotating turbulence

P.-P. Cortet* and F. Moisy

Laboratoire FAST, CNRS, Université Paris-Sud, Orsay, France
(*Received 00 Month 200x; final version received 00 Month 200x*)

The anisotropic energy transfers in the physical space are analyzed in a decaying rotating turbulence experiment. Turbulence is generated by towing a grid in a water-filled container mounted on a rotating platform. Velocity fields are measured in a vertical plane using corotating two-dimensional particle image velocimetry. Two-dimensional surrogates of the two-point velocity correlation $R(\mathbf{r},t)$ and of the energy flux $\Pi(\mathbf{r},t) = \nabla\cdot\mathbf{F}/4$, where $\mathbf{F}(\mathbf{r},t) = \langle\delta\mathbf{u}(\delta\mathbf{u})^2\rangle$ is the flux density and $\delta\mathbf{u}$ the velocity increment over separation $\mathbf{r}$, are computed from ensemble averages over a large number of independent decay realizations. These quantities are used to characterize the anisotropic energy budget based on the Kármán-Howarth-Monin equation. The scale-dependent anisotropy growth is analyzed from the horizontal-to-vertical ratio of the energy and energy flux distributions. The anisotropy of the energy flux $\Pi(\mathbf{r},t)$ is found to be maximum at the smallest resolved scale. On the other hand, the anisotropy of $R(\mathbf{r},t)$ is weaker, with a non-monotonic evolution of the scale of maximum anisotropy r_{aniso}: it first rapidly decreases and then slowly increases. The decrease of r_{aniso} at small time is compatible with the decrease of the Zeman scale (the scale at which the turnover time matches the global rotation rate), although the predicted scaling cannot be verified because of the moderate range of Reynolds and Rossby numbers. The increase of r_{aniso} at large time follows the Kolmogorov scale, because the anisotropic energy transfer becomes negligible compared to viscous diffusion when the Zeman scale is in the dissipative range.

Keywords: turbulence; rotation; anisotropy; Kármán-Howarth equation

1. Introduction

Background rotation, through the action of the Coriolis force, has a strong influence on the statistical and geometrical properties of turbulence [1, 2]. This situation is of major interest in geophysical (atmosphere and ocean), astrophysical and industrial flows. The dynamics of rotating turbulence is governed by the Reynolds and Rossby numbers based on the horizontal velocity U and length scale L (here, horizontal means by convention normal to the rotation axis), $Re = UL/\nu$ and $Ro = U/2\Omega L$. For moderate Rossby number $Ro \simeq O(1)$, the coupling between Coriolis effects and non-linearities is maximum, with a strong energy transfer from the 3D to the 2D modes, resulting in a columnar structuration of the turbulence along the rotation axis [3–7]. In the limit of rapid rotation ($Ro \to 0$), the flow becomes nearly 2 dimensional, but remains 3-component in general (2D-3C), in agreement with the Taylor-Proudman theorem. However, the evolution towards two-dimensionality is intrinsically a nonlinear effect [8–10], and cannot be described by the Taylor-Proudman theorem, which is a purely linear result.

Much work has been devoted to understanding the dynamics of the energy transfers responsible for the anisotropy growth in rotating turbulence. Energy transfers for homogeneous (not necessarily isotropic) turbulence may be described either in the physical space, using the Kármán-Howarth equation, or in the spectral space,

*Corresponding author. Email: ppcortet@fast.u-psud.fr

ISSN: YYYYY (online only)

DOI: XXXXX
http://www.tandfonline.com

using the Lin equation (see references [1] and [11] for recent reviews on the connections between these two frameworks). Although the spectral space is more natural for theoretical or numerical approaches, the physical space is better suited to experiments. The spectral formulation is indeed the natural framework to describe the dynamics of the triadic interactions, which contains the elementary physics of the energy transfers between wave numbers [8, 9, 12]. This framework has also the advantage to implicitly take into account the pressure field through incompressibility. On the other hand, experimental data are available in the physical space, which naturally leads to a description of the energy transfers based on the Kármán-Howarth (KH) equation. This equation is a scale-by-scale energy conservation law, expressed in terms of two-point second-order (for energy) and third-order (for energy transfers) velocity correlations, which can be directly measured experimentally. For 3D isotropic turbulence in the limit of large Reynolds number, KH equation reduces to the Kolmogorov 4/5th law for scales r in the inertial range, $\langle \delta u_L^3 \rangle = -\frac{4}{5}\epsilon r$, where $\delta u_L = [\mathbf{u}(\mathbf{x}+\mathbf{r}) - \mathbf{u}(\mathbf{x})] \cdot \mathbf{r}/r$ is the longitudinal velocity increment over separation $\mathbf{r}$, ϵ the mean dissipation rate per unit mass, and $\langle \cdot \rangle$ the ensemble and spatial average. The KH equation and 4/5th law have been extensively tested experimentally from one-point velocity time series, using hot-wire anemometry [13–17]. If isotropy is assumed, one velocity component along one single direction is indeed sufficient to fully characterize the energy transfers between scales.

Although the KH equation has been mainly investigated in its isotropic form, the assumption of isotropy is actually not required [18]. Its generalized anisotropic form, which still requires homogeneity, has been renamed Kármán-Howarth-Monin (KHM) equation by Frisch [19]. KHM equation must be satisfied in particular for homogeneous rotating turbulence [2, 11, 20]. It describes how the nonlinear energy flux, modified by the Coriolis force, will affect the dynamics of the two-point velocity correlation. In decaying turbulence, apart from viscous effects (which become important at large times), this nonlinear energy flux results in an anisotropy growth of the two-point correlation, a statistical signature of the formation of columnar structures.

The development in the last decade of image-based diagnostics for flow measurements, such as particle image velocimetry (PIV) or particle tracking velocimetry (PTV), has raised the possibility to directly access the energy transfers in the physical space. On the other hand, the limited spatial sampling of velocity measurements using PIV (typically available on grids of order of 100^2 vectors) makes the computation of spectral quantities subject to strong finite size effects. Attempts to compute the energy transfers in the physical space using PIV were first limited to measurements in the plane normal to the rotation axis, hence ignoring the anisotropic nature of the transfers [21, 22]. Anisotropic measurements, in a plane containing the rotation axis, were recently achieved by Lamriben *et al.* [23] in a decaying rotating turbulence experiment. An anisotropy growth of the energy flux density was reported, which was compatible with the anisotropy growth of the two-point velocity correlation. One aim of the present paper is to extend this work, with emphasis given on the time evolution of the scale-dependent anisotropy of energy and energy transfers.

A fundamental issue in rotating turbulence is whether the anisotropy induced by rotation is more pronounced at small or large scales. Classical scaling arguments, based on a scale-dependent Rossby number $Ro_r = \delta u_r / 2\Omega r$ (where δu_r is the horizontal characteristic velocity for a horizontal separation r), suggest that rotation effects are more pronounced at large scales, which would favor stronger anisotropy at large scales too. Scales smaller than the Zeman scale $r_\Omega = \epsilon^{1/2}\Omega^{-3/2} \simeq LRo^{3/2}$

(where Ro is the large-scale, global, Rossby number, and L the horizontal integral scale) should escape from the influence of rotation, and display features similar to classical non-rotating turbulence [24–26]. Contrarily to isotropic turbulence, the connection between time scales and length scales is not straightforward when rotation is present: rotation influences the dynamics of turbulence via inertial waves, for which a given frequency prescribes a direction of propagation only, but not a wavelength. Accordingly, velocity fluctuations slower than the background rotation should be affected by the Coriolis force at all scales.

Recent investigations of the scale-dependent anisotropy of rotating turbulence have lead to different results depending on whether the limit of moderate or rapid rotation is considered. More pronounced anisotropy at small scale is predicted by the wave turbulence formalism [27, 28], valid in the limit of rapid rotation ($Ro \to 0$), which contradicts the above argument based on the scale-dependent Rossby number Ro_r. Galtier [20] provides a qualitative argument for this increasing anisotropy at small scale based on helicity conservation. This stronger anisotropy at small scale is supported by the numerical simulation of Bellet *et al.* [29], in which the finite resolution introduces a moderate effective Reynolds number. In this case, the Zeman scale is smaller than the viscous cutoff, and the anisotropy saturates at an intermediate scale, close to the viscous cutoff. Nazarenko and Schekochihin [30], using the critical balance assumption borrowed from strong magnetohydrodynamic turbulence, suggest that anisotropy should reach a maximum at the critical wavenumber $k_c \simeq L^{-1}Ro^{-4/5}$ corresponding to the breakdown of the wave turbulence limit. This critical wavenumber is smaller than the Zeman wavenumber $k_\Omega \simeq L^{-1}Ro^{-3/2}$, and a return to isotropy is predicted between k_c and k_Ω. In the decaying rotating turbulence experiments reported in reference [23], evidence for stronger anisotropy at small scale is indeed found for the energy flux. The direct numerical simulation of rotating turbulence with helical forcing of Mininni *et al.* [31], on the other hand, shows a decreasing anisotropy for increasing wave number, with a recovery of isotropy for wave numbers larger than k_Ω (see also [32]). A similar recovery of isotropy beyond the Zeman scale is also observed by Naso and Godeferd [33] from the analysis of the geometrical properties of the coarse-grained velocity gradient tensor in forced rotating turbulence simulations.

Although all these studies are compatible with a return to isotropy at small scale, the moderate range of Reynolds and Rossby numbers covered by numerical simulations and experiments (including the ones presented in this paper) make it difficult to draw clear conclusions about which scale concentrates the highest level of anisotropy. We examine experimentally in this paper the scale dependence of anisotropy in decaying rotating turbulence, and find that the highest anisotropy occurs at the smallest resolved scale for the energy flux, and at an intermediate scale r_{aniso} for the energy density, with a non-monotonic evolution of r_{aniso} during the decay.

2. The Kármán-Howarth-Monin equation

2.1. *General anisotropic formulation*

We briefly recall in this section the derivation of the Kármán-Howarth-Monin equation from the Navier-Stokes equation for (anisotropic) homogeneous rotating turbulence. We start from the Navier-Stokes equation for the velocity field $\mathbf{u}$ in a

rotating frame,

$$\partial_t u_i + u_j \partial_j u_i = -\frac{1}{\rho}\partial_i p + f_i + \nu \nabla^2 u_i + \mathcal{F}_i, \tag{1}$$

where $\mathbf{f} = -2\boldsymbol{\Omega} \times \mathbf{u}$ is the Coriolis force (per unit mass), p the pressure field corrected by the centrifugal force, and ν the kinematic viscosity. Although the experiments presented in this paper are concerned with the decaying case only, we also consider in this section an external applied force $\boldsymbol{\mathcal{F}}$ (per unit mass). Introducing this external force is a convenient way to distinguish the stationary and the decaying cases, although such volumic force is not realistic in practical situations.

The Kármán-Howarth equation for the evolution of the two-point velocity correlation $R_{ij}(\mathbf{r},t) = \langle u_i(\mathbf{x},t) u_j(\mathbf{x}+\mathbf{r},t)\rangle$, where $\langle\cdot\rangle$ stands for spatial (over $\mathbf{x}$) and ensemble averages, is obtained by multiplying Equation (1) by $u_j(\mathbf{x}+\mathbf{r})$ and symmetrizing over i and j. We assume here statistical homogeneity (with respect to position $\mathbf{x}$) but not isotropy (with respect to the direction of the separation vector $\mathbf{r}$). Noting the fields at point $\mathbf{x}+\mathbf{r}$ with a prime and at point $\mathbf{x}$ without a prime, we obtain

$$\begin{aligned}\partial_t R_{ij} = {} & \partial_k [S_{ik,j} - S_{kj,i}] + \langle u_i f'_j\rangle + \langle u'_j f_i\rangle \\ & + \partial_i \langle p u'_j\rangle - \partial_j \langle p u'_i\rangle + 2\nu \partial^2_{kk} R_{ij} + \langle u_i \mathcal{F}'_j\rangle + \langle u'_j \mathcal{F}_i\rangle,\end{aligned} \tag{2}$$

where we have introduced the two-point third-order velocity correlation $S_{ij,k}(\mathbf{r},t) = \langle u_i u_j u'_k\rangle$ and where $\partial_i = \partial/\partial r_i$ is now the derivative with respect to the i component of separation vector $\mathbf{r}$. The complexity of this equation originates from the velocity-pressure and the velocity-Coriolis force correlations, which both contribute in the general anisotropic case. However, restricting to the trace $R_{ii}(\mathbf{r},t) = \langle \mathbf{u}\cdot\mathbf{u}'\rangle$, simply denoted $R(\mathbf{r},t)$ in the following, these two contributions vanish, and Equation (2) reduces to

$$\frac{1}{2}\,\partial_t R(\mathbf{r},t) \;=\; \underbrace{\frac{1}{4}\nabla\cdot\mathbf{F}}_{\Pi(\mathbf{r},t)} \;+\; \underbrace{\nu\nabla^2 R}_{-D(\mathbf{r},t)} \;+\; \phi_{\rm inj}(\mathbf{r},t). \tag{3}$$

Following Frisch [19], we call (3) the Kármán-Howarth-Monin (KHM) equation. Here $D(\mathbf{r},t)$ is the viscous damping rate of the two-point correlation and $\Pi(\mathbf{r},t)$ is an energy flux, which derives from the energy flux density

$$\mathbf{F}(\mathbf{r},t) = \langle \delta\mathbf{u}\,(\delta\mathbf{u})^2\rangle, \tag{4}$$

where $\delta\mathbf{u} = \mathbf{u}(\mathbf{x}+\mathbf{r},t) - \mathbf{u}(\mathbf{x},t)$ is the velocity vector increment over separation $\mathbf{r}$. The forcing acts in (3) through the correlation $\phi_{\rm inj}(\mathbf{r},t) = \langle \mathbf{u}\cdot\boldsymbol{\mathcal{F}}' + \mathbf{u}'\cdot\boldsymbol{\mathcal{F}}\rangle/2$. Taking $\mathbf{r}=0$ in (3) simply gives the global energy budget $\partial_t\langle\mathbf{u}^2\rangle/2 = -\epsilon + \epsilon_{\rm inj}$, with $\epsilon(t) = D(0,t) = \nu\langle(\partial_i u_j)^2\rangle$ the mean dissipation rate per unit mass, and $\epsilon_{\rm inj}(t) = \phi_{\rm inj}(0,t) = \langle\mathbf{u}\cdot\boldsymbol{\mathcal{F}}\rangle$ the power per unit mass injected by the forcing. This result follows from the limit $\Pi(\mathbf{r},t)\to 0$ for $|\mathbf{r}|\to 0$, which reflects the fact that nonlinearities redistribute energy among scales without changing the total energy $R(0)/2$. We can note that it also satisfies $\Pi(\mathbf{r},t)\to 0$ for $|\mathbf{r}|\to\infty$ because all correlations must vanish at infinity.

Since the flux density (4) can be written in terms of velocity increments only, it is also of interest to write Equation (3) in terms of the variance of the velocity

increments, $E(\mathbf{r},t) = \langle(\delta\mathbf{u})^2\rangle$, instead of the two-points correlation. Using $E(\mathbf{r},t) = 2[\langle\mathbf{u}^2\rangle(t) - R(\mathbf{r},t)]$, Equation (3) can be rewritten as

$$\partial_t E + \nabla\cdot\mathbf{F} = 2\nu\nabla^2 E - 4\epsilon + 2\langle\delta\mathbf{u}\cdot\delta\boldsymbol{\mathcal{F}}\rangle, \tag{5}$$

(with $\delta\boldsymbol{\mathcal{F}} = \boldsymbol{\mathcal{F}}' - \boldsymbol{\mathcal{F}}$), where $\mathbf{F}$ can now be interpreted as a flux density for the variance E.

Interestingly, the rotation rate Ω does not appear explicitly in Equations (3)-(5), because the Coriolis force produces no work, so that these equations hold both with and without rotation. However, $\boldsymbol{\Omega}$ has a direct influence on the dynamics of $\Pi(\mathbf{r},t)$ or $\mathbf{F}(\mathbf{r},t)$ (governed by 4th order velocity correlations) which in turn will modify the correlation $R(\mathbf{r},t)$. This illustrates the subtle role of the Coriolis force, which leads to an anisotropic structuring of the two-points correlation R through a modification of the nonlinear energy transfers Π.

Homogeneous rotating turbulence is statistically axisymmetric about the rotation axis, which means that all statistical quantities in Equation (3) are axisymmetric with respect to the vector separation $\mathbf{r}$. In the following, we use spherical coordinates, with $\mathbf{e}_z$ the unit vector along $\boldsymbol{\Omega}$, θ the polar angle between $\mathbf{e}_z$ and $\mathbf{r}$, and φ the azimuthal angle in the plane normal to $\mathbf{e}_z$. By axisymmetry, all statistical quantities must depend on (r,θ,t) only, but the energy flux density $\mathbf{F}$ has in general three non-zero components $(F_r, F_\theta, F_\varphi)$. The azimuthal component F_φ is indeed not necessarily zero if the mirror symmetry with respect to vertical planes is broken (a situation which results from the cyclone-anticyclone asymmetry [5, 6]). However this azimuthal component must satisfy $\partial F_\varphi/\partial\varphi = 0$ by axisymmetry, so it does not contribute to the energy flux $\Pi(\mathbf{r},t)$.

2.2. *Energy cascade direction and physical interpretation of KHM*

The energy flux $\Pi(\mathbf{r},t)$ can receive a physical interpretation in the isotropic case only. In this case, all terms in Equations (3) and (5) are functions of $r = |\mathbf{r}|$ and t, and the variance $E(r,t)$ can be interpreted as the cumulated energy of fluid motions of size r or less (see, e.g., reference [34], § 6.6). Accordingly, $\Pi(r,t)$ corresponds to the energy transfer rate through the scale r, i.e., from scales smaller than r towards scales larger than r. For instance, in decaying turbulence, a negative flux $\Pi(r,t)$ increases the cumulated energy $E(r,t)$ from 0 to r, a clear signature of a *direct* cascade of energy toward scales smaller than r. In the isotropic case, the sign (negative or positive) of $\Pi(r,t)$ at a given scale r therefore simply corresponds to the local direction (direct or inverse, respectively) of the energy flux at that scale. Note that if the sign of Π remains constant in a range $[0,r]$, then it also sets the sign of the (scalar) flux density, $F_r(r) = 4r^{-2}\int_0^r \Pi(r)r^2\,dr$.

The counterpart of the KHM equation in the Fourier space is the Lin equation, which in its isotropic form reads $\partial_t e(k,t) = T(k,t) - 2\nu k^2 e(k,t) + \Phi(k,t)$, where $e(k,t)$ is the spectral density of energy, $\Phi(k,t)$ the spectral forcing, and $T(k,t)$ the spectral transfer, accounting for the redistribution of energy among wave numbers k. An important difference between the Lin and KHM equations is that the former governs the dynamics of the energy density $e(k,t)$, whereas the latter governs the dynamics of the "cumulated energy" $E(r,t)$ up to scale r. As a consequence, the equivalent of the physical-space flux $\Pi(r,t)$ of the KHM equation is the spectral flux $\Pi(k,t) = \int_0^k T(k,t)dk$ across the wavenumber k: there is thus a difference of one order of derivation between these two equations. In this isotropic formulation, both $\Pi(k)$ and $\Pi(r)$ are given by $-\epsilon$ in the inertial range at large Reynolds number.

The physical interpretation for $\Pi(\mathbf{r},t)$ cannot be generalized to the anisotropic

case, in which the separation vector $\mathbf{r}$ cannot be simply reduced to a 'scale' $r = |\mathbf{r}|$. In particular, the sign of $\Pi(\mathbf{r}, t)$ or F_r for a given vector separation $\mathbf{r}$ cannot be simply associated to a direction of energy flux. An additional difficulty is that, since the flux density $\mathbf{F}$ acts in the KHM equation only through its divergence, a particular $\mathbf{F}$ or any other flux density $\mathbf{F} + \mathbf{G}$, with $\mathbf{G}$ an arbitrary solenoidal axisymmetric 'gauge' vector field, will have the same effect on the dynamics of R. The flux density $\mathbf{F}$ therefore contains a redundant degree of freedom, which makes delicate any direct physical interpretation of this quantity in general.

2.3. *Stationary forced rotating turbulence*

We examine here the case of stationary (hence, forced) turbulence, by taking $\partial_t R = 0$ in (3). In this case, taking $\mathbf{r} = 0$ simply indicates that $\epsilon = \epsilon_{\rm inj}$, i.e. the injected power is balanced by the viscous dissipation. The KHM equation (3) now only relates the energy flux $\Pi(\mathbf{r})$ to the injection $\phi_{\rm inj}(\mathbf{r})$ (apart from viscous effects), so it cannot provide solution for $R(\mathbf{r})$ without further assumption. The simplest case is to assume an isotropic forcing at a large scale L, characterized by a constant forcing term $\phi_{\rm inj}(\mathbf{r}) \simeq \epsilon_{\rm inj}$ for $|\mathbf{r}| \ll L$, and $\phi_{\rm inj}(\mathbf{r}) \simeq 0$ for $|\mathbf{r}| \gg L$ (note that this assumption implicitly prevents the possibility of an inverse cascade). As a consequence, for inertial scales $r_\nu \ll |\mathbf{r}| \ll L$, where r_ν is a suitably defined viscous cutoff (analogous to the Kolmogorov scale η but possibly modified by rotation), $D(\mathbf{r})$ can be neglected and Equation (3) simply reduces to

$$\Pi(\mathbf{r}) \equiv \frac{1}{4}\nabla \cdot \mathbf{F} = -\epsilon. \tag{6}$$

If isotropy is further assumed, then $\mathbf{F}$ is a purely radial vector, and Equation (6) can be readily integrated, yielding $\mathbf{F} = -\frac{4}{3}\epsilon\mathbf{r}$, i.e.

$$\langle \delta u_L (\delta \mathbf{u})^2 \rangle = -\frac{4}{3}\epsilon r,$$

known as the 4/3rd law [35], with $\delta u_L = \delta\mathbf{u}\cdot\mathbf{r}/r$ the longitudinal velocity increment. Using classical isotropic relations between longitudinal and transverse increments [18], this law is actually identical to the Kolmogorov's 4/5th law, $\langle (\delta u_L)^3 \rangle = -\frac{4}{5}\epsilon r$.

Now, if isotropy cannot be assumed, as for (homogeneous) rotating turbulence, the flux density $\mathbf{F}$ is no longer isotropic, although the flux $\Pi(\mathbf{r})$ itself remains constant (and hence isotropic) for separations $r_\nu \ll |\mathbf{r}| \ll L$. But since $\mathbf{F}$ is no longer radial (it has at least two non-zero components, F_r and F_θ, and also possibly F_φ if the cyclone-anticyclone symmetry is broken), Equation (6) cannot be integrated without further assumption. At this step, only phenomenological arguments have been proposed so far to infer the geometry of $\mathbf{F}$. For example, Galtier [20] suggests from the dispersion relation of inertial waves that $\mathbf{F}$ should be aligned with the vector $\mathbf{e}_T = \mathbf{e}_r + \frac{4}{3}\mathbf{e}_z$ in the limit $Ro \ll 1$, with $\mathbf{e}_z$ oriented along $\mathbf{\Omega}$. From this, he obtains an anisotropic Kolmogorov-like expression for the flux density in the inertial range, $\mathbf{F} = -C(\theta)\epsilon r\, \mathbf{e}_T/|\mathbf{e}_T|$, with a prefactor $C(\theta)$ slowly dependent upon the polar angle θ. A similar approach has been considered by Augier *et al.* [36] for stratified turbulence. This result might be however difficult to check experimentally, because the assumption of an isotropic forcing $\phi_{\rm inj}(\mathbf{r})$ is hardly satisfied in practical situations. Typical forced turbulence experiments in a rotating frame, based on a localized energy injection, e.g. by means of oscillated grid or pumping device, essentially produce inhomogeneous and hence anisotropic forcing.

2.4. *Decaying rotating turbulence*

We finally examine the case of homogeneous decaying turbulence in a rotating frame, which applies to the experiments presented hereafter. Taking $\phi_{\rm inj}(\mathbf{r},t)=0$ in Equation (3) yields

$$\frac{1}{2}\,\partial_t R(\mathbf{r},t) \;=\; \underbrace{\frac{1}{4}\nabla\cdot\mathbf{F}}_{\Pi(\mathbf{r},t)} \;+\; \underbrace{\nu\nabla^2 R}_{-D(\mathbf{r},t)}. \tag{7}$$

This is the key equation of this paper. It shows that, starting from an initially isotropic turbulence, characterized by a correlation $R(\mathbf{r},0)$ independent of the orientation θ, an anisotropy growth in $R(\mathbf{r},t)$ is expected only if the energy flux $\Pi(\mathbf{r},t)$ itself is anisotropic.

Equation (7) shows that two regimes can be expected in decaying rotating turbulence. At short time ("short" being dependent on the considered separation $\mathbf{r}$), the viscous term can be neglected, leading to an anisotropy growth of $R(\mathbf{r},t)$ driven by the anisotropic flux $\Pi(\mathbf{r},t)$, on a timescale which must depend on Ω. At larger time, however, the viscous term becomes dominant, and Equation (7) reduces to $\partial_t R/2=\nu\nabla^2 R$, a simple diffusion equation in the space of separations $\mathbf{r}$. Although in this second regime the Rossby number can be very small, rotation, which acts only through the flux density $\mathbf{F}$, is no longer present in the dynamics of R. During this final viscous regime the shape of the correlation $R(\mathbf{r},t)$ remains unchanged, i.e. the anisotropy at each scale keeps the level reached at the end of the growth regime. This indicates that strong anisotropy may be reached only if the transfer Π acts during a sufficiently large time before viscosity becomes significant. This requires both low Rossby number $Ro=U/2\Omega L$ and large Reynolds number $Re=UL/\nu$. These two limits imply that the initial characteristic velocity U should verify the double condition $\nu/L \ll U \ll 2\Omega L$, indicating that $2\Omega L^2/\nu = Re/Ro \gg 1$ is necessary to reach a significant anisotropy during the decay.

3. Experimental setup and procedures

3.1. *Experimental setup*

The experimental setup is described in [37], and is only briefly recalled here (Figure 1a). Turbulence is generated by rapidly towing a square grid at a velocity $V_g = 1.0$ m s^{-1} from the bottom to the top of a cubic glass tank, of lateral side 60 cm, filled with 52 cm of water. The grid consists in 8 mm thick bars with a mesh size $M = 40$ mm. The whole setup is mounted on the 2 m diameter rotating turntable "Gyroflow" at University Paris-Sud.

Runs for three rotation rates, $\Omega = 0.42, 0.84$ and 1.68 rad s^{-1} (4, 8 and 16 rpm respectively), as well as a reference run without rotation, have been carried out. One has $\Omega M^2/\nu = (6.7-27)\times 10^4$, so that the criterion $\Omega L^2/\nu \gg 1$ necessary for an anisotropy growth before viscous effects become dominant is satisfied (see section 2.4). For each rotation rate, 600 independent decay realizations have been performed. The initial Reynolds number based on the grid mesh is $Re_g = V_g M/\nu = 40\,000$, whereas the initial Rossby number $Ro_g = V_g/2\Omega M$ ranges from 7.4 to 30, indicating that the flow in the close wake of the grid is fully turbulent and weakly affected by rotation.

An important concern about grid turbulence experiments in a confined rotating volume is the excitation of large scale inertial modes [38, 39]. These modes are

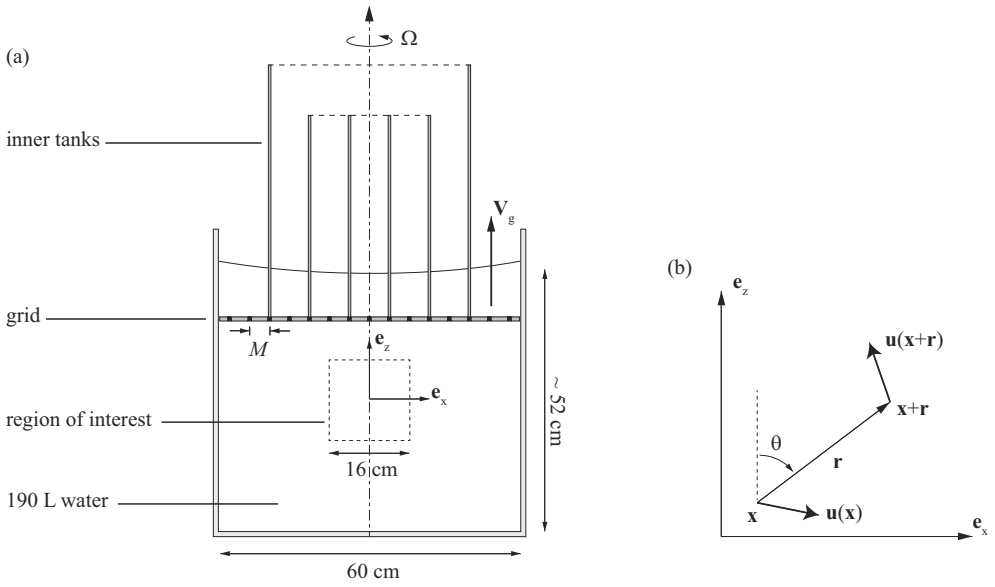

Figure 1. (a) Experimental setup. (b) Velocity increment in the measurement plane $(\mathbf{e_x}, \mathbf{e_z})$, and definition of the spherical coordinate system (r, θ, φ). The azimuthal angle φ (not shown) corresponds to rotation about the axis $\mathbf{e}_z$.

the eigenmodes of inertial waves specific of the container geometry, and have been characterized in detail in the case of a cubic container [40, 41]. Since they are triggered by the grid translation, they have the same phase origin and do not cancel out by ensemble averaging over independent realizations. In this respect, these reproducible inertial modes cannot be considered as turbulence in the sense of the Reynolds decomposition, and constitute an unstationary mean flow.

The excitation of inertial modes have been systematically characterized in [37] for the present geometry. Using a simple grid, we have found that the energy of these modes represents up to 50% of the total energy. The existence of these large-scale modes, which may continuously re-inject energy into the turbulence, break the assumption of homogeneity which is a necessary condition for the validity of the KHM equation (7). However it has been shown in [37] that the excitation of those modes could be significantly reduced by using a specific design of the grid, as sketched in Figure 1(a). A set of vertical sidewalls, in the form of 3 inner tanks without top and bottom walls, are fit together and mounted on the top of the grid. This configuration improves the homogeneity of the flow through the grid meshes, and the energy of the residual reproducible modes represents only 10 to 15% of the total energy. We can therefore consider that the turbulence produced by this setup is reasonably homogeneous and freely decaying, except possibly in the final period of the decay.

3.2. *PIV measurements and two-dimensional surrogates*

During each decay realization, a 2D slice of the velocity field is measured as a function of time in the vertical plane $(\mathbf{e_x}, \mathbf{e_z})$, where z is the rotation axis, in a square area of 16×16 cm^2, using a particle image velocimetry system in the rotating frame. Images are acquired using a double-frame 2048^2 pixels camera, and particles seeding the flow are illuminated using a double pulsed vertical laser sheet mounted on the rotating turntable. 2D velocity fields are computed from image pairs on a 128^2 grid, with a spatial resolution $\Delta x = 1.3$ mm. This resolution is sufficient to resolve the inertial range, but fails to resolve the dissipative scale, at least during the early stage of the turbulence decay (the Kolmogorov scale η is of the order of

0.2 mm right after the grid translation).

For each time after the grid translation, turbulence statistics are ensemble-averaged over the 600 turbulence decay realizations. The restriction to two velocity components (u_x, u_z) has important consequences for the computation of these statistics. Assuming axisymmetry, one has $u'_x = u'_y \neq u'_z$ (with $u'_\alpha = \langle u_\alpha^2 \rangle^{1/2}$ the r.m.s. of the α component), so one-point quantities can be readily computed from the two measured components, e.g. one has $k(t) = (2u_x'^2 + u_z'^2)/2$ for the kinetic energy per unit mass. The situation is less simple for the two-point quantities present in the KHM equation. We actually measure here only two-dimensional surrogates of the energy distribution and flux density (4), namely

$$\widetilde{E}(\mathbf{r}) = \langle \delta u_x^2 + \delta u_z^2 \rangle_{x,z}, \quad \widetilde{\mathbf{F}}(\mathbf{r}) = \langle \delta \mathbf{u} (\delta u_x^2 + \delta u_z^2) \rangle_{x,z} \tag{8}$$

(and similarly for the two-points correlation $\widetilde{R}(\mathbf{r})$), where the spatial average is performed in the measurement plane $(\mathbf{e_x}, \mathbf{e_z})$, and $\mathbf{r} = r_x \mathbf{e}_x + r_z \mathbf{e}_z$ (see Figure 1b).

Exact relations between the surrogate quantities (8) and the exact quantities based on the 3 velocity components (4) can be written for isotropic turbulence (see, e.g., [18]). One has $\widetilde{E}(\mathbf{r}) = \langle \delta u_L^2 + \delta u_T^2 \rangle$ and $E(\mathbf{r}) = \langle \delta u_L^2 + 2\delta u_T^2 \rangle$, with δu_L and δu_T the longitudinal (along $\mathbf{r}$) and transverse increments. For instance, in the dissipative range, isotropy implies $\langle \delta u_T^2 \rangle = 2\langle \delta u_L^2 \rangle$, yielding $E = \frac{5}{3}\widetilde{E}$. Similarly, for the third-order moment, one has $\widetilde{F}_r(\mathbf{r}) = \langle \delta u_L^3 + \delta u_L \delta u_T^2 \rangle$ and $F_r(\mathbf{r}) = \langle \delta u_L^3 + 2\delta u_L \delta u_T^2 \rangle$, yielding $\mathbf{F} = \frac{7}{5}\widetilde{\mathbf{F}}$ in the dissipative range. In the homogeneous and axisymmetric case, kinematics relations between the 2D surrogates (8) and the exact quantities (4) have been derived by Lindborg [42]. However, these relations imply third-order derivatives, so their computation using finite differences from experimental data introduce strong noise. For this reason, we only consider the 2D surrogates here, which will prevent us from verifying quantitatively the budget of the KHM equation. In the following we drop the tildes $\widetilde{\ }$ in Equation (8) for simplicity.

3.3. *Convergence of the statistics*

Ensuring a correct convergence of the ensemble averages is critical, in particular for the computation of the energy flux density $\mathbf{F}(\mathbf{r})$: being a 3rd order moment of velocity increments of zero mean, its statistical convergence requires a very large number of realizations. A systematic evaluation of the convergence of the various fields has been performed as follows. We note in the following $A(\mathbf{r}, t)$ one of the scalar field of interest: E, the two measured components of $\mathbf{F}$ (F_r and F_θ), or $\Pi = \nabla \cdot \mathbf{F}/4$. This field A is computed as the ensemble average over N independent realizations, which we denote $A_n(\mathbf{r}, t)$ with $n = 1...N$. Each $A_n(\mathbf{r}, t)$ is computed from spatial average over $\mathbf{x}$ of combinations of $\delta\mathbf{u}(\mathbf{x}, \mathbf{r}, t)$. For a given time t and a given separation $\mathbf{r}$, the set $\{A_n\}$ thus defines a random variable. The standard deviation of this random variable, $\mathrm{std}(\{A_n\}) = \langle (A_n - A)^2 \rangle^{1/2}$ (with $A = \langle A_n \rangle$) characterizes its intrinsic variability. For a finite number of realizations N, the uncertainty in the determination of the average A can be obtained from the central limit theorem,

$$\sigma_A(\mathbf{r}, t) = \mathrm{std}(\{A_n\})/\sqrt{N}. \tag{9}$$

The convergence of E, $\mathbf{F}$ and Π is illustrated in Figure 2, for a particular rotation rate $\Omega = 16$ rpm, at a time $tV_g/M = 400$ after the grid translation. These quantities

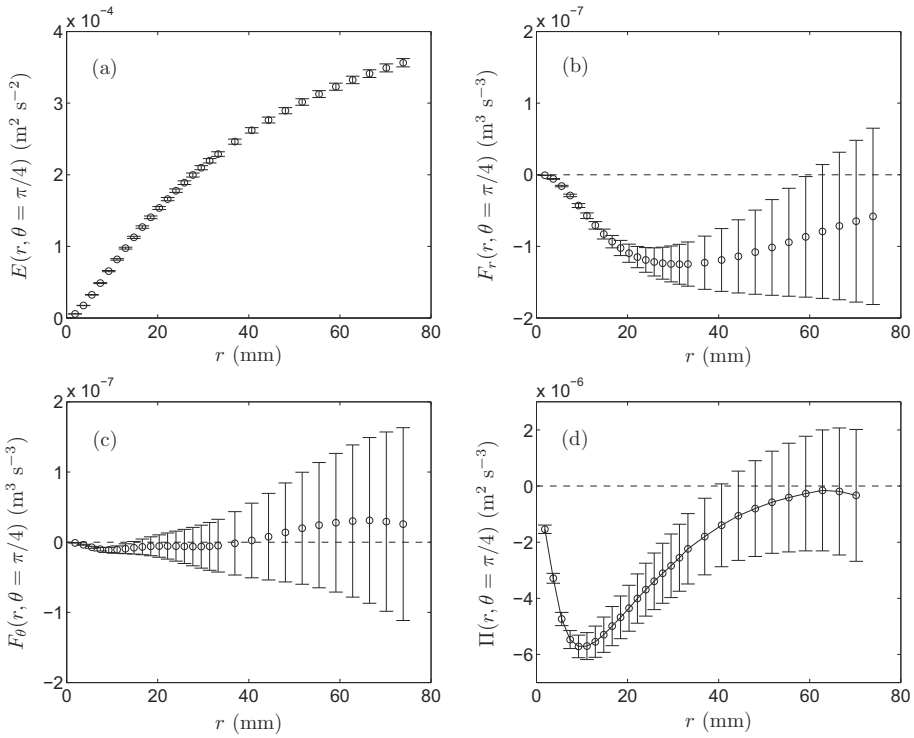

Figure 2. Uncertainty of the statistical quantities as a function of the separation r for a polar angle $\theta = \pi/4$, illustrated by the error bars $\pm\sigma$, with σ defined in Equation (9). (a) Variance of the velocity increments $E(r)$; (b,c) radial and polar components of the energy flux density $\mathbf{F}$; (d) energy flux $\Pi = \nabla\cdot\mathbf{F}/4$. Data obtained at the time $tV_g/M = 400$, for the rotating case at $\Omega = 16$ rpm.

are plotted as a functions of $r = |\mathbf{r}|$, for a fixed angle $\theta = \pi/4$, and the uncertainties (9) are depicted with error bars of length $\pm\sigma_A$. The convergence is excellent for E, showing an accuracy better than 1.5% for all scales up to $r \simeq 2M$. The convergence is not so good for $\mathbf{F}$ and Π, especially at large scales. The increasing uncertainty at large r originates both from a larger intrinsic variability of $\mathbf{F}_n$ at large r and from the decreasing number of available velocity increments when r becomes of the order of the size of the measurement area. Although the uncertainty is significant for $\mathbf{F}$ and Π, improving the convergence of the statistics would require an unrealistic number of realizations ($N = 600$ represents 24 hours of continuous run for each value of Ω).

4. Anisotropy growth and energy transfers

4.1. *Instantaneous Reynolds and Rossby numbers*

We first provide general characteristics of the turbulence decay, by examining the time evolution of the velocity variances $u'_\alpha = \langle u_\alpha^2\rangle^{1/2}$, integral scale, and instantaneous Reynolds and Rossby numbers.

The decay of the horizontal velocity variance (Figure 3a) shows weak effect of the background rotation, following a power law close to $t^{-1.1\pm0.1}$ for $tV_g/M > 50$ at all Ω. The energy decay is slightly reduced at the largest rotation rate, at least for intermediate times, but this effect remains weak and difficult to characterize unambiguously in terms of decay exponent. Sharper effect of the rotation were reported in [6] and [43], but the turbulence statistics of these previous experiments presumably suffered from stronger coupling with reproducible large-scale inertial modes generated by the grid translation. The generation of inertial modes is significantly reduced in the present experiment by the use of a modified grid (see Sec. 3.1),

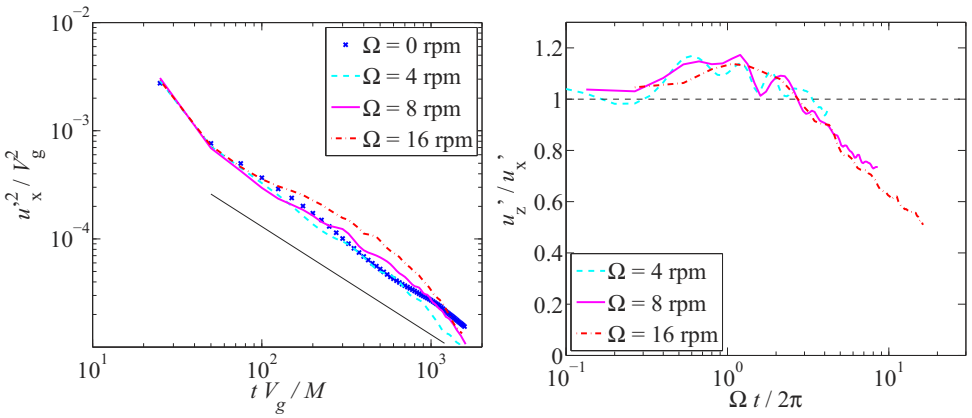

Figure 3. (a) Decay of the horizontal velocity variance. The line shows a power law t^{-1}. (b) Time evolution of the ratio u'_z/u'_x.

so the present results can be considered as more reliable in this respect. But in any case the strong sensitivity of the decay law on the details of the large-scale flows, which are very difficult to fully eliminate in an experiment, makes this issue difficult to address unequivocally.

The time evolution of the vertical-to-horizontal velocity ratio, shown in Figure 3(b) indicates a nearly isotropic energy distribution at small time, characterized by a nearly constant ratio u'_z/u'_x in the range $1.0 - 1.2$ (the stronger variance for the velocity component along the grid translation is a usual property of grid generated turbulence). An anisotropy growth is found for $\Omega t/2\pi > 2$ for the two largest rotation rates, with a good collapse of the curves when rescaled by Ω^{-1}. This anisotropy ratio reaches moderate values, down to $u'_z/u'_x \simeq 0.5$ at the end of the $\Omega = 16$ rpm experiment, confirming that the velocity field remains significantly three-component, although the dynamics of the large scales becomes nearly two-dimensional. This velocity ratio of order 1 is also an indication that even at large time, the Ekman pumping mechanism can be neglected. The Ekman-pumping vertical velocity induced by the horizontal flow would give $u'_z/u'_x \simeq E^{1/2} \simeq 10^{-3}$ (where $E = \nu/2\Omega h^2 \in [0.8, 3]\times 10^{-6}$ is the Ekman number, with h the tank height), which is much smaller than the measured velocity ratio.

In order to compute the instantaneous Reynolds and Rossby numbers, we define the integral scale normal to the rotation axis as

$$L_\perp(t) = \int_0^{r^*} C_\perp(r,t)dr, \qquad \text{with } C_\perp(r,t) = \frac{\langle u_x(\mathbf{x},t)u_x(\mathbf{x}+r\mathbf{e}_x,t)\rangle}{u'^2_x}.$$

The conventional definition is such that $r^* = \infty$, but using here a finite truncation scale is necessary because at large time the correlation function $C_\perp(r,t)$ does not reach 0 at the scale of the PIV field. Following [6] and [44], we chose r^* such that $C_\perp(r^*) = 0.2$. Here again, the background rotation has a weak effect on the integral scale (Figure 4a), all the curves following approximately a power law $L_\perp(t)/M \propto t^{0.30\pm0.05}$ (where M is the grid mesh size). Note that the integral scale parallel to the rotation axis cannot be computed in these experiments, because the vertical correlation rapidly increases and becomes larger than the PIV field in the rotating case.

The instantaneous Reynolds number based on the horizontal velocity fluctuations,

$$Re(t) = \frac{u'_x L_\perp(t)}{\nu},$$

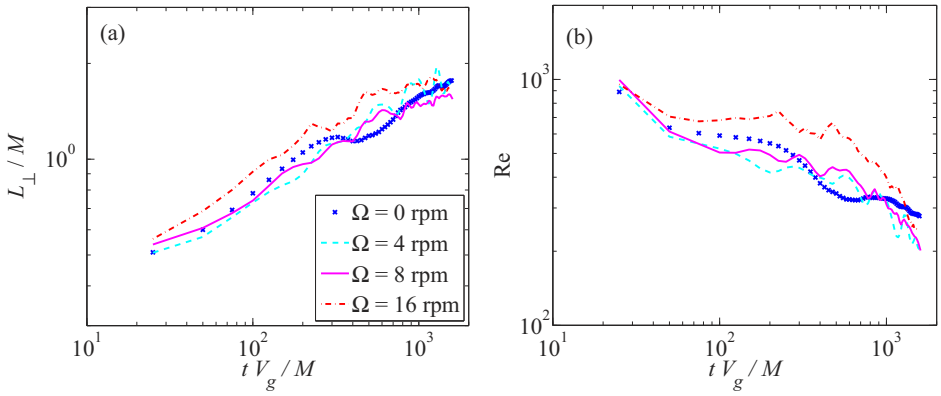

Figure 4. Time evolution of (a) the horizontal integral scale $L_\perp(t)/M$; (b) of the instantaneous Reynolds number $Re(t)$.

is plotted in Figure 4(b), showing a slow decrease from 1000 to about 200, with again a weak influence of the rotation rate. These values indicate that turbulence is moderate in these experiments, and that significant viscous effects must be expected during the decay.

Similarly, we define the instantaneous Rossby number as

$$Ro(t) = \frac{u'_x}{2\Omega\, L_\perp(t)},$$

which decreases from values $O(1)$ down to $O(10^{-1}-10^{-2})$. Interestingly, the curves for the three rotation rates nearly collapse when plotted as a function of the number of tank rotations, $\Omega t/2\pi$ (Figure 5). This collapse is consistent with the analysis of Moisy *et al.* [6], and follows from the fact that in decaying grid turbulence the non-linear time scale $\tau_{nl}(t) \simeq L_\perp/u'_x$ is simply proportional to the elapsed time t after the grid translation, at least at short time (large Ro). It turns out here that the single power law $Ro(t) \propto (\Omega t)^{-0.9\pm0.1}$ provides a reasonable fit for the whole range of time (the above argument would actually predict $Ro(t) \propto (\Omega t)^{-1}$, but at $Ro > 1$ only). The Rossby number at which anisotropy starts for the ratio u'_z/u'_x, i.e. at large scale, is $Ro \simeq 0.1$ (at $\Omega t/2\pi \simeq 2$).

In order to gain more insight into the weak influence of the background rotation on the overall decay of kinetic energy, we can write the decay rate dimensionally as

$$-\frac{du'^2_x}{dt} = G(Ro, Re)\frac{u'^3_x}{L_\perp}. \tag{10}$$

For fully developed turbulence in the absence of rotation ($Re \gg 1$, $Ro \gg 1$), the usual Kolmogorov decay law is recovered with $G \simeq O(1)$. The Ro dependence of G in the presence of rotation ($Ro < 1$) is still a matter of debate [45]. The analysis of Squires *et al.* [46], assuming that the energy decay rate scales as Ω^{-1} for $Ro \ll 1$, $Re \gg 1$, yields $G(Ro, Re) \simeq Ro$. Assuming the conservation of the Saffman (or Loitsanskii) invariant in its isotropic form, this assumption implies that the decay exponent of energy is half the non-rotating decay exponent. This half-exponent prediction has received some numerical [47] and experimental [6] support, but other scalings have also been proposed ($u'^2_x \sim t^{-1}$ based on the conservation of the decay invariant in a modified anisotropic form [45, 48]).

We plot in Figure 6 the prefactor G from Equation (10) as a function of time for the four data sets. Interestingly, all the curves are consistent with a constant value,

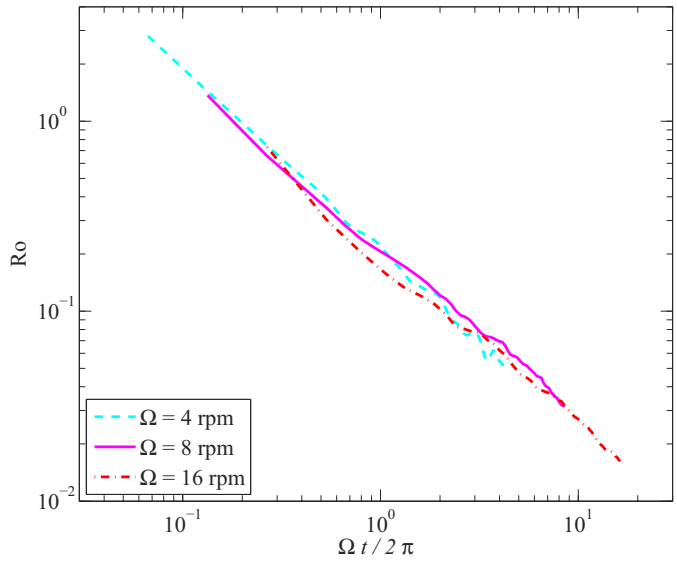

Figure 5. Instantaneous Rossby number as a function of the number of tank rotation.

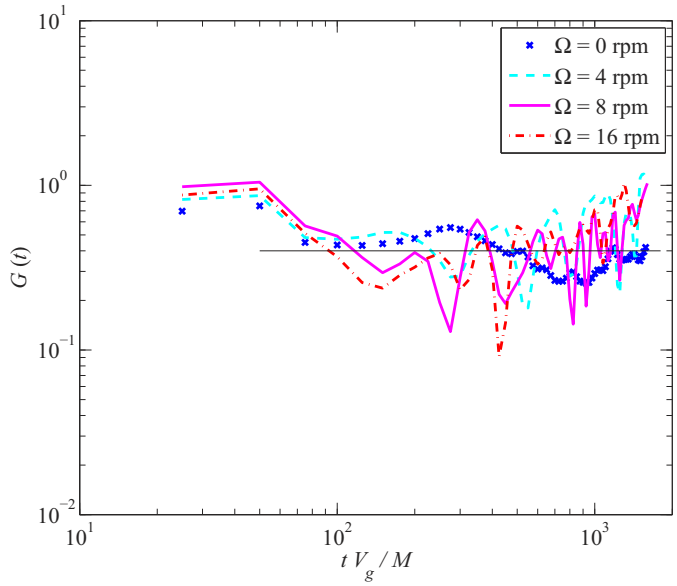

Figure 6. Prefactor $G(t)$ in Equation (10).

$G \simeq 0.4 \pm 0.2$. Although the scatter is large, these curves are not compatible with a $G(Ro) \simeq Ro$ law, since $Ro(t)$ varies over more than one order of magnitude in the same temporal range. This suggests that, at least for the moderate Reynolds and Rossby numbers considered here, the dissipation rate remains well described by the usual non-rotating prediction, $u_x'^3/L_\perp$. It is possible that even smaller Ro are necessary to observe the scaling $G(Ro) \simeq Ro$; however, it must be noted that reaching much smaller Ro while keeping large Re in a decaying turbulence experiment is very difficult.

4.2. *Two-points velocity correlation and energy flux density*

We now turn to two-point statistics in order to probe the scale dependence of the anisotropy growth. The maps of the velocity correlation $R(\mathbf{r}, t)$ for separations $\mathbf{r}$ in the vertical plane are plotted in Figures 7(a,b) for the experiment at $\Omega = 0$,

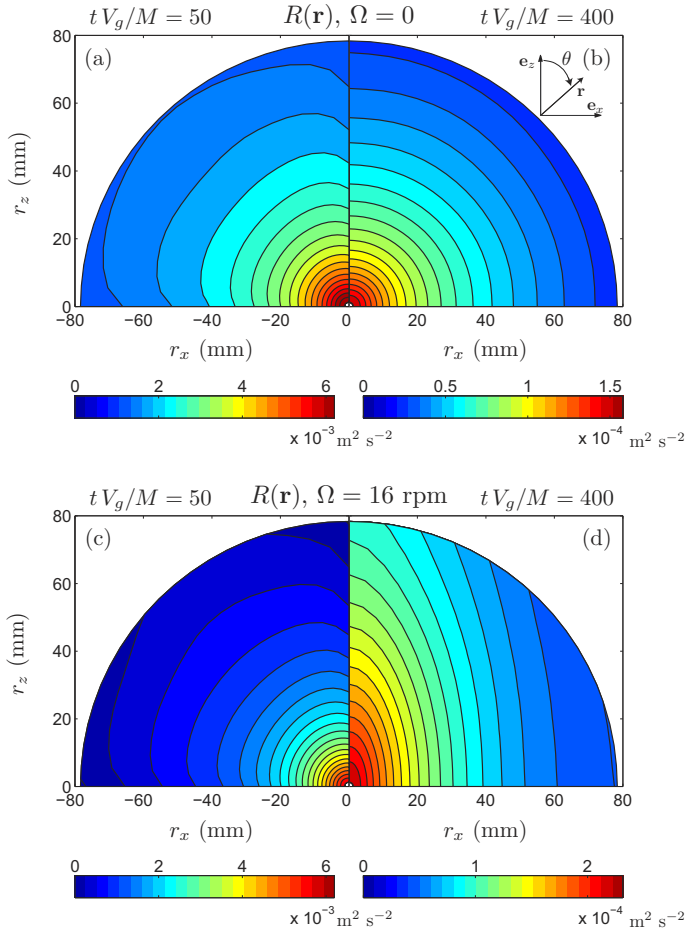

Figure 7. Maps of velocity two-points correlation $R(\mathbf{r})$ at times $tV_g/M = 50$ (a and c) and $tV_g/M = 400$ (b and d) after the grid translation, for $\Omega = 0$ and 16 rpm.

at times $tV_g/M = 50$ and 400 ($t = 2$ and 16 s) after the grid translation. For $tV_g/M = 50$ ($Re \simeq 640$), the iso-level curves are nearly circular, indicating a reasonable level of small-scale isotropy. For scales r larger than $0.6\,M$, we observe a slight decrease of R along the directions $\theta = 0$ and $\theta = \pi/2$ which probably reflects a residual inhomogeneity of the flow induced by the grid. However, for $tV_g/M > 80$, the distribution of $R(\mathbf{r}, t)$ becomes almost perfectly isotropic even at scales r up to $2M$ (Figure 7b). The time needed to reach this isotropy is in good agreement with classical observations of grid turbulence experiments in wind tunnels, which produce approximately isotropic turbulence for distances larger than $40M$ downstream only [49].

We consider now the rotating case at $\Omega = 16$ rpm (Figures 7c,d). At $tV_g/M = 50$ (0.5 tank rotation, $Re = 700$, $Ro = 0.3$), the two-points correlation is almost identical to that found at $\Omega = 0$, confirming that the turbulence generated by the grid is essentially not affected by rotation. This particular time is actually before the start of the anisotropy growth (see Figure 3b). On the other hand, $R(\mathbf{r})$ is strongly anisotropic at time $tV_g/M = 400$ (4.3 tank rotations, $Re = 600$, $Ro = 0.06$), with an enhanced correlation along the rotation axis. This reflects the classical trend towards a 2D-3C turbulence invariant along z (a purely 2D-3C turbulence would correspond to R independent of r_z, i.e. to vertical iso-R lines).

We compare in Figures 8(a,c) the energy flux density $\mathbf{F}(\mathbf{r}, t)$ at time $tV_g/M = 400$ for $\Omega = 0$ ($Ro = \infty$) and $\Omega = 16$ rpm ($Ro = 0.06$). Because the uncertainty on $\mathbf{F}(\mathbf{r}, t)$ for $r > M$ is significantly larger than for second order quantities (see section 3.3), we restrict here to $r \leq M$. At first sight, the vector field $\mathbf{F}$ looks

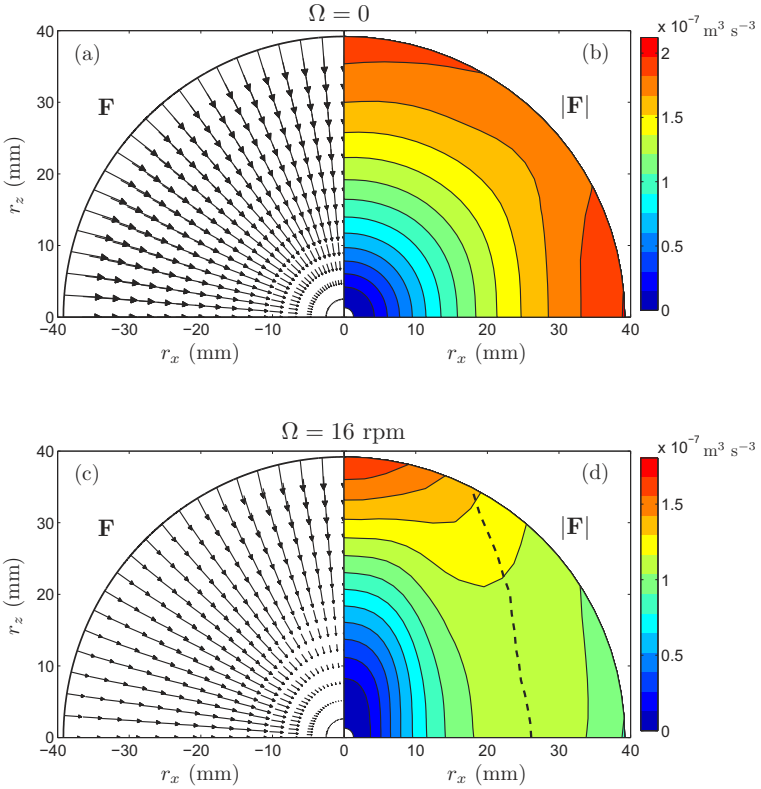

Figure 8. Energy flux density $\mathbf{F}(\mathbf{r})$ at time $tV_g/M = 400$ after the grid translation for $\Omega = 0$ (top, $Re = 400$, $Ro = \infty$) and $\Omega = 16$ rpm (bottom, $Re = 600$, $Ro = 0.06$). In (d), the dashed line shows the "crest line" following the local maximum of $|\mathbf{F}|$.

nearly radial, pointing towards the origin, both in the non-rotating and rotating cases. A departure from the radial direction in the rotating case appears at small scales only, for $r < 10$ mm, where a deflection towards the rotation axis is observed. Although such horizontally tilted $\mathbf{F}$ is consistent with an asymptotic 2D-3C flow (for which $\mathbf{F}$ must be horizontal and independent of r_z), the overall vector field for $r > 10$ mm remains surprisingly radial. This concentration of anisotropy at small scale will be discussed in more detail in section 5.

Differences between the non-rotating and rotating cases are more evident when comparing the iso-magnitude curves of the flux density $\mathbf{F}$ (Figures 8b,d). Note that, since the azimuthal component F_φ is not measured, the magnitude here is actually the 2D norm in the $(\mathbf{e}_x, \mathbf{e}_z)$ plane. The iso-$|\mathbf{F}|$ are nearly circular for $\Omega = 0$, with only slight departure from isotropy near $r \simeq M$, illustrating again the good isotropy of the turbulence without rotation. For $\Omega = 16$ rpm, the iso-$|\mathbf{F}|$ shows a strong anisotropy that extends up to large scales, similar to that of R. Since $\mathbf{F}$ remains nearly radial (except at $r < 10$ mm), the anisotropy of $\mathbf{F}$ is not dominated by the growth of a polar component F_θ, but rather by a θ-dependence of the radial component F_r, at least for $r > 10$ mm. The maximum of $|\mathbf{F}|$ is systematically encountered at rather large scales for vertical separations $\mathbf{r}$ ($r_z \simeq 50-80$ mm in this case), whereas it is found at smaller scales for horizontal separations ($r_x \simeq 30$ mm), as evidenced by the elongated shape of the 'crest line' (dashed line) following the local maximum of $|\mathbf{F}|$.

As noted in Section 2.2, although the flux density $\mathbf{F}$ is the most direct signature of energy transfers that can be computed from the velocity fields, it enters into the KHM equation only through its divergence. The physical interpretation of $\mathbf{F}$ itself is therefore delicate, and the physics of the anisotropic energy transfers is investigated in the following directly from the flux $\Pi = \nabla \cdot \mathbf{F}/4$, which is the source

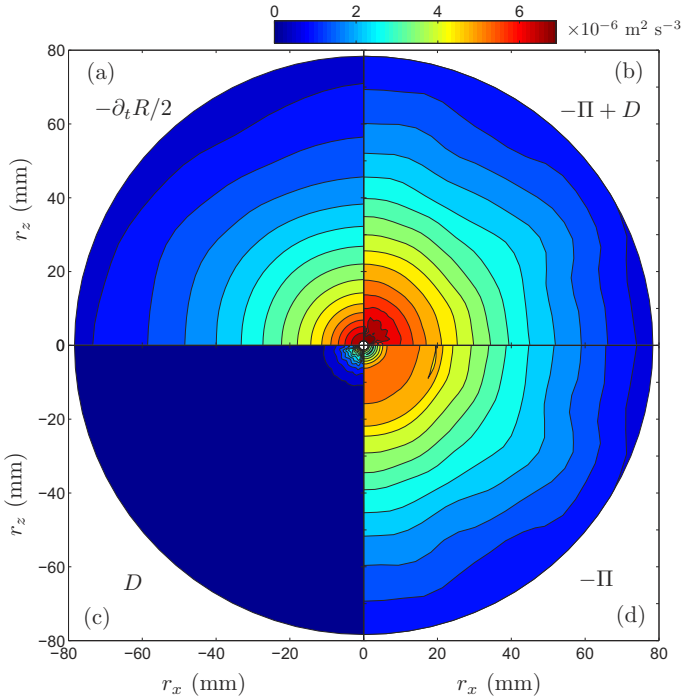

Figure 9. Maps of the terms of the KHM equation for the non-rotating experiment at time $t\,V_g/M = 400$. (a) Unstationary term $-\partial_t R/2$, (c) dissipative term $D = -\nu\nabla^2 R$, (d) transfer term $-\Pi = -\nabla\cdot\mathbf{F}/4$, (b) r.h.s. of the KHM equation $-\Pi + D$.

term for the two-points correlation.

4.3. *Balance between the terms of the KHM equation*

If the assumption of homogeneity remains valid, the KHM equation (7) indicates that the unstationary term $\partial_t R/2$ must be balanced at each separation $\mathbf{r}$ by the flux $\Pi(\mathbf{r},t)$ and the viscous damping $-D(\mathbf{r},t) = \nu\nabla^2 R$. We propose here to check experimentally the consistency of this energy budget, with emphasis on the anisotropy growth of the different terms. It must be noted that an exact verification of the energy budget cannot be achieved here, because of the use of 2D surrogates of R and $\mathbf{F}$ (8). In spite of this limitation, a qualitative comparison between the 3 terms is of first interest to characterize the relation between the geometry of the flux Π and the anisotropy growth of R, and also to estimate the influence of the flow inhomogeneities arising from the container walls and the importance of non-measured out-of-plane contributions $\langle\delta u_y^2\rangle$ and $\nabla\cdot\langle\delta\mathbf{u}(\delta u_y)^2\rangle$.

4.3.1. Non-rotating case

We first present in Figure 9 the spatial structure of the three terms of the KHM equation (7) at time $t\,V_g/M = 400$ for the non-rotating experiment. $R(\mathbf{r},t)$ and $\mathbf{F}(\mathbf{r},t)$ have been remapped on the spherical coordinate system (r,θ,φ), with θ the polar angle between $\mathbf{e}_z$ and $\mathbf{r}$ (see Figure 1b). The divergence and Laplacian operators are approximated by centered second-order finite differences.

The 3 terms of the KHM equation are remarkably isotropic. As expected the energy flux Π tends to zero both at small and large scales, and shows in between a broad negative minimum in an annular region spanning from $r \simeq 5$ to 20 mm, providing a rough indication of the extent of an inertial range. The viscous term D takes significant values only at small scale, for $r \leq 10$ mm. The noise in D originates from discretization effects at small scale in the computation of the Laplacian $\nabla^2 R$ from finite differences. A reasonable match between the shape of the maps

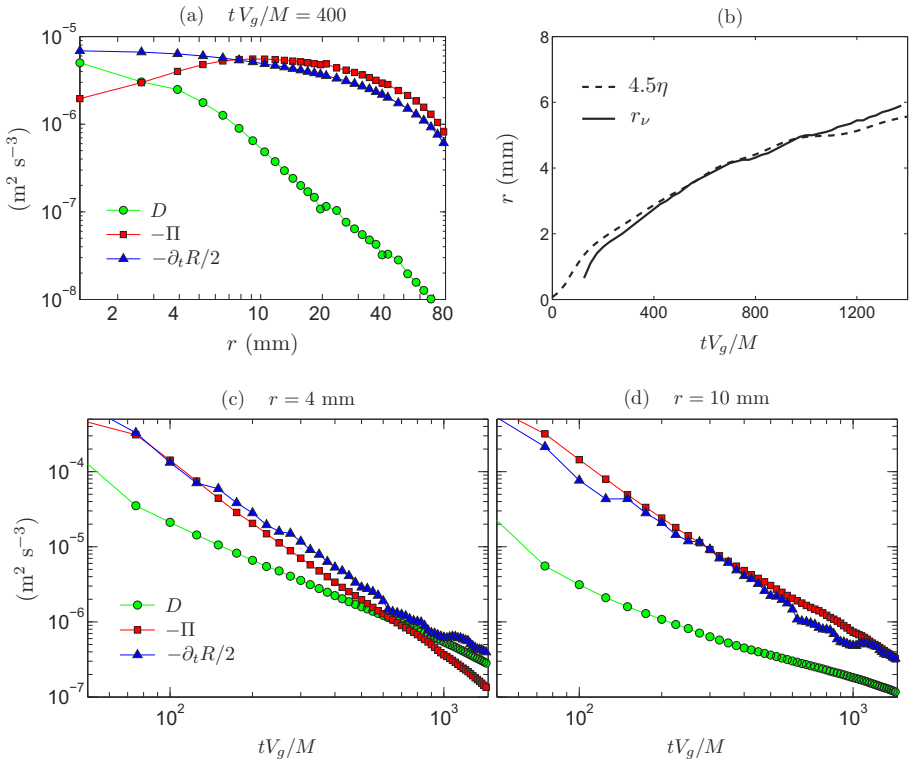

Figure 10. (a) Terms of the KHM equation averaged over θ for the non-rotating experiment as a function of r at $tV_g/M = 400$. (b) Time evolution of the viscous cutoff scales r_ν and 4.5η, with $\eta = (\nu^3/\epsilon)^{1/4}$ the Kolmogorov scale. (c,d) Terms of the KHM equation averaged over θ as a function of time tV_g/M for $r = 4$ mm and $r = 10$ mm.

of $-\partial_t R/2$ and $-\Pi + D$ is observed in Figures 9(a,b). The discrepancy, of order of 30% at this time, probably originates from the missing component u_y in the 2D surrogates (8).

In Figure 10(a) the 3 terms averaged over θ are plotted as a function of the scale r at the same time $tV_g/M = 400$, showing an agreement better than 50% up to 60 mm (larger scales are probably affected by large-scale inhomogeneities). At this time, the unstationary term $-\partial_t R/2$ is essentially governed by the energy transfer $-\Pi$ for $r > r_\nu \simeq 2.5 \pm 1$ mm, whereas the dissipative term D dominates the balance for $r < r_\nu$. The crossover between the inertial and dissipative terms in the KHM equation is found at $(7\pm1)\eta$ in numerical simulations of isotropic turbulence, where $\eta = (\nu^3/\epsilon)^{1/4}$ is the Kolmogorov scale [50]. Estimating here ϵ from $-\partial_t R/2(r \to 0)$ gives $\eta \simeq 0.6$ mm $\simeq r_\nu/4.5$ at $tV_g/M = 400$, which is slightly smaller than the ratio reported in numerical simulations. A good agreement is found in Figure 10(b) between the time evolutions of the measured crossover r_ν and the computed value of $4.5\,\eta$.

Since the dissipative scale is an increasing function of time, the dominant term in the KHM equation is expected to switch from $-\Pi$ to D as time proceeds for a given scale r. This is confirmed in Figures 10(c,d), showing the time evolution of the 3 terms at two scales, $r = 4$ and 10 mm. It is found that, for $r = 4$ mm, the decay is governed by viscosity for $tV_g/M > 630$, whereas for $r = 10$ mm the transfer term Π remains the dominant contribution up to the final time of the experiment.

The limited extent of the inertial range found in Figure 10(a) can be attributed to the moderate Reynolds number of our experiment. Finite Reynolds number effects have been well documented both in forced and decaying isotropic turbulence [15, 50–53]. A true inertial range, where $\Pi(\mathbf{r}) = -\epsilon$, or equivalently $\langle u_L^3 \rangle / r = -4\epsilon/5$ in the isotropic case, actually exists only for very large Reynolds number, but its

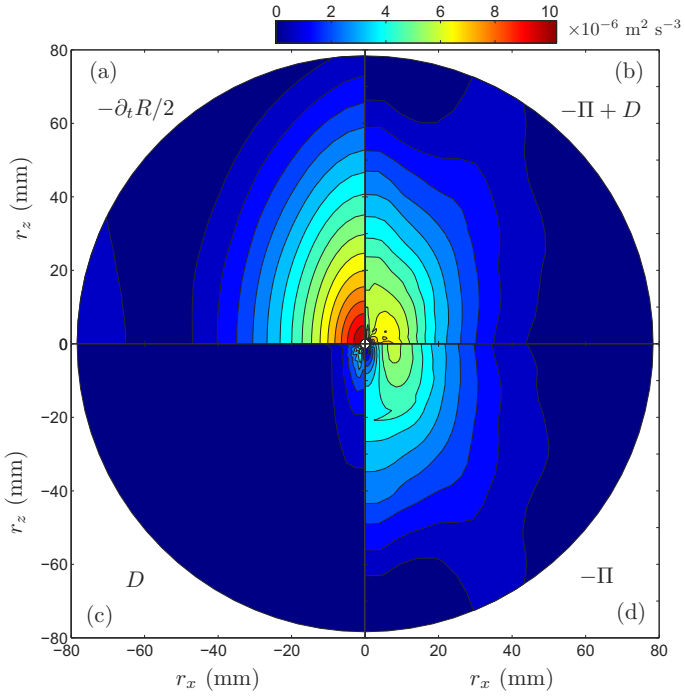

Figure 11. Maps of the terms of the KHM equation for the rotating experiment at $\Omega = 16$ rpm at time $t\,V_g/M = 400$ ($Re = 600$, $Ro = 0.06$). (a) Unstationary term $-\partial_t R/2$, (c) dissipative term $D = -\nu\nabla^2 R$, (d) transfer term $-\Pi = -\nabla\cdot\mathbf{F}/4$, (b) r.h.s. of the KHM equation $-\Pi + D$.

extent is severely limited by viscous and forcing or unstationary effects for the Reynolds numbers usually achieved in laboratory experiments. More precisely, a 'true' inertial range, such that $\langle u_L^3\rangle/r \simeq -4\epsilon/5$ over at least one decade, is observed for $R_\lambda \gg 10^3$ only, where R_λ is the Taylor microscale Reynolds number. The departure between $\langle u_L^3\rangle/r$ and $-4\epsilon/5$ is of order of 50% at $R_\lambda \simeq 100$, and no measurable transfer can be defined at all for $R_\lambda < 30$ [51]. Using the isotropic relation $R_\lambda \simeq \sqrt{15Re}$, Figure 4 indicates that R_λ must be of order 50-100 in the present experiments, so the limited inertial range observed here is in good agreement with the finite Reynolds effects reported in the literature.

4.3.2. Rotating case

In Figure 11, we compare again the maps of the 3 terms of the KHM equation, but now in the rotating case ($\Omega = 16$ rpm), still at time $t\,V_g/M = 400$. All three maps show the characteristic elongated shape along the rotation axis. Although the flux density $|\mathbf{F}|$ is maximum along the rotation axis, it is spread over a wider range of scales, leading to a weaker flux Π along r_z than along r_x. The annular region where Π is negative and approximately constant, marking the inertial range, becomes vertically elongated as time proceeds. Here again, this is consistent with a 2D trend, which would ultimately yield a vanishing energy flux along the rotation axis. The region where Π is most negative is indeed along r_x, inducing a stronger reduction of the velocity correlation R along r_x than along r_z, resulting in a relative growth of the correlation along r_z.

The energy budget is qualitatively similar to that of the non-rotating case, with a dominant energy dissipation D at small scale and a dominant flux $-\Pi$ at large scale (see Figure 12a for the particular choice $\theta = \pi/4$). However, contrarily to the non-rotating case, a correct balance of the terms of KHM is obtained at small time only. At large time, the unstationary term $-\partial_t R/2$ is found systematically larger than the sum of the flux and dissipation terms (Figures 12c,d), by a factor up to 3. This strong discrepancy may originate either from inhomogeneous effects arising

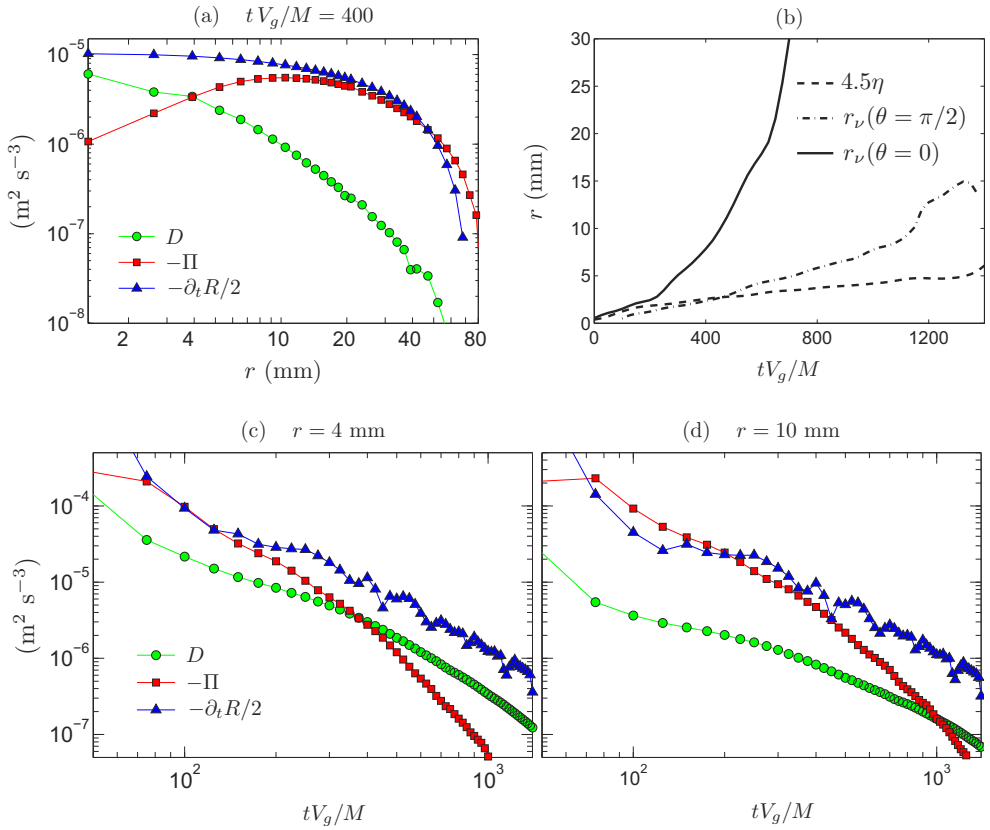

Figure 12. (a) Terms of the KHM equation in the rotating case ($\Omega = 16$ rpm) as a function of r at $\theta = \pi/4$ and $tV_g/M = 400$. (b) Time evolutions of the angle-dependent viscous cutoff $r_\nu(\theta)$, for $\theta = 0$ and $\pi/2$ compared to 4.5η, where the Kolmogorov scale η is computed using the isotropic definition. (c,d) Terms of the KHM equation as a function of time tV_g/M at $\theta = \pi/4$ and for $r = 4$ mm and $r = 10$ mm.

from the container walls or from the missing out-of-plane velocity component u_y. Although it is difficult to determine which contribution dominates this discrepancy, it is possible to estimate the order of magnitude of the former.

Inhomogeneity effects may be of two types in this experiment: they may originate from Ekman pumping or from large-scale reproducible inertial modes triggered by the grid translation. First, since the r.m.s. ratio u'_z/u'_x remains of order 1 throughout the decay (see Section 4.1), the Ekman pumping mechanism, which would give a r.m.s. ratio of order $E^{1/2} \simeq 10^{-3}$, is not expected to contribute significantly. Second, the production term originating from the coupling between turbulence and the large-scale inertial modes can be estimated as $P = -\langle u_i u_j \rangle \partial U_i/\partial x_j$, with $\mathbf{U}$ the ensemble-averaged (unstationary) flow of the inertial modes. In [37] we found that the energy of the residual inertial modes in the present grid configuration was of order of 10-15% of the total energy (see § 3.1). Assuming that the characteristic scale of the inertial modes is given by the tank width L_{tank}, we obtain $P \simeq 0.1 u'^3/L_{tank}$, which is at least one order of magnitude below the unstationary term $\partial_t R \simeq u'^3/L_\perp$. Accordingly, the turbulent production term alone is not likely to explain the observed discrepancy in the budget. This suggests that the missing component u_y is the dominant contribution to the observed discrepancy in the balance of the KHM equation. The influence of the missing component u_y is actually expected to grow in time in the rotating case: as the turbulence tends towards a three-component 2D state, the variance of vertical velocity increments decreases, so the relative weight of the non-measured velocity variance increases, making the use of the surrogates (8) more questionable. Because of this limitation, we can conclude that using 2D surrogates for the correlation and energy flux is ap-

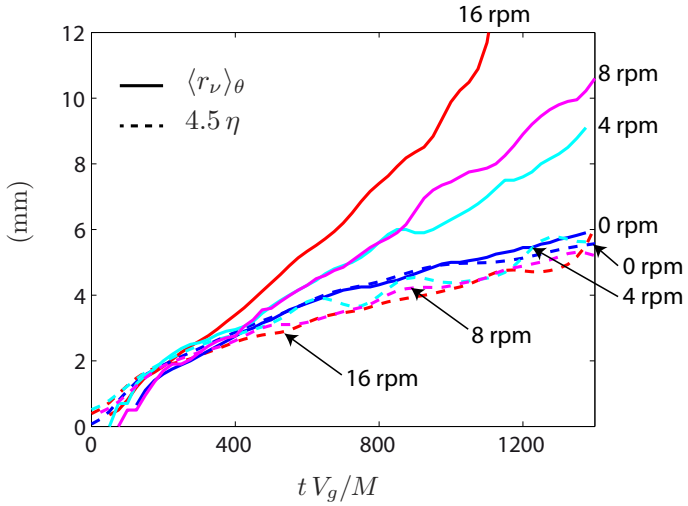

Figure 13. Time evolution of the Kolmogorov scale $\eta = (\nu^3/\epsilon)^{1/4}$, where $\epsilon = -\partial_t R(0)/2$, and of the polar-averaged viscous cutoff $\langle r_\nu \rangle_\theta$ for different rotation rates.

propriate for a qualitative description of the anisotropy growth, but a quantitative assessment of the energy budget would require the full measurement of the three velocity components.

A remarkable feature of Figure 11 is that the balance between the dissipation term D and the energy flux Π now strongly depends on the polar angle θ. In particular, the cross-over $r_\nu(\theta)$ between D and Π has a marked angular dependence, as shown in the time evolution of $r_\nu(\theta)$ for $\theta = 0$ and $\pi/2$ compared to the isotropic result $r_\nu \simeq 4.5\,\eta$ (Figure 12b). The larger r_ν found at $\theta = 0$ (vertical separation) is a simple consequence of the weaker energy flux in the vertical direction. In addition to this θ dependence, the viscous cutoff r_ν also shows a strong dependence on the rotation rate. This is visible in the time evolution of the polar-averaged cutoff $\langle r_\nu \rangle_\theta$ in Figure 13, showing larger values for increasing Ω. This behavior contrasts with the Kolmogorov scale as computed from the isotropic definition $\eta = (\nu^3/\epsilon)^{1/4}$ (with $\epsilon = -\partial_t R(0)/2$), which is almost not influenced by the rotation rate Ω in the range of Ro considered here. This increase of r_ν with Ω is a consequence of the reduced energy transfers in the presence of rotation, resulting in a stronger relative effect of the viscosity in the KHM balance. This effect is also visible in Figure 12(c,d), showing that the crossover between D and Π occurs at a shorter time than in the non-rotating case.

5. Dynamics of the anisotropy

5.1. *Anisotropy ratios*

We characterize now in more detail the scale dependence of the anisotropy in the two-points correlations $R(\mathbf{r}, t)$ and energy flux $\Pi(\mathbf{r}, t)$, with the aim of determining which scale is more anisotropic in rotating turbulence. For this, we define the anisotropy factor for the variance of the velocity increments E,

$$a_E(r,t) = \frac{E(r,\theta=\pi/2,t) - E(r,\theta=0,t)}{E(r,\theta=0,t)},$$

(and similarly $a_\Pi(r,t)$ for the energy flux Π), such that $a_E, a_\Pi > 0$ for vertically elongated E and Π maps. Here, the variance $E(\mathbf{r},t) = 2[\langle \mathbf{u}^2 \rangle(t) - R(\mathbf{r},t)]$ is used instead of $R(\mathbf{r},t)$ in order to probe more accurately the anisotropy at small scale,

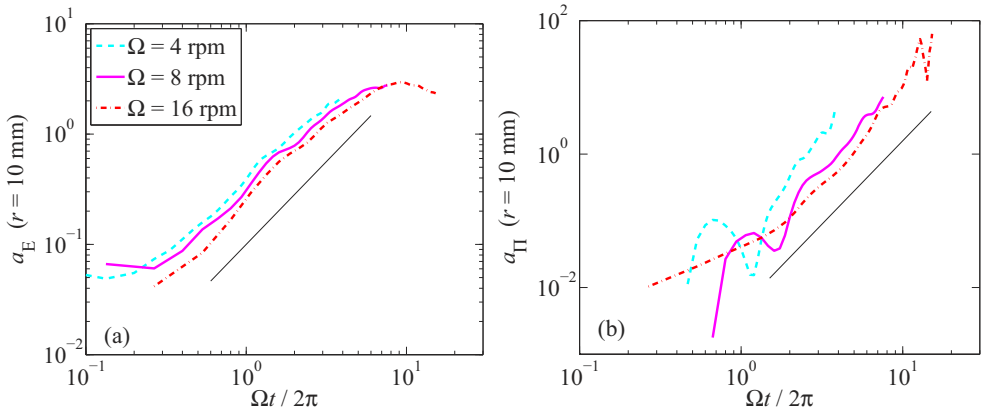

Figure 14. Time evolution of anisotropy ratio of the velocity variance E (a) and of the energy flux Π (b), at a separation $r = 10$ mm, for the 3 rotation rates $\Omega = 4$, 8 and 16 rpm. The solid line shows the power laws $t^{1.5}$ and $t^{2.5}$.

which is hidden in $R(r,\theta)$ by the fact that $R(0,\theta) = \langle \mathbf{u}^2 \rangle$ for all θ.

In Figure 14, the anisotropy ratios $a_E(t)$ and $a_\Pi(t)$ are plotted as functions of the number of tank rotations for the 3 rotating experiments, for a fixed separation $r =$ 10 mm. Both $a_E(t)$ and $a_\Pi(t)$ start from very small values, as expected for isotropic turbulence, and increase as time proceeds. This increase is more pronounced for Π than for the E: for the scale r considered here, a_Π reaches values around 20, while a_E saturates at about 3. This probably originates from the fact that the Coriolis force directly acts on the third-order moments, which in turn affect the dynamics of the second-order moments. The approximate collapse of a_E when plotted as a function of the number of tank rotations indicates that Ω^{-1} is the most relevant timescale for the anisotropy growth of E, which is consistent with the anisotropy growth of the one-point ratio u'_z/u'_x (Figure 3b); we note that this collapse is however less well defined for Π. We can also note that the anisotropy ratio of E saturates at the highest rotation rate, after about 10 tank rotations ($Ro \simeq 0.02$); the acquisition time is probably too short to observe also this saturation for lower Ω. Interestingly, this saturation is not present for the energy flux Π. This may be explained from the balance of the 3 terms in the KHM equation (7): at large time, the flux Π is very anisotropic but its magnitude becomes negligible, so the dynamics of the two-points correlation R becomes dominated by the damping term, $\nu\nabla^2 R$, which conserves the level of anisotropy reached at the end of the growth regime.

5.2. *The scale dependence of anisotropy*

We address now the issue of whether the anisotropy induced by rotation is more pronounced at small or large scales. The scale dependence of anisotropy for the variance E and the flux Π is visualized using spatio-temporal diagrams of $|a_E|$ and $|a_\Pi|$ in Figure 15. Without rotation, both ratios remain very small at all scales throughout the decay. In the presence of rotation ($\Omega = 16$ rpm), the anisotropy essentially concentrates at rather small scales, both for a_E and a_Π. Remarkably, a_E saturates (and even slightly decays) at large times, whereas a_Π continuously increases. This confirms that rotation still acts on the dynamics of the energy flux Π at large time, but the growing anisotropy of Π no longer affects the anisotropy of R because its dynamics becomes dominated by viscous diffusion.

Another remarkable feature of these spatio-temporal diagrams is the time evolution of the scale of maximum anisotropy, shown as bold lines in Figures 15(b,d). For the energy flux Π, the maximum anisotropy is found at a scale initially below the PIV resolution ($\Delta x \simeq 1.3$ mm), which gradually increases throughout the decay,

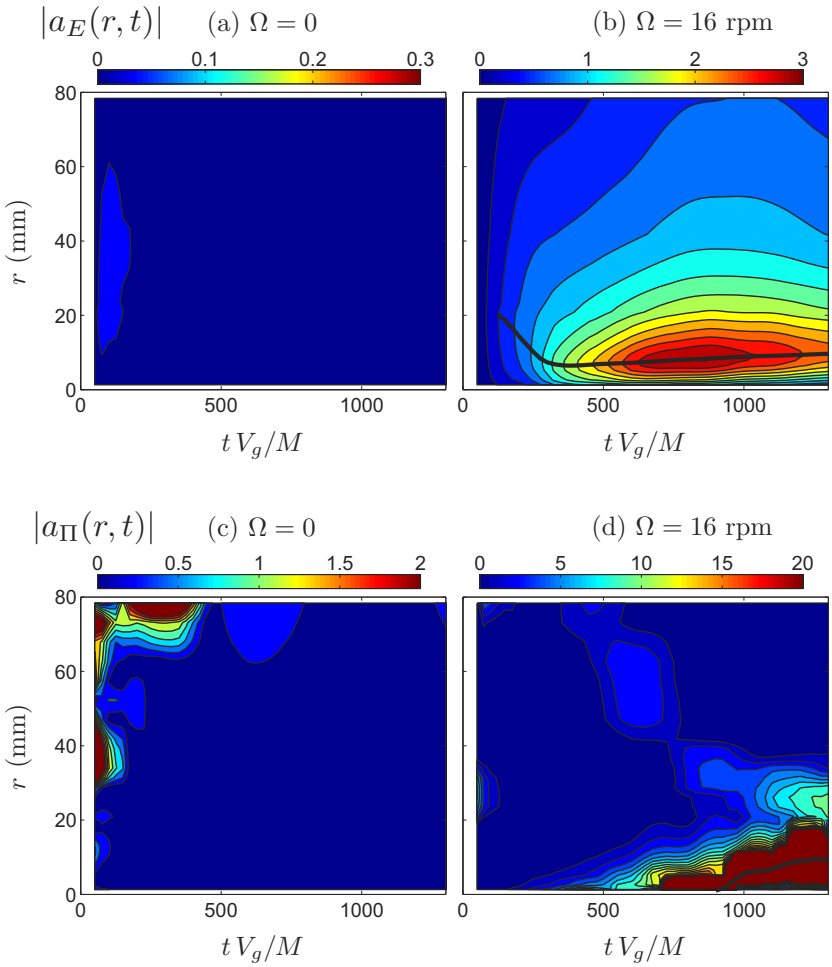

Figure 15. Spatio-temporal maps of the scale-dependent anisotropy ratios $|a_E|$ (top) and $|a_\Pi|$ (bottom), for rotation rates $\Omega = 0$ (a,c) and 16 rpm (b,d). In (b,d), the bold lines show the scale of maximum anisotropy.

up to 9 mm for $\Omega = 16$ rpm. On the other hand, the scale of maximum anisotropy for the velocity variance E, which we denote $r_{\rm aniso}$, shows a non-monotonic behavior: starting from about 20 mm, it first rapidly decreases down to 6 mm at $tV_g/M \simeq 400$, and then slowly re-increases up to 10 mm.

It is tempting to relate the rapid decrease of $r_{\rm aniso}$ at short time with the evolution of the Zeman scale [25, 26],

$$r_\Omega = \left(\frac{\epsilon}{\Omega^3}\right)^{1/2}, \tag{11}$$

which is also a decreasing function of time in decaying turbulence. The Zeman scale is the scale at which the turbulence turnover time is of order of the rotation period Ω^{-1}. Accordingly, scales $r \ll r_\Omega$, being faster than the rotation, should not be affected by the Coriolis force and should display a return to isotropy.

Figure 16 shows that the Zeman scale r_Ω actually provides the right trend and the right order of magnitude for $r_{\rm aniso}$. Although the scaling law cannot be verified here, because of the limited extent of the inertial range, we note that taking $r_{\rm aniso} \simeq 2r_\Omega$ yields a reasonable description of the data for the 3 rotation rates. We must note however that other scalings, such as the critical balance prediction $r_{\rm aniso} \propto \Omega^{-4/5}$ [30], cannot be ruled out by the present data.

The increase of $r_{\rm aniso}$ at larger time can be understood as a viscous effect: at

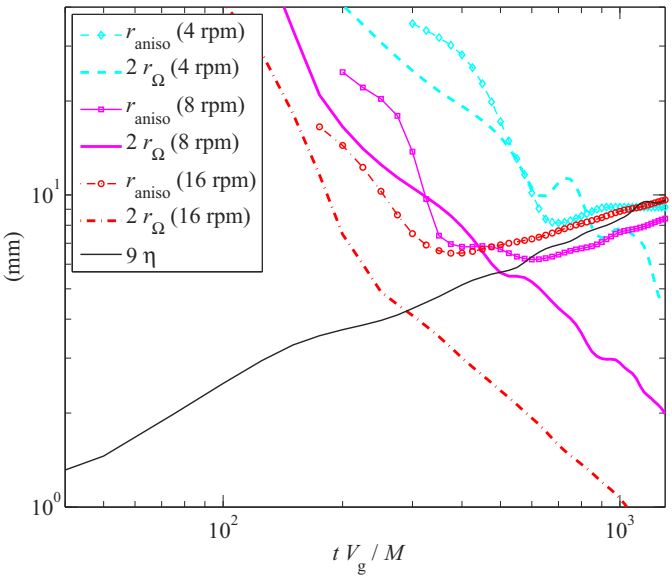

Figure 16. Time evolution of the scale of maximum anisotropy $r_{\rm aniso}$ for the three rotating experiments. Also shown for comparison $2r_\Omega(t)$, where $r_\Omega = (\epsilon/\Omega^3)^{1/2}$ is the Zeman scale, and $9\eta(t)$, where η is the Kolmogorov scale (the curve for η corresponds here to the case $\Omega = 16$ rpm, but curves for other Ω are almost identical; see Figure 13).

some point, the Zeman scale becomes smaller than the Kolmogorov scale, which is slowly increasing during the decay. We actually find that the increase of $r_{\rm aniso}$ in this second regime follows approximately the Kolmogorov scale, with $r_{\rm aniso} \simeq (9 \pm 2)\eta$ for the 3 rotation rates. The crossover between the two regimes occurs sooner as the rotation rate is increased. This is compatible with the criterion $r_\Omega \simeq \eta$, which is reached when the instantaneous dissipation rate ϵ becomes of order of $\nu\Omega^2$, i.e. when $ReRo^2 \simeq O(1)$ [24].

We can summarize these observations by noting that the non-monotonous evolution of the scale of maximum anisotropy for the energy distribution E can be approximately described by

$$r_{\rm aniso} \simeq \max\{2r_\Omega, 9\eta\}. \tag{12}$$

Isotropy is recovered for $r < r_{\rm aniso}$ in both regimes, but this return to isotropy originates from different mechanisms. At short time (when $r_{\rm aniso} \simeq 2r_\Omega$) the return to isotropy is compatible with the Zeman argument, whereas at larger time (when $r_{\rm aniso} \simeq 9\eta$) it results from viscous effects. It must be noted that in this second regime at large time, the return to isotropy for $r \ll \eta$ is a relative effect: the anisotropy of scales r satisfying $r_\Omega \ll r \ll \eta$ no longer increases because the anisotropic energy transfers are negligible compared to the viscous diffusion, and it eventually becomes weaker than the anisotropy of scales $r_\Omega \ll \eta \ll r$ which continues to grow.

Note that in the first regime $r_{\rm aniso} \ll \eta$, the anisotropy concentration at $r_{\rm aniso}$ remains weak, with a maximum anisotropy ratio a_E of order of $1 - 2$ only. On the other hand, in the second regime, the anisotropy becomes more pronounced, with a_E reaching values around 3 at $r_{\rm aniso} \simeq 9\eta$. It is worth noting that this non-monotonous evolution is found only for the energy distribution E. The scale of maximum anisotropy for the energy flux Π, on the other hand, approximately follows the increase of the Kolmogorov scale at large time, but starts below the PIV resolution at small time, and hence well below the Zeman scale (Figure 15d). A similar stronger effect of rotation on the third-order moments is also found in

[33].

The recovery of isotropy for the energy distribution in the sub-range $r \in [\eta, r_\Omega]$ is compatible with the classical Zeman argument [25]. In this sub-range, a scale-dependant Rossby number $Ro_r = (\Omega\tau_r)^{-1}$ can be estimated, with τ_r the time scale of the eddies of horizontal scale r. Using isotropic Kolmogorov scaling, one has $\tau_r \simeq r^{2/3}\epsilon^{-1/3}$, yielding $Ro_r \simeq (r/r_\Omega)^{-2/3}$, which is consistent with the weaker effect of the background rotation expected for $r \ll r_\Omega$. However this simple argument cannot apply in the sub-range $r \in [r_{\rm aniso}, L_\perp]$, in which the Kolmogorov isotropic scaling no longer holds, so it fails to explain why the maximum of anisotropy is actually found at the lower bound $r_{\rm aniso}$ and not at the upper bound $L_\perp$ of this sub-range.

Interestingly, a growing anisotropy for decreasing scales in the sub-range $[r_{\rm aniso}, L_\perp]$ is compatible with the wave turbulence prediction [27, 28, 30] and the numerical simulations of Bellet *et al.* [29], although the Rossby number in the present experiments is far from the requirement $Ro \ll 1$. In order to describe this behavior in terms of a scale-dependent Rossby number, another scaling must be used for the time scale τ_r. Following [20], an alternate choice can be made by taking into account the two invariants of the inviscid equations of motion, energy $\langle \mathbf{u}^2 \rangle/2$ and helicity $\langle \mathbf{u} \cdot \boldsymbol{\omega} \rangle/2$. Each invariant is associated to a cascade with a constant flux [54–56], denoted by ϵ and ϵ_h, respectively. Dimensionally, one has $\langle \delta u_r^3 \rangle \sim \epsilon r$ and $\langle \delta u_r^2 \delta\omega_r \rangle \sim \epsilon_h r$, with $\delta\omega_r$ the characteristic vorticity at scale r. Building now the timescale τ_r from these two conserved fluxes yields $\tau_r = \langle \delta u_r^3 \rangle^{2/3} / \langle \delta u_r^2 \delta\omega_r \rangle$, and hence a scale-dependent helicity Rossby number

$$Ro_r^{(h)} \simeq \frac{\langle \delta u_r^2 \delta\omega_r \rangle}{\Omega \langle \delta u_r^3 \rangle^{2/3}} \simeq \left(\frac{r}{r_h} \right)^{1/3}, \qquad (13)$$

with $r_h = \Omega^3\epsilon^2/\epsilon_h^3$. Accordingly, $Ro_r^{(h)}$ now *increases* at large r, suggesting that larger scales should be *less* affected by the rotation in the sub-range $[r_\Omega, L_\perp]$ (provided that $r_h \gg r_\Omega$), which is compatible with the experiment.

The subtle interplay between helicity and the background rotation has been emphasized by Mininni *et al.* [31]. Unfortunately helicity cannot be measured using 2D PIV, so the helicity Rossby number (13) cannot be determined experimentally. It can however be noted that generating turbulence by towing a grid in a rotating tank is actually expected to inject large-scale helicity at initial time: the stretching of the vertical absolute vorticity lines between the bottom of the tank and the grid bars during the grid translation induces a correlation between vertical velocity $u_z > 0$ and vorticity $\omega_z > 0$, and hence produces a net positive helicity (the same argument applies for the compression of the absolute vorticity lines between the bottom of the tank and the grid holes, inducing $u_z < 0$ and $\omega_z < 0$). Accordingly, a joint energy and helicity cascade is likely to occur in this flow configuration. Although qualitative, the argument based on this scale-dependent helicity Rossby number nonetheless provides an explanation for the observed maximum of anisotropy at a scale significantly smaller than the integral scale.

6. Conclusion

In this paper, the anisotropic energy transfers and the resulting scale-dependent anisotropy in decaying rotating turbulence are characterized from 2-component PIV measurements. The two main results are (i) a detailed analysis of the anisotropy growth of the energy distribution and energy flux based on a balance of the terms of the KHM equation; (ii) a characterization of the scale dependence

of anisotropy, with emphasis given to the non-monotonous evolution of the scale of maximum anisotropy $r_{\rm aniso}$ of the energy distribution.

Thanks to PIV measurements, the anisotropic properties of rotating turbulence can be investigated well beyond conventional one-point statistics. This approach is very promising for anisotropic homogeneous turbulence in general, and should be also of first interest for stratified turbulence (see, e.g., [36]). Extending this approach to (stereoscopic) 3-component PIV is highly desirable, and should in particular allow to achieve exact measurements of the different terms of the KHM equation. In particular, it is expected that the azimuthal component of the energy flux density $\mathbf{F}(\mathbf{r}) = \langle \delta\mathbf{u}\,(\delta\mathbf{u})^2 \rangle$ (not measured in the present work), although it does not contribute to the energy flux $\Pi(\mathbf{r}) = \nabla \cdot \mathbf{F}/4$ because of axisymmetry, should bring new information about the cyclone-anticyclone symmetry breaking, in particular with respect to its scale dependence.

The present results suggest that the scale below which isotropy is recovered, $r_{\rm aniso}$, follows a non-monotonous evolution during the decay. At short time $r_{\rm aniso}$ compares well with the rapid decay of the Zeman scale, whereas at large time $r_{\rm aniso}$ follows the slow increase of the Kolmogorov scale. Decaying turbulence, being characterized by decreasing Reynolds and Rossby numbers, provides a convenient way to explore in a single experiment the two regimes $r_\Omega \gg \eta$ ($ReRo^2 \gg 1$) and $r_\Omega \ll \eta$ ($ReRo^2 \ll 1$), with η the viscous cutoff. The return to isotropy at $r < r_{\rm aniso}$ is compatible with the numerical simulations of a wave turbulence model by Bellet *et al.* [29], for which $r_\Omega \to 0$, and with the forced helical turbulence simulation of Mininni *et al.* [31], for which r_Ω falls in the inertial range. However, whereas the maximum anisotropy is found at $r_{\rm aniso}$ in the present experiments, it is found at the largest scale in [31]. This discrepancy may be due to the specific helical forcing used in their simulations, which could enforce a stronger anisotropy at large scales. Clarifying this issue would require to explore systematically the interplay between the helicity and energy cascades in the different regimes, a point which is well beyond present experimental limitations.

Acknowledgements

We acknowledge C. Lamriben for his contribution to the experiments, A. Aubertin, L. Auffray, C. Borget and R. Pidoux for their experimental help, and C. Cambon, A. Campagne, B. Gallet, S. Galtier, F. Godeferd for fruitful discussions. This work is supported by the ANR grant no. 2011-BS04-006-01 “ONLITUR”. The rotating platform “Gyroflow” was funded by the “Triangle de la Physique”.

References

[1] P. Sagaut and C. Cambon, *Homogeneous turbulence dynamics*, Cambridge University Press, Cambridge, 2008.
[2] P.A. Davidson, *Turbulence in Rotating, Stratified and Electrically Conducting Fluids*, Cambridge University Press, Cambridge, 2013.
[3] E.J. Hopfinger, F.K. Browand, and Y. Gagne, *Turbulence and waves in a rotating tank*, J. Fluid Mech. 125 (1982), pp. 505–534.
[4] P. Bartello, O. Métais, and M. Lesieur, *Coherent structures in rotating three-dimensional turbulence*, J. Fluid Mech. 273 (1994), pp. 1–29.
[5] L. Bourouiba and P. Bartello, *The intermediate Rossby number range and two-dimensional three-dimensional transfers in rotating decaying homogeneous turbulence*, J. Fluid Mech. 587 (2007), pp. 139–161.
[6] F. Moisy, C. Morize, M. Rabaud, and J. Sommeria, *Decay laws, anisotropy and cyclone-anticyclone asymmetry in decaying rotating turbulence*, J. Fluid Mech. 666 (2011), pp. 5–35.
[7] Y. Yoshimatsu, M. Midorikawa, and Y. Kaneda, *Columnar eddy formation in freely-decaying homogeneous rotating turbulence*, J. Fluid Mech. 677 (2011), pp. 154–178.

[8] C. Cambon and L. Jacquin, *Spectral approach to non-isotropic turbulence subjected to rotation*, J. Fluid Mech. 202 (1989), pp. 295–317.
[9] F. Waleffe, *Inertial transfers in the helical decomposition*, Phys. Fluids A 5(3) (1993), pp. 677–685.
[10] L.M. Smith and F. Waleffe, *Transfer of energy to two-dimensional large scales in forced, rotating three-dimensional turbulence*, Phys. Fluids 11(6) (1999), pp. 1608–1622.
[11] C. Cambon, L. Danaila, F.S. Godeferd, and J. Scott, Third-order statistics and the dynamics of strongly anisotropic turbulent flows, J. Turb. 14(3) (2013), pp. 121–160.
[12] G. Bordes, F. Moisy, T. Dauxois, and P.-P. Cortet, *Experimental evidence of a triadic resonance of plane inertial waves in a rotating fluid*, Phys. Fluids 24 (2012), 014105.
[13] F. Anselmet, Y. Gagne, E.J. Hopfinger, and R.A. Antonia, *High-order velocity structure functions in turbulent shear flows*, J. Fluid Mech. 140 (1984), pp. 63–89.
[14] S.G. Saddoughi and S.V. Veeravalli, *Local isotropy in turbulent boundary layers at high Reynolds number*, J. Fluid Mech. 268 (1994), pp. 333-372.
[15] F. Moisy, P. Tabeling, and H. Willaime, *Kolmogorov Equation in a Fully Developed Turbulence Experiment*, Phys. Rev. Lett. 82 (1999), pp. 3994.
[16] T. Zhou and R.A. Antonia, *Reynolds number dependence of the small-scale structure of grid turbulence*, J. Fluid Mech. 406 (1999), pp. 81–107.
[17] Y. Gagne, B. Castaing, C. Baudet, and Y. Malecot, *Reynolds dependence of third-order velocity structure functions*, Phys. Fluids 16 (2004), pp. 482-485.
[18] A.S. Monin and A.M. Yaglom, *Statistical Fluid Mechanics, vol. 2*, MIT Press, Cambridge, 1975.
[19] U. Frisch, *Turbulence - The Legacy of A. N. Kolmogorov*, Cambridge University Press, Cambridge, 1995.
[20] S. Galtier, *Exact vectorial law for homogeneous rotating turbulence*, Phys. Rev. E 80 (2009), 046301.
[21] C.N. Baroud, B.B. Plapp, Z.S. She, and H.L. Swinney, *Anomalous Self-Similarity in a Turbulent Rapidly Rotating Fluid*, Phys. Rev. Lett. 88 (2002), 114501.
[22] C. Morize, F. Moisy, and M. Rabaud, *Decaying grid-generated turbulence in a rotating tank*, Phys. Fluids 17(9) (2005), 095105.
[23] C. Lamriben, P.-P. Cortet, and F. Moisy, *Direct measurements of anisotropic energy transfers in a rotating turbulence experiment*, Phys. Rev. Lett. 107 (2011), 024503.
[24] V.M. Canuto and M.S. Dubovikov, *A dynamical model for turbulence. V. The effect of rotation*, Phys. Fluids 9(7) (1997), pp. 2132–2140.
[25] O. Zeman, *A note on the spectra and decay of rotating homogeneous turbulence*, Phys. Fluids 6(10) (1994), pp. 3221–3223.
[26] Y. Zhou, *A phenomenological treatment of rotating turbulence*, Phys. Fluids 7 (1995), pp. 2092.
[27] C. Cambon, R. Rubinstein, and F.S. Godeferd, *Advances in wave turbulence: rapidly rotating flows*, New J. Phys. 6 (2004), pp. 73.
[28] S. Galtier, *Weak inertial-wave turbulence theory*, Phys. Rev. E 68 (2003), 015301.
[29] F. Bellet, F.S. Godeferd, J.F. Scott, and C. Cambon, *Wave turbulence in rapidly rotating flows*, J. Fluid Mech. 562 (2006), pp. 83–121.
[30] S. Nazarenko and A.A. Schekochihin, *Critical balance in magnetohydrodynamic, rotating and stratified turbulence: towards a universal scaling conjecture,* J. Fluid Mech. 677 (2011), pp. 134–153.
[31] P.D. Mininni, D. Rosenberg, and A. Pouquet, *Isotropization at small scales of rotating helically driven turbulence*, J. Fluid Mech. 699 (2012), pp. 263–279.
[32] P.D. Mininni and A. Pouquet, *Rotating helical turbulence. II. Intermittency, scale invariance, and structures*, Phys. Fluids 22 (2010), 035106.
[33] A. Naso and F.S. Godeferd, *Statistics of the perceived velocity gradient tensor in a rotating turbulent flow*, New J. Phys. 14 (2012), 125002.
[34] P.A. Davidson, *Turbulence: An Introduction for Scientists and Engineers*, Oxford University Press, Oxford, 2004.
[35] R.A. Antonia, M. Ould-Rouis, F. Anselmet, and Y. Zhu, *Analogy between predictions of Kolmogorov and Yaglom*, J. Fluid Mech. 332 (1997), pp. 395–409.
[36] P. Augier, S. Galtier, and P. Billant, *Kolmogorov laws for stratified turbulence*, J. Fluid Mech. 709 (2012), pp. 659–670.
[37] C. Lamriben, P.-P. Cortet, F. Moisy, and L.R.M. Maas, *Excitation of inertial modes in a closed grid turbulence experiment under rotation*, Phys. Fluids 23 (2011), 015102.
[38] G.P Bewley, D.P. Lathrop, L.R.M Maas, and K.R. Sreenivasan, *Inertial waves in rotating grid turbulence*, Phys. Fluids 17 (2007), 071701.
[39] S.B. Dalziel, *Decay of rotating turbulence : some particle tracking experiments*, App. Sc. Res. 49 (1992), pp. 217-244.
[40] J. Boisson, C. Lamriben, L.R.M. Maas, P.-P. Cortet, and F.Moisy, *Inertial waves and modes excited by the libration of a rotating cube*, Phys. Fluids 24 (2012), 076602.
[41] L.R.M. Maas, *On the amphidromic structure of inertial waves in rectangular parallelepiped*, Fluid Dyn. Res. 33 (2003), pp. 373.
[42] E. Lindborg, *Kinematics of homogeneous axisymmetric turbulence*, J. Fluid Mech. 302 (1995), pp. 179–201.
[43] C. Morize and F. Moisy, *Energy decay of rotating turbulence with confinement effects*, Phys. Fluids 18(6) (2006), 065107.
[44] P.J. Staplehurst, P.A. Davidson, and S.B. Dalziel, *Structure formation in homogeneous freely decaying rotating turbulence*, J. Fluid Mech. 598 (2008), pp. 81–105.
[45] P.A. Davidson, *On the decay of Saffman turbulence subject to rotation, stratification or an imposed magnetic field*, J. Fluid Mech 663 (2010), pp. 268–292.
[46] K.D. Squires, J.R. Chasnov, N.N. Mansour, and C. Cambon, *The asymptotic state of rotating homogeneous turbulence at high Reynolds number*, 74th Fluid Dynamics Symposium on "Application of Direct and Large Eddy Simulation to Transition and Turbulence" 4.1 (1994).
[47] L.J.A. van Bokhoven, C. Cambon, L. Liechtenstein, F.S. Godeferd, and H.J.H. Clercx, *Refined vortic-*

ity statistics of decaying rotating three-dimensional turbulence, J. Turbulence 9(6) (2008), pp. 1–24.
[48] T. Teitelbaum and P.D. Mininni, *The decay of turbulence in rotating flows*, Phys. Fluids 23(6) (2011), 065105.
[49] M.S. Mohamed and J. LaRue, *The decay power law in grid-generated turbulence*, J. Fluid Mech. 219 (1990), pp. 195–214.
[50] T. Gotoh, D. Fukayama, and T. Nakano, *Velocity field statistics in homogeneous steady turbulence obtained using a high-resolution direct numerical simulation*, Phys. Fluids 14(3) (2002), pp. 1065–1081.
[51] R.A. Antonia and P. Burattini, *Approach to the 4/5 law in homogeneous isotropic turbulence*, J. Fluid Mech. 550 (2006), pp. 175-184.
[52] L. Danaila, F. Anselmet, T. Zhou, and R.A. Antonia, *Turbulent energy scale budget equations in a fully developed channel flow*, J. Fluid Mech. 332 (2000), pp. 395–409.
[53] E. Lindborg, *Correction to the four-fifths law due to variations of the dissipation*, Phys. Fluids 11 (1999), pp. 510–512.
[54] A. Brissaud, U. Frisch, J. Leorat, M. Lesieur, and A. Mazure, *Helicity cascades in fully developed isotropic turbulence*, Phys. Fluids 16(8) (1973), pp. 1366-1367.
[55] O. Chkhetiani, *On the third moments in helical turbulence*, JETP Lett. 63(10) (1996), pp. 808-812.
[56] T. Gomez, H. Politano, and A. Pouquet, *Exact relationship for third-order structure functions in helical flows*, Phys. Rev. E 61 (2000), pp. 5321–5325.

Chapitre 3

Instabilité dynamique du pelage des adhésifs

Dans ce dernier chapitre, je décris une activité de recherche que j'ai développée au FAST à partir de 2010 en parallèle de mes travaux sur l'hydrodynamique en rotation. Cette activité expérimentale a pour objet d'apporter des éléments nouveaux à la compréhension d'une instabilité dynamique, souvent dite de "stick-slip", qui apparaît de manière fréquente lors du pelage des rubans adhésifs. Cette dynamique instable de l'avancée du front de pelage, alternant régulièrement entre des phases lentes et rapides, constitue à la fois un problème fondamental en mécanique de la rupture et de l'adhésion et un enjeu pour les industriels produisant les adhésifs ou leurs substrats. Elle est connue de tous à travers le son caractéristique qui lui est associé lors du pelage des adhésifs de bureau.

Du point de vue des industriels, cette instabilité est souvent un phénomène aux conséquences négatives : elle peut par exemple conduire à des niveaux de bruit élevés lors du pelage, éventuellement incompatibles avec les limites du code du travail, à une détérioration de la couche adhésive avant l'utilisation effective du ruban, ou encore, à des instabilités sur les lignes industrielles. Malgré ces enjeux, les solutions actuelles pour contrôler cette instabilité, comme les substrats anti-adhésifs, restent relativement peu efficaces et appellent à une meilleure compréhension du phénomène, de la manière de le caractériser efficacement et éventuellement de le prédire à partir de la caractérisation mécanique des matériaux composant le joint substrat-adhésif.

Du point de vue fondamental, cette instabilité est la conséquence d'une décroissance "anormale" de l'énergie de fracture du joint substrat-adhésif sur une gamme spécifique de vitesse de fracture. La compréhension de l'origine rhéologique et géométrique de cette décroissance est un sujet de recherche à part entière qui a reçu de nombreuses contributions. Même si une description théorique quantitative n'a pas encore émergé, il est bien établi que les ingrédients physiques en jeu sont en premier lieu la viscoélasticité du matériau adhésif couplée à son confinement dans une mince couche. L'instabilité dynamique du front de pelage émerge alors du couplage de cette décroissance de l'énergie de fracture avec une élasticité existant entre le point où la traction est imposée et le front de pelage, l'élasticité du ruban jouant généralement ce dernier rôle. On

souligne ici l'analogie entre cette instabilité et celle de la friction solide [152] qui est le fruit d'une décroissance du coefficient de friction avec la vitesse de glissement venant se coupler à l'élasticité du système de traction. La compréhension de la propagation instable du front de pelage constitue finalement un problème dynamique complexe qui recèle encore de nombreuses questions ouvertes. C'est en particulier vrai lorsque l'instabilité intervient à des vitesses de pelage élevées (de l'ordre du mètre par seconde) pour lesquelles des effets inertiels viennent interagir avec la dynamique instable. C'est la caractérisation expérimentale et la modélisation de ce régime de pelage instable à haute vitesse qui constitue le cœur de mon activité sur ce sujet. De manière générale, les études que nous avons menées ont permis d'apporter des éléments nouveaux grâce à la mise en place d'expériences modèles et à l'utilisation d'imagerie rapide numérique, permettant de résoudre temporellement la dynamique du front de pelage dans des conditions contrôlées.

Dans ce chapitre, après avoir discuté les éléments clés pour appréhender la physique de l'instabilité dynamique du pelage des films adhésifs et ses liens avec la mécanique de la rupture, je présente les résultats de deux études expérimentales. La première de ces études consiste en une expérience de pelage d'un adhésif commercial à vitesse imposée depuis un rouleau tournant librement. Ce travail a permis de mettre en évidence une dépendance forte de l'instabilité avec l'angle de pelage qui n'avait pour l'instant pas été clairement identifiée. Cette même étude a par ailleurs révélé des écarts importants de la dynamique à la théorie quasi-statique existante. Ces dernières observations illustrent la nécessité de comprendre les effets inertiels pouvant intervenir lorsque l'instabilité se développe à des vitesses de pelages élevées. Nous résumons dans ce chapitre les résultats de cette étude qui sont décrits plus en détail dans les articles [Cortet *et al.*, Phys. Rev. E, 2013] à la page 174 et [Dalbe *et al.*, Soft Matter, 2014a] à la page 182. La suite de ce chapitre résume les résultats obtenus grâce à une expérience de pelage du même adhésif mais cette fois-ci à vitesse et angle de pelage contrôlés qui nous a permis d'explorer de manière systématique l'instabilité dans l'espace des paramètres. Nous présentons les premiers résultats de cette expérience qui quantifie en fonction de la vitesse et de l'angle de pelage le passage de l'instabilité d'un régime quasi-statique à un régime inertiel. Ces travaux sont décrits en détail dans l'article [Dalbe *et al.*, Soft Matter, 2014b] à la page 189.

Publications associées à ce chapitre (en annexe lorsque le chiffre est encadré)

1. P.-P. Cortet, M.-J. Dalbe, C. Guerra, C. Cohen, M. Ciccotti, S. Santucci, L. Vanel,
Intermittent stick-slip dynamics during the peeling of an adhesive tape from a roller
Physical Review E, **87** 022601 (2013)

2. M.-J. Dalbe, S. Santucci, P.-P. Cortet, L. Vanel,
Strong dynamical effects during stick-slip adhesive peeling
Soft Matter, **10** 132 (2014a)

3. M.-J. Dalbe, S. Santucci, L. Vanel, P.-P. Cortet
Peeling-angle dependence of the stick-slip instability during adhesive tape peeling
Soft Matter, **10** 9637 (2014b)

3.1 Mécanique de la rupture et du pelage des adhésifs

3.1.1 Mécanique linéaire élastique de la rupture

Un des enjeux historiques de la mécanique de la rupture est de décrire la vitesse de propagation d'une fissure préexistante dans un matériau sollicité par des conditions aux limites données [153]. L'objectif ultime est de prédire le temps nécessaire à la rupture complète d'une structure endommagée par une ou plusieurs fissures. Les enjeux économiques et sociaux de cette problématique apparaissent évidemment comme importants : on peut évoquer notamment la résistance à la rupture des éléments de structures (dans les ouvrages de génie civil, les constructions aéronautiques, navales, ferroviaires, automobiles,...) ainsi que de la lithosphère terrestre à l'origine des tremblements de terre.

La réponse à cette problématique a été amorcée par la mécanique linéaire élastique de la rupture qui a pris son essort suite aux travaux pionniers de Griffith (1920) [154] et plus tard de Irwin (1957) [155, 156]. Dans une telle approche, on suppose que le matériau en train d'être fracturé se comporte globalement de manière élastique hormis dans une zone de petite taille, dite "zone de processus", près du front de la fissure. Le critère d'avancée d'une fissure peut alors se formuler de deux manières différentes mais équivalentes. Le critère de Griffith propose d'introduire un coût énergétique Γ, appelé énergie de fracture, à la croissance de la fracture d'une unité de surface. Le critère pour que la fissure avance est alors que l'énergie mécanique G libérée par unité de surface fracturée [*], appelée taux de restitution de l'énergie élastique, dépasse Γ. G est bien entendu une fonction des conditions de chargement et de la géométrie de la fissure. Le critère d'Irwin s'appuie lui sur la notion de facteur d'intensité des contraintes K qui est le préfacteur de la divergence des contraintes prévue par l'élasticité à la pointe de la fissure supposée infiniment fine [†]. Irwin propose que la fissure avance lorsque ce facteur K dépasse un certain seuil critique K_c, appelé ténacité du matériau. Ces deux critères sont en réalité équivalents pour un matériau élastique linéaire puisque le taux de restitution de l'énergie élastique peut être directement relié au facteur d'intensité des contraintes selon $G = K^2\,(1-\nu^2)/E$ où E et ν sont respectivement le module de Young et le coefficient de Poisson du matériau [‡].

Dans un système où l'avancée de la fissure correspondrait au clivage réversible du matériau par rupture des liaisons interatomiques (physiques ou chimiques), l'énergie de fracture serait simplement la mesure de l'énergie des surfaces créées $\Gamma = 2\gamma$. Cette situation ne correspond en fait

∗. $G = \delta U_{\text{méca}}/\delta S$ où S est la surface de la fissure et $U_{\text{méca}}$ l'énergie mécanique du système, mesurée comme la différence de l'énergie élastique stockée dans l'échantillon et du travail des forces extérieures, $U_{\text{méca}} = U_{\text{élastique}} - W$.

†. À une distance r de la pointe d'une fissure infiniment étroite dans un matériau élastique, les contraintes associées à chaque mode d'ouverture de la fissure divergent selon $K_i/\sqrt{2\pi r}$ où K_i est le facteur d'intensité des contraintes associé au mode i. Le mode de sollicitation d'une fissure est une notion locale associée à la direction selon laquelle les lèvres de la fissure se séparent. Le mode I, dit d'ouverture, correspond à une séparation normale au front de fissure et à la direction de propagation de la fissure. Le mode II, dit de cisaillement ou de glissement, correspond à une séparation dans la direction de propagation de la fissure et le mode III, dit de déchirement, dans la direction du front de fissure.

‡. Cette expression est valide sous l'approximation de déformation plane. Sous l'approximation de contrainte plane, on a $G = K^2/E$.

qu'exceptionnellement à la réalité (pour certains cristaux, [157] et les références citées), le phénomène de rupture faisant presque toujours intervenir une zone —nano, micro ou macroscopique— en tête de fissure où se développent des processus dissipatifs, ne serait-ce qu'une déformation plastique pour régulariser la divergence des contraintes prévue par l'approche purement élastique. Ainsi, même les matériaux fragiles que sont les verres présentent à l'échelle nanométrique une zone de déformation plastique [158] associée à une dynamique de rupture par nucléation, croissance et coalescence de cavités [159, 160]. Une conséquence est que leur énergie de fracture Γ est plus grande, d'un ordre de grandeur, que l'énergie des surfaces créées 2γ. Pour les verres de silice, on a par exemple, une énergie de surface de l'ordre de $2\gamma \sim 0.6$ J m^{-2} [161] et une énergie de fracture de l'ordre de $\Gamma \sim 5 - 50$ J m^{-2} [162, 163]. Le rapport $\Gamma/2\gamma$ peut atteindre des valeurs beaucoup plus élevées dans les matériaux viscoélastiques comme les adhésifs. Selon les matériaux, la zone de processus est ainsi le lieu de phénomènes dissipatifs variés (plasticité, fibrillation, microfissuration, dissipation visqueuse, ...) qui, si celle-ci est suffisamment localisée, peuvent être décrits dans le cadre de la mécanique linéaire élastique de la rupture grâce à l'usage d'une énergie de fracture effective $\Gamma = 2\gamma + \Gamma_{\rm pz} \simeq \Gamma_{\rm pz}$.

La dissipation autour de la pointe de fissure décrite par l'énergie surfacique $\Gamma_{\rm pz}$ est de manière usuelle une fonction croissante du taux auquel les processus dissipatifs interviennent. L'énergie de fracture devient ainsi naturellement une fonction (en général croissante) de la vitesse d'avancée de la fissure v. L'équilibre de Griffith $G = \Gamma(v)$ [164] affirme alors que la fracture se propagera à une certaine vitesse v quelles que soient les conditions de chargement pourvu qu'elles produisent le même taux de restitution de l'énergie G. Le succès de ce type de modèles est intimement lié au fait que le matériau considéré possède une énergie de fracture $\Gamma(v)$ bien définie, au sens que celle-ci ne dépend pas du mode du fissuration, ni de la géométrie du problème, mais seulement du matériau et de la vitesse de la fissure.

3.1.2 Taux de restitution de l'énergie en géométrie de pelage

Dans la suite de ce chapitre, nous allons nous intéresser au pelage d'un ruban adhésif depuis un substrat sur lequel il est initialement collé (Figure 3.1). De manière usuelle, le ruban est constitué d'un dos, composé de polymères vitreux, au comportement généralement élastique mais pouvant parfois subir des déformations plastiques lors du pelage du ruban. Ce dos est recouvert d'une couche de mélange d'élastomères ou plus généralement de polymères en phase caoutchoutique [§] constituant le matériau adhésif, au comportement viscoélastique et éventuellement plastique lors du pelage.

Une expérience de pelage d'un tel ruban adhésif peut être vue comme un problème de fracture à la condition de remplacer, dans la définition de l'énergie de fracture Γ, l'énergie surfacique 2γ par une énergie interfaciale d'adhésion $w = \gamma_a + \gamma_s - \gamma_{as}$, où γ_a, γ_s et γ_{as} représentent respectivement les énergies de surface associées à l'adhésif seul, au substrat seul et à l'interface substrat-adhésif. Cette énergie rend compte de la rupture des liaisons de van der Waals à l'in-

§. Un polymère se trouve dans sa phase caoutchoutique ou vitreuse respectivement lorsque la température ambiante est supérieure ou inférieure à sa température de transition vitreuse T_g.

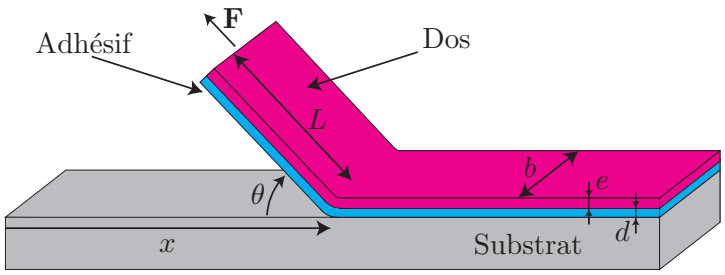

FIGURE 3.1 – Géométrie du pelage d'un ruban adhésif. x est la position du front de pelage telle que dx/dt soit la vitesse du front de pelage. $\mathbf{F}$ est la force de pelage, θ l'angle macroscopique de pelage, L la longueur de ruban pelé, b la largeur du ruban, e l'épaisseur du dos du ruban et d l'épaisseur de la couche adhésive.

terface substrat-adhésif ainsi que de la contribution éventuelle de liaisons chimiques présentes à l'interface. En général, w ne représente qu'une part très faible —de l'ordre de 0.1 à 1 J m^{-2}— de l'énergie de fracture Γ qui pour les adhésifs usuels est de l'ordre de 100 à 1000 J m^{-2}. Le coût énergétique supplémentaire est le fruit de processus dissipatifs, dépendant de la vitesse de la fissure, qui peuvent être localisés près de la pointe de la fissure à l'interface adhésif-substrat (par exemple en lien avec l'existence de chaînes polymères traversant l'interface [165, 166]) ou étendus en volume dans le matériau adhésif (cf. section 3.1.3). Dans ce dernier cas, ils sont principalement de nature visqueuse mais peuvent aussi être partiellement liés à la plastification de la colle selon la vitesse de pelage.

Il est important de remarquer que ces processus dissipatifs sont confinés géométriquement dans un volume limité par l'épaisseur d de la couche de matériau adhésif. Dans une expérience typique, le ruban pelé est long de quelques centimètres à quelques décimètres alors que son épaisseur (e ou d, Figure 3.1) est de l'ordre de quelques dizaines de microns. On note ainsi une séparation d'échelles de trois à quatre ordres de grandeur entre la zone dissipative et la partie élastique du système. Cette séparation donne aux expériences de pelage un caractère modèle dans le cadre de la mécanique de la rupture.

Kendall en 1975 [167] a calculé l'expression du taux de restitution de l'énergie élastique associé à la géométrie de pelage

$$G = \frac{F}{b}(1 - \cos\theta) + \frac{1}{2Ee}\left(\frac{F}{b}\right)^2, \tag{3.1}$$

prenant en compte le travail de la force de pelage $\mathbf{F}$ (Figure 3.1) et la variation de l'énergie élastique stockée dans le ruban pelé. Dans l'expression (3.1), F est la norme de la force $\mathbf{F}$, θ l'angle de pelage macroscopique, b la largeur du ruban, Ee le produit du module de Young E et de l'épaisseur e du dos du ruban pelé. Pour un ruban adhésif commercial de bureau comme le Scotch® 600 [¶], le terme $\frac{1}{2Ee}\left(\frac{F}{b}\right)^2$ lié au stockage de l'énergie élastique dans le ruban pelé

¶. Le ruban adhésif Scotch® 600 est composé d'un adhésif acrylique synthétique déposé sur un dos fait d'un mélange de polyoléfines. $e = 38$ μm, $b = 19$ mm, $E = 1.26$ GPa, Énergie de pelage typique $\Gamma \simeq 100$ J m^{-2}.

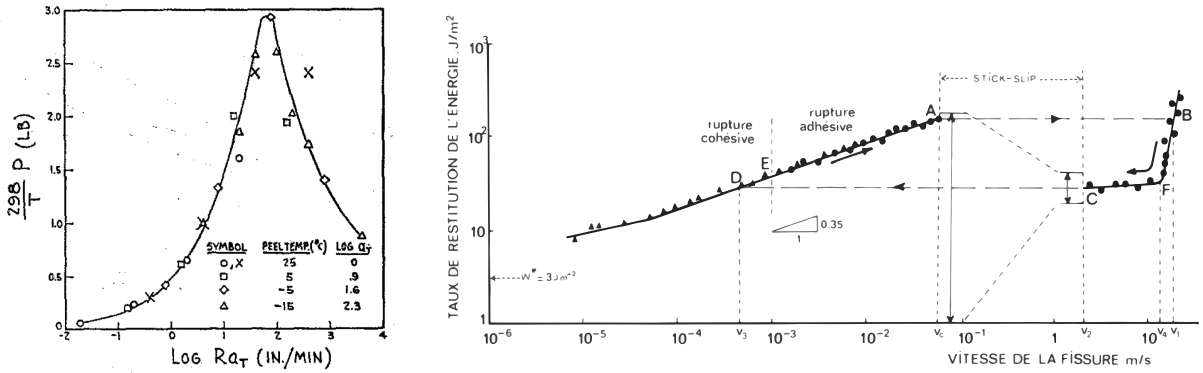

FIGURE 3.2 – **Gauche** : Expériences de pelage de Kaelble [170] d'un adhésif de polyisobutylène sur un dos et un substrat de cellophane. Force de pelage en fonction de la vitesse de pelage pour différentes températures, remise à l'échelle selon le principe WLF (pour Williams, Landel et Ferry [178, 179]). **Droite** : Expériences de pelage de Barquins *et al.* [180] de l'adhésif commercial Scotch® 602 pelé depuis son rouleau. Taux de restitution de l'énergie mesuré en fonction de la vitesse de pelage. Angle de pelage $\theta \simeq 90^o$.

représente moins de 5% de G pour un angle de pelage θ supérieur à 25° et moins de 5‰ pour $\theta > 45^o$. Dans la majorité des situations pratiques, la prise en compte du terme de travail de la force de pelage $\delta W/\delta S = \frac{F}{b}(1-\cos\theta)$, et donc la mesure de cette force, est ainsi suffisante pour estimer précisément le taux de restitution de l'énergie et donc l'énergie de pelage.

3.1.3 Énergie de pelage

La dépendance de l'énergie de fracture des joints substrat-adhésif avec la vitesse du front de pelage v a ainsi été largement étudiée expérimentalement à travers des mesures de la force de pelage F [168–177]. Les résultats de ces études peuvent être synthétisés dans la loi

$$\Gamma(v,T) = \Gamma_0 + \psi(a_T\, v), \tag{3.2}$$

où Γ_0 rend compte des processus dissipatifs interfaciaux à l'origine de l'adhésion à vitesse de pelage nulle. Le terme $\psi(a_T\, v)$ est lui associé à la dissipation dans le volume de l'adhésif : il dépend naturellement de la vitesse d'avancée du front de pelage et s'annule avec celle-ci. Dans ce terme, le facteur thermique a_T est celui introduit par Williams, Landel et Ferry en 1955 [178, 179] pour décrire l'équivalence temps-température des propriétés rhéologiques des polymères amorphes. Il est une fonction de l'écart entre la température ambiante T et la température de transition vitreuse T_g. À partir des années 1960, différents travaux expérimentaux ont ainsi montré que, de manière remarquable, la dépendance en vitesse de l'énergie de pelage des adhésifs suit la même correction avec la température [170–172, 175] que la rhéologie linéaire de l'adhésif, montrant de manière claire le rôle de la viscoélasticité dans le coût énergétique à l'avancée de la fracture (Figure 3.2 Gauche).

Un grand nombre des expériences de pelage citées plus haut ont par ailleurs mis en évidence

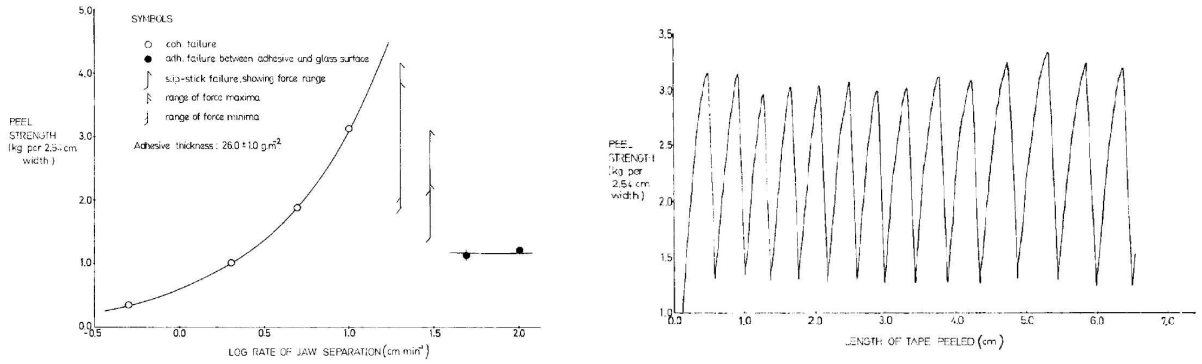

FIGURE 3.3 – Expériences de pelage de Aubrey *et al.* [172] d'un adhésif poly(n-butyl)acrylate sur un dos de polyester et un substrat de verre. **Gauche** : Force de pelage en fonction de la vitesse de pelage. Cette figure illustre une chute de la force de pelage associée à une transition entre un régime de fracture cohésive à basse vitesse et un régime de fracture interfaciale, i.e. adhésive, à haute vitesse. Dans une gamme intermédiaire de vitesse de pelage, les auteurs ont observé de fortes oscillations de la force de pelage, caractéristiques de l'instabilité dynamique de "stick-slip" et en ont reportées les valeur extrêmes. **Droite** : Oscillations saccadées du signal de force mesurées dans le régime instable de "stick-slip" pour une vitesse de pelage $v = 10$ cm min^{-1}.

une gamme de vitesse du front de pelage sur laquelle l'énergie de fracture $\Gamma(v)$ décroît [169–172, 174, 177, 180, 181] (Figures 3.2 et 3.3 Gauche). Une telle décroissance de l'énergie de fracture est parfois associée à une transition du processus de fracture d'un régime cohésif à basse vitesse de pelage, où la fracture se propage dans le cœur du matériau adhésif, vers un régime dit adhésif à haute vitesse, où la fissure se propage à l'interface entre le matériau adhésif et le substrat [171, 172] (Figure 3.3 Gauche). D'autres expériences [174, 177] mettent en évidence une chute de $\Gamma(v)$ associée à une transition entre les deux modes de rupture interfaciaux (entre adhésif et substrat et entre adhésif et dos). D'autres travaux [169, 170, 180, 181] rapportent finalement une chute de l'énergie de fracture qui n'est pas liée à une transition de ce type dans le régime de fissuration qui reste toujours interfacial (Figure 3.2).

Il a été proposé que cette décroissance de l'énergie de fracture avec la vitesse de pelage soit intrinsèquement liée à la viscoélasticité du matériau adhésif [182]. Gent [175] a cependant montré expérimentalement qu'un raisonnement simple essayant de relier l'évolution en fréquence des modules viscoélastiques et celle en vitesse de l'énergie de pelage pour des joints élastomère-élastomère donnait un ordre de grandeur aberrant pour la taille de la zone de processus (1 Å). De Gennes a ensuite proposé à travers son modèle de la "trompette viscoélastique" que le confinement du matériau adhésif entre le substrat et le dos du ruban joue un rôle primordial dans la décroissance de $\Gamma(v)$ à travers une borne fixée à la taille de la zone dissipative [183]. Il est cependant apparu depuis qu'un modèle basé uniquement sur la viscoélasticité linéaire de l'adhésif ne peut décrire quantitativement les observations et qu'une prise en compte du fluage et des larges déformations de l'adhésif semblent nécessaire [184, 185].

On peut noter finalement que pour les adhésifs où la décroissance anormale de $\Gamma(v)$ intervient

à des vitesses de pelage suffisamment élevées —c'est généralement le cas pour les adhésifs de bureau par exemple— la fin de la gamme décroissante de l'énergie de fracture est associée à une forte croissance (Figure 3.2 Droite et Figure 3.7 Gauche) qui traduit un coût énergétique supplémentaire lié à des effets dynamiques. On peut mentionner dans un premier temps un terme spécifique à la géométrie de pelage, le coût en énergie cinétique $\mu v^2(1-\cos\theta)$ associé à la mise en mouvement du ruban initialement collé sur le substrat (μ est la masse surfacique du ruban adhésif [‖]). On note que ce terme vient donner, à grande vitesse, une dépendance avec l'angle de pelage θ à l'énergie de fracture. Au-delà de ce terme et de manière plus générale en mécanique de la rupture dynamique, les processus de radiation sous forme d'ondes des champs de déformation entre la pointe de la fracture et le reste du matériau induisent une diminution du taux de restitution de l'énergie disponible pour faire avancer la fracture par rapport au taux quasi-statique G [153, 186]. Si l'on souhaite conserver formellement une écriture du critère de Griffith sous la forme d'un équilibre entre le taux de restitution quasi-statique G et une énergie de fracture $\Gamma(v)$, celle-ci doit être corrigée par ces effets dynamiques et présente alors une divergence lorsque la vitesse de la fracture approche la vitesse des ondes de Rayleigh à la surface du matériau considéré. Dans le cas du pelage, le "matériau" étant hétérogène (dos + adhésif + substrat) et dans une géométrie à la frontière entre 1D et 2D, la divergence de $\Gamma(v)$ et la vitesse limite pour le front de pelage ne sont pas encore bien comprises théoriquement [187].

3.2 L'instabilité dynamique du pelage des adhésifs

3.2.1 Mises en évidence expérimentales

Parmi les travaux illustrant une décroissance de l'énergie de fracture $\Gamma(v)$, nombreux sont ceux rapportant aussi l'émergence d'oscillations saccadées et de grande amplitude de la force de pelage [169–172, 174, 188, 189] (voir par exemple la Figure 3.3). Ces oscillations sont la signature de l'instabilité dynamique, dite de "stick-slip", du pelage des adhésifs. Pour de nombreux adhésifs commerciaux, comme les adhésifs types de bureau qui vont nous intéresser particulièrement par la suite, la fréquence de ces oscillations est élevée et a été caractérisée expérimentalement de manière indirecte grâce à l'analyse *post-mortem* des empreintes laissées dans l'adhésif [180, 181] ou celle des émissions acoustiques associées à l'instabilité [190, 191]. Grâce aux progrès de l'imagerie rapide numérique, plusieurs travaux ont plus récemment permis l'accès direct à la dynamique du front de pelage dans le régime instable (Cortet *et al.* en 2007 [192] et Thoroddsen *et al.* en 2010 [193]).

Malgré ces nombreuses études expérimentales, la description de la dynamique instable du front de pelage n'a reçu que peu de contributions théoriques. Les travaux les plus significatifs, présentés par Barquins et Maugis [180, 181] dans les années 1980, qui modélisent la dynamique de "stick-slip" par une approche quasi-statique, ont permis à ces auteurs de décrire quantitativement

‖. Pour le Scotch® 600 déjà évoqué, $\mu \simeq 44,4$ g m^{-2}. Le terme d'énergie cinétique μv^2 devient du même ordre de grandeur que le pic de dissipation visqueuse $\Gamma \sim 100$ J m^{-2} (Figure 3.7 Gauche) pour une vitesse $v \simeq 48$ m s^{-1} pour $\theta = 90°$.

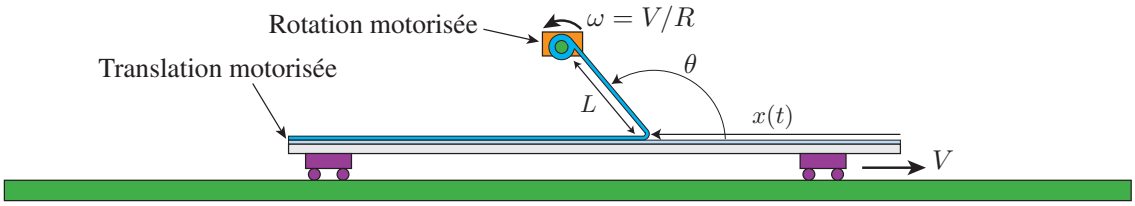

FIGURE 3.4 – Schéma de principe de l'expérience de pelage à angle θ et vitesse V imposés. La vitesse V de translation de la barre rigide constituant le support de l'adhésif et celle d'enroulement du ruban pelé $R\omega$ sont asservies électroniquement. Une première couche d'adhésif a été déposée sur la barre en translation constituant le substrat de l'adhésif pelé.

la période des oscillations sur la partie basse de la gamme instable de l'adhésif étudié. Nous décrirons plus en détail ces travaux qui constituent le point de départ de notre étude dans la section 3.2.3.

3.2.2 Les origines de l'instabilité

Pour comprendre l'origine de l'instabilité de stick-slip, il faut expliciter l'équilibre énergétique de Griffith $G = \Gamma(v)$ dans la géométrie de pelage. En faisant l'hypothèse que le ruban pelé, entre le point où la vitesse de pelage V est imposée (par enroulement) et le front de pelage est toujours tendu de manière uniforme, la force F exercée par l'opérateur peut être reliée à l'allongement du ruban u à travers son élasticité $F \simeq \frac{Eeb}{L} u$ [**]. L'équilibre de Griffith prévoit alors que la vitesse du front de pelage $v(t) = V$ et que l'allongement du ruban $u(t) = u_0$ avec $(1 - \cos\theta)u_0 Ee/L = \Gamma(V)$.

On veux tester la stabilité de cet équilibre en étudiant l'amplification ou l'amortissement d'une petite perturbation $\delta x(t)$ de la position $x(t)$ du point de pelage par rapport à sa position d'équilibre $x_0(t) = Vt$. La description de l'allongement du ruban $u(t)$ en fonction de la position $x(t)$ du point de pelage dépendant de la géométrie de l'expérience, nous allons considérer ici la situation modèle où l'opérateur enroule le ruban à une vitesse V sur un rouleau et où le substrat est plan et translaté à la même vitesse V parallèlement à sa surface (Figure 3.4). Dans cette géométrie, qui fixe cinématiquement l'angle de pelage $\theta(t)$ à une valeur constante lorsque le pelage est stationnaire $v(t) = V$, l'allongement du ruban est décrit par $u(t) = u_0 + (1 - \cos\theta_0)(Vt - x(t))$ où θ_0 est l'angle de pelage moyen. On montre alors que le taux de restitution de l'énergie associé au système perturbé, i.e. à $x(t) = x_0(t) + \delta x(t)$, vaut

$$G = \frac{Ee}{L} u(t)(1 - \cos\theta(t)) = \Gamma(V) - \left(\frac{\Gamma(V)}{L}(1 + \cos\theta_0) + \frac{Ee}{L}(1 - \cos\theta_0)^2 \right) \delta x, \tag{3.3}$$

au premier ordre en δx. Le premier terme du membre de droite en δx, qui est lié à la variation de l'angle de pelage, est généralement négligeable sauf pour un angle θ_0 faible. Cette propriété émerge du fait que l'énergie d'adhésion $\Gamma(V)$ est de manière générale très petite devant la

**. De manière exacte, $F = \frac{Eeb}{\mathcal{L}} u$ où $\mathcal{L} = L - u$ est la longueur de ruban dans l'état relâché.

raideur Ee : pour le Scotch® 600 déjà évoqué, on a par exemple $\Gamma(V)/Ee \leqslant 2\ 10^{-3}$. En faisant l'hypothèse que l'équilibre de Griffith est toujours vérifié pour le système perturbé, on obtient aux temps courts

$$\left.\frac{d\Gamma}{dv}\right|_V \frac{d\delta x}{dt} \simeq -\frac{Ee}{L}(1-\cos\theta_0)^2\,\delta x. \tag{3.4}$$

Lorsque $\left.\frac{d\Gamma}{dv}\right|_V > 0$, une perturbation positive de la position du front de pelage $\delta x > 0$ engendrera une perturbation négative de la vitesse de pelage amortissant la perturbation. Au contraire, lorsque $\left.\frac{d\Gamma}{dv}\right|_V < 0$, la perturbation sera amplifiée et le pelage instable. On comprend ici que c'est le couplage entre l'élasticité du ruban pelé et la décroissance de $\Gamma(v)$ qui est à l'origine de l'instabilité. Selon cette approche élémentaire, le système est donc instable dès que $\Gamma(V)$ est décroissant.

3.2.3 Le modèle quasi-statique et les expériences de Barquins et Maugis

Le modèle de l'instabilité du pelage adhésif proposé par Barquins et Maugis [180, 181] dans les années 1980 prolonge le raisonnement précédent en décrivant la dynamique du pelage une fois que l'instabilité a atteint sa saturation. Dans ce modèle quasi-statique, l'hypothèse est faite que l'équilibre de Griffith reste vérifié instantanément lorsque la vitesse du front de pelage $v(t)$ appartient aux gammes croissantes de l'énergie de fracture. La dynamique de pelage décrit alors les cycles ABCD représentés à la Figure 3.2 (Droite), sautant entre les branches croissantes lente et rapide de la courbe $\Gamma(v)$ dès que le système tend à entrer dans la branche décroissante. Ces discontinuités de la vitesse du front de pelage sont associées à l'hypothèse que le mouvement de la fracture $x(t)$ n'est affecté d'aucune inertie, même effective. Ce modèle permet alors de prédire à partir des mesures des branches croissantes lente $\Gamma_{\text{lent}}(v)$ et rapide $\Gamma_{\text{rapide}}(v)$ de $\Gamma(v)$ la durée des phases de "stick" et de "slip"

$$T_{\text{stick}} = \frac{L}{Ee(1-\cos\theta_0)^2}\int_{\Gamma_{\min}}^{\Gamma_{\max}} \frac{dG}{V-\Gamma_{\text{lent}}^{-1}(G)}, \tag{3.5}$$

$$T_{\text{slip}} = \frac{L}{Ee(1-\cos\theta_0)^2}\int_{\Gamma_{\min}}^{\Gamma_{\max}} \frac{dG}{\Gamma_{\text{rapide}}^{-1}(G)-V}, \tag{3.6}$$

où $\Gamma_{\min}$ et $\Gamma_{\max}$ mesurent respectivement les minimum et maximum locaux de $\Gamma(v)$.

Barquins et Maugis [180, 181] ont validé les prédictions de ce modèle pour un angle de pelage $\theta \simeq 90^{\text{o}}$ grâce à des expériences de pelage à vitesse imposée V de l'adhésif commercial Scotch® 602 pour lequel la gamme de vitesse instable est $0.06 \leqslant V \leqslant 2.1$ m s^{-1} (Figure 3.2 Droite). Sur la partie basse de cette gamme instable, $0.06 \leqslant V \leqslant 0.60$ m s^{-1}, les mesures de la période des cycles de stick-slip $T_{\text{ss}} = T_{\text{stick}} + T_{\text{slip}}$ grâce à la détection *post-mortem* des marques laissées dans la colle par l'instabilité, ont ainsi montré un accord quantitatif avec la prédiction (3.5) pour la période de "stick". Elles ont par la même occasion confirmé la pré-

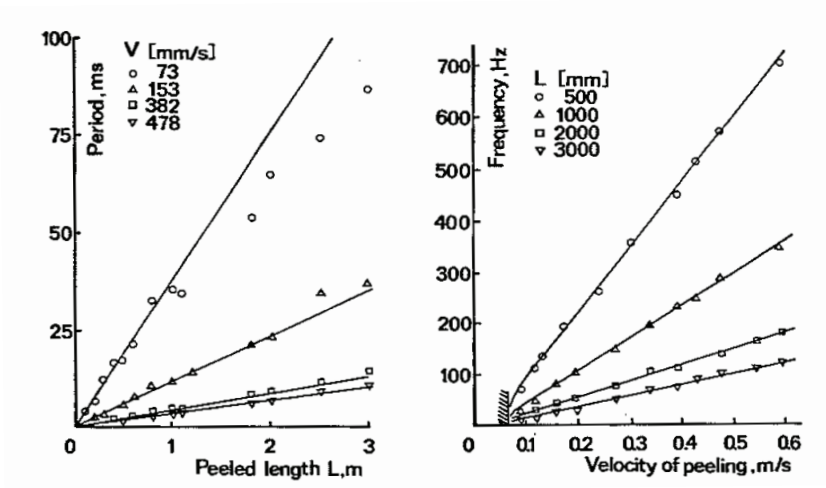

FIGURE 3.5 – Période de l'oscillation dynamique du pelage en fonction de la longueur du ruban L (Gauche) et de la vitesse de pelage V (Droite). Expériences de pelage de Barquins et Maugis [180, 181] à vitesse imposée V de l'adhésif commercial Scotch® 602 depuis son rouleau monté sur une poulie (angle de pelage $\theta \simeq 90°$). Les lignes continues représentent les prédictions du modèle quasi-statique pour la période de "stick" (3.5).

diction d'une période de "slip" négligeable (Figure 3.5) devant T_{ss}. Dans ce travail, Barquins et Maugis [180, 181] n'ont cependant pas été capables de mesurer la période des oscillations de stick-slip, et donc de tester leur modèle, aux vitesses de pelage plus grandes, les marques laissées par l'instabilité ayant disparu.

3.3 Expériences de pelage depuis un rouleau tournant librement

- Collaboration avec M.-J. Dalbe (ENS Lyon/Univ. Lyon 1), S. Santucci (ENS Lyon) et Loïc Vanel (Univ. Lyon 1)

Le point de départ de notre projet expérimental sur le pelage des adhésifs est né de la volonté de tester de manière plus exigeante la validité de l'approche quasi-statique proposée par Barquins et Maugis en accédant à l'ensemble de la gamme instable de vitesse de pelage ainsi qu'au détail de la dynamique du front de pelage $v(t)$, au-delà de la mesure de la période des oscillations. De manière plus générale, notre objectif est de mieux caractériser l'instabilité du pelage des adhésifs lorsqu'elle intervient à des vitesses de pelage suffisamment élevées pour que des effets dynamiques ou inertiels soient en jeu. De la même manière que pour les études de la turbulence en rotation présentées au chapitre 2, ce projet est rendu possible par les progrès techniques de l'imagerie numérique : l'accès à ce type de dynamiques de pelage, associées à des fréquences d'oscillation élevées (Figure 3.5), est aujourd'hui possible grâce aux caméras rapides.

Nous avons ainsi revisité l'expérience de pelage à vitesse imposée depuis un rouleau tournant

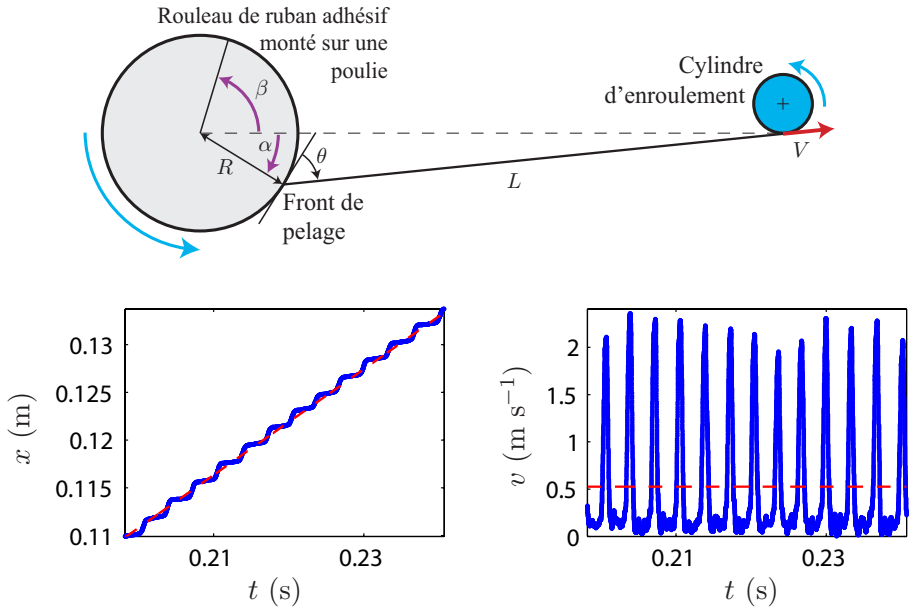

FIGURE 3.6 – **Haut** : Géométrie du pelage à vitesse imposée V d'un rouleau de ruban adhésif monté sur une poulie. R est le rayon du rouleau pelé ($R = 25 \pm 5$ mm). $\alpha(t)$ et $\beta(t)$ sont respectivement les positions angulaires du front de pelage et du rouleau dans le référentiel du laboratoire et $\theta(t)$ l'angle de pelage. **Bas gauche** : Dynamique de la position du front de pelage $x(t) = R(\alpha(t) + \beta(t))$ pour une expérience à vitesse imposée $V = 0.55$ m s^{-1} et une longueur de ruban pelé $L = 0.48$ m. La ligne tiretée représente la dynamique associée à la vitesse imposée si le pelage était stationnaire, i.e. $x = Vt$. **Bas droite** : Vitesse correspondante du front de pelage dx/dt. La ligne tiretée représente la vitesse imposée.

librement (Figure 3.6 Haut). Lors de ces expériences, réalisées avec le ruban adhésif Scotch® 600 (légèrement différent de celui de Barquins et Maugis), nous avons pu résoudre la dynamique de la position $x(t)$ du point de pelage le long de la surface du substrat (Figure 3.6 Bas) par analyse numérique d'images de caméra rapide. Nous avons par ailleurs mesuré la composante selon l'axe de pelage (trait pointillé sur la Figure 3.6 Haut) de la force exercée par le ruban pelé sur le rouleau grâce à un capteur de force linéaire placé sur le support du rouleau. Cette force s'identifie à la norme de la force $\mathbf{F}$ transmise par le ruban lorsque le pelage a lieu avec un angle $\theta = 90^o$ (Figure 3.6 Haut).

Dans un premier temps, nous avons caractérisé l'amplitude de l'instabilité de stick-slip en fonction de la vitesse imposée V à partir de l'analyse des séries temporelles de la vitesse du front de pelage $v(t) = dx(t)/dt$ (Figure 3.6 Bas). Ces mesures ont révélé une gamme instable allant de $V_a = 0.10 \pm 0.03$ m s^{-1} à $V_b = 2.45 \pm 0.10$ m s^{-1} qui est incluse dans la gamme décroissante de l'énergie de fracture $\Gamma(v)$ à laquelle nous avons pu accéder à travers les mesures de la force moyenne de pelage. On peux noter que nos mesures de $\Gamma(v)$ dans le régime de pelage stable à basse vitesse sont en accord avec celles réalisées sur le même adhésif par Barquins et Ciccotti [194] (Figure 3.7 Gauche) qui avaient alors aussi réussi à caractériser la branche rapide stable pour les vitesses $V > 19$ m s^{-1}. Ces deux études combinées laissent cependant légèrement incertaine, dans l'intervalle $V_b \leqslant V \leqslant 19$ m s^{-1}, la vitesse de transition entre la branche décroissante et la branche stable rapide de $\Gamma(v)$.

Le premier résultat remarquable de cette étude a été la mise en évidence d'oscillations lentes (vis-à-vis du stick-slip) de la rotation $\beta(t)$ du rouleau d'adhésif autour de la rotation moyenne $\beta_0(t) = Vt/R$. Ces oscillations très légères dans la gamme de basses vitesses instables deviennent de plus en plus marquées pour les vitesses imposées $V > 1.5$ m s^{-1}. Nous avons montré de manière quantitative que ces oscillations pendulaires sont le fruit de l'interaction entre la force de pelage et l'inertie du rouleau pelé. Elles induisent une oscillation lente de l'angle de pelage $\theta(t)$, qui se superpose aux oscillations plus rapides (d'un ou deux ordres de grandeur) liées à l'instabilité de stick-slip. De manière remarquable, la vitesse moyenne (sur le temps caractéristique du stick-slip) du front de pelage $\int_t^{t+T_{ss}} v(s)ds/T_{ss}$ est insensible à ces oscillations pendulaires et reste égale à la vitesse imposée V. La dynamique pendulaire du rouleau, qui nous est dans un premier temps apparue comme un phénomène parasite, permet ainsi d'explorer de manière quasi-statique la dépendance de l'instabilité de stick-slip avec l'angle de pelage. Ces expériences ont ainsi révélé que, aux grandes vitesses instables au moins, l'instabilité de stick-slip voit son amplitude décroître rapidement lorsque l'angle de pelage θ passe de 70 à 120^o. Aux plus grandes vitesses instables —où les oscillations pendulaires sont les plus marquées— on observe même une dynamique intermittente de l'instabilité de stick-slip, fortement corrélée à la valeur de l'angle de pelage θ (Figure 3.7 Droite). Le lecteur trouvera une description plus détaillée de ces résultats dans l'article [Cortet *et al.*, Phys. Rev. E, 2013] en annexe à ce chapitre à la page 174.

Il est à noter que seuls Aubrey *et al.* [172] avaient auparavant fait état d'une dépendance des seuils de l'instabilité avec l'angle de pelage à travers quelques expériences non systématiques. Ce fort effet de l'angle de pelage sur l'amplitude et le seuil de l'instabilité peut être compris dans le cadre du critère d'instabilité associé au signe de $\frac{d\Gamma}{dv}\big|_V$ (partie 3.2.2) uniquement si la gamme

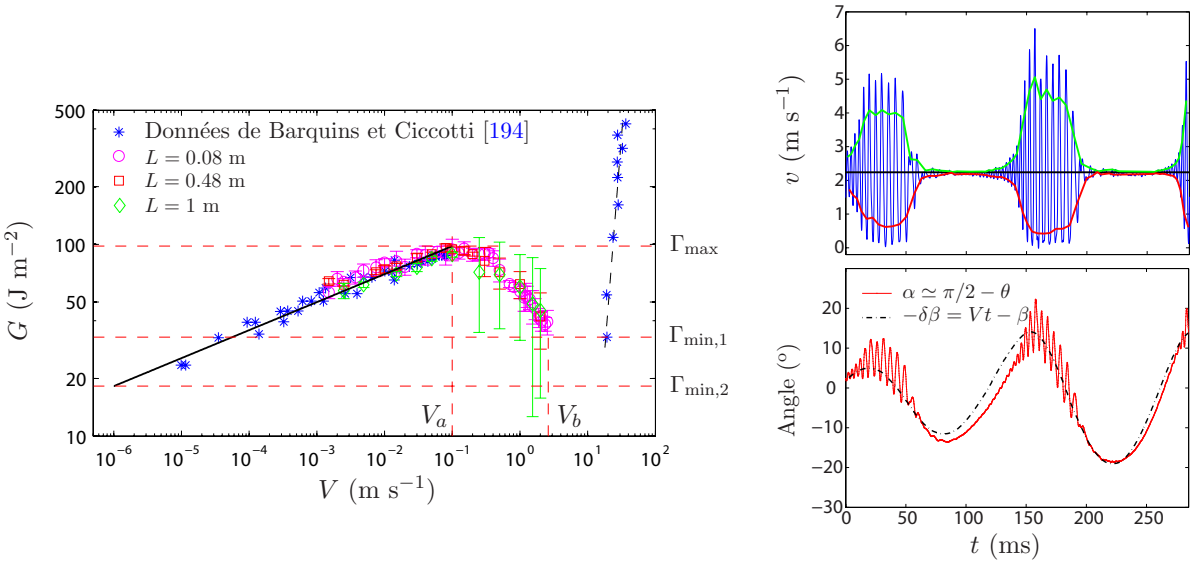

FIGURE 3.7 – **Gauche** : Taux de restitution de l'énergie $G = F/b$ en fonction de la vitesse de pelage V. Les étoiles reportent les données de Barquins et Ciccotti [194] pour le même adhésif. Les barres d'erreur représentent la déviation standard des fluctuations de la force (en unité de G) pendant une expérience. Lorsque l'instabilité du pelage est présente, pour $V_a < V < V_b$, les mesures de force révèlent des fluctuations importantes. **Droite** : Vitesse $v(t)$ du front de pelage (en haut) et sa position angulaire $\alpha(t)$ dans le référentiel du laboratoire (en bas) ainsi que le mouvement pendulaire du rouleau $-\delta\beta = Vt - \beta$ en fonction du temps t pour une expérience à $V = 2.24$ m s^{-1} et $L = 1$ m.

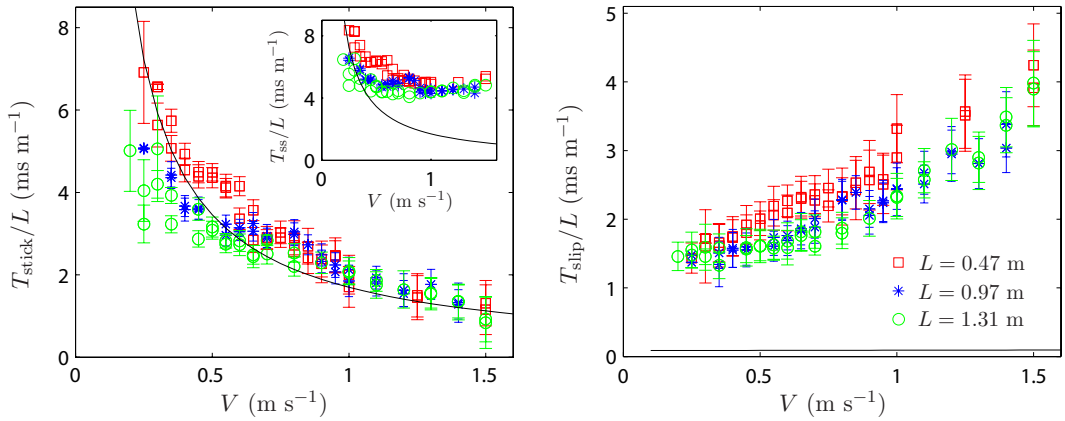

FIGURE 3.8 – $T_{\rm stick}/L$ et $T_{\rm ss}/L$ (gauche) et $T_{\rm slip}/L$ (droite) en fonction de la vitesse de pelage V pour trois longueurs de ruban pelé L ($T_{\rm ss} = T_{\rm stick} + T_{\rm slip}$). Chaque point correspond à la moyenne et chaque barre d'erreur à la déviation standard de la statistique d'une expérience. Dans chacune des figures, la ligne continue représente la prédiction théorique du modèle quasi-statique de Maugis et Barquins (3.5).

décroissante de l'énergie de fracture $\Gamma(v)$ se révèle elle-même être une fonction marquée de l'angle de pelage, ce qui reste à ce jour une question encore ouverte. En effet, aucun travail expérimental publié dans la littérature n'a clairement mis en évidence une dépendance de l'énergie de pelage avec l'angle de pelage [167, 195, 196], mis à part des dépendances qui semblent ne pas impacter directement l'instabilité de stick-slip : on pense ici au travail de Kaelble [197] qui a rapporté une dépendance de l'énergie de pelage avec l'angle à de très faibles vitesses, interprétée comme une transition dans la sollicitation de l'adhésif d'un mode de clivage à un mode de cisaillement. Cette transition n'interagit cependant aucunement avec une gamme décroissante de $\Gamma(v)$. On note finalement le travail de Gent et Hamed [198] qui met en évidence une dépendance de l'énergie de pelage avec l'angle, cette fois-ci liée à la plastification du dos du ruban adhésif aux grands angles de pelage.

La caractérisation et la compréhension de la dépendance de l'instabilité dynamique du pelage des adhésifs avec l'angle de pelage a constitué, à la suite du travail expérimental que nous venons de décrire, un des objectifs principaux de notre activité.

Les expériences de pelage sur rouleau libre que nous venons de décrire nous ont par ailleurs permis, sur la gamme de vitesse instable où les oscillations pendulaires du rouleau sont faibles et l'angle de pelage proche de 90° ($V < 1.5$ m s^{-1}), d'extraire pour la première fois séparément les dépendances des durées des phases de "stick" et de "slip". Nous avons ainsi pu montrer que, sur la partie basse de la gamme de vitesse instable, les prédictions du modèle quasi-statique de Maugis et Barquins décrivent quantitativement la période de "stick" (Figure 3.8 Gauche). Cependant, contrairement à ce qui avait été proposé dans ce modèle, la durée de la phase de pelage rapide de "slip" devient rapidement du même ordre de grandeur que celle de la phase de "stick" lorsque la vitesse de pelage croît. La prédiction quasi-statique pour la durée de la phase de slip se révèle en pratique deux ordres de grandeurs plus faibles que les durées observées (Figure 3.8 Droite). Cette confrontation quantitative des prédictions du modèle quasi-statique avec les données de

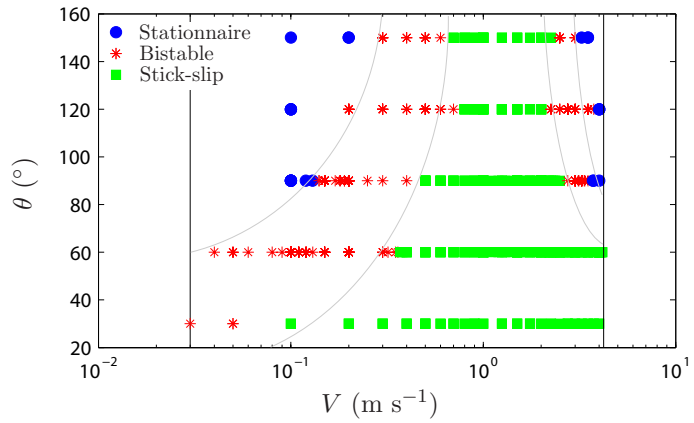

FIGURE 3.9 – Diagramme de stabilité du pelage dans l'espace vitesse-angle de pelage (V, θ). Chaque point représente une expérience. Les lignes verticales correspondent aux limites expérimentales du dispositif. Les lignes courbes sont un guide pour le yeux soulignant les frontières de stabilité du système.

périodes de l'instabilité est décrit en détail dans l'article [Dalbe *et al.*, Soft Matter, 2014a] que le lecteur trouvera à la page 182.

Les écarts que nous venons de mettre en évidence entre la dynamique du front de pelage et les prédictions du modèle quasi-statique suggèrent la probable intervention d'effets inertiels pendant le pelage qui viennent empêcher la fissure de sauter à sa guise entre les branches lentes et rapides de l'équilibre statique de Griffith $G = \Gamma(v)$. La dynamique du rouleau étant visiblement insensible à celle du pelage aux échelles de temps du stick-slip, les effets inertiels en jeu dans l'instabilité ne semblent pas liés à l'inertie du rouleau et sont donc probablement associés plus intrinsèquement à la dynamique du pelage des adhésifs. La compréhension de ces effets inertiels a constitué le deuxième axe selon lequel nous avons développé nos efforts expérimentaux.

3.4 Expériences de pelage à angle et vitesse imposés

- Collaboration avec M.-J. Dalbe (ENS Lyon/Univ. Lyon 1), S. Santucci (ENS Lyon) et Loïc Vanel (Univ. Lyon 1)

Les expériences de pelage depuis un rouleau tournant librement, décrites dans la partie précédente, nous ont permis d'identifier deux questions clés et encore ouvertes sur la dynamique de l'instabilité de stick-slip : (i) À travers quel processus l'angle de pelage modifie-t-il les seuils et l'amplitude de l'instabilité ? (ii) Quels sont les effets inertiels qui expliquent les écarts à la théorie quasi-statique ? Pour répondre à ces questions, nous avons mis en place une nouvelle expérience où le ruban est pelé depuis un substrat plan grâce à son enroulement à vitesse constante sur un cylindre. Le substrat est lui-même translaté à une vitesse identique grâce à un asservissement électronique. Ce montage met en œuvre le principe expérimental que nous avons déjà évoqué brièvement à la partie 3.2.2 et dans la Figure 3.4. Son intérêt principal est qu'il contraint ciné-

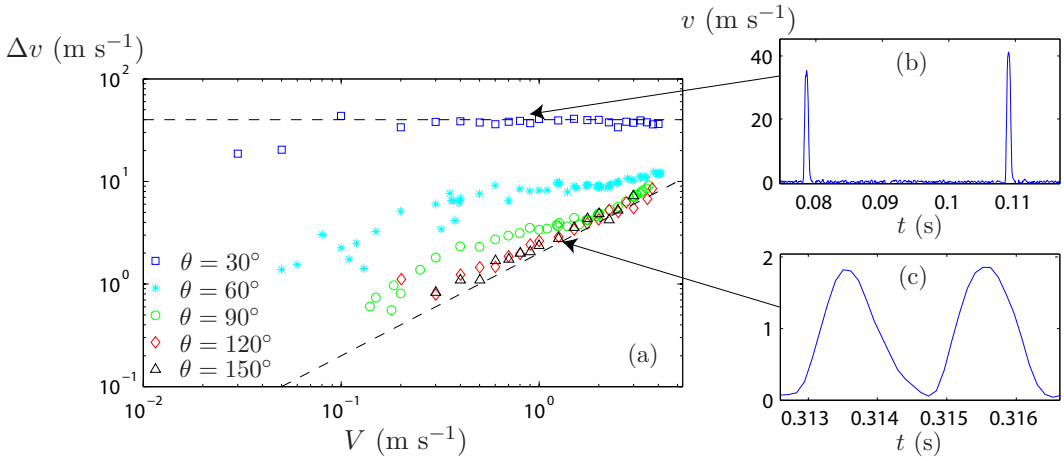

FIGURE 3.10 – (a) Amplitude moyenne de l'instabilité Δv en fonction de la vitesse de pelage V pour différents angles de pelage. Chaque point représente la moyenne sur différentes longueurs de ruban pelé. La ligne tiretée du bas représente $\Delta v = 2V$ et celle du haut $\Delta v = 40$ m s^{-1}. (b - c) Vitesse du front de pelage en fonction du temps pour (b) $V = 0.9$ m s^{-1}, $\theta = 30°$, $L = 0.51$ m et (c) $V = 0.9$ m s^{-1}, $\theta = 150°$, $L = 0.54$ m.

matiquement l'angle de pelage (et la longueur de ruban pelé) à une valeur constante, lorsque le pelage est stable (cf. section 3.2.2). Lorsque l'instabilité dynamique intervient, les fluctuations de l'angle de pelage et de la longueur de ruban pelé restent aussi très faibles : lors de nos expériences, elles sont respectivement de l'ordre de 0.1° à 1° et de 0.1% à 1%. En parallèle, la vitesse de pelage $v(t)$ oscille fortement mais suit cependant précisément la vitesse imposée V aux échelles de temps supérieures à la période de l'instabilité. Ce système expérimental présente le deuxième intérêt de supprimer l'inertie du substrat en tant que paramètre du problème en imposant sa vitesse. Il permet ainsi à la fois de contrôler la vitesse moyenne et l'angle instantané de pelage et de restreindre les effets inertiels intervenant pendant l'instabilité aux effets "intrinsèques" au ruban.

Ce système expérimental nous a ainsi permis de sonder les domaines de stabilité du pelage en fonction des paramètres de contrôle que sont la vitesse moyenne de pelage (0.03 m s$^{-1} < V < 4$ m s^{-1}), l'angle de pelage ($30° < \theta < 150°$) et la longueur de ruban pelé (0.25 m $< L < 1.35$ m). Cette étude s'appuie à nouveau sur une analyse des séries temporelles de la vitesse du front de pelage $v(t)$ extraites d'images de caméra rapide. Ces analyses ont révélé une série de résultats que nous listons ci-après de manière synthétique et qui sont (pour partie) détaillés dans l'article [Dalbe *et al.*, Soft Matter, 2014b] à la page 189 :

1. À un angle de pelage donné, les seuils en vitesse d'apparition et de disparition de l'instabilité sont associés à des bifurcations sous-critiques. Plus précisément, on observe près de ces seuils une gamme de vitesse (Figure 3.9) où le système est bistable entre le régime de pelage stationnaire et un régime de pelage oscillant, d'amplitude finie au seuil. Le pelage présente en pratique des intermittences temporelles entre les deux régimes (stationnaire et oscillant). Cette nature sous-critique de la bifurcation du système n'est pas compatible

avec le critère simple qui relie univoquement la stabilité du pelage au signe de $\frac{d\Gamma}{dv}\big|_V$.

2. La gamme instable (et bistable) s'élargit vers les grandes et les petites vitesses lorsque l'angle de pelage θ décroît (Figure 3.9) confirmant de manière systématique et contrôlée la forte influence de θ sur les seuils de l'instabilité, déjà observée lors des expériences de pelage depuis un rouleau libre.
3. Dans les gammes instables de vitesses, lorsque l'angle de pelage augmente, les oscillations de la vitesse du front de pelage évoluent progressivement d'oscillations de relaxation d'amplitude fixe ~ 40 m s^{-1}, typiques du stick-slip quasi-statique, à des oscillations sinusoïdales d'amplitude $2V$ (Figure 3.10). Aux faibles vitesses et/ou faibles angles de pelage, la période des oscillations (de relaxation) est bien décrite par le modèle quasi-statique (section 3.2.3) de l'instabilité. Dans le régime d'oscillations sinusoïdales, aux grandes vitesses et/ou aux grands angles de pelage, la période de l'instabilité s'écarte en revanche fortement du modèle quasi-statique et devient compatible en ordre de grandeur avec le temps de propagation d'une onde de déformation longitudinale (de vitesse $c = \sqrt{Ee/\mu}$) le long du ruban pelé. Dans les deux régimes limites mentionnés ici, que l'on qualifiera respectivement de quasi-statique et d'inertiel, la période et l'amplitude de l'instabilité sont cependant toujours respectivement proportionnelle et indépendante de la longueur L du ruban pelé.

3.5 Développements actuels et perspectives

Les résultats des expériences de pelage à angle et vitesse imposés que nous venons de décrire fournissent un support solide pour progresser dans la compréhension de l'instabilité du pelage des adhésifs, au-delà de la description quasi-statique et du critère de stabilité basé sur le signe de $\frac{d\Gamma}{dv}\big|_V$. Les questions fondamentales ouvertes par ces résultats appellent à la construction de modèles théoriques plus élaborés, mais aussi à des études expérimentales complémentaires. Nous évoquons dans cette dernière partie les développements actuels de notre étude et les pistes de travail à plus long terme.

3.5.1 Énergie de fracture $\Gamma(v, \theta)$

- Collaboration avec M. Ciccotti et C. Creton (ESPCI) et David Yarusso (3M Company)
- Post-doctorat de R. Villey (février 2014 - présent)

La dépendance avec l'angle de pelage de la gamme instable de vitesse que nous venons de mettre en évidence nous guide naturellement vers une caractérisation expérimentale de la dépendance angulaire de l'énergie de pelage $\Gamma(V, \theta)$ et, notamment, de sa gamme décroissante. Nous sommes actuellement en train de réaliser ce travail à travers des mesures de la force de pelage grâce à un couplemètre dynamique monté sur le cylindre d'enroulement de notre expérience de pelage à angle et vitesse imposés. Dans ce cadre, il est important d'accéder à la branche lente de l'énergie de fracture sur une large gamme de vitesse pour pouvoir évaluer les prédictions du modèle quasi-statique (voir section 3.2.3) et donc ses limites. Nous complétons

ainsi les mesures au couplemètre dynamique par des mesures réalisées sur une machine de traction Instron® couplée à une platine de translation. Au final, ces expériences nous permettront de sonder une gamme de vitesse allant de 1 μm s^{-1} à 4 m s^{-1}. Cette étude est encore en cours, mais semble d'ores et déjà révéler une croissance globale de l'énergie de pelage avec l'angle de pelage, et ce sur toute la gamme de vitesse étudiée. Cette augmentation semble compatible avec une croissance de la période de l'instabilité avec l'angle de pelage, observée pour les expériences en régime quasi-statique présentées à la partie 3.4. Cette étude met par ailleurs en évidence une dépendance angulaire, cependant modérée, de la gamme décroissante de $\Gamma(V)$. Nous travaillons actuellement à la modélisation des implications de ces mesures de l'énergie de fracture en régime stable sur les seuils et la dynamique de l'instabilité de stick-slip (voir la perspective 3.5.2) en résonance avec les résultats expérimentaux décrits à la partie 3.4.

Un autre aspect de cette étude est de mieux appréhender les origines de la dépendance angulaire de l'énergie de fracture qui, comme nous l'avons décrit dans la section 3.3, n'a été que peu étudiée par le passé. Les pistes de recherche consisteront ici à caractériser de manière systématique les structures internes, les dimensions et la forme de la zone de processus grâce à des observations microscopiques pendant le pelage (toujours en régime stable). Un autre objectif consistera à estimer les contraintes dans la zone de processus : l'idée est ici d'ajuster à la forme réelle du ruban pelé près du front de pelage les prédictions de la théorie de l'Elastica en prenant en compte l'existence de contraintes surfaciques exercées par le matériau adhésif. La connaissance de ces contraintes est un ingrédient important pour modéliser les processus dissipatifs ou tout du moins quantifier localement la dissipation intervenant dans le matériau adhésif.

Finalement, une autre ambition de ce projet est d'étudier les liens entre la forme anormale de l'énergie de pelage et la rhéologie des matériaux avec comme objectif de mieux comprendre comment cette rhéologie détermine l'instabilité. Nous entamons dans ce contexte une collaboration avec le centre de recherche américain de la société 3M (St. Paul, Minnesota) qui synthétise pour nous des échantillons "sur-mesure" proches des adhésifs commerciaux Scotch® 600 que nous avons étudié jusqu'à présent. L'atout principal de ce projet est que 3M est capable de modifier de manière contrôlée certains paramètres rhéologiques de la colle :

- La température de transition vitreuse, en changeant la concentration de résine "tackifiante" dans le matériau adhésif acrylique.
- L'extensibilité limite et l'élasticité de l'adhésif aux grandes déformations ainsi que son élasticité linéaire à basse fréquence, en changeant le taux de réticulation des chaînes polymères.
- Le comportement visco-plastique et en particulier la fibrillation aux grandes déformations ainsi que le comportement visqueux à basse fréquence, en changeant le niveau d'enchevêtrement des chaînes polymères.

Un objectif de cette partie est de tester si la gamme décroissante de l'énergie de pelage est contrôlée uniquement par la température de transition vitreuse T_g de l'adhésif. Cette dépendance avec T_g a déjà largement été mise en évidence à travers le respect par l'énergie de pelage du principe d'équivalence temps-température de Williams, Landel et Ferry [178, 179]. Nous souhaitons au contraire mieux caractériser l'influence des changements de la rhéologie non-linéaire

et aux grandes déformations de l'adhésif sur la décroissance de l'énergie de fracture et donc indirectement sur l'instabilité de stick-slip.

3.5.2 Modélisation de la dynamique instable et mesures dynamiques de la force de pelage

- Collaboration avec M. Ciccotti (ESPCI), S. Santucci (ENS Lyon) et Loïc Vanel (Univ. Lyon 1)
- Post-doctorat de R. Villey (février 2014 - présent)

Les mesures de la dépendance angulaire de l'énergie de pelage que nous venons d'évoquer seront évidemment un support fondamental à la compréhension de la dépendance angulaire de la dynamique instable du pelage et, notamment, des seuils de l'instabilité.

Cependant, une deuxième voie d'exploration dans la perspective de comprendre cette dépendance angulaire semble liée à la compréhension des effets inertiels intervenant pendant le pelage instable. Une partie de nos efforts est ainsi actuellement consacrée à modéliser les résultats des expériences de pelage à angle et vitesse imposés en prenant en compte la physique de la propagation sous forme d'ondes des déformations dans le ruban pelé. Le fait que la période de l'instabilité de pelage que nous avons mesurée dans le régime "inertiel" corresponde en ordre de grandeur au temps de propagation des ondes longitudinales dans le ruban pelé suggère en effet la probable importance de celles-ci dans l'écart au régime quasi-statique. Il semble ainsi primordial, pour bien comprendre le régime "inertiel" de l'instabilité, de ne pas considérer le ruban comme uniformément tendu pendant le pelage, contrairement aux équations développées dans les parties 3.2.2 et 3.2.3. La dépendance angulaire de l'instabilité de pelage pourrait en pratique trouver une partie de son origine dans la dépendance angulaire de son régime inertiel.

Le défi de cette partie "théorique" de notre projet consiste à complexifier de manière pertinente l'équilibre de Griffith entre le taux de restitution de l'énergie G et l'énergie de fracture $\Gamma(v)$ pour prendre en compte les effets dynamiques intervenants dans le régime inertiel. Au-delà des ondes se propageant le long du ruban pelé, un ingrédient important à prendre en compte sera la contribution de l'énergie de flexion, stockée dans la courbure du ruban près du front de pelage, dans la libération d'énergie nécessaire à l'avancée non-stationnaire du front [††].

Finalement, il est important de rappeler que l'observation expérimentale de gammes de vitesse où le système est bistable aux seuils de l'instabilité remet en cause le critère de stabilité "simple" basé sur le signe de $\frac{d\Gamma}{dv}\big|_V$. Cette bistabilité traduit en effet l'existence, près du maximum local de la courbe $\Gamma(V)$, de deux états métastables (au sens des systèmes dynamiques) associés à un pelage stationnaire et un pelage oscillant. Le seuil de stabilité du système associé à une telle bifurcation sous-critique ne peut évidemment pas être décrit à travers un test de stabilité vis-à-vis d'une petite perturbation comme celui qui mène au critère sur le signe de $\frac{d\Gamma}{dv}\big|_V$ (voir partie 3.2.2). Pour compléter cette discussion, il est intéressant d'évoquer les résultats expérimentaux de Yamazaki et Toda [189] qui ont réalisé des expériences de pelage en variant sur plusieurs ordres de grandeur la raideur du système de pelage pour un même adhésif. Dans leurs

††. Cette énergie de courbure ne contribue pas à l'avancée de la fissure en régime stationnaire.

expériences, pour les plus faibles raideurs, le pelage est instable sur toute la gamme de vitesse où $\frac{d\Gamma}{dv}\big|_V < 0$. Cependant, une augmentation de deux ordres de grandeur de la raideur permet de stabiliser le pelage temporellement pour l'ensemble des vitesses. Une disparition analogue de l'instabilité de stick-slip de la friction solide est aussi observée lorsque la raideur du système de traction augmente fortement [152]. Ces observations illustrent le fait que la raideur du système de pelage doit, lorsqu'elle dépasse un certain seuil, être prise en compte dans la construction du critère de stabilité [‡‡]. La description des seuils de stabilité apparaît finalement comme une autre question encore largement ouverte d'un point de vue théorique.

D'un point de vue expérimental, nous travaillons en parallèle à la mesure de la force instantanée exercée par le rouleau d'enroulement sur l'extrémité du ruban pelé grâce au couplemètre dynamique utilisé pour les mesures de l'énergie de fracture en régime stable. Ces mesures sont particulièrement difficiles car l'oscillateur formé par l'élasticité en torsion du couplemètre associée à l'inertie du rouleau d'enroulement vient se coupler aux fluctuations de la force de pelage. Le signal mesuré doit donc être corrigé *a posteriori* à travers un modèle de cette partie du système pour pouvoir finalement accéder à la force réelle à l'extrémité du ruban pelé. L'autre objectif de ce développement expérimental est de mesurer en parallèle la force réelle au point de pelage à travers l'introduction d'un capteur de force compact encastré dans la barre de translation constituant le substrat de l'adhésif et recouvert d'une fine et courte plaque reconstruisant la surface du substrat. L'objectif global de ces mesures est de reconstruire les évolutions temporelles parallèles des oscillations de la vitesse du front de pelage, de la force au point de pelage et de la force au point d'enroulement. La mesure simultanée de ces trois signaux temporels, qui constitue un vrai défi expérimental, permettra finalement de sonder le cœur de la dynamique instable du pelage des adhésifs et de baliser précisément les ingrédients physiques importants pour décrire celle-ci de manière quantitative.

‡‡. Les mécanismes en jeu ici sont possiblement liés au fait que la période et l'amplitude (en longueur d'avancée du front) de l'instabilité décroissent avec la raideur du ruban, selon le modèle quasi-statique. La disparition de l'instabilité peut alors être liée à l'entrée en jeu d'une inertie locale (associée à une fréquence caractéristique à travers l'élasticité des matériaux) ou à celle des hétérogénéités de l'adhésif (associées à une échelle caractéristique) qui inhibent l'instabilité lorsqu'elle essaie de se développer à des échelles temporelles ou spatiales plus petites.

Intermittent stick-slip dynamics during the peeling of an adhesive tape from a roller

Pierre-Philippe Cortet,[1] Marie-Julie Dalbe,[2,3] Claudia Guerra,[2] Caroline Cohen,[3] Matteo Ciccotti,[4] Stéphane Santucci,[3] and Loïc Vanel[2]

[1]*Laboratoire FAST, CNRS, Univ Paris Sud, UPMC Univ Paris 06, France*

[2]*Institut Lumière Matière, UMR5306 Université Lyon 1-CNRS, Université de Lyon, France*

[3]*Laboratoire de Physique de l'Ecole Normale Supérieure de Lyon, CNRS and Université de Lyon, France*

[4]*Laboratoire PPMD/SIMM, UMR7615 (CNRS, UPMC, ESPCI Paristech), Paris, France*

(Received 31 July 2012; revised manuscript received 7 December 2012; published 19 February 2013)

We study experimentally the fracture dynamics during the peeling at a constant velocity of a roller adhesive tape mounted on a freely rotating pulley. Thanks to a high speed camera, we measure, in an intermediate range of peeling velocities, high frequency oscillations between phases of slow and rapid propagation of the peeling fracture. This so-called stick-slip regime is well known as the consequence of a decreasing fracture energy of the adhesive in a certain range of peeling velocity coupled to the elasticity of the peeled tape. Simultaneously with stick slip, we observe low frequency oscillations of the adhesive roller angular velocity which are the consequence of a pendular instability of the roller submitted to the peeling force. The stick-slip dynamics is shown to become intermittent due to these slow pendular oscillations which produce a quasistatic oscillation of the peeling angle while keeping constant the peeling fracture velocity (averaged over each stick-slip cycle). The observed correlation between the mean peeling angle and the stick-slip amplitude questions the validity of the usually admitted independence with the peeling angle of the fracture energy of adhesives.

DOI: 10.1103/PhysRevE.87.022601 PACS number(s): 82.35.Gh, 62.20.mm, 68.35.Np

I. INTRODUCTION

The stick-slip instability that can develop during the high speed peeling of adhesives, and which consists in strong oscillations between phases of slow and rapid propagation of the peeling fracture, constitutes a major problem in the polymer industry. The scratchy sound that anyone can experience when pulling on an adhesive tape, which is a trace of this instability, can indeed cause a level of acoustic noise that is simply unbearable in the industrial context. Another negative impact of stick slip is the damage caused to the adhesive coating [1,2] when the instability occurs during the peeling of a temporary substrate layer before the adhesive is effectively used. It is, for example, a severe problem for hard disk drive (HDD) manufacturers as stick slip will deteriorate the quality of the adhesive seal which can lead to HDD failure. These industrial concerns have recently conducted many patents on this issue to be deposited (e.g., [3]). Overall, adhesive stick slip reduces industrial productivity and its current hard-to-predict nature hinders the development of new technical applications.

From a fundamental perspective, this unstable stick-slip crack growth is admitted to be the consequence of a decreasing fracture energy $\Gamma(v_p)$ in a certain range of peeling fracture velocity v_p. This anomalous drop of the fracture energy has been proposed to be related to structural transitions, from cohesive to interfacial failure [4], or between different interfacial failure modes [5]. It has, however, also been proposed [6] that the rheological transition of adhesive materials, from soft to hard rubber or from rubber to glass, as a function of the strain rate could be, in the presence of confinement (which is the case for adhesive tapes), at the origin of a drop in the cohesive fracture energy. Overall, the stick-slip motion, resulting from this decreasing zone of fracture energy coupled to the compliance of the peeled tape or peeling machine, corresponds to an oscillation of the crack velocity between two (usually) very different values. There are several factors that may influence the peeling velocity range in which stick slip effectively appears. For instance, the stick-slip velocity thresholds can show a dependence on the glass transition temperature of the adhesive [5,7], the thickness of the adhesive layer [8,9], the substrate roughness [10], and its viscoelastic properties [11]. Remarkably, when stick slip occurs, the details of its dynamics change with the imposed peeling velocity but also with the length of the tape submitted to the peeling load [12] and sometimes the stiffness of the loading machine [2].

As proposed and verified experimentally by Kendall [13], the fracture energy of a peeled adhesive tape does not depend on the peeling angle in the regular and slow (with respect to the stick-slip domain) peeling regime, which result is widely extrapolated to larger peeling velocities. An effect of the peeling angle on the velocity range for which stick slip exists was nevertheless already reported in some early experiments [14], however, in conditions where the length of the peeled tape was not constant but instead linearly increasing with time during the peeling.

In this paper, we describe experiments of adhesive tape peeling from a freely rotating roller in which we aim at imposing the peeling velocity and the peeled tape length, defined as the distance between the peeling fracture front on the roller and a winding cylinder. Keeping these two parameters constant is indeed necessary to produce a well-defined stick-slip dynamics [12]. Thanks to a fast imaging camera coupled to image correlation velocimetry, we are able to extract the full dynamics of the peeling fracture velocity with respect to the substrate. In practice, we do not impose the peeled tape length but only the distance between the adhesive roller and the winding cylinder (Fig. 1). During an experiment at constant pulling velocity, superimposed on the stick-slip instability, we may observe a slow oscillation of the angular position at which the tape pulls on the roller. This slow dynamics causes the effective peeling angle (averaged over one stick-slip event)

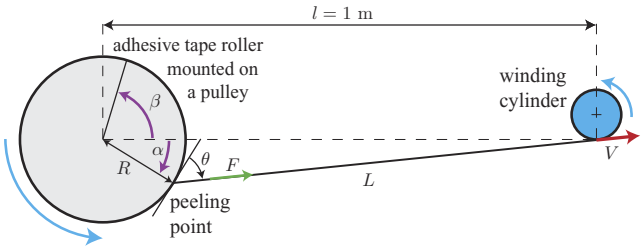

FIG. 1. (Color online) Schematic view of the experimental setup. The angles α and β are oriented *clockwise* and *counterclockwise*, respectively. Roller diameter: 40 mm $< 2R <$ 58 mm; roller and tape width: $b = 19$ mm; tape thickness: $e = 58$ μm.

to oscillate with significant amplitude, but in a quasistatic manner for the stick slip. We report that the value of the effective peeling angle has a strong effect on the triggering and amplitude of the stick-slip instability, even though the mean fracture velocity and peeled tape length remain constant or at least not significantly affected by the slow oscillations. This effect of the peeling angle on stick slip can not be simply understood by taking into account its influence on the work term of the elastic energy release rate as proposed by Kendall [13]. We suggest that the detailed features of any adhesive stick-slip motion should depend not only on the peeling velocity and peeled tape stiffness, but also strongly on the effective peeling angle.

II. EXPERIMENTAL SETUP

We peel a roller adhesive tape, mounted on a freely rotating pulley, by winding up the peeled ribbon extremity on a cylinder at a constant linear velocity V using a servo-controlled brushless motor (Fig. 1). The distance between the pulley and the winding cylinder is fixed to $l = 1$ m. It is defined between the adhesive roller center and the point, assumed to be fixed, at which the peeled tape joins the winding spool. The adhesive tape used, 3M Scotch® 600, of the same kind as in Refs. [15,16], is made of a polyolefin blend backing (38 μm thick) coated with a 20-μm layer of a synthetic acrylic adhesive. Each experiment consists in increasing the winding velocity from 0 up to the target velocity V at a rate of 1 m s^{-2}. Once the peeling velocity V is reached, it is maintained constant to a precision better than $\pm 2\%$ during two seconds, before decelerating back to zero. We have varied the imposed velocity V from 0.15 to 2.55 m s^{-1} in order to cover the whole range where stick-slip instability is observed for the considered adhesive tape and peeling geometry.

The local dynamics of the peeling fracture line, viewed as a point from the side, is imaged using a high speed camera (Photron Ultima 1024) at a rate of $f = 8000$ fps and a resolution of 512×64 pixels. The field of view being approximately 2.5 cm wide, the resolution is about 50 μm/pixel. The recording of each movie is triggered once the peeling has reached a constant average velocity V in order to obtain a stationary condition for the peeling experiment. Following the method presented in Ref. [16], correlations between images of the movie, separated of a time $\delta t = N/f$ ($N \in \mathbb{N}$), allow us to access the following:

(i) the curvilinear position of the peeling point in the laboratory reference frame $\ell_\alpha = R\,\alpha$, where α is the angular position of the peeling point (chosen positive in the *clockwise* direction, $\alpha > 0$ in Fig. 1) and R is the roller radius (between 20 and 29 mm);

(ii) the curvilinear position of the adhesive roller $\ell_\beta = R\,\beta$, in the laboratory reference frame, where β is the unwrapped angular position of the roller (chosen positive in the *counterclockwise* direction, $\beta > 0$ in Fig. 1).

We are finally able to compute the curvilinear position ℓ_p of the peeling fracture point in the roller reference frame (ℓ_p is chosen so that it increases when the peeling front advances)

$$\ell_p = \ell_\alpha + \ell_\beta = R(\alpha + \beta). \tag{1}$$

We can then compute the peeling fracture velocity v_p relative to the substrate

$$v_p = \frac{d\ell_p}{dt} = R(\dot{\alpha} + \dot{\beta}). \tag{2}$$

Here, the substrate simply consists in the backing of the adhesive tape remaining to peel.

The separation number N between the images used for correlation is chosen such that the moving matter at the periphery of the roller displaces of about 5 pixels ($\sim$250 μm) between the two images. Since the correlation is subpixel interpolated, we reach a precision of about 1 pixel/10 $\sim$ 5 μm on the displacement, i.e., 2%. We finally get the same precision of 2% on the average peeling point velocity v_p over a time scale $dt \sim (250 \times 10^{-6}\,\text{m})/V$, varying between 1.7 ms at the lowest imposed velocity and down to 0.1 ms at the largest imposed velocity.

III. EQUATIONS OF MOTION

The equation ruling the motion of the adhesive roller can be written as

$$I\ddot{\beta} = FR\,\cos\theta, \tag{3}$$

where I is the moment of inertia of the roller and F the tensile force transmitted along the peeled tape. Here, the angle θ and α are linked by the geometrical constraint

$$l\cos(\theta + \alpha) = R\cos\theta, \tag{4}$$

where $l = 1$ m is the constant distance between the roller center and the point at which the tape joins the winding spool. An interesting limit case of Eq. (3) is then obtained [17] when the roller radius R is small compared to the distance l, so that $\theta + \alpha \simeq \pi/2$. In our experiments, it is almost the case, with $R/l < 3\%$, and the roller equation of motion (3) can be approximated by

$$I\ddot{\beta} \simeq FR\,\sin\alpha. \tag{3b}$$

Then, assuming a uniform tensile strain in the peeled tape, the force F transmitted to the roller is simply

$$F = \frac{Ebe}{L - u}\,u, \tag{5}$$

where u is the elongation of the tape of Young modulus E, thickness e, and width b. The assumption of a uniform peeled tape strain amounts to neglect transverse waves in the tape under tension. It is worth to note that these waves may,

however, influence the high frequency stick-slip instability in some peeling regimes. In Eq. (5), the peeled tape length L is not a constant (see Fig. 1) and varies with the angle α according to

$$L(t)^2 = l^2 + R^2 - 2lR\cos\alpha(t). \tag{6}$$

Experimentally, the observed instantaneous values of α range between -25° and $+25^{\circ}$ at most. Such variations of α induce peeled tape length variations of $\delta L/L \sim 0.3\%$ in our geometry. These very small variations of L during the peeling experiments should have no significant impact on the velocity thresholds and the other features of the stick-slip instability [2].

Finally, the following kinematical constraint on the peeled tape elongation applies:

$$V = v_p + \dot{u} - R\cos\theta\,\dot{\alpha}. \tag{7}$$

Note the sign change in the last term of Eq. (7) compared to Ref. [17] due to the opposite orientation chosen for α. Using the approximation $\theta \simeq \pi/2 - \alpha$, Eq. (1) and the integration over time of Eq. (7) give

$$\ell_p - Vt = R(\alpha + \delta\beta) = u_0 - u + R(\cos\alpha_0 - \cos\alpha), \tag{7b}$$

in which $\delta\beta = \beta - Vt/R$ measures the unsteady part of the roller rotation. In Eq. (7b), u_0 and α_0 are constants corresponding to the values of u and α at $t = 0$ for which $\ell_p = 0$ by definition. Then, since the peeling crack length averaged over a long time $\langle \ell_p \rangle$ simply equals to Vt, one gets $\langle u \rangle = u_0 + R(\cos\alpha_0 - \langle\cos\alpha\rangle)$, where $\langle\cdots\rangle$ denotes the time average, which measures the mean level of deformation of the peeled tape during the experiment.

To close the system of equations describing the peeling experiments, one needs to model how the peeling fracture velocity v_p is set. Such physical condition for peeling is usually expressed as a balance between the elastic energy release rate G of the system and the fracture energy Γ required to peel a unit surface such that

$$G = \Gamma(v_p). \tag{8}$$

$\Gamma(v_p)$ accounts for the energy cost of the dissipative processes near the fracture front during the fracture growth. In general, this fundamental quantity in fracture mechanics is characteristic of the type of material to fracture, of the fracture geometry, and of the fracture velocity. For a given material and geometry, it is therefore classically considered to be a function of the fracture velocity v_p only. In the context of adhesive peeling, Γ is therefore also characteristic of the rheology of the adhesive material, of the backing, and of the substrate. Finally, it is *a priori* also a function of the local geometry near the fracture front: the thickness of adhesive, the local peeling angle, ... However, most of theoretical works on stick-slip adhesive peeling considers only the dependence of fracture energy on fracture velocity $v_p(t)$, except in some models which assume that Γ is also dependent on the imposed velocity V [17,18].

The elastic energy release rate G corresponds to the amount of mechanical energy released by the growth of the fracture by a unit surface. This quantity, which is geometry dependent, both takes into account the work done by the operator and the changes in the recoverable energy stored in material strains. The following expression is traditionally used for the peeling fracture geometry [13,17]

$$G = \frac{F}{b}(1 - \cos\theta). \tag{9}$$

This is a very good approximation for most adhesive tapes and peeling geometries, except when the peeled tape stretching energy can not be neglected for very small peeling angles [13] or when its curvature elasticity has to be taken into account [19], especially for very short peeled tape length.

It is usually assumed that in the fracture propagation equation (8), the effect of peeling angle θ is fully taken into account by its appearance in the energy release rate (9). In other words, it is usually considered that Γ itself does not depend on θ. Consequently, the velocity range in which stick slip appears is expected to be independent of the peeling angle and to be set mainly by the region where $\Gamma(v_p)$ has a negative slope, with some limitations due to an influence of the peeled tape stiffness [2].

Altogether, we can identify three independent degrees of freedom (for example α, β, and u) related to each other by the system of Eqs. (2)–(9) involving three differential equations: (3), (7), and (8). An interesting exact solution is the steady state, or fixed-point, solution corresponding to a regular peeling and given by

$$\begin{aligned} &\alpha = 0; \quad \dot{\beta} = \frac{V}{R}; \quad \frac{u}{L} = \frac{1}{1 + Ee/\Gamma(V)}; \\ &\theta = \frac{\pi}{2}; \quad v_p = V; \quad L = l - R; \quad \frac{F}{b} = \Gamma(V). \end{aligned} \tag{10}$$

IV. RESULTS

A. Basic stick-slip features

In Fig. 2, we plot a typical signal of peeling fracture velocity $v_p(t)$ for an imposed peeling velocity $V = 0.90\,\mathrm{m\,s^{-1}}$. The observed large and oscillating fluctuations of $v_p(t)$ are the characteristic signature of the stick-slip motion. Note that the amplitude of these oscillations is roughly as large as the mean peeling velocity. In particular, the peeling

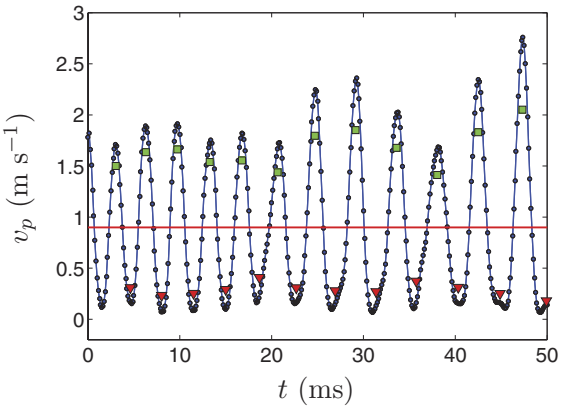

FIG. 2. (Color online) Peeling point velocity $v_p(t)$ in the roller reference frame for an experiment performed at $V = 0.90$ m s^{-1}. Triangles and squares, respectively, show the averaged stick v_{stick} and slip v_{slip} velocities for each stick-slip cycle. The horizontal straight line shows the imposed peeling velocity V.

experiences an almost complete arrest with a very low fracture velocity (here, fluctuating between 0.05 m s^{-1} $\sim 0.06\,V$ and 0.15 m s^{-1} $\sim 0.17\,V$) once every stick-slip cycle. The period of these oscillations is quite stable during an experiment (here, 3.9 ± 0.4 ms for $V = 0.90$ m s^{-1}).

Now considering all the experiments, over the whole range of peeling velocities $0.25 < V < 2.45$ m s^{-1} for which we observe stick-slip instability, the stick-slip oscillations period (averaged over all the stick-slip events for each experiment) is very stable, in the range 3.9 ± 0.3 ms. This result is in contrast with the data reported in Refs. [12,20] for a different adhesive roller tape (3M Scotch® 602) also peeled at constant velocity. In Refs. [12,20], the stick-slip period was extracted from torque time series provided by the winding motor and was indeed shown to be proportional to L and approximatively proportional to the inverse of V over the whole range of instable peeling velocities (which was $0.06 < V < 2.1$ m s^{-1}). The linearity of the stick-slip period with L/V reported in Ref. [12] agrees with a model where the limit of stability of the stick phase, before the system jumps into the slip phase, corresponds to the reach of a constant threshold in strain or stress in the peeled ribbon. Indeed, during the stick phase the peeled tape strain almost linearly increases with time as Vt/L. An important assumption of the model developed in Refs. [12,20] is that the slip phase duration is negligible compared to the stick phase one. However, in these works, this assumption remained untested since the torque measurements did not allow a direct access to the peeling fracture dynamics contrary to our measurements. As can be seen in Fig. 2, the assumption of a negligible slip phase duration is obviously far from being true in our experiments, which could explain why this model fails here and also suggests that we are not investigating a comparable stick-slip regime.

In our experiments, as a consequence of the constancy of the mean stick-slip cycle duration T_{ss}, the mean amplitude of the fracture propagation A_{ss} during stick-slip cycles increases almost proportionally to the peeling velocity V according to $A_{ss} = V\,T_{ss}$. It is, however, remarkable to note that the dispersion inside a given experiment of the stick-slip cycles amplitude and period is increasing significantly from about 5% to 40% with the imposed velocity V going from 0.25 to 2.45 m s^{-1}. We will see in the following that this increasing dispersion is the trace of the growth with V of low frequency oscillations of the mean peeling angle (averaged over one stick-slip event) which induce intermittencies in the stick-slip instability.

From the signal of instantaneous peeling velocity, we actually search for all the moments at which the sign of $v_p(t) - V$ changes. When $v_p(t) - V$ goes from positive to negative, it defines the beginning of a stick event and when it goes from negative to positive, it defines the beginning of a slip event. We then compute the mean stick v_{stick} and slip v_{slip} velocities as the average value of the velocity $v_p(t)$ during the phases where $v_p(t) < V$ (stick) and $v_p(t) > V$ (slip). Finally, only the events during which v_p is successively smaller than $0.95\,V$ and larger than $1.05\,V$ are considered as true stick-slip events. This allows us to avoid measurement noise and small velocity fluctuations to be taken into account as stick-slip events during periods where no stick-slip is present. These stick and slip velocities are reported in Fig. 2 as triangle and square symbols, respectively. We observe that the stick and slip mean velocities are fluctuating in time during a peeling experiment at constant velocity V. This is probably mainly because of heterogeneities in the adhesion properties of the peeled tape and also maybe, to a lesser extent, because of the fluctuations of the imposed velocity.

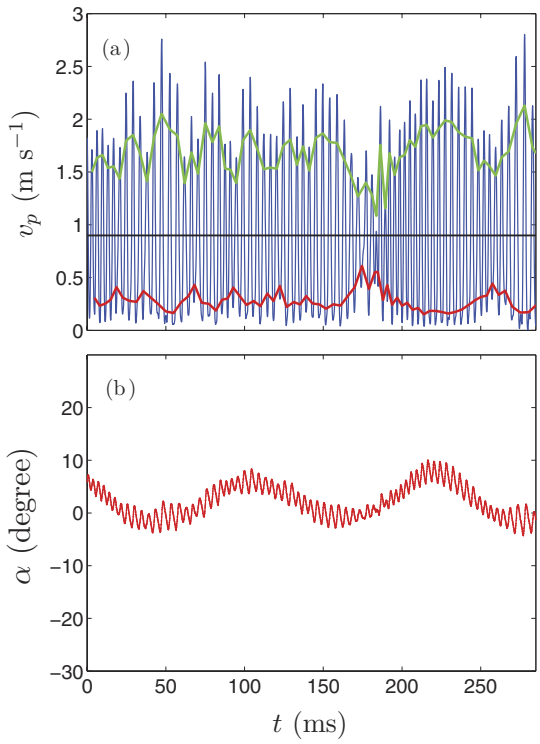

FIG. 3. (Color online) (a) Peeling point velocity v_p in the roller reference frame as a function of time for an experiment performed at $V = 0.90$ m s^{-1}. The top and bottom continuous lines, respectively, trace the slip and stick local mean velocities. The horizontal straight line shows the average peeling velocity V. (b) shows the corresponding instantaneous peeling point angular position α as a function of time.

At the lower peeling velocities belonging to the instable interval, the stick and slip velocities are, however, relatively stable throughout the peeling cycles during an experiment as can be seen in Fig. 3(a) (same experiment at $V = 0.90$ m s^{-1} as in Fig. 2). We nevertheless observe in this figure at time $t \sim 180$ ms that the stick-slip amplitude decreases abruptly and temporarily during three stick-slip cycles. We believe such "accident" may be related to rare large scale defects in the adhesion of the commercial tape.

B. Stick-slip intermittencies and roller pendular oscillations

Remarkably, as the average peeling velocity V is increased, we observe that the stick-slip dynamics becomes intermittent, alternating regularly between periods of time with fully developed stick-slip cycles and periods of time without or at least with strongly attenuated stick-slip amplitude. A typical example of such intermittencies is shown in Fig. 4(a) where a period of about 140 ms (∼7 Hz) can be seen. Comparing these data with the instantaneous angular position of the peeling point in the laboratory $\alpha(t)$ in Fig. 4(b), we see that the intermittent stick-slip behavior is strongly correlated with low

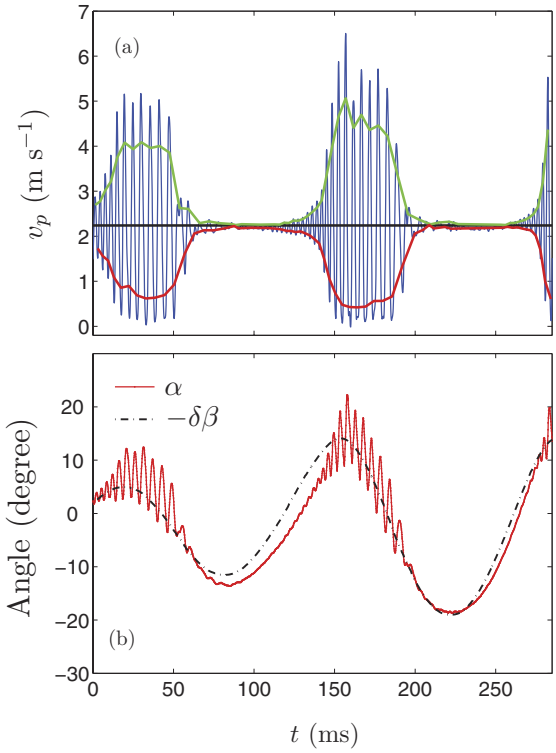

FIG. 4. (Color online) (a) Peeling point velocity v_p in the roller reference frame and (b) angular positions $\alpha(t)$ and $-\delta\beta(t) \equiv Vt/R - \beta(t)$ as functions of time for an experiment performed at $V = 2.24\,\mathrm{m\,s^{-1}}$. Same layout as in Fig. 3.

frequency variations of this angle, whereas high frequency variations of $\alpha(t)$ (at about ∼250 Hz) are directly correlated to the stick-slip motion.

The slow oscillations of the angular peeling position $\alpha(t)$ are the direct consequence of a low frequency pendulumlike motion of the adhesive roller, in addition to its mean rotation at a rate V/R. Indeed, as can be seen in Fig. 4(b), the angle $\delta\beta(t) = \beta(t) - V\,t/R$, which measures the unsteady part of the roller rotation, matches rather well the low frequency oscillations of $-\alpha(t)$ when smoothing over the fast stick-slip oscillations. This observation $\langle\alpha + \delta\beta\rangle_{ss} \simeq 0$, where $\langle\cdots\rangle_{ss}$ stands for the average over a stick-slip cycle, can be understood in the following way. Experimentally, we observe that the mean (averaged over a stick-slip cycle) fracture velocity $\langle v_p\rangle_{ss}$ is always equal to the imposed peeling velocity V to better than 7%. Therefore, to a good approximation, we have $\langle \ell_p\rangle_{ss} \simeq Vt$. Finally, using the first equality in Eq. (7b), this shows that $\langle\alpha\rangle_{ss} \simeq -\langle\delta\beta\rangle_{ss}$ as is indeed verified in Fig. 4(b). Furthermore, averaging Eq. (3b) over a stick-slip cycle and using $\langle\alpha\rangle_{ss} \simeq -\langle\delta\beta\rangle_{ss}$, we get

$$\langle\ddot{\delta\beta}\rangle_{ss} + \frac{FR}{I}\langle\sin\delta\beta\rangle_{ss} \simeq 0, \tag{11}$$

which predicts pendular oscillations of the unsteady part of the roller rotation at a frequency close to $\omega = \sqrt{FR/I}$ for small amplitudes of $\delta\beta$.

To check this interpretation of the pendular oscillations, we have made some measurements of the mean peeling force $\langle F\rangle$, time averaged over the whole constant velocity peeling experiment. This is done with a force gage (Interface® SML-5), aligned with the direction $\alpha = 0$, and placed between the adhesive roller pulley and its mechanical support. In Table I, we compare the frequency of the slow oscillations with the characteristic frequency $\omega = \sqrt{\langle F\rangle R/I}$ replacing F by its temporal average value. Although this framework is only approximate, we find a rather good agreement between the direct measurement of the period and the theoretical prediction $2\pi/\omega$. We conclude that the low frequency dynamics develops due to the interplay between the inertia of the roller and the moment applied to the roller by the peeling force as already suggested in Ref. [16].

TABLE I. Comparison between the direct measurement of the low frequency oscillations period T and the period $2\pi/\omega = 2\pi/\sqrt{\langle F\rangle R/I}$ estimated using the average peeling force $\langle F\rangle$ in Eq. (11).

V (m s^{-1})	$\langle F\rangle$ (N)	T (s)	$2\pi/\omega$ (s)
0.36 ± 0.01	1.71 ± 0.07	0.109 ± 0.005	0.092 ± 0.002
0.50 ± 0.01	1.40 ± 0.06	0.115 ± 0.005	0.102 ± 0.002
0.72 ± 0.02	1.18 ± 0.05	0.118 ± 0.005	0.111 ± 0.002
1.53 ± 0.03	0.91 ± 0.04	0.130 ± 0.005	0.126 ± 0.003

In the two previous paragraphs, we have shown that the slow pendular oscillations of the adhesive roller are independent of the physics of the adhesive fracture propagation. We have indeed verified that the roller rotation $\beta(t) = Vt/R + \delta\beta(t)$ is unsensitive to the high frequency stick-slip oscillations of $\alpha(t)$ and $v_p(t)$ because of the roller inertia. Consequently, we feel entitled in the following to consider the slowly oscillating mean peeling angle $\langle\theta\rangle_{ss} \simeq \pi/2 - \langle\alpha\rangle_{ss} \simeq \pi/2 + \langle\delta\beta\rangle_{ss}$ as an effective control parameter for the fracture problem [i.e., Eq. (8)], which is quasistatically varying.

In order to quantify the slow oscillations of the peeling point angular position for various imposed velocity V, we plot as a function of V the mean angle α during each experiment and the corresponding standard deviation of its oscillations as error bars (Fig. 5). We also report the maximum and minimum angle α reached during each experiment. We can note the regular increase of the oscillation amplitude of α from ∼±2° up to ∼±25° as the imposed velocity increases in the instable range, whereas its mean value is quite stable in the range $\alpha \in [-4,3]^\circ$. Since the effective peeling angle verifies $\theta \simeq \pi/2 - \alpha$, it has a mean value always close to $\theta \simeq 90^\circ$, corresponding to the steady state solution (10), and variations up to ±25° around the mean at large peeling velocities.

In Fig. 4, we see that large amplitude stick slip occurs mostly for the larger and positive values of $\alpha(t)$ (i.e., $\theta < 90^\circ$), whereas for negative values (i.e., $\theta > 90^\circ$), stick slip almost disappears. Such straightforward correlation is, however, a simplistic picture since it can also be noted that there is some hysteresis in the angle α at which stick slip appears and disappears. Guesses could be that the hysteresis is due to a delayed response of the peeling instability when the angle α changes, which would correspond to a value of the stick-slip instability growth rate comparable to the pendular oscillations frequency. More generally, this hysteresis may reveal dynamical effects related to $d\theta/dt$. At low peeling

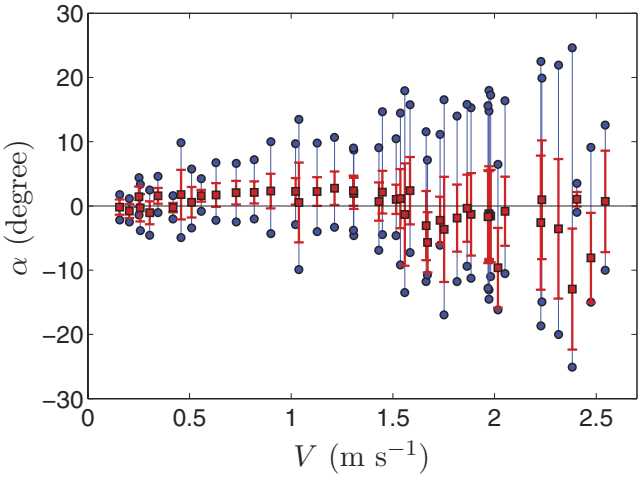

FIG. 5. (Color online) Mean angle α (squares) during each experiment and the corresponding standard deviation of its oscillations as error bars. Circles show the maximum and minimum angle α reached during each experiment.

velocity [Fig. 3(b)], low frequency oscillations of the peeling point angle do actually already exist but, as we have seen, are of smaller amplitude. They moreover apparently do not correlate with small stick-slip amplitude modulations. This suggests that the slow oscillations of α must overtake a certain amplitude to trigger a significant time modulation of the stick-slip amplitude.

C. Stick and slip velocities, and correlation with peeling angle

In Fig. 6(a), we plot the average (over all the events in each experiment) stick and slip velocities as a function of the imposed peeling velocity V. For the lower peeling velocities, we have plotted $v_{\text{stick}} = v_{\text{slip}}$ which means that the peeling is regular without observation of stick-slip events. The stick slip actually initiates at a peeling velocity threshold of $0.25 \pm 0.02\,\text{m s}^{-1}$ with average stick and slip velocities starting to deviate from the imposed peeling velocity V (continuous line). This threshold corresponds very well to the value measured for the same roller adhesive tape peeled by falling loads [16]. The stick and slip velocities increase gradually for V varying from 0.25 up to 2.45 ± 0.10 m s^{-1} for which value they collapse on the average velocity V. The measured disappearance threshold for stick slip at large velocities, 2.45 ± 0.10 m s^{-1}, is also compatible with the previously measured value in peeling experiments by falling loads where it was about 2.6 m s^{-1}.

In Fig. 6(a), the data are accompanied with their corresponding statistical standard deviation inside each experiment. These standard deviations are quite low (∼5% to 10%) from $V = 0.25$ to 1.5 m s^{-1} which means that the corresponding stick-slip features are quite stable during a given experiment. For average velocities V larger than 1.5 m s^{-1} and up to the disappearance of the stick slip at 2.45 ± 0.10 m s^{-1}, we observe larger standard deviations (∼10% to 20%) for the stick and slip velocities. This increase is obviously the trace of the stick-slip intermittencies that lead to alternate periods of strong and weak stick-slip oscillations.

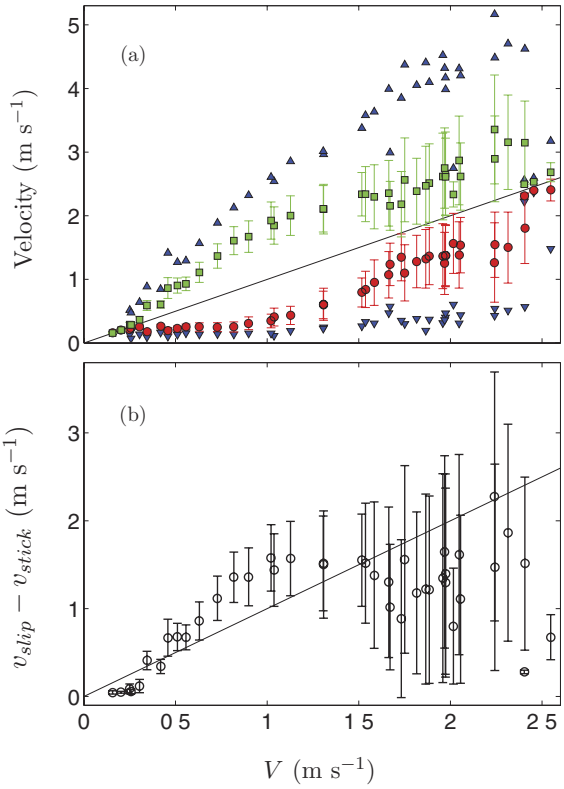

FIG. 6. (Color online) (a) Average slip (squares) and stick (circles) velocities and maximum slip (up triangle) and minimum stick (down triangle) velocities and (b) average of the difference $v_{\text{slip}} - v_{\text{stick}}$, as a function of the imposed peeling velocity V. In (a) and (b), the continuous line corresponds to the imposed peeling velocity. Each data point is an average and the error bar the standard deviation over all stick-slip events in a single experiment. The large values of standard deviation at large peeling velocities are the trace of the intermittent occurrence of stick slip.

Finally, in Fig. 6(a), we also plot the maximum slip and minimum stick velocities measured during each experiment. We see that as the peeling becomes more and more intermittent with the increasing peeling velocity V, the extreme values of the stick and slip velocities are further and further away from the average ones which reveals the amplitude of the stick-slip modulations. Focusing on the two experiments at imposed velocity $V = 2.40$ m s^{-1}, we can observe one experiment with a developed stick slip and one experiment with almost no remaining stick slip with mean stick and slip velocities about only 4% smaller and larger than V, respectively. These observations reveal the unprecise definition of the stick-slip disappearance threshold which is an intrinsic feature of adhesive stick slip, amplified in the present case by the slow oscillations of the peeling angle. Regarding the mean velocities, the last two data points, at 2.47 and $2.55\,\text{m s}^{-1}$, show an almost complete absence of stick slip. On the contrary, we see that the maximum slip and minimum stick velocities are very close to V for 2.47 m s^{-1} but quite far anew for the experiment at 2.55 m s^{-1}: in the last case, this is simply the trace of very marginal stick-slip events existing only during short phases of the pendular oscillations where the angle $\alpha(t)$ is large.

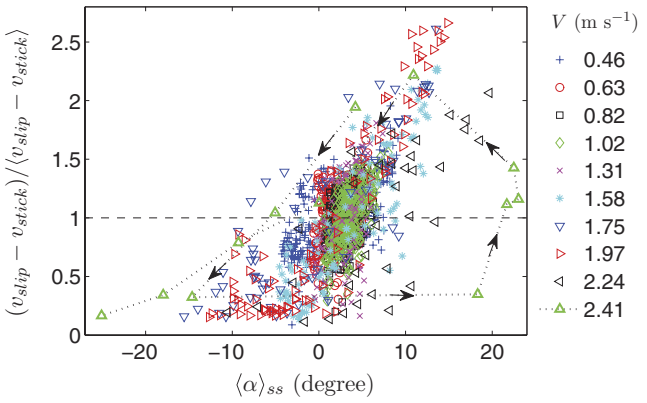

FIG. 7. (Color online) Parameter $(v_{\rm slip} - v_{\rm stick})/\langle v_{\rm slip} - v_{\rm stick}\rangle$, quantifying the normalized dependence of the velocity contrast between the slip and stick phases with the angular position of the peeling point $\langle\alpha\rangle_{ss}$ for various imposed peeling velocities V. Each data point corresponds to a single stick-slip event. The dotted line and the arrows indicate the time sequence of successive stick-slip events in the $V = 2.41$ m s^{-1} experiment which reveals a large hysteresis loop.

To study these intermittencies in more details, in Fig. 6(b), we plot as a function of the imposed velocity the quantity $v_{\rm slip} - v_{\rm stick}$ averaged over all stick-slip cycles in each experiment. We see that the mean velocity amplitude of stick slip is first larger than the imposed velocity up to $V = 1.5$ m s^{-1} before being overall lower and quite scattered as a consequence of the stick-slip intermittencies. Here, again the error bars correspond to the standard deviation of the plotted statistical quantity. These data illustrate very well the strong increase of the explored range of stick-slip amplitudes as the peeling velocity V increases. One can indeed observe in Fig. 6(b) that the standard deviation of the stick-slip amplitude becomes almost as large as its mean value for $V > 1.7$ m s^{-1}, which is the trace of the strongly intermittent behavior.

Finally, in order to quantify the correlations between the peeling point angular position and the amplitude of stick-slip, we introduce an order parameter defined as the difference between the slip and stick velocities for each stick-slip event $(v_{\rm slip} - v_{\rm stick})/\langle v_{\rm slip} - v_{\rm stick}\rangle$, normalized by its average over all the events at a given imposed velocity. Figure 7 shows the evolution of this parameter as a function of the mean angular position of the peeling point $\langle\alpha\rangle_{ss}$ for each stick-slip cycle during the experiments and for a wide selection of imposed velocity V. We first see that the average operating point in each data series at a given imposed velocity V, which is defined by $v_{\rm slip} - v_{\rm stick} = \langle v_{\rm slip} - v_{\rm stick}\rangle$, corresponds for a large majority of events to angles in the region $\langle\alpha\rangle_{ss} \in [0^{\rm o},5^{\rm o}]$. This observation is the trace of the fact that, without the parasitic pendular oscillations of the roller which generate the intermittencies, the stick-slip peeling would naturally proceed with a mean peeling angle in the range $\langle\theta\rangle_{ss} \in [85^{\rm o},90^{\rm o}]$. Around this operating point ($v_{\rm slip} - v_{\rm stick} = \langle v_{\rm slip} - v_{\rm stick}\rangle$, $\langle\alpha\rangle_{ss} \in [0^{\rm o},5^{\rm o}]$), the statistics of the stick-slip events gather on a cloud, which can be (roughly) modeled by

$$v_{\rm slip} - v_{\rm stick} = g(V) \times f(\langle\alpha\rangle_{ss}),$$

with f a rapidly increasing function and a separation of the variables V and $\langle\alpha\rangle_{ss}$. Here, g is defined as the mean velocity contrast $g(V) = \langle v_{\rm slip} - v_{\rm stick}\rangle(V,\alpha = \alpha_0)$ for a given stable peeling angle α_0. These data confirm that the stick-slip instability increases dramatically in amplitude with $\langle\alpha\rangle_{ss}$ and occurs preferentially when $\langle\alpha\rangle_{ss} > -5^{\rm o}$, whereas it tends to disappear when $\langle\alpha\rangle_{ss} < -5^{\rm o}$. These results overall point out an important effect of the peeling angle $\theta \simeq \pi/2 - \alpha$ (Fig. 1) on the stick-slip instability thresholds and amplitude.

Speaking more accurately, the order parameter $(v_{\rm slip} - v_{\rm stick})/\langle v_{\rm slip} - v_{\rm stick}\rangle$ dependence as a function of the angle $\langle\alpha\rangle_{ss}$ does obviously not collapse perfectly on a master curve f in Fig. 7. It actually shows a hysteresis that becomes stronger at large velocities (see the arrows indicating the time sequence of successive stick-slip events in the $V = 2.41$ m s^{-1} experiment). As already mentioned, we attribute this hysteresis to a delay in the response of the peeling instability to a change in the experimental peeling angle θ or to the dynamical effects of $d\theta/dt$. Nevertheless, this hysteresis is far beyond our current understanding of the adhesive stick-slip peeling. To the first order, we therefore believe that this overall dependence of the stick-slip amplitude with the local mean (over each stick-slip cycle) peeling angle $\langle\theta(t)\rangle_{ss}$ reflects a general intrinsic dependence of the peeling fracture process with the peeling angle θ, which should be explored in peeling experiments at imposed mean angle $\langle\theta\rangle_{ss}$.

V. DISCUSSION

Theoretically, the angle θ at which the peeling of an adhesive tape is performed is usually taken into account in the calculation of the elastic energy release rate G through Eq. (9). If one further assumes that the fracture energy $\Gamma(v_p)$ is independent of the peeling angle as suggested by Kendall's experiments in the regular peeling regime, the velocity thresholds for the onset of stick-slip instability, related to the zone where $\Gamma(v_p)$ is a decreasing function, should also be roughly independent of the effective peeling angle θ. In that case, there are consequently no clear reasons for stick slip to be strongly dependent on the peeling angle at a given mean fracture velocity $\langle v_p\rangle_{ss} = V$ in the instable range of $\Gamma(v_p)$. The susceptibility of the stick-slip instability to the peeling angle that we report in this paper therefore questions which are the correct dissipation mechanisms that should be taken into account in the fracture energy Γ during the instable regime of the peeling.

The behavior we have observed in Fig. 4 resembles to some extent the dynamics predicted by some models [see for instance Fig. 4(b) in Ref. [17]]. Here, the authors have assumed that the fracture energy is a function of both the local peeling velocity v_p and the imposed velocity V so that $\Gamma(v_p,V)$, which can be viewed as an *ad hoc* guess. In the roller geometry, this model sometimes predicts a stick-slip dynamics corresponding to high frequency oscillations of the angle α superimposed to a lower frequency and larger amplitude variation. The authors explain that this behavior is obtained either when increasing peeling velocity for a given inertia of the roller or when increasing the roller inertia for a given peeling velocity. Thus, the intermittent appearance and disappearance of stick slip observed in this model seems to be the consequence of a subtle

balance between the effect of inertia of the roller and the effect of a fracture energy depending explicitly on both the pulling velocity V and the fracture velocity v_p.

Another possibility to understand the observed stick-slip dynamics would be that the fracture energy itself depends on the peeling angle θ so that $\Gamma(v_p,\theta)$. From static equilibrium considerations, it is clear that varying the angle of peeling will change the relative contribution of normal and shear load on the adhesive at the peeling front. Since it has been observed that shear can have an effect on the resistance of adhesives to rupture [21], one could think that it can also have an effect on the dependence of the fracture energy with velocity, contrary to the results of Kendall [13]. The onset of stick-slip instability would then naturally become dependent on the peeling angle.

At this point, it is not possible to conclude whether the intermittent stick-slip behavior observed in our experiments is due to inertial effects of the roller combined with a $\Gamma(v_p,V)$ dependence of the fracture energy as proposed in Ref. [17], or if it is rather due to a direct dependence $\Gamma(v_p,\theta)$ with the angle. Experiments performed in a different geometry, such as peeling from a flat surface at constant angle θ, would help distinguish between the two proposed mechanisms.

ACKNOWLEDGMENT

This work has been supported by the French ANR through Grant "STICKSLIP" No. 12-BS09-014-01.

[1] G. Ryschenkow and H. Arribart, J. Adhes. **58**, 143 (1996).
[2] Y. Yamazaki and A. Toda, Phys. D (Amsterdam) **214**, 120 (2006).
[3] T. Nonaka, S. Inokuchi, and O. Masahiro, US Patent-7534478 (2009).
[4] A. Gent and R. Petrich, Proc. R. Soc. London, Ser. A **310**, 433 (1969).
[5] C. Derail, A. Allal, G. Marin, and P. Tordjeman, J. Adhesion **61**, 123 (1997); **68**, 203 (1998).
[6] P.-G. de Gennes, Langmuir **12**, 4497 (1996).
[7] D. W. Aubrey and M. Sherriff, J. Polym. Sci., Part A: Polym. Chem. **18**, 2597 (1980).
[8] J. L. Gardon, J. Appl. Polym. Sci. **7**, 625 (1963).
[9] J. Kim, K. S. Kim, and Y. H. Kim, J. Adhes. Sci. Technol. **3**, 175 (1989).
[10] J. L. Racich and J. A. Koutsky, J. Appl. Polym. Sci. **19**, 1479 (1975).
[11] J. Renvoise, D. Burlot, G. Marin, and C. Derail, J. Adhesion **83**, 403 (2007).
[12] M. Barquins, B. Khandani, and D. Maugis, C. R. Acad. Sci. serie II **303**, 1517 (1986).
[13] K. Kendall, J. Phys. D: Appl. Phys. **8**, 1449 (1975).
[14] D. W. Aubrey, G. N. Welding, and T. Wong, J. Appl. Polym. Sci. **13**, 2193 (1969).
[15] M. Barquins and M. Ciccotti, Int. J. Adhes. Adhes. **17**, 65 (1997).
[16] P.-P. Cortet, M. Ciccotti, and L. Vanel, J. Stat. Mech. (2007) P03005.
[17] R. De, A. Maybhate, and G. Ananthakrishna, Phys. Rev. E **70**, 046223 (2004).
[18] R. De and G. Ananthakrishna, Phys. Rev. E **71**, 055201 (2005).
[19] A. J. Kinloch, C. C. Lau, and J. G. Williams, Int. J. Fract. **66**, 45 (1994).
[20] D. Maugis and M. Barquins, in *Adhesion 12*, edited by K. W. Allen (Elsevier ASP, London, 1988), p. 205.
[21] N. Amouroux, J. Petit, and L. Leger, Langmuir **17**, 6510 (2001).

Soft Matter

PAPER

Strong dynamical effects during stick-slip adhesive peeling

Cite this: *Soft Matter*, 2014, **10**, 132

Marie-Julie Dalbe,*[ab] Stéphane Santucci,[a] Pierre-Philippe Cortet[c] and Loïc Vanel[b]

Received 12th July 2013
Accepted 9th October 2013

DOI: 10.1039/c3sm51918j

www.rsc.org/softmatter

We consider the classical problem of the stick-slip dynamics observed when peeling a roller adhesive tape at a constant velocity. From fast imaging recordings, we extract the dependence of the stick and slip phase durations on the imposed peeling velocity and peeled ribbon length. Predictions of Maugis and Barquins [in *Adhesion 12*, edited by K. W. Allen, Elsevier ASP, London, 1988, pp. 205–222] based on a quasistatic assumption succeed to describe quantitatively our measurements of the stick phase duration. Such a model however fails to predict the full stick-slip cycle duration, revealing strong dynamical effects during the slip phase.

1. Introduction

Everyday examples of adhesive peeling are found in applications such as labels, stamps, tape rollers, self-adhesive envelopes or post-it notes. During the peeling of those adhesives, a dynamic instability of the fracture process corresponding to a jerky advance of the peeling front called "stick-slip" may occur. This stick-slip instability has been an industrial concern since the 1950's because it leads to noise levels above the limits set by work regulations, to adhesive layer damage and/or to mechanical problems on assembly lines. This instability is still a limiting factor for industrial productivity due to the limitations of generic technical solutions applied to suppress it, such as anti-adhesive silicon coating.

From a fundamental point of view, the stick-slip instability of adhesive peeling is generally understood as the consequence of an anomalous decrease of the fracture energy $\Gamma(v_p)$ of the adhesive–substrate joint in a specific range of peeling front velocities v_p.[1–8] Indeed, when the peeling process also involves a compliance between the point where the peeling velocity is imposed and the fracture front, this decreasing fracture energy naturally leads to oscillations of the fracture velocity v_p around the mean velocity V imposed by the operator. Often, it is simply the peeled ribbon elasticity which provides compliance to the system. From a microscopic perspective, such an anomalous decrease of the fracture energy $\Gamma(v_p)$ (correctly defined for stable peeling only) could correspond (but not necessarily) to the transition from cohesive to adhesive failure[2,3] or between two different interfacial failure modes.[4,7] More fundamentally, this decrease of the fracture energy has been proposed to be the consequence of the viscous dissipation in the adhesive material.[9] De Gennes[10] further pointed out the probable fundamental role of the adhesive material confinement (which was evidenced experimentally in ref. 3) in such viscoelastic theory. Since then, it has however appeared that a model based on linear viscoelasticity solely cannot be satisfactory and that the role of creep, large deformations and temperature gradient in the adhesive material is important (ref. 11–14 and references therein).

Experimentally, the stick-slip instability was first characterized thanks to peeling force measurements which revealed strong fluctuations in certain ranges of peeling velocity.[1,3,5,6] Since then, it has also been studied through indirect measurements of the periodic marks left on the tape[5,6,15,16] or of the emitted acoustic noise.[17,18] Thanks to the progress in high speed imaging, it is now possible to directly access the peeling fracture dynamics in the stick-slip regime.[19–21]

In the late 1980's, Barquins and co-workers[5,6] performed a series of peeling experiments of a commercial adhesive tape (3M Scotch® 602) at a constant pulling velocity V and for various lengths of peeled ribbon L. For the considered adhesive, the velocity range for which stick-slip was evidenced, thanks to peeling force fluctuation measurements, was shown to be $0.06 < V < 2.1$ m s^{-1}. In a sub-range of unstable peeling velocity $0.06 < V < 0.65$ m s^{-1}, the authors succeeded to access the stick-slip cycle duration thanks to the post-mortem detection of periodic marks left on the tape by stick-slip events. Moreover, they managed to model quantitatively the measured stick-slip period,[5,6] assuming the fracture dynamics to remain a quasistatic problem during the stick phase and backing on measurements of the stable branch of the fracture energy $\Gamma(v_p)$ at low peeling velocities below the instability onset.

In this article, we revisit these experiments by studying the stick-slip dynamics during the peeling of a roller adhesive tape at an imposed velocity. The principal improvement compared to

[a]*Laboratoire de Physique de l'ENS Lyon, CNRS and Université de Lyon, France. E-mail: mariejulie.dalbe@ens-lyon.fr; stephane.santucci@ens-lyon.fr*

[b]*Institut Lumière Matière, UMR5306 Université Lyon 1-CNRS, Université de Lyon, France. E-mail: loic.vanel@univ-lyon1.fr*

[c]*Laboratoire FAST, CNRS, Univ. Paris Sud, France. E-mail: ppcortet@fast.u-psud.fr*

Barquins's seminal work is that, thanks to a high speed camera coupled to image processing, we are able to access the dynamics of the peeling fracture front. We focus on the study of the duration of the stick-slip cycle and its decomposition into stick and slip events, for which data are inaccessible through other techniques. We present experimental data of the stick and slip durations for a wide range of imposed peeling velocities V and for different peeled ribbon lengths L. We show that the model proposed by Barquins and co-workers[5,6] describes the evolution of the duration of the stick phase, but fails to predict the duration of the whole stick-slip cycle due to unexpectedly long slip durations.

2. Experimental setup

In this section, we describe briefly the experimental setup which has already been presented in detail in a recent study.[21] We peel an adhesive tape roller (3M Scotch® 600, made of a polyolefin blend backing coated with a layer of a synthetic acrylic adhesive, also studied in ref. 8, 19, and 21), mounted on a freely rotating pulley, by winding up the peeled ribbon extremity on a cylinder at a constant velocity V using a servo-controlled brushless motor (see Fig. 1). The experiments have been performed at a temperature of $23 \pm 2°$ and a relative humidity of $45 \pm 5\%$. The width of the tape is $b = 19$ mm, its thickness $e = 38$ μm and its Young's modulus $E = 1.26$ GPa.

Each experiment consists of increasing the winding velocity from 0 up to the target velocity V. Once the velocity V is reached, it is maintained constant for two seconds before decelerating the velocity back to zero. When stick-slip is present this 2-second stationary regime of peeling provides sufficient statistics to compute well converged stick-slip mean features. We have varied the imposed velocity V from 0.0015 to 2.5 m s^{-1} for different values of the peeled tape length between $L = 0.08$ and 1.31 m. During the experiment, the peeled tape length L (Fig. 1) is submitted to variations, due to the stick-slip fluctuations and slow oscillations of the peeling point angular position, which however always remain negligible compared to its mean value (less than 0.3%).[21]

3. Peeling force measurement

Thanks to a force sensor (Interface® SML-5) on the holder maintaining the pulley, we are able to measure the mean value of the force F transmitted along the peeled tape during one experiment. When peeling is stable, we compute the strain energy release rate G from the mean value of the force F, following the traditional relationship for the peeling geometry[22,23]

$$G = \frac{F}{b}(1 - \cos\theta) + \frac{1}{2Ee}\left(\frac{F}{b}\right)^2 \simeq \frac{F}{b}, \qquad (1)$$

for a peeling angle $\theta \simeq 90°$ (see Fig. 1). The quantity G corresponds to the amount of mechanical energy released by the growth of the fracture by a unit surface. The right-hand term of eqn (1) finally simply takes into account the work done by the operator but discards the changes in the elastic energy stored in material strains (term $(F/b)^2/2Ee$ in eqn (1))[23] which are negligible here. Indeed, the maximum encountered force in our experiments is typically of about 2 N, which gives $F/b \approx 100$ J m^{-2}, to be compared to $(F/b)^2/2Ee \approx 0.12$ J m^{-2}.

In the context of elastic fracture mechanics, the condition for a fracture advance at a constant velocity v_p is a balance between the release rate G and the fracture energy $\Gamma(v_p)$ required to peel a unit surface and accounting for the energy dissipation near the fracture front. When the fracture velocity v_p approaches the Rayleigh wave velocity v_R, $\Gamma(v_p)$ also takes into account the kinetic energy stored in material motions which leads to a divergence when $v_p \to v_R$.[24] In our system, the strain energy release rate G, computed through eqn (1), therefore stands as a measure of the fracture energy $\Gamma(v_p)$ when the peeling is stable only, *i.e.* when v_p is constant. We will nevertheless compute G for the experiments in the stick-slip regime for which the peeling fracture velocity $v_p(t)$ is strongly fluctuating in time. In such a case, G cannot be used as a measure of the fracture energy: it is simply the time average of the peeling force F in units of G.

In Fig. 2, we plot G as a function of the imposed peeling velocity V for three different peeled tape lengths L. When the peeling is stable, the peeling force is nearly constant in time, whereas it fluctuates strongly when the stick-slip instability is

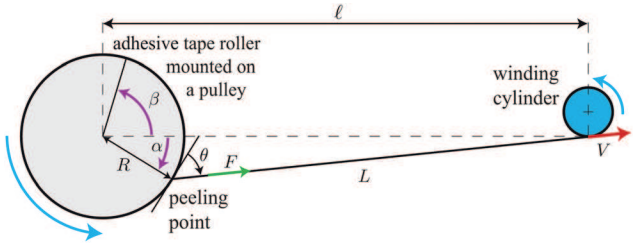

Fig. 1 Schematic view of the experimental setup. The angles α and β are oriented *clockwise* and *counterclockwise* respectively. Roller diameter: 40 mm < 2R < 58 mm, roller and tape width: $b = 19$ mm.

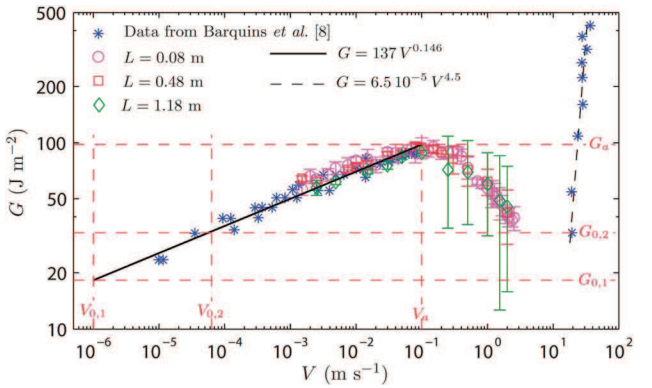

Fig. 2 Mean value of the peeling force F, in units of the strain energy release rate $G = F/b$, as a function of V for 3 different peeled tape lengths L. Stars report the data of Barquins and Ciccotti[8] for the same adhesive. The solid line is a power law fit $G = 137V^{0.146}$ of the data in the low velocity stable branch. Error bars represent the standard deviation of the force fluctuations during one experiment.

present. The standard deviation of these fluctuations is represented in Fig. 2 with error bars. Large error bars are indicative of the presence of stick-slip.

Between $V = 0.0015$ m s^{-1} and $V = 0.10 \pm 0.03$ m s^{-1}, we observe that $G = F/b$ increases slowly with V and that its temporal fluctuations are nearly zero, revealing that the peeling is stable. This increasing branch $G(V)$ is therefore a measure of the adhesive fracture energy $\Gamma(v_p = V) = G(V)$ for $V < 0.10 \pm 0.03$ m s^{-1}. Our results are compatible with the data reported by Barquins and Ciccotti[8] for the same adhesive tape (see Fig. 2). However, they explored a much larger range of velocities in this stable branch of peeling, down to $V = 10^{-5}$ m s^{-1}. By using both series of measurements, it is reasonable to model the stable peeling branch with a power law, $G(V) = aV^n$, with $n = 0.146$ and $a = 137$. For 0.10 ± 0.03 m s$^{-1} < V \leq 2.5$ m s^{-1}, we observe that the measured value of $G(V)$ decreases with V. This tendency, which was already observed in previous experiments,[25] is accompanied with the appearance of temporal fluctuations which are the trace of the stick-slip instability. From these data, we can estimate the onset of the instability to be $V_a = 0.10 \pm 0.03$ m s^{-1}. The measured decreasing branch of $G(V)$ for $V > V_a$ appears as a direct consequence of the anomalous decrease of the fracture energy at the origin of the instability. It is important to note that the measured mean value of $G = F/b$ is nearly independent of the length of peeled ribbon L. This result is natural in the stable peeling regime but was *a priori* unknown in the stick-slip regime.

Barquins and Ciccotti[8] succeeded to measure a second stable peeling branch for $V \geq 19$ m s^{-1}. This increasing branch constitutes a measure of the peeling fracture energy $\Gamma(v_p = V) = G(V)$ in a fast and stable peeling regime. In ref. 8, this branch is inferred to exist for velocities even lower than $V = 19$ m s^{-1}, although it was not possible to measure it. Backing on the data of ref. 6 for a very close adhesive, one can however guess that the local minimum value of $G(V)$, corresponding to a velocity in the range 2.5 m s$^{-1} < V < 19$ m s^{-1}, would be bound by $G_{0,1} = 18 < G < G_{0,2} = 33$ J m^{-2}.

4. Peeling point dynamics

The local dynamics of the peeling point is imaged using a high speed camera (Photron FASTCAM SA4) at a rate of 20 000 fps. The recording of each movie is triggered once the peeling has reached a constant average velocity V ensuring that only the stationary regime of the stick-slip is studied. Through direct image analysis,[21] the movies allow access to the curvilinear position of the peeling point $\ell_\alpha(t) = R\alpha$ in the laboratory frame (with α being the angular position of the peeling point and R being the roller diameter, $\alpha > 0$ in Fig. 1). Image correlations on the adhesive tape roller contrast pattern further allow direct access to its angular velocity $\mathrm{d}\beta/\mathrm{d}t$ in the laboratory frame (where β is the unwrapped angular position of the roller, $\beta > 0$ in Fig. 1, $\ell_\beta(t) = R\beta$). We finally compute numerically the curvilinear position $\ell_p(t) = \ell_\beta(t) + \ell_\alpha(t)$ and velocity $v_p(t) = \mathrm{d}\ell_p/\mathrm{d}t$ of the peeling point in the roller reference frame.

The curvilinear position of the peeling point $\ell_\alpha(t)$ in the laboratory frame is actually estimated from the position of the peeled ribbon at a small distance of 0.30 ± 0.05 mm from the peeling fracture front on the roller surface. We therefore do not detect strictly the peeling fracture front position but a very close quantity only. This procedure can consequently introduce some bias in our final estimation of the fracture front velocity $v_p(t)$. This bias is notably caused by the changes in the radius of curvature of the tape at the junction with the substrate which are due to the force oscillations in the peeled tape characteristics of the stick-slip instability. Such an effect actually biases the measurement toward larger velocities during the stick phase and lower velocities during the slip phase. Another effect that leads to uncertainties in velocity measurement is the emission of a transverse wave in the peeled tape when the fracture velocity abruptly changes at the beginning and at the end of slip phases.

Fig. 3(a) and (c) represent the fracture position $\ell_p(t)$ and velocity $v_p(t)$ as a function of time for a typical experiment performed at $V = 0.55$ m s^{-1} and $L = 0.47$ m. In these figures, we observe alternate phases of slow (stick phase) and fast (slip phase) peeling which are the signatures of the stick-slip motion. These large velocity fluctuations are quite regular in terms of duration and to a lesser extent in terms of amplitude at least at the considered peeling velocity. Our general data analysis further consists of the decomposition of the signal of instantaneous peeling velocity $v_p(t)$ into stick-slip cycles by setting the beginning of each cycle at times t_n (n denoting the n^{th} cycle) when $v_p(t_n) = V$ and $\mathrm{d}v_p(t_n)/\mathrm{d}t < 0$. From these data, we extract the duration T_{ss} of each stick-slip cycle for which we define a rescaled time $t' = (t - t_n)/T_{ss}$. We further compute the phase averaged evolution of the peeling fracture velocity $v_p(t')$ from $t' = 0$ to 1 considering all the stick-slip cycles in one experiment. With this procedure, we finally extract for each peeling velocity V and peeled tape length L the typical fracture velocity evolution during a stick-slip cycle getting rid of intrinsic fluctuations of

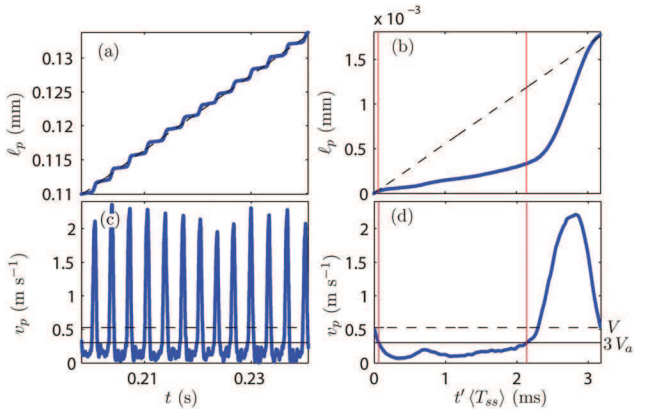

Fig. 3 (a) Peeling point position $\ell_p(t)$ in the roller reference frame for an experiment performed at $V = 0.55$ m s^{-1} and $L = 0.47$ m. The dashed line shows $\ell_p = Vt$, with V the average peeling velocity. (b) Corresponding phase averaged peeling point position as a function of $t'\langle T_{ss}\rangle$ (see the main text). (c and d) Corresponding instantaneous (c) and phase averaged (d) peeling point velocity v_p. The dashed horizontal lines show the average peeling velocity V and the continuous horizontal lines show $3V_a$. In (b) and (d), the vertical lines show the transitions between the stick ($v_p < 3V_a$) and the slip ($v_p > 3V_a$) phases.

the stick-slip period. In Fig. 3(b) and (d), we show the phase averaged position and velocity profiles, corresponding to Fig. 3(a) and (c) respectively, as a function of $t = t'\langle T_{ss}\rangle$ ($\langle\rangle$ denotes the ensemble averaged value over all the cycles in one experiment).

From these phase averaged velocity profiles, we define, for each experimental condition V and L, stick events as continuous periods during which $v_p(t) < 3V_a$ and slip events as continuous periods during which $v_p(t) > 3V_a$. According to the model of Barquins *et al.*[5,6] a natural threshold in order to separate the stick and slip phases is the onset of the instability V_a (as defined in Fig. 2). However, as discussed previously, due to the procedure used for the detection of the peeling point, our measurement of the fracture velocity can be affected by biases caused by the variation of the tape curvature at the peeling point and by the propagation of transverse waves in the tape. The effect of the latter can be observed in Fig. 3(d) in the early stage of the stick phase. In order to avoid taking into account the velocity biases in the decomposition of the stick-slip cycle, we chose for the threshold separating the stick and slip phases a value little larger than the "theoretical" threshold V_a, that is to say $3V_a$.

Finally, as we have shown recently in ref. 21, when the peeling velocity V is increased, low frequency pendular oscillations of the peeling angle θ develop. Due to the dependence of the stick-slip instability onset on the mean peeling angle, these oscillations lead to intermittence in the stick-slip dynamics for peeling velocities $V > 1.5$ m s^{-1}. We therefore exclude the experiments with $V > 1.5$ m s^{-1}in the sequel. For the studied experiments, we have a mean peeling angle $\langle\theta\rangle = 90 \pm 3°$ with slow temporal variations in the range $\Delta\theta = \pm 15°$ during one experiment.

5. Stick-slip cycle duration

From the signal of peeling point position $\ell_p(t)$ (see Fig. 3(a)), we define the stick-slip amplitude A_{ss} as the distance travelled by the fracture during a stick-slip cycle. In Fig. 4, we report this amplitude A_{ss} for each stick-slip event as a function of the corresponding stick-slip period T_{ss}, for all events in 6 different experiments. These data gather close to the curve $A_{ss} = VT_{ss}$. The large spread of the data along the curve $A_{ss} = VT_{ss}$ reflects the statistics of the stick-slip cycle amplitude and duration which could be due for instance to adhesive heterogeneities. In contrast, the dispersion of the data around the curve $A_{ss} = VT_{ss}$ is much smaller. It actually estimates the discrepancy between the imposed velocity V and the averaged fracture velocity for each stick-slip cycle. The observed small discrepancy actually traces back both measurement errors in the instantaneous fracture velocity and intrinsic fluctuations of the dynamics.

In Fig. 4, one can already see that the statistically averaged values of A_{ss} and T_{ss} increase with L for a given peeling velocity V. In the following, we will focus on the study of the statistical average $\langle T_{ss}\rangle$ of the duration of the stick-slip oscillation and its decomposition into stick and slip phases with in mind the aim of testing the description of Barquins, Maugis and co-workers.[5,6] There is no need to study the averaged stick-slip amplitude $\langle A_{ss}\rangle$ since it is unequivocally related to $\langle T_{ss}\rangle$ through $\langle A_{ss}\rangle = V\langle T_{ss}\rangle$.

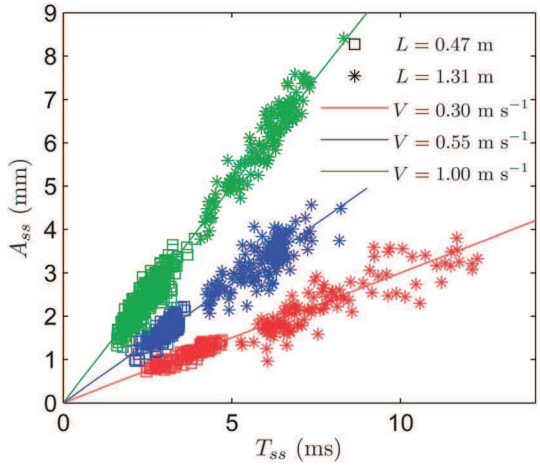

Fig. 4 Stick-slip amplitude A_{ss} as a function of stick-slip period T_{ss} for each stick-slip cycle in 6 different experiments with $L = 0.47$ and 1.31 m and $V =$ 0.30, 0.55 and 1.00 m s^{-1}. The lines represent the curves $A_{ss} = VT_{ss}$.

In Fig. 5(a), we plot the mean stick-slip duration T_{ss} as a function of V for three different lengths L of the peeled ribbon. The data correspond to the average $\langle T_{ss}\rangle$ and the error bars correspond to the standard deviation of the statistics of T_{ss} over

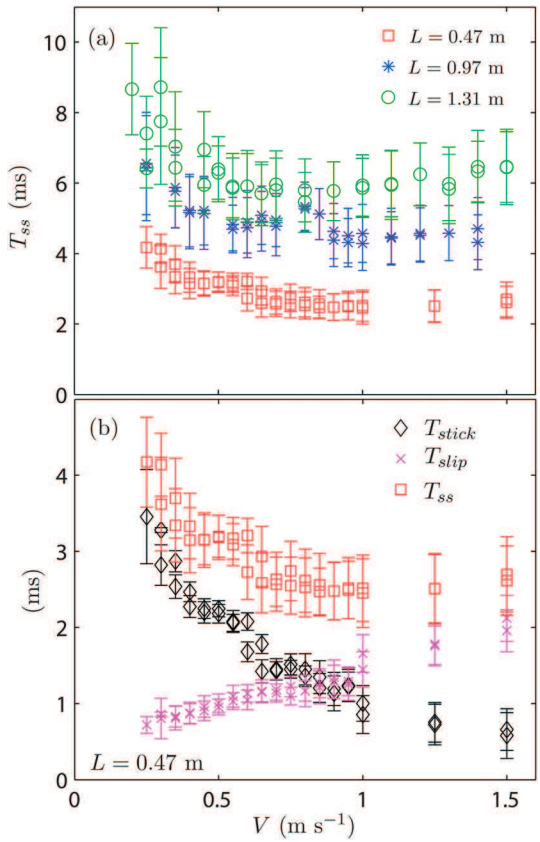

Fig. 5 Average stick-slip cycle duration T_{ss} as a function of the average peeling velocity V, for different lengths of the peeled ribbon L. (b) Average stick-slip, stick and slip durations as functions of the average peeling velocity for $L = 0.47$ m. Each data point corresponds to the average and each error bar to the standard deviation of the statistics over one experiment.

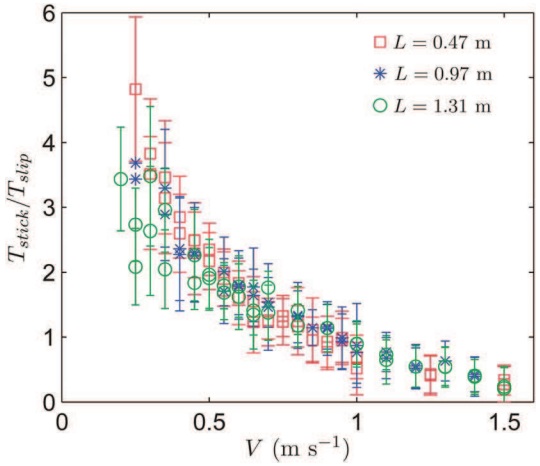

Fig. 6 T_{stick}/T_{slip} *vs.* V for 3 different L. Each data point corresponds to the average and each error bar to the standard deviation of the statistics over one experiment.

all the stick-slip events in each experiment. In the following, since we will consider the averaged values only, we will skip the brackets $\langle\rangle$. At first sight, it appears that, within the error bars, the stick-slip duration T_{ss} is stable over the major part of the explored range of peeling velocity V. One can however note that, independently of L, T_{ss} tends to decrease with V for $V \leq V_c = 0.6 \pm 0.1$ m s^{-1}. Such behavior is compatible with the observations of Barquins *et al.*[5] but appears here over a rather limited velocity range. The characteristic velocity $V_c = 0.6 \pm 0.1$ m s^{-1} above which T_{ss} is nearly constant seems not to depend strongly on the length of the peeled ribbon L.

In Fig. 5(b), we show the mean durations of stick and slip events, T_{stick} and T_{slip} respectively, as a function of the imposed peeling velocity V for the experiments performed with the peeled length $L = 0.47$ m. Interestingly, we observe that the stick and slip phases evolve differently with V: the stick duration decreases with V, while the slip duration increases over the whole explored range of V. In consequence, the ratio T_{stick}/T_{slip}, presented in Fig. 6, decreases with V from $T_{stick}/T_{slip} \sim 4 \pm 1$ down to $T_{stick}/T_{slip} \sim 0.3 \pm 0.2$. Such behavior of T_{stick}/T_{slip} appears to be very little dependent on L according to Fig. 6. For $V \geq 0.90 \pm 0.05$ m s^{-1}, T_{stick}/T_{slip} becomes smaller than 1, meaning that the slip phase is longer than the stick one. Our data therefore show that it is not possible to neglect the slip duration compared to the stick duration in general.

6. Model

In this section, we compare our experimental data with the model proposed by Barquins, Maugis and co-workers in ref. 5 and 6. This model is based on measurements of the stable branch of the fracture energy $\Gamma(v_p)$ for low peeling velocities below the instability onset V_a, and on the following assumptions:

• During the stick phase, the equilibrium between the instantaneous energy release rate $G = F/b$ and the fracture energy $\Gamma(v_p)$ (of the low velocity stable branch) is still valid dynamically, *i.e.* $G(t) = \Gamma(v_p(t))$.

• The peeled ribbon remains fully stretched during the peeling, which means

$$G = \frac{F}{b} = \frac{Ee}{L}u, \tag{2}$$

where u is the elongation of the tape with Young's modulus E and thickness e.

• The slip duration is negligible compared to the stick duration.

Backing on these hypotheses, it is possible to derive a prediction for the stick-slip duration T_{ss}. Introducing the inverted function $v_p = \Gamma^{-1}(G)$ and noting that $du/dt = V - v_p$ (see the next paragraph and ref. 21), eqn (2) leads to the dynamical relationship

$$\frac{dG}{dt} = \frac{Ee}{L}\left(V - \Gamma^{-1}(G)\right), \tag{3}$$

which can be integrated over the stick phase to get

$$T_{stick} = \frac{L}{Ee}\int_{G_0}^{G_a} \frac{dG}{V - \Gamma_{slow}{}^{-1}(G)}. \tag{4}$$

G_a is the maximum value of $\Gamma(v_p)$ at the end of the "slow" stable branch $\Gamma_{slow}(v_p)$. G_0 is the minimum value of $\Gamma(v_p)$ at the beginning of the "fast" stable branch $\Gamma_{fast}(v_p)$ (see Fig. 2) and is assumed to be also the value of G at which the stick phase starts on the slow branch after a slip phase.

In this model, the ribbon is assumed to remain taut during the whole stick-slip cycle. In order to challenge the validity of this hypothesis, let us estimate the evolution of the elongation $u(t)$ of the tape as a function of time. If we note $P(t)$ the peeling point position and M the point where the peeled tape is wound, we can define the quantity $u(t)$ as the difference between the distance $|\overline{MP(t)}|$ and the length of the peeled tape in the unstrained state. If $u(t)$ is positive, this quantity indeed measures the elongation of the tape as in eqn (2), whereas it measures the excess of slack tape if it is negative. Following ref. 21, one can show that

$$u(t) = u_0 + \int_0^t \left(V - v_p(t)\right)dt - \cos\theta \int_0^t \left(R\dot{\beta} - v_p(t)\right)dt. \tag{5}$$

Since in our experiments the peeling angle θ is close to 90° and the roller rotation velocity $Rd\beta/dt$ sticks to the imposed peeling velocity V to a precision always better than ±1.5%,[21] we finally have $u(t) \simeq u_0 + \int_0^t (V - v_p(t))dt$. The elongation/slack $u(t)$ increases with $\Delta u = \int_0^{T_{stick}} (V - v_p(t))dt$ during the stick phase and decreases with the same amplitude $\Delta u = -\int_{T_{stick}}^{T_{ss}} (V - v_p(t))dt$ during the slip phase. This compensation is ensured by the fact that the averaged velocity over the stick-slip cycle matches the imposed velocity V, *i.e.* $\int_0^{T_{ss}} (V - v_p(t))dt = 0$, and is valid whether or not the tape remains always taut during the stick-slip cycle.

To test the relevance of the hypothesis of a tape always in tension, one can actually compare the increase/decrease Δu of the quantity $u(t)$ during the stick/slip phase with the one predicted by the quasistatic model of Barquins and co-workers

$$\Delta u_{\text{theo}} = \frac{L}{Eeb}(F_a - F_0) = \frac{L}{Ee}(G_a - G_0), \quad (6)$$

for an always taut tape. Throughout our data, the relative discrepancy $(\Delta u_{\text{theo}} - \Delta u)/\Delta u$ is typically less than 15% which confirms the relevance of the assumption of a tape in tension during the whole stick-slip cycle.

An equivalent but more instructive way to test the model of Barquins and co-workers is to integrate numerically eqn (4) and compare it with experimental measurements of the stick duration. To do so, we use the fit of the data of the energy release rate $G(V)$ in Fig. 2, *i.e.* $G(V) = \Gamma_{\text{slow}}(V) = aV^n$, with $n = 0.146$ and $a = 137$. The value of G_0 is affected by a significant uncertainty in our data. We will therefore use two different guesses corresponding to the limit values introduced in page 3 (see $G_{0,1}$ and $G_{0,2}$ in Fig. 2). These values of G_0 correspond to two limit values of the fracture velocity at the beginning of the stick phase: $V_{0,1} = 10^{-6}$ m s^{-1} measured in another adhesive but with a close behavior,[6] and $V_{0,2} = 6.3 \times 10^{-5}$ m s^{-1} which is an upper limit for V_0 according to the data of Fig. 2.

In the inset of Fig. 7(b), we report the measured data for T_{ss}/L as a function of V for three different lengths L as well as the predictions of eqn (4) with $V_{0,1}$ (solid line) and $V_{0,2}$ (dashed line).

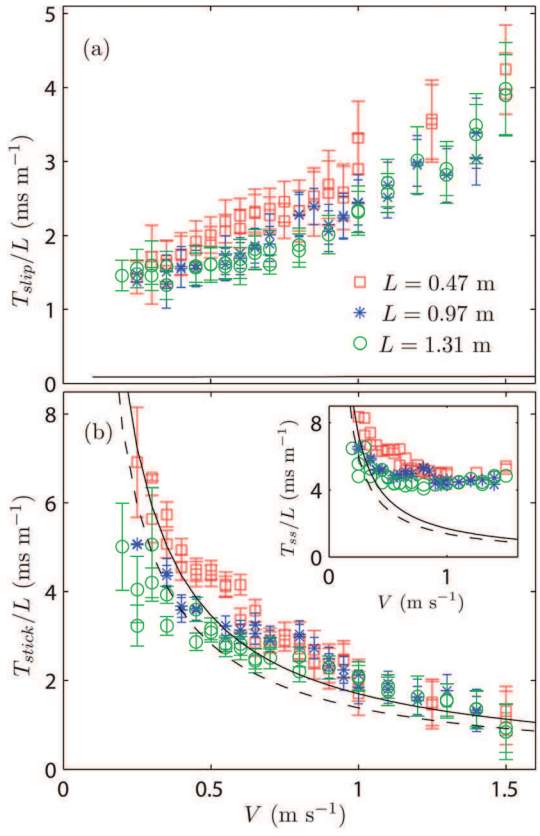

Fig. 7 (a) T_{slip}/L, (b) T_{stick}/L and T_{ss}/L (insert) *vs.* V for 3 different L. Each data point corresponds to the average and each error bar to the standard deviation of the statistics over one experiment. In (a), the curve close to the x-axis represents the theoretical prediction for a quasistationary slip phase. In (b), the lines show the predictions of eqn (4) with $V_a = 0.10$ m s^{-1} and $V_{0,1} = 10^{-6}$ m s^{-1} (solid line) or $V_{0,2} = 6.3 \times 10^{-5}$ m s^{-1} (dashed line).

The model appears compatible with the experimental data only for a marginal range of very low peeling velocities. Once $V > 0.5$ m s^{-1}, the measured values of T_{ss}/L indeed deviate more and more from the theoretical prediction. A first natural explanation for this discrepancy is that the assumption of a negligible slip duration T_{slip} (barely verified for low velocities for which $0.25 < T_{\text{slip}}/T_{\text{stick}} < 0.5$) becomes more and more false as V is increased (see Fig. 6).

In Fig. 7(b) we therefore directly plot T_{stick}/L as a function of V, along with the prediction (4). One can note that the theoretical predictions using the two limit guesses for V_0 are not very different. A first interesting result is that the stick duration appears, to the first order, proportional to the peeled tape length L as evidenced by the reasonable collapse of the data T_{stick}/L on a master curve, which is compatible with the analytical prediction of the model (4). But more importantly, we observe that for the range of velocities explored, the model for T_{stick}, which does not use any adjustable parameter, reproduces very well the experimental data.

Obviously, one can consider an equivalent quasistationary approximation during the slip phase in order to predict the slip duration using ${\Gamma_{\text{fast}}}^{-1}(G)$ instead of ${\Gamma_{\text{slow}}}^{-1}(G)$ in eqn (4). Here, ${\Gamma_{\text{fast}}}^{-1}(G)$ corresponds to the inverse of the energy fracture $G = \Gamma_{\text{fast}}(v_{\text{p}})$ in the fast and "stable" peeling regime of Fig. 2. The integration using the model of the fast branch $\Gamma_{\text{fast}}(V) = 6.5 \times 10^{-5} V^{4.5}$ (see Fig. 2) however leads to values of T_{slip} always 2 orders of magnitude smaller than the experimental values as evidenced in Fig. 7(a). It is however worth noting that the collapse of the data T_{slip}/L for the different L values shows that T_{slip} increases nearly linearly with L.

7. Discussion

In this paper, we report experiments on a roller adhesive tape peeled at a constant velocity focusing on the regime of stick-slip instability. From fast imaging recordings, we extract the dependence of the stick and slip phase durations on the imposed peeling velocity V and peeled ribbon length L.

The stick phase duration T_{stick} of the stick-slip oscillations is shown to be nearly proportional to the peeled tape length L and to decrease with the peeling velocity V. These data moreover appear in quantitative agreement with the predictions of a model proposed by Barquins, Maugis and co-workers in ref. 5 and 6 which do not introduce any adjustable parameter. This successful comparison confirms the relevance of the two main assumptions made in the model: (i) the tape remains in tension during the whole stick-slip cycle; (ii) the principle of an equilibrium between the instantaneous energy release rate $G(t) = F(t)/b$ and the fracture energy $\Gamma(v_{\text{p}}(t))$, as measured in the steady peeling regime, is valid dynamically during the stick phase.

Describing the peeling dynamics as a function of time t by the knowledge of the fracture velocity $v_{\text{p}}(t)$ and of the force $F(t) = bG(t)$ in the peeled tape, the considered model further assumes that the system jumps instantaneously, at the end of the stick phase, from the "slow" stable branch to the "fast" stable branch of the steady fracture energy $G = \Gamma(v_{\text{p}})$ and then instantaneously backward from the "fast" branch to the "slow" branch at the end

of the slip phase. In such a framework, reproducing the assumptions (i) and (ii) for the slip phase leads to a prediction for the slip duration. We have shown that this prediction is at least hundred times smaller than the slip phase duration T_{slip} measured in our experiments. We actually report that in contrast to what is finally proposed in ref. 5 and 6, the slip duration T_{slip} cannot be neglected compared to the stick one T_{stick}, since it is at best 4 times smaller, and becomes even larger than T_{stick} for $V \geq 0.90 \pm 0.05$ m s^{-1}.

These last experimental results account for the existence of strong dynamical effects during the slip phase which can therefore not be described by a quasistatic hypothesis. These dynamical effects could be due to the inertia of the ribbon close to the fracture front. Some models also predict a strong influence of the roller inertia.[18,26] Notably, thanks to numerical computation, De and Ananthakrishna[26] have shown that for certain values of the roller inertia, the slip phase could consist of several jumps from the "fast stable" branch to the "slow stable" branch in the (v_p, $G = \Gamma(v_p)$) diagram. Such a process would certainly produce a longer slip time than expected in the framework of Barquins's model. It would be most interesting to confront our experimental observations to the predictions of this model, based on a detailed set of dynamical equations and *ad hoc* assumptions made on the velocity dependence of Γ. However, such a comparison is not straightforward in our current setup since we do not have the temporal and spatial resolutions to detect such eventual fast oscillations. Besides, in order to obtain a quantitative comparison, measurement of the instantaneous peeling force $F(t)$ is required but it remains a challenge.

Acknowledgements

This work was supported by the French ANR through Grant "STICKSLIP" no. 12-BS09-014. We thank Costantino Creton and Matteo Ciccotti for fruitful discussions and Matteo Ciccotti for sharing data with us.

References

1 J. L. Gardon, *J. Appl. Polym. Sci.*, 1963, **7**, 625–641.
2 A. N. Gent and R. P. Petrich, *Proc. R. Soc. London, Ser. A*, 1969, **310**, 433–448.
3 D. W. Aubrey, G. N. Welding and T. Wong, *J. Appl. Polym. Sci.*, 1969, **13**, 2193–2207.
4 D. W. Aubrey and M. Sherriff, *J. Polym. Sci.*, 1980, **18**, 2597–2606.
5 M. Barquins, B. Khandani and D. Maugis, *C. R. Acad. Sci., Ser. II: Mec., Phys., Chim., Sci. Terre Univers*, 1986, **303**, 1517–1519.
6 D. Maugis and M. Barquins, in *Adhesion 12*, ed. K. W. Allen, Elsevier ASP, London, 1988, pp. 205–222.
7 C. Derail, A. Allal, G. Marin and P. Tordjeman, *J. Adhes.*, 1997, **61**, 123–157, 1998, **68**, 203–228.
8 M. Barquins and M. Ciccotti, *Int. J. Adhes. Adhes.*, 1997, **17**, 65–68.
9 D. Maugis, *J. Mater. Sci.*, 1985, **20**, 3041–3073.
10 P.-G. de Gennes, *Langmuir*, 1996, **12**, 4497–4500.
11 A. N. Gent, *Langmuir*, 1996, **12**, 4492–4496.
12 G. Carbone and B. N. J. Persson, *Phys. Rev. Lett.*, 2005, **95**, 114301.
13 E. Barthel and C. Fretigny, *J. Phys. D: Appl. Phys.*, 2009, **42**, 19.
14 H. Tabuteau, S. Mora, M. Ciccotti, C.-Y. Hui and C. Ligoure, *Soft Matter*, 2011, **7**, 9474–9483.
15 J. L. Racich and J. A. Koutsky, *J. Appl. Polym. Sci.*, 1975, **19**, 1479–1482.
16 G. Ryschenkow and H. Arribart, *J. Adhes.*, 1996, **58**, 143–161.
17 M. Gandur, M. Kleinke and F. Galembeck, *J. Adhes. Sci. Technol.*, 1997, **11**, 11–28.
18 M. Ciccotti, B. Giorgini, D. Vallet and M. Barquins, *Int. J. Adhes. Adhes.*, 2004, **24**, 143–151.
19 P.-P. Cortet, M. Ciccotti and L. Vanel, *J. Stat. Mech.: Theory Exp.*, 2007, P03005.
20 S. T. Thoroddsen, H. D. Nguyen, K. Takehara and T. G. Etoth, *Phys. Rev. E: Stat., Nonlinear, Soft Matter Phys.*, 2010, **82**, 046107.
21 P.-P. Cortet, M.-J. Dalbe, C. Guerra, C. Cohen, M. Ciccotti, S. Santucci and L. Vanel, *Phys. Rev. E: Stat., Nonlinear, Soft Matter Phys.*, 2013, **87**, 022601.
22 R. S. Rivlin, *Paint Technol.*, 1944, **9**, 215–216.
23 K. Kendall, *J. Phys. D: Appl. Phys.*, 1975, **8**, 1449–1452.
24 L. B. Freund, *Dynamic fracture mechanics*, Cambridge University Press, London, 1998.
25 Y. Yamazaki and A. Toda, *Physica D*, 2006, **214**, 120–131.
26 R. De and G. Ananthakrishna, *Eur. Phys. J. B*, 2008, **61**, 475–483.

Soft Matter

PAPER

Cite this: *Soft Matter*, 2014, **10**, 9637

Peeling-angle dependence of the stick-slip instability during adhesive tape peeling

Marie-Julie Dalbe,[ab] Stéphane Santucci,[a] Loïc Vanel[b] and Pierre-Philippe Cortet[c]

Received 19th August 2014
Accepted 6th October 2014

DOI: 10.1039/c4sm01840k

www.rsc.org/softmatter

The influence of peeling angle on the dynamics observed during the stick-slip peeling of an adhesive tape has been investigated. This study relies on a new experimental setup for peeling at a constant driving velocity while keeping constant the peeling angle and peeled tape length. The thresholds of the instability are shown to be associated with a subcritical bifurcation and bistability of the system. The velocity onset of the instability is moreover revealed to strongly depend on the peeling angle. This could be the consequence of peeling angle dependance of either the fracture energy of the adhesive-substrate joint or the effective stiffness at play between the peeling front and the point at which the peeling is enforced. The shape of the peeling front velocity fluctuations is finally shown to progressively change from typical stick-slip relaxation oscillations to nearly sinusoidal oscillations as the peeling angle is increased. We suggest that this transition might be controlled by inertial effects possibly associated with the propagation of the peeling force fluctuations through elongation waves in the peeled tape.

1 Introduction

In standard fracture mechanics, crack growth is usually described by velocity-dependent fracture energy, accounting for the rate dependence of the energy cost of elementary dissipative rupture processes close to the fracture tip.[1] Then, the condition for a crack to propagate at a given velocity is that the amount of mechanical energy released by a unit area of crack growth provides the corresponding fracture energy.[2] When the fracture energy becomes a decreasing function of crack velocity, *i.e.* it costs less energy for the crack to grow faster, a dynamical instability often occurs. In that case, the crack velocity starts to oscillate as well as the energy release rate. Such oscillations are a common feature of crack propagation and can be observed for very different ranges of mean crack velocity depending on the considered material.[3,4] The stick-slip oscillations observed during the peeling of adhesive films is a very-well known example of such dynamic rupture instability.[5–8]

The unstable "stick-slip" dynamics of adhesive film peeling is admitted to be the consequence of a decrease of the fracture energy $\Gamma(v_p)$ of the substrate–adhesive joint within a specific range of fracture velocity v_p combined with the compliance between the location where the peeling velocity V is imposed and the peeling fracture front.[5–12] This decrease has been proposed to proceed from the viscoelasticity of the adhesive material coupled to the effects of material confinement and large deformations.[13–17] Peeling an adhesive tape from a freely rotating roller is a standard configuration which has received much experimental and theoretical attention.[7,8,12,18–24] However, in some circumstances, the stick-slip peeling may become intermittent when pendulum-like oscillations of the roller develop as a result of the interplay between the peeling force and the roller inertia.[23] This intermittent behavior has been attributed to the possibility of an intrinsic dependance of the instability with the peeling angle which, in these experiments, oscillates quasi-statically as a consequence of the slow unsteady roller dynamics.[23]

In order to study the influence of the peeling angle on the stick-slip instability, regarding which very few experimental results exist,[6] we have developed an innovative experimental setup where the adhesive tape end is pulled at a controlled velocity from a plane substrate which is translated at the same velocity. Unlike usual peeling geometries which allow control of the peeling angle, we can also keep fixed the length of the peeled tape, which controls the elastic compliance of the peeling system and is an important control parameter of the instability. Furthermore, in contrast with the roller geometry, the inertia of the substrate (which becomes effectively infinite) will not be anymore a parameter of the peeling problem. This new setup, associated with a high speed imaging of the fracture dynamics, has allowed us to quantify for the first time, at a fixed peeled tape length, the dependance of the instability velocity thresholds and amplitude with the peeling angle.

[a]*Laboratoire de Physique de l'ENS de Lyon, CNRS and Université de Lyon, France. E-mail: mariejulie.dalbe@ens-lyon.fr; stephane.santucci@ens-lyon.fr*
[b]*Institut Lumière Matière, UMR5306 Université Lyon 1-CNRS, Université de Lyon, France. E-mail: loic.vanel@univ-lyon1.fr*
[c]*Laboratoire FAST, CNRS, Univ. Paris Sud, France. E-mail: ppcortet@fast.u-psud.fr*

2 Experimental methods

The experimental setup (Fig. 1) consists of a 3 m long, 45 mm wide rigid bar which can be translated at a controlled velocity V up to 4.5 m s^{-1} thanks to a CC servo-motor. The bar is covered with a layer of adhesive tape which constitutes the substrate of a second layer of the same adhesive. The adhesive tape, 3M Scotch® 600 (as in ref. 12 and 22–24), is made of a polyolefin blend backing (38 μm thick, 19 mm wide, Young modulus $E =$ 1.26 GPa) coated with a 20 μm layer of a synthetic acrylic adhesive. The experiments have been performed at a temperature of 22.3 ± 0.9 °C and a relative humidity of 43 ± 9%.

During an experiment, the top layer adhesive tape is peeled from its substrate thanks to a second servo-motor which winds the peeled tape on a cylinder of radius R at a rotation rate ω (Fig. 1). The rotation rate ω is slaved electronically to the velocity of the rigid bar translation, *i.e.* $\omega(t) \propto V(t)$, such that $R\omega(t) \simeq V(t)$ even during acceleration and deceleration transients of the experiment. Whatever the target velocity V of the experiment—between 0.03 and 4.5 m s^{-1}—the two motors are able to accelerate and decelerate enough strongly so that a stationary regime at velocity V can be observed over at least 1 m of peeling. When the imposed velocity V does not fall in the stick-slip unstable range, the peeling front velocity $v_p(t)$ is constant and kinematically set to V by this system. In this situation, the coupled translation and winding motions actually impose to the peeling point to remain fixed in the laboratory frame, setting consequently the peeling angle $\theta(t)$ and the peeled tape length $|\mathbf{MP}|$ to constant values (see Fig. 1).

It is worth pointing out two experimental subtleties that need to be managed carefully for the experimental setup to work properly. First, if one sets the winding velocity $R\omega$ and the translation velocity V to the exact same value, a slow drift of the peeling point in the laboratory frame is observed during the stationary phase of the experiment. This drift is due to the fact the tape is peeled from the substrate in an unstretched state whereas it is wound in a stretched state. Second, during the peeling, the radius $R(t)$ of the winding cylinder – initially of 39.5 mm – increases of 0.6% per meter of peeled tape due to the thickness of the tape being wound, which drives an acceleration of the winding with respect to the translation. In practice, we compensate these two effects simultaneously by setting the target winding rotation rate ω to a value slightly faster (of a few 0.1%) than the target translation velocity V. With this method, we succeed to limit the slow drift of the peeling point in the laboratory frame during the stationary stage of peeling to values corresponding to drifts of the peeling angle lower than 1° and drifts of the peeled tape length lower than 3%.

The real value of our setup is that when the stick-slip instability is present, the instantaneous fluctuations of the peeling angle and of the peeled tape length still remain small: throughout all the experiments presented in this paper, they respectively range from 0.1° to 2° and from 0.1% to 5%. At the same time, the peeling front velocity oscillates strongly with amplitudes larger or much larger than V. Note however that the peeling front velocity follows precisely the imposed velocity V once averaged over timescales larger than the stick-slip instability period.

The peeling dynamics is imaged up to 20 000 frames per second (Photron Fastcam APX RS). The corresponding images of 896 × 512 to 384 × 224 pixels have a resolution in the range 40 to 80 μm per pixel. From the recorded image time series, we detect the location of the peeled tape in the laboratory frame at a small distance of 0.7 ± 0.1 mm from the substrate. This measurement provides an estimate for the position $\ell_{lab}(t)$ of the fracture front in the laboratory frame (Fig. 1) and is used to compute the velocity $d\ell_{lab}/dt$ with a typical error of ±1%. We also measure the instantaneous velocity of the substrate, $d\ell_{bar}/dt$, with a typical relative precision of ±0.4%. We finally compute the fracture velocity relative to the substrate $v_p(t) = d\ell_{lab}/dt + d\ell_{bar}/dt$.

3 Subcritical instability

In Fig. 2(a), we show a sequence of the peeling fracture velocity time series $v_p(t)/V$ for a typical experiment for which stick-slip

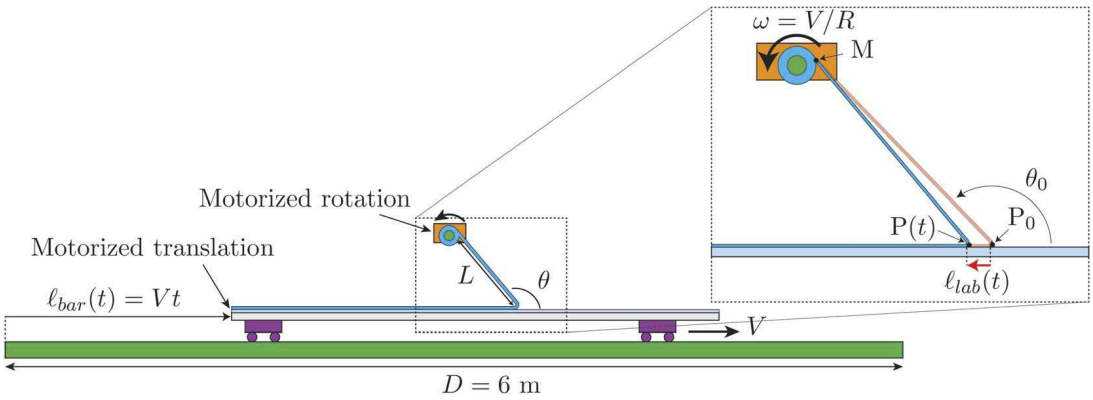

Fig. 1 Scheme of the peeling experiment at controlled velocity V, angle θ and peeled tape length L. The translation velocity V of the rigid bar and the winding velocity $R\omega$ are slaved electronically to each other. ℓ_{bar} is the position of the rigid bar and $\ell_{lab}(t) = \overline{P_0P}(t)$ is the position of the peeling front in the laboratory frame. M is the location of the point where the winding of the peeled tape proceeds, P_0 is the average location of the peeling point and $P(t)$ is its location as a function of time t. θ_0 is the average peeling angle. We denote $L = |\mathbf{MP}_0|$ as the average peeled tape length.

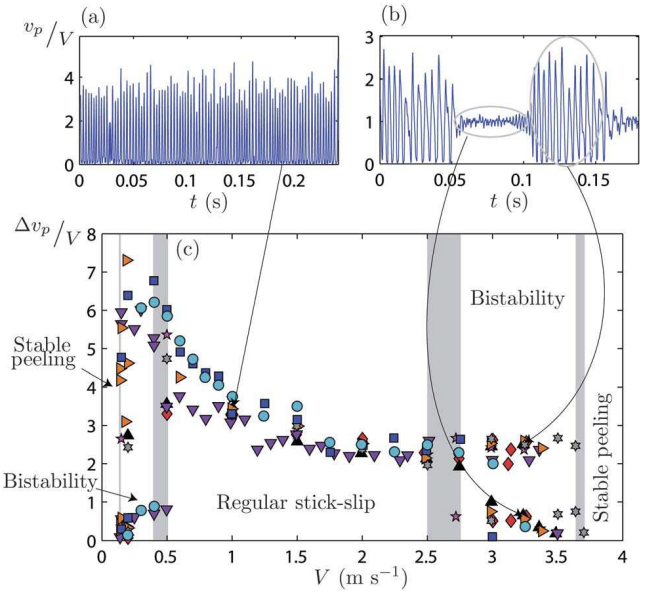

Fig. 2 Portions of the measured time series $v_p(t)/V$ for typical experiments at $\theta = 90°$: (a) $L = 45$ cm, $V = 1$ m s^{-1}, regular stick-slip; (b) $L = 69$ cm, $V = 3.25$ m s^{-1}, bistable peeling. (c) Statistical average $\Delta v_p/V$ of the amplitude of fracture velocity fluctuations $\delta v_p(t)/V$ as a function of V for $\theta = 90°$ and various peeled tape lengths L (♦: $L = 25$ cm; ▲: $L = 34$ cm; ⋆: $L = 45$ cm; ▼: $L = 54$ cm; ►: $L = 69$ cm; ✳: $L = 81$ cm; ■: $L = 100$ cm; ●: $L = 134$ cm). The standard deviation of $\delta v_p(t)/V$ over all velocity fluctuations in one experiment is typically of the order of the symbol size.

instability is observed, consisting in high frequency alternation between slow and fast phases of peeling. When the peeling is unstable, we typically observe from a few dozen (for $\theta = 30°$) to a few hundred (for large θ) stick-slip cycles during the complete stationary regime of peeling in one experiment. Over this statistical ensemble of stick-slip oscillations in a given experiment, we always observe a very stable period of stick-slip from cycle to cycle, which illustrates that the stick-slip instability has reached a "stationary state".

In the following, we focus on the characterization of the instability velocity amplitude as a function of the peeling control parameters V, θ and L. To do so, we start by defining, from the fracture velocity time series, the instantaneous amplitude of the peeling instability as the velocity contrast, $\delta v_p(t) = \max(v_p(t), t \in [t - T/2, t + T/2]) - \min(v_p(t), t \in [t - T/2, t + T/2])$, between the maximum and minimum values of the fracture velocity $v_p(t)$ over a sliding time interval T of the order of the typical stick-slip cycle duration. Practically, we also compute this quantity when stick-slip instability is not present, in which case δv_p measures the amplitude of the fracture velocity fluctuations due to spatial heterogeneities in adhesion or to the fluctuations of the velocity enforced by the motors.

In Fig. 2(c), we report the average of the amplitude of fracture velocity fluctuations $\Delta v_p/V = \langle \delta v_p(t) \rangle / V$ as a function of the driving velocity V for several experiments performed with a peeling angle $\theta = 90°$ and various peeled tape lengths L. For imposed velocities V below $V_{onset} = 0.135 \pm 0.005$ m s^{-1} and above $V_{disp} = 3.7 \pm 0.04$ m s^{-1}, the peeling dynamics is stable with limited velocity fluctuations $|\Delta v_p/V| < 0.2 \pm 0.01$. For peeling velocities up to $V = 0.45 \pm 0.05$ m s^{-1}, a change in the fracture dynamics occurs with the appearance of intermittencies between phases of a noisy but rather stable peeling and phases of well-developed stick-slip instability (Fig. 2(b)). In this bistable regime, the probability distribution of $\delta v_p(t)$ has two bumps with a minimum around $1.5V$. We analyze separately events with $\delta v_p < 1.5V$ corresponding to noisy stationary peeling and events with $\delta v_p > 1.5V$ corresponding to stick-slip peeling. This data processing leads to two average values Δv_p, in Fig. 2(c) which are characteristic of the coexisting two types of peeling dynamics. For peeling velocities V larger than 0.45 ± 0.05 m s^{-1}, bistability is no longer present and the fully developed stick-slip regime of peeling is the unique stable state of the system. A typical time series of $v_p(t)/V$ in the pure stick-slip regime is provided in Fig. 2(a). For $2.63 \pm 0.13 < V < V_{disp} = 3.7 \pm 0.04$ m s^{-1}, the peeling dynamics is bistable again, and can be characterized by two average values of $\delta v_p/V$ for a given peeling velocity. The bistability of the peeling dynamics at the appearance and disappearance thresholds suggests that the stick-slip instability onsets, as a function of the imposed velocity V, are associated with subcritical bifurcations. This result constitutes very valuable information that excludes theoretical models predicting supercritical bifurcations (at least for the considered adhesive tape).[8]

4 Impact of the peeling angle

We study how the features of the instability reported in Fig. 2 for a peeling angle of $\theta = 90°$ depend on the two control parameters that are the peeled tape length and the peeling angle. In Fig. 2(c), we see that the different instability thresholds and the value of the instability amplitude do not significantly depend on the length of the peeled tape L, at least over the limited range of L investigated here, from 25 to 134 cm. This invariance moreover remains a robust feature when varying θ. In contrast, the instability thresholds depend strongly on the peeling angle as can be seen in Fig. 3 and 4. Fig. 3 presents a state diagram in the (V, θ)-space showing the domains where the peeling is stable,

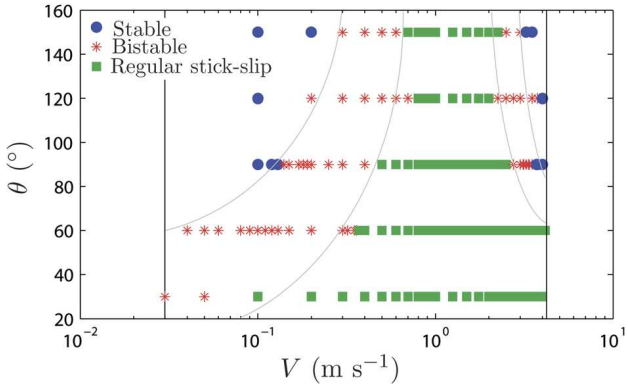

Fig. 3 Diagram of the peeling regime in (V, θ)-space. Each marker corresponds to one experiment. The vertical lines show the experimental limits of our setup. The continuous gray lines are a guide to the eye.

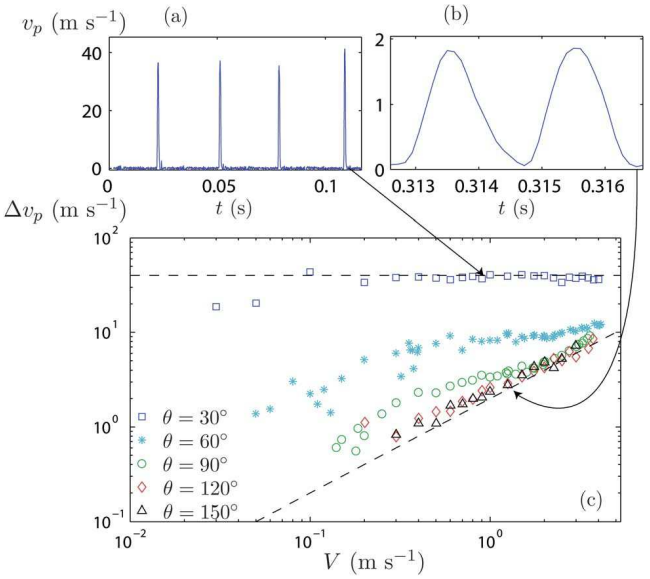

Fig. 4 Short portions of the measured time series of the instantaneous peeling velocity for (a) $V = 0.9$ m s^{-1}, $\theta = 30°$, $L = 0.51$ m and (b) $V = 0.9$ m s^{-1}, $\theta = 150°$, $L = 0.54$ m. (c) Instability amplitude Δv_p as a function of peeling velocity V for different peeling angles θ. Each marker represents data averaged over different peeled tape lengths L. The lower dashed line is $\Delta v_p = 2V$ and the upper one $\Delta v_p = 40$ m s^{-1}.

bistable or fully unstable. We find that the velocity range over which the adhesive peeling is dynamically unstable tends to increase of at least an order of magnitude as the peeling angle decreases. This is observed for the two frontiers between stable and bistable, as well as between bistable and stick-slip regimes. For $\theta \leq 60°$, the limitations of the experimental setup in peeling velocity V did not allow us to reach neither the low velocity stable domain, nor the high velocity bistable and stable domains. For θ increasing above 120°, the velocity thresholds seem to saturate to constant values. It is important to highlight here that, to the best of our knowledge, only Aubrey *et al.*[6] had previously reported evidence for the dependence of the instability with the peeling angle thanks to the observation of the disappearance of the instability when θ is increased at a specific imposed velocity. They however did not perform a systematic study of the instability as a function of the control parameters and the peeled tape length varied during a tensile test. The marked dependence of the stick-slip instability with the peeling angle that we report here is consequently an important feature that has however not been considered by current theories of adhesive peeling instability. This point is discussed in more detail in the final paragraphs of the paper.

Fig. 4 shows the dependance of the velocity amplitude Δv_p of the dynamical instability with peeling angle θ and driving velocity V. Each data point corresponds here to an average of $\delta v_p(t)$ over experiments for which the peeling is fully unstable or on time intervals over which stick-slip is observed for bistable experiments. Taking advantage of the fact that the instability amplitude $\Delta v_p(V, \theta, L)$ does not depend significantly on the peeled tape length L, data for a fixed velocity V and peeling angle θ are averaged over L. For a given peeling velocity V, the instability amplitude decreases with the peeling angle θ, initially rapidly for small angles but more slowly as θ increases. The instability amplitude finally seems to saturate to a low limit value for $\theta \geq 120°$. The dependance of the instability amplitude Δv_p with the peeling velocity V actually changes drastically with θ. For $\theta = 30°$, the instability amplitude is nearly constant with the peeling velocity V whereas, as θ increases up to 150°, $\Delta v_p(V)$ tends towards linearity with V. The strong difference in behavior between the stick-slip velocity amplitude at a small and large peeling angle is an intriguing result.

5 Discussion

5.1 Effect of peeling angle on the instability thresholds

To get some insight into the reported effects of peeling angle on the stick-slip instability, we start from the dynamical equations derived originally by Barquins *et al.*[7] Under stationary peeling conditions, the adhesive peeling dynamics is described by the balance equation $G = \Gamma(v_p)$ between the fracture energy $\Gamma(v_p)$, which accounts for the energy dissipated near the fracture front, and the strain energy release rate G which corresponds to the release of mechanical energy, both per unit surface of fracture growth. The strain energy release rate is[25]

$$G = \frac{F}{b}(1 - \cos\theta) + \frac{F^2}{2b^2eE} \simeq \frac{F}{b}(1 - \cos\theta), \quad (1)$$

where F is the force transmitted to the fracture along the tape, b is the tape width, e its thickness and E its Young modulus. Neglecting the second term in eqn (1), corresponding to the elastic energy stored in the tape, is a very good approximation for most adhesive tapes and peeling geometries. In our case, this term goes from 2 to 3 orders of magnitude smaller than the first term when θ increases from 30° to 150°.

In order to estimate the force F in the peeled tape, we need to generalize for any peeling angle the relationship between the tape elongation u and the peeling velocity v_p which was originally expressed as $du/dt = V - v_p$ in ref. 7 but, as we show below, is valid for $\theta = 90°$ only. To demonstrate this, we introduce the following notations (see Fig. 1): M is the location of the point where the winding of the peeled tape proceeds, $P(t)$ is the location of the peeling point as a function of time t and P_0 its average location during a stick-slip cycle (for stationary peeling, $P(t) = P_0$). In the reference frame of the laboratory, the peeling location $P(t)$ tends to move at a velocity V due to the translation motion of the substrate and moves in the opposite direction due to the peeling front propagation, such that

$$\overline{P_0P}(t) = \ell_p(t) - Vt. \quad (2)$$

The distance between the winding and peeling points can be written as

$$\begin{aligned} |\mathbf{MP}|(t) &= \sqrt{(\mathbf{MP}_0 + \mathbf{P}_0\mathbf{P}(t))^2}, \\ &\simeq |\mathbf{MP}_0| + \overline{P_0P}\cos\theta_0, \end{aligned} \quad (3)$$

where θ_0 corresponds to the peeling angle when the peeling front is at location P_0. The approximation made in eqn (3) is

valid to a precision better than 0.4‰ in our experiments since in practice we always observe that $|\overline{P_0P}| < 4\times10^{-2}|\mathbf{MP}_0|$. The distance $|\mathbf{MP}|(t)$ can also be related to the elongation $u(t)$ through the equation

$$|\mathbf{MP}|(t) = \mathscr{L}(t) + u(t), \tag{4}$$

where $\mathscr{L}(t)$ is the unstretched peeled tape length. $\mathscr{L}(t)$ is not a constant and varies according to the rate of tape creation at the peeling front and the rate of tape disappearance at the winding point

$$\mathscr{L}(t) = \mathscr{L}_0 + \int_0^t \left(v_p(\tau) - R\omega \frac{\mathscr{L}(\tau)}{|\mathbf{MP}|(\tau)} \right) \mathrm{d}\tau. \tag{5}$$

Here, the tape on the substrate is assumed to have been applied in an unstretched state while the tape wound on the cylinder is stretched. As already discussed in Section 2, in our experiments, the deviation of the stretch ratio from 1, *i.e.* $|\mathbf{MP}|/\mathscr{L}$, ranges typically from 0.1% to 1.5% and the winding roller radius $R(t)$ slowly increases during the peeling. Practically, the velocity of the winding ω in the stationary stage is set to a constant value such that $\omega R(t)\frac{\mathscr{L}(t)}{|\mathbf{MP}|(t)}$ matches V to a precision always better than 1.5% at the worst moments (of the less favorable experiments): the match is most of the time much better. We can therefore safely approximate (5) by

$$\mathscr{L}(t) \simeq \mathscr{L}_0 + \int_0^t \left(v_p(\tau) - V\right)\mathrm{d}\tau = \mathscr{L}_0 + \ell_p(t) - Vt. \tag{6}$$

This approximation actually amounts to neglecting the drift during a stick-slip cycle of the peeling point position $\ell_p(t) - Vt$ in the laboratory frame due to the mismatch between $\omega R(t)\frac{\mathscr{L}(t)}{|\mathbf{MP}|(t)}$ and V with respect to its stick-slip oscillation amplitude: this approximation is truly relevant since the former is never larger than 2% of the latter in our experiments.

From eqn (2)–(6), we obtain the following kinematical constraint for the peeled tape elongation

$$u = u_0 + (Vt - \ell_p)(1 - \cos\theta_0), \tag{7}$$

where $u_0 = |\mathbf{MP}_0| - \mathscr{L}_0$ is the mean elongation during the peeling. In our geometry, the extension of Barquins *et al.*'s equation[7] for any peeling angle is thus

$$\frac{\mathrm{d}u}{\mathrm{d}t} = \left(V - v_p\right)(1 - \cos\theta_0). \tag{8}$$

If we assume a uniform tensile stress in the ribbon, we can further write

$$F = \frac{Ebe}{\mathscr{L}}u \simeq \frac{Ebe}{L}u, \tag{9}$$

(the approximation $\mathscr{L} \simeq L = |\mathbf{MP}_0|$ being valid to a precision better than 1% and generally much better). From eqn (1), we finally deduce the energy release rate

$$G \simeq \frac{Ee}{L}(1 - \cos\theta(t))\left[u_0 + \left(Vt - \ell_p\right)(1 - \cos\theta_0)\right], \tag{10}$$

where $\theta(t)$ corresponds to the peeling angle at location $P(t)$.

In our geometry (see Fig. 1), we have

$$\cos\theta(t) = \frac{|\mathbf{MP}_0|\cos\theta_0 + \overline{P_0P}}{\sqrt{|\mathbf{MP}_0|^2 + |\mathbf{P}_0\mathbf{P}|^2 + 2\mathbf{MP}_0\cdot\mathbf{P}_0\mathbf{P}}}. \tag{11}$$

Since $|\overline{P_0P}| < 4\times10^{-2}|\mathbf{MP}_0|$, we can develop (11) to the first order in $\overline{P_0P}/|\mathbf{MP}_0| = (\ell_p - Vt)/L$ which leads to

$$\cos\theta(t) \simeq \cos\theta_0 + \frac{\ell_p - Vt}{L}\left(1 - \cos^2\theta_0\right). \tag{12}$$

Finally injecting (12) into (10) and noting that $u_0/L = \Gamma(V)/Ee(1 - \cos\theta_0)$ is typically of order of 10^{-3} for the studied adhesive tape† and therefore smaller than $|\ell_p - Vt|/L$, the energy release rate can be written to first order in $(\ell_p - Vt)/L$

$$G = \frac{Ee}{L}(1 - \cos\theta_0)\left[u_0 + \left(Vt - \ell_p\right)(1 - \cos\theta_0)\right]. \tag{13}$$

Its time derivative finally verifies

$$\frac{\mathrm{d}G}{\mathrm{d}t} = \frac{k_{\mathrm{eff}}}{b}\left(V - v_p\right). \tag{14}$$

where $k_{\mathrm{eff}} = (1 - \cos\theta_0)^2\, Ebe/L$ is an effective stiffness. We stress here that one of the factors $(1 - \cos\theta_0)$ comes from the geometry dependence of the energy release rate, while the other one arises from the unstable peeling dynamics.

Finally, assuming that the quasistatic relationship $G = \Gamma$ still holds instantaneously when peeling is not stationary, we obtain the following dynamical equation

$$\left.\frac{\mathrm{d}\Gamma}{\mathrm{d}v_p}\right|_{v_p}\frac{\mathrm{d}v_p}{\mathrm{d}t} = \frac{k_{\mathrm{eff}}}{b}\left(V - v_p\right). \tag{15}$$

The stationary solution $v_p(t) = V$ of eqn (15) becomes unstable as soon as the fracture energy $\Gamma(v_p)$ becomes a decreasing function. According to this simple approach, the instability onset should be the velocity V_a at the end of the "slow" increasing branch of $\Gamma(v_p)$ where it reaches a local maximum (see Fig. 2 in ref. 24 representing $\Gamma(V)$ for the Scotch® 600 adhesive tapes). Therefore, one may ask if the effect of peeling angle on the stick-slip instability onset and amplitude could be related to a peeling angle dependance of the velocity $V_a(\theta)$ and more generally of the fracture energy $\Gamma(v_p, \theta)$. This dependance should however be strong enough to explain the reported change of an order of magnitude in the instability velocity range over the studied range of the peeling angle. To the best of our knowledge, there is no indication from the literature for such strong angle dependence of the fracture energy. It has actually received only a few experimental validations, which tend to rule out such peeling angle dependence.[25–27] The only evidence for an angular dependance of Γ has been reported by Kaelble,[28] who related it to a transition from cleavage to

† The fracture energy for Scotch® 600 adhesive tapes is typically of the order of or less than 100 J m^{-2}.[12]

shearing loading of the adhesive at very small peeling velocities, and by Gent & Hamed,[29] who related it to the appearance of plastic deformations of the tape backing at a large peeling angle. All these studies however involved adhesives which are significantly different from ours. It would therefore be valuable to measure systematically the fracture energy dependence with the peeling velocity and angle for the adhesive tape considered here.

In contrast, previous experimental observations of the stick-slip instability of peeling[30] have shown that increasing the stiffness of the loading system when peeling at 90° leads to a reduction of the stick-slip unstable domain and may even suppress it entirely. A similar effect is known in the case of frictional stick-slip instability.[31] From that perspective, the reduction in the stick-slip velocity range with increasing peeling angle could be due to an increase in effective stiffness k_{eff}. Indeed, a strong increase of k_{eff} by a factor of 200 is obtained when increasing the peeling angle from $\theta = 30°$ to 150°. Likewise, the lack of detectable effect of the peeled length on the unstable velocity range could simply be due to the corresponding weak variation in effective stiffness, limited to a factor of 5 in our experiments. From a theoretical point of view, the physical origin of the reduction of the unstable velocity range when the elastic stiffness of the loading becomes large is still unclear in the case of adhesive tape peeling.

5.2 Effect of the peeling angle on the instability limit cycles: an inertial effect?

In addition to the instability thresholds, it is also fundamental to carefully consider how the instability velocity fluctuations, once developed, are strongly dependent on the peeling angle.

For a small angle, the stick-slip amplitude Δv_{p} is nearly constant around the value 40 m s^{-1}. These experiments actually correspond to the archetypal stick-slip relaxation dynamics, with the peeling being alternatively very slow during long stick phases and very fast during very short slip phases as illustrated in Fig. 4(a). Barquins and Maugis[7,8] proposed that in this regime the stick-slip dynamics is such that the peeling explores quasistatically the "slow" stable velocity branch of $\Gamma(v_{\mathrm{p}})$ during the stick phase, *i.e.* $G(t) = \Gamma(v_{\mathrm{p}}(t))$, in alternance with infinitely short dynamical slip phases approaching the fast stable branch of $\Gamma(v_{\mathrm{p}})$ (see Fig. 2 in ref. 24 representing $\Gamma(V)$). This theoretical framework leads to quantitative prediction of the stick period which has received several experimental validations.[7,8,24] It predicts in particular that the stick-slip oscillation period decreases almost as $1/V$ which we have checked to be valid for the data presented here for $\theta = 30°$. In the framework of this relaxation stick-slip dynamics, one would also expect very large values of Δv_{p}, independent of the average peeling velocity, exactly as observed in our experiments at $\theta = 30°$.

For large angles, in contrast, Δv_{p} becomes dependant on the peeling velocity, converging towards $\Delta v_{\mathrm{p}} = 2V$ (Fig. 4(c)), and the time evolution of v_{p} during a stick-slip cycle consists in nearly sinusoidal oscillations around V (Fig. 4(b)). This behavior occurs at large effective stiffness $k_{\mathrm{eff}} \propto (1 - \cos\theta)^2$ which, according to eqn (15), imposes a smaller and smaller quasistatic time scale for the velocity dynamics as θ increases. Whereas the quasistatic time scale gets smaller, some inertial effects may eventually become important: they could be associated with the propagation of elongation waves in the backing tape or to the changes in the tape bending close to the peeling fracture front. Before building a complete description of the interaction between the crack growth criterion at the peeling fracture front and the dynamics of the elastic deformations of the backing tape, one may try to take into account empirically the effective influence of these inertial effects on the quasistatic balance equation $G = \Gamma(v_{\mathrm{p}})$ by replacing it with a dynamical equation

$$\mu\ddot{x} = G - \Gamma(\dot{x}), \tag{16}$$

where x is the position of the peeling front, so that $v_{\mathrm{p}} = \dot{x}$, and μ represents a yet unknown effective inertial mass per unit length. Eqn. (16) was originally proposed by Webb and Aifantis[32] in order to describe oscillatory crack propagation in polymeric materials.

A stationary solution of eqn (16) is $x_{\mathrm{s}} = Vt$ and $\dot{x}_{\mathrm{s}} = V$. Introducing the fluctuations around the stationary solution $\delta x = x - x_{\mathrm{s}}$ (hence, $\delta\dot{x} = \dot{x} - V$), eqn (16) becomes

$$\mu\delta\ddot{x} + \frac{k_{\mathrm{eff}}}{b}\delta x = \Gamma(V) - \Gamma(\dot{x}). \tag{17}$$

The left hand side of this equation corresponds to a harmonic oscillator with angular frequency $\omega = \sqrt{k_{\mathrm{eff}}/b\mu}$. As can be seen in Fig. 4(b), the experimental motion of the peeling front when the peeling angle is large is not very far from a sinusoidal oscillation. The corresponding experimental period of oscillations T_{ss} can be used to get an estimate of the effective mass per unit length μ. For $\theta = 150°$ and $V = 0.9$ m s^{-1}, we have for example $T_{\mathrm{ss}} = 2.2 \pm 0.4$ ms and $k_{\mathrm{eff}} = 5.9 \times 10^3$ N m^{-1}, so that we would predict $\mu \simeq 0.038 \pm 0.013$ kg m^{-1}. This value is close to the mass of the peeled tape per unit width of the peeling front: $\alpha = 0.024$ kg m^{-1}.

Furthermore, for the same experiment, we have measured stick-slip amplitudes of about 2 mm. Taking therefore $\delta x = 1$ mm, we find that $\frac{k_{\mathrm{eff}}}{b}\delta x \simeq \pm 309$ J m^{-2}, hence an amplitude of about 600 J m^{-2}. In the ideal stick-slip cycle described by Barquins *et al.*, the variation of fracture energy corresponds to the two extreme values of the decreasing branch of $\Gamma(V)$. It was measured to be at most 100 J m^{-2} when peeling at 90° from a roller for the Scotch® 600 adhesive tapes.[24] Provided the order of magnitude of Γ does not depend strongly on θ, we can thus expect that fluctuations of the elastic energy release rate are about 6 times larger than the fluctuations of fracture energy during a stick-slip cycle. This observation confirms that a strong discrepancy between G and $\Gamma(\dot{x})$ may appear and shall be accounted for by a new physical term in the equations. If we do assume that $\Gamma(\dot{x}) - \Gamma(V)$ can consequently be neglected at large peeling angle and that $\dot{x} = 0$ when $u = 0$, which is the case when the peeled tape has not been loaded yet, we obtain the following asymptotic solution of eqn (17)

$$x = Vt - \frac{V}{\omega}\sin(\omega t),$$
$$\dot{x} = V(1 - \cos(\omega t)). \quad (18)$$

This asymptotic solution is consistent with the experimental velocity oscillation observed at a large angle (Fig. 4(b)). It moreover predicts exactly $\Delta v_p = 2V$ for the instability amplitude which is the experimentally observed asymptotic limit.

This analysis shows that, at a large peeling angle, when the effective stiffness of the peeled tape is large, the fracture energy seems to be eventually not important in the determination of the fracture velocity limit cycles, although it surely remains important to make the peeling unstable, *i.e.* to trigger the instability. For smaller peeling angles, we expect the unstable peeling dynamics to be due to a combination of inertial effects, geometry-dependent stiffness and fracture energy decreasing with fracture velocity. The fact that geometry has a determinant role on the dynamical instability of adhesive peeling, which is stronger than expected from the simple geometry dependence of the energy release rate, is intrinsically connected to the action of an effective inertial mass of the crack whose physical origin is still to be uncovered.

Acknowledgements

We thank A. Aubertin, L. Auffray, C. Borget and R. Pidoux for their help in the conception of the experiment, M. Ciccotti, C. Creton, and J.-P. Hulin for fruitful scientific discussions and F. Moisy, P. Holdsworth and T. Dauxois for a careful reading of the manuscript. This work has been supported by the French ANR through Grant "StickSlip" no. 12-BS09-014. The peeling experiments were funded by the University Paris-Sud.

References

1 L. B. Freund, *Dynamic fracture mechanics*, Cambridge University Press, London, 1990.
2 B. Lawn, *Fracture of brittle solids*, Cambridge University Press, 1995.
3 J. Fineberg and M. Marder, *Phys. Rep.*, 1999, **313**(1–2), 1.
4 K. Tsunoda, J. J. C. Busfield, C. K. L. Davies and A. G. Thomas, *J. Mater. Sci.*, 2000, **35**(20), 5187.
5 J. L. Gardon, *J. Appl. Polym. Sci.*, 1963, **7**, 625–641.
6 D. W. Aubrey, G. N. Welding and T. Wong, *J. Appl. Polym. Sci.*, 1969, **13**, 2193–2207.
7 M. Barquins, B. Khandani and D. Maugis, *C. R. Acad. Sci., Ser. II: Mec., Phys., Chim., Sci. Terre Univers*, 1986, **303**, 1517–1519.
8 D. Maugis and M. Barquins, *Adhesion 12*, ed. K. W. Allen, Elsevier ASP, London, 1988, pp. 205–222.
9 A. N. Gent and R. P. Petrich, *Proc. R. Soc. London, Ser. A*, 1969, **310**, 433–448.
10 D. W. Aubrey and M. Sherriff, *J. Polym. Sci.*, 1980, **18**, 2597–2606.
11 C. Derail, A. Allal, G. Marin and P. Tordjeman, *J. Adhes.*, 1997, **61**, 123–157; C. Derail, A. Allal, G. Marin and P. Tordjeman, *J. Adhes.*, 1998, **68**, 203–228.
12 M. Barquins and M. Ciccotti, *Int. J. Adhes. Adhes.*, 1997, **17**, 65–68.
13 D. Maugis, *J. Mater. Sci.*, 1985, **20**, 3041–3073.
14 P.-G. de Gennes, *Langmuir*, 1996, **12**, 4497–4500.
15 A. N. Gent, *Langmuir*, 1996, **12**, 4492–4496.
16 E. Barthel and C. Fretigny, *J. Phys. D: Appl. Phys.*, 2009, **42**, 19.
17 H. Tabuteau, S. Mora, M. Ciccotti, C.-Y. Hui and C. Ligoure, *Soft Matter*, 2011, **7**, 9474–9483.
18 R. De and G. Ananthakrishna, *Phys. Rev. E: Stat., Nonlinear, Soft Matter Phys.*, 2004, **70**, 046223.
19 M. Ciccotti, B. Giorgini and M. Barquins, *Int. J. Adhes. Adhes.*, 1998, **18**, 35.
20 R. De and G. Ananthakrishna, *Phys. Rev. Lett.*, 2006, **97**, 165503.
21 M. Ciccotti, B. Giorgini, D. Vallet and M. Barquins, *Int. J. Adhes. Adhes.*, 2004, **24**, 143–151.
22 P.-P. Cortet, M. Ciccotti and L. Vanel, *J. Stat. Mech.: Theory Exp.*, 2007, P03005.
23 P.-P. Cortet, M.-J. Dalbe, C. Guerra, C. Cohen, M. Ciccotti, S. Santucci and L. Vanel, *Phys. Rev. E: Stat., Nonlinear, Soft Matter Phys.*, 2013, **87**, 022601.
24 M.-J. Dalbe, S. Santucci, P.-P. Cortet and L. Vanel, *Soft Matter*, 2014, **10**, 132.
25 K. Kendall, *J. Phys. D: Appl. Phys.*, 1975, **8**, 1449–1452.
26 D. H. Kaelble, *Trans. Soc. Rheol.*, 1959, **3**, 161.
27 D. Maugis and M. Barquins, *J. Phys. D: Appl. Phys.*, 1978, **11**, 1989.
28 D. H. Kaelble, *Trans. Soc. Rheol.*, 1960, **4**, 45.
29 A. N. Gent and G. R. Hamed, *J. Appl. Polym. Sci.*, 1977, **21**, 2817.
30 Y. Yamazaki and A. Toda, *Physica D*, 2006, **214**, 120–131.
31 T. Baumberger and C. Caroli, *Adv. Phys.*, 2006, **55**(3), 279.
32 T. Webb and E. Aifantis, *Int. J. Solids Struct.*, 1995, **32**, 2725–2743.

Bibliographie

[1] H. Greenspan, *The theory of rotating fluids* (Cambridge University Press, Cambridge, 1968).

[2] J. Lighthill, *Waves in fluids* (Cambridge University Press, Cambridge, 1978).

[3] J. Pedlosky, *Geophysical Fluid Dynamics* (Springer-Verlag, Heidelberg, 1987).

[4] L.M. Smith, F. Waleffe, "Transfer of energy to two-dimensional large scales in forced, rotating three-dimensional turbulence," Phys. Fluids **11**, 1608 (1999).

[5] C. Cambon, "Turbulence and vortex structures in rotating and stratified flows," Eur. J. Mech. B : Fluids **20**, 489 (2001).

[6] P. Sagaut, C. Cambon, *Homogeneous turbulence Dynamics* (Cambridge University Press, Cambridge, 2008).

[7] G. Veronis, "The analogy between rotating and stratified fluids," Ann. Rev. Fluid Mech. **2**, 37 (1970).

[8] S.T. Suess, "Viscous flow in a deformable rotating container," J. Fluid Mech. **45**, 189 (1971).

[9] C. Morize, M. Le Bars, P. Le Gal, A. Tilgner, "Experimental Determination of Zonal Winds Driven by Tides," Phys. Rev. Lett. **104**, 214501 (2010).

[10] F.H. Busse, "Steady fluid flow in a precessing spheroidal shell," J. Fluid Mech. **33**, 739 (1968).

[11] K.D. Aldridge, A. Toomre, "Axisymmetric inertial oscillations of a fluid in a rotating spherical container," J. Fluid Mech. **37**, 307 (1969).

[12] P. Melchior, B. Ducarme, "Detection of inertial gravity oscillations in the Earth's core with a superconducting gravimeter," Phys. Earth Planet. Inter. **42**, 129 (1986).

[13] K.D. Aldridge, L.I. Lumb, "Inertial waves identified in the Earth's fluid outer core," Nature **325**, 421 (1987).

[14] W. Munk, C. Wunsch, "Abyssal recipes ii : energetics of tidal and wind mixing," Deep Sea Res. Part I : Ocean. Res. Papers **45**, 1977 (1998).

[15] F.P. Bretherton, "On the mean motion induced by internal gravity waves," J. Fluid Mech. **36**, 785 (1969).

[16] A. Tilgner, "Zonal Wind driven by Inertial Modes," Phys. Rev. Lett. **99**, 194501 (2007).

[17] M.H. Alford, R. Pinkel, "Observations of overturning in the thermocline : The context of ocean mixing," J. Phys. Ocean. **30**, 805 (2000).

[18] O.M. Phillips, "Energy transfer in rotating fluids by reflection of inertial waves," Phys. Fluids **6**, 513 (1963).

[19] D.E. Mowbray, B.S.H. Rarity, "A theoretical and experimental investigation of the phase configuration of internal waves of small amplitude in a density stratified liquid," J. Fluid Mech. **28**, 1 (1967).

[20] B.R. Sutherland, S.B. Dalziel, G.O. Hughes, P.F. Linden, "Visualization and measurement of internal waves by 'synthetic Schlieren'. Part 1. Vertically oscillating cylinder," J. Fluid Mech. **390**, 93 (1999).

[21] M.R. Flynn, K. Onu, B.R. Sutherland, "Internal wave excitation by a vertically oscillating sphere," J. Fluid Mech. **494**, 65 (2003).

[22] N.H. Thomas, T.N. Stevenson, "A similarity solution for viscous internal waves," J. Fluid Mech. **54**, 495 (1972).

[23] B. Voisin, "Limit states of internal wave beams," J. Fluid Mech. **496**, 243 (2003).

[24] Cited in [1] : H. Görtler, "On forced oscillation in rotating fluids," 5th Midwestern Conf. on Fluid Mech. **3**, 192 (1957).

[25] L. Messio, C. Morize, M. Rabaud, F. Moisy, "Experimental observation using particle image velocimetry of inertial waves in a rotating fluid," Exp. Fluids **44**, 519 (2008).

[26] A.D. Mc Ewan, "Inertial oscillations in a rotating fluid cylinder," J. Fluid Mech. **40**, 603 (1970).

[27] A.A.M. Manders, L.R.M. Maas, "Observations of inertial waves in a rectangular basin with one sloping boundary," J. Fluid Mech. **493**, 59 (2003).

[28] K.K. Zhang, X.H. Liao, P. Earnshaw, "On inertial waves and oscillations in a rapidly rotating spheroid," J. Fluid Mech. **504**, 1 (2004).

[29] M. Rieutord, "Linear theory of rotating fluids using spherical harmonics. II. Time-periodic flows," Geophys. Astrophys. Fluid Dyn. **59**, 185 (1991).

[30] A. Tilgner, "Driven inertial oscillations in spherical shells," Phys. Rev. E **59**, 1789 (1999).

[31] J. Noir, F. Hemmerlin, J. Wicht, S. Baca, J. Aurnou, "An experimental and numerical study of librationally driven flow in planetary cores and subsurface oceans," Phys. Earth Planet. Inter. **173**, 141 (2009).

[32] M. A. Calkins, J. Noir, J.D. Eldredge, J.M. Aurnou, "Axisymmetric simulations of libration-driven fluid dynamics in a spherical shell geometry," Phys. Fluids **22**, 086602 (2010).

[33] R.R. Kerswell, "On the internal shear layers spawned by the critical regions in oscillatory Ekman boundary layers," J. Fluid Mech. **298**, 311 (1995).

[34] J. Noir, D. Jault, P. Cardin, "Numerical study of the motions within a slowly precessing sphere at low Ekman number," J. Fluid Mech. **437**, 283 (2001).

[35] W.V.R. Malkus, "Precesion of earth as cause of geomagnetism," Science **160**, 259 (1968).

[36] A. Sauret, D. Cébron, M. Le Bars, S. Le Dizès, "Fluid flows in a librating cylinder," Phys. Fluids **24**, 026603 (2012).

[37] A. Sauret, D. Cébron, C. Morize, M. Le Bars, "Experimental and numerical study of mean zonal flows generated by librations of a rotating spherical cavity," J. Fluid Mech. **662**, 260 (2010).

[38] F.H. Busse, "Mean zonal flows generated by librations of a rotating spherical cavity," J. Fluid Mech. **650**, 505 (2010).

[39] G.K. Batchelor, *An introduction to Fluid Dynamics* (Cambridge University Press, Cambridge, 1967).

[40] L.R.M. Maas, "On the amphidromic structure of inertial waves in rectangular parallelepiped," Fluid Dyn. Res. **33**, 373 (2003).

[41] H. Bondi, R.A. Lyttleton, "On the dynamic theory of the rotation of the Earth : the effect of precession on the motion of the liquid core," Proc. Camb. Phil. Soc. **49**, 498 (1953).

[42] J. Noir, P. Cardin, D. Jault, J.-P. Masson, "Experimental evidence of nonlinear resonance effects between retrograde precession and the tilt-over mode within a spheroid," Geophys. J. Int. **154**, 407 (2003).

[43] D. Cébron, M. Le Bars, P. Meunier, "Tilt-over mode in a precessing triaxial ellipsoid," Phys. Fluids **22**, 116601 (2010).

[44] S. Kida, "Steady flow in a rapidly rotating sphere with weak precession," J. Fluid Mech. **680**, 150 (2011).

[45] M.H. Poincaré, "Sur la précession des corps déformables," Bull. Astron. **27**, 321(1910).

[46] M. Greff-Lefftz, H. Legros, "Core rotational dynamics and geological events," Science **286**, 1707 (1999).

[47] R.R. Kerswell, "Upper bounds on the energy dissipation in turbulent precession," J. Fluid Mech. **321**, 335 (1996).

[48] A. Tilgner, "Precession driven dynamos," Phys. Fluids **17**, 034104 (2005).

[49] J.P. Vanyo, J.R. Dunn, "Core precession : flow structures and energy," Geophys. J. Int. **142**, 409 (2000).

[50] S.A. Triana, D.S. Zimmerman, D.P. Lathrop, "Precessional states in a laboratory model of the Earth's core," J. Geophys. Res. **117**, B04103 (2012).

[51] J.P. Vanyo, "A geodynamo powered by luni-solar precession," Geophys. Astrophys. Fluid Dyn. **59**, 209 (1991).

[52] J. Vanyo, P. Wilde, P. Cardin, P. Olson, "Experiments on precessing flows in the Earth's liquid core," Geophys. J. Int. **121**, 136 (1995).

[53] P.M. Goldreich, J.L. Mitchell, "Elastic ice shells of synchronous moons : Implications for cracks on Europa and non-synchronous rotation of Titan," Icarus **209**, 631 (2010).

[54] R.R. Kerswell, "Elliptical instability," Ann. Rev. Fluid Mech. **34**, 83 (2002).

[55] K. Aldridge, B. Seyed-Mahmoud, G. Henderson, W. van Wijngaarden, "Elliptical instability of the Earth's fluid core," Phys. Earth Planet. Inter. **103**, 365 (1997).

[56] R.R. Kerswell, W.V.R. Malkus, "Tidal instability as the source for Io's magnetic signature," Geophys. Res. Lett. **25**, 603 (1998).

[57] L. Lacaze, P. Le Gal, S. Le Dizès, "Elliptical instability in a rotating spheroid," J. Fluid Mech. **505**, 1 (2004).

[58] M. Le Bars, S. Le Dizès, P. Le Gal, "Coriolis effects on the elliptical instability in cylindrical and spherical rotating containers," J. Fluid Mech. **585**, 323 (2007).

[59] D. Cébron, M. Le Bars, J. Noir, J.M. Aurnou, "Libration driven elliptical instability,". Phys. Fluids **24**, 061703 (2012).

[60] J. Noir, D. Cébron, "Precession driven flows in non-axisymmetric ellipsoids," J. Fluid Mech. **737**, 412 (2013).

[61] D. Cébron, S. Vantieghem, W. Herreman, "Libration driven multipolar instability," J. Fluid Mech. **739**, 502 (2014).

[62] S. Goto, N. Ishii, S. Kida, M. Nishioka, "Turbulence generator using a precessing sphere," Phys. Fluids **19**, 061705 (2007).

[63] S. Goto, M. Fujiwara, M. Yamato, "Turbulence sustained in a precessing sphere and spheroids," Proceedings of 7th International Symposium on Turbulence and Shear Flow Phenomena, (Ottawa, Canada, 2011).

[64] R.R. Kerswell, "The instability of precessing flow," Geophys. Astrophys. Fluid Dyn. **72**, 107 (1993).

[65] S. Lorenzani, A. Tilgner, "Inertial instabilities of fluid flow in precessing spheroidal shells," J. Fluid Mech. **492**, 363 (2003).

[66] S. Lorenzani, A. Tilgner, "Fluid instabilities in precessing spheroidal cavities," J. Fluid Mech. **447**, 111 (2001).

[67] S. Kida, "Instability by weak precession of the flow in a rotating sphere," Procedia IUTAM **7**, 183 (2013).

[68] P.A. Davidson, *Turbulence in rotating, stratified and electrically conducting fluids* (Cambridge University Press, Cambridge, 2013).

[69] L. Jacquin, O. Leuchter, C. Cambon, J. Mathieu, "Homogeneous turbulence in the presence of rotation," J. Fluid Mech. **220**, 1 (1990).

[70] C. Cambon, N.N. Mansour, F.S. Godeferd, "Energy transfer in rotating turbulence," J. Fluid Mech. **337**, 303 (1997).

[71] E.J. Hopfinger, F.K. Browand, Y. Gagne, "Turbulence and waves in a rotating tank," J. Fluid Mech. **125**, 505 (1982).

[72] P. Bartello, O. Métais, M. Lesieur, "Coherent structures in rotating three-dimensional turbulence," J. Fluid Mech. **273**, 1 (1994).

[73] R.A. Wigeland, H.M. Nagib, "Effects of rotation on decay of turbulence," Bull. Am. Phys. Soc. **23**(8), 998 (1978).

[74] C. Morize, F. Moisy, "On the energy decay of rotating turbulence in confined geometry," Phys. Fluids **18**, 065107 (2006).

[75] C. Morize, F. Moisy, M. Rabaud, "Decaying grid-generated turbulence in a rotating tank," Phys. Fluids **17**, 095105 (2005).

[76] C. Cambon, L. Jacquin, "Spectral approach to non-isotropic turbulence subjected to rotation," J. Fluid Mech. **202**, 295 (1989).

[77] C. Lamriben, P.-P. Cortet, F. Moisy, "Direct measurements of anisotropic energy transfers in a rotating turbulence experiment," Phys. Rev. Lett. **107**, 024503 (2011).

[78] P.D. Mininni, D. Rosenberg, A. Pouquet, "Isotropization at small scales of rotating helically driven turbulence," J. Fluid Mech. **699**, 263 (2012).

[79] A. Delache, C. Cambon, F. Godeferd, "Scale by scale anisotropy in freely decaying rotating turbulence," Phys. Fluids **26**, 025104 (2014).

[80] O. Praud, J. Sommeria, A.M. Fincham, "Decaying grid turbulence in a rotating stratified fluid," J. Fluid Mech. **547**, 389 (2006).

[81] L. Bourouiba, P. Bartello, "The intermediate Rossby number range and two-dimensional three-dimensional transfers in rotating decaying homogeneous turbulence," J. Fluid Mech. **587**, 139 (2007).

[82] F. Moisy, C. Morize, M. Rabaud, J. Sommeria, "Decay laws, anisotropy and cyclone-anticyclone asymmetry in decaying rotating turbulence," J. Fluid Mech. **666**, 5 (2011).

[83] J. Proudman, "On the motion of solids in a liquid possessing vorticity," Proc. R. Soc. Lond. A **92**, 408 (1916)

[84] G.I. Taylor, "Motion of solids in fluids when the flow is not irrotational," Proc. R. Soc. Lond. A **93**, 92 (1917).

[85] L. Gostiaux, H. Didelle, S. Mercier, T. Dauxois, "A novel internal waves generator," Exp. Fluids **42**, 123 (2007).

[86] M. Mercier, D. Martinand, M. Mathur, L. Gostiaux, T. Peacock, T. Dauxois, "New wave generation," J. Fluid Mech. **657**, 310 (2010).

[87] D. Benielli, J. Sommeria, "Excitation and breaking of internal gravity waves by parametric instability," J. Fluid Mech. **374**, 117 (1998).

[88] C. Staquet, J. Sommeria, "Internal gravity waves : From instabilities to turbulence," Ann. Rev. Fluid Mech. **34**, 559 (2002).

[89] C.R. Koudella, C. Staquet, "Instability mechanisms of a two-dimensional progressive internal gravity wave," J. Fluid Mech. **548**, 165 (2006).

[90] S. Galtier, "Weak inertial-wave turbulence theory," Phys. Rev. E **68**, 015301 (2003).

[91] C. Cambon, R. Rubinstein, F.S. Godeferd, "Advances in wave turbulence : rapidly rotating flows," New J. Phys. **6**, 73 (2004).

[92] S.V. Nazarenko, A.A. Schekochihin, "Critical balance in magnetohydronamic, rotating and stratified turbulence : towards a universal scaling conjecture," J. Fluid Mech. **677**, 134 (2011).

[93] S. Nazarenko, *Wave Turbulence* (Springer-Verlag, Berlin, 2011).

[94] F. Waleffe, "The nature of triad interactions in homogeneous turbulence," Phys. Fluids A **4**, 350 (1992).

[95] F. Waleffe, "Inertial transfers in the helical decomposition," Phys. Fluids A **5**, 677 (1993).

[96] A. Craya, *Contribution à l'analyse de la turbulence associée à des vitesses moyennes*, (Publications Scientifiques et Techniques, Ministère de l'air, Paris, 1958).

[97] J.R. Herring, "Approach of axisymmetric turbulence to isotropy," Phys. Fluids **17**, 859 (1974).

[98] D. Benney, P. Saffman, "Nonlinear interaction of random wave in a dispersive medium," Proc. R. Soc. Lond. A **289**, 301 (1966).

[99] A. Newell, "Rossby wave packet interactions," J. Fluid Mech. **35**, 255 (1969).

[100] V. Zakharov, V. L'vov, G. Falkovich, *Wave Turbulence* (Springer, Berlin, 1992).

[101] L.S. Smith, Y. Lee, "On near resonances and symmetry breaking in forced rotating flows at moderate Rossby number," J. Fluid Mech. **535**, 111 (2005).

[102] Q. Chen, S. Chen, G. Eyink, D. Holm, "Resonant interactions in rotating homogeneous three-dimensional turbulence," J. Fluid Mech. **542**, 139 (2005).

[103] P. Tabeling, "Two-dimensional turbulence : a physicist approach," Phys. Rep. **362**, 1 (2002).

[104] L. Bourouiba, D.N. Straub, M.L. Waite, "Non-local energy transfers in rotating turbulence at intermediate Rossby number ," J. Fluid Mech. **690**, 129 (2012).

[105] J.F. Scott, "Wave turbulence in a rotating channel," J. Fluid Mech. **741**, 316 (2014).

[106] U. Frisch, *Turbulence - The Legacy of A. N. Kolmogorov* (Cambridge University Press, Cambridge, 1995).

[107] F. Moisy, P. Tabeling, H. Willaime, "Kolmogorov Equation in a Fully Developed Turbulence Experiment," Phys. Rev. Lett. **82**, 3994 (1999).

[108] F.S. Godeferd, "Relating statistics to dynamics in axisymmetric homogeneous turbulence," Physica D **241**, 794 (2012).

[109] A.S. Monin, A.M. Yaglom, *Statistical Fluid Mechanics, vol. 2* (MIT Press, Cambridge, 1975).

[110] A.N. Kolmogorov, Dokl. Akad. Nauk SSSR, "The local structure of turbulence in incompressible viscous fluids at very large Reynolds numbers," **30**(4), 299 (1941) ; "On the degeneration of isotropic turbulence in an incompressible viscous fluids," **31**(6), 538 (1941) ; "Dissipation of energy in isotropic turbulence," **32**(1) 19 (1941).

[111] R. Kraichnan, "Inertial ranges in two-dimensional turbulence," Phys. Fluids **10**, 1417 (1967).

[112] D. Bernard, "Three-point velocity correlation functions in two-dimensional forced turbulence," Phys. Rev. E **60**, 6184 (1999).

[113] E. Lindborg, "Can the atmospheric kinetic energy spectrum be explained by two-dimensional turbulence ?," J. Fluid Mech. **388**, 259 (1999).

[114] U. Frisch, P.L. Sulem, "Numerical-simulation of the inverse cascade in two-dimensional turbulence," Phys. Fluids **27**, 1921 (1984).

[115] J. Sommeria, "Experimental-study of the two-dimensional inverse energy cascade in a square box," J. Fluid Mech. **170**, 139 (1986).

[116] J. Paret, P. Tabeling, "Experimental observation of the two-dimensional inverse energy cascade," Phys. Rev. Lett. **79**, 4162 (1997).

[117] G. Boffetta, A. Celani, M. Vergassola, "Inverse cascade in two-dimensional turbulence : deviations from Gaussianity," Phys. Rev. E **61**, 29 (2000).

[118] A. Babiano, T. Dubos, "On the contribution of coherent vortices to the two-dimensional inverse energy cascade," J. Fluid Mech. **529**, 97 (2005).

[119] G. Boffetta, S. Musacchio, "Evidence for the double cascade scenario in two-dimensional turbulence," Phys. Rev. E **82**, 016307 (2010).

[120] M. Hossain, "Reduction in the dimensionality of turbulence due to a strong rotation," Phys. Fluids **6**, 1077 (1994).

[121] L.M. Smith, J.R. Chasnov, F. Waleffe, "Crossover from Two- to Three-Dimensional Turbulence," Phys. Rev. Lett. **77**, 2467 (1996).

[122] P.K. Yeung, Y. Zhou, "Numerical study of rotating turbulence with external forcing," Phys. Fluids **10**, 2895 (1998).

[123] P.D. Mininni, A. Alexakis, A. Pouquet, "Scale interactions and scaling laws in rotating flows at moderate Rossby numbers and large Reynolds numbers," Phys. Fluids **21**, 015108 (2009).

[124] A. Sen, P.D. Mininni, D. Rosenberg, A. Pouquet, "Anisotropy and nonuniversality in scaling laws of the large-scale energy spectrum in rotating turbulence," Phys. Rev. E **86**, 036319 (2012).

[125] A. Pouquet, A. Sen, D. Rosenberg, P.D. Mininni, J. Baerenzung, "Inverse cascades in turbulence and the case of rotating flows," Phys. Scripta **T155**, 014032 (2013).

[126] E. Deusebio, G. Boffetta, E. Lindborg, S. Musacchio, "Dimensional transition in rotating turbulence," Phys. Rev. E **90**, 023005 (2014).

[127] M. Thiele, W.-C. Muller, "Structure and decay of rotating homogeneous turbulence," J. Fluid Mech. **637**, 425 (2009).

[128] T. Teitelbaum, P.D. Mininni, "The decay of turbulence in rotating flows," Phys. Fluids **23**, 3592325 (2011).

[129] C.N. Baroud, B.B. Plapp, Z.-S. She, H.L. Swinney, "Anomalous Self-Similarity in a Turbulent Rapidly Rotating Fluid," Phys. Rev. Lett. **88**, 114501 (2002).

[130] E. Yarom, Y. Vardi, E. Sharon, "Experimental quantification of inverse energy cascade in deep rotating turbulence," Phys. Fluids **25**, 085105 (2013).

[131] P. Billant, J.-M. Chomaz, "Experimental evidence for a new instability of a vertical columnar vortex pair in a strongly stratified fluid," J. Fluid Mech. **418**, 167 (2000).

[132] P. Augier, P. Billant, M.E. Negretti, J.-M. Chomaz, "Experimental study of stratified turbulence forced with columnar dipoles," Phys. Fluids. **26**, 046603 (2014).

[133] B. Gallet, A. Campagne, P.-P. Cortet, F. Moisy, "Scale-dependent cyclone-anticyclone asymmetry in a forced rotating turbulence experiment," Phys. Fluids **26**, 035108 (2014).

[134] M. Lesieur, J. Herring, "Diffusion of a passive scalar in two-dimensional turbulence," J. Fluid Mech. **161**, 77 (1985).

[135] A.M. Yaglom, "On the local structure of a temperature field in a turbulent flow," Dokl. Akad. Nauk SSSR **69**, 743 (1949).

[136] O. Zeman, "A note on the spectra and decay of rotating homogeneous turbulence," Phys. Fluids **6**, 3221 (1994).

[137] Y. Zhou, "A phenomenological treatment of rotating turbulence," Phys. Fluids **7**, 2092 (1995).

[138] V.M. Canuto, M.S. Dubovikov, "A dynamical model for turbulence. V. The effect of rotation," Phys. Fluids **9**, 2132 (1997).

[139] S. Galtier, "Exact vectorial law for homogeneous rotating turbulence," Phys. Rev. E **80**, 046301 (2009).

[140] O. Chkhetiani, "On the third moments in helical turbulence," JETP Lett. **63**, 808 (1996).

[141] T. Gomez, H. Politano, A. Pouquet, "Exact relationship for third-order structure functions in helical flows," Phys. Rev. E **61**, 5321 (2000).

[142] F. Bellet, F.S. Godeferd, J.F. Scott, C. Cambon, "Wave turbulence in rapidly rotating flows," J. Fluid Mech. **562**, 83 (2006).

[143] K. Yoshimatsu, M. Midorikawa, Y. Kaneda, "Columnar eddy formation in freely decaying homogeneous rotating turbulence," J. Fluid Mech. **677**, 154 (2011).

[144] A. Naso, F.S. Godeferd, "Statistics of the perceived velocity gradient tensor in a rotating turbulent flow," New J. Phys. **14**, 125002 (2012).

[145] G.P. Bewley, D.P. Lathrop, L.R.M. Maas, K.R. Sreenivasan, "Inertial waves in rotating grid turbulence," Phys. Fluids **19**, 071701 (2007).

[146] C. Lamriben, P.-P. Cortet, F. Moisy, L.R.M. Maas, "Excitation of inertial modes in a closed grid turbulence experiment under rotation," Phys. Fluids **23**, 015102 (2011).

[147] C. Cambon, L. Danaila, F.S. Godeferd, J.F. Scott, "Third-order statistics and the dynamics of strongly anisotropic turbulent flows," J. Turb. **14**, 121 (2013).

[148] K.D. Squires, J.R. Chasnov, N.N. Mansour, C. Cambon, "The asymptotic state of rotating turbulence at high Reynolds number," AGARD-CP-551, 4.1 (1994).

[149] P.A. Davidson, "On the decay of Saffman turbulence subject to rotation, stratification or an imposed magnetic field," J. Fluid Mech. **663**, 268 (2010).

[150] L.J.A. van Bokhoven, C. Cambon, L. Liechtenstein, F.S. Godeferd, H.J.H. Clercx, "Refined vorticity statistics of decaying rotating three-dimensional turbulence," J. Turb. **9**, 1 (2008).

[151] P.J. Staplehurst, P.A. Davidson, S.B. Dalziel, "Structure formation in homogeneous freely decaying rotating turbulence," J. Fluid Mech. **598**, 81 (2008).

[152] T. Baumberger, C. Caroli, "Solid friction from stick-slip down to pinning and aging," Adv. Physics **55**, 279 (2006).

[153] L.B. Freund, *Dynamic Fracture Mechanics* (Cambridge University Press, New York, 1990).

[154] A.A. Griffith, "The phenomena of rupture and flow in solids," Phil. Trans. Royal Soc. London **221**, 163 (1920).

[155] G.R. Irwin, "Analysis of stresses and strains near the end of a crack traversing a plate," J. Appl. Mech. **24**, 361 (1957).

[156] G.R. Irwin, *Fracture : Handbuch der physik*, **6**, 557 (Springer-Verlag, Berlin, 1958).

[157] A. Gleizer, D. Sherman, "The cleavage energy at initiation of (110) silicon," Int. J. Fract. **187**, 1 (2014).

[158] K. Han, M. Ciccotti, S. Roux, "Measuring nanoscale stress intensity factors with an atomic force microscope," EPL **89**, 66003 (2010).

[159] F. Célarié, S. Prades, D. Bonamy, L. Ferrero, E. Bouchaud, C. Guillot, C. Marlière, "Glass breaks like metal but at the nanometer scale," Phys. Rev. Lett. **90**, 075504 (2003).

[160] D. Bonamy, S. Prades, L. Ponson, D. Dalmas, C.L. Rountree, E. Bouchaud, C. Guillot, "Experimental investigation of damage and fracture in glassy materials at the nanometer scale," Int. J. Prod. Tech. **26**, 339 (2006).

[161] T. Sarlat, A. Lelarge, E. Søndergård, D. Vandembroucq, "Frozen capillary waves on glass surfaces : an AFM study," Eur. Phys. J. B **54**, 121 (2006).

[162] M. Ciccotti, "Stress-corrosion mechanisms in silicate glasses," J. Phys. D : Appl. Phys. **42**, 214006 (2009).

[163] S.M. Wiederhorn, T. Fett, J.-P. Guin, M. Ciccotti, "Griffith Cracks at the Nanoscale," Int. J. Appl. Glass Sc. **4**, 76 (2013).

[164] B.R. Lawn, *Fracture of brittle solids*, (Cambridge University Press, New-York, 1993).

[165] C. Creton, H.R. Brown, K.R. Shull, "Molecular weight effects in chain pullout," Macromolecules **27**, 3174 (1994).

[166] L. Léger, E. Raphaël, H. Hervet, "Surface-anchored polymer chains : their role in adhesion and friction," Adv. Polym. Sci. **138**, 185 (1998).

[167] K. Kendall, "Thin-film peeling - the elastic term," J. Phys. D : Appl. Phys. **8**, 1449 (1975).

[168] R.S. Rivlin, "The effective work of adhesion," Paint Technol. **9**, 215 (1944).

[169] J.L. Gardon, "Peel Adhesion. 1. Some Phenomenological Aspects of the Test," J. Appl. Polym. Sci. **7**, 625 (1963).

[170] D.H. Kaelble, "Theory and analysis of peel adhesion : rate-temperature dependance of visocelastic interlayers," J. Colloid Sci. **19**, 413 (1964).

[171] A.N. Gent, R.P. Petrich, "Adhesion of viscoelastic materials to rigid substrates," Proc. R. Soc. Lond. A **310**, 433 (1969).

[172] D.W. Aubrey, G.N. Welding, T. Wong, "Failure Mechanisms in Peeling of Pressure-Sensitive Adhesive Tape," J. Appl. Polym. Sci., **13** 2193 (1969).

[173] E.H. Andrews, A.J. Kinloch, "Mechanics of adhesive failure. I," Proc. R. Soc. Lond. A **332** 385 (1973).

[174] D.W. Aubrey, M. Sherriff, "Peel Adhesion and Viscoelasticity of Rubber-Resin Blends," J. Polym. Sci. **18**, 2597 (1980).

[175] A.N. Gent, "Adhesion and Strength of Viscoelastic Solids. Is There a Relationship between Adhesion and Bulk Properties ?," Langmuir **12**, 4492 (1996).

[176] A.N. Gent, S.-M. Lai, "Interfacial bonding, energy dissipation, and adhesion," J. Polym. Sci., Part B, **32**, 1543 (1994).

[177] C. Derail, A. Allal, G. Marin, P. Tordjeman, "Relationship between Viscoelastic and Peeling Properties of Model Adhesives. Part 2. The Interfacial Fracture Domains," J. Adhes. **68**, 203 (1998).

[178] M.L. Williams, R.F. Landel, J.D. Ferry, "The Temperature Dependence of Relaxation Mechanisms in Amorphous Polymers and Other Glass-forming Liquids," J. Am. Chem. Soc. **77**, 3701 (1955).

[179] J.D. Ferry, *Viscoelastic properties of polymers*, (Wiley, New York, 1961).

[180] M. Barquins, B. Khandani, D. Maugis, "Propagation saccadée de fissure dans le pelage d'un solide viscoélastique," C. R. Acad. Sci. série II **303**, 1517 (1986).

[181] D. Maugis, M. Barquins, "Stick-slip and peeling of adhesive tapes," Adhesion **12**, 205 (Elsevier ASP, London, 1988).

[182] D. Maugis, "Subcritical crack growth, surface energy, fracture toughness, stick-slip and embrittlement," J. Mat. Sci. **20**, 3041 (1985).

[183] P.-G. de Gennes, "Soft Adhesives," Langmuir **12**, 4497 (1996).

[184] E. Barthel, C. Fretigny, "Adhesive contact of elastomers : effective adhesion energy and creep function," J. Phys. D : Appl. Phys. **42**, 195302 (2009).

[185] H. Tabuteau, S. Mora, M. Ciccotti, C.-Y. Hui, C. Ligoure, "Propagation of a brittle fracture in a viscoelastic fluid," Soft Matter **7**, 9474 (2011).

[186] J. Fineberg, M. Marder, "Instability in dynamic fracture," Phys. Rep. **313**, 1 (1999).

[187] G. Lazzaroni, R. Bargellini, P.-E. Dumouchel, J.-J. Marigo, "On the role of kinetic energy during unstable propagation in a heterogeneous peeling test," Int. J. Fract. **175**, 127 (2012).

[188] G. Ryschenkow, H. Arribart, "Adhesion Failure in the Stick-Slip Regime : Optical and AFM Characterizations and Mechanical Analysis," J. Adhes. **58**, 143 (1996).

[189] Y. Yamazaki, A. Toda, "Pattern formation and spatiotemporal behavior of adhesive in peeling," Physica D **214**, 120 (2006).

[190] M. Gandur, M. Kleinke, F. Galembeck, "Complex dynamic behavior in adhesive tape peeling," J. Adhes. Sci. Technol. **11**, 11 (1997).

[191] M. Ciccotti, B. Giorgini, D. Vallet, M. Barquins, "Complex dynamics in the peeling of an adhesive tape," Int. J. Adhes. Adhes. **24**, 143 (2004).

[192] P.-P. Cortet, M. Ciccotti, L. Vanel, "Imaging the stick-slip peeling of an adhesive tape under a constant load," J. Stat. Mech. P03005 (2007).

[193] S.T. Thoroddsen, H.D. Nguyen, K. Takehara, T.G. Etoth, "Stick-slip substructure in rapid tape peeling," Phys. Rev. E **82**, 046107 (2010).

[194] M. Barquins, M. Ciccotti, "On the kinetics of peeling of an adhesive tape under a constant imposed load," Int. J. Adhes. Adhes. **17**, 65 (1997).

[195] D. Maugis, M. Barquins, "Fracture mechanics and adherence of viscoelastic bodies," J. Phys. D : Appl. Phys. **11**, 1989 (1978).

[196] D.H. Kaelble, "Theory and analysis of peel adhesion : mechanisms and mechanics," Trans. Soc. Rheol. **3**, 161 (1959).

[197] D.H. Kaelble, "Theory and analysis of peel adhesion : bond stresses and distributions," Trans. Soc. Rheol. **4**, 45 (1960).

[198] A.N. Gent, G.R. Hamed, "Peel mechanics for an elastic-plastic adherend," J. Appl. Pol. Sci. **21**, 2817 (1977).